Lehrstuhl für Elektrische Energiespeichertechnik
Fakultät für Elektrotechnik und Informationstechnik
Technische Universität München

Performance and Safety of Lithium-Ion Electrodes and Cells: Modeling, Simulation, and Validation at Elevated Temperatures and Currents

Dipl.-Ing. Univ. Jan Alexander Gerrit Rheinfeld

Vollständiger Abdruck der von der Fakultät für Elektrotechnik und Informationstechnik der Technischen Universität München zur Erlangung des akademischen Grades eines

Doktor-Ingenieurs (Dr.-Ing.)

genehmigten Dissertation.

Vorsitzender:		Prof. Dr.-Ing. Martin Buss
Prüfer der Dissertation:	1.	Prof. Dr.-Ing. Andreas Jossen
	2.	Prof. Dr. rer. nat. Jürgen Garche

Die Dissertation wurde am 18.06.2019 bei der Technischen Universität München eingereicht und durch die Fakultät für Elektrotechnik und Informationstechnik am 30.07.2019 angenommen.

Abstract

Guaranteeing a high level of safety of lithium-ion batteries is an essential requirement which must be fulfilled at all times. In order to design such intrinsically safe products which also meet the desire for ever increasing energy densities and reduced cost, advanced tools and methods are required. In this thesis, experimental and computational methods are developed and combined on electrode and cell level in order to allow for a thorough evaluation of high performance and safety characteristics of lithium-ion batteries, focusing on a characterization of cell thermal runaway. Means of studying the evolution, initiation, and possible mitigation of cell thermal runaway are presented. Due to the thermal nature of this problem, the focus is laid on the investigation of heat generation and heat dissipation at elevated temperatures and currents. The kinetics of individual exothermic decomposition reactions involving a cell's electrodes and electrolyte are derived by means of a model based data analysis of calorimetric measurements, which describes the evolution of cell thermal runaway at elevated temperatures. Rate capability tests as well as newly developed quasi-isothermal short circuit tests are combined with a physical-chemical model in order to describe the heat generation during high rate operation, resulting in an excessive temperature increase which may initiate cell thermal runaway. Multidimensional multiphysics modeling and simulation as well as experiments are applied to study the heat dissipation capabilities of cells with different formats and sizes at varying cooling strategies, which may mitigate or suppress cell thermal runaway during short circuit events. By combining the presented experimental and simulation-based approaches, a lithium-ion battery's performance and safety characteristics can be most thoroughly evaluated on the electrode and cell level enabling a comprehensive design of lithium-ion batteries for a given application.

Kurzfassung

Eine Grundvoraussetzung für die Verwendung von Lithium-Ionen-Batterien ist ein hohes Maß an Sicherheit. Dieses muss stets gewährleistet sein. Neue, ganzheitliche Auslegungsmethoden werden benötigt, um solch eigensichere Lithium-Ionen-Batterien entwickeln zu können, welche gleichsam dem wachsenden Drang nach höheren Energiedichten und geringeren Kosten gerecht werden. Im Rahmen der vorliegenden Arbeit werden experimentelle und simulationsbasierte Methoden auf Elektroden- und Zellebene entwickelt und kombiniert, um das Sicherheitsverhalten von Batterien im Hinblick auf das exotherme Abreagieren bzw. thermische Durchgehen von Lithium-Ionen-Zellen beurteilen zu können. Hierbei werden Ansätze vorgestellt, um den eigentlichen Verlauf, die zugrundeliegenden Auslösemechanismen sowie ein mögliches Einschreiten zur Abschwächung eines thermischen Durchgehens beschreiben und bewerten zu können. Um der thermischen Natur des Problems gerecht zu werden, liegt der Fokus der Betrachtungen auf der Wärmeerzeugung und der Wärmeabgabe bei erhöhten Zelltemperaturen und -strömen. Die Ausprägung eines thermischen Durchgehens bei erhöhten Zelltemperaturen wird durch die Reaktionskinetik von einzelnen thermischen Zersetzungsreaktionen zwischen den jeweiligen Elektroden der Zelle und dem Elektrolyt beschrieben, welche anhand einer modellgestützten Analyse von kalorimetrischen Messdaten bestimmt werden. Um die Wärmerzeugung zu beschreiben, welche zu einer übermäßigen Temperaturerhöhung und einem möglichen Auslösen eines thermischen Durchgehens führen kann, werden Ratenfähigkeitstests sowie ein neuentwickelter quasi-isothermer Kurzschlusstest mit physikalisch-chemischen Simulationsrechnungen kombiniert. Durch die Anwendung mehrdimensionaler multiphysikalischer Modellbildung und Simulation und die Durchführung experimenteller Untersuchungen können Zellen verschiedener Formate und Größen bei unterschiedlichen Kühlbedingungen hinsichtlich ihrer Wärmeabgabe bewertet werden. Dies erlaubt es, Maßnahmen zu identifizieren, welche eine Abschwächung und gar eine gänzliche Unterdrückung eines thermischen Durchgehens ermöglichen. Durch die Kombination der dargestellten experimentellen und simulationsgestützten Ansätze können sowohl die Leistungsfähigkeit als auch das Sicherheitsverhalten von Lithium-Ionen-Batterien auf Elektroden- und Zellebene umfassend bewertet werden, wodurch eine ganzheitliche Auslegung von Lithium-Ionen-Batterien für eine bestimmte Anwendung ermöglicht wird.

Contents

Abbreviations **III**

Symbols **VII**

1 Introduction to Lithium-Ion Battery Safety **1**

1.1 Lithium-ion battery hazard analysis and risk assessment . . . 3
1.1.1 Nature of lithium-ion battery hazards . . . 4
1.1.2 Cause of lithium-ion battery hazards . . . 5
1.1.3 Risks associated with lithium-ion batteries . . . 8
1.2 Battery design: Between performance, cost, and safety . . . 12
1.3 The runaway problem . . . 17
1.4 Experimental evaluation of lithium-ion battery safety . . . 22
1.4.1 Thermal stability investigations from material to cell level . . . 22
1.4.2 Abuse tests and emulation of internal short circuits on the cell level . . . 27
1.4.3 Propagation tests on multiple cell arrangements . . . 30
1.5 Modeling and simulation in the context of battery safety . . . 30
1.6 Thesis outline . . . 34

2 Heat Generation due to Exothermic Side Reactions **37**

2.1 Kinetic description of exothermic side reactions . . . 37
2.2 Influence of state of charge and state of health on reaction kinetics . . . 39

3 Heat Generation due to High Rate Operation **59**

3.1 Rate capability of active materials, electrodes, and cells . . . 60
3.2 Understanding liquid phase rate limitations via electrochemically engineered electrodes . 61
3.3 External short circuit behavior of lithium-ion cells under quasi-isothermal conditions . . 76
3.4 Impact of rate limitations on external short circuit behavior of lithium ion cells . . . 103

4 Heat Dissipation due to Thermal Design **135**

4.1 Influence of thermal design on external short circuit behavior of lithium-ion cells . . . 136
4.2 Electro-thermal validation of large-format lithium-ion cell models . . . 174

5 Summary and Conclusion **197**

References **201**

List of Publications **225**

Acknowledgment **227**

Abbreviations

Al_2O_3	aluminum oxide
CO_2	carbon dioxide
CO	carbon monoxide
HF	hydrogen fluoride
Li_2CO_3	lithium carbonate
Li_2O	lithium oxide
$LiAsF_6$	lithium hexafluoroarsenate
$LiBF_4$	lithium tetrafluoroborate
LiBOB	lithium bis(oxalato) borate
$LiClO_4$	lithium perchlorate
LiF	lithium fluoride
$LiPF_6$	lithium hexafluorophosphate
PF_5	phosphorus pentafluoride
POF_3	phosphoryl fluoride
SiO_2	silicon dioxide
TiO_2	titanium dioxide
ARC	accelerating rate calorimetry
ASIL	automotive safety integrity level
BA	balanced
BEV	battery electric vehicle
BMS	battery management system
CID	current interrupt device
CT	computed tomography
DC	direct current
DEC	diethyl carbonate
DMC	dimethyl carbonate

DPMO . . . . . defects per million opportunities

DSC . . . . . differential scanning calorimetry

EC . . . . . ethylene carbonate

ECM . . . . . equivalent circuit model

EDX . . . . . energy dispersive X-ray spectroscopy

EMC . . . . . ethylmethyl carbonate

EUCAR . . . . . European Council for Automotive Research and Development

EV . . . . . electric vehicle

HE . . . . . high energy

HEV . . . . . hybrid electric vehicle

HP . . . . . high power

HV . . . . . high voltage

HWS . . . . . heat-wait-search

ICE . . . . . internal combustion engine

IR . . . . . infrared

LCO . . . . . lithium cobalt oxide

LFP . . . . . lithium iron phosphate

LMO . . . . . lithium manganese oxide

LNO . . . . . lithium nickel oxide

LTO . . . . . lithium titanate

MCMB . . . . . mesocarbon microbeads

MuDiMod . . . . multidimensional modeling

NCA . . . . . lithium nickel cobalt aluminum oxide

NCM . . . . . lithium nickel cobalt manganese oxide

NHTSA . . . . . National Highway Traffic Safety Administration

NMC . . . . . see NCM

OEM . . . . . original equipment manufacturer

OPD . . . . . overcharge protection device

PA . . . . . polyamide

PAN . . . . . polyacrylonitrile

PC . . . . . propylene carbonate

PCM . . . . . phase change material

PE . . . . . polyethylene

PEM . . . . . proton exchange membrane

PET . . . . . polyethylene terephthalate

PHEV . . . . . plug-in hybrid electric vehicle

PI . . . . . polyimide

PMMA . . . . . poly(methyl methacrylate)

PP . . . . . polypropylene

PTC . . . . . positive temperature coefficient

PVDF . . . . . poly(vinylidene fluoride)

SEI . . . . . solid electrolyte interphase

SEM . . . . . scanning electron microscopy

SHR . . . . . self-heating rate

SIL . . . . . safety integrity level

SoC . . . . . state of charge

SoH . . . . . state of health

TGA . . . . . thermogravimetric analysis

UNECE . . . . . United Nations Economic Commission for Europe

UV . . . . . ultraviolet

VC . . . . . vinylene carbonate

VTOL . . . . . vertical take-off and landing

XAS . . . . . X-ray absorption spectroscopy

XRD . . . . . X-ray diffraction

Symbols

Please note that the symbols listed here are defined as used within the main part of this thesis and may vary from each individual article included in this work due to specific standards set by the journals or unique requirements within the integrated articles. Hence, all symbols are defined once again within each article individually.

Constants

F	Faraday's constant $96485\,\mathrm{C\,mol^{-1}}$	
k_B	Boltzmann's constant $1.360649 \cdot 10^{-23}\ \mathrm{J\,K^{-1}}$	
R	universal gas constant $8.314\,\mathrm{J\,mol^{-1}\,K^{-1}}$	

Greek symbols

α	degree of conversion	
$\alpha_{\mathrm{a/c}}$	anodic/cathodic charge transfer coefficients	
Δ	referring to a difference	
η	overpotential	V
γ	frequency factor	$\mathrm{s^{-1}}$
Φ	potential	V

Latin symbols

c	concentration	$\mathrm{mol\,m^{-3}}$
C_p	overall heat capacity	$\mathrm{J\,K^{-1}}$
c_p	specific heat capacity	$\mathrm{J\,kg^{-1}\,K^{-1}}$
E	voltage	V
E_a	activation energy	J
E_eq	equilibrium potential	V
$f(\alpha)$	reaction order	
H	specific reaction heat	$\mathrm{J\,kg^{-1}}$
h_c	convection coefficient	$\mathrm{W\,m^{-2}\,K^{-1}}$
I	current	A
i_0	exchange current density	$\mathrm{A\,m^{-2}}$
j_n	pore wall flux	$\mathrm{mol\,m^{-2}\,s^{-1}}$
k	reaction rate constant of exothermic side reaction	$\mathrm{s^{-1}}$
$k_{\mathrm{a/c}}$	anodic/cathodic rate constant of charge-transfer reaction	$\mathrm{m\,s^{-1}}$
m	mass	kg
$\dot{Q}$	heat rate	W
T	absolute temperature	K
t	time	s

Subscripts

0	referring to an initial condition
dis	referring to a dissipated quantity
gen	referring to a generated quantity
∞	referring to the surroundings or environment
l	referring to the liquid phase
max	referring to the maximum value
min	referring to the minimum value
onset	referring to the onset of a thermal runaway event
ref	referring to a reference state
runaway	referring to a thermal runaway event
s	referring to the solid phase
stable	referring to a stable operation
start	referring to a start of a reaction
unstable	referring to an unstable operation

1 Introduction to Lithium-Ion Battery Safety

Moving on from an era that has been considerably shaped by various means of combusting hydrocarbons for the purpose of producing thermal, kinetic, and electrical energy, the current transformation toward a low-carbon society is characterized by an advancing substitution of fossil fuels with renewable energy sources — which is inevitably linked to a growing need for efficient storage and extraction of electrical energy whenever and wherever required.[1]

This transition becomes especially apparent when considering the recent progressive increase in worldwide initiatives ranging from governmental incentives encouraging the sale of emission-free vehicles to legislative bans prohibiting the sale, or even use, of diesel-powered cars and cars with internal combustion engines (ICEs) of any kind, starting from as early as 2019 (see overview in Fig. 1.1).[2] Such development is vital considering that road transportation of passengers and goods alone accounted for approximately 18 % of global carbon dioxide (CO_2) emissions in 2016.[3]

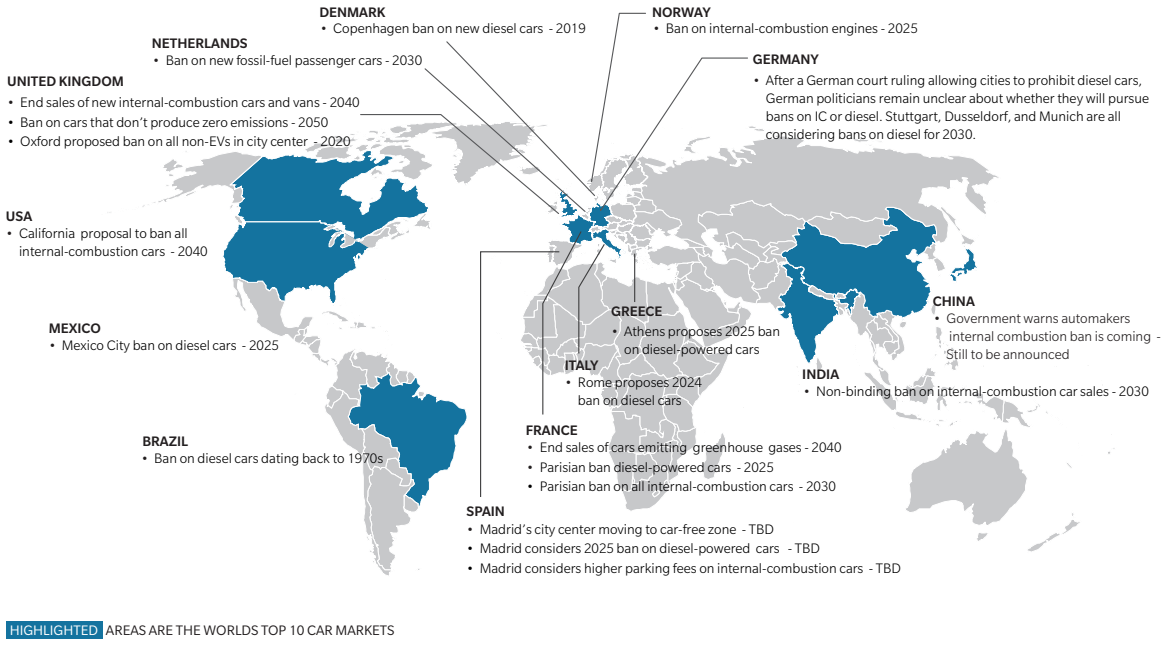

Figure 1.1: Global overview of countries prohibiting or considering a ban on the sale or use of ICE vehicles (data as from March 2018, figure taken from Ref. [2]).

With the 25 year anniversary of lithium-ion batteries in 2016, today's electrochemical energy storage solution of choice underlined its ongoing importance throughout this process.[4] Not only a multitude of today's applications, ranging from portable electronic devices and power tools to electric vehicles (EVs) and even stationary energy storage systems, rely on the appealing combination of high energy (HE) and high power (HP) density,[5] but also novel technologies, such as vertical take-off and landing (VTOL) aircrafts, are using Li-ion batteries as an enabler to potentially revolutionize daily life.[6,7]

Despite the technological maturity that Li-ion batteries have gained throughout the last three decades, to date there is still need for major improvements in order to push both gravimetric and volumetric energy and power densities to even higher levels whilst reducing the price tag per kilowatt and kilowatt hour.[1,8,9] This ongoing development is crucial in order to meet the requirements set by technologically demanding and economically competitive applications. As an example, traction batteries for EVs demand for all-electric driving ranges of up to 300 miles (i.e. almost 500 km) and beyond which requires ambitious energy densities of more than 235 $\mathrm{Wh\,kg^{-1}}$ or 500 $\mathrm{Wh\,L^{-1}}$ on the pack level.[9,10]

In order to achieve not only a driving range but also a price for battery electric vehicles (BEVs), which is comparable to vehicles with an ICE, reductions in cost are essential in order to fall below the critical threshold of $125 per kWh on the pack level.[10] With the battery pack as a whole accounting for approximately 35 % of the total BEV cost in 2018 (25 % battery cells and 10 % battery integration), the extent of market penetration of EVs such as BEVs, plug-in hybrid electric vehicles (PHEVs), and hybrid electric vehicles (HEVs) is heavily dependent on battery price development in the next years.[11] Together with the electric motor and power electronics which make up about 15 % of the total BEV cost, BEVs are currently about 35 % more expensive than ICE vehicles of which the entire powertrain makes up only 16 % of the total vehicle cost.[11] Starting from over $1000 per kWh before 2010,[12,13] the cost of the battery pack needs to decrease even further than the current price range between $176 to $195 per kWh.[11,14] This considerable drop in battery pack cost per kWh of 80 % to 85 % until 2018 is based on an annual cost reduction ranging between 8 % and 35 % of the battery pack which can be traced back to continuous improvements in battery cell manufacturing,[10,12,14,15] high learning rates in pack integration,[12] and a growing importance of economies of scale.[10,12] Together with an annual increase in energy density of 5 % to 7 % of the battery pack,[13] BEVs which are comparable to ICE vehicles both in terms of range and manufacturing cost are expected to be available between 2025 and 2030, resulting in an electrification of more than half of all new car sales and an electrification of up to a third of the global car fleet by 2040.[9,11,13]

Promising alternative active materials for state-of-the-art Li-ion batteries (e.g. conversion materials or polyanionic cathode materials[16]), post Li-ion batteries (e.g metal-air batteries[17]), and alternative technologies (e.g. H_2 proton exchange membrane (PEM) fuel cells[18]) have been thoroughly discussed in the past as possible candidates to enable cheap production of EVs with a boost in driving range. However, battery pack costs of advanced Li-ion batteries are expected to reduce to $153 per kWh by 2021,[11] based on an increasing degree of automation and an assumed average learning rate of 18 %,[10,11,14] and are predicted to further decrease to $94 per kWh by 2024 and to drop as low as $62 to $70 per kWh by 2030.[13,14] The implications being that upcoming alternative technologies might just not be competitive at the time industrialization comes within reach.[10] Hence, advanced Li-ion batteries based on intercalation materials, such as lithium nickel cobalt aluminum oxide (NCA), nickel-rich lithium nickel cobalt manganese oxides (NCMs or NMCs), lithium- and manganese-rich HE-NMC, and high voltage (HV) spinels as the cathode active material,[9,16,19] are likely to dominate the near-term to mid-term product range of EVs offered by original equipment manufacturers (OEMs).[20,21] These cathode materials will most likely be paired with high-capacity anodes combining state-of-the-art intercalation materials such as graphite with an increasing share of alloying materials such as silicon.[16,22]

This development implies that besides remaining economical and ecological challenges in Li-ion battery manufacturing,[23–25] on the one hand, a possible future shortage in supply of main commodities, such as cobalt and nickel, might limit the pace and extent of EV market penetration.[20,21] On the other hand, safety concerns of state-of-the-art Li-ion batteries linked to both the employed materials and to the design of electrodes, cells, modules, and battery packs or systems will remain a key challenge in research and development.[4,26]
The seemingly conflicting goals of cheaply producing EVs that offer a driving range at a price which customers are used to whilst guaranteeing a high level of safety are both of utmost importance in order to realize not only an economical but also a safe transition from fuel combustion to electrification. However, designing safe yet economically and technologically appealing Li-ion batteries requires substantial scientific attention. The development of powerful experimental and simulation based methods and tools is necessary in order to enable the optimization problem to be solved. Developing such methods and tools is the focus of this work.

1.1 Lithium-ion battery hazard analysis and risk assessment

The term *Li-ion battery* can be misleading as it is often synonymously used to describe various levels of integration of the basic electrochemical unit cell which is fundamentally based on the transfer and movement of Li-ions enabling both discharge and charge.
In its simplest form, the electrochemical unit cell is enclosed in a flexible or rigid housing, forming a single Li-ion battery *cell*. The cell's voltage level is solely defined by the material combination of the electrochemical unit cell, whereas the amount of electrical charge stored within the cell is dependent on both the material combination of the electrochemical unit cell and the amount of active material incorporated within the cell's housing. The voltage level and the amount of electrical charge stored then define the cell's electrochemical energy content. A mechanical assembly of cells electrically connected in series and/or parallel forms a Li-ion battery *module*. Whilst the module's voltage level is based on the number of cells connected in series, the amount of electrical charge stored within the module depends on the number of cells connected in parallel, both of which define the module's electrochemical energy content. A mechanical assembly of cells or modules electrically connected in series and/or parallel including additional control and protection systems (e.g. battery management system (BMS), thermal management system, etc.) forms a Li-ion battery *pack* or *system*. The voltage level, electrical charge stored, and resulting electrochemical energy content of the pack or system are defined by the series and parallel configuration of the assembled cells or modules.

Safety can generally be understood as the absence of harm or danger. In terms of *Li-ion battery safety*, this harm or danger arises from both hazards and risks associated with Li-ion batteries ranging from cells to modules and packs or systems. Whilst a hazard is something that has the potential to cause harm in the first place, a risk is the potential that a hazard will eventually cause harm. In the following subsections, both the nature and cause of Li-ion battery hazards are characterized before potential risks arising from handling and operating Li-ion batteries are summarized.

1.1.1 Nature of lithium-ion battery hazards

Hazards associated with a failure of HV Li-ion battery systems as in EVs (>60 V direct current (DC), voltage class B defined in ISO 6469[27]) can be categorized into functional, electrical, thermal, chemical, and kinetic hazards.[28,29] These hazards, which can pose significant harm or danger to individuals involved in accidents, are schematically summarized in Fig. 1.2.

Amongst others, the general functionality of a Li-ion battery system involves delivering the required electrical energy and power level throughout the designated operation whilst maintaining its safe operating window. Functional hazards in this context can range from an uncontrollable function to a complete loss of function of a battery which, in turn, may result in a dangerous condition when a flawless operation of the HV Li-ion battery system is vital (e.g. a sudden lack or loss of an EV's propulsion during overtaking).

Electrical hazards can involve the exposure to HV environments resulting in severe injuries or even death when making direct contact with current-carrying components at such raised voltage levels. Furthermore, HV Li-ion battery systems containing unnoticeably overcharged or overheated cells (e.g. resulting from a BMS malfunction or misconstruction[31,32]) or cells with a hidden internal fault (e.g. based on manufacturing impurities or a violation of manufacturing tolerances[33]) can also pose severe electrical hazards.

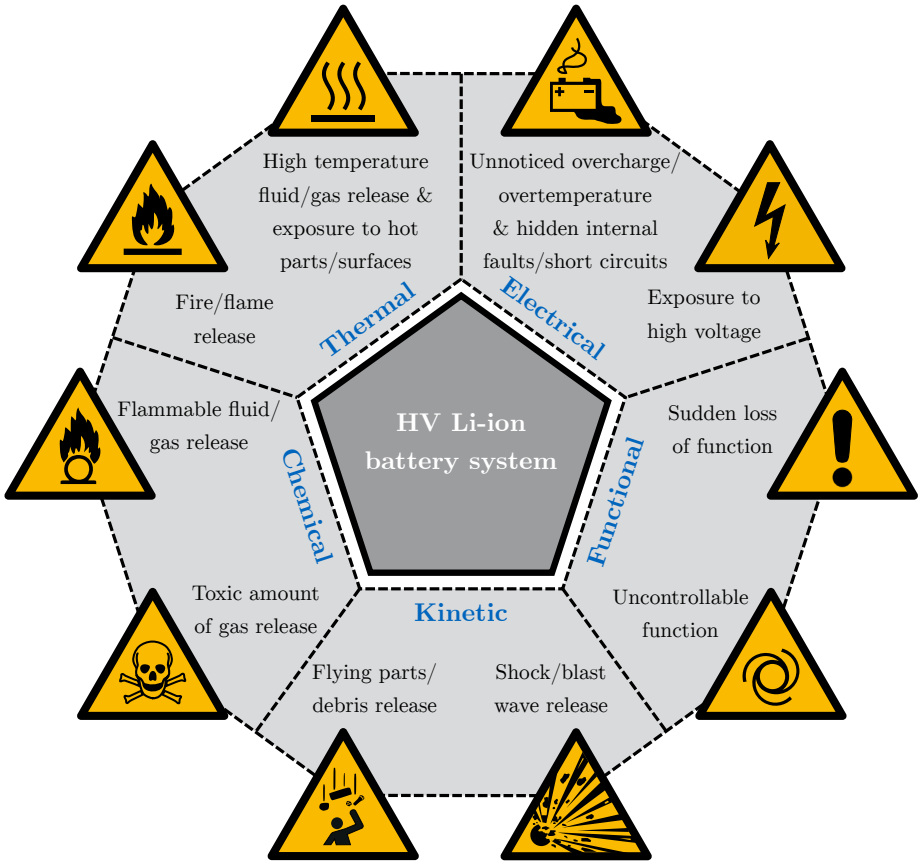

Figure 1.2: Schematic representation of main hazards associated with the failure of a HV Li-ion battery system (modified from Refs. [28; 29]). The warning signs were taken from ISO 7010 and were used in a related but not identical context as indicated in the standard.[30]

Electrical hazards are mostly accompanied by thermal hazards involving violent exothermic reactions due to structural and thermal instabilities of the employed materials[34] and/or internal short circuits with large local currents and heat generation rates.[35] Thermal hazards evolving from such events involve, for example, an exposure to hot surfaces and a release of hot liquid and gaseous fluids which, when ignited, may even result in a release of fire and flame. Besides these thermal hazards, chemical hazards are also accompanied by the release of volatile fluids as well as smoke, which can result in a toxic environment (e.g. carbon monoxide (CO), hydrogen fluoride (HF), phosphoryl fluoride (POF_3), etc.) when sufficiently concentrated.[36,37] Furthermore, if a failure of a HV Li-ion battery system is violent enough, not only flammable fluids and smoke are released, but also solid components and debris may be ejected from the battery system. The resulting severe kinetic hazards may be accompanied with a shock or blast wave, in the event that a sufficiently high pressure build up is not released in a controlled fashion.

1.1.2 Cause of lithium-ion battery hazards

The reason behind these often thermally related hazards lies within the working principle and consequently material combination of Li-ion batteries and is closely linked to the chosen architecture.[38] A schematic representation of the basic electrochemical unit cell is shown in Fig. 1.3. Li-ion batteries, and batteries in general, consist of three main functional components: Two electrodes forming anode and cathode and an electrolyte enabling ion exchange between the two. From an electrochemical perspective, the anode is the electrode that is oxidized whilst the cathode is the electrode that is reduced.

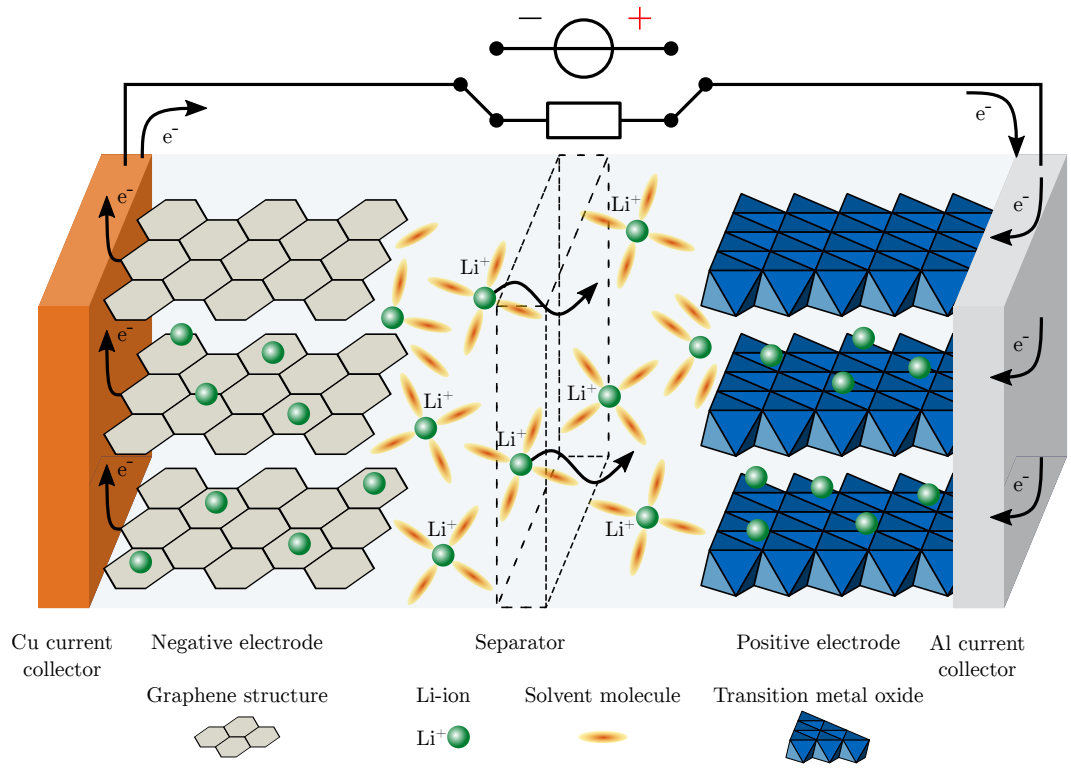

Figure 1.3: Schematic representation of the working principle of a Li-ion battery during discharge (i.e. galvanic cell, charge: electrolytic cell) based on an anodic deintercalation reaction at the carbonaceous negative electrode and a simultaneously occurring cathodic intercalation reaction at the transition metal oxide based positive electrode (modified from Ref. [39]).

This applies to both discharge and charge of a battery and consequently implies alternating naming for the two electrodes, depending on the battery's operating mode. In order to avoid confusion, the discharge process is considered as a reference, implying that the more negative electrode is the anode (i.e. the negative electrode) and the less negative electrode is the cathode (i.e. the positive electrode) by definition.

In state-of-the-art Li-ion batteries, the anode is made from one of various types of carbon (e.g. synthetic or natural graphite, soft or hard carbon, or mesocarbon microbeads (MCMB)) or lithium titanate (LTO), whereas the cathode is made from layered oxides (e.g. lithium cobalt oxide (LCO), NCA, or NMC), spinels (e.g. lithium manganese oxide (LMO)), or polyanion compounds (e.g. lithium iron phosphate (LFP)).[16,40] The commonly applied non-aqueous liquid electrolyte typically consists of a solvent based on a mixture of organic cyclic carbonates or esters (e.g. ethylene carbonate (EC) and/or propylene carbonate (PC) combined with linear carbonates such as diethyl carbonate (DEC), dimethyl carbonate (DMC), and/or ethylmethyl carbonate (EMC)) and a lithium salt forming non-coordinating anions as the solute (e.g. lithium hexafluorophosphate ($LiPF_6$), lithium perchlorate ($LiClO_4$), lithium hexafluoroarsenate ($LiAsF_6$), or lithium tetrafluoroborate ($LiBF_4$)).[39,40] In order to physically separate and, hence, electronically isolate the two electrodes from one another, whilst still allowing for an ion exchange between them, polyolefin based materials such as polyethylene (PE) and/or polypropylene (PP) are generally used to create single- or multi-layered microporous membranes as the separator of 25 µm in thickness or less with porosities of 40 % or more.[40–44] Other commonly applied but commercially less significant separator materials are based on polymers such as poly(vinylidene fluoride) (PVDF), polyacrylonitrile (PAN), and poly(methyl methacrylate) (PMMA) to create not only single- and multilayered microporous membranes but also non-woven mats.[44] Besides using different polymers (e.g. polyamides (PAs), polyimide (PI), and polyethylene terephthalate (PET)), key attributes of polymer separators (e.g. wettability, mechanical strength, porosity as well as shrinkage and thermal stability) can be enhanced by surface modifications (e.g. plasma treatment, ultraviolet (UV) irradiation, and electron beam irradiation) or by coating/filling polymers with thermally and mechanically extremely robust ceramics (e.g. aluminum oxide (Al_2O_3), and silicon dioxide (SiO_2), or other inorganic materials such as titanium dioxide (TiO_2)) to form composite separators.[44,45]

As long as a Li-ion battery is operated within its designated operating window, defined by its temperature limits T, voltage level E, and applied current range I (i.e. $T_{\min} \leq T \leq T_{\max}$, $E_{\min} \leq E \leq E_{\max}$, and $|I| \leq |I_{\max}|$), the main reaction occurring is based on a deintercalation and intercalation reaction within anode and cathode during both discharge and charge which is characterized by low losses, slow side reactions, and little heat being generated.[38] For a carbonaceous negative electrode and a metal oxide based positive electrode, the simplified half-cell and full-cell reactions are defined as follows (with M representing e.g. Ni, Co, and/or Mn):[40]

Negative half-cell reaction:
$$\mathrm{Li}_x\mathrm{C}_n \underset{\text{charge}}{\overset{\text{discharge}}{\rightleftharpoons}} x\,\mathrm{Li}^+ + n\,\mathrm{C} + x\,\mathrm{e}^- \tag{1.1}$$

Positive half-cell reaction:
$$\mathrm{Li}_{1-x}\mathrm{MO}_2 + x\,\mathrm{Li}^+ + x\,\mathrm{e}^- \underset{\text{charge}}{\overset{\text{discharge}}{\rightleftharpoons}} \mathrm{LiMO}_2 \tag{1.2}$$

Overall full-cell reaction:
$$\mathrm{Li}_{1-x}\mathrm{MO}_2 + \mathrm{Li}_x\mathrm{C}_n \underset{\text{charge}}{\overset{\text{discharge}}{\rightleftharpoons}} \mathrm{LiMO}_2 + n\,\mathrm{C} \tag{1.3}$$

The balance between generated and dissipated heat then defines the temperature evolution of the battery which can be readily regulated by the BMS and/or an additionally integrated thermal management system.

Considering that strongly oxidizing (i.e. the cathode) and reducing agents (i.e. the anode) that are electronically isolated from one another by a thin porous separator, which tends to shrink or melt at elevated temperatures, are combined with an electrolyte containing highly flammable organic solvents, state-of-the-art Li-ion batteries pose a considerable danger when accidentally or intentionally operated outside of this designated operating window (i.e. misuse or abuse) or when quality or wear-and-tear related malfunctions occur. This dilemma is schematically shown in Fig. 1.4 in the representation of a so called fire tetrahedron.[46] As soon as the battery is operated outside its designated operating window, e.g. when the battery's temperature T exceeds the maximum tolerable temperature T_{max}, additional and generally undesired exothermic side reactions dominate the battery's behavior.[34] For state-of-the-art Li-ion batteries, these exothermic side reactions include reactions within the negative electrode such as the thermal decomposition reaction of the passivating solid electrolyte interphase (SEI) which can be found on graphite anodes enabling stable battery operation[47] (ca. 80 °C to 120 °C), as well as reactions of the negative active material with electrolyte and fluorinated binders (ca. 150 °C to 300 °C). Reactions within the positive electrode involve the decomposition reaction of the positive active material accompanied by oxygen release (as for layered oxides), as well as the reaction of the positive active material with electrolyte (ca. 150 °C to 300 °C). Further reactions involve the decomposition reaction of the liquid electrolyte including the reaction of salt with solvent (ca. 250 °C to 400 °C) and the combustion reaction of carbonaceous materials included within the battery such as solvent, negative active material, separator, binder, and conductive agents with oxygen released from the positive active material (partial combustion) and/or oxygen from the environment in case of leakage, venting, or rupture (self-ignition >450 °C).[26,33,34,48–50]

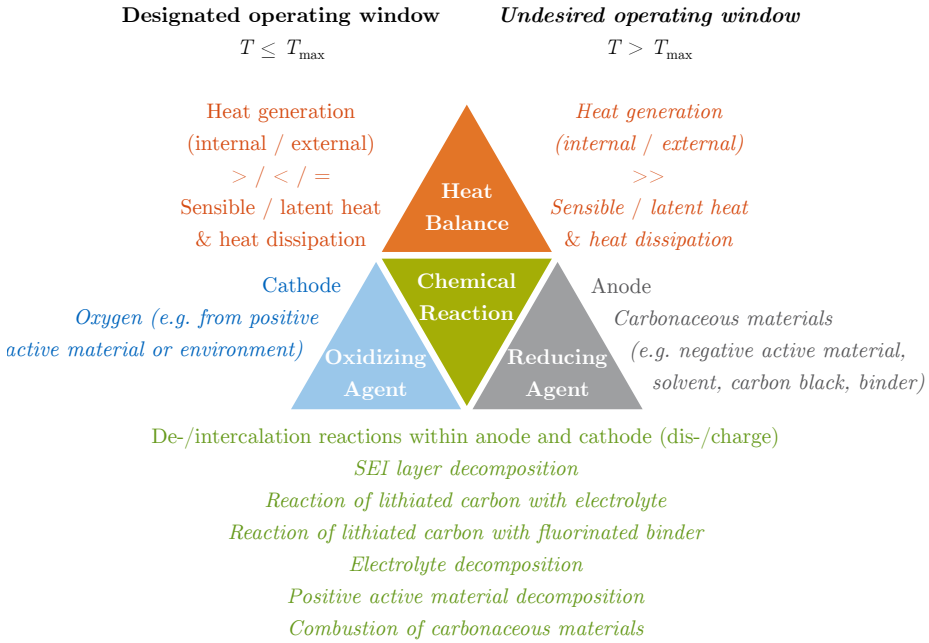

Figure 1.4: Fire tetrahedron summarizing dominating reactions (green), reactants (blue and grey), and resulting heat balances (orange) within a Li-ion battery depending on the operating window (reduced to the battery's temperature T). Main reactions occurring within the designated operating window are shown in roman whilst undesired reactions occurring outside this window are represented in italic (oxidizing and reducing agents of undesired reactions are exemplarily shown for the combustion reaction of carbonaceous materials). Schematic representation modified from Ref. [46] and extended based on Refs. [34; 38].

When considering a Li-ion battery with an energy density of 235 $\mathrm{Wh\,kg^{-1}}$ and a specific heat capacity c_p ranging between 800 $\mathrm{J\,kg^{-1}\,K^{-1}}$ and 1000 $\mathrm{J\,kg^{-1}\,K^{-1}}$,[51,52] a complete conversion of the stored electrochemical energy into thermal energy (e.g. during a short circuit) would result in an adiabatic temperature rise of approximately 850 °C to 1050 °C. In practice, these temperature values are not reached as the electrochemical reaction does not run completely (e.g. due to cell venting or rupture) and as adiabatic conditions do not prevail. However, such increase in temperature is more than sufficient to exceed the threshold temperature triggering additional chemical, exothermic side reactions. Starting from a temperature of 25 °C, under adiabatic conditions only 5.2 % to 6.5 % of the stored electrochemical energy would be required to trigger the decomposition reaction of the SEI within the negative electrode starting from as low as 80 °C. Another 6.6 % to 8.3 % of the electrochemical energy would be then sufficient to initiate the decomposition reaction of the positive electrode and the reaction of both electrodes with the electrolyte, assuming a starting temperature of approximately 150 °C. Further considering a generic Li-ion battery containing hard carbon as the negative electrode and LCO as the positive electrode as initially commercialized by Sony in 1991 whilst assuming a complete conversion of all reactions, approximately 31 % compared to the cell's electrochemical energy content would be released as heat, based on chemical exothermic side reactions within the negative electrode. Relative to the stored electrochemical energy, another 64 % would be released due to chemical reactions within the positive electrode, and additionally 11 % would be released based on the decomposition of the electrolyte. In total, 106 % compared to the cell's electrochemical energy content would be released as heat based on chemical reactions of the active materials and the electrolyte alone. Further assuming a complete combustion of the solvent, another 306 % would be released as heat, which could increase toward 1028 %, in the event that the graphite from the negative electrode were also to be completely combusted.[33]

This implies that Li-ion batteries contain not only the reactants but also the required electrical and, hence, thermal energy to both trigger and sustain additional exothermic side reactions. Depending on the battery's chemistry, a Li-ion battery may generate 11 times or more the amount of electrical energy stored in the form of heat due to chemical exothermic side reactions. The self-accelerating nature of these reactions makes it very difficult, or even impossible, to control or limit a further heat up as soon as a certain critical temperature limit is exceeded. This is generally understood as a so called *thermal runaway*, which involves not only thermal hazards but may eventually also lead to chemical and kinetic hazards when the battery leaks, vents, ruptures, or even explodes (see Fig.1.2).

1.1.3 Risks associated with lithium-ion batteries

In order to be able to evaluate Li-ion battery safety, not only direct hazards involving Li-ion batteries need to be analyzed but related risks must also be thoroughly assessed. These risks are schematically summarized in Fig. 1.5. On the one hand, risks associated with Li-ion batteries are highly dependent on the intended field of application and, on the other hand, they are intrinsically connected to design and quality related aspects. A potential misuse or abuse of a cell, module, pack or system can be therefore linked to the battery's operational life, as well as to its handling during production, shipping, maintenance, and recycling. Deriving possible test scenarios to evaluate a battery's abuse tolerance is therefore rather straightforward as the test parameters can be related to requirements set by a given application and/or can be aligned with foreseeable accidents or manipulations. These so called *abuse tests* can be categorized into mechanical, electrical, and thermal or environmental abuse scenarios, depending on the nature of the external trigger and the initial fault the trigger is producing.

Hence, a crash or crush of a Li-ion battery cell, module, pack or system will first of all lead to a mechanical fault such as a separator rupture within one or more cells. If this mechanical fault has no further impact on the battery, the consequence of this test can be considered as an uncritical fault. This fault may only affect the functionality of the battery and proves the abuse tolerance of the battery in connection with this test. If, however, the separator rupture leads to a further electrical fault such as a local or widespread cell-internal short circuit within the battery cell or cells, a continuation or progression of the fault toward a thermal fault with local or global overheating and eventually heat generation rates exceeding by far the heat dissipation, a critical battery fault including a thermal event with all its consequences is possible (see Fig. 1.2).
Similar Li-ion battery abuse tests referring to varying test parameters and test specimens have been defined throughout the last years in both standards and regulations, not only for traction batteries in automotive applications, but also for batteries included in portable electronics, aeronautics, as well as marine, military, and stationary applications.[53,54]

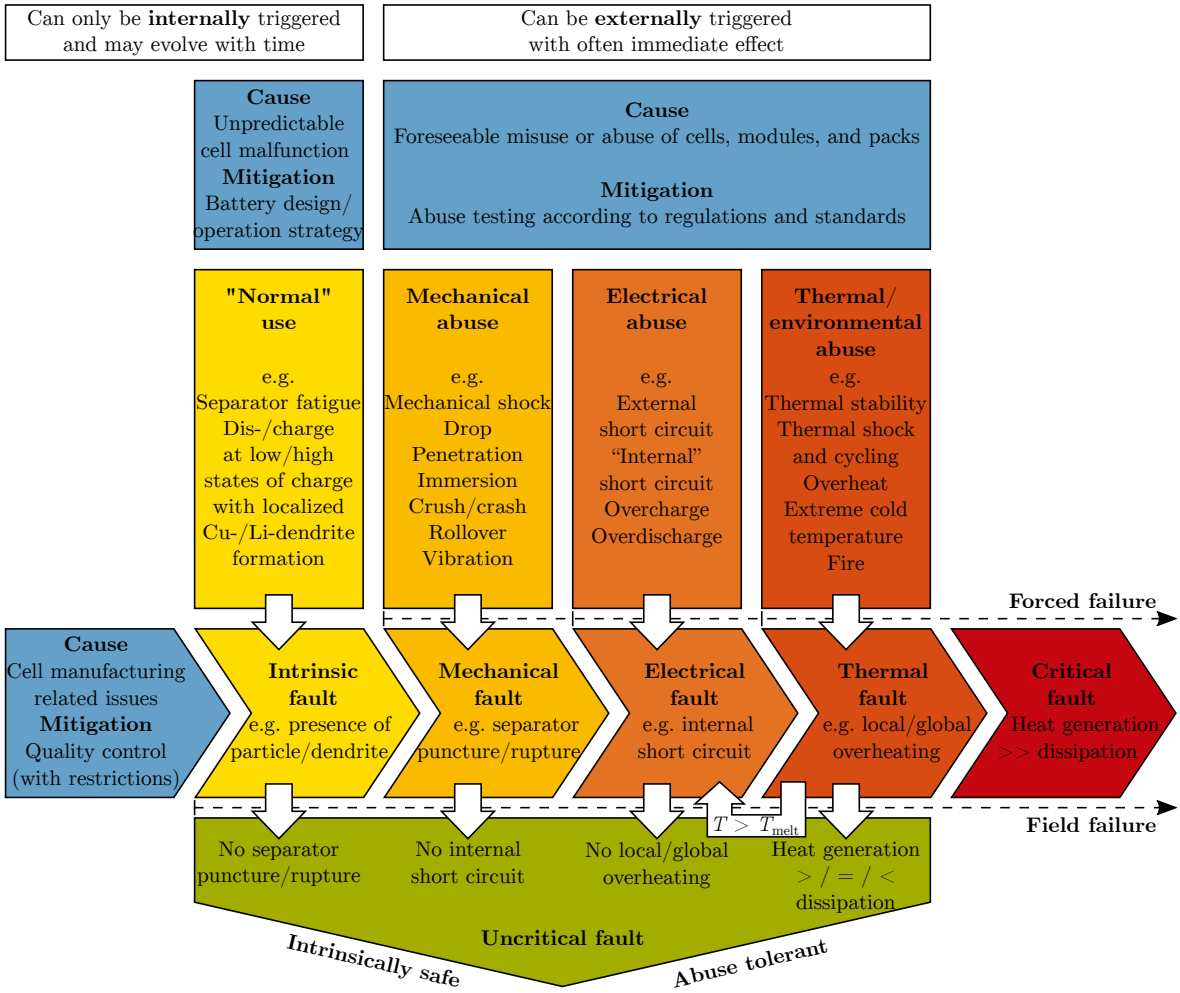

Figure 1.5: Schematic representation of risks associated with Li-ion batteries distinguishing between internally and externally triggered faults that may either result in a critical battery fault including field failures or forced failures (horizontal arrow, left to right) or lead to an uncritical fault due to battery's intrinsic safety or abuse tolerance (vertical arrow, top to bottom). Exemplary abuse tests are listed in accordance with Ref. [53].

Resulting from the vast field of utilization combined with the need for nationally and internationally valid requirements, a large variety of standards and regulations applicable to Li-ion batteries can be found. Whilst standards are issued by non-governmental institutions, documenting the current state of research and being voluntary by nature, regulations are released by governmental authorities having the force of law (e.g. type approval regulations in the automotive sector such as issued by the United Nations Economic Commission for Europe (UNECE) or the National Highway Traffic Safety Administration (NHTSA) in the USA).[53] Evaluating a Li-ion battery's abuse tolerance in accordance with standards and regulations with specified pass/fail criteria (e.g. tolerable maximum hazard levels as specified by the European Council for Automotive Research and Development (EUCAR)[55]) guarantees high quality standards of battery equipped products by minimizing the risk of harm to individuals due to accidents and manipulations involving Li-ion battery cells, modules, and packs or systems.

The "holy grail" of Li-ion battery safety research and development can be found, however, in the form of so called *field failures* which are predominantly based on internal short circuits occurring during otherwise "normal" operation.[33,56] Similar to *forced failures* which may result from a misuse or abuse of the Li-ion battery, field failures also involve a critical battery fault including heat generation rates exceeding by far the heat dissipation rates entailing an uncontrollable heat up of a single battery cell (i.e. thermal runaway) which may then lead to a cascading fault of adjacent cells affecting whole modules or even the entire pack or system (i.e. thermal propagation).
In contrast to forced failures, field failures are based on intrinsic faults and can therefore neither be externally triggered, nor do they develop an immediate effect after an intrinsic fault is formed. With field failures occurring at frequencies of just one failure in 5-10 million cells or 0.1 to 0.2 defects per million opportunities (DPMO) for the most established and experienced cell manufacturers after the cells had been operating normally for months to years,[33,35] studying the development until the field failure occurs and/or investigating the course of the field failure itself is very difficult. The lack of publicly available data documenting such field failures in a scientific manner prevents true progress in research and development in this particular field. This implies that neither the evolution of an internal short circuit, nor the transition of an internal short circuit toward a cell thermal runaway including a possible consecutive thermal propagation are fully understood so far.[33]
Possible mechanisms leading to internal short circuits in the field have been thoroughly discussed in literature, however, often without clear evidence or conclusion. This is due to the fact that, firstly, even a thorough forensic investigation of failed Li-ion batteries often does not allow the identification of the internal short circuit trigger due to the extensive damage that the subsequent thermal event produced within the battery and, secondly, that different kinds of triggers are likely to produce similar outcomes supporting the stochastic nature of field failures. Unless cell assembly or quality control related issues can be directly linked to repeatedly occurring field failures as those identified throughout the Boeing Dreamliner incidents in 2013/2014,[57,58] or for the Samsung Galaxy Note 7 mobile phones in 2016/2017,[59] cells with internal faults remain unobserved, fulfilling quality standards far beyond six sigma (i.e. 3.4 DPMO). A large proportion of internal faults leading to field failures are estimated to be caused by foreign metal particles which contaminate cells throughout electrode fabrication, including cutting and shaping manufacturing processes or during cell assembly. These foreign particles, which have been reported to be made from metals such as iron or nickel, might be located on the cathode side which would lead to particle dissolution at typical cathode potentials >3.5 V vs. Li/Li^+ with subsequent plating on the anode at characteristic potentials <1.5 V vs. Li/Li^+, growing through the separator toward the cathode (standard potentials ranging between 2.6 V to 2.9 V for Fe/Fe^{2+} and Ni/Ni^{2+} vs. Li/Li^+).[33]

With melting points >1450 °C, iron and nickel dendrites can theoretically sustain a considerably high short circuit current before the short circuit is interrupted or fused by a melting of the dendrite. Another likely mechanism leading to an internal short circuit resulting from particle contamination would be a separator puncture due to fatigue occurring as a reason of consecutive volume changes within the Li-ion cell including stress and strain experienced within the separator during discharge and charge (especially as for Li-ion cells with graphite anodes exhibiting volume changes of the graphite lattice structure of as much as 13 % between the fully lithiated and delithiated state[60]). However, field failures linked to internal short circuits may not only arise from a contamination with foreign metal particles, but may also result from dendrite formation due to localized lithium plating on nucleation sites fostering dendrite growth on the anode at local potentials below 0 V vs. Li/Li^+ experienced during charging at too high currents, at a too high state of charge (SoC) (e.g. overcharge), and/or at too low temperatures.[61–66] Similarly, a dissolution of the copper current collector at anode potentials exceeding 3.1 V vs. Li/Li^+[67] with subsequent deposition of copper on the cathode at potentials below this threshold, as experienced during discharging at too high currents and/or at a too low SoC (e.g. overdischarge), could grow through the separator and form an internal short circuit.[68–70] Whilst copper combines an excellent electronic conductivity with a high melting point of 1085 °C which may allow for sustaining a substantially high short circuit current for a considerable amount of time (similar to iron and nickel particles) lithium already melts around 180 °C which speaks against an enduring short circuit leading to a thermal event.[33,62] However, a large current occurring locally for a short amount of time might already be sufficient to shrink or melt the surrounding separator material which could then lead to a more pronounced internal short circuit accompanied by a thermal runaway.

Without being able to reproduce field failures by means of an adequate test, only the abuse tolerance of a battery can be evaluated with regard to foreseeable misuse or abuse — the intrinsic safety of a battery, however, cannot be assessed through tests so far. Considering the limited choice of mitigation strategies reducing the risk of an internal short circuit such as introducing even higher and therefore costly quality standards in cell manufacturing (if even possible) or setting tight operation boundaries limiting the battery's capabilities, a satisfying solution to this dilemma seems somewhat out of reach. Strategies involving designing battery packs or systems that tolerate an internal short circuit as well as the consequences of cell thermal runaway including (partial) thermal propagation allow this issue to be tackled on the pack or system level. A further approach to work around the seemingly inevitable risk of field failures is to detect the initiation of internal short circuits or so called "soft" internal short circuits, with relatively high short circuit resistances[56] >1000 Ω,[35] before a "hard" short circuit with a low short circuit resistance and consequently large local currents and high heat generation rates can develop.[33,35,71–74]

Such early warning or detection, however, is only effective when a battery pack or system can react to the developing internal short circuit, reducing its impact. Such intelligence and functionality must then be considered as part of the pack's or system's *functional safety*, which can be described as the ability of an electrical, electronic, or programmable electronic device to maintain or return to a safe operating mode when an error occurs.[28] A systematic hazard analysis and risk assessment determining relevant safety integrity levels (SILs) is vital in order to appropriately design a battery system including specific functions that guarantee a battery's functional safety at all times. Such systematic hazard analysis and risk assessment following industrial standards (e.g. IEC 61508[75]), standards relevant to the processing industry (e.g. IEC 61511[76]), or automotive standards (e.g. ISO 26262[77]) to determine SILs or automotive safety integrity levels (ASILs) is therefore a crucial part of battery development today.

1.2 Battery design: Between performance, cost, and safety

Despite the desire to design batteries which excel in each individual aspect of functionality, facilitating market penetration, a tradeoff between a battery's characteristics is most often the only option in order to create a suitable product for a targeted application. This implies that enhancing a certain attribute of a battery can often only be realized at the expense of diminishing other properties.
Several key requirements such as a battery's volumetric and gravimetric energy and power density, depending on its temperature and the applied current, as well as its longevity are performance related — however, cost and safety of a battery are also crucial. These conflicting goals between a battery's performance, cost, and safety are simplified in Fig. 1.6, which identifies a certain optimum depending on the battery's energy density when keeping the overall electrochemical energy content constant. The chosen combination of materials and electrodes has the largest impact on a battery's energy density, cost, and safety. This means that the cell design including cell safety devices as well as battery integration on the module and pack or system level can only enhance the battery's safety characteristics to a certain extent without impacting too heavily on the cost and energy density.

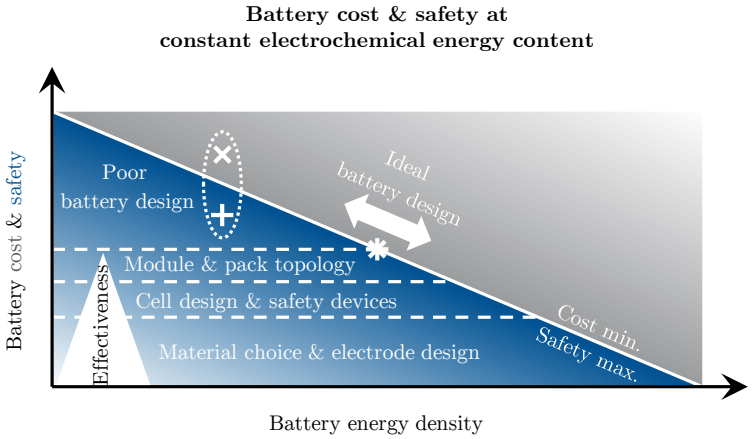

Figure 1.6: Schematic representation of conflicting goals between a battery's performance, cost (gray, ×), and safety (blue, +) in the context of the chosen materials and electrodes, cell design, and battery integration at a constant electrochemical energy content of the battery.

Material choice The dilemma between the desire to develop intrinsically safe, yet technologically and economically appealing Li-ion batteries that fulfill the demand for high energy densities at low cost becomes especially apparent when considering the current trend toward establishing cathode materials with increasingly high nickel contents, such as NCA and nickel-rich NMCs.[78] Since the commercialization of Li-ion batteries by Sony in 1991, the gravimetric energy density of Li-ion cells increased from from just 98 $\mathrm{Wh\,kg^{-1}}$ to over 300 $\mathrm{Wh\,kg^{-1}}$, whilst the volumetric energy density grew from 220 $\mathrm{Wh\,L^{-1}}$ to 650 $\mathrm{Wh\,L^{-1}}$ and beyond.[79] This could only be achieved by increasingly substituting cobalt within the LCO cathode with other transition metals such as nickel allowing for higher capacities.[19] For two decades, $LiCoO_2$ had been the most widely applied cathode material in commercial consumer Li-ion secondary batteries due to its ease of fabrication as well as its sufficiently high rate capability. However, its comparably low capacity in practical applications below 150 $\mathrm{mAh\,g^{-1}}$ at a high cost, combined with its toxicity and low thermal stability, as well as its limited cycle life makes it unsuitable for high performance, high volume applications as, for example, experienced in traction batteries for EVs.[16,79]

Fully substituting cobalt with nickel as in lithium nickel oxide (LNO) or $LiNiO_2$ cathodes seems therefore very promising at first glance, as nickel offers a high theoretical capacity around $275\,mAh\,g^{-1}$ for intercalating Li-ions whilst reducing cost and ruling out toxicity issues of LCO.[16,80] However, such substitution also comes with an increasing power loss[81] and a strongly reduced capacity retention throughout cycling[82,83] as well a considerably reduced thermal stability.[84] Several attempts have been made to stabilize $LiNiO_2$ during cycling, e.g. via ZrO_2 coating[85] or Zr doping.[82] It has been further shown that a partial substitution of cobalt with nickel, resulting in $LiNi_{1-x}Co_xO_2$, allowed for the desired tradeoff between compromising both capacity retention during cycling and thermal stability in favor of an increase in theoretical capacity. By means of aluminum doping, these characteristics could be even enhanced in terms of a reduced cell polarization leading to $LiNi_{1-x-y}Co_xAl_yO_2$ also known as NCA with its popular form of $LiNi_{0.8}Co_{0.15}Al_{0.05}O_2$, allowing for practical capacities around $200\,mAh\,g^{-1}$.[16,19,86] Together with the development of $LiNi_{1-x}Mn_xO_2$[87] forming a solid solution with $LiCoO_2$, $LiNi_xCo_yMn_zO_2$ (with $x+y+z=1$) or NCM/NMC was obtained.[88,89] This development showed successful stabilization of the layered crystal structure[90] and was shortly after fabricated in its popular form of $LiNi_{1/3}Co_{1/3}Mn_{1/3}O_2$[91,92] or NMC-111 exhibiting a high capacity retention combined with a high thermal stability at a moderate practical capacity of $160\,mAh\,g^{-1}$ to $170\,mAh\,g^{-1}$.[16] With nickel offering a high capacity at a low thermal stability, manganese showing a high cycling performance at a high thermal stability, and cobalt coming with a good rate capability at a comparably high cost, the composition of NMC can be tuned to a specific set of requirements, formed of energy and power density, longevity, cost, and safety.[78,79,93]

Considering the strong need for a significant increase in energy density of Li-ion batteries at a simultaneously reduced price per kWh within the next years especially within large-scale automotive applications, the current pathway of the battery industry toward nickel-rich cathode materials seems rather inevitable, simply due to the lack of technologically mature alternatives.[9] However, with increasing nickel content of NMC materials, not only increases the capacity but also compromises the thermal stability, which especially holds for nickel-rich representatives of NMC.[78,79,93–95] Specific capacities of $215\,mAh\,g^{-1}$ and beyond for $LiNi_{0.8}Co_{0.1}Mn_{0.1}O_2$ or NMC-811 electrodes, not only come with a dramatic reduction in onset temperature of thermal decomposition reactions based on phase transitions from layered to spinel and rocksalt phases, but also involve a more pronounced heat and oxygen release throughout this process.[94,95]

NMC materials with moderate nickel contents such as NMC-433, NMC-442, and NMC-532 exhibit a comparably well-balanced behavior, with an increase in capacity at the expense of a reduced cycling performance and thermal stability. This hints at an optimum composition of NMC aside from nickel-rich representatives such as NMC-622, NMC-811,[93–95] and the newly discussed NMC-9.5.5.[20] Besides finding the optimum composition of NMC for a given application, approaches involving concentration gradients and core-shell materials are also discussed. Such designs include nickel-rich regions within the center of the active material particles and, for example, manganese-rich outer layers combining a high capacity with a high cycling performance and thermal stability.[9,79,93,96,97] These approaches are considered as possible candidates to achieve the energy, power, cycling performance, cost, and safety targets set by automotive representatives until 2025,[9] including a maximum EUCAR cell hazard level of 4 which implies "no fire or flame; no rupture; no explosion; weight loss $\geq$50 % of electrolyte weight (electrolyte = solvent + salt)".[55] Together with morphological adaptions of primary and secondary particles as well as a modification of electrode packing densities and coating thicknesses defining the electrode loading, electrochemically engineered and optimized electrodes seem to represent a promising route forward which is worth studying in further detail.[96,97]

Cell format and size When looking at the amount of cell formats (see Fig. 1.7) and sizes commercially available today it becomes obvious that so far no cell design has proven to be superior even for a given application. For example, cell designs including cylindrical, prismatic, and pouch-type formats, with capacities which start from several Ah and below and rise toward 100 Ah and beyond are all being used for the same application as traction batteries for electric vehicles (e.g. Tesla's Roadster, Model S, Model X, and Model 3 using thousands of 18650 or 21700 cylindrical NCA cells ranging below 6 Ah or BMW's i3 using around a hundred prismatic NMC-based cells ranging from 60 Ah, over 94 Ah, and up to 120 Ah).[9,98–100]

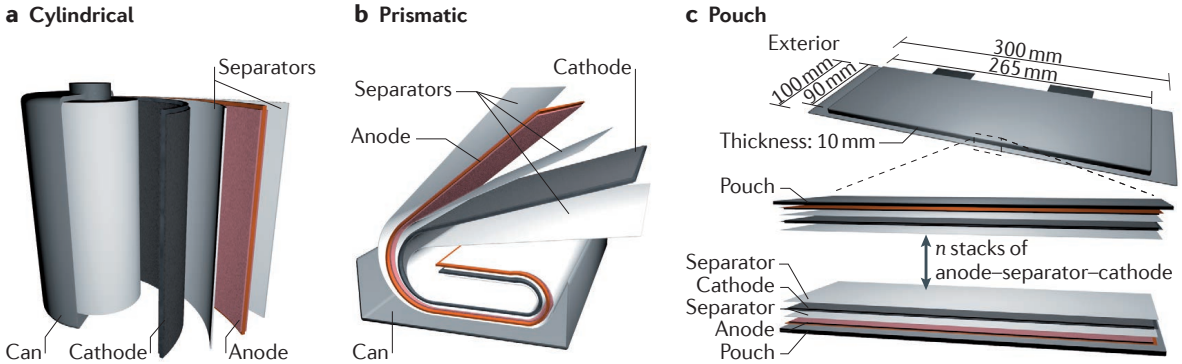

Figure 1.7: Commonly available Li-ion cell formats such as cylindrical (a), prismatic (b), and pouch-type cells (c). Figure taken from Ref. [17].

This implies that the decision for or against a certain combination of active materials, electrode morphologies and designs, as well as cell formats and sizes can be only made together with choosing the geometry and topology of the battery modules and pack or system. This includes additional monitoring and control strategies, such as implemented in the BMS and the battery's thermal management system. The necessary requirements of the battery system and its sub-components need to be derived from both the targeted application and prevailing production constraints in order to allow for a vertically integrated battery design from the material and electrode level to the cell, module, and pack or system level. Several studies have been published throughout the years taking on individual aspects of Li-ion battery design and especially cell design. From a cost of production perspective, large-format prismatic Li-ion cells are considered to have an advantage compared to smaller-sized cylindrical cells in the mid- to long-term. This is due to vast possibilities in cell design optimization combined with synergistic effects in handling larger, but fewer cells during production, as well as so far unexploited economies of scale. In comparison, the production of smaller-sized cylindrical cells has already or will approach its optimum in the near future.[101] Efforts to standardize prismatic and pouch-type Li-ion cell formats across the automotive industry to increase or accelerate the impact of economies of scale following the example of cylindrical 18650 or 21700 cells,[100] are, however, yet ongoing.[102]

With the quest to find the ideal cell design for a given application being a highly proprietary task, which strongly depends on battery system related constraints, only very little data considering cell design specific questions has been reported by battery manufacturers or OEMs so far. Determining thermal gradients across cells depending on the cell's format under various operating conditions[103,104] can give an indication of the homogeneity of cell operation throughout its lifetime. This can identify potential hot spots which can either lead to accelerated aging or to local overheating, including the risk of a thermal event in case the chosen cooling strategy cannot resolve this issue. However, such investigation requires not only external but also elaborately integrated internal temperature sensors,[105–110] which is complicated and hazardous for the personnel involved.

This becomes especially apparent when considering that cells often need to be manipulated throughout the assembly process or, with regard to most commercially sourced cells, that cells need to be opened and manipulated after assembly has already been carried out by the manufacturer. Besides the impact of the cell's format, the influence of a cell's electrode and tab design on its electrochemical and thermal performance has also been studied.[111,112] To be able to evaluate not only thermal gradients for this purpose, local currents[113] and potentials[114–118] or even local displacements[119] can be used indicating not only inhomogeneities within the electrodes during operation but also during resting phases[117] and characterization procedures.[116] Such data can be further used to validate models that describe the distribution in temperature, potential, and current within cells[115,118] in order to study the impact of cell format[120] and/or electrode and tab designs[111,120–126] on a broad data basis with a high degree of freedom choosing from endless cell formats, electrode designs, and tab configurations.
However, such cell format and/or electrode and tab design related considerations are most often lacking a holistic evaluation of the impact of the investigated design variables on a battery system's performance, cost, and safety. In this regard, a generalization of the made observations is cumbersome, due to the nature of the studies carried out, and/or because a projection from the electrode and cell level to the system level is not possible, based on the underlying data.
One of the most complete studies trying to assess the impact of a cell's format and size on the battery as a whole was recently published by Fraunhofer battery alliance.[127] Cylindrical 18650 and 21700 cells were compared to large-format prismatic (PHEV2 and BEV2), as well as pouch-type cell formats (in accordance with DIN 91252[102]). The study considers the cell's energy densities and cooling capabilities, resulting module energy densities including cost breakdown from electrode fabrication to module assembly, and finally, evaluates the impact of a cell's format and size on battery safety. Despite the larger energy content of the BEV2 cell which will inevitably produce more heat during a possible internal short circuit posing a severe hazard, it is considered overall safer than small-sized 18650 or 21700 cylindrical cells, the smaller prismatic PHEV2 cell, or large-format pouch-type cells containing the same chemistry. This is thanks to the safety mechanisms that can be included in the large, rigid cell housing.[127] These include a safety vent which releases an excessive pressure build-up in a controlled manner, a current interrupt device (CID) which breaks the electrical contact at the positive terminal at too high pressure, and an overcharge protection device (OPD) which similarly fuses the cell based on a triggering pressure as a result from gas generation during overcharge. Safety vents and CIDs can be also found in cylindrical cells, whereas the flexible housing of pouch-type cells does not allow for additional safety devices to be included. Another advantage of the BEV2 cells comes with the detection of a critical cell state (e.g. cell overcharging or overheating) or even a possible cell fault (e.g. a sudden drop in cell voltage) by the BMS.[127] With less cells to be equipped with sensors and data to be logged, BMS topologies which allow for a complete battery monitoring and control can be included in the battery system. Furthermore, smaller cells require a complex electrical interconnection to build larger battery modules, packs or systems which can be more prone to failure resulting from mechanical loads (e.g. shocks and vibrations) than a rigid cell interconnection. Despite its considered high safety, the BEV2 cell format is estimated to range behind both 21700 and large pouch-type cells in the mid- to long-term future when it comes to energy density and cost. A final conclusion, however, cannot yet be drawn from this study. Even though it offers remarkably high detail in the considerations made, the substantial extent of presumptions that (still) needed to be made throughout preparing this design study leaves questions yet unanswered. These can be only resolved by knowing precisely all constraints of the battery system that is to be designed.[127]

Cell safety devices In order to be able to keep the safety level of cells even with nickel-rich cathodes at least at the same level as cells using NMC-111,[9] additional approaches on the material, electrode, and cell level need to be evaluated which allow for counteracting a material related increase in both hazards and risks associated with Li-ion cells. Besides safety vents, CIDs, and OPDs, further current interrupting or limiting devices such as one-shot fuses or self-resetting positive temperature coefficient (PTC) elements can be included in the cell averting the cell reaching critical temperatures due to an external fault such as an external short circuit.[128]
However, these devices not only add weight and cost the cell consuming space but may also affect the cell's reliability, performance, and cooling requirements. This is due to the possibility of premature or faulty tripping and based on an increased electrical resistance of the cell, resulting from the series configuration of the additionally integrated components and the cell's and electrode's electrical interconnections.[129]
Other possibilities to render cells intrinsically safe are to include safety mechanisms on the electrode and material level such as using separators with shutdown functionality as PP/PE/PP tri-layer separators. The middle PE layer softens and eventually melts at temperatures near 135 °C, clogging the pores of the outer PP layers exhibiting a higher thermal stability with melting temperatures around 165 °C, which effectively hinders the movement of Li-ions and consequently interrupts the current at too high temperatures.[42,43,128–131] Applying alternative electrolytes[129,132–134] and/or electrolyte additives[129,132–138] that improve electrode passivation, or which enhance the electrolyte's thermal stability, reduce its flammability, and/or include additional functionalities to the electrolyte such as an intrinsic bypass overcharge protection (e.g. redox-shuttle additives involving comparably low heat generation due to Joule heating[139]) or even a shutdown mechanism triggered at too high potentials or temperatures (e.g. polymerizing shutdown additives) may also be an elegant way to increase a cell's intrinsic safety without incorporating additional devices. However, similar to passivating and/or functional coatings applied to electrodes, such an approach should neither impair the electrochemical performance of the electrodes and cell as a whole nor substantially increase the cell's cost. This restricts the quantities which can be added to the cell and, consequently, limits the desired effect.[129,132,138]
Both additionally included safety devices on the cell level as well as modifications on the material and electrode level, however, have their individual restrictions making, for example, a fuse incorporated in the cell's terminals ineffective toward an internal short circuit within the cell which, therefore, does not reduce the associated risk of a field failure. Hence, it needs to be distinguished between engineered solutions that increase a cell's abuse tolerance (such as Samsung SDI's "nail safety device"[140]) and mechanisms that make a cell intrinsically safe.

The described overall trend of applying high capacity materials in Li-ion cells which further tend to increase in size, means that additional measures are also likely to be considered on the module and pack or system level in order to protect the battery's environment from a cell failure, including the associated possibilities of thermal runaway and thermal propagation.[31,32] This must be ultimately taken into account when designing a Li-ion battery for a specific application.
As pointed out in Fig. 1.6, not only a tradeoff between cost and safety, but also the effectiveness of modifications on different levels of battery integration need to be considered. This implies that tackling safety related issues already on the material and electrode level will facilitate the development of an intrinsically safe battery system, whereas secondary measures on the module and pack or system level will be limited in the overall effectiveness in terms of both cost and safety (see Fig. 1.6).

1.3 The runaway problem

In literature, Li-ion battery safety is most often associated with (the absence of) thermal runaway of a Li-ion cell. The term *thermal runaway* in the context of Li-ion battery safety, however, is not clearly defined, leading to confusion regarding what is actually referred to.[141] This circumstance has resulted in a rather excessive and colloquial use of the term, especially when a hazardous condition such as fire or explosion of a Li-ion cell is described.
According to the Oxford English Dictionary, a *runaway reaction* is "a chemical or nuclear reaction that is accelerated by the products of the reaction or its effects (such as a rise in temperature), so that it becomes uncontrollable and continues until there are no reactants left".[142] Hence, a *thermal* runaway reaction can be generally understood as a reaction that becomes uncontrollable specifically due to the effect of produced heat and the accompanied increase in temperature which itself accelerates underlying reactions and consequently the heat generation rate, temperature rise, and so forth. From a pyrotechnics perspective, a thermal runaway is "the situation where the rate of energy production for a pyrotechnic material exceeds the rate of energy loss. This results in a continuing temperature rise, which leads to spontaneous ignition and possibly an explosion".[143] These two definitions already give a quite good overview of the involved scientific disciplines and the related emphasis of what is to be considered during a thermal runaway of a Li-ion cell. On the one hand, a fundamentally reaction kinetics based consideration of thermal runaway is crucial for a most quantitative evaluation which, on the other hand, also needs room for the involved hazards such as auto-ignition and explosion.
In the context of Li-ion battery safety, a thermal runaway reaction can often be identified as the cause of subsequent thermal, chemical, and even kinetic hazards such as the exposure to high temperature fluids and gases which may be released together with fire and flame during venting, rupture, or explosion of a battery (see Fig. 1.2) — however, a thermal runaway is not the hazard itself in the first place.

The theory behind the development of a thermal runaway can be best visualized with the aid of a so called Semenov diagram originating in thermal explosion theory,[144] which can be also applied to Li-ion batteries (see Fig. 1.8).[49,145,146] In such a diagram, the heat generation rate resulting from underlying exothermic reactions and the heat dissipation rate based on the thermal interaction of the reaction vessel (i.e. the cell's housing in this case) with its surroundings are shown as a function of temperature. For clarity, a Semenov diagram explicitly does not describe a system's transient change of heat rate with temperature — this would add a third dimension to the diagram. Whilst the heat generation rate is assumed to rise in an exponential fashion with temperature following Arrhenius law, the heat dissipation is considered to only increase in a linear fashion with temperature due to Newton's law of cooling primarily accounting for convective heat transfer, whilst neglecting the impact of radiation. If the cooling performance is large enough, two intersections with the heat generation rate can be observed (see Fig. 1.8). At lower temperatures, the cooling performance is smaller than the reaction heat (1). This leads to a temperature rise toward the first intersection which can be considered as a stable operating point (2). A further increase in temperature beyond this point is intrinsically suppressed with the heat dissipation then exceeding the heat generation rate (3). If the temperature is further raised by additional means toward the second intersection between cooling performance and reaction heat, an unstable operating point is formed (4) allowing for no further cooling down to reach a stable operation. *Vice versa*, with no further heat added to the system, no uncontrolled heat up would occur. However, as soon as the unstable operating point is exceeded, the cooling performance becomes too small in comparison and cannot stop the system from heating up excessively (5), which can be understood as a point of no return or a thermal runaway event.

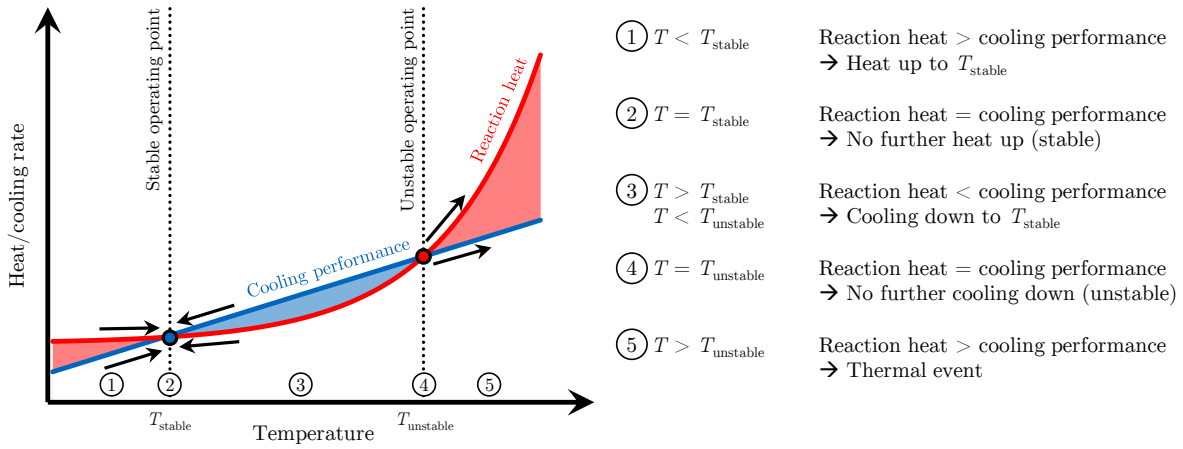

Figure 1.8: Semenov diagram representing the tendency of a Li-ion cell to develop a thermal runaway event depending on the underlying reaction heat due to exothermic side reactions (red line) and the prevailing cooling performance defined by the interaction of the cell with its surroundings (blue line) as a function of its temperature. If the reaction heat exceeds the cooling performance, the cell heats up (red area), whereas it cools down if the cell's heat dissipation surpasses its heat generation (blue area). A stable operating point forms (blue marker), if both a lower and a higher temperature results in an equalization between heat generation and heat dissipation which inhibits a further heat up beyond this point. An unstable operating point occurs (red marker), if a further temperature increase beyond this point cannot be controlled by the prevailing cooling condition. Modified in accordance with Refs. [49; 145; 146].

Hence, Li-ion battery safety is inherently related to a thermal problem.[147,148] The characteristics of heat generation are primarily defined by the thermal stability of the employed materials, whilst the heat dissipation is dependent not only on the cooling strategy with its prevailing heat dissipation mechanisms,[149] but is also defined by the format and size of a Li-ion cell with its intrinsically limited heat dissipation capabilities.[129,145]

However, what makes a true scientific evaluation of Li-ion cell thermal runaway difficult is the aforementioned lacking definition of the thermal runaway itself with its specific triggers, related mechanisms, and consequences. Strictly speaking, an operation past the unstable operating point as shown in Fig. 1.8 is referring to a thermal runaway.[143] However, in practical applications it is often not possible to quantify heat rates without a calorimetric setup under which all relevant thermal boundary conditions are well-defined, making an identification of the thermal runaway initiation difficult or impossible.
With the temperature and transient temperature evolution of a specimen being relatively easy to address and quantify, often a temperature related criterion is considered.[150] The so called onset temperature of a thermal runaway at which a potentially critical self-heat up of a Li-ion cell can be detected earliest is mostly defined by the accuracy and resolution of the measurement based on the applied measurement equipment and prevailing thermal test conditions.
In literature, the onset temperature of a thermal runaway is therefore mostly defined as the temperature at which a self-heating rate (SHR) of $0.2\,°C\,min^{-1}$ can be reliably detected.[150] Such defined onset temperature can be considered close to, but slightly higher than, the temperature of unstable operation.

As a self-heating due to discharge and charge operation can easily exceed this value within the cell's designated operating window, depending on the prevailing cooling conditions,[151] this criterion is better understood as an abnormal or additional heating outside a cell's designated temperature range. At this SHR threshold, it is considered that a properly designed thermal management system should be able to detect such an undesired temperature rise in the first place and to adequately increase its cooling performance in the second place so that a stable operation can be again achieved. However, if the SHR exceeds $10\,^{\circ}\mathrm{C\,min^{-1}}$ at higher temperatures, no cooling system is considered efficient enough to be able to reach stable operation which can be considered as a fully developed thermal runaway.[150] With the sensible heat of a system defined by its overall heat capacity C_p ($\mathrm{J\,K^{-1}}$) and transient temperature increase neglecting latent heat effects due to melting and evaporation, the heat balance between heat generation $\dot{Q}_{\mathrm{gen}}$ (W) and heat dissipation rate $\dot{Q}_{\mathrm{dis}}$ (W) can be written as follows:

$$C_p \frac{\mathrm{d}T}{\mathrm{d}t} = \dot{Q}_{\mathrm{gen}} - \dot{Q}_{\mathrm{dis}} \tag{1.4}$$

which results in

$$\mathrm{SHR} = \frac{\mathrm{d}T}{\mathrm{d}t} = \frac{\dot{Q}_{\mathrm{gen}} - \dot{Q}_{\mathrm{dis}}}{C_p} \tag{1.5}$$

This implies that a SHR criterion characterizing thermal runaway of a Li-ion cell not only accounts for the balance between heat generation and dissipation but also involves its thermal inertia. Furthermore, considering the impact of a cell's geometry on its temperature distribution as well as the limited capability of surface-mounted temperature sensors to capture a cell's overall temperature, let alone its core temperature, certain limitations of this approach become apparent. These limitations make a SHR criterion on its own more of a qualitative than a quantitative method to describe a cell's thermal runaway characteristics.

In order to be able to derive a generally applicable thermal runaway definition in the context of Li-ion battery safety, first of all, the characteristics of the individual exothermic side reactions defining the heat generation rate which eventually leads to cell thermal runaway need to be evaluated and quantified. Secondly, with cell thermal runaway being closely related to cell-internal triggers as a frequent root cause for locally exceeding a certain threshold temperature, internal short circuit related conditions need to be exclusively analyzed. Lastly, with both the trigger and heat rate of a runaway reaction characterized, the thermal interaction of a cell with its surroundings needs to be considered which depends not only on the prevailing cooling condition but also on the cell's format and size with its inherent thermophysical properties and, hence, thermal inertia and resistivity.

Heat generation at elevated temperatures When considering an exothermic decomposition reaction with a starting temperature T_{start} and a convective cooling with a convection coefficient h_{c} ($\mathrm{W\,m^{-2}\,K^{-1}}$), defining the slope of the heat dissipation curve, and an environmental temperature T_{∞}, defining the stable operating point T_{stable} as shown in Fig. 1.9 a, it becomes obvious that neither the starting temperature nor the heat generation rate of the exothermic decomposition reaction can be easily assessed especially without precisely knowing the heat dissipation rate. This problem can be solved by ensuring adiabatic conditions which implies that the heat dissipation rate becomes zero and, hence, forms a horizontal line with the effect that the unstable operating point T_{unstable} and the starting temperature of the exothermic decomposition reaction coincide (see Fig. 1.9 b).

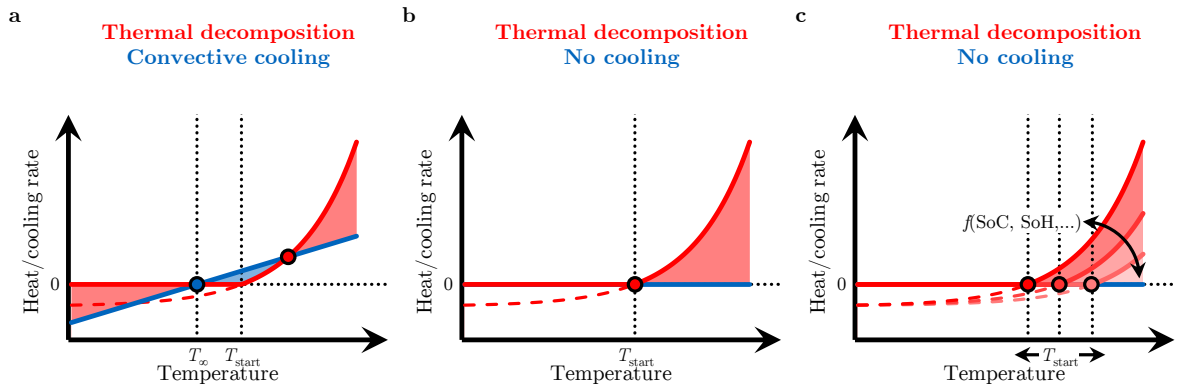

Figure 1.9: Schematic representation of strategies aiming at quantifying both the starting temperature T_{start} and heat generation rate of additional exothermic side reactions at prevailing convective cooling conditions (a) as well as under adiabatic conditions (b and c) qualitatively showing the influence of a cell's SoC and SoH on the heat generation characteristics of additional exothermic side reactions (c). Lines, markers, and coloring are chosen in accordance with Fig. 1.8.

Such conditions can be guaranteed by applying so called accelerating rate calorimetry (ARC) or adiabatic reaction calorimetry which uses this principle to determine the heat generation rate of exothermic reactions knowing the specimen's heat capacity.[152] In order to increase the specimen's temperature to the starting temperature of exothermic side reactions, the sample is incrementally heated up by the calorimeter followed by a resting phase in which a self-heating due to an exothermic reaction of the specimen is to be detected (lower ARC threshold often chosen at $0.02\,°C\,min^{-1}$). This so called heat-wait-search (HWS) operation is then followed by an adiabatic operation in which the calorimeter temperature follows the specimen's temperature until the reaction is completed or the temperature limits and/or heat rate limits of the calorimeter are exceeded.[152] With the aid of such considerations, not only the impact of various materials and material combinations on the kinetic characteristics of the exothermic reactions can be studied but also the associated dependency on state variables can be evaluated, such as SoC and state of health (SoH), which characterize a cell's operational voltage range as well as its operational life (see Fig. 1.9 c).

Heat generation at elevated currents The same principle of adiabaticity can also be applied to study an exothermic cell-internal trigger resulting in the investigated exothermic decomposition reactions (see hatched area in Fig. 1.10 a). Examining a high rate discharge experienced during an external or internal short circuit, the starting temperature of exothermic decomposition reactions can be rapidly exceeded without the need of artificially raising the cell's temperature by means of external heating. However, as only a small fraction of the cell's electrochemical energy is required to rise its temperature beyond the starting temperature of exothermic side reactions (see section 1.1.2), a complete evaluation of the electrochemical and electrical trigger mechanism is often not possible as the cell's response and behavior becomes rapidly dominated by an interference with the triggered chemical exothermic side reactions. In order to be able to separate a cell's short circuit characteristics from its sequence of thermal failure mechanisms, an approach of ideal cooling to prevail an isothermal cell temperature can be applied. This is schematically shown in Fig. 1.10 b resulting in a vertical heat dissipation curve.
If the cell's size and geometry allow for such an approach, the cell is constantly held at or near its stable operating point defined by the environmental temperature. The heat rate can be then determined by the extracted heat accumulated in a defined passive or active heat sink.

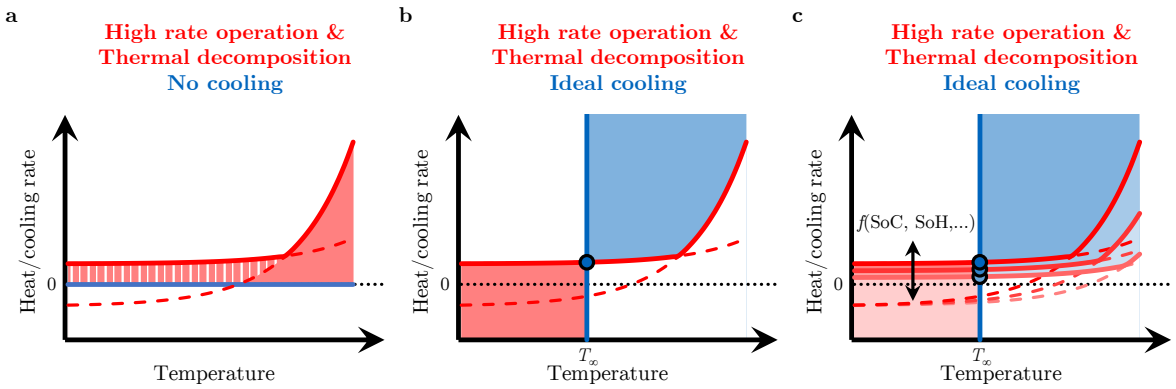

Figure 1.10: Schematic representation of strategies aiming at quantifying the heat generation rate resulting from high rate cell operation such as experienced during external or internal short circuits under adiabatic conditions (a, hatched area) as well as at prevailing ideal cooling conditions (b and c) qualitatively showing the influence of a cell's SoC and SoH on the heat generation characteristics resulting of both high rate cell operation and additional exothermic side reactions (c). For the purpose of simplicity of the graph, only one reaction is assumed to take place at a certain temperature. Lines, markers, and coloring are chosen in accordance with Fig. 1.8.

By varying the isothermal temperature and, hence, the stable operating point, a more complete picture of thermal runaway can be drawn including the role of cell-internal triggering mechanisms. Similar to adiabatic conditions, the influence of different materials and electrodes, as well as the impact of SoC and SoH, can be studied which can be further extended by varying test parameters (1.10 c).

Heat dissipation in the context of thermal runaway Together with the characterized exothermic decomposition reactions and studied trigger mechanisms, the influence of a cell's thermal interaction with its surroundings on cell thermal runaway can be evaluated. This is schematically shown in Fig. 1.11 a. Whilst the same convective cooling condition as shown in Fig. 1.9 a is sufficiently high to form a stable operating point when solely exothermic decomposition reactions occur, the combination with a triggering short circuit only allows for the development of an unstable operating point in this example. By reducing the environmental or coolant temperature as shown in Fig. 1.11 b, stable operation can be achieved through shifting the heat dissipation curve toward lower temperatures. Another approach to achieve such stable operation is to enhance the overall cooling capability at a constant environmental or coolant temperature as shown in Fig. 1.11 c which is represented by an increasing slope of the heat dissipation curve. This can be obtained by either increasing the environmental heat transfer coefficient or by improving the thermal design of the cell (i.e. reducing its thermal resistance). Assuming that additional exothermic side reactions dominate a cell's heat generation at a certain temperature even during high rate operation as shown in Fig. 1.11, the graphic representation in Fig. 1.11 b and c suggests that a cooling strategy preventing thermal runaway resulting from an internal or external short circuit can be only found if a stable operating point is possible before additional exothermic side reactions take over.

By combining the approaches presented here, a cell's thermal runaway mechanism can be most thoroughly characterized facilitating eventually a definition of thermal runaway itself. Additionally, the choice of materials as well as the design of a battery's electrodes, cells, and modules, with its pack or system topology including an inherent thermal management can be optimized toward an intrinsically safe configuration.

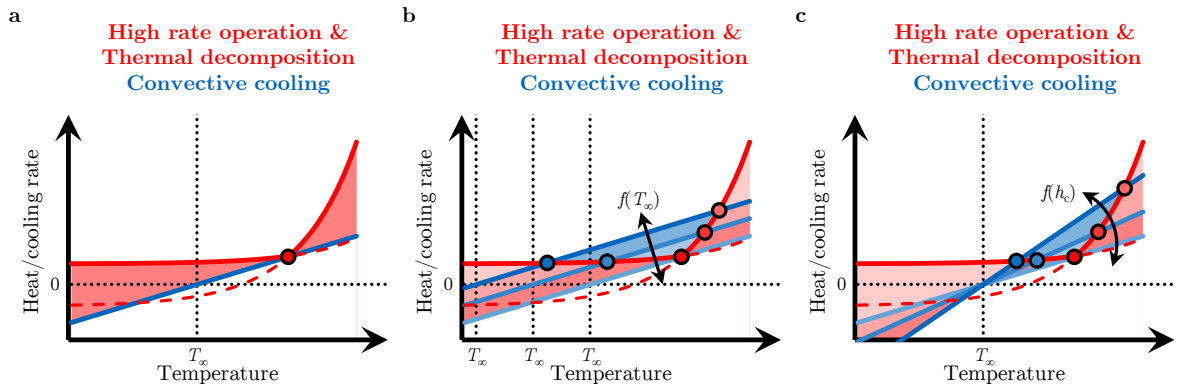

Figure 1.11: Schematic representation of strategies aiming at evaluating the interplay of the heat generation rate resulting from high rate cell operation and additional exothermic side reactions with convective cooling as shown in Fig. 1.9 a (a) for varying temperatures of the environment or coolant (b) as well as for varying convective heat transfer coefficients (c). For the purpose of simplicity of the graph, only one reaction is assumed to take place at a certain temperature. Lines, markers, and coloring are chosen in accordance with Fig. 1.8.

If not otherwise specified in the further course of this work, a cell's thermal runaway is denoted as a general self-accelerating heat up involving exothermic side reactions.

1.4 Experimental evaluation of lithium-ion battery safety

With the example of cell thermal runaway revealing the complex nature of Li-ion battery safety, experimental assessment of all safety-related characteristics of a Li-ion battery powered product is vital. Such assessment is not only relevant to material, cell, and battery manufacturers, improving the quality of their products, but is also crucial for OEMs to develop and distribute solutions which fulfill legally binding regulations guaranteeing a safe handling and operation at all times.[54]

Extensive reviews of reported Li-ion battery safety related experimental efforts have been published throughout the last years covering thermal stability investigations on the material and electrode level, as well as abusive tests on the cell, module, and pack or system level.[26,48–50] These experimental efforts have helped to achieve a basic understanding of the key mechanisms resulting in cell thermal runaway and its associated effects.[26,34,49,150]

Considering the increasingly high effort in terms of testing infrastructure guaranteeing a safe test execution required with an increasing energy content of the specimens, a substantial amount of literature can be found on the material and electrode level, which gradually decreases when moving forward to the cell, module, and pack or system level. An excerpt of most relevant experimental activities and findings is briefly given in the following.

1.4.1 Thermal stability investigations from material to cell level

With Li-ion battery safety being inherently related to a thermal problem, as thoroughly discussed in chapter 1.3, both the thermal stability of the employed individual materials and the interaction amongst them needs to be assessed. As a means of quantifying a specimen's thermal stability characteristics, defined thermal boundary conditions allowing for a calorimetric evaluation are required.

In order to be able to correlate the observed thermal characteristics of the studied specimens to underlying mechanisms resulting in such thermal behavior, additional methods, such as thermogravimetric analysis (TGA) as well as diffraction and mass spectroscopy based methods are frequently used. Commonly applied calorimetric methods in Li-ion battery safety research involve ARC,[152,153] differential scanning calorimetry (DSC),[154] or a combination of both[155] in order to determine the thermal stability of cells and cell components initiating and fueling thermal runaway. Less frequent calorimetric methods also try to quantify associated fire hazards during cell opening, venting, rupture, and explosion e.g. by means of a fire calorimeter such as so called Tewarson or cone calorimeters.[156,157]
Calorimeters are often used to determine the overall characteristics of a thermal decomposition reaction such as the temperature at which the reaction initiates, the amount of heat produced throughout the reaction characterizing the reaction enthalpy, and the peak heat rate together with its corresponding temperature. Furthermore, they can also be used to analyze decomposition reaction kinetics including frequency factor, activation energy, and reaction mechanism or reaction order.[152,158,159] Such consideration of reaction kinetics is crucial to allow for a sophisticated evaluation of thermal stability characteristics of a given material or material combination as experienced in Li-ion cells.[34,160]

Thermal stability of graphite anodes Starting from a temperature of approximately 80 °C[33,161] or less (temperatures reported as low as 69 °C[162] or 57 °C[163]), the passivating SEI layer starts to exothermically decompose, peaking in its reaction heat around 100 °C,[164] until completed around 120 °C.[33,34] The SEI layer predominantly consists of stable inorganic components, such as lithium fluoride (LiF), lithium oxide (Li_2O), and lithium carbonate (Li_2CO_3), as well as metastable organic components, such as polymers and semicarbonates ($ROCO_2Li$) with R representing a low-molecular-weight alkyl group.[165] Besides additional reactions, the most likely reaction mechanism of the exothermic SEI layer decomposition is considered to be:[164,166]

$$(CH_2OCO_2Li)_2 \longrightarrow Li_2CO_3 + C_2H_4 + CO_2 + 0.5\,O_2 \tag{1.6}$$

or in combination with intercalated or metallic lithium

$$2\,Li + (CH_2OCO_2Li)_2 \longrightarrow 2\,Li_2CO_3 + C_2H_4 \tag{1.7}$$

These observations have been supported not only by ARC measurements carried out by Richard et al.[164] and MacNeil et al.[161] for various types of carbon, but also by manifold DSC studies carried out by Maleki et al.,[155] Zhang et al.,[154] Roth et al.,[167] Wang et al.,[162] and Ryou et al.[168] Beyond this temperature, the graphite anode is no longer protected by the SEI layer, allowing for a direct contact between lithiated graphite and the electrolyte, which is considered to result in a balanced reaction of secondary SEI layer re-formation and decomposition[164,169] within a temperature range of 120 °C to 250 °C. In the presence of EC ($C_3H_4O_3$), SEI layer formation is assumed to follow:[170]

$$2\,C_3H_4O_3 + 2\,Li^+ + 2\,e^- \longrightarrow (CH_2OCO_2Li)_2 + C_2H_4 \tag{1.8}$$

Beyond this temperature range, this balanced reaction is overruled by the thermal decomposition reaction and reaction of the graphite anode with the electrolyte.[26,166] In the presence of EC, such reaction could follow:[34]

$$2\,Li + C_3H_4O_3 \longrightarrow Li_2CO_3 + C_2H_4 \tag{1.9}$$

Combined calorimetric and high energy X-ray diffraction (XRD) analysis of the thermal stability of lithiated graphite supported the theory of a balanced reaction of SEI layer re-formation and decomposition occurring between 110 °C to 230 °C, based on a continuous decrease of intercalated lithium within this temperature range.[171] Further, less noticed,[172] exothermic reactions within the graphite composite anode include the reaction of metallic or intercalated lithium with fluorinated binders such as PVDF,[155,166,173,174] which starts around 200 °C[174] to 240 °C, with its reaction peak around 290 °C until completion around 350 °C.[147]
Besides a straightforward dependency of the graphite anode's thermal stability on the composition of the electrolyte including solvent and salt[175] as well as the nature of the composite electrode referring to its active components,[161,171] also the electrode morphology including its specific surface area defined by the size and shape of the active material particles has been observed to have a considerable influence.[161,176]

Thermal stability of cathodes Such dependency of an electrode's thermal stability on its electrode morphology, however, is not exclusive to graphite anodes alone but can be equally observed for cathode materials such as LCO and NCA.[177,178] Amongst others, the thermal stability of various cathode materials was compared via DSC by MacNeil et al.[84] as well as via ARC by Jiang et al.,[179] Wang et al.,[180] Roth,[181] and Doughty et al.[150] suggesting a decreasing thermal stability from LFP, LMO, NMC, NCA, LCO, to LNO, whereas the thermal stability of NMC decreases considerably with increasing nickel content approaching the thermal stability level of NCA/LCO for its nickel-rich representatives.[26,93,95] Whilst the strong P=O covalent bond of the LFP phosphate octahedral structure increases its thermal stability preventing an excessive oxygen release during decomposition,[26] cathodes based on transition metal oxides, and especially layered oxides, tend to release substantial amounts of oxygen accompanied by a strong exothermal decomposition reaction which, in the case of LNO, has been reported to be sufficient to completely combust the electrolyte solvent.[182]
Amongst others, MacNeil et al.[183–185] studied the thermal stability of LCO via both DSC and ARC investigating the kinetics of its thermal decomposition reaction, which was extended by the work of Yamaki et al.[186] through combined TGA and mass spectroscopy measurements and supported the work of Biensan et al.[147] by reporting noticeably exothermic decomposition reactions of LCO with electrolyte starting from as low as 130 °C.[185] In the absence of electrolyte, Li_xCoO_2 (with $x = 0.5$) is expected to exothermically decompose at elevated temperatures according to:[185]

$$Li_{0.5}CoO_2 \longrightarrow 0.5LiCoO_2 + \frac{1}{6}Co_3O_4 + \frac{1}{6}O_2 \tag{1.10}$$

which in combination with electrolyte solvent (e.g. EC) assuming full solvent combustion proceeds to

$$Li_{0.5}CoO_2 + 0.1C_3H_4O_3 \longrightarrow 0.5LiCoO_2 + 0.5CoO + 0.3CO_2 + 0.2H_2O \tag{1.11}$$

With NCA showing a comparable, if not slightly higher, thermal stability compared to LCO at a considerably higher specific capacity and energy content,[38,180] the material has received growing attention throughout the last years. Starting from a temperature around 160 °C to 170 °C, a strong exothermic reaction can be determined via ARC,[180] and DSC,[187] which can be correlated to a severe oxygen release due to the sudden phase transformation from layered to disordered spinel phase around 175 °C and the subsequent formation of a rock salt phase (face-centered cubic unit cells with different space groups) examined via XRD combined with mass spectroscopy and X-ray absorption spectroscopy (XAS).[188]

With NMC materials of various composition exhibiting a highly appealing combination of high specific capacity, low cost, and a substantial thermal stability, NMC grades have been not only thoroughly examined in terms of their electrochemical performance but also with respect to their thermal stability.[79,95] NMC-111 for instance, shows superior thermal stability compared to both NCA and LCO.[180] With exothermic reactions observed from temperatures of 180 °C and beyond determined via ARC,[95,180] a delayed transition to rock salt after the transformation to spinel phase is considered to be one reason for the enhanced thermal stability of NMC-111 compared to other layered, nickel based materials such as NCA and LNO.[189] Besides XRD studies supporting this theory,[189] XAS results also underline the importance of cobalt inhibiting the phase transformation to rock salt, further revealing the impact of manganese stabilizing the layered structure at lower temperatures.[190] Increasing the nickel content whilst inevitably reducing the share of cobalt and manganese, compromises this stabilizing effect.[190] Such destabilization results not only in lower temperatures at which the thermal decomposition of the cathode material is initiated decreasing from over 180 °C for NMC-111 to approximately 120 °C for NMC-811, but also in an increased specific heat generation by more than 75 % (i.e. from 512.5 $\mathrm{J\,g^{-1}}$ for NMC-111 to 904.8 $\mathrm{J\,g^{-1}}$ for NMC-811).[93,95] Hence, alternative NMC materials containing a high share of manganese such as NMC-442 show a promising balance between energy content and thermal stability.[95] As pointed out in section 1.2, doping, concentration gradient or core shell materials, as well as primary and secondary particle surface modifications can enhance the thermal stability of nickel-rich NMC grades which is worth further investigation.[79,93,96,97]
The relatively high thermal stability of LMO was studied by MacNeil et al.[191] via ARC and Zhang et al.[154] via DSC showing relevant exothermic decomposition reactions starting from temperatures of 200 °C and beyond.

Thermal stability of electrolytes Besides the reaction of the electrolyte with anode materials $< 1.0\,\mathrm{V}$ (vs. $\mathrm{Li/Li^+}$) and cathode materials $> 4.3\,\mathrm{V}$ (vs. $\mathrm{Li/Li^+}$), a decomposition reaction which is coupled with a solvent oxidation is common to all layered cathode materials at elevated temperatures. The exact mechanism, however, is not understood as of yet. Both the positive active material itself (see Eqs. 1.10 and 1.11) or excessive oxygen released throughout the cathode decomposition process can react with the solvent leading to complete or partial combustion, which in the case of EC results in:[26,34]

$$2.5\mathrm{O_2} + \mathrm{C_3H_4O_3} \longrightarrow 3\,\mathrm{CO_2} + 2\,\mathrm{H_2O} \tag{1.12}$$

for a sufficient amount of oxygen available, or with not enough oxygen provided by the cathode resulting in an incomplete combustion releasing CO

$$\mathrm{O_2} + \mathrm{C_3H_4O_3} \longrightarrow 3\,\mathrm{CO} + 2\,\mathrm{H_2O} \tag{1.13}$$

Hence, through reduction and oxidation reactions at the anode and cathode, the electrolyte plays an important role in the thermal stability of both electrodes, which makes thermal stability measurements in the presence of electrolyte inevitable. The yet partly unclear oxidation mechanism of the electrolyte at the cathode leaves, however, the question unanswered to what extent exactly the electrolyte defines the thermal stability of materials, electrodes, and cells.[34]
Furthermore, both solvent and salt can decompose exothermically at elevated temperatures.[134] In dry conditions, $\mathrm{LiPF_6}$ salt, for example, starts to decompose to LiF and phosphorus pentafluoride ($\mathrm{PF_5}$) already below 100 °C, which is even further reduced when in contact with solvent.[134,192]

Mixtures of 1 M $LiPF_6$ or $LiClO_4$ with electrolyte solvents such as 1:1 PC:DMC, EC:DMC, PC:DEC, or EC:DEC revealed considerable exothermic peaks between 230 °C and 280 °C.[193] Depending on both $LiPF_6$ salt concentration and solvent mixture, Botte et al.[194] identified endothermic reactions below 200 °C, which were assumed to be related to a decomposition or phase change of the salt. First exothermic reactions were detected from approximately 200 °C onwards together with subsequent, more pronounced exothermic reactions starting from approximately 250 °C both increasing in reactivity with increasing salt concentration.[194]
Whilst the specific reaction heat that can be assigned to the electrolyte's thermal decomposition reaction alone lies below the heat generated from both anode and cathode, a partial or complete combustion of the solvent with oxygen released from cathode decomposition or from the environment, in case of cell leakage or venting, can exceed the contribution from both electrodes by far.[195] With a specific heat of combustion ranging between 11 kJ g^{-1} and 16 kJ g^{-1} for common $LiPF_6$ based electrolyte mixtures,[196] the process of venting including electrolyte evaporation, ignition, and combustion deserves further attention.[26,197] Until safer, yet electrochemically applicable, electrolytes are developed that reduce or rule out the likeliness of partial or complete combustion as expected from advanced ionic liquids,[198] inorganic liquid electrolytes,[199] or solid electrolytes,[200] such considerations are vital to understand and eventually control fire and explosion related Li-ion battery hazards.

Full cell thermal stability tests In order to evaluate the interplay of the partly simultaneously occurring and, hence, interacting exothermic decomposition reactions of anode, cathode, and electrolyte, thermal stability investigations of full cells are required. For this purpose, both quantitative calorimetric ARC tests[150,167,181,201–216] and rather qualitative thermal abuse tests,[215,217–223] such as so called oven tests or thermal ramp tests applying a constant environmental temperature or a constant heat rate, are used to examine small laboratory-scale (e.g. coin cells),[211] consumer-sized (e.g. 18650, 21700, or smaller sized prismatic or pouch-type cells),[150,167,181,201–203,206–210,212–215,218–221,223] and even large-format Li-ion cells (e.g. prismatic or pouch-type EV cells).[204,205,216,217,222]
Whilst cell level ARC tests can be considered to represent a worst-case scenario for a Li-ion cell not being able to dissipate the generated heat to its surroundings as soon as cell-internal exothermic side reactions occur, thermal abuse tests tend to represent a more realistic scenario in which cells also interact with their environment during cell thermal runaway. Such differing conditions will inevitably also lead to slightly different test outcomes which needs to be taken into consideration when comparing test results from different test procedures. Reported cell level tests underline the aforementioned impact of cathode material choice on the thermal stability of Li-ion cells.[150,181,202,206,207,209,214]
A further dependency of cell thermal stability on state functions such as a cell's SoC,[167,201,207,210,213,214] describing the cell's electrical energy content due to the degree of lithiation within both electrodes, as well as a cell's SoH,[208–210,213,216,219,224] describing a cell's degradation resulting from aging processes throughout its lifetime, can be evaluated by means of such tests which will be discussed in chapter 2. Besides a qualitative investigation of the interplay of various decomposition reactions, more quantitative investigations are also possible, which aim at separating the underlying reactions occurring during cell thermal runaway by combining material level calorimetric measurements with experiments on full cells.[211] Furthermore, thermal stability investigations on the cell level also allow for evaluating the impact of the separator's thermal and mechanical integrity inhibiting or fostering internal short circuits during cell heat up which may accelerate a cell's thermal runaway due to the additionally generated heat from high rate discharge operation.[26,43,223]

With ARC and thermal abuse tests not always representing real-life environmental conditions as the available air volume is often limited or minimized (e.g. when testing in an enclosed containment of finite size or when testing under inert conditions in nitrogen environment), the excessive heat that can be produced outside the cell housing due to the combustion of ejected carbonaceous materials is not evaluated properly.[225] Hence, a combination of cell thermal stability studies with tests examining the burning or fire behavior of cells during thermal runaway are required.[156,157,224–229] A quantitative analysis of the heat produced during the combustion of ejected material during cell venting and rupture can be carried out by using cone calorimeters,[157,224,229] Tewarson calorimeters,[156] or novel calorimetric configurations trying to break down all relevant heat fluxes from a cell's boundaries to its environment during cell thermal runaway.[224,225] By further examining the venting and ejection process *in-situ* during thermal stability tests by means of high speed radiography and X-ray computed tomography (CT),[220,221] a most complete picture of cell thermal runaway can be assessed that enables improvement of a cell's thermal stability by designing, for example, safety vents in such a way that an uncontrolled rupture or explosion can be avoided reducing cell related hazards.[220,221]

1.4.2 Abuse tests and emulation of internal short circuits on the cell level

A cell's intrinsic thermal stability combined with both internal and external triggers define the hazard and risk of a cell thermal runaway. Therefore, not only cell thermal stability tests need to be considered but also tests representing a likely mechanical or electrical abuse, or even an unlikely manufacturing related internal short circuit, are required (see Fig. 1.5). Compared to the quantity of reported literature dealing with the thermal stability of a cell and its components, approaches and findings characterizing a cell's behavior during mechanical and electrical abuse are limited — and even more so considering experimental means of triggering a representative internal short circuit. The most relevant results are summarized briefly in the following.

Mechanical abuse tests Due to the limited mechanical strength of a Li-ion cell, mechanical cell abuse may result in a critical deformation of the cell's external and/or internal structure that can trigger consecutive events such as rupture of the cell's casing including leakage and/or separator failure, which can result in electrode contact and, hence, local short circuits within the cell.[230] With cells being most often an integral part of a module, pack or system which should reduce an external mechanical impact to a minimum, static mechanical abuse tests on the cell level, such as pinch tests, crush or punch tests, compression tests, and three-point bending tests, can be considered as a means of evaluating the mechanical abuse tolerance of a cell when the external enclosure of the cells fails and/or when misused during cell handling.[231] With the capability of mechanical cell abuse tests to provoke cell-internal defects that may result in local short circuits within the cell, a considerable amount of activities in this area is focusing on developing tests which can reproducibly cause separator rupture and short circuit formation as a possible way to approach a realistic field-like internal short circuit.[232] Especially pinch tests and round blunt tests have attracted growing attention in this field forming a promising alternative to rather rigorous nail penetration tests by provoking only few layers to form a short circuit whilst keeping the cell casing airtight.[232–234]

The most established mechanical cell abuse test, however, is the nail penetration test which is also an essential part of several abuse testing standards.[53] This test is mostly carried out with a sharp steel rod or nail (e.g. 3 mm in diameter at a velocity of $80\,\mathrm{mm\,s^{-1}}$) penetrating the cell geometry completely.

Nail penetration tests are generally considered not to represent a realistic internal short circuit due to the violence of the short circuit formed, involving multiple layers of the cell to short via a comparably substantial conductor, a premature cell opening, and a considerable heat dissipation extracted via the nail from the cell's center to its surroundings (i.e. the nail actuating device).[232,233,235] Despite the reported dependency of the test outcome on the nail's size, speed, and location of penetration,[53,236,237] its reproducibility in triggering cell thermal runaway and its general acceptance for cell, module, and pack or system level tests in international standards and regulations make it a commonly applied mechanical cell abuse test today.[217,237–239]
Maximizing the insights gained from test execution by, for example, including temperature sensors within the nail or by simultaneously analyzing the mechanical damage pattern the nail causes during penetration form a promising route which is worth following.[236,240–242] Further varying the configuration of the nail,[243] by using a ceramic shaft with a nickel tip as suggested in IEC TR 62660-4:2017,[244] enables development of the nail penetration test toward a more realistic internal short circuit scenario where strongly localized short circuits around the nail's tip combined with a reduced thermal interaction of the cell with its surroundings would be possible.

Internal short circuit emulation The focus of mechanical cell abuse tests reveals the necessity of developing a test which can trigger a truly realistic internal short circuit that would eventually cause field-like failures if unnoticed. Several promising approaches to reproduce realistic internal short circuits have been discussed in literature, however, without yet revealing a clear favorite. Besides the controlled, slow external indentation with, for example, a sphere, cylinder, or round blunt,[232,245] most suggested solutions involve a manipulation of the cell to include cell-internal defects, ideally during cell manufacturing. These modifications involve, for example, incorporating a particle between the electrodes formed of a low melting-point metal or metal alloy which can be melted at moderate temperatures to soak into the separator and eventually form a short circuit between the electrodes (e.g. gallium or Bi/Sn/In melting at temperatures <40 °C or <70 °C).[245] Further, more rigorous modifications involve placing an L-shaped nickel particle between the electrodes before assembly (as suggested in IEC 62660-3:2016[246] and IEC 62133-2:2017[247]) which is supposed to trigger an internal short circuit within the cell upon external pressure. A similar approach, which does not require external pressure but external heat, is to include a particle formed of a shape memory alloy which pierces the separator at its trigger temperature of approximately 70 °C.[248] Another concept showing promising results is the incorporation of a small phase change material (PCM) platelet whilst introducing a defined hole in the separator before cell assembly.[249–251] By external heating, the PCM platelet melts at 70 °C or below (paraffin wax) and allows for a contact between the electrodes through the hole in the separator. By further modifying the platelet and the electrodes, various kinds of internal short circuits can be triggered (e.g. between negative and positive current collectors, between negative current collector and positive composite electrode, between negative composite electrode and positive current collector, or between negative and positive composite electrode), which is expected to result in differing short circuit resistances, heat dissipation, and amounts of heat being produced which, consequently, leads to a varying severity of the triggered short circuit.[252,253] By combining such approaches with further techniques such as high speed radiography, X-ray CT, infrared (IR) thermography, and calorimetric measurements analyzing the dissipated heat from the cell via its surface and via material ejection, a thorough evaluation of thermal runaway evolution from internal short circuits is possible.[250,251] This further allows the development of novel strategies that mitigate internal short circuit formation and/or thermal runaway initiation.[254]

External short circuit tests Despite the lack of a strongly localized heating, external short circuits are closely related to internal ones. However, external short circuit tests applied to Li-ion cells have yet not received a thorough evaluation in literature even though external short circuit tests range among the most common tests applied from Li-ion cells to packs or systems. This minor attention can be partly explained by rather mild test outcomes reported, in which no cell thermal runaway could be observed either based on the applied test conditions, the investigated combination of active materials, or due to additional safety devices that might protect the cell from overheating during external short circuits.[217,218,255,256]

A closer investigation into external short circuits applied to NMC and NCA pouch-type cells was provided by Kriston et al.[257] The study suggests some rate limiting effects occurring during short circuit scenarios that are worth further consideration in order to understand the short circuit or high rate discharge behavior of electrodes and cells, which may explain observations made throughout both internal and external short circuits. This will be more closely investigated in chapter 3.

Overcharge and overdischarge tests Due to the additional electrochemical energy charged into Li-ion cells, combined with growing structural instabilities of transition metal oxide based cathodes including oxygen release at a low stoichiometry,[258–260] as well as a fostering of significant lithium plating at high degrees of lithiation and low potentials within the graphite anode,[260–262] cell overcharge significantly differs from other thermal, mechanical, and electrical abuse scenarios, posing a severe hazard which needs to be evaluated further via systematic cell overcharge tests.[217,218,263,264]

Contrary to the general awareness of hazards associated with cell overcharge, cell overdischarge, and its related side reactions have as of yet received little consideration. Similar to the risk of cell overcharge, a BMS should in theory avoid cell overdischarge by monitoring individual cell voltages and by consequently maintaining each cell within its designated voltage related operational window. However, in case of BMS malfunction or inappropriate parametrization, the safe voltage limits of individual cells might not be kept, leading to either an overcharge or overdischarge during operation.

Whilst there is no evidence of an increased thermal instability due to the overdischarge process,[265] a repeated violation of the cell's lower voltage limit can eventually result in anode potentials exceeding 3.1 V vs. Li/Li^+, which may trigger copper dissolution at the anode with a subsequent deposition on the cathode.[67,68,70,266] Such a process might result in the formation of copper dendrites, which can grow through the separator and may lead to internal short circuits with associated cell thermal runaway and battery field failure.[68] Similar to an overcharge which can trigger internal short circuits due to lithium dendrite formation,[264] a forced overdischarge can potentially be used to provoke representative internal short circuits.[33,68,266] However, further evaluation of such an approach is necessary in order to avoid interference of the test outcome with possible structural instabilities of cathode materials during overcharge and/or an excessive capacity fading affecting electrode stoichiometry during both overcharge and overdischarge.

1.4.3 Propagation tests on multiple cell arrangements

With the growing understanding of the interplay between cell thermal stability, internal short circuits, and battery pack or system topology influencing the occurrence of field failures and defining the intrinsic safety of Li-ion batteries, an evaluation of the impact of a single cell thermal runaway on the module and pack level has become increasingly important.[141] This understanding has recently resulted in legislative activities reviewing the need for so called (thermal) propagation tests in both automotive regulations and air transportation standards involving Li-ion batteries.[141] Early theoretical work in this field has highlighted the impact of both cell thermal stability and thermal interaction among the cells within a battery pack or system on the tendency for the development of a full battery failure based on the propagation of thermal runaway.[267] First experimental work investigated the behavior of multiple cell configurations of consumer-sized cylindrical[268,269] and prismatic[269] Li-ion cells as well as large-format prismatic[270] Li-ion cells studying the influence of geometrical, thermal, and electrical configuration on the propagation characteristics due to a single cell thermal runaway which was induced via nail penetration[268,270] or selective cell heating.[269] Alternatively, replacing one cell within the multiple cell configuration with a resistive cell-shaped heater also showed successful results in triggering thermal propagation.[271,272] The results suggest that the thermal interaction between the cells can be significantly altered by including defined gaps between the cells as well as strategically placing heat sinks and heat shields within the geometric configuration of the cells, which can affect the propagation characteristics such as its speed as well as its likelihood of occurrence.[53,268,269]
However, these efforts demonstrate the urgent need for a properly designed method that reliably triggers a field-like internal short circuit, which may initiate a cell thermal runaway with a subsequent thermal propagation on the module and pack or system level.[141] Such development is crucial to be able to assess a Li-ion battery's intrinsic safety, which eventually enables the design of safe Li-ion batteries.

1.5 Modeling and simulation in the context of battery safety

On the one hand, with Li-ion battery models becoming increasingly elaborate and, on the other hand, with sufficient computational resources becoming more easily available, Li-ion battery modeling and simulation has gained substantial attention throughout the last years. Examples ranging from fully mechanistic to strictly empirical models describing Li-ion battery behavior over a wide range of length and time scales during a manifold of operating conditions and applications have been presented in the last years.[273] Furthermore, due to the increasing maturity of Li-ion battery safety models, computational modeling and simulation in this particular field has also increased in popularity. Most safety-related Li-ion battery models focus on a cell's behavior during abusive conditions such as those experienced during mechanical overload, short circuit scenarios, and overheating. Due to the variety of phenomena and the complexity of interactions occurring during safety-related events, a combination of two or more modeling disciplines is mostly required in order to guarantee general applicability and validity of the model.[274,275]
In the following, mechanical, electrical-/electrochemical-thermal, and chemical-thermal modeling and simulation works in the field of Li-ion battery safety are highlighted before fully coupled modeling approaches combining these disciplines are summarized. Such coupled approaches allow for a most thorough evaluation of the interplay between a trigger mechanism and not only its direct but also its subsequent effects (e.g. a cell thermal runaway that is initiated by the heat generation from a local short circuit within the cell which itself is triggered by mechanical cell abuse).

Modeling short circuit triggers Related to the experimentally observed possibility of triggering local short circuits within Li-ion cells upon mechanical abuse, mechanical Li-ion battery models have become increasingly popular as a means of studying the underlying mechanisms resulting in such short circuits in more detail.[231] The mechanical behavior of Li-ion cells has been thoroughly investigated in the past by simulating a cell's behavior during numerous static mechanical load profiles such as those resulting from pinch tests, crush or punch tests, compression tests, and three-point bending tests. Within these mechanical models, the cell's jelly roll is being considered as either a homogeneous solid with effective mechanical parameters[276–282] or as a layered structure accounting for individual components of the cell.[283–285] With the experimentally observed simultaneous drop in cell voltage (indicating a short circuit) and a drop in mechanical load (indicating a softening or cracking of one or more layers), mechanical cell abuse models are capable of determining a critical load which may trigger a local short circuit within the cell due to an external mechanical load.[276,279,281,282,284,285]
However, so far little modeling work has been reported which investigates the formation of a field-like internal short circuit. The work of Jana et al.[286] describes lithium dendrite formation and growth through the separator by using a phase field method, depicting localized processes of electrodeposition and electrodissolution defining the growth and shrinkage of lithium dendrites. With the aid of such models, not only critical current densities can be identified that will result in a suppression or in a fostering of lithium dendrite formation, but also geometrical requirements of the separator can be derived that will block lithium dendrites from growing through the separator forming a short circuit (e.g. by defining a maximum pore size). This modeling approach can be further used to investigate the formation of other metallic dendrites such as copper dendrites on the cathode resulting from repeated overdischarge[68] or discharge at too high currents with anode potentials exceeding the copper dissolution threshold, as well as the suggested dissolution of foreign nickel or iron particles on the cathode with its accompanied deposition on the anode.[33,35]
A model that can describe a particle-induced separator fatigue, due to the localized stress and strain imposed on the separator coming with a reversible swelling and contraction of the active materials and electrodes during charging and discharging[287] as well as an irreversible expansion during aging,[119,288] however, is still missing today and requires further attention.

Modeling thermal runaway triggers With a short circuit often being accompanied by excessive currents and heat generation rates, local or global overheating of the cell is likely, which potentially triggers additional exothermic side reactions and will eventually result in cell thermal runaway if the heat is not dissipated adequately. Whilst the implementation of a short circuit within an equivalent circuit model (ECM) is a rather straightforward task which allows for studying the effects of short circuits with little computational effort,[289] the predictability of such an empirical model is generally limited, due to its defined parametrization window and its intrinsic shortcoming in the modeling approach, simplifying a cell's behavior to predominantly resistive and capacitive effects. This model assumption makes ECMs incapable of describing rate limiting effects based on ion movement and/or limited reaction kinetics which are likely to occur during a high rate discharge operation.
In order to be able to describe a cell's electrochemical response during short circuit scenarios with relevant mechanisms, electrochemical or physical-chemical modeling approaches are required. Homogenized Newman-type models have been widely accepted and applied in Li-ion battery modeling and simulation for years, describing reaction kinetics as well as mass and charge transport within the liquid and solid components of porous electrodes, whilst accounting for effects which are characteristic for concentrated solutions.[273,290,291]

Due to their general versatility,[292–294] Newman-type models have consequently also found their application in short circuit modeling and simulation with slight modifications in order to guarantee numerical stability.[295,296] By further accounting for reversible[297] and especially irreversible heat effects, which are rather common sources of heat generation in Li-ion battery modeling and simulation,[298] together with a cell's heat capacity as well as its interaction with the environment due to heat conduction, convection, and radiation,[148,298] a cell's electrochemical and thermal response to short circuit conditions can be readily described.[295,296] Considering not only local concentrations, potentials, and current densities between the electrodes, but also the current density distribution along or across the electrodes due to the finite dimensions of the electrode geometry,[115,121,299,300] allows the electrical and thermal effects across the cell's dimensions to be described for various types of short circuits. These effects depend on the geometry of the electrodes and cell, the electrical characteristics of both the short circuit and the electrodes, as well as the thermophysical properties of the cell's components. An early representative of such a model which couples electrical and electrochemical effects to thermal effects was presented by Yamauchi et al.[301] describing local currents and heat generation rates resulting from nail penetration within a spirally wound electrode configuration, as found in cylindrical cells. Despite demonstrating the general applicability of such modeling approach to describe the local short circuit behavior of Li-ion cells, a key finding of the presented results was the observation that a cell's rate capability making it suitable for HP applications, also increases its heat generation throughout shorting which leads to a higher tendency of overheating and, consequently, cell thermal runaway.[301]

A work presented by Santhanagopalan et al.[252] studying the nature of internal short circuits by comparing the impact of individual cell components involved in internal short circuit formation, revealed that a short circuit between the positive electrode's aluminum current collector and the negative electrode's composite electrode poses a worst-case scenario. This can be attributed to the combination of a comparably small short circuit resistance, poor heat dissipation capabilities, and low temperature levels at which exothermic side reactions are triggered.

Further works, focusing on local short circuits formed as a result of pinch tests[235] or nail penetration tests[155,302–306] revealed a significant impact of a cell's SoC,[235,302,306] its format and size,[235,303,304,306] and the cell' inherent resistance on the electrical and thermal characteristics of the short circuit.[305,306] Furthermore, the influence of the resistance of a short circuit,[303,306] its location,[235,303,305] and the overall shorted area[303,305,306] can also be evaluated with the presented models deriving implications considering suitable cooling conditions[235,303] depending on the cell's local temperature distribution.[235,303–305]

A simulation-based comparison of various short circuit scenarios such as an external short circuit resulting from a contact of the cell's current collecting components,[253] a local short circuit due to nail penetration,[253,307] and an internal short circuit induced by impurities[253,307] was given by Zavalis et al.[253] and Zhao et al.[307] The results suggest that true internal short circuits formed, for example, via particle contamination result in quite different current and heat generation characteristics compared to local short circuits resulting from, for example, nail penetration.[253,307] This can be explained with the effect that the entire short circuit current, coming from all electrode layers of a cell, needs to pass through one small spot within only one electrode layer in the case of a true internal short circuit.[307] Despite the smaller electrical contact area and, hence, comparably larger electrical resistance of an internal short circuit leading to smaller overall currents, this strongly localized effect can easily lead to so called hot spots with large temperatures due to Joule heating at the short circuit site.[253] An observed effect of rate limitation occurring during various types of short circuits limiting the evolving current[253] was supported by the modeling and simulation work of Fang et al.,[308] based on experiments of Ramadass et al.[238] Within this work, the possibility of self-limiting internal short circuits was discussed,

which could be observed during short circuits with a small electrical resistance. As a result from the large initial currents, saturation and depletion effects within the solid and liquid components of the positive electrode could be observed, that led to rapidly diminishing currents and, consequently, heat generation rates.[308] Whilst an externally triggered overheating of Li-ion cells is mostly implemented by a simple modification of the boundary conditions of a thermal model, other means of provoking exothermic side reactions due to cell-internal events such as overcharging have not received noticeable attention in the battery safety modeling and simulation community so far.[34]

Modeling thermal propagation triggers With exothermic side reactions being inherently associated with cell thermal runaway which, in the context of multiple cell arrangements, may result in thermal propagation, the focus of thermal runaway related models lies within the thermal description of heat produced throughout chemical reactions such as decomposition and combustion reactions.
Besides few first principle or *ab initio* calculations describing the process of electrolyte decomposition based on molecular orbital calculations,[309] most models describing cell thermal runaway are based on thermal decomposition reaction models derived from DSC and/or ARC measurements by fitting power functions or kinetic triplets formed of frequency factor, activation energy, and reaction mechanism or reaction order to the measured heat rate and temperature data.[147,152,158,159,310,311]
A commonly applied model, describing a cell's thermal response due to decomposition reactions of both graphite and LCO with electrolyte, was first introduced by Hatchard et al.[311] This model is based on extensive experimental and theoretical work presented by Dahn's group, with Richard et al.[164,169] describing the decomposition reactions of lithiated graphite with electrolyte and MacNeil et al.[183,184] characterizing the decomposition reaction of LCO with electrolyte. With the aid of the model, a cell's thermal response due to cell thermal abuse as experienced, for example, in an oven test could be reliably described based on the kinetics of the underlying reactions.[311] This lumped or 0D thermal model was further extended by an electrolyte decomposition reaction and solved within a 3D cell geometry which allowed for the investigation of the local initiation and cell-internal propagation mechanism of thermal decomposition reactions triggered by a localized heat source representing an internal short circuit.[34,312] Besides various applications of this approach investigating different cell geometries and thermal boundary conditions,[313–316] a coupling of this chemical-thermal decomposition model to electrical-[317] and electrochemical-thermal models[26,318] has been reported in literature, in order to describe the initiation of thermal decomposition reactions with possible cell thermal runaway as a result from internal short circuits, such as experienced during separator melting[26,318] or as a result from local short circuits triggered by nail penetration.[317]
Recent adaptions and extensions to the original chemical-thermal modeling approach account for: An electrochemically motivated SEI layer formation and thermal decomposition reaction,[319] an extended dependency of the graphite's chemical decomposition reaction on its specific surface area,[320] an additional reaction of residual lithiated graphite with electrolyte,[321] and a substitution of kinetic triplets in order to study cells with cathode materials differing from LCO.[34,160,322] Further extensions of the original model include the mathematical description of endothermic effects due to electrolyte evaporation and subsequent venting[323–325] as well as a simplified depiction of additional heat sources such as cell external combustion reactions.[326] Despite the considerable experimental effort in preparing material samples and conducting calorimetric measurements combined with the associated data analysis to identify suitable kinetic triplets as well as the crucial model validation via full cell experiments, the discussed commonly applied thermal-chemical modeling approach enables high validity and allows for an easy adaptability.

However, reported validated sets of kinetic triplets are scarce which makes model parametrization for active materials other than MCMB and LCO within an $LiPF_6$ and EC based electrolyte difficult, not to mention dependencies on electrode morphologies or state functions such as SoC and SoH.

Modeling thermal propagation and fully coupled phenomena With slight adaptions of the original chemical-thermal modeling approach to account for a cell stack formed of six 25 Ah prismatic NMC cells, thermal propagation within this configuration was successfully modeled and validated with experimental data showing good agreement.[270,327] An approach to simplify the complexity of thermal propagation models and to save both experimental resources and computational time is to apply a single reaction kinetic model for the simultaneously occurring thermal decomposition and combustion reactions within Li-ion cells.[328] Such a reduced cell model can be parametrized via calorimetric data gained from full cell measurements instead of DSC and/or ARC measurements of individual materials and material combinations.[224] Thermal propagation measurements of defined multiple cell arrangements can be used to validate the chosen modeling approach as presented for 18650 sized graphite/LCO cells.[328] However, in order to adequately describe the process of cell thermal runaway or thermal propagation which is triggered, for example, by mechanical abuse such as indentation or nail penetration, fully coupled approaches are required that describe mechanical, electrical, electrochemical, thermal, and chemical effects.[275] Such models can be increasingly found in literature which pose a promising field of further research.[329–332] With ever growing model complexity, alternative computational approaches are required to reduce computational time for solving coupled models which account for a variety of mechanisms and effects. This is crucial, in order to not only be able to describe single Li-ion cells but also multiple cell arrangements, modules, and packs.[275,333]

1.6 Thesis outline

As shown in sections 1.4 and 1.5, battery safety testing and battery safety modeling and simulation have been so far treated as more or less two individual disciplines. Recent activities in both fields have emphasized the need for developing a complementary picture that uses the capabilities of battery safety modeling and simulation, revealing insights into failure mechanisms that are too difficult or too expensive to test, together with engineered battery safety tests, providing an invaluable data basis for both assessing a battery's safety performance and for validating and enhancing the prediction accuracy of battery models.[275] All of which is the motivation for this work.
Within this thesis, a workflow is presented, combining experimental work with modeling and simulation, in order to first separate a Li-ion cell's thermal behavior from its electrochemical and electrical performance before the interaction between these characteristics is evaluated. This approach allows ruling out the difficulty of trying to asses a cell's safety related characteristics by evaluating superimposed phenomena such as those that occur during a short circuit triggered cell thermal runaway.

As pointed out in section 1.3, different experimental approaches need to be followed in order to be able to achieve such task. However, despite readily available calorimetric measurements such as DSC and ARC to determine the heat generation of both materials and cells at elevated temperatures, novel and alternative experimental methods need to be developed and applied for the evaluation of a cell's electrochemical and thermal short circuit characteristics as well as a cell's cooling capabilities.
From a modeling perspective, the required separation of mechanisms is an inherent key feature which makes simulation based studies attractive in the very first place.

However, with the experimental difficulty of separating individual characteristics of a cell which rate it safe or unsafe, true model validation is often lacking which generally diminishes the significance of simulation results.

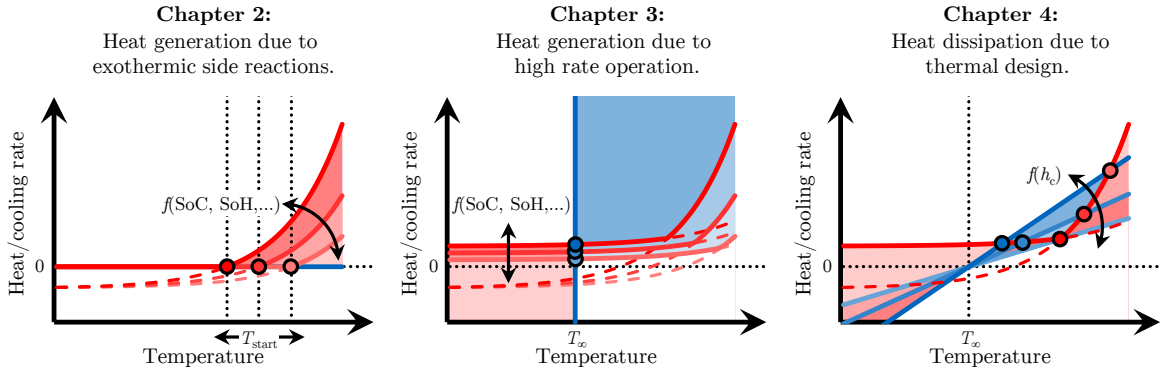

Figure 1.12: Schematic representation of thesis outline in accordance with Figs. 1.8 to 1.11.

With the problem of Li-ion cell thermal runaway and the associated lack of common understanding, key characteristics of **thermal runaway evolution** (see chapter 2), its **initiation** (see chapter 3), and possible **mitigation strategies** (see chapter 4) are evaluated in this thesis as suggested in chapter 1.3, which is schematically shown in Fig. 1.12.

In order to first of all characterize the dynamics and magnitude of heat generation following exothermic side reactions, calorimetric measurements on the material and cell level need to be carried out at elevated temperatures, e.g. under adiabatic conditions (see left of Fig. 1.12). In section 2.1, current activities reporting the further use of calorimetric measurement data to derive kinetic parameters are reviewed and put in the context of modeling and simulation.
With the described current attention of Li-ion battery research activities toward NMC materials of various grades, exothermic side reactions evolving from thermal decomposition of manganese rich NMC-442, as well as its interaction with electrolyte including electrolyte oxidation, are characterized and described via kinetic triplets in section 2.2. These kinetic triplets are derived from two-component ARC measurements following a reaction model based data analysis. Together with the adequately mathematically described thermal decomposition reaction and interaction of MCMB with electrolyte, the resulting thermal runaway characteristics of a 5 Ah pouch-type Li-ion cell is mathematically described and compared to full-cell measurement data. Furthermore, a dependency of exothermic side reactions and associated kinetic triplets on state functions such as SoC describing a cell's relative electrochemical energy content as well as SoH covering its degradation throughout lifetime is evaluated.
Based on these findings, the self-accelerating nature of a Li-ion cell's heat generation can be described resulting from individual exothermic side reactions which occur at elevated temperatures. These considerations are the basis for characterizing the **evolution of cell thermal runaway**.

In order to derive critical heat generation rates that may overheat a Li-ion cell and eventually trigger exothermic side reactions, high rate discharge operations such as those experienced during short circuits need to be evaluated. Hence, such investigation not only involves the rate capability of Li-ion electrodes and cells but even more importantly characterizes the associated heat generation rate. In order to study a complete short circuit, which is not interrupted by electrolyte leakage or venting, and to further not interfere with exothermic side reactions, the cell's temperature must be kept within an uncritical range (see middle of Fig. 1.12).

In section 3.1, mechanisms defining the rate capability of materials, electrodes, and Li-ion cells are briefly described and put into the context of high rate discharge operation as well as abusive short circuit conditions. In section 3.2, the rate capability of graphite/NMC-111 coin cells with defined variations in anode morphology are studied by both isothermal experiments and physical-chemical modeling and simulation. Within this context, observed characteristics of a premature rate limitation can be correlated to severe salt concentration gradients within the liquid electrolyte resulting in local depletion and large overpotentials. These concentration gradients can be directly altered by the electrode morphology and the associated transport length for Li-ions to travel from the anode to the cathode. In order to guarantee numerical stability of the developed homogenized three-dimensional electrode model under such extremes, a concept of salt diffusion limited reaction kinetics is applied.
In section 3.3, a quasi-isothermal calorimetric test setup is further suggested that allows to determine both the electrical and thermal response of single-layered pouch-type Li-ion cells to external short circuits. By varying the characteristics of the studied graphite/NMC-111 cells such as electrode loading and tab configuration, a cell's electrical and thermal short circuit behavior can be most thoroughly investigated. These investigations are further extended by varying test conditions such as temperature, SoC, and external short circuit resistance. The presented experimental data serves as an excellent basis for model validation which is carried out in section 3.4. By analyzing simulated transient concentration profiles and calculated overpotentials, the experimentally observed short circuit characteristics and rate limitations can be explained. This allows for a systematic study of design parameters that may result in a short circuit tolerant electrode and cell design.
With the presented experimental data basis and the validated physical-chemical modeling approach, heat generation due to high rate operation such as occurring during short circuits can be evaluated. These methods are essential for describing an **initiation of thermal runaway**.

By coupling the validated physical-chemical modeling approach with higher dimensional models, accounting for electrical effects along the current collectors, as well as thermal effects across the cell's electrode stack or jelly roll, the response of larger sized cells to short circuits as well as the effect of prevailing cooling conditions can also be mathematically described. An adequate maximum control of cooling conditions throughout experiments is therefore necessary to evaluate the interplay between a cell's geometry and its cooling capabilities (see right of Fig. 1.12).
In section 4.1, a coupled modeling approach is introduced, which is based on the physical-chemical model describing the cell's local high rate discharge as presented in section 3.4, an electrical model accounting for differences in current density distribution along the electrodes, and a thermal model depicting the effect of local heat generation and dissipation. By altering the boundary conditions within the thermal model in order to account for different cooling strategies, the possibility of mitigating an initiation of cell thermal runaway is discussed, depending on the format and size of the studied cells.
In order to be also able to validate cell models, which calculate the thermal response of Li-ion cells of various formats and sizes as a result of heat generation and heat dissipation, novel experimental setups are required which allow for a maximum control of prevailing cooling conditions. In section 4.2, a strategy to parametrize and validate a semi-empirical electro-thermal cell model is described and exemplarily shown for a large-format pouch-type cell containing a graphite anode and a blend of NMC and LMO as the cathode.
With the presented methods, not only cooling conditions can be studied which allow for a maximized cooling performance for a given format and size of a cell, but also geometric cell designs can be evaluated which allow for a cooling strategy that might reduce or minimize the risk of overheating during short circuits. Such an approach is crucial for developing **thermal runaway mitigation strategies**.

2 Heat Generation due to Exothermic Side Reactions

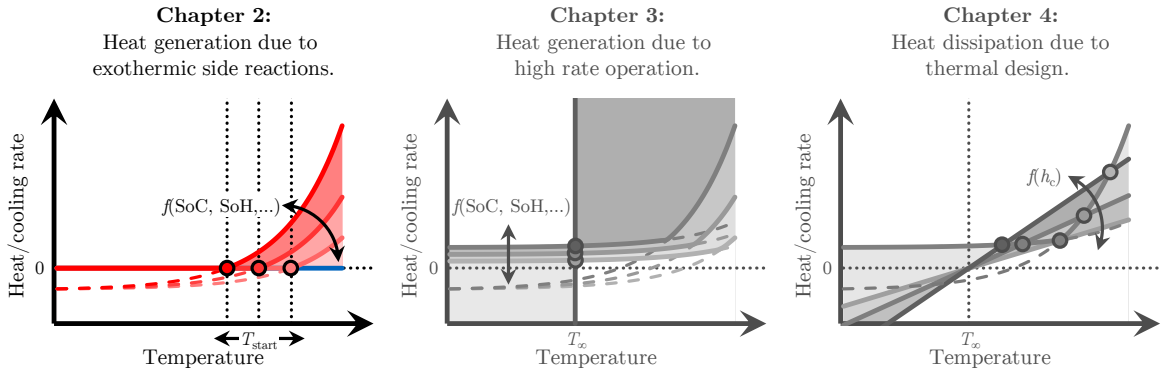

Figure 2.1: Outline of chapter 2.

Quantifying the heat generation arising from exothermic side reactions associated with the thermal stability of a cell's composite electrodes and electrolyte is crucial in order to evaluate the evolution of cell thermal runaway.
As described in section 1.4.1, readily available and widely applied calorimetric methods such as DSC and ARC can be used to assess these characteristics and to further evaluate the kinetics of the involved reactions. With a reliable kinetic description of exothermic side reactions, dominating reactions leading to a certain cell response can be identified by means of modeling and simulation. Such considerations are indispensable to evaluate the impact of individual materials and material combinations, as well as their interplay on the resulting thermal behavior of the cell during thermal runaway.
In this chapter, reported studies and approaches evaluating the kinetics of exothermic side reactions of a cell's components are briefly reviewed before ARC studies are presented, which aim at a model based data analysis of exothermic side reactions for MCMB/NMC-442 cells accounting for a varying SoC and SoH (see Fig. 2.1).

2.1 Kinetic description of exothermic side reactions

As pointed out in section 1.5, a strong discrepancy between the growing need for valid models, that can describe a cell's thermal runaway characteristics based on individual exothermic side reactions, and the sparse data that is available and has yet been used to parametrize such models can be observed.
On the one hand, this lies within the vast experimental effort to supply the necessary measurement data as summarized in section 1.4.1 and, on the other hand, can be explained with the lack of standardized and commonly accepted methods of analyzing the experimental data in order to derive a valid set of parameters describing the underlying exothermic side reactions.

This lack of suitable data and methods has resulted in the erroneous application of exothermic side reaction models parametrized toward MCMB/LCO cells, even when completely different electrode materials are supposed to be described with the chosen model.[334] The combined work of Richard et al.,[164,169] MacNeil et al.,[183,184] and Hatchard et al.[311] as well as the extensions and modifications reported Spotnitz et al.[34] and Kim et al.[312] forms the most widely accepted and applied cell thermal runaway model reported in literature today (see section 1.5). With the current trend of growing attention to NCA and nickel rich NMC materials, there is, however, an urgent need to re-evaluate model parameters reported almost 20 years ago for LCO cells.

Besides the calorimetry related works presented in section 1.4.1, which predominantly aim at a first identification and description of underlying exothermic side reactions, Dahn's group suggested to use the data of both two-component DSC and ARC measurements to also identify reaction parameters as already suggested by Kissinger,[158] Ozawa,[159] and Townsend et al.[152] All suggested methods essentially try to fit the following equation to experimental data:

$$\frac{\mathrm{d}\alpha}{\mathrm{d}t} = k \cdot f(\alpha) = \gamma \cdot e^{-\frac{E_\mathrm{a}}{k_\mathrm{B} T}} \cdot f(\alpha) \tag{2.1}$$

The rate of reaction conversion $\frac{\mathrm{d}\alpha}{\mathrm{d}t}$ is consequently defined by a reaction rate constant k (s^{-1}) and the associated reaction mechanism or reaction order $f(\alpha)$. The reaction rate constant k can be essentially related to the frequency factor γ (s^{-1}), activation energy E_a (J), and Temperature T of a reaction together with Boltzmann's constant k_B as described by the Arrhenius equation. The combination of frequency factor γ, activation energy E_a, and reaction mechanism $f(\alpha)$ can be also referred to as a so called "kinetic triplet". Together with the specific heat of the reaction H ($\mathrm{J\,kg}^{-1}$), the heat produced throughout the reaction can be fully described as a function of the degree of reaction conversion α which is essentially linked to the heat rate $\frac{\mathrm{d}T}{\mathrm{d}t}$ ($\mathrm{K\,s}^{-1}$) and, consequently, to the temperature T of the reaction.

Whilst an extraction of a reaction's frequency factor γ and activation energy E_a can be easily achieved via, for example, Kissinger's method applied to DSC measurements of a sample's thermal behavior at varying heat rates,[158] the reaction mechanism $f(\alpha)$ cannot be easily determined from such an approach, which is essentially treating the sample's kinetic behavior as being independent from the reaction mechanism.[334] With DSC profiles being furthermore rather insensitive to the chosen reaction mechanism $f(\alpha)$,[184] ARC measurements can be used to identify a function that resembles the shape of both DSC and ARC profiles over a wide range of temperatures and heat rates.

Several works have reported an extraction of kinetic parameters from DSC[171,334,335] and TGA[177,186] experiments for electrolytes,[335] anode,[171,186,334] and cathode materials[177,334] based on Kissinger's and Ozawa's method. Furthermore, novel approaches such as deconvolution methods have also been discussed in order to enhance and facilitate a kinetic description of exothermic side reactions.[336]

However, an extraction of such kinetic parameters from ARC measurements can scarcely be found in literature, except for the original results reported by Richard et al.[164,169] and MacNeil et al.[183,184] Such an approach, however, essentially allows the inclusion of the reaction mechanism $f(\alpha)$ in the extraction of kinetic parameters such as frequency factor γ and activation energy E_a.[152] This implies that different combinations of kinetic triplets are seemingly possible in order to describe the same reaction. The kinetic triplet that shows the best match with the experimental data can, hence, be regarded as the most suitable description of the exothermic decomposition reaction.

An efficient approach that allows the evaluation of kinetic triplets from ARC measurements will be discussed in the following section for a variety of reaction mechanisms, describing two-component systems formed of electrolyte wetted MCMB and NMC-442 materials.

2.2 Influence of state of charge and state of health on reaction kinetics

Within this section, the article titled *Thermal Analysis of $LiNi_{0.4}Co_{0.2}Mn_{0.4}O_2$/Mesocarbon Microbeads Cells and Electrodes: State-of-Charge and State-of-Health Influences on Reaction Kinetics* is presented.

Fresh and cycled 5 Ah pouch-type cells were investigated formed of an MCMB anode and an NMC-442 cathode together with an electrolyte containing 1 M $LiPF_6$ in EC:DMC 3:7 (by weight) with 2 wt% vinylene carbonate (VC) and 0.5 wt% lithium bis(oxalato) borate (LiBOB). Results from ARC measurements of electrolyte wetted electrode materials are analyzed and correlated to full-cell ARC measurements by using an iterative reaction model based data analysis. The suggested approach allows for further calculation of the thermal full-cell behavior based on the identified exothermic side reactions. Whilst the reactions within the cathode are considered to dominate the full-cell thermal behavior at temperatures from ca. 160 °C onwards due to a comparably higher reactivity, an SEI decomposition and re-formation reaction is most likely to be defining the cell's behavior below this temperature. Yet, exothermic side reactions involving the SEI were not detected within the two-component measurements. A possible contribution of exothermic side reactions within the anode at temperatures beyond 200 °C was predicted by the thermal cell model, which is most likely overruled by further structural changes within the NMC cathode including considerable electrolyte oxidation. The presented method of iteratively fitting frequency factor γ and activation energy E_a of a chosen reaction mechanism $f(\alpha)$ to the two-component ARC measurements, combined with adapting the reaction's initial degree of conversion α_0, its initial temperature T_0, and its overall temperature rise ΔT, enables a meaningful kinetic triplet to be derived. Knowing the specific heat capacities c_p and masses m of active and inactive materials, the specific heat H as well as the starting temperature of the reaction T_{start} can be determined (i.e. $\alpha = 0$, see Fig. 1.9).

By applying the presented methods, not only a significant sensitivity of calculated reaction parameters on the assumed reaction mechanism can be pointed out, but also a considerable influence of both SoC and SoH on the reactivity of the two-component system can be quantified based on the specific heat and the calculated reaction rate constant. For the studied material combinations, Avrami-Erofeev expressions which have been applied in the past to describe e.g. non-isothermal solid-phase decompositions and phase transformations,[337] show slightly superior prediction accuracies of the underlying ARC HWS traces compared to the reported autocatalytic reaction mechanism to describe exothermic side reactions of LCO with electrolyte.[183,184] Whilst a lower SoC increases the thermal stability of both two-component systems and full-cells, a lower SoH reduces the thermal stability of the cathode which adequately compromises the thermal stability on the full-cell level. These observations can be correlated to XRD measurements of fresh and aged cathode samples at 100% SoH and 80% SoH with SoCs ranging from 100%, over 50%, to 0% which reveal a comparably lower degree of lithiation and, hence, reduced thermal stability for aged cathode materials especially at lower SoCs compared to the fresh counterparts. This shift in electrode balancing seems to be responsible for the observed increased reactivity of the cathode samples and, hence, reduced full-cell thermal stability for the chosen aging procedure. If, however, this effect is the only cause for the observed characteristics and whether Li-ion cells generally behave in the same way with ongoing aging remains unclear. Therefore, especially the impact of the chosen aging strategy needs to be further studied in order to to allow for a more thorough evaluation of the interplay of aging and safety.[208,338]

Despite remaining discrepancies between the predicted and measured full-cell behavior, this work shows the importance of combining two-component and full-cell ARC measurements with model based data analysis of individual exothermic side reactions. The kinetics of the underlying exothermic side reactions must be known and understood before full-cell thermal stability measurements can be sufficiently evaluated, identifying the contribution of each reaction to the observed full-cell behavior within a certain temperature range.
The described approach of combining measurement data with simulation results forms the basis for investigating the evolution of cell thermal runaway, depending not only on the chosen material combination but also on the cell's SoC and SoH. With the cell's electrochemical energy content and its age further affecting the amount and rate at which this electrochemical energy is released during a short circuit, such considerations are of utmost importance to fully study a cell's tolerance to both abusive conditions and field-like internal short circuits throughout its operating range and lifetime.

Author contribution Stephan Hildebrand designed and carried out ARC and XRD measurements and supported the model development. Alexander Rheinfeld initiated the experimental work, developed and carried out the model based data analysis, and conducted the simulation studies. Alex Friesen helped with the cell preparation and carried out aging experiments, whilst Jan Haetge initiated and coordinated the experimental work. The data was analyzed by Alexander Rheinfeld and Stephan Hildebrand. The manuscript was written by Alexander Rheinfeld and Stephan Hildebrand and was edited by Falko M. Schappacher, Andreas Jossen, and Martin Winter. All authors discussed the data and commented on the results.

Thermal Analysis of $LiNi_{0.4}Co_{0.2}Mn_{0.4}O_2$/Mesocarbon Microbeads Cells and Electrodes: State-of-Charge and State-of-Health Influences on Reaction Kinetics

Stephan Hildebrand, Alexander Rheinfeld, Alex Friesen, Jan Haetge, Falko M. Schappacher, Andreas Jossen, Martin Winter

Journal of The Electrochemical Society 165 (2), pp. A104–A117, 2016

Permanent weblink:
http://dx.doi.org/10.1149/2.0361802jes

Thermal Analysis of $LiNi_{0.4}Co_{0.2}Mn_{0.4}O_2$/Mesocarbon Microbeads Cells and Electrodes: State-of-Charge and State-of-Health Influences on Reaction Kinetics

S. Hildebrand,[1,2,=,*] A. Rheinfeld,[3,=,*,z] A. Friesen,[1] J. Haetge,[1] F. M. Schappacher,[1,z] A. Jossen,[3] and M. Winter[1,2,4,]**

[1]*MEET Battery Research Center, Westfälische Wilhelms-Universität Münster, D-48149 Münster, Germany*
[2]*Institute of Physical Chemistry, Westfälische Wilhelms-Universität Münster, D-48149 Münster, Germany*
[3]*Institute for Electrical Energy Storage Technology, Technical University of Munich, D-80333 Munich, Germany*
[4]*Helmholtz-Institute Münster, IEK-12, Research Center Jülich GmbH, D-48149 Münster, Germany*

The thermal stability of lithium ion batteries was studied by means of Accelerating Rate Calorimetry in Heat-Wait-Search operation on both electrode and cell level. Fresh and aged samples were investigated depending on the state-of-charge (SoC) of a 5 Ah pouch cell comprising mesocarbon microbeads and $LiNi_{0.4}Co_{0.2}Mn_{0.4}O_2$ as the anode and cathode materials. 1 M $LiPF_6$ in EC:DEC 3:7 (by weight) containing 2 wt% VC and 0.5 wt% LiBOB was chosen as the electrolyte. Measurements on the electrode level revealed a higher self-heating rate (SHR) of the cathode compared to the anode for all SoC and state-of-health (SoH) combinations in the temperature range where a self-sustaining decomposition reaction could be detected. A lower SoC showed a lower SHR of the electrode/electrolyte mixture with no reaction detected on the anode side $\leq$ 50% cell SoC. Cyclic aging led to a decrease in thermal stability of the cathode at lower SoC values with no significant influence on the anode implying a larger safety threat on the cell level. Avrami-Erofeev and autocatalytic reaction models were used to quantify the influences of SoC and SoH on reaction kinetics. Full cell measurements confirmed the observations at a higher SHR.
 [DOI: 10.1149/2.0361802jes]

Manuscript submitted November 13, 2017; revised manuscript received December 20, 2017. Published January 5, 2018.

Based on their high energy and power density combined with a long cycle life, high energy efficiency and low costs, lithium ion batteries are currently the state-of-the-art energy source for electric vehicles (EV).[1–3] A long cycle life requires excellent aging behavior, whereas a high energy and power density demands for a high level of safety in order to comply with automotive prerequisites.[4–6] Many studies have dealt with the investigation of aging and safety individually as well as their interplay.[4,7–13] Yet, these interactions are not fully understood. Accelerating Rate Calorimetry (ARC) has been reported to be a promising method to measure the thermal stability of samples under quasi-adiabatic conditions. This method can be applied from single battery materials[14–20] up to full cells.[11,13,21] Based on the prevailing quasi-adiabatic conditions, a worst-case scenario can be simulated. With no heat dissipation taking place, the generated heat can be evaluated by measuring the temperature increase of the sample, knowing its total heat capacity.[22] This behavior can be readily transferred to real life scenarios where heat dissipation during cell failure is partially inhibited by the cell surroundings.

Predicting a cell's behavior during thermal abuse conditions is a topic of major interest in order to prevent hazardous situations on the battery pack level such as the propagation of thermal runaway after a single cell failure.[23] Due to the complexity of cell thermal runaway dynamics influenced e.g. by material composition[14,15] and morphology,[24–26] modeling and simulation can help to identify the dominating processes and interactions within a single cell based on individual material decomposition reactions.[27–29] Characteristic kinetic parameters of predominantly empirical decomposition reaction models were reported to be determined via calorimetric measurements such as Differential Scanning Calorimetry (DSC) and ARC.[22]

Richard et al. started to use data of ARC Heat-Wait-Search (HWS) experiments in order to determine the activation energy of the reaction between a lithiated anode and the surrounding electrolyte for modeling and simulation purposes.[20,30] Further work in that direction was carried out to study the thermal decomposition reaction of delithiated cathodes containing $LiCoO_2$ (LCO).[14,31–33] These findings were the basis for numerous model implementations to describe the overall cell behavior during a thermal runaway[27,28,34] as well as its local effects.[35,36]

The work presented here focuses on studying the influences of a cell's state-of-charge (SoC) and state-of-health (SoH) on both the single electrode and the full cell thermal stability. In the first part of this work, ARC-HWS measurements are conducted and discussed on the electrode level. These findings are further correlated with X-ray powder diffraction (XRD) measurements in order to identify the underlying decomposition reaction mechanism within the cathode. In the second part of this work, the kinetics of the occurring decomposition reactions are investigated more closely by means of model based data analysis as previously suggested.[33] Based on this data analysis, influences of SoC and SoH on parameters of Arrhenius-type "kinetic triplets" are investigated. In the final part of this work, the identified reaction models are used to correlate the carried out ARC-HWS measurements on the electrode level with those conducted on the full cell level.

The studied electrode materials were harvested from medium sized (i.e. approximately 5 Ah) pouch type cells which were manufactured with the aid of an in-house laboratory scale manufacturing line. On the electrode level, two-component systems of composite electrode material and electrolyte (1 M $LiPF_6$ in ethylene carbonate (EC): diethyl carbonate (DEC) 3:7 (by weight) containing 2 wt% vinylene carbonate (VC) and 0.5 wt% lithium bis(oxalate)borate (LiBOB)) were examined individually. On the cell level, the corresponding pouch cells comprising electrodes with $LiNi_{0.4}Co_{0.2}Mn_{0.4}O_2$ (NCM-424, this work expressed as: NMC-442) as the cathode and mesocarbon microbeads (MCMB) as the anode active material were tested.

Experimental

Electrode manufacturing and cell assembly.—Pouch cells were assembled containing 18 cathode sheets (66 × 119 mm) and 19 anode sheets (68 × 121 mm) with the aid of an in-house laboratory scale manufacturing line. The composite electrode on the cathode side consisted of NMC-442 (BASF, Germany) as the active material, Super P (TIMCAL, Switzerland) as the conductive additive and polyvinylidene difluoride (PVdF) (Solvay, Belgium) as the binder with a mass ratio of 93:3:4. The resulting single-sided mass loading of the electrode after calendaring was 15 mg cm^{-2} at an average thickness of

[=]These authors contributed equally to this work.
[*]Electrochemical Society Member.
[**]Electrochemical Society Fellow.
[z]E-mail: alexander.rheinfeld@tum.de; falko.schappacher@uni-muenster.de

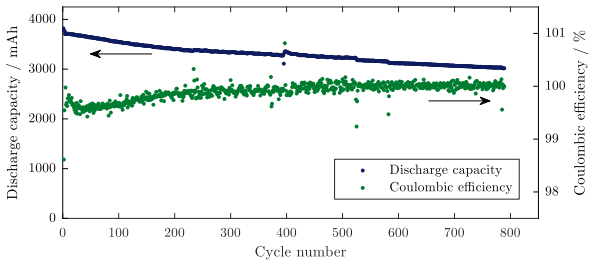

Figure 1. Cycling data of a 5 Ah pouch cell at 4C containing NMC-442 as cathode, MCMB as anode and a mixture of 1 M $LiPF_6$ in EC:DEC 3:7 (by weight) + 2 wt% VC and 0.5 wt% LiBOB as electrolyte, Data covers the first cycle after formation until the capacity faded to 80% of its initial capacity at 4C (i.e. 80% SoH, by definition in this work).

50 μm of the composite electrode. The slurry was cast on Al foil (15 μm thickness) as the current collector. The composite electrode on the anode side consisted of MCMB (10–28, Osaka Gas Chemicals, Japan) as the active material, hard carbon (Kureha, USA) and Super P (TIMCAL, Switzerland) as the conductive additives and PVdF (Solvay, Belgium) as the binder. The mass ratio was chosen as 83.2:9.3:0.5:7. The resulting single-sided mass loading of the electrode on the Cu current collector (10 μm thickness) was 10 mg cm^{-2} with an average thickness of 65.5 μm of the composite electrode after calendaring. A mixture of 1 M $LiPF_6$ in EC:DEC 3:7 (by weight) blended with 2 wt% VC and 0.5 wt% LiBOB (BASF, Germany) was used as the electrolyte. A Mitsubishi OZ-S30 polyester non-woven membrane with ceramic coating (30 μm thickness, Mitsubishi Paper Mills Ltd., Japan) was used as the separator.

Formation procedure.—The formation procedure consisted of five constant-current (CC) charge (first charge at 0.05C then at 0.1C) and discharge steps (0.1C) between 3.0 and 4.2 V at an ambient temperature of 20°C. The SoC was adjusted with a constant current step of 0.5C, followed by a constant voltage phase at 4.2 V until the current dropped below 0.05C (CC/CV, I < 0.05C) and the desired SoC was reached based on the discharge capacity of the previous cycle.

Aging procedure.—The aging procedure consisted of a sequence of a CC/CV (I < 0.05C) charge step to the charge voltage of 4.2 V followed by a CC discharge step until 3.0 V was reached. The charge and discharge steps were both performed at 4C in order to accelerate the aging procedure. The aging procedure was stopped at 80% SoH, whereas the SoH was defined by relating the discharge capacity at 4C to the discharge capacity at 4C of the third cycle after the formation procedure. This implies that the SoH determination chosen here includes effects of both capacity fade and resistance increase. The aging procedure as described was carried out at an ambient temperature of 20°C. Both the formation and cycling procedures were performed with the aid of a Series 4000 Battery Tester (Maccor, USA). Exemplary test data of cell aging is shown in Fig. 1. The cell shown was cycled for more than 750 cycles until the end-of-life criterion (i.e. 80% SoH) was reached. All cells cycled showed a similar aging behavior. Although at higher C-rates, accelerated aging phenomena like Li plating can occur during charging,[12,37,38] the discharge capacity faded without major drops during these cycles so that the aging process can be considered as fairly constant throughout the whole cycling procedure and therefore suitable for the carried out investigations. After cell opening, the cells also did not show any indication toward Li plating which supports this consideration. The same cells cycled at 1C showed comparable results, with a capacity fade to 80% after approximately 4000 cycles.

X-ray powder diffraction.—XRD measurements on the electrodes were performed on a D8 Advance Diffractometer (Bruker, Germany) with Cu K_α radiation ($\lambda = 0.154$ nm) equipped with a Lynxeye detector in order to investigate crystalline changes after aging. The diffractograms were measured with a step width of 0.021° 2Θ in the range of 15 to 90° 2Θ. A duration of 2 s per step was chosen.

ARC sample preparation.—For the ARC full cell measurements, the cells were placed in a stainless steel holder and were then transferred into the ARC. For the electrode measurements, the cells were first disassembled at the adjusted SoC within a dry room (dew point below −60°C). After the disassembly, the separated electrodes were transferred into a glove box (M. Braun Inertgas-Systeme GmbH, Germany) under argon atmosphere (6.0 purity, Westfalen Gas; O_2 < 0.1 ppm, H_2O < 0.1 ppm). Opening the 5 Ah pouch cells in a dry room environment before transferring the samples into a glove box was chosen for safety reasons as all cells were opened at a defined SoC which poses a certain risk to the personnel involved in the procedure. With this approach, necessary counter-measures could have been provided if the cell had been shorted during cell dismantling. The electrode sheets were then cut into pieces with a size of around 1 mm^2. Spherical titanium vessels (Netzsch, Germany) with a wall thickness of 0.5 mm, a volume of 1 mL and a mass of 3 g were filled with 0.7 mL of electrolyte and 0.7 g of composite electrode material. The Al and Cu current collectors were kept in the sample mixture and are generally considered as thermally inactive material. At least two ARC-HWS experiments were carried out per material, SoC and SoH combination.

ARC measurements.—ARC experiments on the electrode level were carried out with a standard Enhanced System Accelerating Rate Calorimeter (ES-ARC) manufactured by Thermal Hazard Technology (THT, UK) whereas for the cell level experiments, a larger ARC (EV-ARC) of the same manufacturer was used. A stainless steel holder was used for the full cell ARC-HWS experiments in order to guarantee a thermal contact between the pouch foil and the electrode stack throughout the duration of the experiments. A thermocouple was attached to the center of the cell's surface with the aid of Al tape. The spherical Ti vessels chosen for the two-component material tests guaranteed a gastight environment throughout the measurements. A standard HWS mode was conducted in order to detect the onset temperature of a self-sustaining exothermal reaction ($T_{dT/dt>0.02°C/min}$), the onset temperature of a thermal runaway ($T_{dT/dt>0.2°C/min}$) and the temperature of the thermal runaway itself ($T_{dT/dt>10°C/min}$). All samples were heated stepwise from the starting temperature of 50°C to the limiting temperature of 350°C with a temperature increment of 5°C. After heating the sample by a 5°C step, the ARC switched from heating mode to wait mode for 30 min allowing for a temperature equalization at this temperature. Thereafter, the mode was changed to search mode, scanning for an exothermic reaction with a defined self-heating rate threshold of 0.02°C min^{-1}. In the consecutive exothermic mode, the vessel temperature of the ARC followed the sample temperature to simulate adiabatic test conditions. Overall, the temperature limit was set to 400°C if an exothermic reaction was detected. The sample temperature corresponding to a self-heating rate exceeding 0.2°C min^{-1} ($T_{dT/dt>0.2°C/min}$) was regarded to be the onset temperature of thermal runaway following the definition stated by Doughty et al.[4,39]

Results and Discussion

Within this section, the measurement data gained from ARC-HWS and XRD experiments on the electrode level is presented first, which is then discussed in terms of the underlying reaction kinetics by means of model based data analysis. These findings are compared to ARC-HWS experiments on the cell level. An overview of the carried out ARC-HWS experiments is given in Table I. The SoC and SoH range was chosen in accordance with the expected operating window of Li ion batteries, which is assumed to lie between 100% and 0% SoC as well as between 100% and 80% SoH.

Table I. ARC-HWS measurements carried out in this work.

		100% SoC	50% SoC	0% SoC
100% SoH	Anode	x	n/a*	n/a*
	Cathode	x	x	x
	Cell	x	x	x
80% SoH	Anode	x	n/a	n/a*
	Cathode	x	n/a	x
	Cell	x	n/a	n/a

x: measured.
n/a: not available as not measured.
n/a*: not available as no signal detected.

Electrode level tests.—Fig. 2 shows the results of ARC-HWS thermal stability investigations of harvested NMC-442 composite electrodes mixed with electrolyte at different SoC and SoH combinations. The higher the SoC, the lower the onset temperature of thermal runaway gets for both fresh and aged samples as shown in Figs. 2a and 2b. The impact of degree of lithiation on the onset temperature of thermal runaway for different grades of $LiNi_xCo_yMn_zO_2$ was shown previously, which supports the observations made here.[17] The sample at 100% SoC and 100% SoH showed an onset temperature of 179°C compared to 181°C and 187°C for 50% and 0% SoC. The measurements generally revealed a standard deviation of 1°C between two measurements and therefore, the observed difference in $T_{dT/dt>0.2°C/min}$ for 100% and 50% SoC is minor. The samples at 100% SoC and 80% SoH showed an onset temperature of 173°C compared to 178°C at 0% SoC. So, there is a considerable increase in onset temperature of thermal runaway of around 8°C and 5°C from the highest to the lowest SoC for the fresh and aged NMC-442 composite electrodes mixed with electrolyte. Similarly, the temperature rise of the first exothermic reaction (i.e. ΔT), represented by the width of the ARC-HWS plot in Fig. 2 increases with increasing SoC for both fresh and aged samples. This effect can be attributed to a decreasing structural stability of the active material during delithiation resulting not only in an increase in the total amount of heat release but also affecting the heat generation rate, which is resembled by the height of the ARC-HWS plot in Fig. 2.

Figs. 2c and 2d show ARC-HWS results of NMC-442 electrolyte mixtures depending on the SoH for both fully charged cells (i.e. 100% SoC, see Fig. 2c) and discharged cells (i.e. 0% SoC, see Fig. 2d). Both aged samples at 100% and 0% SoC showed a significant decrease in onset of thermal runaway from 179°C to 173°C and from 187°C to 178°C. This suggests that in the very beginning of an exothermic reaction, an aged cathode at an elevated degree of lithiation (i.e. 80% SoH and 0% SoC) shows a quite similar thermal behavior compared to a fresh cathode at a lower degree of lithiation (i.e. 100% SoH and 100% SoC). When further comparing the general shape of the ARC traces shown in Figs. 2c and 2d, the thermal stability seems to decrease with ongoing aging (i.e. a lower SoH) especially at higher degrees of lithiation (i.e. a lower SoC) confirming the observed trend of a decreasing onset temperature. Literature results from nail penetration experiments on commercially available full cells confirm the results showing that aging significantly decreases the time until a cell undergoes a thermal runaway.[11] The decreased thermal stability of the aged cathodes at lower levels of cell SoC can be explained by a lack of relithiation during aging caused e.g. by the growth of the cathode electrolyte interphase (CEI)[40] layer and/or by a contact loss of the cathode particles. The process of contact loss based on the formation of a CEI was shown previously.[41] The lacking relithiation during aging was confirmed via XRD measurements (see Fig. 3).[42] The (003) reflex is shifted to lower and the (101), (006) as well as the (102) reflexes are shifted to higher angles due to the expansion of the *c*-axis and the contractions of the *a*- and *b*-axis of the crystal structure during delithiation[43] (see Figs. 3a and 3b). The reflexes for the aged sample in the lithiated state corresponding to 0% cell SoC can be found at

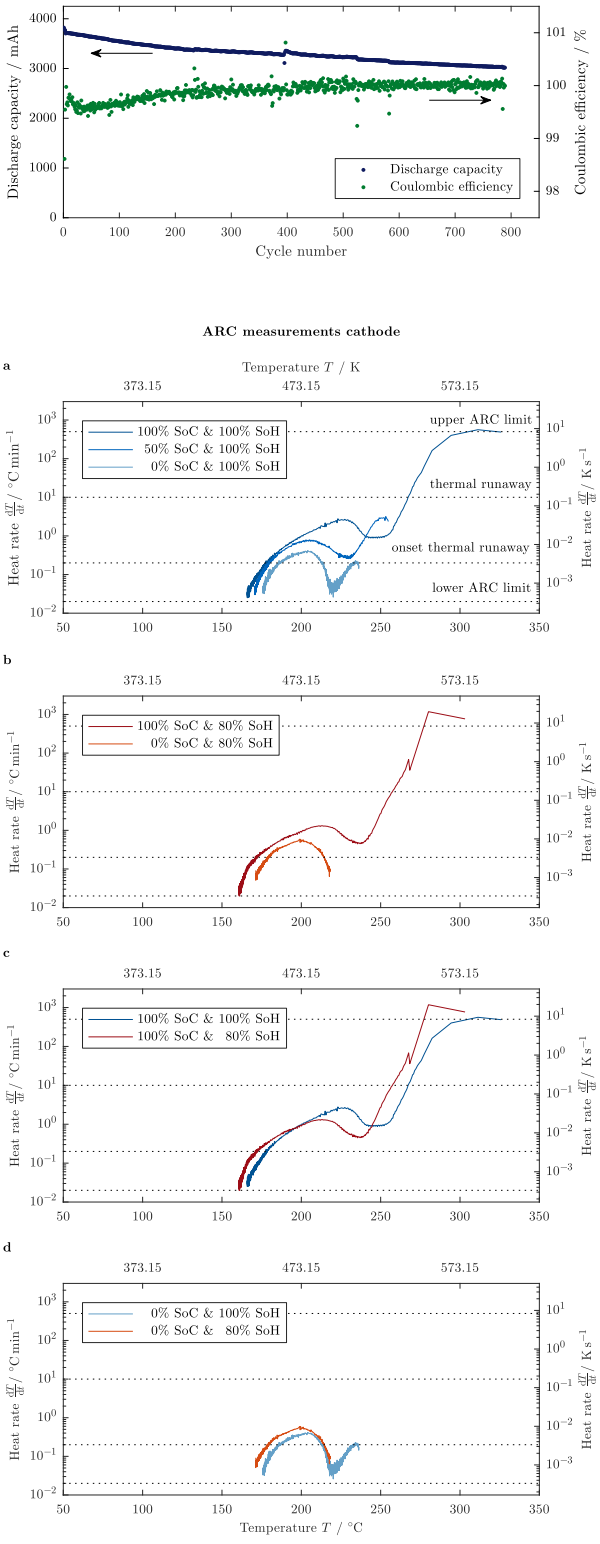

Figure 2. ARC-HWS results comparing the self-heating rate of NMC-442/electrolyte mixtures as a function of sample temperature indicating the SoC influence at 100% SoH (a), the SoC influence at 80% SoH (b), the impact of SoH at 100% SoC (c) and the impact of SoH at 0% SoC (d).

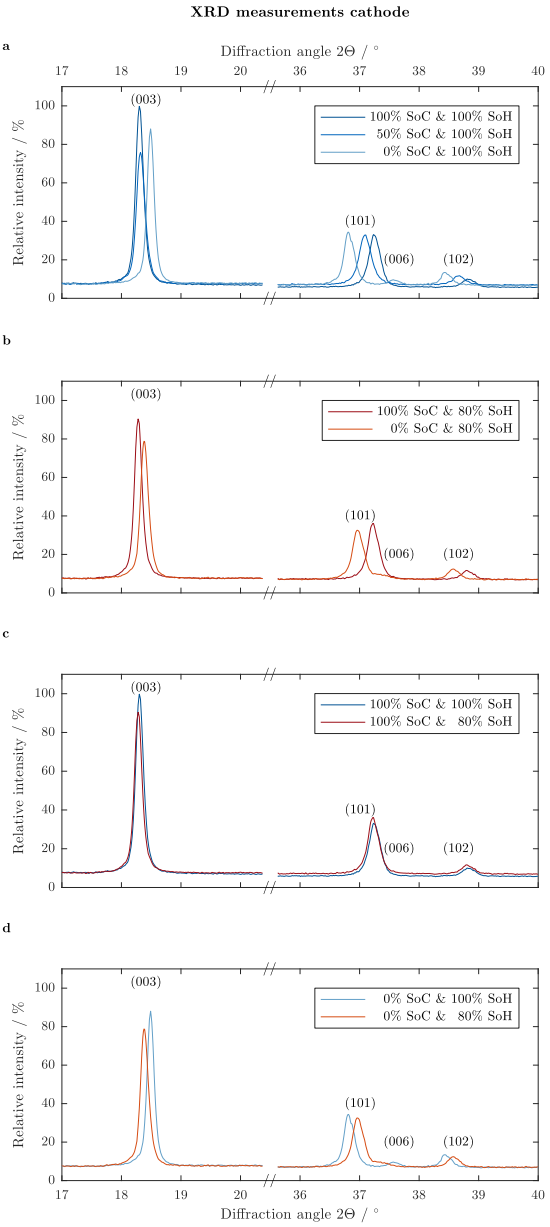

Figure 3. X-ray diffractograms of NMC-442/electrolyte mixtures indicating the SoC influence at 100% SoH (a), the SoC influence at 80% SoH (b), the impact of SoH at 100% SoC (c) and the impact of SoH at 0% SoC (d).

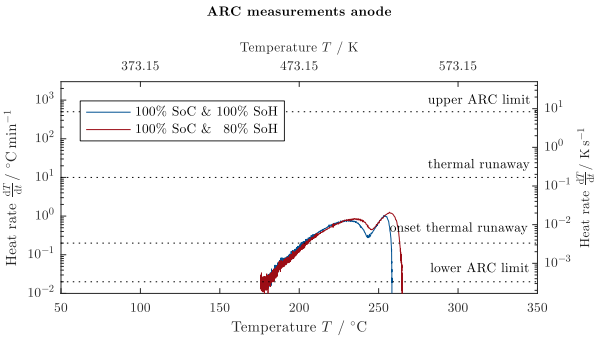

Figure 4. ARC-HWS results comparing the self-heating rate of MCMB/electrolyte mixtures as a function of sample temperature indicating the SoH influence at 100% SoC.

2Θ values in between the fresh samples at 0% and 100% SoC (see Fig. 3d) which indicates an incomplete relithiation during discharge. The comparably more delithiated structure remains less thermally stable and can therefore lead to a shift in $T_{dT/dt>0.2°C/min}$ to lower temperatures. In addition, the degree of lithiation for the samples at 100% SoC occurs to be similar for 80% and 100% SoH according to nearly equal 2Θ values observed in the X-ray diffractograms (see Fig. 3c).

Fig. 4 shows the ARC-HWS results of MCMB composite electrode/electrolyte mixtures. For anodes at 100% cell SoC, $T_{dT/dt>0.2°C/min}$ increases slightly from 100% to 80% SoH. Experiments on anodes at 50% and 0% SoC showed negligible exothermic reactions for both fresh and aged cells and are therefore not shown here. The values for the measured onset temperatures of thermal runaway on the electrode level are summarized in Table II.

It is also worth mentioning, that even with a comparably vast amount of composite electrode material (i.e. 0.55 g to 0.63 g) guaranteeing a thorough soaking with electrolyte (i.e. 0.63 g to 0.72 g), an exothermic decomposition reaction around 80°C to 120°C as previously reported[20] could not be observed in this work when testing the anode/electrolyte mixtures. On the cathode side, similar sample quantities were used for the composite electrode materials (i.e. 0.67 g to 0.76 g) and electrolyte (i.e. 0.74 g to 0.94 g). Also, it should be stated that the anode seems to be less reactive than the cathode within the whole temperature range from 160°C onwards for all SoC and SoH combinations never undergoing a runaway scenario which has been recently reported conversely for cells formed of artificial graphite and NMC-111.[44] Based on the electrode level measurements and the surprisingly not detectable decomposition and reformation reaction of the solid electrolyte interphase (SEI),[45] the authors cannot comment on any changes in the anode's reactivity below that temperature.

Electrode level reaction kinetics.—In order to quantify the observations made when comparing the ARC trace gathered during measurements, the underlying reaction kinetics are more closely investigated in this part. As already briefly discussed in the cathode section,

Table II. Temperature values for detected onset of thermal runaway on the electrode level $T_{dT/dt>0.2°C/min}$.

		100% SoC $T_{dT/dt>0.2°C/min}$ (°C)	50% SoC $T_{dT/dt>0.2°C/min}$ (°C)	0% SoC $T_{dT/dt>0.2°C/min}$ (°C)
100% SoH	Anode	202	-	-
	Cathode	179	181	187
80% SoH	Anode	203	-	-
	Cathode	173	-	178

The measured values exhibit a standard deviation of 1°C.

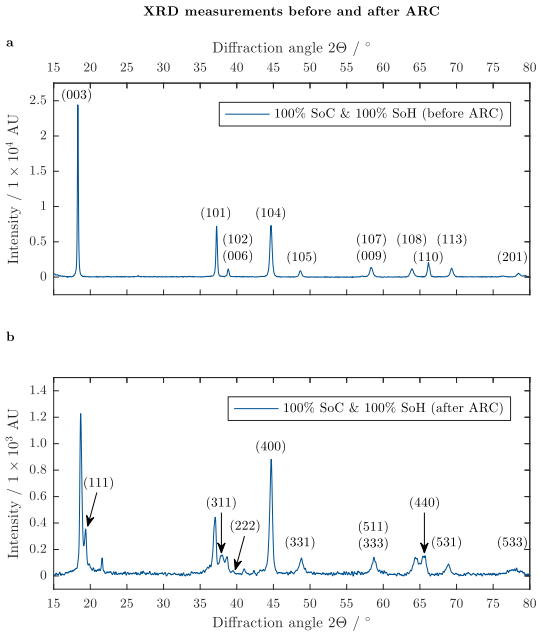

Figure 5. X-ray diffractograms of delithiated NMC-442 before (a) and after (b) ARC-HWS measurement up to 255°C.

ΔT can be assigned to the first exothermic reaction taking place involving a structural conversion from layered (space group $R\bar{3}m$) to cubic spinel phase (space group $Fd\bar{3}m$) via oxygen release and a subsequent combustion of the electrolyte.[46]

The transition to spinel phase was confirmed via XRD measurements which are shown in Fig. 5.[46–48] To obtain the presented powder diffractogram, the sample was heated to 255°C, stopping the ARC-HWS experiment to prevent further phase conversion. The (111) reflex is well visible and identifies besides other reflexes the formation of the spinel phase[46] (see Fig. 5b).

The highly reactive oxygen released during conversion can subsequently combust the flammable organic electrolyte via

$$C_3H_4O_3 + \frac{5}{2}O_2 \rightarrow 3CO_2 + 2H_2O \quad [1]$$

$$C_5H_{10}O_3 + 6O_2 \rightarrow 5CO_2 + 5H_2O \quad [2]$$

Previous works in the field have shown that ARC-HWS measurement data can be used to study reaction kinetics in order to obtain so called "kinetic triplets" including frequency factor γ (min^{-1}), activation energy E_a (eV) and reaction mechanism $f(\alpha)$ as a function of reaction conversion α.[20,32,33,49] These kinetic triplets can be used to simulate e.g. the underlying ARC-HWS trace or similar thermal stability tests. Due to the potential capability to predict the process of heat evolution during ARC-HWS measurements, deriving such kinetic triplets of the carried out two-component measurements as a function of both SoC and SoH is regarded to be of high importance for the community and this work.

The self-heating rate $\frac{dT}{dt}$ of a reaction follows Eq. 3.[33]

$$\frac{dT}{dt} = \frac{h}{C_{tot}} \cdot \frac{d\alpha}{dt} \quad [3]$$

With h as the total heat of the reaction (J), C_{tot} ($J\,K^{-1}$) as the total heat capacity of the sample and α as the degree of reaction conversion ($0 \leq \alpha \leq 1$). Hence, $\frac{d\alpha}{dt}$ represents the rate of reaction conversion depending on the rate constant k and the reaction model $f(\alpha)$ (see Table III).

$$\frac{d\alpha}{dt} = k \cdot f(\alpha) \quad [4]$$

Table III. Common reaction models and corresponding equations to describe the trace of the self-heating rate in ARC-HWS experiments.[50]

Reaction model (*m-n-p*)	$\frac{d\alpha}{dt} = \boldsymbol{k} \cdot \boldsymbol{f(\alpha)} = \boldsymbol{k} \cdot \boldsymbol{\alpha^m} \cdot (1-\boldsymbol{\alpha})^{\boldsymbol{n}} \cdot (-\ln(1-\boldsymbol{\alpha}))^{\boldsymbol{p}}$
0 order (0-0-0)	k
1st order (0-1-0)	$k \cdot (1-\alpha)$
2nd order (0-2-0)	$k \cdot (1-\alpha)^2$
Autocatalytic (1-1-0)	$k \cdot \alpha \cdot (1-\alpha)$
Avrami-Erofeev 1/2 (0-1-1/2)	$k \cdot (1-\alpha) \cdot (-\ln(1-\alpha))^{\frac{1}{2}}$
Avrami-Erofeev 2/3 (0-1-2/3)	$k \cdot (1-\alpha) \cdot (-\ln(1-\alpha))^{\frac{2}{3}}$
Avrami-Erofeev 3/4 (0-1-3/4)	$k \cdot (1-\alpha) \cdot (-\ln(1-\alpha))^{\frac{3}{4}}$

The rate constant k can be described via Eq. 5.

$$k = \gamma \cdot e^{-\frac{E_a}{k_B T}} \quad [5]$$

With γ as the frequency factor, E_a as the activation energy and the Boltzmann constant k_B.

$\frac{h}{C_{tot}}$ can be described as the total temperature increase for the reaction ΔT assuming a full conversion (i.e. $\alpha = 0 \ldots 1$) of the reaction (see Eq. 6).

$$\frac{h}{C_{tot}} = \Delta T \quad [6]$$

ΔT is mainly influenced by the so called phi-factor ϕ of the measurement.[22] It describes the ratio between material which takes part in the reaction (thermally active material) and material which only serves as a thermal mass (thermally inactive material) such as the calorimeter bomb or the current collector foils. It affects the temperature rise according to Eq. 7, whereas ΔT is the measured temperature rise as defined in Eq. 6. ϕ is defined in Eq. 8.

$$\Delta T_{ad} = \phi \cdot \Delta T \quad [7]$$

$$\phi = 1 + \frac{\sum \left(m_{inactive} \cdot c_{p,\ inactive}\right)}{\sum \left(m_{active} \cdot c_{p,\ active}\right)} \quad [8]$$

The estimated phi-factor values for the electrode level measurements ($\phi_{cathode} = 1.74$ and $\phi_{anode} = 1.90$) are higher but still comparable to the cell level measurements ($\phi_{cell} = 1.52$). The masses of each sample components and underlying heat capacities are summarized in Table IV. Combining Eq. 3 with Eq. 4, Eq. 5, and Eq. 6, the overall equation for the self-heating rate calculates as shown in Eq. 9

$$\frac{dT}{dt} = \Delta T \cdot \gamma \cdot e^{-\frac{E_a}{k_B T}} \cdot f(\alpha) \quad [9]$$

whereby γ, E_a and $f(\alpha)$ form the kinetic triplet which has to be determined to describe the reaction properly. Due to the nature of the equation and its number of variables, there are several solutions to fit ARC-HWS results.[20,32,33,57] To narrow down the choice of significant parameters to describe the function of self-heating rate vs. temperature, a linearization according to the reaction model was conducted. Self-heating rate curves were obtained which, in principle, are independent from any reaction model. By using this approach, the reaction mechanism can be eliminated from the equation, and γ as well as E_a can be then determined via the intersection with the y-axis and the slope of the linear part of the natural logarithm of the self-heating rate plotted against the reciprocal temperature (see Eq. 10).

$$\ln \frac{d\alpha}{dt} - \ln(f(\alpha)) = \ln \gamma - \frac{E_a}{k_B T} \quad [10]$$

Then, the linear part of the Arrhenius plot in Figs. 6b and 6d can be fitted for the cathode and anode side to obtain meaningful values for γ and E_a. As shown in Figs. 6a and 6c, the optimization procedure shows comparable results for both assumed reaction mechanisms even

Table IV. Sample masses studied in this work and corresponding heat capacities.

		Sample mass cell (g)	Sample mass anode (g)	Sample mass cathode (g)	Specific heat capacity c_p (J g^{-1} K^{-1})
Neg. current collector	Cu	14.42	0.27	-	0.385[a]
Neg. composite electrode	MCMB	31.27	0.55-0.63	-	0.800[b]
Separator	Polyester	8.69	-	-	2.480[c]
Pos. composite electrode	NMC-442	42.42	-	0.67-0.76	0.800[b,d]
Pos. current collector	Al	5.86	-	0.14	0.903[a]
Electrolyte	EC:DEC	27.60	0.63-0.72	0.74-0.94	2.055[a]
Pouch case	PA/Al/PP	5.65	-	-	1.212[e]
Ti vessel	Ti	-	2.97-3.05	2.98-3.04	0.523[f]
Steel holder	Fe	47.00	-	-	0.449[f]

[a]in accordance with.[51]
[b]approximated in accordance with.[52]
[c]in accordance with.[53]
[d]approximated in accordance with.[54]
[e]in accordance with.[55]
[f]in accordance with.[56]

though two similar but not identical sets of linear fits were derived from the linearization procedure (see Figs. 6b and 6d). The autocatalytic and Avrami-Erofeev type reaction mechanisms were chosen in the following as these were reported to show the most promising results for describing the decomposition of LCO/electrolyte mixtures[32,57] which could be confirmed for the studied NMC-442/electrolyte mixtures in this work. The exothermic reactions of the anode with the electrolyte involve the reaction of lithiated graphite with the conducting salt $LiPF_6$ and the solvent.[6,58,59] To allow for a most straightforward comparison between the electrodes, the same reaction mechanisms were chosen for the anode.

In order to find the most suitable set of γ and E_a for describing the ARC-HWS trace, an iterative least squares fit was carried out. First of all, the time equidistant data sets which were gathered every 30 s during the experiment were transformed to temperature equidistant data sets at temperature steps of 0.05°C via linear interpolation. This procedure is essential to not lay the focus of the fitting on measurement data gathered at the very early stages of thermal decomposition but to allow for a most thorough fit throughout the entire reaction. In the next step, the temperature ranges of both optimizing and linearizing needed to be defined. For both cathode and anode, the optimization range was chosen between the first detection of a self-sustaining decomposition reaction and the deflection point of the self-heating rate as a function of temperature (see Figs. 6a and 6c). The linearization range was reduced by 5 to 10°C from both the lower and upper end of the optimization range, approaching the peak heat generation rate at the top end of the linearization range (see Figs. 6b and 6d). This procedure showed most robust, reproducible and comparable results for all data sets based on the elimination of signal noise at lower temperatures and the exclusion of non-linear parts based on the applied reaction mechanism at elevated temperatures.

With a first guess for ΔT derived from the width of the ARC-HWS trace in Figs. 6a and 6c and assuming an almost negligible initial degree of conversion (i.e. $\alpha_0 \leq 1 \times 10^{-6}$) at the measured starting temperature T_0, a first linearization can be carried out. Based on this first linearization step and the derived values for γ and E_a, the ARC-HWS trace can be calculated numerically according to Eq. 9. In order to allow for an optimization, a cost function needs to be defined, which the authors chose as the sum of normalized squared errors (*SSE*) for both the predicted temperature and self-heating rate over all time steps in the optimization range

$$SSE = \sum_t \left(\left(1 - \frac{T_s}{T_m}\right)^2 + \left(1 - \frac{\frac{dT_s}{dt_s}}{\frac{dT_m}{dt_m}}\right)^2 \right) \quad [11]$$

whereas the subscript s and m denote simulated and measured values with $t_s \equiv t_m$. Together with the initial values as well as lower and upper limits for γ, E_a, ΔT, T_0 and α_0, these five values are iteratively varied to minimize the cost function *SSE*. The number of function evaluations and iterations is set to 1×10^5 and the absolute and relative tolerances are set to 1×10^{-9}. The lower and upper bounds for γ and E_a are derived from the standard deviation of the carried out linearization procedure which follows a standard linear least squares fit. The lower bound of ΔT is chosen as 0°C and the upper bound is the measured temperature increase for the entire ARC trace. The initial temperature of the reaction T_0 is chosen to lie between the minimum and maximum measured temperature and the corresponding initial degree of conversion α_0 is defined between 0 and 1. After this first optimization step, the whole procedure of linearizing and optimizing is repeated based on the calculated values for ΔT, T_0 and α_0. This results in a new set of γ and E_a, which is then the basis for the next optimization step. This procedure is repeated until a converged state can be observed after a maximum of 50 iterations. The convergence criterion is defined by the mean value of the derived coefficients of determination R^2_{tot} for the linearization procedure and the simulated values for the sample's temperature and self-heating rate.

$$R^2_{tot} = \frac{1}{3} \cdot \left(R^2_{lin} + R^2_T + R^2_{\frac{dT}{dt}} \right) \quad [12]$$

After R^2_{tot} does not alter more than 0.01% between two iterations, the solution corresponding to the maximum value of R^2_{tot} is chosen as the final solution of the linearization and optimization procedure. Exemplary values of R^2_{tot} for each measurement point are given in Table V for an Avrami-Erofeev 2/3 reaction model, which in sum showed the best performance in predicting the ARC-HWS trace of all studied reaction models for both electrodes.

The resulting simulated ARC-HWS traces for the studied Avrami-Erofeev 2/3 reaction model can be seen in Fig. 7 and Fig. 8 for the cathode and the anode side which were presented in analogy to Fig. 2 and Fig. 4. The results are also given in Table VI. It can be stated, that all derived fits show an excellent behavior for predicting the ARC-HWS trace with almost no visible deviation between the simulated and the measured values in the optimization range.

Except for the 0-order reaction, all reaction types summarized in Table III were used for the linearization and optimization procedure of all electrode samples presented in this work. First and second order reaction types are not shown due to their comparably poor performance in predicting the ARC-HWS trace for both electrodes. Generally, both autocatalytic and Avrami-Erofeev type reaction models showed similar R^2_{tot} values. Therefore, these reaction mechanisms are examined more closely in the following.

This procedure further allows for deriving the influence of SoC and SoH on kinetic parameters such as γ and E_a as presented in Fig. 9 and Table VI as well as the starting temperature T_{start} (i.e. $\alpha = 0$) and the specific heat of the reaction H (J g^{-1}) as shown in Fig. 10

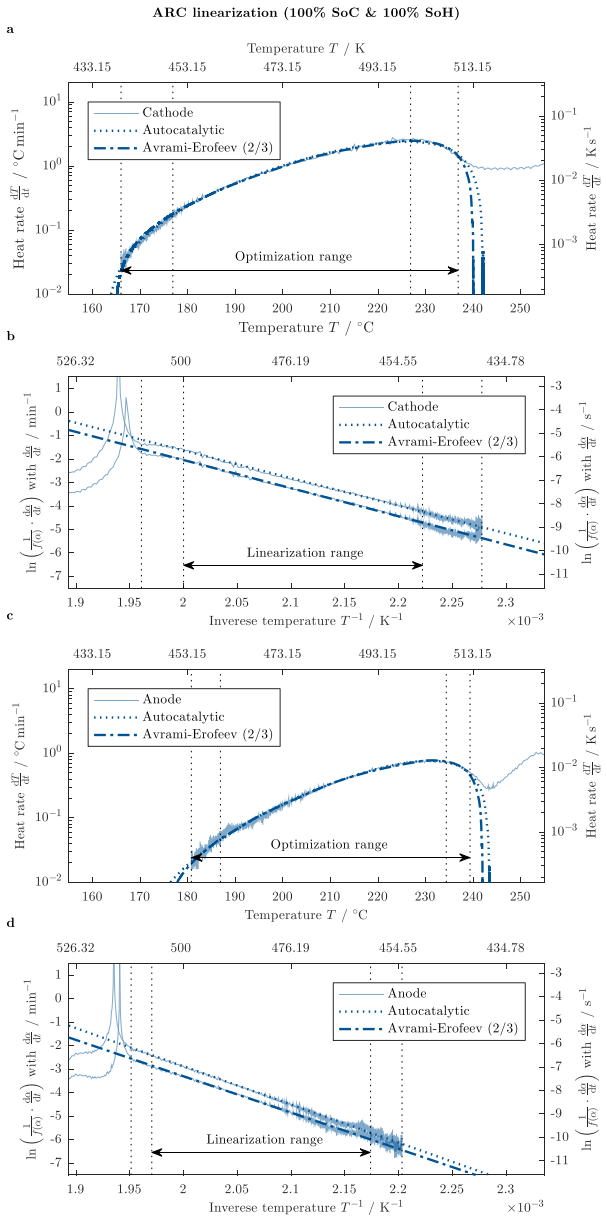

Figure 6. Linearization process of ARC-HWS measurements of NMC-442/electrolyte mixtures (a and b) and MCMB/electrolyte mixtures (c and d) at 100% SoC and 100% SoH applying two different reaction mechanisms.

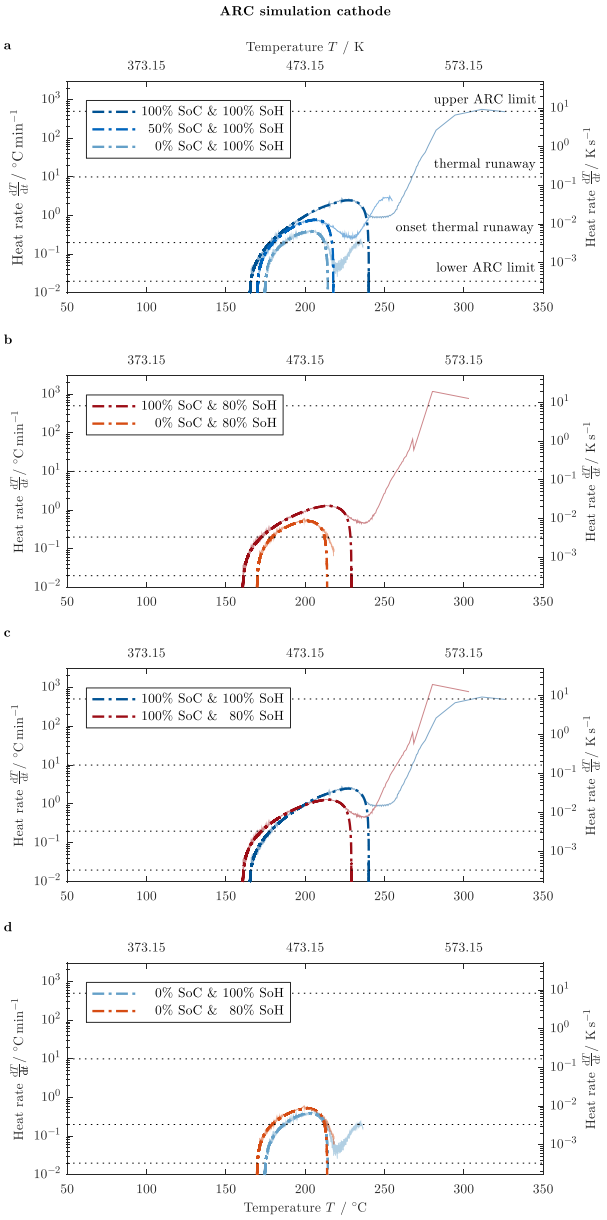

Figure 7. Simulated (Avrami-Erofeev 2/3, dash-dotted lines) and measured (solid lines) ARC-HWS results comparing the self-heating rate of NMC-442/electrolyte mixtures as a function of sample temperature indicating the SoC influence at 100% SoH (a), the SoC influence at 80% SoH (b), the impact of SoH at 100% SoC (c) and the impact of SoH at 0% SoC (d).

Table V. Mean values of the derived coefficients of determination R^2_{tot} for the linearization procedure and the simulated values for the sample's temperature and self-heating rate compared to measurement data (Avrami-Erofeev 2/3).

		100% SoC	50% SoC	0% SoC
100% SoH	Anode	99.65%	-	-
	Cathode	99.64%	99.27%	98.66%
80% SoH	Anode	99.69%	-	-
	Cathode	99.69%	-	98.53%

and Table VII with

$$H = \frac{h}{m_{\text{electrode}}} = \Delta T \cdot \frac{\sum_i m_i \cdot c_{p,i}}{m_{\text{electrode}}} \qquad [13]$$

whereas the indexes i accounts for all components of a sample as summarized in Table VI. All graphs are shown as a function of a decrease in capacity. As can be seen for all relevant reaction models, similar trends can be observed as long as the assumed reaction model is not altered for varying SoC and SoH combinations. The magnitude of the SoC and SoH influence varies slightly with the chosen reaction model as can be seen from the slopes and the absolute values in the

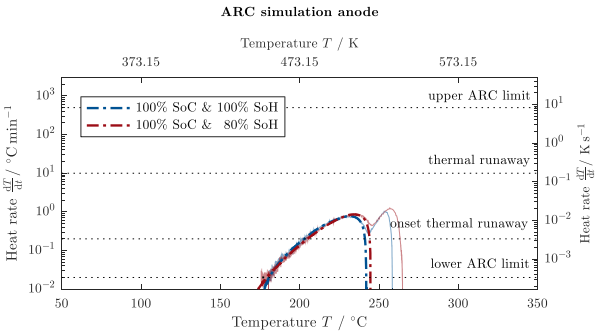

Figure 8. Simulated (Avrami-Erofeev 2/3, dash-dotted lines) and measured (solid lines) ARC-HWS results comparing the self-heating rate of MCMB/electrolyte mixtures as a function of sample temperature indicating the SoH influence at 100% SoC.

graphs. It can be also observed that both autocatalytic and Avrami-Erofeev type reaction models show similar results, which especially holds for the 2/3 and 3/4 shape on the cathode side and the 1/2 and 2/3 shape on the anode side.

At 100% SoH, the cathode reveals an exponential decrease of γ and a linear decrease of E_a with decreasing SoC (see Figs. 9a and 9b). At the same SoH, the cathode shows a linear increase of T_{start} and a quadratic decrease in H with decreasing SoC forming a minimum at 0% SoC (see Figs. 10a and 10b). For all remaining observations revealing the SoH influence, only trends can be described as only two data points are accessible in this work (i.e. 100% SoH and 80% SoH). On the cathode side, we can observe a strong decrease in both γ and E_a with decreasing SoH (see Figs. 9c and 9d). It is worth mentioning, that a cathode at 80% SoH with a low degree of lithiation (i.e. 100% cell SoC) shows similar values for γ and E_a as a cathode at 100% SoH at a high degree of lithiation (i.e. 0% cell SoC). With this observation alone, a simple influence of cell capacity or degree of lithiation on the thermal stability can be ruled out on the cathode side. As already observed from the ARC measurements, both the starting temperature of the reaction and the specific heat decrease with ongoing aging (see Figs. 10b and 10d). The anode in comparison reveals a contrary behavior in terms of γ and E_a compared to the cathode with ongoing aging. Both values increase with lower values in SoH (see Figs. 9e and 9f). Similar to the cathode, the starting temperature decreases for the anode, however, in a stronger manner (see Fig. 10e). Again contrary to the cathode, the specific heat increases with ongoing aging (see Fig. 10f).

When comparing the influence of SoC and SoH on each parameter, a straightforward tendency in terms of the overall reactivity cannot be stated without further considerations. From a reaction model perspective, a higher frequency factor combined with a lower activation energy would somewhat hint at a higher tendency to react whereas a lower frequency factor and a higher activation energy would indicate a lower tendency to react. This is not the case here as both frequency factor and activation energy either decrease or increase simultaneously. Together with the specific heat of the reaction, these factors represent the thermal stability of a sample over a wide range of temperatures (see Eq. 9). Therefore, they should be simultaneously evaluated to make a somewhat clearer statement.

For this purpose, the product of specific heat H and the reaction rate k are shown as a function of temperature for the cathode in Fig. 11 and for the anode in Fig. 12 highlighting the derived starting temperature of the reaction T_{start}. This product is further denoted as the specific reactivity of the sample (W g^{-1}). To further distinguish between the calculated values for varying SoC and SoH combinations, relative values are shown on the right side of both figures. From these figures, the influence of SoC and SoH becomes more apparent. On the cathode side, the reactivity is generally reduced at lower SoC levels for both fresh and aged cells, especially when considering the shift in T_{start} to higher values (Figs. 11b and 11d) resulting in an increased thermal stability with decreasing SoC. At temperatures below approximately 115°C, the reactivity for 0% SoC is slightly higher compared to 100% SoC but at this temperature, the reaction has not even started yet. With ongoing aging, the effect of SoC seems to be reduced which can be observed when comparing Figs. 11b to 11d. This becomes even more pronounced when comparing Figs. 11f to 11h. At 100% SoC, the cathode is more reactive at 80% SoH compared to 100% SoH at temperatures up to approximately 195°C but is less reactive afterwards. At 0% SoC, the aged cathode is more reactive throughout the entire duration of the first reaction (i.e. < 220°C, as shown in Fig. 7d). Combined with the observed reduced T_{start}, aged cathodes are generally becoming more reactive than fresh cathodes at lower temperatures (see Fig. 11f). The temperature range, in which aged cathodes are more reactive than their fresh counterpart, also becomes larger at lower SoC values (Fig. 11h). This results in a comparably reduced thermal stability with ongoing aging especially at increasing degrees of lithiation.

Looking into the anode, the reactivity is reduced with ongoing aging at temperatures above approximately 175°C and below 230°C at 100% SoC (Figs. 12a and 12b). Beyond this temperature, the aged lithiated anode is more reactive than its fresh counterpart. Before the fresh anode starts to react at approximately 175°C, the aged anode is more reactive, as the reaction has already started at approximately 162°C. As no reaction could be detected at lower SoC values for both fresh and aged anodes, the SoC seems to be dominating the SoH influence in this case. It remains worth mentioning here, that for all SoC and SoH combinations, the cathode is more reactive than the anode for the temperature range, which we considered for fitting the presented reaction models (i.e. $150°C < T < 250°C$) which agrees well with the observations made from comparing the ARC-HWS measurements shown in Fig. 2 and Fig. 4. Below this temperature range, the anode might be dominating based on the SEI-decomposition and reformation reaction, which will be discussed in the next section. Above that temperature range, a second, more reactive reaction seems to be dominating on the cathode side at lower degrees of lithiation (see Fig. 2c), which is by magnitudes larger than the small second reaction peak forming on the anode side (see Fig. 3b).

Cell level tests and simulations.—Results of ARC-HWS experiments on full cells with a nominal capacity of 5 Ah (i.e. < 4 Ah at 4 C) consisting of MCMB as the anode and NMC-442 as the cathode are presented in Fig. 13 in order to show the influence of SoC and SoH on the full cell behavior. As already observed during the measurements on electrolyte wetted anodes and cathodes, the self-heating rate is highly dependent on the cell's SoC. The same can be seen in

Table VI. Values for frequency factor γ and activation energy of the reaction E_a derived from the optimization procedure (Avrami-Erofeev 2/3).

		100% SoC γ (s^{-1}) / E_a (J)	50% SoC γ (s^{-1}) / E_a (J)	0% SoC γ (s^{-1}) / E_a (J)
100% SoH	Anode	$1.66 \times 10^{+10}$ / 2.14×10^{-19}	-	-
	Cathode	$5.50 \times 10^{+07}$ / 1.65×10^{-19}	$7.12 \times 10^{+06}$ / 1.51×10^{-19}	$6.02 \times 10^{+05}$ / 1.38×10^{-19}
80% SoH	Anode	$6.08 \times 10^{+11}$ / 2.40×10^{-19}	-	-
	Cathode	$2.48 \times 10^{+05}$ / 1.30×10^{-19}	-	$3.23 \times 10^{+04}$ / 1.17×10^{-19}

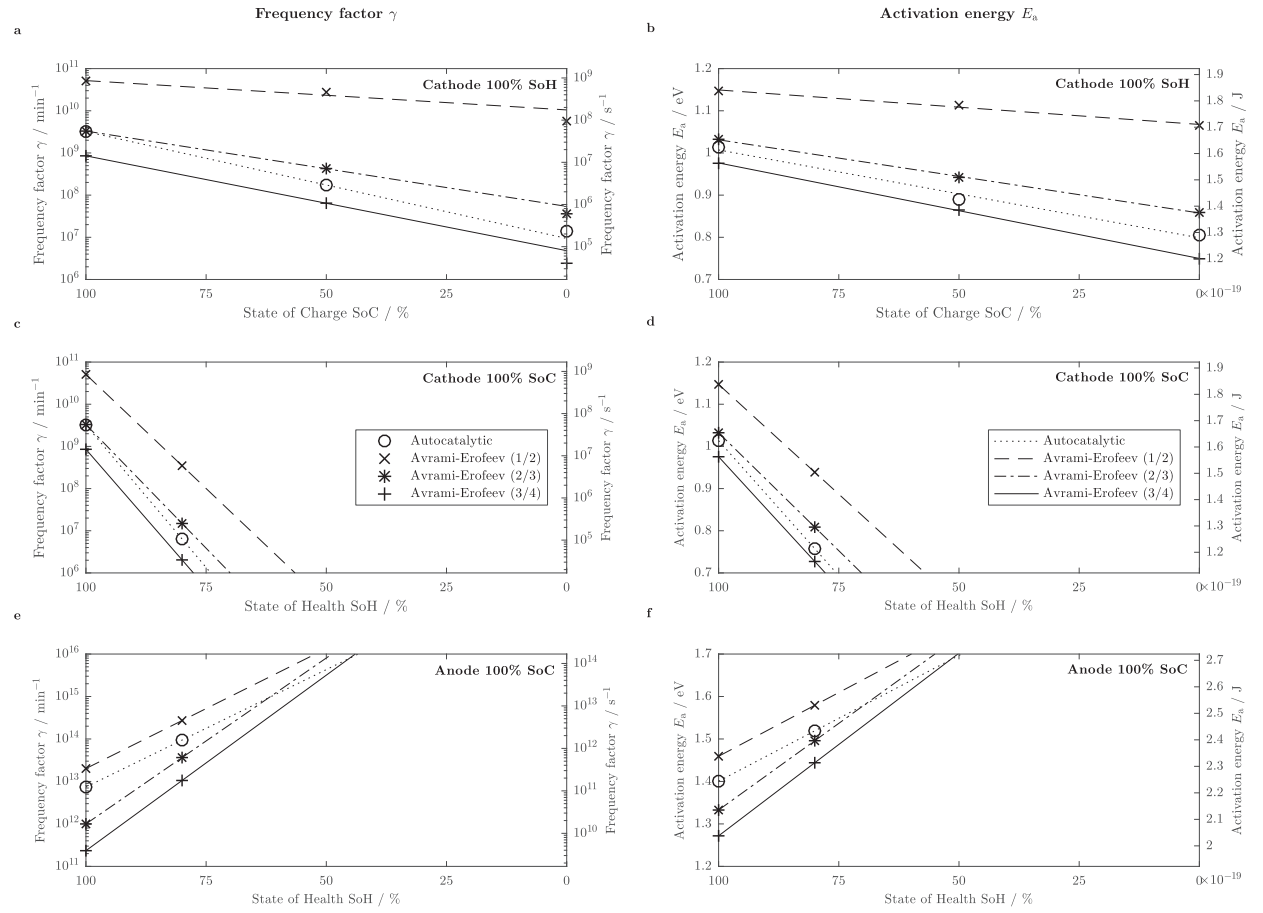

Figure 9. Frequency factor γ (left) and activation energy E_a (right) – influence of SoC (a and b) at 100% SoH as well as the influence of SoH (c and d) at 100% SoC on the cathode side and influence of SoH (e and f) at 100% SoC on the anode side for four different reaction models. Markers represent values summarized in Table VI and lines represent the underlying fit types shown in the Appendix.

Fig. 13a. In accordance with the two-component measurements, the reactivity increases with increasing SoC. Cells charged to 100% SoC undergo a thermal runaway whereas cells at 50% SoC just about border a runaway scenario and cells at 0% SoC do not cross the threshold of 10°C min^{-1} at all. This fits well to the two-component measurements performed on electrolyte wetted cathodes. Between 80°C and 135°C where the SEI is supposed to decompose and reform,[60] the self-heating rate is significantly lower for the cells which are not fully charged. The reason for the lower reactivity is probably based on the limited reformation of the SEI. After the SEI decomposes in fully charged cells, the SEI is directly reformed due to the low electrode potential and the high Li ion concentration at the surface of the active material particles.[6,20,61] Once the SEI is decomposed and the Li ion concentration in the anode is too low combined with a higher potential of the anode, the SEI can be only partially reformed. Generally, the heat release of the SEI decomposition is relatively small compared to what was observed in other studies.[21,62] The reactivity at temperatures from around 160°C onwards is similar to the two-component measurements on cathodes reported in this study (see Fig. 2) similarly showing a decrease in reactivity with decreasing SoC. Within this temperature range, the anode plays only a minor role in heat generation as already stated.

In order to investigate the influence of aging on the thermal stability of a full cell, ARC-HWS measurements were also carried out at 80% SoH (see Fig. 13b). Although the capacity of the whole cell is reduced by 20% at 4C, the reactivity seems to increase below temperatures of 160°C. This is well in line with the presented XRD results revealing the degree of lithiation within the cathode, which is not majorly affected by the SoH at 100% SoC (see Fig. 3c). Furthermore, ARC-HWS results in Fig. 2c and Fig. 12f show that the cathode reactivity is even increased at lower temperatures. In the case of a full cell, the self-heating rate from 160°C onwards is, however, not significantly influenced by aging. According to the here presented results, the reaction of the cathode with the electrolyte is expected to dominate within that temperature range. Only the temperature range before 160°C reveals a stronger reactivity for the aged cell. In this area, the anode (i.e. lithium within the anode) is supposed to react with the electrolyte.[6] As already mentioned, ARC-HWS results on fully charged anodes presented in this work do not show any exothermic reactions at such an early stage. On the one hand, this may be attributed to the comparably lower active material share and the consequently higher ϕ-factor during the two-component measurement. On the other hand, the electrode composition could have changed after cell opening; oxygen from the air in the dry room could have reacted with the lithium in the anode and possible decomposition products could have evaporated. Studying these effects should be within the scope of further work. If, however, these assumptions hold true, measurements on the cell level are very important to gain in-situ information about the processes occurring during thermal abuse. For a distinct analysis of each material's reactivity in a full cell, the measurement is, however, not sensitive enough due to simultaneously occurring reactions, which are difficult to separate in the overall

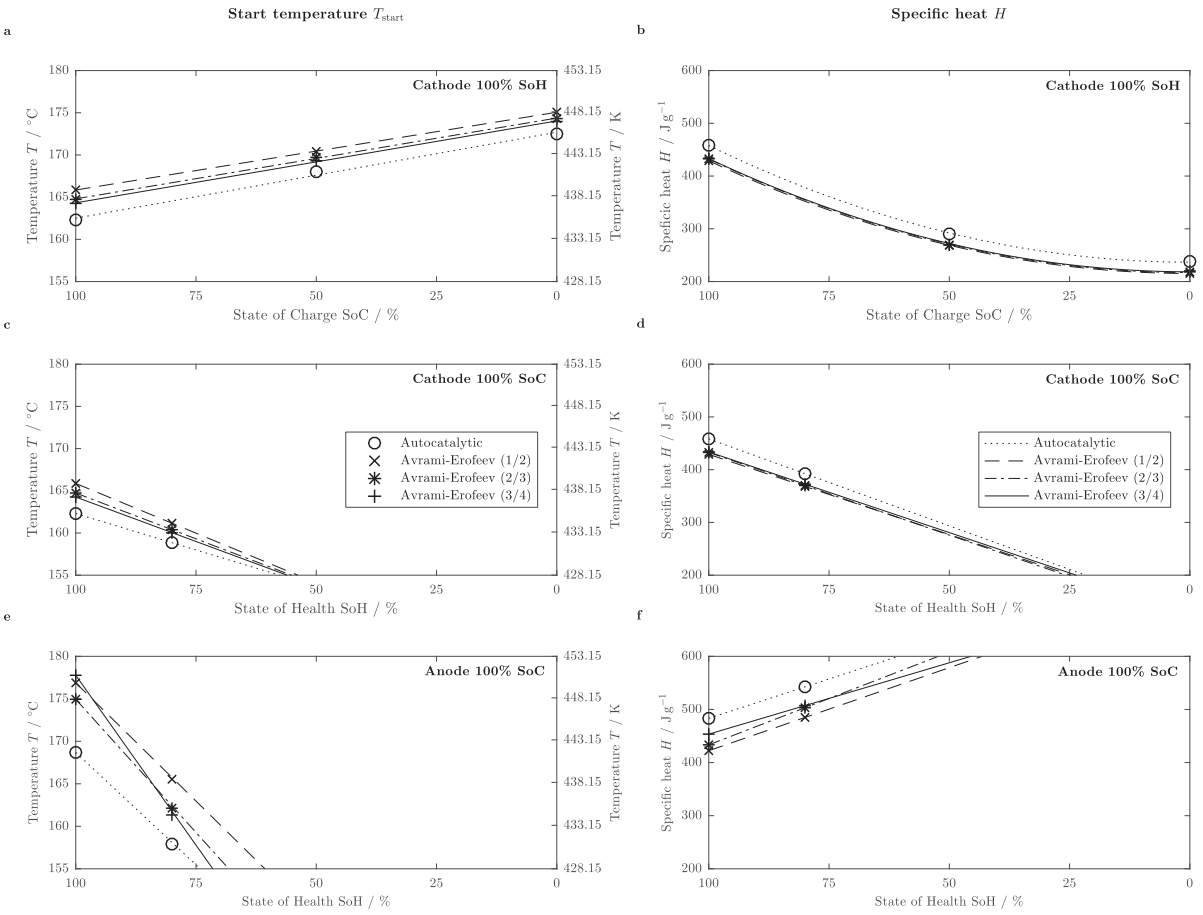

Figure 10. Start temperature T_{start} (left) and specific heat H (right) – influence of SoC (a and b) at 100% SoH as well as the influence of SoH (c and d) at 100% SoC on the cathode side and influence of SoH (e and f) at 100% SoC on the anode side for four different reaction models. Markers represent values summarized in Table VII and lines represent the underlying linear fits for T_{start} and the fit types shown in the Appendix for H.

ARC-HWS trace. Therefore, it depends on the scope of a study which level should be preferably investigated. In this work, both electrode and cell level are considered to draw a more complete picture of cell thermal stability.

In order to describe the full cell behavior based on the identified two-component reaction kinetics, their individual impact on the temperature evolution needs to be considered via

$$\frac{dT}{dt} = \frac{1}{C_{p,\,\mathrm{cell}}} \sum_i \left(m_i \cdot H_i \cdot e^{-\frac{E_{a,i}}{k_B T}} \cdot (1-\alpha_i) \cdot (-\ln(1-\alpha_i))^{\frac{2}{3}} \right) \quad [14]$$

whereas the indexes i denotes the decomposition reaction on the anode or cathode side weighed with the respective composite electrode mass m_i and degree of reaction conversion α_i, which is calculated individually according to Eq. 4 and Eq. 5.

The kinetic description of the full cell behavior based on the two-component measurements appeared to be challenging as can be seen in Fig. 14. Exothermic reactions involving several reaction partners from both anode and cathode take place at the same time, which seems to be difficult to depict via two-component measurements alone. Furthermore, the two-component measurements did not show any exothermic reactions below 160°C so that the kinetics could not be determined for this temperature range. That makes a complete description impossible based on the here presented results. For this temperature range, the reader is referred to previous publications which form the basis for this work.[20,30] Basically, five different events can be identified when comparing the simulated cell behavior to the measured cell

Table VII. Values for start temperature T_{start} (i.e. $\alpha = 0$) and specific heat of the reaction H (i.e. $\alpha = 0 \ldots 1$) derived from the optimization procedure (Avrami-Erofeev 2/3).

		100% SoC T_{start} (°C) / H (J g^{-1})	50% SoC T_{start} (°C) / H (J g^{-1})	0% SoC T_{start} (°C) / H (J g^{-1})
100% SoH	Anode	174.95 / 433.40	-	-
	Cathode	165.95 / 432.74	170.82 / 269.14	175.82 / 218.33
80% SoH	Anode	162.13 / 503.22	-	-
	Cathode	161.03 / 370.02	-	171.30 / 258.20

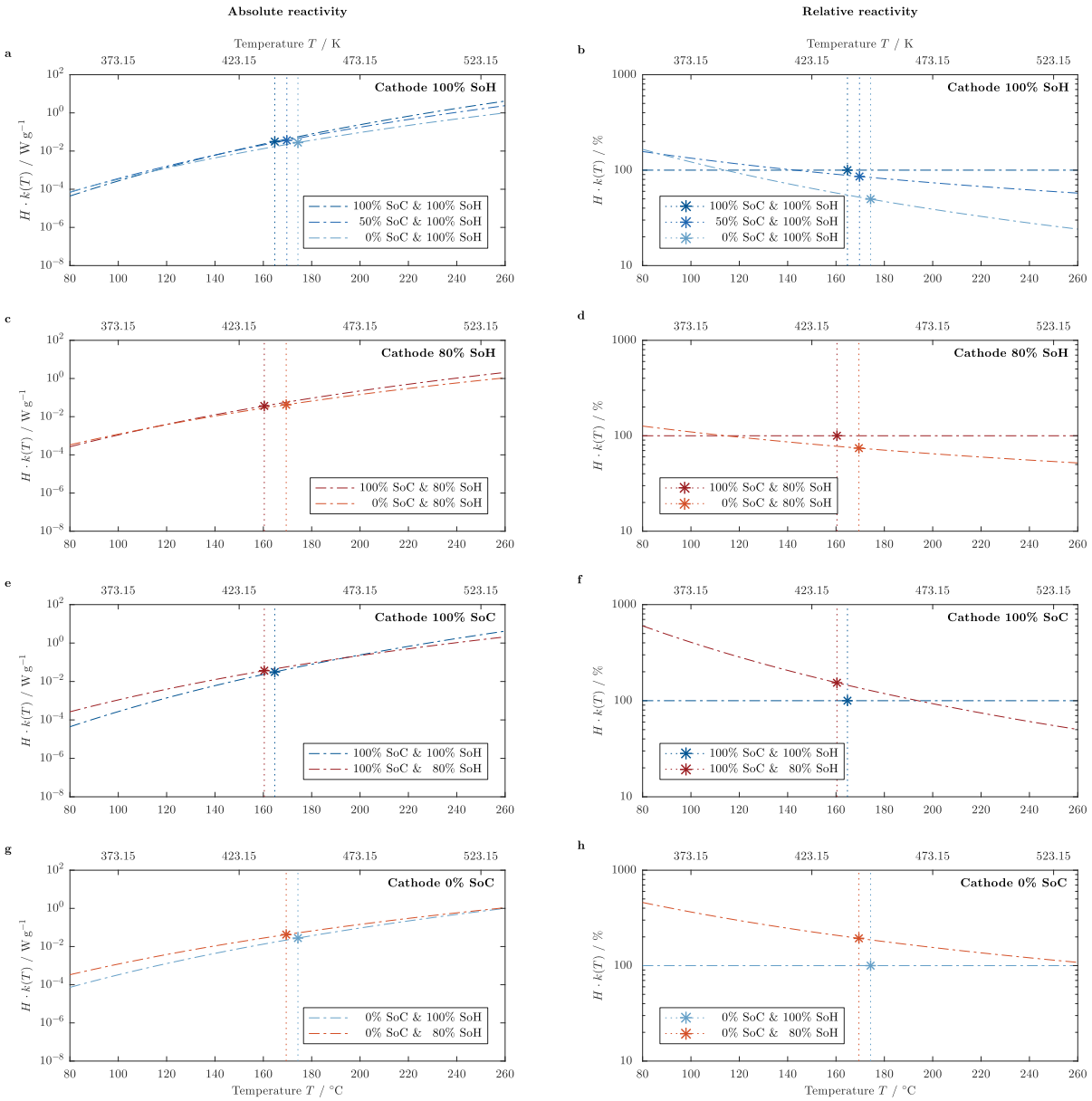

Figure 11. Results from the linearization and optimization procedure (Avrami-Erofeev 2/3) comparing the reactivity of NMC-442/electrolyte mixtures as a function of sample temperature (dash-dotted lines, T_{start} marked with asterisks and vertical lines) indicating the SoC influence at 100% SoH (a and b), the SoC influence at 80% SoH (c and d), the impact of SoH at 100% SoC (e and f) and the impact of SoH at 0% SoC (g and h).

behavior at 100% SoC. From ∼80°C to ∼135°C, the SEI is supposed to decompose (1) and subsequently it is reformed (2) from ∼135°C to ∼160°C.[20] From ∼160°C onwards, the cathode starts to decompose and react with the electrolyte (3) as we showed in our study. Between ∼215°C and ∼235°C, the polyester based separator is expected to melt consuming heat during the melting process leading to consecutive short circuits in the cell (4). This temperature span falls in the range of the melting point of polyesters. According to the manufacturer, the heat resistivity of the separator lies around 270°C due to its ceramic coating, which could even prevent the formation of severe internal short circuits up to this temperature. Above ∼235°C the cathode is expected to release further oxygen accelerating the reaction with the electrolyte (5) as also shown in Fig. 2c. The reaction of the anode with the electrolyte seems to play only a minor role within that temperature range, and is expected to significantly contribute to the self-heating of the cell at temperatures from ∼250°C onwards based on the lower reactivity compared to the cathode as discussed in the previous section and shown by the simulated second peak shown in Fig. 14. As a result of the combination of events and the varying dominance of reactions, each reaction's impact on the ARC trace may be shifted to higher temperatures in comparison to the two-component measurements as can be observed when looking into the impact of the anode on the simulated cell behavior.

In general, the self-heating rate during the full cell measurement is higher compared to the two-component measurements. On the one hand, this can be attributed to the already mentioned combination

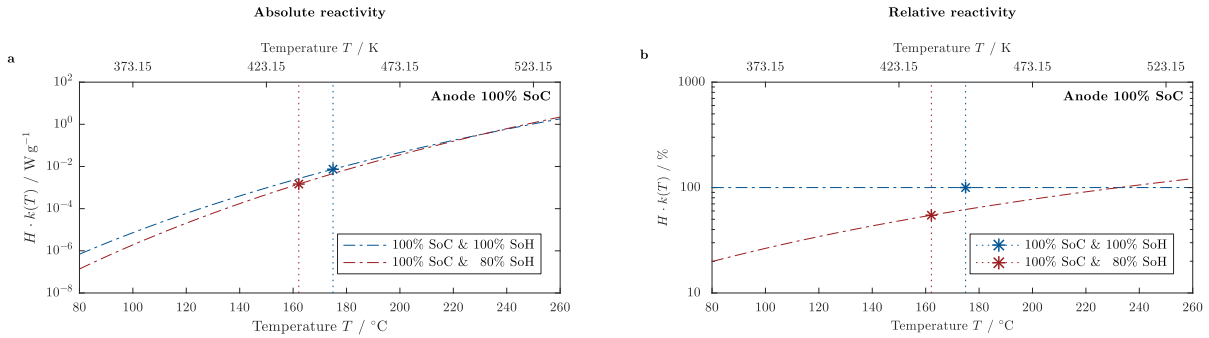

Figure 12. Results from the linearization and optimization procedure (Avrami-Erofeev 2/3) comparing the self-heat rate of MCMB/electrolyte mixtures as a function of sample temperature (dash-dotted lines, T_{start} marked with asterisks and vertical lines) indicating the SoH influence at 100% SoC.

and interaction of reactions within the full cell. On the other hand, the slightly larger share of thermally active mass in the pouch cell ($\phi_{cell} = 1.52$) leads to a higher self-heating rate compared to the two-component measurements ($\phi_{cathode} = 1.74$ and $\phi_{anode} = 1.90$), according to Eq. 7 and Table IV. Furthermore, a leakage or a rupture of the pouch foil resulting from a gassing of the electrolyte (evaporation of DEC starting at ∼127°C[63]) could have led to a contact between the electrolyte wetted electrode materials with environmental oxygen which could significantly increase the overall intensity of the reaction. At a temperature of ∼162°C, an abrupt voltage drop to 0 V could be observed which might hint at a severe electrolyte leakage or even the formation of a hard internal short involving excessive heating. In the two-component measurements carried out in this work, a contamination of the electrolyte wetted electrode materials with environmental oxygen was not possible due to the applied gastight Ti vessels. Based on the two-component systems investigated, also short circuits were not possible to form.

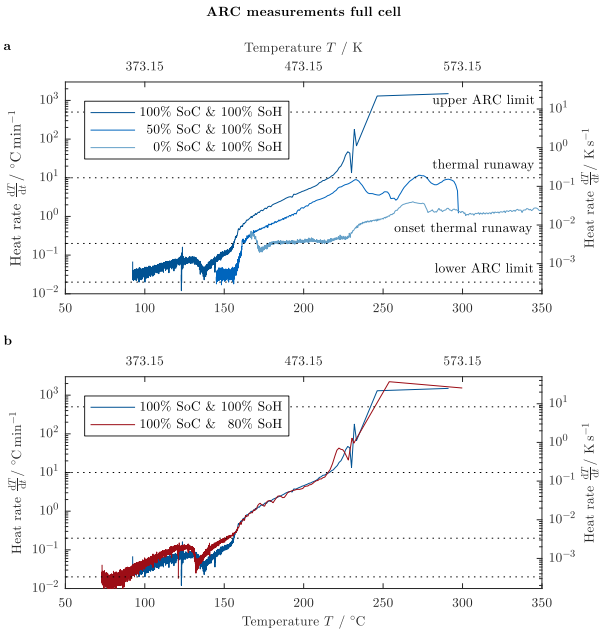

Figure 13. ARC-HWS results comparing the self-heating rate of 5 Ah pouch cells with MCMB as the anode and NMC-442 as the cathode as a function of sample temperature indicating the SoC influence at 100% SoH (a) and the impact of SoH at 100% SoC (b).

Conclusions

Within this work, a comprehensive thermal study on 5 Ah pouch cells (NMC-442/MCMB) and its thermally active components was presented based on combined ARC-HWS and XRD measurements. Composite anode and cathode materials were harvested from the studied 5 Ah pouch cells at defined states (i.e. 100%, 50%, and 0% cell SoC & 100% and 80% cell SoH) which were mixed with the used electrolyte (1 M $LiPF_6$ in EC:DEC 3:7 (by weight) + 2 wt% VC + 0.5 wt% LiBOB) and placed in gastight Ti vessels. The studied cathode samples showed an increase in the onset temperature of thermal runaway between 8°C and 5°C with decreasing SoC from 100% to 0% SoC for fresh and aged samples. Aging from 100% to 80% SoH led a decrease in onset temperature of thermal runaway up to 6°C for more delithiated cathodes (i.e. 100% cell SoC) and up to 9°C for more lithiated cathodes (i.e. 0% cell SoC). XRD measurements revealed that aged cathodes showed a lower degree of lithiation at 0% SoC which explains the higher reactivity in mixture with electrolyte with ongoing aging especially at a low cell SoC. The studied anode samples showed a comparably lower self-heating rate for all SoC and SoH combinations. For SoC values lower than 100%, no self-sustaining exothermic reaction could be detected at all. At 100% SoC, a negligible increase in onset temperature of thermal runaway could be observed with ongoing aging.

Avrami-Erofeev and autocatalytic reaction models were considered to describe the ARC trace of the two-component measurements, which allowed for a comparison of kinetic parameters such as the activation energy as well as the frequency factor of each reaction. For this purpose, a linearization of the ARC trace was performed based on the assumed reaction model, which was fitted in an iterative least squares

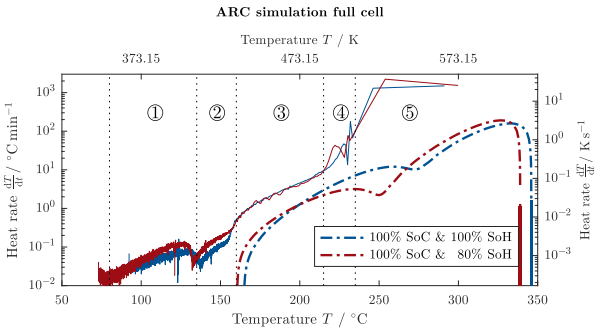

Figure 14. Simulated (Avrami-Erofeev 2/3, dash-dotted lines) and measured (solid lines) ARC-HWS results comparing the self-heating rate of 5 Ah pouch cells with MCMB as the anode and NMC-442 as the cathode as a function of sample temperature indicating the SoH influence at 100% SoC.

manner to the measurement data. It could be shown, that considering these parameters on their own did not necessarily lead to a straightforward conclusion in terms of relative changes in the reactivity of a sample as both activation energy and frequency factor simultaneously increased or decreased but never changed in opposing directions which would have been much easier to interpret. The authors showed that by evaluating the reaction rate constant together with the specific heat and the starting temperature of the reaction, the tendency observed during the ARC-HWS measurements could be analytically explained. With this approach, the qualitatively observed increase in reactivity of the cathode with ongoing aging at reduced SoC levels could be quantitatively confirmed. As the cathode was dominating in terms of the overall reactivity in this case, this implied a larger safety threat for cyclic aged cells compared to fresh cells, which especially holds for lower SoC values.

In accordance with the two-component measurements, full cells also showed a comparably lower reactivity with decreasing SoC and a relatively higher reactivity with ongoing aging. However, the first exothermic reactions occur at much lower temperatures compared to the two-component measurements, which may be attributed to the decomposition and reformation reaction of the SEI. This reaction could not be observed during the two-component measurements of the corresponding anode, which the authors believe to be primarily based on the chosen sample preparation in a dry room environment and the comparably higher ϕ-factor of the two-component measurements itself. Based on the identified reaction models from the two-component measurements, the full cell ARC trace could be simulated. However, the predicted ARC trace did not fully resemble the tendencies observed during the full cell measurements. On the one hand, this could be attributed to the already mentioned lacking description of the SEI decomposition and reformation reaction as well as the lacking description of further processes such as separator melting or cell shorting in this study. On the other hand, possible cross-interactions between reaction species from the anode and the cathode could not be depicted via two-component measurements alone. What is more, a possible rupture of the pouch seam during the full cell measurement might resulted in a contamination of the reaction with environmental oxygen. Further research will be conducted regarding the active mass ratio of the two-component measurements to increase the detectable signal and considering the sample preparation to avoid the evaporation of volatile components as can be found e.g. in the SEI. Based on the depicted reaction models, the thermal stability of NMC-442/MCMB cells can be described during various abuse scenarios as both a function of SoC and SoH, which will be of particular interest for modeling and simulation purposes of this cell chemistry.

Acknowledgment

The work presented here was supported by the German Federal Ministry of Education and Research (03X4631N and 03X4631P, *SafeBatt*). The authors thank Oliver Nolte from Volkswagen AG and Juhyon Lee from BMW AG for supporting the work with fruitful discussions.

Appendix

In order to be able to describe the underlying reaction kinetics of a cell individually as a function of SoC (0. . . 1) and SoH (0.8. . . 1), relevant kinetic parameters (see Table VI and Table VII) such as the frequency factor γ (s^{-1}), the activation energy E_a (J) and the specific heat of the reaction H (J g^{-1}) were fitted according to an Avrami-Erofeev 2/3 reaction model. For the cathode side, Eq. A1, Eq. A2 and Eq. A3 apply.

$$\gamma_{ca}\,(SoC,\,SoH) = 0.0535 \cdot e^{(-6.2607 \cdot SoC + 10.3735 \cdot SoC \cdot SoH + 16.6386 \cdot SoH)} \quad [A1]$$

$$E_{a,ca}(SoC,\,SoH) = ((0.7487 \cdot SoH - 0.4707) \cdot SoC + (1.0341 \cdot SoH + 0.3400)) \cdot 1 \times 10^{-19} \quad [A2]$$

$$H_{ca}(SoC,\,SoH) = (517.2133 \cdot SoH - 301.9439) \cdot SoC^2 + (-205.7713 \cdot SoH + 422.8129) \quad [A3]$$

As no self-sustaining exothermal decomposition reaction could be detected for SoC values of 50% and 0%, reaction kinetics on the anode side can be only described as a function of SoH (0.8. . . 1) at 100% SoC.

$$\gamma_{an}\,(SoH) = 1.0849 \times 10^{18} \cdot e^{-17.9926 \cdot SoH} \quad [A4]$$

$$E_{a,an}\,(SoH) = (-1.3077 \cdot SoH + 3.4429) \cdot 1 \times 10^{-19} \quad [A5]$$

$$H_{an}\,(SoH) = -349.1208 \cdot SoH + 782.5197 \quad [A6]$$

ORCID

A. Rheinfeld https://orcid.org/0000-0003-0995-7266

References

1. P. Meister, H. Jia, J. Li, R. Kloepsch, M. Winter, and T. Placke, *Chem. Mater.*, **28**(20), 7203 (2016).
2. T. Placke, R. Kloepsch, S. Dühnen, and M. Winter, *J Solid State Electrochem*, **21**(7), 1939 (2017).
3. R. Wagner, N. Preschitschek, S. Passerini, J. Leker, and M. Winter, *J. Appl. Electrochem.*, **43**(5), 481 (2013).
4. D. H. Doughty and E. P. Roth, *Electrochem. Soc. Interface*, **21**(2), 37 (2012).
5. P. G. Balakrishnan, R. Ramesh, and T. Prem Kumar, *J. Power Sources*, **155**(2), 401 (2006).
6. P. Biensan, B. Simon, J. P. Pérès, A. de Guibert, M. Broussely, J. M. Bodet, and F. Perton, *J. Power Sources*, **81–82**(0), 906 (1999).
7. M. Börner, A. Friesen, M. Grützke, Y. P. Stenzel, G. Brunklaus, J. Haetge, S. Nowak, F. M. Schappacher, and M. Winter, *J. Power Sources*, **342**, 382 (2017).
8. E. P. Roth and D. H. Doughty, *J. Power Sources*, **128**(2), 308 (2004).
9. P. Röder, B. Stiaszny, J. C. Ziegler, N. Baba, P. Lagaly, and H.-D. Wiemhöfer, *J. Power Sources*, **268**, 315 (2014).
10. M. Fleischhammer, T. Waldmann, G. Bisle, B.-I. Hogg, and M. Wohlfahrt-Mehrens, *J. Power Sources*, **274**, 432 (2015).
11. S. Hildebrand, A. Friesen, J. Haetge, V. Meier, F. Schappacher, and M. Winter, *ECS Trans.*, **74**(1), 85 (2016).
12. J. Vetter, P. Novák, M. R. Wagner, C. Veit, K.-C. Möller, J. O. Besenhard, M. Winter, M. Wohlfahrt-Mehrens, C. Vogler, and A. Hammouche, *J. Power Sources*, **147**(1–2), 269 (2005).
13. M. Reichert, J. Haetge, D. Berghus, C. Wendt, V. Meier, U. Rodehorst, S. Passerini, F. Schappacher, and M. Winter, *ECS Trans.*, **61**(27), 87 (2014).
14. J. Jiang and J. R. Dahn, *Electrochem. Commun.*, **6**(1), 39 (2004).
15. Y. Wang, J. Jiang, and J. R. Dahn, *Electrochem. Commun.*, **9**(10), 2534 (2007).
16. S. Hildebrand, C. Vollmer, M. Winter, and F. M. Schappacher, *J. Electrochem. Soc.*, **164**(9), A2190 (2017).
17. L. Ma, M. Nie, J. Xia, and J. R. Dahn, *J. Power Sources*, **327**, 145 (2016).
18. S. Brox, S. Roser, T. Husch, S. Hildebrand, O. Fromm, M. Korth, M. Winter, and I. Cekic-Laskovic, *ChemSusChem*, **9**(13), 1704 (2016).
19. S. Brox, S. Röser, B. Streipert, S. Hildebrand, U. Rodehorst, X. Qi, R. Wagner, M. Winter, and I. Cekic-Laskovic, *ChemElectroChem*, **4**(2), 304 (2017).
20. M. N. Richard and J. R. Dahn, *J. Electrochem. Soc.*, **146**(6), 2068 (1999).
21. A. Friesen, F. Horsthemke, X. Mönnighoff, G. Brunklaus, R. Krafft, M. Börner, T. Risthaus, M. Winter, and F. M. Schappacher, *J. Power Sources*, **334**, 1 (2016).
22. D. I. Townsend and J. C. Tou, *Thermochim. Acta*, **37**(1), 1 (1980).
23. X. Feng, J. Sun, M. Ouyang, F. Wang, X. He, L. Lu, and H. Peng, *J. Power Sources*, **275**, 261 (2015).
24. J. Geder, H. E. Hoster, A. Jossen, J. Garche, and D. Y. Yu, *J. Power Sources*, **257**, 286 (2014).
25. S. EL Khakani, D. Rochefort, and D. D. MacNeil, *J. Electrochem. Soc.*, **163**(7), A1311 (2016).
26. G.-Y. Kim and J. R. Dahn, *J. Electrochem. Soc.*, **160**(8), A1108 (2013).
27. R. Spotnitz and J. Franklin, *J. Power Sources*, **113**(1), 81 (2003).
28. T. D. Hatchard, D. D. MacNeil, A. Basu, and J. R. Dahn, *J. Electrochem. Soc.*, **148**(7), A755 (2001).
29. S. U. Kim, P. Albertus, D. Cook, C. W. Monroe, and J. Christensen, *J. Power Sources*, **268**, 625 (2014).
30. M. N. Richard and J. R. Dahn, *J. Electrochem. Soc.*, **146**(6), 2078 (1999).
31. D. D. MacNeil, T. D. Hatchard, and J. R. Dahn, *J. Electrochem. Soc.*, **148**(7), A663 (2001).
32. D. D. MacNeil, L. Christensen, J. Landucci, J. M. Paulsen, and J. R. Dahn, *J. Electrochem. Soc.*, **147**(3), 970 (2000).
33. D. D. MacNeil and J. R. Dahn, *J. Phys. Chem. A*, **105**(18), 4430 (2001).
34. P. Peng, Y. Sun, and F. Jiang, *Heat Mass Transfer*, **50**(10), 1405 (2014).
35. P. T. Coman, E. C. Darcy, C. T. Veje, and R. E. White, *J. Electrochem. Soc.*, **164**(4), A587 (2017).
36. G.-H. Kim, A. Pesaran, and R. Spotnitz, *J. Power Sources*, **170**(2), 476 (2007).
37. C. von Lüders, V. Zinth, S. V. Erhard, P. J. Osswald, M. Hofmann, R. Gilles, and A. Jossen, *J. Power Sources*, **342**, 17 (2017).
38. V. Zinth, C. von Lüders, M. Hofmann, J. Hattendorff, I. Buchberger, S. Erhard, J. Rebelo-Kornmeier, A. Jossen, and R. Gilles, *J. Power Sources*, **271**, 152 (2014).

39. D. H. Doughty, *Vehicle Battery Safety Roadmap Guidance*, (2012).
40. R. Wagner, B. Streipert, V. Kraft, A. Reyes Jiménez, S. Röser, J. Kasnatscheew, D. R. Gallus, M. Börner, C. Mayer, H. F. Arlinghaus, M. Korth, M. Amereller, I. Cekic-Laskovic, and M. Winter, *Adv. Mater. Interfaces*, **3**(15), 1600096 (2016).
41. Y. Qian, P. Niehoff, M. Börner, M. Grützke, X. Mönnighoff, P. Behrends, S. Nowak, M. Winter, and F. M. Schappacher, *J. Power Sources*, **329**, 31 (2016).
42. B. J. Hwang, Y. W. Tsai, D. Carlier, and G. Ceder, *Chem. Mater.*, **15**(19), 3676 (2003).
43. M. Balasubramanian, X. Sun, X. Yang, and J. McBreen, *J. Power Sources*, **92**(1-2), 1 (2001).
44. T. Inoue and K. Mukai, *Electrochem. Commun.*, **77**, 28 (2017).
45. M. Winter, *Z. Phys. Chem.*, **223**(10-11), 1395 (2009).
46. S.-M. Bak, E. Hu, Y. Zhou, X. Yu, S. D. Senanayake, S.-J. Cho, K.-B. Kim, K. Y. Chung, X.-Q. Yang, and K.-W. Nam, *ACS Appl. Mater. Interfaces*, **6**(24), 22594 (2014).
47. H. Wang, Y.-I. Jang, B. Huang, D. R. Sadoway, and Y.-M. Chiang, *J. Electrochem. Soc.*, **146**(2), 473 (1999).
48. S.-T. Myung, K.-S. Lee, C. S. Yoon, Y.-K. Sun, K. Amine, and H. Yashiro, *J. Phys. Chem. C*, **114**(10), 4710 (2010).
49. D. D. MacNeil and J. R. Dahn, *J. Electrochem. Soc.*, **148**(11), A1205 (2001).
50. M. E. Brown, D. Dollimore, A. K. Galwey, C. H. Bamford, C. F. H. Tipper, and Editors, *Reactions in the solid state*, New York, Amsterdam, New York, Elsevier Scientific Pub. Co (1980).
51. S. C. Chen, C. C. Wan, and Y. Y. Wang, *J. Power Sources*, **140**(1), 111 (2005).
52. A. Loges, S. Herberger, P. Seegert, and T. Wetzel, *J. Power Sources*, **336**, 341 (2016).
53. V. Vishwakarma and A. Jain, *J. Power Sources*, **272**, 378 (2014).
54. P. Gotcu and H. J. Seifert, *PCCP*, **18**(15), 10550 (2016).
55. A. Rheinfeld, S. Kosch, S. V. Erhard, P. J. Osswald, B. Rieger, and A. Jossen, *J. Electrochem. Soc.*, **163**(14), A3046 (2016).
56. David R. Lide, Editor, *CRC Handbook of Chemistry and Physics: 84th Edition*, CRC Press (2003).
57. D. D. MacNeil and J. R. Dahn, *J. Electrochem. Soc.*, **149**(7), A912 (2002).
58. T. Inoue and K. Mukai, *ACS Appl. Mater. Interfaces*, **9**(2), 1507 (2017).
59. J. Yamaki, H. Takatsuji, T. Kawamura, and M. Egashira, *Solid State Ion.*, **148**(3-4), 241 (2002).
60. H. H. Lee, C. C. Wan, and Y. Y. Wang, *J. Electrochem. Soc.*, **151**(4), A542 (2004).
61. H. Park, T. Yoon, Y. Kim, J. G. Lee, J. Kim, H.-s. Kim, J. H. Ryu, J. J. Kim, and S. M. Oh, *J. Electrochem. Soc.*, **162**(6), A892 (2015).
62. Z. Zhang, D. Fouchard, and J. R. Rea, *J. Power Sources*, **70**(1), 16 (1998).
63. D. Li, W. Fang, Y. Xing, Y. Guo, and R. Lin, *J. Hazard. Mater.*, **161**(2-3), 1193 (2009).

Erratum: Thermal Analysis of $LiNi_{0.4}Co_{0.2}Mn_{0.4}O_2$/Mesocarbon Microbeads Cells and Electrodes: State-of-Charge and State-of-Health Influences on Reaction Kinetics [*J. Electrochem. Soc.*, 165, A104 (2018)]

S. Hildebrand,[1,2] A. Rheinfeld,[3] A. Friesen,[1] J. Haetge,[1] F. M. Schappacher,[1] A. Jossen,[3] and M. Winter[1,2,4]

[1]*MEET Battery Research Center, Westfälische Wilhelms-Universität Münster, D-48149 Münster, Germany*
[2]*Institute of Physical Chemistry, Westfälische Wilhelms-Universität Münster, D-48149 Münster, Germany*
[3]*Institute for Electrical Energy Storage Technology, Technical University of Munich, D-80333 Munich, Germany*
[4]*Helmholtz-Institute Münster, IEK-12, Research Center Jülich GmbH, D-48149 Münster, Germany*

 [DOI: 10.1149/2.0851802jes] Published January 20, 2018.

Figure 2 on page A106 should appear as shown at right.

Equation 14 on page A113 should appear as

$$\frac{\mathrm{d}T}{\mathrm{d}t} = \frac{1}{C_{p,\mathrm{cell}}} \sum_i \left(m_i \cdot H_i \cdot \gamma_i \cdot e^{-\frac{E_{\mathrm{a},i}}{k_\mathrm{B} T}} \cdot (1-\alpha_i) \cdot (-\ln(1-\alpha_i))^{\frac{2}{3}} \right) \quad [14]$$

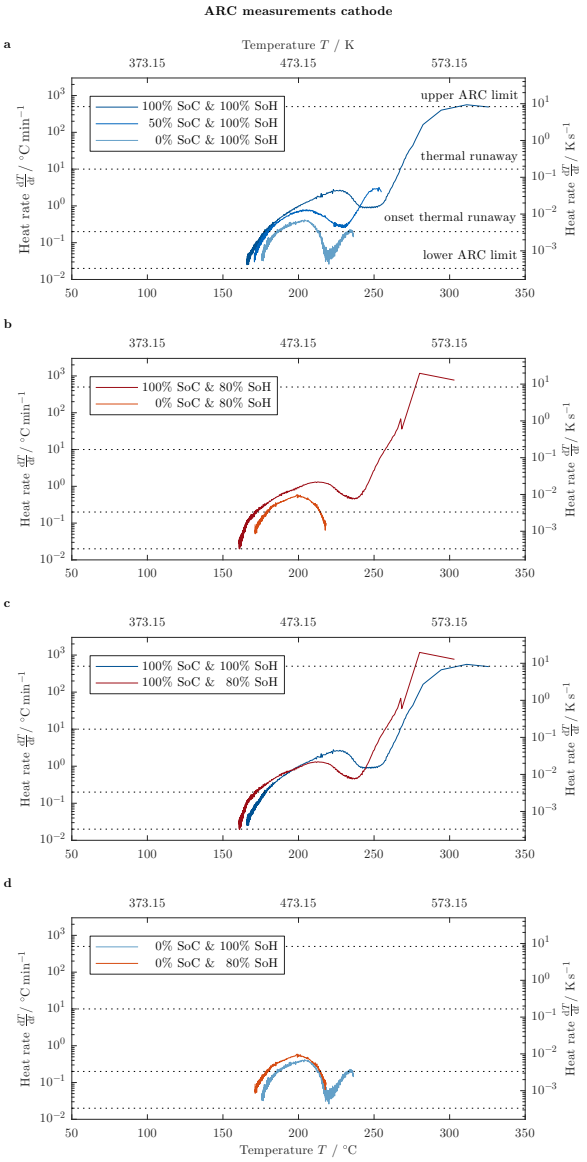

Figure 2. ARC-HWS results comparing the self-heating rate of NMC-442/electrolyte mixtures as a function of sample temperature indicating the SoC influence at 100% SoH (a), the SoC influence at 80% SoH (b), the impact of SoH at 100% SoC (c) and the impact of SoH at 0% SoC (d).

3 Heat Generation due to High Rate Operation

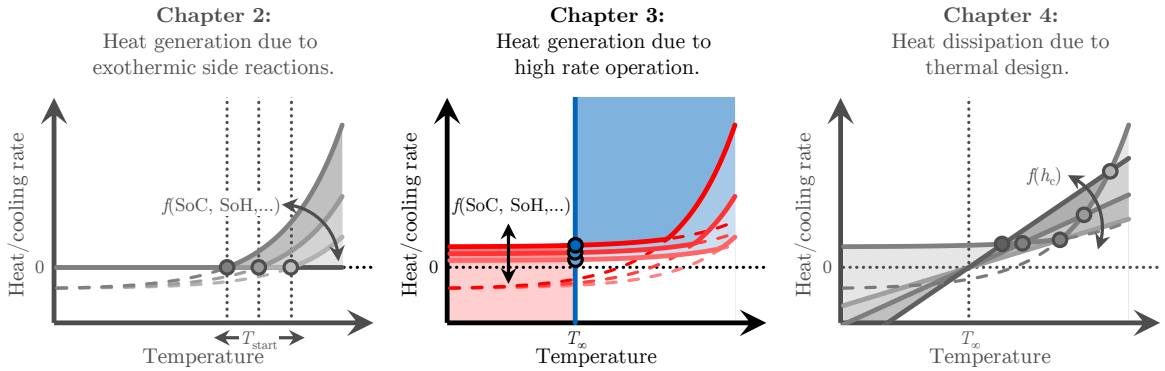

Figure 3.1: Outline of chapter 3.

Quantifying the heat generation arising from both reversible and especially irreversible heat effects associated with a high rate discharge operation of a Li-ion cell such as short circuits is essential in order to evaluate the initiation of cell thermal runaway.

As already pointed out in section 1.4.2, the lack of experimental data extracting a cell's electrochemical short circuit characteristics under well-defined electrical and thermal test conditions makes a thorough evaluation of a cell's behavior before a thermal runaway might occur difficult, which will eventually dominate the measured signals. Consequently, the lack of experimental data that specifically addresses the electrochemical short circuit characteristics of electrodes and cells under controlled electrical and thermal test conditions means that validated modeling approaches are scarce, as described in section 1.5.

Within this chapter, an approach combining isothermal measurements with modeling and simulation in order to determine a cell's heat generation due to high rate discharge operation is presented (see Fig. 3.1). First of all, the dominating mechanisms that define the rate capability of materials, electrodes, and cells are briefly reviewed in section 3.1, with respect to excessively high discharge rates as experienced during hard short circuits. With these rate limiting mechanisms in mind, liquid phase rate limitations are examined via both experiment and modeling and simulation during constant current discharge for coin cells comprising electrochemically engineered electrodes within section 3.2. By introducing a custom experimental setup which allows for a maximum control of electrical and thermal test conditions throughout external short circuit tests applied to small-sized pouch-type cells, the quasi-isothermal short circuit behavior of Li-ion cells is experimentally evaluated in section 3.3. With this experimental data basis, a physical-chemical model describing a cell's short circuit behavior is validated and used to identify underlying mechanisms and rate limiting effects in section 3.4, which result in the experimentally observed characteristics discussed in section 3.3.

3.1 Rate capability of active materials, electrodes, and cells

As described in sections 1.4.2 and 1.5, a Li-ion cell's short circuit characteristics can be closely related to effects which are generally associated with rate limitation. In the context of Li-ion cells, rate limitation can be understood as a significantly decreasing capacity retention with increasing current or current density and/or reduced temperature. Such noticeable decrease in retrievable capacity can be correlated to a premature approach of a cell's voltage limits due to a comparably large electrode polarization arising from limitations in electron transport, ion movement, and/or reaction kinetics.
The rate capability of materials, electrodes, and cells has been thoroughly investigated in the past in order to understand the reason for an undesired decay in capacity retention so that cells with both HE and HP characteristics can be obtained. Depending on the chosen combination of active materials exhibiting a certain size and shape of the active material particles as well the chosen electrode configuration including electrode thickness and morphology, either a balanced or unbalanced contribution of individual mechanisms to the overall polarization of the electrodes and separator can be achieved. With one or more mechanisms dominating a cell's overvoltage, rate limitation can be observed, whereas a maximized capacity retention is possible for a certain material combination when each underlying mechanism contributes more or less equally to the cell's behavior.[339]
Whilst considerations associated with rate limitations are rather common when trying to assess the suitability of a certain material or electrode design for a given application, such evaluation can barely be found in the context of a cell's short circuit behavior. Little work has yet been presented that specifically tries to correlate observations made throughout short circuit conditions in connection with rate limiting effects, as the focus is commonly laid on the triggering mechanism of exothermic side reactions. With the simulation based works of Yamauchi et al.,[301] Zavalis et al.,[253] and Mao et al.,[295,296] rate limiting effects observed throughout both internal and external short circuit conditions could be explained by describing underlying mechanisms, such as a depletion of Li-ions within the liquid phase of the positive electrode with ongoing short circuit duration. A similar effect was also reported by Gallagher et al.[340] as part of rate capability investigations of thick electrodes.
Experimental investigations of external short circuits carried out by Kriston et al.[257] indicate varying rate limiting mechanisms occurring during short circuits as already pointed out by Mao et al.[295,296] Hence, not only a cathodic liquid phase depletion of Li-ions may limit the evolving short circuit current, but also solid phase limitations leading to a cathodic saturation or an anodic depletion are likely to occur. These mechanisms will ultimately affect charge transfer kinetics resulting in large reaction overpotentials and, consequently, strongly decreasing currents.
In order to be able to describe rate limiting mechanisms based on depletion and saturation effects accompanied with ion movement and reaction kinetics, physical-chemical models such as Newman-type p2D (i.e. 1D+1D) models are applied considering mass and charge transport throughout the solid and liquid components of the electrodes and separator (x-dimension) as well as concentration gradients throughout the active material particles (r-dimension) and associated charge-transfer reactions at the interface between solid and liquid phase.[290,291] However, numerical issues associated with the nature of the applied Butler-Volmer equation and the calculated exchange current density i_0 ($\mathrm{A\,m^{-2}}$) in order to derive the pore wall flux j_n ($\mathrm{mol\,m^{-2}\,s^{-1}}$), as suggested by the Newman group,[290,341] need to be handled at such extremes. The pore wall flux can be calculated as follows:

$$j_\mathrm{n} = \frac{i_0}{F}\left[\exp\left(\frac{\alpha_\mathrm{a}F}{RT}\eta\right) - \exp\left(\frac{\alpha_\mathrm{c}F}{RT}\eta\right)\right] \tag{3.1}$$

with α_a and α_c representing the anodic and cathodic charge transfer coefficients of the reaction and η (V) describing the reaction overpotential together with Faraday's constant F (96485 C mol^{-1}) and the universal gas constant R (8.314 J mol^{-1} K^{-1}). By including experimentally measured half-cell equilibrium potentials E_{eq} (V) in the Butler-Volmer equation, η can be written as:[290,341]

$$\eta = \Phi_s - \Phi_l - E_{eq} \tag{3.2}$$

based on the potentials Φ_s and Φ_l (V) in the solid and liquid phase of the electrodes. The exchange current density is commonly calculated as:[290,341]

$$i_0 = F k_c^{\alpha_a} k_a^{\alpha_c} \left(\frac{c_l}{c_{l,\,ref}} \right)^{\alpha_a} (c_{s,\,max} - c_{s,\,surf})^{\alpha_a} (c_{s,\,surf})^{\alpha_c} \tag{3.3}$$

with the anodic and cathodic reaction rate constants k_a and k_c (m s^{-1}), the salt concentration in the liquid electrolyte c_l (mol m^{-3}) and its associated reference concentration $c_{l,\,ref}$ of 1 mol m^{-3}, as well as the maximum Li-ion concentration and surface concentration of the solid active material particles $c_{s,\,max}$ and $c_{s,\,surf}$. If not further modified, this combination of equations leads to numerical instabilities and, consequently, fails to describe the cell's behavior if i_0 approaches 0, as experienced during depletion and saturation processes, whilst E_{eq} attains a finite value.[342] In order to overcome these issues, a modification of the initially stated Butler-Volmer equation can be applied.[295,296,343]
Rate limiting mechanisms will be more closely investigated via both experiments and modeling and simulation in the further course of this chapter in order to be able to describe high rate operation and associated losses resulting in heat generation based on the applied current as well as a Li-ion cell's effective overvoltage.

3.2 Understanding liquid phase rate limitations via electrochemically engineered electrodes

Within this section, the article titled *Increasing the Discharge Rate Capability of Lithium-Ion Cells with Laser-Structured Graphite Anodes: Modeling and Simulation* is presented. This work forms the basis for understanding rate limiting mechanisms occurring throughout high rate discharge operation, which can be correlated to charge and mass transport limitations in the liquid and solid components of Li-ion cells, as well as reaction kinetics. These considerations help to understand characteristics throughout related high rate discharge operation profiles such as short circuit conditions.
Previously reported experimental results[344] of coin cells comprising laser-structured graphite anodes and NMC-111 cathodes together with an electrolyte containing 1 M $LiPF_6$ in EC:EMC 3:7 (by weight) with 2 wt% VC were analyzed with the aid of a newly developed 3D+1D homogenized physical-chemical model of the structured electrode geometry. Based on the structuring process, a bi-tortuous electrode morphology is created[345,346] which reduces the comparably high through-plane tortousity[347,348] within the graphite anode facilitating ion transport. Similar to the homogenized p2D approach of Newman-type models,[290,291] the homogenized three-dimensional porous electrode model, depicting the hole-like electrode structuring pattern, is coupled to the one-dimensional representation of the active material particles which allows the depiction of the local distribution of concentrations and potentials in both the liquid and solid phase including the associated current densities and overpotentials.

With the aid of the model, three observed stages in capacity retention improvement compared to cells with unstructured, pristine graphite anodes could be identified and correlated to the simulated distribution in liquid and solid phase concentration throughout the cell. At C-rates below 1C, the structuring process and, hence, electrode morphology plays only a minor role leading to an almost identical solid phase concentration distribution within the electrodes and, therefore, to a similar capacity retention between coin cells with unstructured and structured anodes. At higher C-rates, the liquid phase concentration becomes increasingly inhomogeneous, which can be reduced by the anode structuring process, enhancing ion transport by creating a bi-tortuous electrode structure reducing the impact of the comparably large tortuousity of pristine graphite anodes.[347,348] This homogenization in liquid phase concentration comes with a reduced polarization resulting from ion movement within the liquid electrolyte which leads to an enhanced utilization of the active materials and, consequently, higher capacity retention. However, beyond 3C, this effect diminishes until it is completely faded at C-rates as large as 10C. With liquid phase concentrations within the cathode approaching complete depletion throughout the entire electrode, the homogenizing effect on liquid and solid phase concentration within the anode becomes more and more irrelevant as reaction overpotentials within the cathode tend to dominate. This effect not only results in a reduction of the difference in capacity retention between the two cell types but also in a general decrease in capacity retention to around 15 % at 10C compared to the discharged capacity at C/5.
The presented results suggest a dominating effect of a cathodic liquid phase depletion and associated overpotentials limiting the rate capability of Li-ion cells at very high currents. This effect can only be marginally influenced by the electrode morphology resulting in large reaction based overpotentials. Hence, a similar rate limiting effect may easily be observable under such extreme conditions as occurring during short circuits which supports earlier findings described in the previous section.[253,295,296,301,340] Furthermore, extensive simulation studies showed the importance of implementing diffusion limited reaction kinetics in order to guarantee smooth model operation. Both effects will be more closely evaluated in the following sections of this chapter.

Author contribution Jan B. Habedank initiated the idea of laser-structuring graphite anodes and supplied the coin cell measurement data. Ludwig Kraft carried out simulation studies, supported the model development, and helped to optimize the model parameters. Alexander Rheinfeld developed the homogenized three-dimensional electrode model to describe structured electrode morphologies. Christina Krezdorn supported both model development and simulation studies. The data was analyzed and interpreted by Alexander Rheinfeld, Ludwig Kraft, and Jan B. Habedank. The manuscript was written by Ludwig Kraft, Alexander Rheinfeld, and Jan B. Habedank and was edited by Andreas Jossen and Michael F. Zaeh. All authors discussed the data and commented on the results.

Increasing the Discharge Rate Capability of Lithium-Ion Cells with Laser-Structured Graphite Anodes: Modeling and Simulation

Jan B. Habedank, Ludwig Kraft, Alexander Rheinfeld, Christina Krezdorn, Andreas Jossen, Michael F. Zaeh

Journal of The Electrochemical Society 165 (7), pp. A1563–A1573, 2018

Permanent weblink:
http://dx.doi.org/10.1149/2.1181807jes

Increasing the Discharge Rate Capability of Lithium-Ion Cells with Laser-Structured Graphite Anodes: Modeling and Simulation

Jan B. Habedank,[1,=] Ludwig Kraft,[2,=,*,z] Alexander Rheinfeld,[2,=,*] Christina Krezdorn,[1] Andreas Jossen,[2] and Michael F. Zaeh[1]

[1]*Institute for Machine Tools and Industrial Management, Technical University of Munich (TUM), Munich, Germany*
[2]*Institute for Electrical Energy Storage Technology, Technical University of Munich (TUM), Munich, Germany*

A physical-chemical model is suggested, which is able to describe the enhanced discharge rate capability of lithium-ion cells by using laser-structured graphite anodes. Recently published test data of coin cells comprising unstructured and structured graphite anodes with $LiNi_{1/3}Co_{1/3}Mn_{1/3}O_2$ cathodes is used for the presented purpose of modeling, simulation and validation. To minimize computational demand, a homogenized three-dimensional model of a representative hole structure is developed, accounting for charge and mass transport throughout the cell layers and one-dimensional diffusion within radial-symmetric particles. First, a standard pseudo-two-dimensional model is calibrated against rate capability test data of coin cells with unstructured anodes. The calibrated parameter set is transferred to the three-dimensional model in order to simulate the transient voltage response and the discharged capacity depending on the applied C-rate. The simulation data shows excellent agreement with experimental data for both cell types. Three stages of rate capability enhancement are identified showing an improved relative capacity retention of 11−24% at 3C. Experimental and simulation data reveal a restricted C-rate window, which can be positively affected by the structuring process, whereas both shape and pattern of the structuring process can be further optimized with the model.
 [DOI: 10.1149/2.1181807jes]

Manuscript submitted March 26, 2018; revised manuscript received May 4, 2018. Published May 23, 2018.

Lithium-ion batteries (LIBs) are the predominant energy storage solution for consumer electronics, electric vehicles and stationary energy storage devices. However, especially LIBs with high energy densities struggle to deliver sufficient energy at high discharge rates.[1] This rate limitation is caused by internal cell resistances of diverse origins, which has recently been reported to be dominated by the ionic resistance in the liquid electrolyte for common LIB electrode morphologies and operation strategies.[2,3] The electrodes of LIBs typically consist of active material particles mixed with binders and conductive agents and are coated onto metallic current collector foils. The pores of the electrodes and the electronically insulating separator are filled with the electrolyte solution, enabling ion transport between the electrodes. In most automotive LIBs, lithium nickel cobalt manganese oxide $Li(Ni_xCo_yMn_z)O_2$ (NMC) is employed as the cathode active material due to its high specific capacity and voltage level vs. Li/Li^+. For nearly all commercially available cells, graphite is used as the anode active material. Natural graphite particles have a flake-like shape, which makes them align parallel to the current collector foil during the coating and the subsequent calendering process. This particle orientation implies a strong tortuosity anisotropy within the graphite anodes, creating particularly long diffusion pathways for Li-ion transport through the electrode.[4] This results in large Li-ion concentration gradients within the electrode at high charge and discharge rates, causing concentration overpotentials and, consequently, a premature approach of the voltage limits resulting in an insufficient usage of the available capacity.[3]

Previously, it has been demonstrated that structured electrodes can have a positive impact on the cell's performance at higher current rates.[5] Multiple fabrication processes have been introduced, such as co-extrusion of the active material[6] and combinations of extrusion and sintering processes.[7] Many of the battery concepts involve a three-dimensional (3D) cell setup, in which the electrodes interlock on a micro or nano scale, creating a large reaction surface area and excellent charge transfer characteristics.[8] As laser-based manufacturing processes have been gaining importance in the processing industry over the past decades, particular attention has been given to laser-structuring of state-of-the-art electrodes. This concept involves high-precision ablation of a small fraction of the active material from the initial coating, generating additional diffusion pathways, which are solely filled with electrolyte. Significant improvements in rate capability were observed for laser-structured cathodes, e.g. consisting of lithium manganese oxide $LiMn_2O_4$,[9] as well as for graphite anodes.[10]

A few simulation-based approaches have been published in the past, explaining the improved rate capability for structured cathodes[6,11] and anodes[12] due to the reduced overall tortuosity of the electrodes. Based on the structuring process, a more homogeneous active material utilization is achieved and overpotentials are reduced during operation. To the knowledge of the authors, no experimentally validated physical-chemical model of LIBs with structured graphite anodes has been presented so far. Such a model, however, is needed to optimize the geometry of the superimposed structure while taking manufacturing constraints into account. In the work presented here, a homogenized 3D model of an NMC/graphite cell with laser induced microstructures within the anode is introduced taking one-dimensional (1D) diffusion within the solid particles into account. The adapted 3D+1D electrochemical model is based on Newman's pseudo two-dimensional (p2D) model of a LIB[13] accounting for both theories of porous electrodes and concentrated solutions.[14] The presented model is implemented and solved with the aid of a commercially available finite element method (FEM) tool. Geometrical features of the electrodes are matched to previously measured data.[10] Most relevant material parameters, such as the open circuit potentials of the used materials, were determined experimentally. The model is utilized to not only predict the transient voltage curves for discharge rates from C/5 to 10C and the derived capacity at the end of discharge, but also to determine Li-ion concentration gradients throughout the cell representing the cause of overpotentials during operation. The simulation results show excellent accordance with experimental data collected during the considered rate capability tests. Based on these results, the presented model can be used for optimizing a superimposed electrode structure, allowing for further improvements in terms of rate capability of LIBs.

Experimental

In this section, the experimental procedures for electrode fabrication, laser-structuring of the anodes as well as cell assembly and testing are described.

Electrode fabrication.—The components for the electrode inks were mixed with N-methyl-2-pyrrolidone (NMP, Sigma-Aldrich, USA) in a planetary vacuum mixer (Thinky Mixer ARV-310, Thinky, USA) for 10 min at ambient pressure and temperature. The graphite

=These authors contributed equally to this work.
*Electrochemical Society Student Member.
zE-mail: ludwig.kraft@tum.de

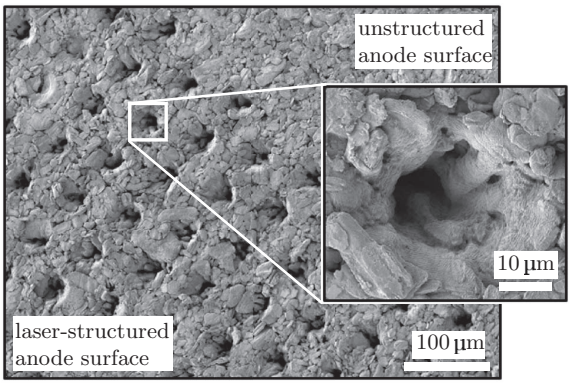

Figure 1. SEM image of a laser-structured anode with structured and unstructured parts.

ink contained 95 wt% graphite (SGL Carbon, Germany) and 5 wt% polyvinylidene fluoride (PVDF, Kynar, Arkema, France). The NMC ink was made of 96 wt% $LiNi_{1/3}Co_{1/3}Mn_{1/3}O_2$ (BASF, Germany), 2 wt% PVDF and 2 wt% conductive carbon (C65, Timcal, Switzerland). Slot die coating was performed in an industrial roll-to-roll coating machine (Coatema, Germany) equipped with an infrared dryer at a coating speed of 1 m min^{-1}. Subsequently, the coatings were calendered to a final porosity of approximately 35%. After calendering, the average coating thickness was 64 µm for both anode and cathode.

Laser-structuring of anodes.—For laser-structuring, a femtosecond laser (Spirit One 1040-8, Spectra-Physics, USA), operating at an infrared wavelength of $\lambda = 1040$ nm with a pulse duration τ_p of 400 fs was used. Only the anodes were structured, the NMC cathodes remained pristine as a larger effect on the overall tortuosity can be achieved in comparison. The beam diameter d_0 in the focal plane (on the electrode surface) was 17.2 µm and the peak fluence Φ_0 was 33.6 J cm^{-2}. The repetition rate f_{rep} used for ablation was 1 kHz and a pulse number $n = 100$ was applied to achieve an average structure depth d_s of approximately 52 µm and an average structure diameter of approximately 20 µm at the electrode's surface, measured with a confocal microscope. Toward deeper parts of the electrode (close to the current collector), the structures narrowed. The structures were spatially distributed in a hexagonal shape with a lateral length of 70 µm, resulting in approximately 20400 structures per cm^2. The ablated fraction of the coating materials for the chosen process parameters was around 5 wt% of the composite electrode material, determined by weighing electrodes before and after structuring. For more details on the experimental setup, the reader is referred to Habedank et al.[10] An image of the resulting structure distribution and geometry gained by means of scanning electron microscopy (SEM) is presented in Fig. 1. It becomes apparent, that the laser-induced structures are not uniformly shaped as the electrode consists of particles of different sizes and shapes. The local electrode conditions thus play a decisive role in the resulting characteristics of the structure.

Half cell assembly and open circuit potentials.—The open circuit potential curves of the utilized unstructured graphite and NMC electrodes were measured in 2032 type coin cells vs. a lithium metal electrode. The half cells were assembled in an argon filled glove box (M. Braun Inertgas-Systeme, Germany) with $H_2O < 0.1$ ppm and $O_2 < 0.1$ ppm. Each cell was filled with 150 µl of electrolyte (LP57, BASF, Germany), containing ethylene carbonate (EC) and ethyl-methyl-carbonate (EMC) in a ratio of 3:7 (by weight) with 1 M lithium-hexaflourophosphate ($LiPF_6$). As a separator, a glass microfiber sheet (Type 691, VWR, USA) was employed. In its uncompressed state, the separator has a thickness of 260 µm. Due to the compression during cell assembly, the separator thickness was estimated to be 200 µm.[15] For the measurement of the quasi open circuit potential as a function of the degree of lithiation, the cells were charged and discharged three times at rates of C/50 in a dry room at a controlled temperature of 20°C between 4.3 V and 2.9 V (NMC) and between 1.6 V and 0.05 V (graphite). In order to derive representative open circuit potential curves from this procedure, an averaging between lithiation (NMC) and delithiation (graphite) of the considered working electrode was carried out for all three C/50 cycles. The averaged open circuit potential curves that were used for modeling and simulation are shown in Fig. A1 in the Appendix. The individual cell capacities for specifying the applied C/50 current were calculated by determining the coating mass assuming mass specific capacities of 150 mAh g^{-1} for NMC and 360 mAh g^{-1} for graphite.

Full cell fabrication.—Three 2032 type coin cells with unstructured anodes and three coin cells with laser-structured anodes were assembled analogously to the half cell assembly described in the previous section. As common practice for Li-ion cells, the areal capacities of the graphite anodes were slightly overdimensioned compared to the NMC cathodes in order to account for irreversible losses during formation and to avoid anode potentials below 0 V, which would result in an undesired Li-plating reaction during charge. In the case presented here, an overdimensioning factor of approximately 1.2 of the pristine anode was chosen so that Li-plating could be avoided at all times during cycling. As only 5 wt% of the coating was removed during the laser-structuring process, this overdimensioning was considered sufficient so that Li-plating during charging could also be avoided in this case. As the mass loading of the pristine graphite anodes was kept constant, the structuring process inevitably resulted in a change in the capacity balancing of the electrodes. This effect needs to be taken into account especially during modeling and simulation and will be further discussed in the modeling section. As the electrolyte, LP572 (BASF, Germany) was used, which consists of EC and EMC in a gravimetric mixing ratio of 3:7 with 1 M $LiPF_6$ conductive salt and 2 wt% vinylene carbonate (VC). As the full cell test data has already been published elsewhere,[10] no further details on the cell fabrication procedure are discussed here. The focus of the work presented here lies on model validation by means of this experimental test data, which is why only essential information is given. Material and fabrication parameters relevant for modeling and simulation purposes are listed in the Appendix of this paper.

Formation procedure.—All cells went through a formation procedure of three charge and discharge cycles at a C-rate of C/10 in order to sufficiently form the solid electrolyte interphase (SEI) on the surface of the graphite particles before the subsequent rate capability test was carried out. Charging was conducted using a constant current/constant voltage (CCCV) operation with a cutoff current of C/20 and discharging was performed in a constant current (CC) procedure within a voltage window of 4.2 V to 3.0 V at a constant temperature of 20°C.

Rate capability test.—After formation, the cells underwent a rate capability test at a controlled temperature of 20°C whereas the applied current was derived from the capacity of the cell after the last formation cycle at C/10. The area-specific values for the adapted C/10 discharge current are shown in Table I for each individual cell considered in this study. As can be seen from this table, all cells investigated in this work showed comparable areal capacities with only slight deviations between the samples. This was considered to be of major importance in order to allow for a straightforward comparison in absolute capacity retention. Higher C-rates are a multiple of the corresponding C/10 discharge current. Charging was carried out following a CCCV procedure and discharging was performed in a CC procedure within a voltage window between 4.2 V and 3.0 V from C/10 to 10C. The constant voltage (CV) phase during charge was terminated when a charging current smaller than C/20 was reached. Charging currents were C/10 and C/5 for the corresponding discharge cycles of C/10 and C/5, respectively. After that, a charging current of C/2 was applied.

Table I. C/10 discharge currents matched to cell capacities of coin cells comprising unstructured and structured anodes.

		Discharge current in mA cm^{-2}
Unstructured anode	Cell 1	0.2399
	Cell 2	0.2535
	Cell 3	0.2597
	Average	0.2510
Structured anode	Cell 4	0.2597
	Cell 5	0.2445
	Cell 6	0.2501
	Average	0.2514

The resulting discharge rate capability is shown in Fig. 2. As can be seen from this figure, all investigated cells show quite comparable behavior. The cells containing structured anodes show an even more reproducible behavior compared to the cells with unstructured anodes. As can be clearly seen from the experiments in Fig. 2, the structuring process results in an overall improvement of the cell's absolute capacity retention, which becomes dominant beyond 2.5 mA cm^{-2} or 1C and fades again before 25 mA cm^{-2} or 10C. This effect will be further evaluated in the following sections.

Cyclic aging test.—Subsequent to the rate capability tests, the six coin cells comprising unstructured and structured anodes underwent a cycling test of 1000 cycles. The cells were charged with a CCCV procedure following a charging current of 1C until the cutoff voltage of 4.2 V and a cutoff current of C/5 in the CV phase. The discharge was carried out with a CC phase at a 1C discharge current until a cutoff voltage of 3.0 V. Similar to the rate capability tests, the ambient temperature was set to 20°C. The capacity retention of the first CC discharge cycle was used as a reference. The capacity fade of each cell as a result of cyclic aging is displayed in Fig. 3.

Modeling

In accordance with the homogenized p2D modeling approach for porous microstructures developed by Newman, Doyle and Fuller,[13,14,16] the model presented here consists of an anode, a separator, and a cathode domain in which both charge and mass transport are accounted for. The governing equations rely on porous electrode and concentrated solution theories and are listed in the appendix for the reader's convenience. Relevant model parameters representing the investigated coin cells are summarized in Table AI in the appendix. The Newman model originally considers a 1D representation through the layers of the electrochemical cell which is coupled to a second dimension representing radial-symmetric active material particles (i.e. 1D+1D, hence p2D). This approach has proven to be valid if the cell shows a homogeneous behavior in the second and third in-plane dimension which allows to neglect gradients in these dimensions as the cell behavior is dominated by through-plane charge and mass transport.[17,18] Only if these gradients cannot be ruled out due to e.g. the non-ideal spatial configuration of the current collectors and the positioning of the corresponding tabs, further means of model development need to be considered.[19,20]

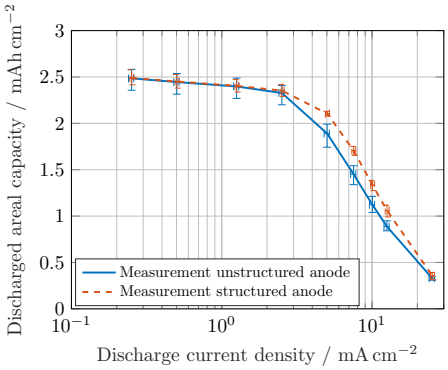

Figure 2. Measured area-specific discharge capacity as a function of applied current density of coin cells comprising unstructured and structured anodes.

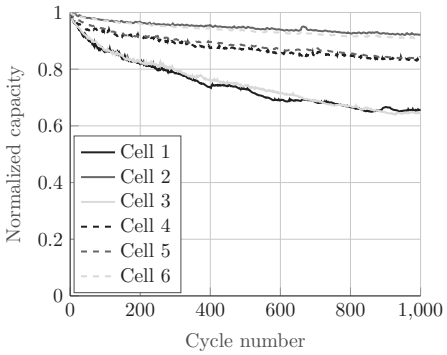

Figure 3. Normalized capacity retention during cycling of cells comprising unstructured anodes (Cell 1, Cell 2 and Cell 3) and structured anodes (Cell 4, Cell 5 and Cell 6).

In the case presented here, 1D and 2D models cannot be used to appropriately describe the hole structure created by the laser ablation process as gradients are expected to occur due to the spatial distribution of the superimposed structure. Furthermore, as already stated in the laser-structuring section, the hole structure is not uniform throughout the entire electrode but is highly dependent on the size and shape of the particles which are affected by the ablation process resulting in a rather coarse hole structure when visually comparing the holes one by one. In order to account for a representative hole structure on the one hand and in order to limit computational effort on the other hand, a homogenized 3D representation of the electrode layers is considered which is coupled to the aforementioned additional radial dimension representing the active material particles. This simplification follows the same line of thought initially suggested by the Newman group in order to efficiently describe porous insertion materials. If the electrode is large enough in terms of its planar dimensioning, every location along an electrode's normal vector can be represented by one particle that will be in contact with the surrounding electrolyte leading to the p2D approach, which is widely accepted and applied. The same principle accounts for a representative hole structure describing the general behavior of the structured electrode. Following this idea, there will be a particle at every location within the representative 3D structure which will be in contact with the surrounding electrolyte at this very location. Furthermore, a generalized or simplified hole structure representing the 20400 holes per cm^2 can be introduced. The specified differential equations have to be consequently solved in all three spatial dimensions of the homogenized 3D cell setup which implies:

$$\nabla := \left(\frac{\partial}{\partial x}, \frac{\partial}{\partial y}, \frac{\partial}{\partial z} \right) \quad [1]$$

Due to the increased spatial discretization effort, 3D models tend to have larger degrees of freedom (DOF), which inevitably causes a higher computational demand and, hence, longer computing times. To minimize the computational effort for solving the set of partial differential equations, the modeled electrode section takes most advantage of symmetry planes representing the structuring pattern. The definition of the modeled geometry is shown in Fig. 4. The laser ablation process creates holes in a hexagonal pattern as can be seen from Fig. 1. The x-direction of the modeled section represents the direction perpendicular to the layers of the cell following the same notation

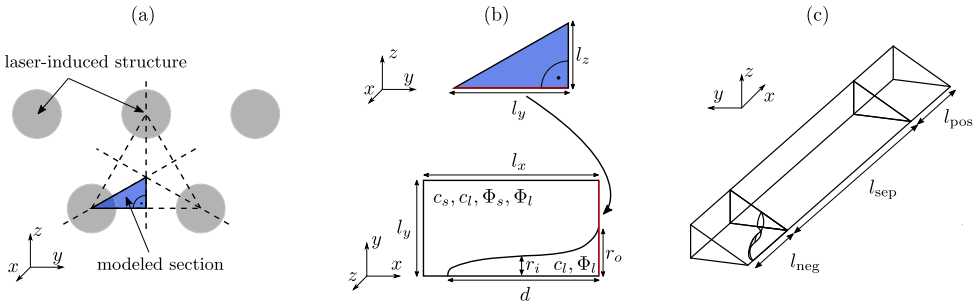

Figure 4. Definition of the modeled geometry using symmetry characteristics of the laser-structured anode. Representative anode surface (a), anode cross section (the state variables solved per domain are the solid and liquid phase Li-ion concentration c_s and c_l and the solid and liquid phase potential Φ_s and Φ_l, respectively) (b) and final 3D geometry implemented in the FEM tool (c).

as the original Newman model. As the holes are homogeneously distributed across the cell, a triangular section of the structured anode is sufficient to describe the entire cell behavior, see Fig. 4a. In this case, a 30° sector of the hexagonal structuring pattern is specified. The cross section of the anode is shown in Fig. 4b with l_x, l_y and l_z representing the length in x-, y- and z-direction, respectively. In this case, l_x is equal to the thickness of the negative electrode l_{neg}. The distance between the centers of two adjacent holes accounts for $2l_y$. The inner radius of the hole is described by r_i, the outer radius by r_o and the depth by d. As the structures are not perfectly cylindrical, the shape was built by using a cubic Bézier curve

$$B(t) = (1-t)^3 P_0 + 3(1-t)^2 t P_1 + 3(1-t)t^2 P_2 + t^3 P_3 \qquad [2]$$

The Bézier curve runs in the interval $0 \leq t \leq 1$. It starts at P_0 for $t = 0$ and terminates in the last control point for $t = 1$. Each control point P_n is defined by its x_n and y_n component, the shape of the curve was controlled by the weighting coefficients w_1 and w_2. The control points are provided in Table II.

$$P_n = \begin{pmatrix} x_n \\ y_n \end{pmatrix}, \; n = 0, 1, 2, 3 \qquad [3]$$

All remaining parameters are listed in the Appendix in Table AI. The resulting idealized 3D geometry is displayed in Fig. 4c. The volume fraction of the modeled hole is 5.1% of the initial anode volume, which is in good agreement with the results of the laser-structuring process. To account for a reduced anode volume, the initial degree of lithiation of the unstructured anode was increased from $0.78 \cdot c_{s,\,max,\,neg}$ (see Table AI) to $0.82 \cdot c_{s,\,max,\,neg}$ for the structured anode which represents this relative decrease. The thicknesses of the separator l_{sep} and the positive electrode l_{pos} are added to the geometry in x-direction.

The presented model of the Li-ion cell was implemented in the FEM-based software platform *COMSOL Multiphysics 5.3*. In order to depict the geometrical features of the hole, a high spatial discretization around the hole boundaries was chosen resulting in approximately 30000 DOF which need to be solved during computation. For comparison, a 3D model of an unstructured cell with a similar spatial discretization along the x-axis results in approximately 9000 DOF. For describing the unstructured cell, a classic p2D model with around 2000 DOF was chosen in order to save computing time.

Table II. x and y components of the four control points.

	x_n	y_n
P_0	$l_{neg} - d$	0
P_1	$l_{neg} - d$	$r_i w_1$
P_2	l_{neg}	$r_i w_2$
P_3	l_{neg}	r_o

In order to describe charge and mass transport in the porous microstructures of a Li-ion cell, a correction of the electrolyte's transport properties is necessary. An often used correction factor is the Bruggeman exponent which was empirically determined for porous structures formed of spherical particles. Recent research findings showed that the Bruggeman correction often underestimates the limitation of the transport properties especially in graphite electrodes formed of platelet-like particles.[4,21–24] In order to evaluate effective transport parameters, the tortuosity τ of the porous electrode structure needs to be known, which can be defined as the ratio of the direct path length to the effective path length of ion transport

$$D_{l,\,eff} = D_l \frac{\varepsilon_l}{\tau} = \frac{D_l}{N_M} \qquad [4]$$

$$\kappa_{eff} = \kappa \frac{\varepsilon_l}{\tau} = \frac{\kappa}{N_M} \qquad [5]$$

with D_l representing the diffusion coefficient in the liquid phase (i.e. the electrolyte), κ its conductivity and ε_l the volume fraction of the electrolyte, also known as the porosity of the porous structure. The ratio of the tortuosity to the volume fraction is also known as the MacMullin number N_M.[24–26] Ebner et al. further demonstrated that the electrode's tortuosity for spherical particles (e.g. NMC) shows an isotropic behavior, but for cylindrical (e.g. lithium cobalt oxide $LiCoO_2$ (LCO)) and platelet-shaped particles (e.g. graphite), an anisotropy of tortuosity can be observed that cannot be neglected when considering charge and mass transport in all spatial dimensions of an electrode.[4] Especially the through-plane tortuosity of graphite τ_x is significantly higher than the in-plane tortuosity (with $\tau_y = \tau_z$). In order to account for this effect, an anisotropic tortuosity was implemented in the graphite anode with $\tau_x = 8$ and $\tau_y = \tau_z = 2.5$.[4] The separator and the NMC cathode were considered to inhibit an isotropic tortuosity of $\tau_x = \tau_y = \tau_z = 1.2$ and $\tau_x = \tau_y = \tau_z = 1.7$, respectively (see Table AI).

Results and Discussion

In this section, the data gained from the rate capability tests carried out for this work is presented and then discussed with the aid of simulation studies derived from the developed modeling approach. The results of the cyclic aging experiments carried out after the rate capability tests are discussed at the end of the section.

Effects of structuring on rate capability.—All rate capability tests were carried out as described in the experimental section at C/10, C/5, C/2, 1C, 2C, 3C, 4C, 5C and 10C at an ambient temperature of 20°C. As the coulombic efficiency of the C/10 cycles after the formation procedure was only 99.1% on average, this data is not considered in the further process of this work. The authors believe that the process of formation was not completely finished at this stage, which might falsify the observed trends if taken into consideration here. From the

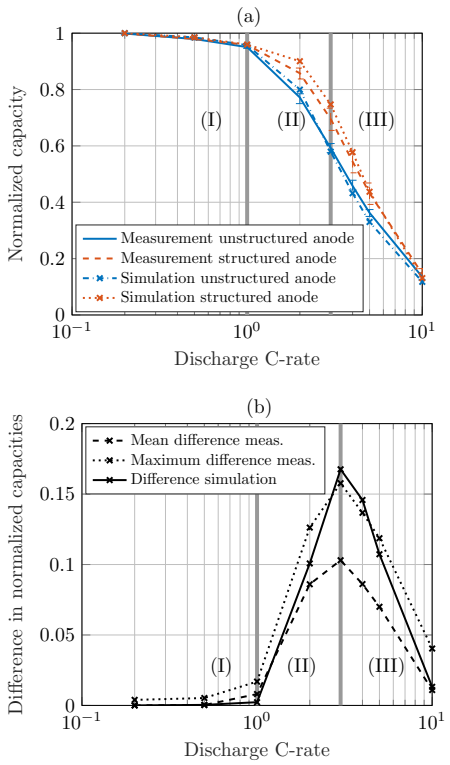

Figure 5. Comparison of measured and simulated C/5-normalized discharge rate capability of coin cells comprising unstructured and structured anodes (a) and observed difference in normalized discharge rate capability (b) within the three stages (I), (II) and (III).

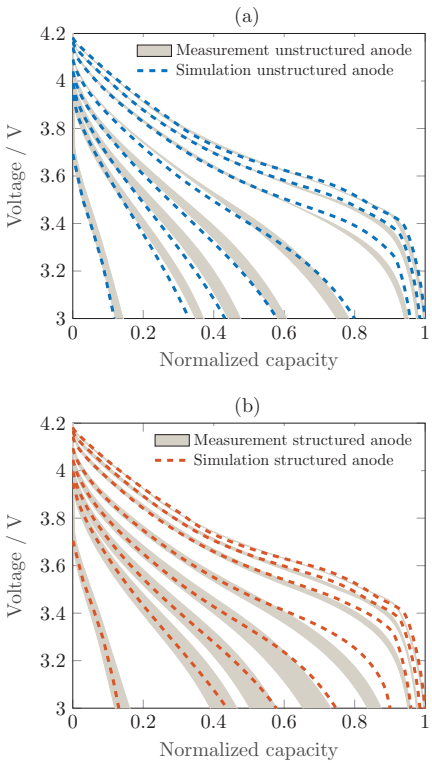

Figure 6. Comparison of measured and simulated discharge voltage curves as a function of C/5-normalized capacity for coin cells comprising unstructured (a) and structured anodes (b) for C-rates of C/5, C/2, 1C, 2C, 3C, 4C, 5C, and 10C (from right to left).

C/5 cycles onwards, all cycles showed efficiencies above this value rising toward 99.7%. Therefore, all further observations were focused on C-rates larger than C/10.

In Fig. 2, the mean area-specific discharged capacity is shown as a function of applied current density. As indicated by the error bars, a variation in both directions occurs, whereas the variation in applied current follows the notation presented in Table I, which is based on the derived capacity at the end of the carried out formation cycles. The cathode samples used for building the coin cells were chosen in such way, that the loading of the capacity limiting electrode, i.e. the cathode, was very similar for both unstructured and structured cells (see experimental section). This approach resulted in a highly reproducible area-specific capacity of approximately 2.5 mAh cm^{-2} at low current densities for all cells considered within this study, which guarantees a most straightforward comparison of the results gained from the rate capability tests. For the reader's convenience, besides area-specific values (see Fig. 2), also the capacity retention normalized to the C/5 discharge rate (see Fig. 5a) and the difference in normalized capacity retention (see Fig. 5b) is shown in this work. When looking into the difference in normalized capacity retention, the impact of electrode structuring can be categorized in three different stages depending on the applied C-rate and increase in derived capacity. The area-specific energy density is not shown here, as the voltage level only merely varies between coin cells with structured and unstructured anodes. Therefore, the area-specific capacity and area-specific energy density as a function of applied C-rate show very similar characteristics in this work. As the volume of the anode does not change with the structuring process, the volumetric energy density of the cell directly follows this trend. Based on the lower density of the electrolyte compared to the composite anode, the overall weight of the electrolyte soaked anode is reduced by approximately 3%. This will slightly improve the gravimetric energy density of the full cell. For all applied currents, the coin cells comprising structured anodes generally showed a larger discharged capacity compared to their unstructured counterpart, as can be seen in Fig. 2. In the case presented in this study, this effect suddenly becomes dominant at discharge current densities above 2.5 mA cm^{-2} or 1C reaching its peak impact around 7.5 mA cm^{-2} or 3C and steadily declines at current densities above this value as shown in Fig. 5b. As can also be seen from Figs. 2 and 5a, there is a rather gentle decrease of the discharged capacity with increasing current density up to 2.5 mA cm^{-2} or 1C, which then becomes more pronounced up to 7.5 mA cm^{-2} or 3C and then finally decreases again in its steepness. In order to understand the interplay of mechanisms leading to this effect, the presented model was applied. For this purpose, a standard p2D Newman model was considered first, in order to match the parameter set to the results of the rate capability tests with cells comprising unstructured anodes. As shown in Figs. 5a and 6a, the relative decline in capacity retention with rising C-rate at the end of the discharge as well as the transient characteristics of the voltage response during discharge can be depicted very well with the parameter set given in the Appendix.

This parameter set was then transferred to the 3D representation of the homogenized structured electrode model. With a simulated hole diameter of roughly 20 µm, 80% of penetration depth and 70 µm of distance between the centers of the holes, the rate capability tests performed on cells comprising structured anodes could also be depicted very well. Again, this accounts for both the absolute and the relative decline in discharged capacity with rising C-rate at the end of the discharge procedure (see Fig. 5a) as well as the transient characteristics of the voltage response during discharge (see Fig. 6b).

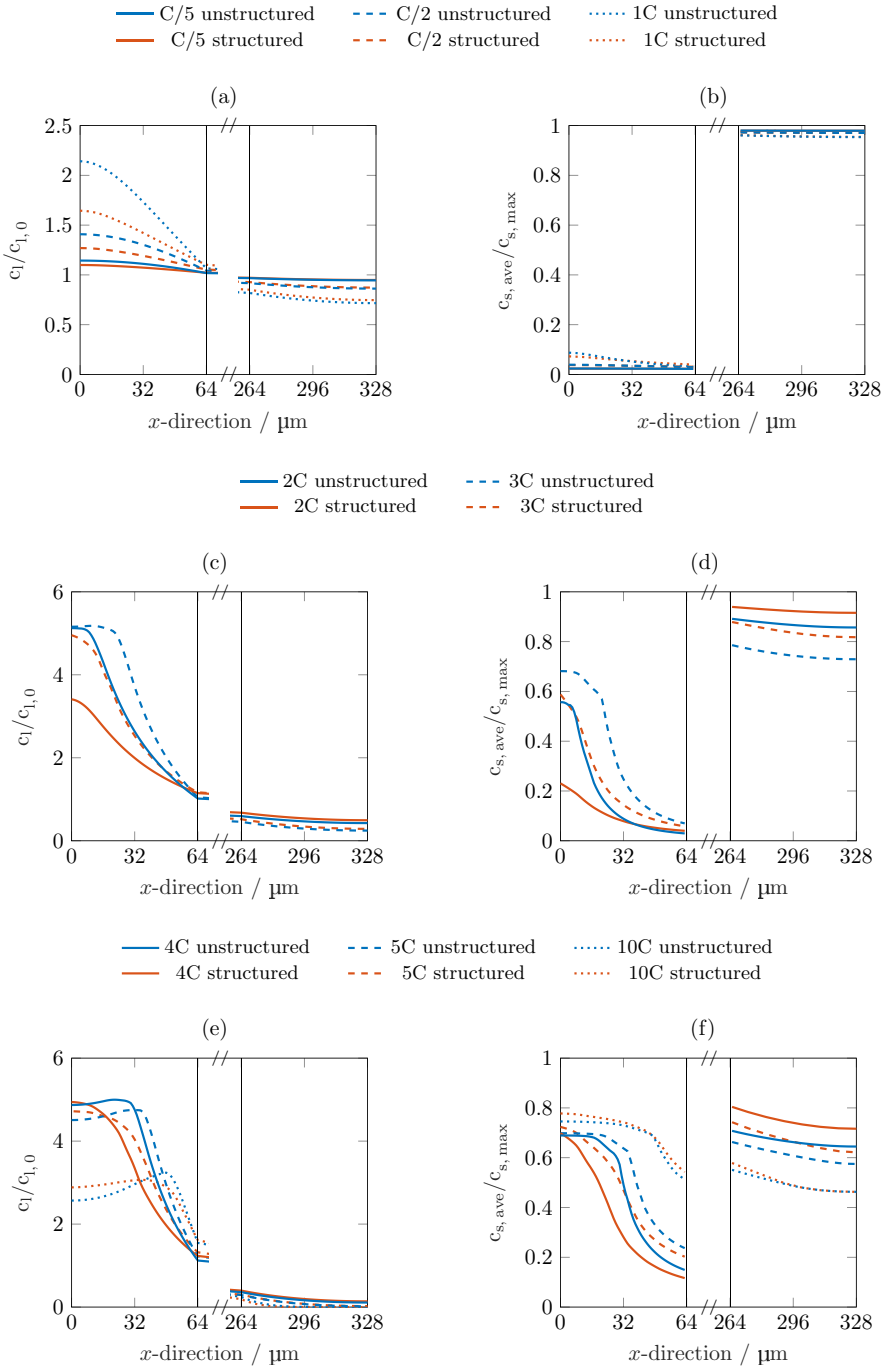

Figure 7. Li-ion concentration in both liquid (left) and solid phase (right) averaged along y- and z-direction at the end of the corresponding discharge step; solid phase concentration accounts for the mean concentration within the particle dimension.

Mechanisms of rate limitation.—When looking into Fig. 5a, the C-rates of C/5, C/2 and 1C are almost not affected by the structuring process. Also, the similar trend of the decline in discharged capacity hints at a limiting effect which is not influenced by the structuring process and consequently charge and mass transport in the liquid phase. This assumption can be proven when looking into Figs. 7a and 7b. The spatial distribution in liquid phase concentration at the end of the discharge procedure is almost identical for both the unstructured and structured cells with rising gradients between the anode and cathode for increasing C-rate. The same holds true for the spatial distribution in solid phase concentration. The utilization of the electrodes is constantly above 90% with almost no gradients along the thickness of the electrodes. At C-rates of 1C and below, this observation leads to the assumption that the capacity retention is mainly influenced by an increased potential drop based on ohmic losses and charge transfer kinetics with increasing C-rate. From 2C onwards, a

more homogeneous liquid phase concentration can be observed for the cells with structured anodes compared to those with unstructured anodes with lower maximum values, which positively influences the transport properties of the electrolyte (see Fig. 7c). This results in a considerably homogenized solid phase concentration along the electrode with lower mean values on the anode side which leads to higher overall solid phase concentrations on the cathode side at the end of the discharge procedure (see Fig. 7d). At C-rates of 4C and above, the homogenizing influence of laser beam structuring on both the liquid and the solid phase concentration is considerably diminished as shown in Figs. 7e and 7f. At these C-rates, the limiting influence in the liquid phase on the cathode side becomes increasingly dominant, reaching almost a complete depletion of Li-ions, which results in large overpotentials related to charge transfer kinetics (see Fig. 7e). In addition, the liquid phase concentration within the anode domain rises above 4 mol l^{-1} which significantly reduces both its conductivity and diffusivity resulting in large ohmic and diffusion based overpotentials. The electrolyte conductivity is reduced to 35% and the diffusivity to 14% at 4 mol l^{-1} compared to the values at the initial liquid Li-ion concentration of 1 mol l^{-1}. In order to improve the rate capability of the cell at these high discharge rates, further modifications need to be considered such as different electrolytes with enhanced transport properties at such high levels of Li-ion concentration or an additional structuring of the cathode to avoid a complete depletion of Li-ions.

These observations suggest a classification of the influence of laser beam structured anodes on the rate capability of the cells: At low C-rates, electrode morphology plays only a minor role in capacity retention making laser beam structuring obsolete in general, i.e. stage (I) between 0.1C and 1C in this case. At moderate C-rates, the effect of anode morphology and related effective transport properties becomes dominant, showing the largest benefit of laser beam structured anodes, i.e. stage (II) between 1C and 3C in this case. At high C-rates, not only the anode morphology is mainly influencing the occuring overpotentials, but also the electrolyte's inherent transport properties as well as the morphology of the separator and cathode are becoming increasingly important approaching a depletion of the electrolyte near the cathode current collector, i.e. stage (III) between 3C and 10C in this case. It is worth mentioning here, that the chosen glass fiber separator is not representative for commercial Li-ion cells, where separators are used which are about a magnitude thinner (i.e. approximately 10–30 μm). The glass fiber separator was used in this case due to ease of handling and comparability between half cell and full cell measurements. For the here presented results, this circumstance should only have a mere influence on the investigated rate capability as the overpotentials within the separator are dominated by the effective transport properties of the electrolyte, resembling an effective path-length of ion movement. The chosen glass fiber separator shows a MacMullin number of approximately 1.7 in its compressed state of 200 μm, which results in an effective path-length for the Li-ions of 340 μm. A standard polyolefin based separator with a thickness of 25 μm and a porosity of 40% inhibits a MacMullin number between 10 to 15,[24] resembling an effective path-length of 250–375 μm, which is very comparable to the chosen glass fiber separator.

In order to not only evaluate the through-plane but also the in-plane penetration depth of the structuring procedure, the 3D spatial distribution of Li-ion concentration in the solid and liquid phase was studied at the end of a 3C discharge step. For this purpose, five cut planes were introduced along the thickness of the structured anode (compare Fig. 4c) at a constant distance of 16 μm between them (see Figs. 8a and 8b). Looking into the spatial distribution of both the liquid and solid phase concentration, a fairly homogeneous coloring of the cut planes can be observed, whereby the coloring level is mainly dominated by the through-plane distribution in Li-ion concentration. This implies that the concentration gradients along the hole's axis are generally larger than the concentration gradients along the hole's radial direction.

Near the interface between the anode and the separator (i.e. planes V and IV), there is only little variation in Li-ion concentration throughout the cut planes in both the liquid and the solid phase. This tendency is confirmed when looking into the normalized liquid and solid phase concentration along the hypotenuse symmetry axis of the considered triangular electrode domain (see Figs. 8c and 8d). Furthermore, we observe an increasing gradient from the bulk material between the holes to the center of the hole with increasing distance to the separator along the depth of the holes (i.e. planes III and II). In case of the liquid phase concentration, the spatial distribution within the unstructured part of the electrode (i.e. plane I) becomes fairly homogeneous again, however, at significantly elevated levels of concentration. This jump becomes especially apparent when looking into the level of liquid phase Li-ion concentration within the hole (i.e. at $y = z = 0$ within planes V, IV and III) compared to the unstructured part of the electrode (i.e. at $y = z = 0$ within plane I). A similar trend in the solid phase concentration can be observed, whereas a considerable gradient in Li-ion concentration remains near the current collector in the range of a third to a half of the total through-plane concentration difference, which can be explained by the comparably slow diffusion-based equalization process within the solid phase compared to the liquid phase.[17] These observations imply that the penetration depth of the structuring process not only varies for the liquid and solid phase concentration but is highly dependent on the size and the depth of the hole as well as the distance between the holes. These results suggest that the size, the depth and the shape of the hole itself as well as the structuring pattern can be optimized in order to obtain an improved rate capability within a certain operating window and price range.

Cyclic aging behavior.—From the overall cycling behavior displayed in Fig. 3, no distinct indication can be observed that coin cells comprising structured or unstructured graphite anodes show superior aging characteristics. What is more, the developing spread between the cells might be a result of the manual cell assembly process or partial deterioration during the rate capability tests with high C-rates. Nevertheless, all cells comprising structured anodes reveal a capacity retention above 83% after 1000 cycles, whereas two cells with unstructured anodes already showed a capacity fade toward 65%. This leads to the conclusion that the laser-structuring process of the graphite anodes has no negative impact on the cyclic aging behavior of the coin cells. If coin cells comprising structured anodes even show an enhanced aging behavior needs to be evaluated by means of further measurements including more cells and cells that did not undergo a rate capability test before the carried out aging study.

Conclusions

Within this work, a combination of experimental and simulation-based evaluation of laser-beam structured graphite electrodes for enhancing the discharge rate capability of a NMC/graphite Li-ion cell was presented. As the experimental basis of this work, coin cells with a constant loading of approximately 2.5 mAh cm^{-2} were manufactured, whereas the NMC cathode was the capacity limiting electrode and the pristine graphite anode was oversized by approximately 20% in capacity so that the laser beam ablation of roughly 5 wt% did not result in an elevated risk of Li-plating during cycling. For simulation purposes, a representative homogenized microstructure model of the considered laser-beam-structured graphite electrode was developed and validated against rate capability tests, which were performed on both coin cells with unstructured and structured graphite electrodes.[10] In a first step, the underlying physical and chemical model parameters were adapted toward the unstructured coin cells with the aid of a standard p2D Newman-type model resulting in an excellent agreement between experimental and simulated rate capability tests. This parameter set was then transferred to the homogenized 3D+1D microstructure model, forming a representative triangular section of the structuring pattern making most use of symmetry planes in order to minimize computational effort. Due to the inevitably higher spatial discretization effort around the hole geometry, which was qualitatively approximated by a cubic Bézier curve toward SEM pictures, the computational demand

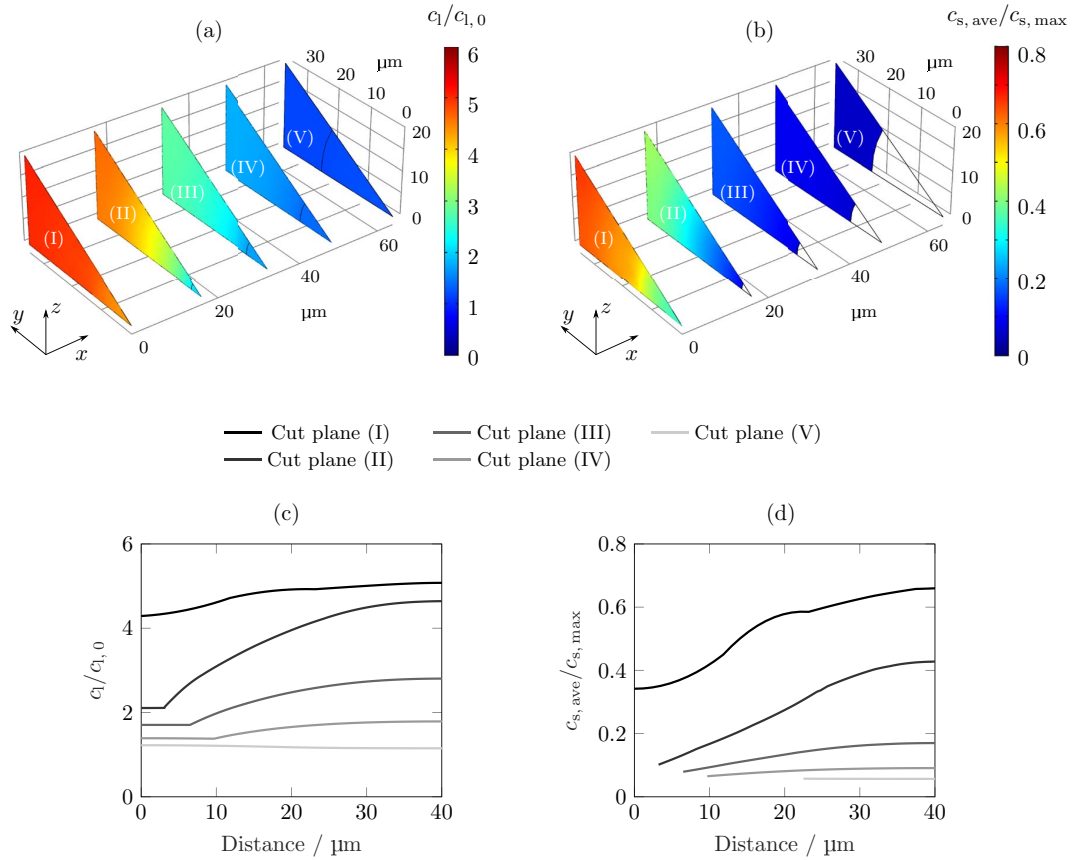

Figure 8. Liquid (a) and solid phase (b) Li-ion concentration on defined cut planes (I), (II), (III), (IV) and (V) (distance in x-direction: 0 µm, 16 µm, 32 µm, 48 µm and 64 µm, respectively) and liquid (c) and solid phase (d) Li-ion concentration along hypotenuse of cut planes at the end of a 3C discharge step within the structured graphite anode.

increased by a factor of approximately 15 compared to a standard p2D model (30000 DOF vs. 2000 DOF).

Simulated rate capability tests, which were carried out with the aid of the parametrized structured electrode model, were validated against experimental data showing again excellent agreement in terms of the transient voltage decline during discharge as well as the observed reduced capacity retention with increasing C-rate. It was shown, that for the electrode morphologies and materials considered in this case, the maximum benefit of structuring the graphite electrode was around a discharge rate of 3C. At low discharge rates, there is merely an influence of the structuring process (here up to 1C), which then suddenly changes at 2C rising toward its maximum impact at 3C of gaining between 10% and 15% in capacity compared to cells without structured graphite anodes at C/5. This corresponds to a relative improvement of capacity retention of 11–24% at 3C, at which the minimum and maximum capacity retention of the structured cells at 3C are related to the mean capacity retention of the unstructured cells at 3C. Beyond 3C, the impact of the structuring process declines again, however, at a comparably lower rate. This implies, that there forms a certain C-rate region in which the use of structured electrodes can considerably enhance a cell's rate capability forming an optimum. In other words, structured electrodes do not necessarily come with an overall improvement in rate capability of Li-ion cells at all applied currents as mass transport limitations within the electrolyte are still dominating at large currents despite the locally homogenized distribution in Li-ion concentration (e.g. overall electrolyte depletion in the NMC cathode[3]). When looking into the simulated spatial Li-ion concentration in the liquid and the solid phase at the end of discharge, the effect of the structuring process on the rate limitation becomes apparent. At low C-rates (i.e. C/5, C/2 and 1C or stage (I)), the structuring process has almost no influence on the solid phase concentration in both anode and cathode. Consequently, the amount of discharged capacity is rather limited by an increasing polarization due to ohmic losses and charge transfer kinetics instead of transport limitations in the liquid electrolyte. At higher C-rates (i.e. 2C and 3C or stage (II)), the homogenized liquid phase concentration has a more dominant impact on the distribution in liquid and solid phase concentration especially in the graphite anode which results in higher degrees of utilization within both electrodes. When further increasing the discharge rate (i.e. 4C, 5C and 10C or stage (III)), the positive impact of electrode structuring on the homogeneity of liquid phase concentration fades, which then results in a similarly inhomogeneous utilization of the graphite anode. What also becomes apparent is that the level in liquid phase concentration within the cathode generally decreases with increasing C-rate which is based on the ongoing depletion of the electrolyte resulting in increased charge transfer overpotentials. Similarly, the liquid phase concentration within the anode becomes excessively high ($> 4\,\mathrm{mol\,l^{-1}}$), which significantly reduces the inherent transport properties of the electrolyte, resulting in large ohmic and diffusion based overpotentials. This effect cannot be significantly influenced by a structuring of the anode but needs further modifications such as using enhanced electrolytes or including an additional structuring of the cathode.

The results shown in this work imply that not only the anode structuring process can enhance the discharge rate capability of the entire cell in a certain range but also that modeling and simulation

can help to understand the underlying mechanisms and interactions resulting in this enhancement. By evaluating the through-plane and in-plane distribution in Li-ion concentration throughout the electrodes, the ideal hole size, geometry and pattern can be identified in order to maximize the rate capability within a limited operating window. By further considering the costs of the electrode structuring process and also of the excess electrolyte within the holes, a cost-effective rate capability enhancement can be achieved. This can be best explained when considering Fig. 5b, where the peak location, height and width of the curve can be altered by changing the size, the shape and the pattern of the superimposed structure. In order to be able to reliably optimize the structure, inherent transport properties of the applied electrolyte need to be characterized well throughout the entire concentration range occurring during operation before salt precipitation takes place (i.e. beyond 4 mol l^{-1} in this case). The same holds true for a thorough characterization of the anisotropic electrode morphology. Further work will focus on this optimization procedure, not only for the graphite anode, but also for the NMC cathode during both discharge and charge operation for various electrode loadings. Furthermore, the model error accompanied with the homogenization of the microstructure will be evaluated and investigated in terms of means of a further model order reduction.

Acknowledgment

This work was financially supported by the German Federal Ministry of Education and Research (BMBF) under grant number 03XP0081 (ExZellTUM II) and 03XP0027G (MiBZ).

Appendix

In the experimental section, the open circuit potential measurements of the half cells were described. In Fig. A1, the derived curves are plotted as a function of degree of lithiation.

The developed model is based on the subsequent equations. For a more detailed description, the reader is referred to the work of the Newman group.[13,14,16] The most relevant model parameters used in this work are listed in Table AI. The mass balance is applied in the porous intercalation electrodes

$$\varepsilon_l \frac{\partial c_l}{\partial t} = \nabla \left(D_{l,\,\mathrm{eff}} \nabla c_l - \frac{i_l t_+}{F} \right) + \frac{3\varepsilon_s}{r_p} j_n \qquad [A1]$$

where ε_l is the porosity or the liquid phase fraction of the electrode domain, $D_{l,\,\mathrm{eff}}$ the effective diffusivity, i_l the ionic current density, F the Faraday constant, ε_s the solid phase fraction, r_p the particle radius and j_n the pore wall flux. In the separator, there is no charge transfer reaction taking place, hence, the mass balance simplifies to

$$\varepsilon_l \frac{\partial c_l}{\partial t} = \nabla \left(D_{l,\,\mathrm{eff}} \nabla c_l - \frac{i_l t_+}{F} \right) \qquad [A2]$$

The ionic current density accounts for the interaction between the different species in the electrolyte which is why the activity dependence is essential

$$i_l = -\kappa_{\mathrm{eff}} \nabla \Phi_l + \frac{2\kappa_{\mathrm{eff}} RT}{F} \left(1 + \frac{\partial \ln f_\pm}{\partial \ln c_l} \right) (1 - t_+) \nabla \ln c_l \qquad [A3]$$

with κ_{eff} being the effective ionic conductivity, Φ_l the potential in the liquid phase and R the ideal gas constant. At high C-rates the Li-ion concentration in the electrolyte can locally become very low due to transport limitations. To prevent the concentration from becoming zero or even negative, which causes instability of the model, a kinetic modification introduced by the Newman group[27] was implemented. The Butler-Volmer equation, which describes the charge transfer between the solid and the liquid phase on the particle surface is divided by a limitation term with $c_{\mathrm{lim}} = 1$ mol m^{-3}

$$j_n = \frac{i_0}{F} \frac{\exp\left(\frac{\alpha_a F}{RT}\eta\right) - \exp\left(-\frac{\alpha_c F}{RT}\eta\right)}{1 + \frac{c_{\mathrm{lim}}}{c_l} \exp\left(-\frac{\alpha_c F}{RT}\eta\right)} \qquad [A4]$$

α_a and α_c are the anodic and cathodic charge-transfer coefficients. The exchange current density i_0 is defined as

$$i_0 = F k_c^{\alpha_a} k_a^{\alpha_c} (c_{s,\,\max} - c_s)^{\alpha_a} c_s^{\alpha_c} \left(\frac{c_l}{c_{l,\,\mathrm{ref}}} \right)^{\alpha_a} \qquad [A5]$$

with $c_{l,\,\mathrm{ref}} = 1$ mol m^{-3}. $c_{s,\,\max}$ is the maximum Li-ion concentration in the solid phase and k_a and k_c are the anodic and cathodic reaction rates, respectively. The overpotential η is defined as a subtraction of the potential of the liquid phase Φ_l and the equilibrium voltage E_{eq} from the potential of the solid phase Φ_s

$$\eta = \Phi_s - \Phi_l - E_{\mathrm{eq}} \qquad [A6]$$

Finally, the following boundary conditions have to be maintained

$$\left. \frac{\partial c_l}{\partial x} \right|_{x=0 \& x=L} = 0 \qquad [A7]$$

$$\left. \frac{\partial \Phi_l}{\partial x} \right|_{x=0 \& x=L} = 0 \qquad [A8]$$

with $L = l_{\mathrm{neg}} + l_{\mathrm{sep}} + l_{\mathrm{pos}}$.

$$\left. \frac{\partial \Phi_s}{\partial x} \right|_{x=0 \& x=L} = -\frac{i_s}{\sigma} \qquad [A9]$$

with i_s being the electric current density.

$$\left. \frac{\partial \Phi_s}{\partial x} \right|_{x=l_{\mathrm{neg}} \& x=l_{\mathrm{neg}}+l_{\mathrm{sep}}} = 0 \qquad [A10]$$

$$\nabla i_l = -\nabla i_s \qquad [A11]$$

$$\left. \frac{\partial c_s}{\partial r} \right|_{r=0} = 0 \qquad [A12]$$

$$\frac{\partial c_s}{\partial r} = D_s \left(\frac{\partial^2 c_s}{\partial r^2} + \frac{2}{r} \frac{\partial c_s}{\partial r} \right) \qquad [A13]$$

$$-D_s \left. \frac{\partial c_s}{\partial r} \right|_{r=r_p} = j_n \qquad [A14]$$

In literature, only a few electrolytes used in Li-ion cells have been characterized adequately so that they can be used for the purpose of model parameterization.[27–31] Necessary characteristics are diffusivity, ionic conductivity and activity dependence of the electrolyte. These characteristics depend on the Li-ion concentration and on the

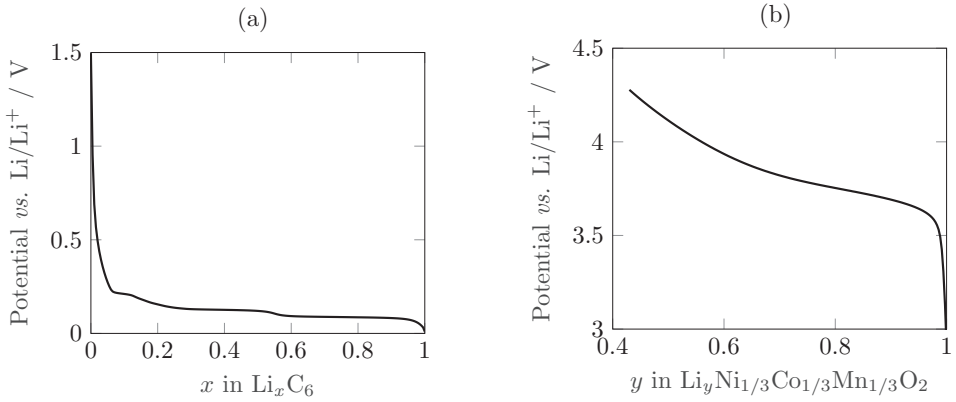

Figure A1. Open circuit potential curves for the graphite anode (a) and the NMC cathode (b) considered in this work.

Table AI. Model parameters used within this work; superscript *m* indicates measured values, *e* indicates estimated values (* value derived from D50 mass-median-diameter from datasheet, ** value derived from weight ratio of electrode composition); numeric values and magnitudes of parameters chosen in this study were referenced to literature where applicable.

Parameter	Anode	Separator	Cathode
Geometry			
Thickness l	64 µm ^{m}	200 µm[15]	64 µm ^{m}
Particle radius r_p	5 µm *		5.5 µm *
Solid phase fraction ϵ_s	0.59 **		0.52 **
Liquid phase fraction ϵ_l	0.32 ^{m}	0.7 ^{e}	0.35 ^{m}
Tortuosity through-plane τ_x	8[4]	1.2 ^{e}	1.7[4]
Tortuosity in-plane $\tau_{y,z}$	2.5[4]	1.2 ^{e}	1.7[4]
Thermodynamics			
Equilibrium voltage E_{eq}	Fig. A1a		Fig. A1b
Maximum lithium concentration $c_{s,max}$	32000 mol m^{-3}[32,33]		50000 mol m^{-3}[33]
Initial state of charge $\frac{c_{s,0}}{c_{s,max}}$	0.78 ^{e}		0.43 ^{e}
Kinetics			
Anodic reaction rate k_a	1×10^{-9} m s^{-1}[27]		1×10^{-9} m s^{-1}[27]
Cathodic reaction rate k_c	1×10^{-9} m s^{-1}[27]		1×10^{-9} m s^{-1}[27]
Anodic charge-transfer coefficient α_a	0.5[32,34]		0.5[32,34]
Cathodic charge-transfer coefficient α_c	0.5[32,34]		0.5[32,34]
Transport			
Solid diffusivity D_s	1×10^{-14} m^{2}s^{-1}[27,32]		1.8×10^{-13} m^{2}s^{-1}[33,35]
Solid conductivity σ	100 S m^{-1}[21,36]		10 S m^{-1}[35,36]

Parameter	Hole
Inner radius r_i	7.5 µm ^{m}
Outer radius r_o	22.5 µm ^{m}
Depth d	$0.8 \cdot l_{neg}$ ^{m}
Weighting factor w_1	1.1
Weighting factor w_2	0.6
Distance $2l_y$	70 µm ^{m}

Parameter	Electrolyte
Electrolyte diffusivity D_l	Eq. A15
Electrolyte conductivity κ_{fit}	Eq. A17
Activity dependence $\frac{\partial \ln f_\pm}{\partial \ln c_l}$	Eq. A18
Transport number t_+	0.4[27]

Parameter	Global
Temperature T	293.15 K ^{m}
Ohmic contact resistance R_Ω	1.3×10^{-3} Ωm^2 ^{e}

temperature, which is kept constant in this case. Due to various electrolyte compositions, the resulting curves differ slightly but overall show a similar trend.

The electrolyte diffusion coefficient and the electrolyte ionic conductivity were adopted according to Mao et al.[27] The corresponding unit for the following characteristic electrolyte functions is mol l^{-1} for the Li-ion concentration c_l and K for the temperature T

$$D_l = 5.34 \times 10^{-10} \exp(-0.65 c_l) \exp\left(\frac{2000(T-298)}{298T}\right) f \quad [A15]$$

$$\kappa = (0.0911 + 1.9101 c_l - 1.052 c_l^2 + 0.1554 c_l^3) \exp\left(\frac{1690(T-298)}{298T}\right) \quad [A16]$$

The electrolyte diffusion coefficient was slightly reduced by multiplying a factor $f = 0.85$. Mao et al.[27] used a polynomial fitting function for the ionic conductivity that is only valid in a certain concentration range. For concentrations above 3 mol l^{-1}, the conductivity starts to increase again due to the considered cubic fitting function. As larger Li-ion concentrations were observed in this work, the following fit was used, which is based on Eq. A16 with a constant temperature $T = 293.15$ K

$$\kappa_{fit} = 2.034 \left(\frac{c_l}{2.512}\right)^{0.55} \exp\left(-\left(\frac{c_l}{2.512}\right)^{1.55}\right) \quad [A17]$$

The effective diffusivity and ionic conductivity can be determined using the correction presented in Eqs. 4 and 5. The electrolyte activity dependence was taken from Valøen and Reimers[28] as it was neglected by Mao et al.[27]

$$\frac{\partial \ln f_\pm}{\partial \ln c_l} = \frac{0.601 - 0.24 c_l^{0.5} + 0.982 c_l^{1.5}(1 - 0.0052(T-294))}{1 - t_+} - 1 \quad [A18]$$

The equation contains a dependence of the transport number t_+, which was set constant, see Table AI.

ORCID

Jan B. Habedank http://orcid.org/0000-0003-2057-7037
Ludwig Kraft http://orcid.org/0000-0003-4324-426X
Alexander Rheinfeld http://orcid.org/0000-0003-0995-7266

References

1. M. Singh, J. Kaiser, and H. Hahn, "Thick Electrodes for High Energy Lithium Ion Batteries," *Journal of the Electrochemical Society*, **162**, A1196 (2015).
2. A. Nyman, T. G. Zavalis, R. Elger, M. Behm, and G. Lindbergh, "Analysis of the Polarization in a Li-Ion Battery Cell by Numerical Simulations," *Journal of The Electrochemical Society*, **157**, A1236 (2010).
3. K. G. Gallagher, S. E. Trask, C. Bauer, T. Woehrle, S. F. Lux, M. Tschech, P. Lamp, B. J. Polzin, S. Ha, B. Long, Q. Wu, W. Lu, D. W. Dees, and A. N. Jansen, "Optimizing Areal Capacities through Understanding the Limitations of Lithium-Ion Electrodes," *Journal of The Electrochemical Society*, **163**, A138 (2015).
4. M. Ebner, D.-W. Chung, R. E. García, and V. Wood, "Tortuosity Anisotropy in Lithium-Ion Battery Electrodes," *Advanced Energy Materials*, **4**, 1 (2014).
5. M. Osiak, H. Geaney, E. Armstrong, and C. O'Dwyer, "Structuring materials for lithium-ion batteries: Advancements in nanomaterial structure, composition, and defined assembly on cell performance," *Journal of Materials Chemistry*, **A 2**, 9433 (2014).

6. C. L. Cobb and M. Blanco, "Modeling mass and density distribution effects on the performance of co-extruded electrodes for high energy density lithium-ion batteries," *Journal of Power Sources*, **249**, 357 (2014).
7. C.-J. Bae, C. K. Erdonmez, J. W. Halloran, and Y.-M. Chiang, "Design of battery electrodes with dual-scale porosity to minimize tortuosity and maximize performance," *Advanced materials*, **25**, 1254 (2013).
8. S. Ferrari, M. Loveridge, S. D. Beattie, M. Jahn, R. J. Dashwood, and R. Bhagat, "Latest advances in the manufacturing of 3D rechargeable lithium microbatteries," *Journal of Power Sources*, **286**, 25 (2015).
9. J. Pröll, H. Kim, A. Piqué, H. J. Seifert, and W. Pfleging, "Laser-printing and femtosecond-laser structuring of $LiMn_2O_4$ composite cathodes for Li-ion microbatteries," *Journal of Power Sources*, **255**, 116 (2014).
10. J. B. Habedank, J. Endres, P. Schmitz, H. P. Huber, and M. F. Zaeh, "Femtosecond laser structuring of graphite anodes for improved lithium-ion batteries: Ablation characteristics and process design," *Journal of Laser Applications* (2018) (accepted for publication) 2018.
11. C. L. Cobb and S. E. Solberg, "Communication—Analysis of Thick Co-Extruded Cathodes for Higher-Energy-and-Power Lithium-Ion Batteries," *Journal of The Electrochemical Society*, **164**, A1339 (2017).
12. V. P. Nemani, S. J. Harris, K. C. Smith, and Design of Bi-Tortuous, "Anisotropic Graphite Anodes for Fast Ion-Transport in Li-Ion Batteries," *Journal of The Electrochemical Society*, **162**, A1415 (2015).
13. J. Newman and K. E. Thomas-Alyea, *Electrochemical Systems*, 3rd ed.; John Wiley & Sons, Inc.: Hoboken, New Jersey, 2004.
14. M. Doyle, T. F. Fuller, and J. Newman, "Modeling of Galvanostatic Charge and Discharge of the Lithium/Polymer/Insertion Cell," *Journal of the Electrochemical Society*, **140**, 1526 (1993).
15. J. Landesfeind, D. Pritzl, and H. A. Gasteiger, "An Analysis Protocol for Three-Electrode Li-Ion Battery Impedance Spectra: Part I. Analysis of a High-Voltage Positive Electrode," *Journal of the Electrochemical Society*, **164**, A1773 (2017).
16. T. F. Fuller, M. Doyle, and J. Newman, "Simulation and Optimization of the Dual Lithium Ion Insertion Cell," *Journal of the Electrochemical Society*, **141**, 1 (1994).
17. F. M. Kindermann, P. J. Osswald, G. Ehlert, J. Schuster, A. Rheinfeld, and A. Jossen, "Reducing Inhomogeneous Current Density Distribution in Graphite Electrodes by Design Variation," *Journal of The Electrochemical Society*, **164**, E3105 (2017).
18. F. M. Kindermann, P. J. Osswald, S. Klink, G. Ehlert, J. Schuster, A. Noel, S. V. Erhard, W. Schuhmann, and A. Jossen, ", Measurements of lithium-ion concentration equilibration processes inside graphite electrodes," *Journal of Power Sources*, **342**, 638 (2017).
19. S. V. Erhard, P. J. Osswald, J. Wilhelm, H. E. Hoster, and A. Jossen, "Simulation and Measurement of Local Potentials of Modified Commercial Cylindrical Cells: II: Multi-Dimensional Modeling and Validation," *Journal of The Electrochemical Society*, **162**, A2707 (2015).
20. S. V. Erhard, et al. Simulation and Measurement of the Current Density Distribution in Lithium-Ion Batteries by a Multi-Tab Cell Approach," *Journal of The Electrochemical Society*, **164**, A6324 (2017).
21. M. Doyle and J. Newman, "Comparison of Modeling Predictions with Experimental Data from Plastic Lithium Ion Cells," *Journal of the Electrochemical Society*, **143**, 1890 (1996).
22. K. K. Patel, J. M. Paulsen, and J. Desilvestro, "Numerical simulation of porous networks in relation to battery electrodes and separators," *Journal of Power Sources*, **122**, 144 (2003).
23. I. V. Thorat, D. E. Stephenson, N. A. Zacharias, K. Zaghib, J. N. Harb, and D. R. Wheeler, "Quantifying tortuosity in porous Li-ion battery materials," *Journal of Power Sources*, **188**, 592 (2009).
24. J. Landesfeind, J. Hattendorff, A. Ehrl, W. A. Wall, and H. A. Gasteiger, "Tortuosity Determination of Battery Electrodes and Separators by Impedance Spectroscopy," *Journal of The Electrochemical Society*, **163**, A1373 (2016).
25. R. B. MacMullin and G. A. Muccini, "Characteristics of porous beds and structures," *AIChE Journal*, **2**, 393 (1956).
26. M. J. Martínez, S. Shimpalee, and J. W. van Zee, "Measurement of MacMullin Numbers for PEMFC Gas-Diffusion Media," *Journal of the Electrochemical Society*, **156**, B80 (2009).
27. J. Mao, W. Tiedemann, and J. Newman, "Simulation of temperature rise in Li-ion cells at very high currents," *Journal of Power Sources*, **271**, 444 (2014).
28. L. O. Valøen and J. N. Reimers, "Transport Properties of $LiPF_6$-Based Li-Ion Battery Electrolytes," *Journal of the Electrochemical Society*, **152**, A882 (2005).
29. A. Nyman, M. Behm, and G. Lindbergh, "Electrochemical characterisation and modeling of the mass transport phenomena in $LiPF_6$–EC–EMC electrolyte," *Electrochimica Acta*, **53**, 6356 (2008).
30. M. Guo and R. E. White, "A distributed thermal model for a Li-ion electrode plate pair," *Journal of Power Sources*, **221**, 334 (2013).
31. H. Lundgren, M. Behm, and G. Lindbergh, "Electrochemical Characterization and Temperature Dependency of Mass-Transport Properties of $LiPF_6$ in EC:DEC," *Journal of the Electrochemical Society*, **162**, A413 (2014).
32. P. Ramadass, B. Haran, P. M. Gomadam, R. White, and B. N. Popov, "Development of First Principles Capacity Fade Model for Li-Ion Cells," *Journal of The Electrochemical Society*, **151**, A196 (2004).
33. S. Tippmann, D. Walper, L. Balboa, B. Spier, and W. G. Bessler, "Low-temperature charging of lithium-ion cells part I: Electrochemical modeling and experimental investigation of degradation behavior," *Journal of Power Sources*, **252**, 305 (2014).
34. M. Doyle and Y. Fuentes, "Computer Simulations of a Lithium-Ion Polymer Battery and Implications for Higher Capacity Next-Generation Battery Designs," *Journal of The Electrochemical Society*, **150**, A706 (2003).
35. M. Park, X. Zhang, M. Chung, G. B. Less, and A. M. Sastry, "A review of conduction phenomena in Li-ion batteries," *Journal of Power Sources*, **195**, 7904 (2010).
36. K. Smith and C.-Y. Wang, "Power and thermal characterization of a lithium-ion battery pack for hybrid-electric vehicles," *Journal of Power Sources*, **160**, 662 (2006).

3.3 External short circuit behavior of lithium-ion cells under quasi-isothermal conditions

Within this section, the article titled *Quasi-Isothermal External Short Circuit Tests Applied to Lithium-Ion Cells: Part I. Measurements* is presented. In the first part of this combined work, the experimental data basis for the consecutive model-based evaluation of a Li-ion cell's external short circuit characteristics is discussed. The experimental findings shown within this work are indispensable when validating physical-chemical short circuit models which will allow the study of underlying rate limitations and influencing factors in more detail.

For this purpose, an experimental setup was designed that allows not only well-defined external short circuit conditions to be imposed on small-sized pouch-type Li-ion cells, but to also both the cell's electrical and thermal signals to be measured, whilst guaranteeing quasi-isothermal test conditions. This enables a very detailed study of a cell's external short circuit behavior without commonly accompanied effects such as cell overheating, exothermic side reactions, and eventually cell thermal runaway, which would result in a premature interruption of the external short circuit current. The idea of quasi-isothermal external short circuit tests was inspired by previously published results studying the difference in external short circuit characteristics of 10 Ah pouch-type Li-ion cells under non-isothermal conditions as well as small coin cells comprising the same materials with capacities of less than 5 mAh, which can be considered isothermal.[257] Laboratory-scale pouch-type Li-ion cells were investigated containing graphite and NMC-111 as the anode and cathode active materials as well as 1 M $LiPF_6$ in EC:DMC 1:1 (by weight) with 2 wt% VC as electrolyte. Three different electrode loadings were investigated ranging from 1 mAh cm^{-2} (HP loading), over 2 mAh cm^{-2} (balanced (BA) loading), to 3.5 mAh cm^{-2} (HE loading). Furthermore, varying tab configurations resulting in a homogeneous or inhomogeneous current density distribution were studied. By additionally varying the test conditions such as the cell's temperature, its SoC, and the applied external short circuit resistance, a most thorough evaluation of individual factors influencing a cell's short circuit behavior can be guaranteed.

Depending on the cell characteristics and test conditions, initial C-rates from 100C up to 800C and beyond can be observed when applying "hard" external short circuits approaching an initial cell voltage of 0 V, which is accompanied by large heat generation rates. Test results of all investigated cells suggest that different rate limiting effects occur throughout the duration of the short circuit. This can be both observed in strongly diminishing cell currents as well as heat generation rates with ongoing discharge. The impact of electrode loading reveals that cells which are designed for delivering a HP capability also come with an accelerated short circuit behavior which results in relatively large currents and heat generation rates as well as a shorter duration until completely discharged or overdischarged, as already assumed by Yamauchi et al.[301] Furthermore, distinct transient plateaus in short circuit current and heat generation rate can be correlated to underlying mechanisms and limitations which can be fostered or reduced by altering the characteristics of the cells and test conditions. Whilst the early stage of a short circuit, which forms within less than a second, seems to be primarily defined by ohmic and reaction based overpotentials, an ongoing short circuit duration leads to a second plateau which can be correlated to likely mass transport based limitations within the cathode. The mature stage of a short circuit which forms in the range of hundreds to thousands of seconds depending on the electrode's energy and power characteristics, however, seems to be defined by an additionally occurring copper dissolution process which allows for a significant overdischarge of the cell beyond the cell's electrode balancing window which could be confirmed via energy dispersive X-ray spectroscopy (EDX) measurements.

With the cell's in-plane inhomogeneity in electrode current density distribution affecting the mechanical stress occurring within the electrodes,[119,124,288] mechanical damage of the electrode structure can be observed via scanning electron microscopy (SEM), especially for thicker electrodes. This is accompanied by highly resistive behavior of the cells throughout the short circuit. Varying the cell's temperature raises or lowers the observed plateaus in current and heat generation rate by generally enhanced transport properties and accelerated reaction kinetics with increasing temperature. The cell's SoC has almost no impact on the transient behavior of the cell until the cell is fully discharged, which reveals a sequence of rate limiting effects which also dominate throughout a variation of external short circuit resistances.
The presented extensive experimental data is further used to first validate a physical-chemical model before the underlying rate limiting mechanisms are studied in more detail within the following section.

Author contribution Alexander Rheinfeld developed the idea of quasi-isothermal short circuit tests, carried out the measurements, and analyzed the data. Andreas Noel helped to design the measurement setup and to establish the testing protocols, whereas Jörn Wilhelm helped throughout *post mortem* analysis. Akos Kriston and Andreas Pfrang shared their experience within the field of external short circuit measurements and provided related measurement data. The manuscript was written by Alexander Rheinfeld and was edited by Andreas Noel, Jörn Wilhelm, Akos Kriston, Andreas Pfrang, and Andreas Jossen. All authors discussed the data and commented on the results.

Quasi-Isothermal External Short Circuit Tests Applied to Lithium-Ion Cells: Part I. Measurements

Alexander Rheinfeld, Andreas Noel, Jörn Wilhelm, Akos Kristion, Andreas Pfrang, Andreas Jossen

Journal of The Electrochemical Society 165 (14), pp. A3427–A3448, 2018

Permanent weblink:
http://dx.doi.org/10.1149/2.0451814jes

Quasi-Isothermal External Short Circuit Tests Applied to Lithium-Ion Cells: Part I. Measurements

Alexander Rheinfeld,[1,*,z] Andreas Noel,[1] Jörn Wilhelm,[1] Akos Kriston,[2] Andreas Pfrang,[2] and Andreas Jossen[1]

[1]*Institute for Electrical Energy Storage Technology, Technical University of Munich, D-80333 Munich, Germany*
[2]*European Commission, Joint Research Centre (JRC), Directorate for Energy, Transport and Climate, Energy Storage Unit, 1755 LE Petten, The Netherlands*

Single-layered pouch-type cells were exposed to quasi-isothermal external short circuit tests to study the influence of electrode loading and tab configuration on the short circuit characteristics. Additionally, test conditions such as initial cell temperature, cell voltage and external short circuit resistance were varied. Keeping the cell's temperature increase below 1°C whilst using a calibrated calorimetric setup, a direct correlation between the electrical and thermal behavior could be shown without occurring exothermal side reactions. Previously studied step-like characteristics in the transient current profile could be confirmed for all cells and test conditions, showing differing durations and magnitudes of the observed plateaus based on ohmic resistances, transport processes and reaction kinetics. Lower electrode loadings, counter-tab configurations homogenizing the current density distribution and higher initial cell temperatures accelerate the short circuit by increasing the cell current due to a reduced effective cell resistance. Whilst the chosen initial cell voltages and external short circuit resistances showed a minor impact on the short circuit dynamics, the initial state of charge revealed a noticeable influence defining the discharged capacity and the amount of generated heat. By post mortem analysis, the observed over-discharge could be correlated to an anodic dissolution of the negative electrode's copper current collector.

 [DOI: 10.1149/2.0451814jes]

Manuscript submitted July 19, 2018; revised manuscript received September 25, 2018. Published November 2, 2018.

Because of their comparably high gravimetric and volumetric energy and power density combined with a high degree of technological maturity and meanwhile low overall cost, lithium-ion batteries are the energy storage solution of choice for multiple of today's applications ranging from mobile devices to electric vehicles and even stationary energy storage solutions. With Li-ion batteries being widely applied in our daily life, reported safety incidents involving this technology have resulted in an increased public attention toward the topic.[1–3] Li-ion battery safety is mainly defined by chemical/toxicological safety and thermal safety. The latter is related to thermal characteristics of the applied materials and chosen architecture which, on the one hand, guarantee a smooth operation of the battery, but, on the other hand, pose a certain risk for a so called thermal runaway if a battery heats up too much.[4–6] Such a heat up, which can exceed the cooling capacity of the battery system, can be either caused by an external misuse of the battery or by an internal fault.[7] In order to guarantee a high level of safety for Li-ion batteries entering the market, a substantial number of regulations and standards has been developed in the past covering mechanical, electrical and environmental or thermal abuse scenarios that may trigger a battery failure.[8]

One of the most common electrical tests is the external short circuit test, which is intended to simulate an accidental connection of the battery terminals.[9–14] For a hard external short circuit, the short circuit resistance is in the same order or lower than the internal high frequency resistance of the battery, resulting in a battery response predominantly affected by its inherent characteristics and not by the test conditions. With increasing battery size and consequently reduced internal high frequency resistance which can easily range below 1 mΩ, a thorough experimental realization of such a truly hard external short is becoming technically difficult.[14] This partly explains why both mechanical and electrical tests provoking a cell-internal short circuit are gaining a lot of attention recently, as such an incident can approach a worst-case scenario for a battery independent of the battery size. Besides the short circuit of the cell, an additional localized heat up is triggered. The combination of a short circuit and a strongly localized heating can rapidly exceed the onset temperature of thermal decomposition reactions often resulting in a violent failure of the investigated cell. Various triggers for provoking an internal short circuit have been reported in the past ranging from sharp nails [15] and blunt rods[16] to phase change materials[17] and metal pieces[18,19] that need to be elaborately included within the cell during manufacturing. Besides the efforts for designing such a test, the influence of the test parameters on the cell behavior is not quite understood so far which may cause variations in the cell response making an interpretation of reported test data difficult. This becomes especially apparent when looking into the design of e.g. a nail penetration test within which not only the nail's material, surface, diameter, and tip angle can be varied but also the penetration speed, depth, and location of a nail entering a cell may be altered.[8] These test parameters can significantly affect the outcome which has been shown recently for 18650 sized cells in terms of the location and penetration depth of the nail.[20,21] Moreover, the electrical behavior of a battery can mostly not be separated from its thermal behavior, which makes a scientific evaluation of the battery response complicated. Furthermore, the thermal behavior during battery failure is not only dependent on the chemical composition of the active and passive materials used within the cells,[22,23] but also affected by the state of charge (SoC) and state of health (SoH) of the cell and the respective electrodes.[24,25] A dedicated experimental investigation enabling a separation of effects is required for understanding the underlying mechanisms during a short circuit event. This accounts for both internal as well as external short circuits, whereas the focus of this work is laid on the latter in order to study the overall short circuit behavior of a battery in the first place.

Within the first part of this combined work, the experimental basis for a model-based investigation of hard external short circuits is presented which elaborates on a continuation of previously published experimental results.[14] As an enhancement of the external short circuit test, a quasi-isothermal calorimetric setup is presented, which allows a straightforward separation of the electrical and thermal behavior of the investigated single-layered pouch-type cells. Test results of quasi-isothermal external short circuit tests are presented, whereas both the characteristics of the cells itself and the test conditions were altered individually. Following this approach, the influence of (intrinsic) cell specific characteristics and (extrinsic) test conditions on the dynamic response of a battery during external short circuits can be evaluated.

*Electrochemical Society Student Member.
[z]E-mail: alexander.rheinfeld@tum.de

Table I. Cell and electrode characteristics.

		Negative electrode				Separator	Positive electrode			
		Current collector	Composite electrode				Composite electrode			Current collector
		Copper	Graphite			Polyolefin	NMC-111			Aluminum
	Unit		HP	BA	HE		HP	BA	HE	
Areal capacity[s]	mAh cm^{-2}		1.1	2.2	3.9		1.0	2.0	3.5	
Active material content[s]	wt%		96	96	96		86	86	86	
Binder content[s]	wt%		2	2	2		6	6	6	
Conductive carbon content[s]	wt%		2	2	2		8	8	8	
Gravimetric capacity[s]	mAh g^{-1}		350	350	350		145	145	145	
Thickness[m]	µm	18	39	67	124	25	32	79	141	20

[s]supplier information.
[m]measured with a micrometer screw at three different locations during post mortem analysis.

Experimental

In this section, the investigated cells and chosen short circuit test conditions are presented first. The quasi-isothermal calorimetric setup is described before the calibration and test procedure are characterized. At the end of the section, the carried out qualitative post-mortem analysis is described.

Cells and test conditions.—Within this work, 18 single-layered pouch-type cells were exposed to external short circuit scenarios under quasi-isothermal test conditions. Cells and test conditions were chosen to achieve a most extensive evaluation of both intrinsic cell designs and extrinsic short circuit conditions. The investigated cells were manufactured by Custom Cells Itzehoe GmbH (Germany) comprising graphite anodes and $LiNi_{1/3}Co_{1/3}Mn_{1/3}O_2$ cathodes (NCM-111, in the following written as NMC-111). A mixture of 1 M $LiPF_6$ in ethylene carbonate (EC) : dimethyl carbonate (DMC) 1:1 (by weight) containing 2 wt% vinylene carbonate (VC) was used as electrolyte. The cells varied in terms of electrode loading from approximately 1 mAh cm^{-2} (i.e. high power loading, HP), 2 mAh cm^{-2} (i.e. balanced loading, BA) up to 3.5 mAh cm^{-2} (i.e. high energy loading, HE) following the overall trend toward higher area specific capacities.[26] Within the specified voltage range of the cell during cycling between 3.0 V and 4.2 V, the NMC cathode was the capacity limiting electrode in order to avoid lithium plating during charging. An overview of the graphite and NMC electrode characteristics for each loading is given in Table I. A summary of the investigated cells and applied test conditions is given in Table II. Besides the targeted electrode loading, the investigated cells varied in terms of the tab configuration. Most cells investigated within this work were configured with wide tabs on opposing sides (i.e. counter-tab design, CT, cells 1 to 14) to optimize the homogeneity of current density distribution along the electrodes. Four of the studied 18 cells were equipped with smaller tabs on the same side (i.e. aligned-tab design, AT, cells 15 to 18) to provoke a more inhomogeneous current density distribution during the short circuit tests compared to the CT cells. Whilst the loading and tab configuration were altered within this study, the width and height of the electrodes of 56 mm × 31 mm was not changed which resulted

Table II. Investigated cells and test conditions.

Cell specifications			Test conditions					Before test			During test			After test		
No.	Design	C_{th} mAh	T_∞ °C	E_{cell} V	SoC %	Short	t_{rest} h	$C_{4.20\,V}$ mAh	C_{test} mAh	$R_{1\,kHz}$ mΩ	$I_{sc,\,max}$ A	C-rate	C_{sc} mAh	SoC %	E_{cell} V	$R_{1\,kHz}$ mΩ
1[†]	CT	17	25	4.15	96	0 V	15	14.4	13.8	316	9.91	689	16.2	−17	2.12	337
2	CT	17	25	4.15	96	0 V	48	13.6	12.9	306	9.91	730	15.0	−15	2.55	319
3	CT	17	45	4.15	96	0 V	15	13.9	13.3	309	10.59	761	16.2	−20	1.72	524
4	CT	17	55	4.15	96	0 V	15	12.3	11.7	319	10.20	828	14.5	−22	1.47	507
5[†]	CT	35	25	4.15	96	0 V	15	29.7	28.5	328	9.72	327	33.3	−16	2.44	346
6[*†]	CT	35	25	4.15	96	0 V	48	30.1	28.8	338	9.42	313	32.3	−11	2.64	359
7	CT	35	25	4.30	108	0 V	15	29.5	31.9	330	9.26	313	36.5	−16	2.36	522
8	CT	35	25	4.00	82	0 V	15	29.1	23.9	329	9.61	330	27.4	−12	2.64	337
9	CT	35	25	3.85	67	0 V	15	30.0	20.1	321	9.34	310	24.0	−13	2.48	355
10[†]	CT	60	25	4.15	96	0 V	15	60.5	58.1	397	9.01	149	66.2	−13	2.31	430
11	CT	60	25	4.15	96	0 V	48	61.9	59.4	432	8.91	144	67.2	−13	2.52	464
12[*]	CT	60	25	4.15	96	5 mΩ	15	56.6	54.2	470	8.37	148	60.9	−12	2.40	928
13	CT	60	25	4.15	96	50 mΩ	15	60.7	58.7	409	8.33	137	66.6	−13	2.45	472
14	CT	60	25	4.15	96	576 mΩ	15	59.3	57.0	411	5.90	99	63.8	−11	2.63	434
15[†]	AT	17	25	4.15	96	0 V	15	13.8	13.2	293	9.93	719	15.1	−14	2.47	338
16[†]	AT	35	25	4.15	96	0 V	15	33.2	31.9	349	9.59	289	37.0	−15	2.33	367
17[*†]	AT	60	25	4.15	96	0 V	15	56.7	54.3	470	8.55	150	47.9	11	3.49	936
18	AT	60	25	4.15	96	0 V	15	62.4	59.9	470	8.55	137	66.2	−10	2.49	670

[*]Cell showed high-resistance behavior during test.
[†]Cell was opened after test.

in overall nominal capacities of 17 mAh (HP), 35 mAh (BA), and 60 mAh (HE) between 3.0 V and 4.2 V. In accordance with previous work,[14] the influence of cell temperature (cells 1 to 4) and short circuit resistance (cells 10 to 14) was again studied within this work in order to compare the test results to previous results and to study the behavior during solely hard shorts with varying external short circuit resistances. The previous results were obtained from non-isothermal short circuit tests on 10 Ah pouch-type cells and short circuit tests on 4.5 mAh coin cells which were assumed to be isothermal. Within both previous work and the work presented here, cells from the same cell manufacturer were studied. An electrode loading of 2 mAh cm^{-2} was investigated in previous work which is very similar to the here presented BA loading. Furthermore, the influence of initial cell voltage and, hence, SoC was studied (cells 5 to 9). Again, to enable a most straightforward comparison between the test results presented within this study and previous work, the initial cell voltage was set to 4.15 V in most cases.

To sum up, the scope of the chosen cells and test conditions was, on the one hand, to study the influence of inherent cell characteristics such as the electrode loading and tab design and, on the other hand, to evaluate the influence of test conditions such as initial cell temperature, initial cell voltage or SoC and external short circuit resistance.

Experimental setup.—The single-layered electrode configuration of the investigated cells allows for designing a simple, yet quantitative quasi-isothermal calorimetric test. This can help to understand the cell's behavior during excessively high currents beyond its designated operating window by correlating thermal to simultaneously measured electrical signals. Such a test configuration allows to investigate only the main short circuit event, eliminating the effect of exothermal side reactions (e.g. solid electrolyte interphase layer decomposition, reaction of intercalated lithium with electrolyte and fluorinated binder, electrolyte and positive active material decomposition),[4] which can easily dominate the cell behavior at temperatures exceeding 80°C. In order to keep the overall temperature rise of the investigated cells below 1°C (considered quasi-isothermal within this study) without having to apply an active cooling strategy, the cells were placed in-between two copper bars of 45 mm × 45 mm × 90 mm (CW004A, purity 99.9%). To guarantee a good thermal contact between the cell's pouch foil and the two copper bars, thermally conductive (6 W m^{-1} K^{-1}) yet compressible ceramic foils of 0.5 mm thickness (86/600 Softtherm, Kerafol Keramische Folien GmbH, Germany) were used. To reduce the thermal interaction of the setup with the environment, the copper bars were insulated with a 60 mm thick layer of extruded polystyrene foam (XPS, approximately 0.04 W m^{-1} K^{-1}). For measuring the overall temperature rise, Pt100 temperature sensors (accuracy ±0.15°C at 0°C, DIN/IEC Class A) were placed in the center of the copper bars. The Pt100 sensors were attached to the copper bars with a thermal adhesive which also sealed the hole that was necessary to include the sensors. A schematic overview of the experimental setup including the investigated cell designs is shown in Fig. 1. The two Pt100 sensors and another Pt100 sensor attached with Kapton tape to the surface of the positive tab were connected to three individual digital multimeters (34470A, Keysight Technologies Inc., USA). Based on the four-wire temperature measurement and the chosen time-averaging sampling of approximately 1 s per data point, a temperature resolution of ±0.001°C was achieved. In order to reproducibly simulate highly dynamic short circuit conditions, the cells were connected to a single-channel potentiostat including a 10 A/5 V booster in a two-electrode configuration (SP-300, Bio-Logic Science Instruments, France). The entire calorimetric setup excluding the measurement equipment was placed within a custom-built climate chamber which was cooled by Peltier elements and heated with resistive heaters. For the investigated temperatures, the standard deviation of the environmental temperature regulation was ranging below ±0.03°C which was determined with the aid of a reference thermometer (1524, Fluke Corp., USA) equipped with a fast response reference platinum resistance thermometer (5622, Fluke Corp., USA) resulting in a combined accuracy of ±0.015°C to ±0.019°C between

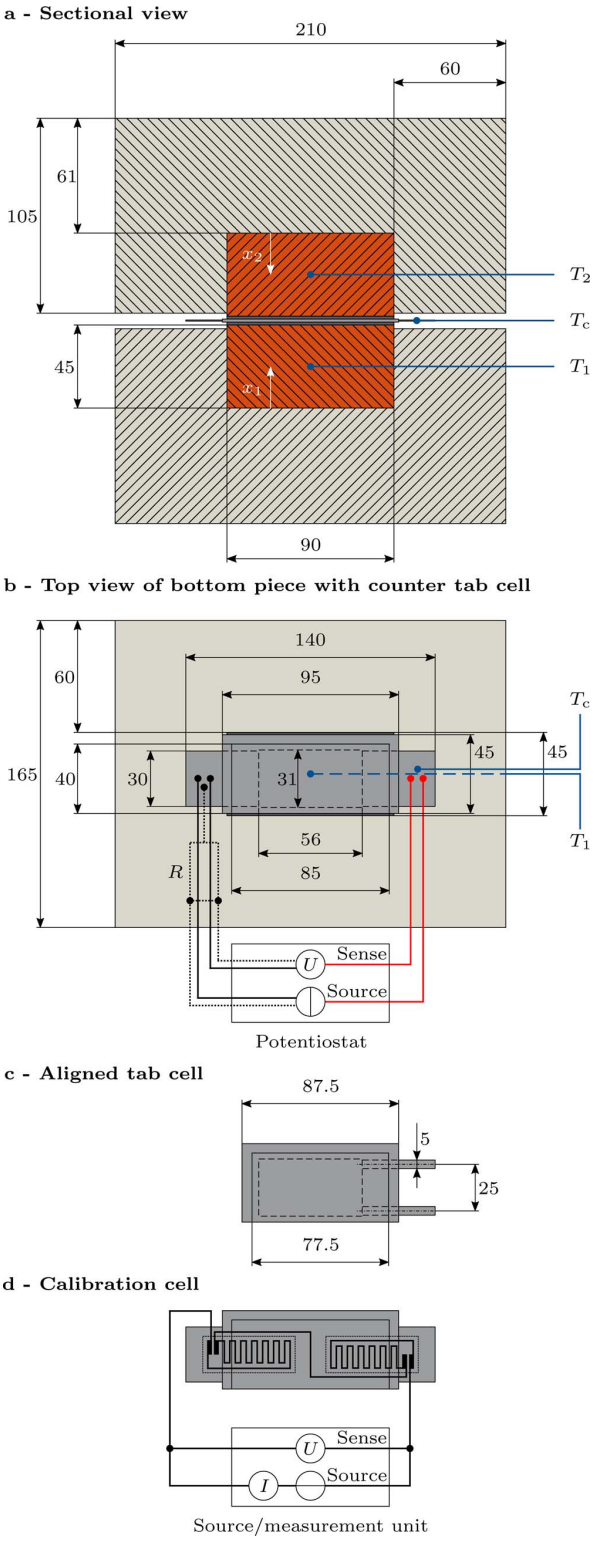

Figure 1. Schematic drawing of the calorimetric setup including a sectional view (a), a top view on the bottom piece of the calorimeter including a representative counter-tab cell (b), a representative aligned-tab cell (c), and a cell used for calibration purposes (d).

Table III. Calibration procedure.

R_{foil} Ω	E_{app} V	I_{app} mA	$\dot{Q}_{app}$ W	t s	Q_{app} J
1218.4	11.0	9.1	0.1	7200	720
1218.4	34.9	28.6	1.0	720	720
1218.4	78.1	64.1	5.0	144	720
1218.4	110.4	90.6	10.0	72	720

0°C and 100°C during the experiments. The measurement equipment was placed outside the climate chamber within the laboratory environment of 25 ± 2°C and was connected to a single desktop computer to allow for a time-synchronization among the used software programs.

Calibration.—Prior to the tests, the measured temperature signal of each Pt100 sensor was corrected by adapting the overall offset and slope of the measurement signal within the considered temperature range toward the reference thermometer. At temperature levels of 25°C, 45°C, and 55°C, the calorimetric setup was rested for 24 h within the custom-built climate chamber to allow for a thorough temperature equalization between the sensors and the environment whilst the temperature was simultaneously measured by the three digital multimeters and the reference thermometer. In order to calibrate the calorimetric test setup, i.e to determine the calorimetric constant associated with the overall heat capacity of the setup and losses to the environment, an over-discharged CT dummy cell was equipped with two resistive heater foils. The heater foils were attached on both sides of the cell's surface and were electrically connected in a series configuration. A precision source/measurement unit (B2901A, Keysight Technologies Inc., USA) was used to provide the driving voltage whilst precisely measuring the current so that the generated heat could be calculated (see Fig. 1d). Different voltages were applied to the heater foils, resulting in a heat generation rate of 0.1 W, 1 W, 5 W, and 10 W for a limited amount of time leading to an applied heat of 720 J in each case (see Table III). This value was chosen based on the estimated electrical energy content of the investigated cells ranging from 225 J (HP) to 800 J (HE). The resulting slope of the temperature increment multiplied by the total heat capacitance of the system whilst including losses to the environment represents the applied heat rate. In this configuration (see Figs. 1a, 1b, and 1d), the cell including the attached wiring is considered to be able to exchange heat only with the two copper bars which results in

$$E_{app} \cdot I_{app} = C_{p,1}\frac{d\overline{T}_1}{dt} + C_{p,2}\frac{d\overline{T}_2}{dt} + C_{p,c}\frac{d\overline{T}_c}{dt} + UA_1\left(\overline{T}_1 - T_\infty\right) + UA_2\left(\overline{T}_2 - T_\infty\right) \quad [1]$$

where $C_{p,i}$ (J K^{-1}) refers to the total heat capacity, $\overline{T}_i$ (K) to the mean temperature, and UA_i (W K^{-1}) to the overall heat transfer to the environment for each copper bar i. T_∞ represents the environmental temperature. Based on the combined effective heat transfer coefficient U_i (W m^{-2} K^{-1}) and effective heat transfer surface A_i (m^2), UA_i accounts for all heat losses of the calorimeter to the environment including both insulation and wiring. $C_{p,c}$ and $\overline{T}_c$ refer to the total heat capacity and mean temperature of the cell respectively. With the given specific heat capacity $c_{p,Cu}$ (CW004A: 386 J kg^{-1} K^{-1} at 20°C) and the measured mass m_{Cu} of 1.62 kg for each copper bar, the total heat capacity $C_{p,i}$ is obtained via

$$C_{p,i} = m_{Cu} \cdot c_{p,Cu} \qquad (i = 1,\ 2) \quad [2]$$

With an average mass m_c of 6.5 g and a specific heat capacity $c_{p,c}$ ranging between 800 J kg^{-1} K^{-1} and 1000 J kg^{-1} K^{-1},[27,28] the total heat capacity of the investigated cells can be estimated analogously via

$$C_{p,c} = m_c \cdot c_{p,c} \quad [3]$$

The mean copper bar temperature $\overline{T}_i$ and mean cell temperature $\overline{T}_c$ are considered to be represented by the measured temperatures. In order to determine UA_i, the cooling phase after heating up the setup was considered assuming a homogeneous temperature distribution among the components. This assumption allows to separate the individual temperature equalization processes of the two copper bars with the environmental temperature

$$C_{p,i}\frac{d\overline{T}_i}{dt} = UA_i\left(T_\infty - \overline{T}_i\right) \qquad (i = 1,\ 2) \quad [4]$$

By introducing the dimensionless temperature Θ_i based on the initial temperature $T_{i,0}$ at the end of the heat-up and the environmental temperature T_∞

$$\Theta_i = \frac{\overline{T}_i - T_\infty}{\overline{T}_{i,0} - T_\infty} \qquad (i = 1,\ 2) \quad [5]$$

the solution to this ordinary differential equation can be written as follows[29]

$$\Theta_i = \exp\left(-\frac{UA_i}{C_{p,i}} \cdot t\right) \qquad (i = 1,\ 2) \quad [6]$$

which can be individually fitted to the measured exponential temperature decrease and environmental temperature. Knowing each parameter, the theoretical adiabatic temperature $\overline{T}_{ad,i}$ can be determined which is relevant for considering appropriately the generated heat

$$\overline{T}_{ad,i} = \overline{T}_i + \frac{UA_i}{C_{p,i}}\int\left(\overline{T}_i - T_\infty\right)dt \qquad (i = 1,\ 2) \quad [7]$$

Including the calculated adiabatic temperature $\overline{T}_{ad,i}$ of the two copper bars in Eq. 1, the effective overall heat capacities of the two copper bars and cell need to be adjusted so that the calculated total heat rate resembles the applied heat rate $\dot{Q}_{app}$ (W) based on the applied voltage E_{app} (V) and resulting current I_{app} (A)

$$\dot{Q}_{app} \stackrel{!}{=} \dot{Q}_{tot} \quad [8]$$

whereas the total heat rate $\dot{Q}_{tot}$ calculates as

$$\dot{Q}_{tot} = \dot{Q}_1 + \dot{Q}_2 + \dot{Q}_c = C_{p,1}\frac{d\overline{T}_{ad,1}}{dt} + C_{p,2}\frac{d\overline{T}_{ad,2}}{dt} + C_{p,c}\frac{d\overline{T}_c}{dt} \quad [9]$$

Allowing for a linear fit of the effective overall heat capacities toward the temperature data, Q_{tot} (J) is further considered here

$$Q_{tot} = Q_1 + Q_2 + Q_c = C_{p,1}\left(\overline{T}_{ad,1} - T_{0,1}\right) + C_{p,2}\left(\overline{T}_{ad,2} - T_{0,2}\right) + C_{p,c}\left(\overline{T}_c - T_{0,c}\right) \quad [10]$$

with $T_{0,i}$ and $T_{0,c}$ representing the initial temperature of each individual component. By iteratively repeating the steps summarized in Eq. 6, Eq. 7 and Eq. 10 for the applied heat rates, an effective overall heat capacity of 660.7 J K^{-1} for each copper bar and 3.7 J K^{-1} for the cell was determined fulfilling Eq. 8. In the case of the two copper bars, the effective specific heat capacity of 406.5 J kg^{-1} K^{-1} is 5.3% larger than the theoretical value which can be correlated to the influence of the surrounding insulating material, cell wiring and the additional thermal adhesive that was used for attaching the Pt100 sensors. In the case of the pouch cell, an effective specific heat capacity of 562.4 J kg^{-1} K^{-1} can be determined which is lower than the reported data in the literature. This can be explained with the temperature of the tab not fully resembling the mean temperature of the cell based on the location of the Pt100 sensor. With this calibration procedure, the mean error in predicting the applied heat rate can be reduced to as little as 0.1% within the chosen range from 0.1 W to 10 W.

As a measurement setup with a high thermal inertia compared to the specimen was used and local temperatures were measured instead of the mean temperature of the components, an evaluation of this

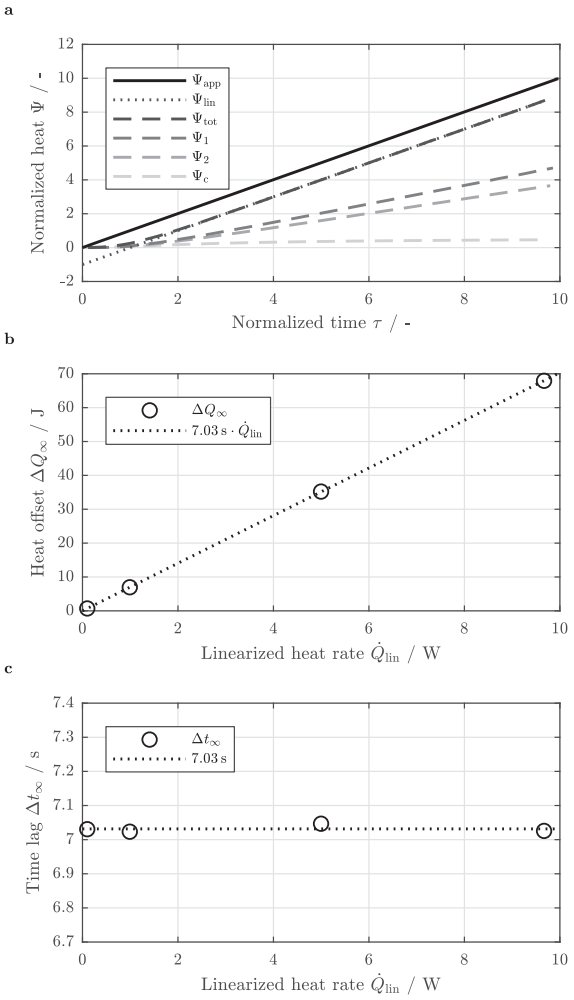

Figure 2. Normalized heat measurement during a calibration procedure at a constant applied heat rate of 10W for 72s (a) and derived absolute measurement error showing the offset in detected heat (b) and the time lag (c) as a function of the linearized measured heat rate ($\tau > 3$). Ψ_j is derived by relating Q_j to ΔQ_∞ (j = app, lin, tot, 1, 2, c).

combined measurement error is needed. Whilst the error accompanied with the positioning of the Pt100 temperature sensors falls below the combined resolution the measurement equipment (see appendix), the measurement error related to the system's thermal inertia cannot be neglected. This *type I thermometer error* is further discussed here.[29] For comparing the carried out calibration tests, the dimensionless heat Ψ and the dimensionless time τ are introduced

$$\Psi = \frac{Q}{\Delta Q_\infty} \quad [11]$$

$$\tau = \frac{t}{\Delta t_\infty} \quad [12]$$

which are based on the asymptotic absolute offset in measured heat ΔQ_∞ (J) and the time lag of the measurement Δt_∞ (s). Based on linearizing Q_{tot} as a function of time, both ΔQ_∞ and Δt_∞ can be determined. ΔQ_∞ is represented by the intercept of Q_{lin} with the ordinate and Δt_∞ is defined by the intercept of Q_{lin} with the abscissa. In Fig. 2a, normalized calibration test data is shown for an applied heat rate of 10 W. Due to the normalization procedure following Eq. 11 and Eq. 12, the 5 W, 1 W, and 0.1 W calibration test data look almost identical with increasing measurement signal noise at lower heat rates. As shown in this figure, an offset between the predicted and the applied overall heat can be observed. With progressing time, this offset becomes constant. Beyond approximately 3τ, the slope of the predicted heat is also becoming constant allowing for the presented linear fit of the setup's specific heat capacities during calibration. At $\Psi_{lin} = 0$, $\tau = 1$ which resembles the time delay of the measurement. At $\tau = 0$, $\Psi_{lin} = -1$ which represents the offset in the heat measurement. Whilst ΔQ_∞ follows the applied and measured heat rate in a linear fashion (see Fig. 2b), Δt_∞ remains fairly constant around 7s (see Fig. 2c).
With

$$\Psi_{app} = \tau \quad [13]$$

Ψ_{tot} can be further described by the inhomogeneous differential equation

$$\frac{d\Psi_{tot}}{d\tau} + \Psi_{tot} = \tau \quad [14]$$

which can be solved analytically based on the sum of its particular and homogeneous solution[29]

$$\Psi_{tot}(\tau) = \exp(-\tau) + \tau - 1 \quad [15]$$

With this solution, the measurement error $\Delta\Psi$ and its derivative $\Delta\dot{\Psi}$ can be quantified in the course of the measurement

$$\begin{aligned}\Delta\Psi &= \Psi_{app} - \Psi_{tot} \\ &= 1 - \exp(-\tau)\end{aligned} \quad [16]$$

$$\begin{aligned}\Delta\dot{\Psi} &= \frac{d\Psi_{app}}{d\tau} - \frac{d\Psi_{tot}}{d\tau} \\ &= \exp(-\tau)\end{aligned} \quad [17]$$

This allows to derive the errors ΔQ (J) and $\Delta\dot{Q}$ (W) in measuring the overall heat and heat rate respectively

$$\begin{aligned}\Delta Q &= Q_{app} - Q_{tot} \\ &= \Delta Q_\infty \left(1 - \exp\left(-\frac{t}{\Delta t_\infty}\right)\right)\end{aligned} \quad [18]$$

$$\begin{aligned}\Delta\dot{Q} &= \dot{Q}_{app} - \dot{Q}_{tot} \\ &= \frac{\Delta Q_\infty}{\Delta t_\infty} \exp\left(-\frac{t}{\Delta t_\infty}\right)\end{aligned} \quad [19]$$

The short circuit test data Q_{sc} and $\dot{Q}_{sc}$ presented in this work is corrected based on these findings accordingly

$$Q_{sc} = Q_{tot} + \Delta Q \quad [20]$$

$$\dot{Q}_{sc} = \dot{Q}_{tot} + \Delta\dot{Q} \quad [21]$$

whereas t_∞ is considered to be independent of the applied heat rate (7.03s) and Q_∞ is assumed to be directly related to t_∞ and $\dot{Q}_{tot}$

$$\Delta Q_\infty = \Delta t_\infty \cdot \dot{Q}_{tot} \quad [22]$$

as shown in Figs. 2b and 2c.

Short circuit test procedure.—All cells investigated within this study were first cycled outside the calorimetric test setup for 10 cycles at C/2 between the lower and upper cutoff voltage of 3.0 V and 4.2 V using a battery test system (CTS, BaSyTec GmbH, Germany), after which the 1 kHz impedance of the cells was measured at 50% SoC (BT3564, Hioki E.E Corporation, Japan). The discharge capacity of the cells was determined right before the test between 4.2 V and 3.0 V as well as between the upper cutoff voltage of the test (i.e. 4.3 V, 4.15 V, 4.0 V, and 3.85 V) and 3.0 V. For this purpose, a C/2 constant

current (CC) charge and discharge procedure was applied followed by a constant voltage (CV) phase until the current dropped to C/100 at the respective lower and upper cutoff voltage. After the cell voltage or SoC was adjusted according to Table II following a CC/CV charging procedure, the cells were rested for at least 4 h before they were shorted. The cell's discharge capacity between 100% SoC (4.2 V) and 0% SoC (3.0 V) based on the CC/CV procedure was used as the reference for the SoC determination. All tests outside the calorimetric setup were carried out at 25°C within a climate chamber. The main short circuit condition chosen in this work was set to simulate a worst-case scenario, which can be achieved by applying a 0 V CV condition between the working electrode (positive electrode) and the counter/reference electrode (negative electrode) within the used EC-Lab software. The regulation of the 0 V condition was based on a four-wire measurement of the potentiostat. Varying short circuit resistances were simulated as well, whereas the highest resistance chosen in this work (576 mΩ or 1 mΩ m^2 referred to the electrode area) was applied by using the constant resistance operating mode within the software. Any resistance level below the 1 kHz impedance of the cell caused problems with the stability of the voltage regulation supplied by the potentiostat. Therefore, precision resistors (accuracy ±1%) of 50 mΩ or 0.087 mΩ m^2 and 5 mΩ or 0.0087 mΩ m^2 (Power Metal Strip, Vishay Intertechnology Inc., USA) were connected in series to the investigated cells applying the 0 V CV condition (see Fig. 1b dotted lines). Additional resistances due to wiring and electrical contact were ranging below 1 mΩ at 1 kHz. In order to be still able to measure the cell's voltage response during the test, the precision source/measurement unit used for calibrating the calorimetric setup was additionally connected to the cell's tabs (not explicitly shown in Fig. 1b). The short circuit condition was stopped as soon as the current dropped below 0.2 mA or until a control of the potentiostat was no longer possible. This generally resulted in a short circuit duration between 1 h and 3 h depending on the cell behavior. After the short circuit condition was stopped by the potentiostat, the cell remained within the closed calorimetric setup between 15 h and 48 h in order to determine the calorimetric constant for each individual test. A resting time of 48 h before and after the test, both within a closed configuration, was carried out once for each electrode loading in order to determine possible variations throughout the entire test phase. A resting time of 15 h after the test within a closed configuration and an equalization time of 3 h before the test in an opened configuration allowed for performing one test per day without drawbacks in the temperature equalization prior to the short circuit test and in determining the calorimetric constant after the short circuit.

Post mortem analysis.—In order to qualitatively study the impact of the short circuit condition on the investigated cells and electrodes, selected cells were opened in a glove box (M. Braun Inertgas-Systeme GmbH, Germany) under argon atmosphere after short circuit. Punched out electrode samples were washed with DMC and dried subsequently before they were studied by scanning electron microscopy (SEM) and energy-dispersive X-ray spectroscopy (EDX). For this purpose, a benchtop SEM (JCM-6000, JEOL Ltd., Japan) equipped with a MP-00040EDAP detector was used at an acceleration voltage of 15 kV and a working distance of 19-20 mm. EDX mapping was performed at a magnification of 150 and 1000, whereas at the lower magnification the observable area which can be studied by means of the EDX detector is maximized at the chosen working distance (ca. 0.8 mm × 0.6 mm = 0.48 mm^2).

Results and Discussion

Within this section, results from the quasi-isothermal short circuit tests are presented and discussed. First, experimental data from an exemplary short circuit test as well as derived calorimetric data is shown. Based on this, the influence of electrode loading, initial cell temperature, initial cell voltage or SoC, short circuit resistance, and tab design is evaluated in terms of absolute values and cell capacity related data. Observed discrepancies in the behavior of certain cells are further correlated to the occurring effective overvoltage and cell resistance. At the end of the section, selected results from the qualitative post mortem analysis are shown before the underlying mechanisms are discussed leading to the observed behavior which allows for deriving implications in order to design cells and electrodes which may increase a cell's tolerance toward external short circuits.

Short circuit characteristics.—A representative short circuit test is shown in Fig. 3 which was conducted on a HE cell with a CT design (cell 11, see Table II and Figs. 1a and 1b) including a 48 h resting period before and after the test. As can be seen from the voltage data plotted for the entire test duration in Fig. 3a, the applied 0 V condition results in a short circuit duration of approximately 2 h before the test is stopped by the potentiostat and the cell voltage relaxes. Within this condition, the investigated cell delivers a maximum current approaching 9 A (ca. 150C, see Fig. 3b) resulting in a sudden temperature increment of almost 0.6°C of the measured copper bar temperature with respect to the time-averaged environmental temperature ΔT_∞ (Fig. 3c). After the short circuit is interrupted, the cell voltage relaxes above 2.5 V (Fig. 3a) and the temperature of the overall calorimetric setup decreases in an exponential manner (Fig. 3c). Based on this exponential temperature decrease, the unknown parameters of Eq. 6 can be fitted in the same manner as for the calibration procedure. With the aid of these parameters, the heat exchanged with the environment can be determined for the entire setup which is represented by the right term in Eq. 4 for each copper bar. The obtained total heat exchange rate with the environment is shown in Fig. 3g. Looking into the time scales and magnitudes occurring (see Figs. 3b, 3d, and 3f), a logarithmic representation of the short circuit duration and short circuit current is useful.[14] The potentiostat is capable of simulating a worst-case 0 V condition within 50-100 ms for most of the investigated cells (see Fig. 3b). A constant offset of approximately 100 μV toward the electrical ground could be observed for all tests which can be directly correlated to the accuracy of the potentiostat which is 100 μV between 0 V and the maximum voltage of 4.3 V. As has been previously reported,[14] the discharge current reveals a strong step-like behavior within a double-logarithmic representation (see Fig. 3d). Between the initiation of the short circuit and 1s of elapsed short circuit time, a plateau forms at a current level exceeding 8 A (ca. 130C), after which the current drops within a few seconds before a second plateau forms at current values ranging between 1 A (ca. 17C) and 0.1 A (ca. 1.7C). This second plateau lasts from several seconds after the short circuit was triggered up to several hundred seconds before the current drops within a few thousand seconds approaching a third plateau at a current level of 1 mA (ca. C/60) and below. The measured temperature rise shows that both copper bars behave identical throughout the entire short circuit duration. Due to the chosen time averaging sampling condition and the associated resolution of the temperature measurement, a temperature rise below 0.001°C or within 1s cannot be accurately detected with the method presented here, which is why only data is considered beyond this threshold. Whilst there is a continuous rise of the measured temperature up to approximately 1 h, the temperature decreases beyond this point as the generated heat becomes less than the heat transferred to the environment (ca. 25 mW). The measured temperature rise of the positive tab shows a more dynamic behavior of the cell's temperature evolution from the beginning up to approximately 200 s before it follows the temperature of the copper bars (see Fig. 3f). By accounting for the calculated overall heat losses shown in Fig. 3g, the theoretical adiabatic temperature of the test setup can be determined according to Eq. 7. This procedure allows for a determination of the heat generation rate throughout the entire short circuit duration by calculating the slope of the adiabatic temperature rise of the system knowing its total heat capacity as summarized in Eq. 9. By correcting the calculated heat generation rate with the measurement error of the setup as presented in Eq. 21, the true heat rate can be approximated. The result is shown in Fig. 3h, which reveals a very strong resemblance with the measured cell current despite the aforementioned time delay of ca. 7 s which only becomes apparent at early times. The presented correction of the heat signal cannot completely rule out this delay due to the limited

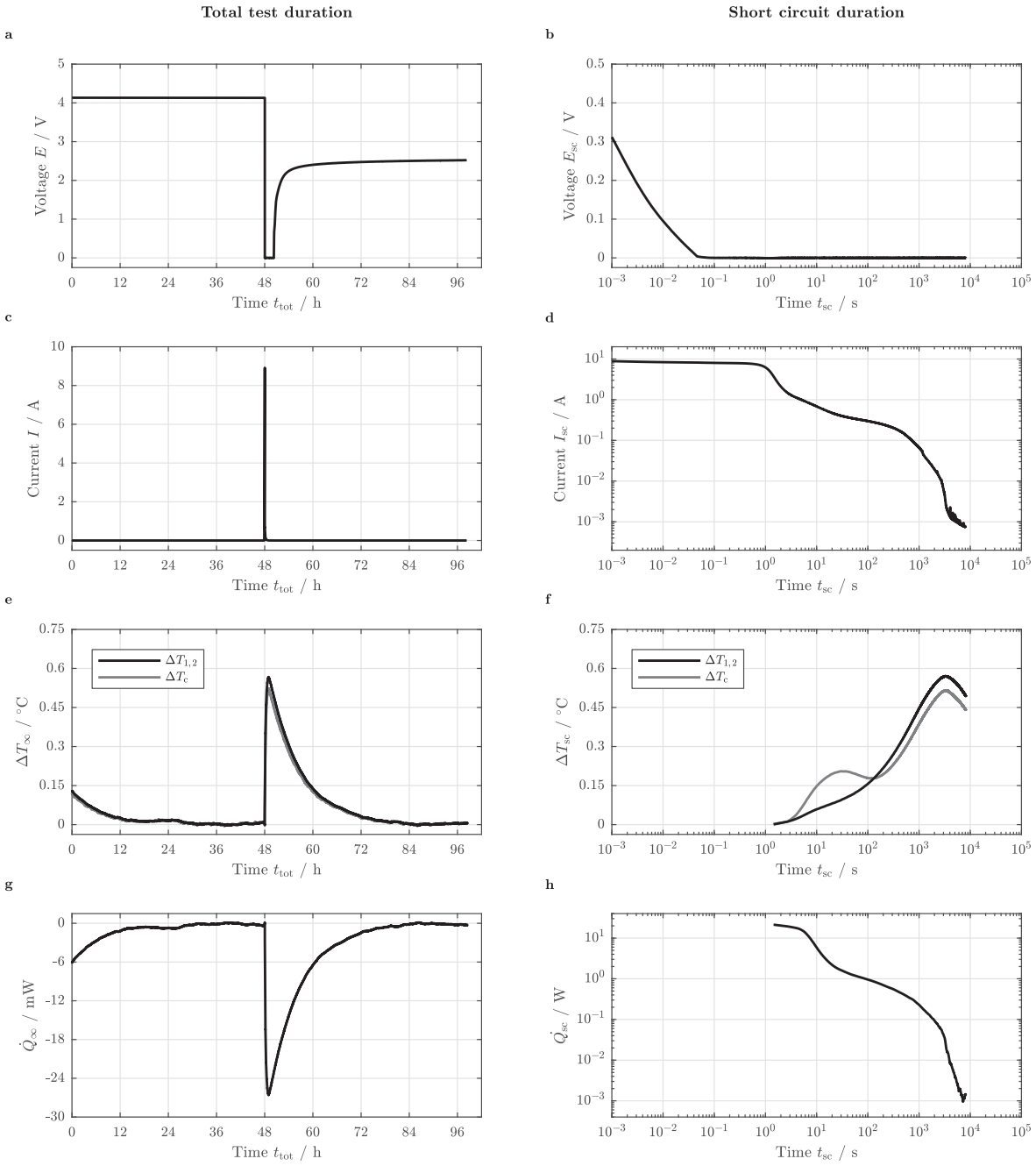

Figure 3. Representative electrical cell behavior (cell 11) during a short circuit test including a 48 h resting period before and after the short circuit event measured with the used potentiostat (a to d) including the thermal behavior measured with the calorimetric setup (e to h) for the entire test duration (left: a, c, e, and g) and the short circuit duration (left: b, d, f, and h).

resolution of the measurement and the unknown heat rate of the cell in the first place. Beyond 21 s ($3\Delta t_\infty$), the heat generation rate can be accurately determined as observed during calibration. The calculated heat generation rate exceeds 10 W in the beginning of the short circuit, forming a similarly shaped plateau between approximately 1 W and 0.1 W before the heat generation rate drops below 1 mW.

By comparing the transient behavior of the investigated cells by both potentiostatic and calorimetric measurements in the following subsections, similarities and differences between the test results become apparent which can be correlated to the altered cell characteristics and test conditions.

Influence of electrode loading.—In Fig. 4, the short circuit current I_{sc} and time-integrated discharged capacity C_{sc} (mAh) gained from potentiostatic measurements is presented on the left (a, c, and e) whereas the calculated heat generation rate $\dot{Q}_{sc}$ and generated heat

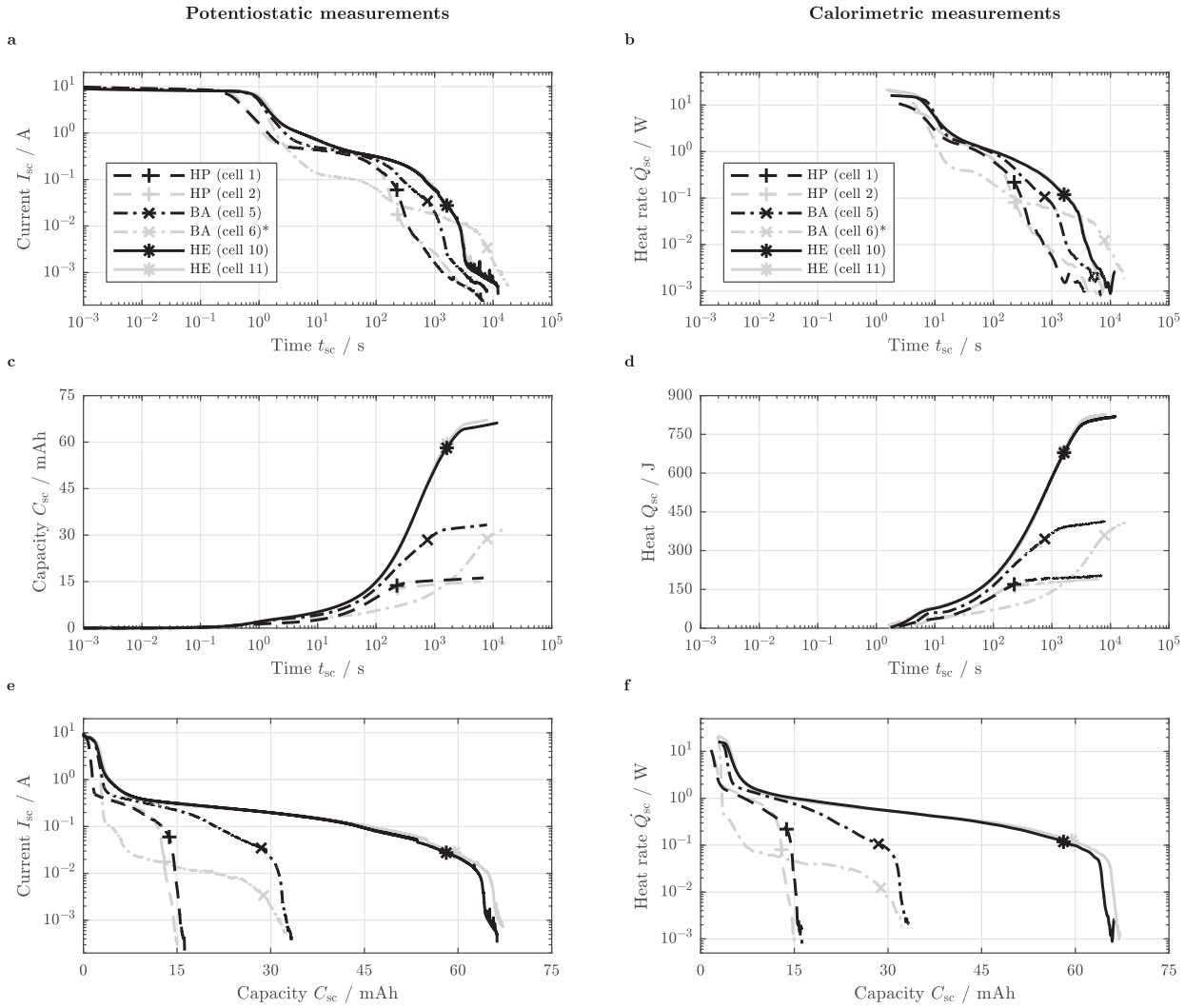

Figure 4. Cell behavior during a 0 V CV short circuit event applied to the HP (dashed lines), BA (dash-dotted lines), and HE loading (solid lines) with a CT design as a function of short circuit duration (a to d) and as a function of discharged capacity (e and f) for the cell current (a and e), heat generation rate (b and f), discharged capacity (c), and generated heat (d) measured with the potentiostat (left: a, c, and e) and the calorimetric setup (right: b, d, and f). Markers indicate 0% SoC. Cell 6 shows a high-resistance behavior (*).

Q_{sc} based on the calorimetric measurements are presented on the right (b, d, and f). All tests were conducted at 25°C applying a 0 V condition to the investigated HP, BA, and HE cells with a CT design (see Table II and Figs. 1a and 1b). As can be seen from Fig. 4, the CT cells investigated in this study generally showed very reproducible characteristics in terms of short circuit current and heat generation rate as a function of short circuit duration t_{sc} (s) (see Figs. 4a and 4b) and discharged capacity (see Figs. 4e and 4f). The strong resemblance between the electrical and thermal behavior of the cells becomes further obvious when comparing the discharged capacity with the total generated heat (see Figs. 4c and 4d). One of the cells shown here comprising a BA loading (cell 6) behaved differently in that respect, which hints at a high-resistance characteristics beyond 1s based on the comparably lower cell current and heat generation rate throughout the second plateau. This will be further discussed in a later part of this section. The peak current $I_{sc,\,max}$ delivered by the three electrode loadings at the very beginning of the short circuit varies between approximately 9.9 A, 9.6 A and 9.0 A for the HP (cells 1 and 2), BA (cells 5 and 6), and HE loading (cells 10 and 11) respectively. Previous tests with 18650 cells have shown that a stable control up to 12 A can be achieved with the potentiostat when applying a sudden voltage drop which is sufficient for the investigations made here. The varying peak currents imply that cells with a lower area specific capacity and therefore overall capacity deliver a higher absolute initial short circuit current. Looking into the levels of the 1 kHz impedance measured prior to the tests (310 mΩ, 330 mΩ, and 415 mΩ), a certain correlation to the peak current can be drawn as previously suggested.[30] With increasing the electrode loading in general, both the cell current and the heat generation rate are extended to longer times (see Figs. 4a and 4b). Whilst the current for the HP loading starts dropping toward its second plateau after 0.3 s, both the BA and HE loading take approximately twice as long (i.e. 0.6 s). Furthermore, the HP loading drops below 0.1 A after approximately 200 s, whilst the BA and HE loading can sustain a cell current above this threshold in the range of 300 s and 700 s (see Fig. 4a). This implies that the higher the electrode loading and cell capacity, the longer a certain current level can be sustained, whereas

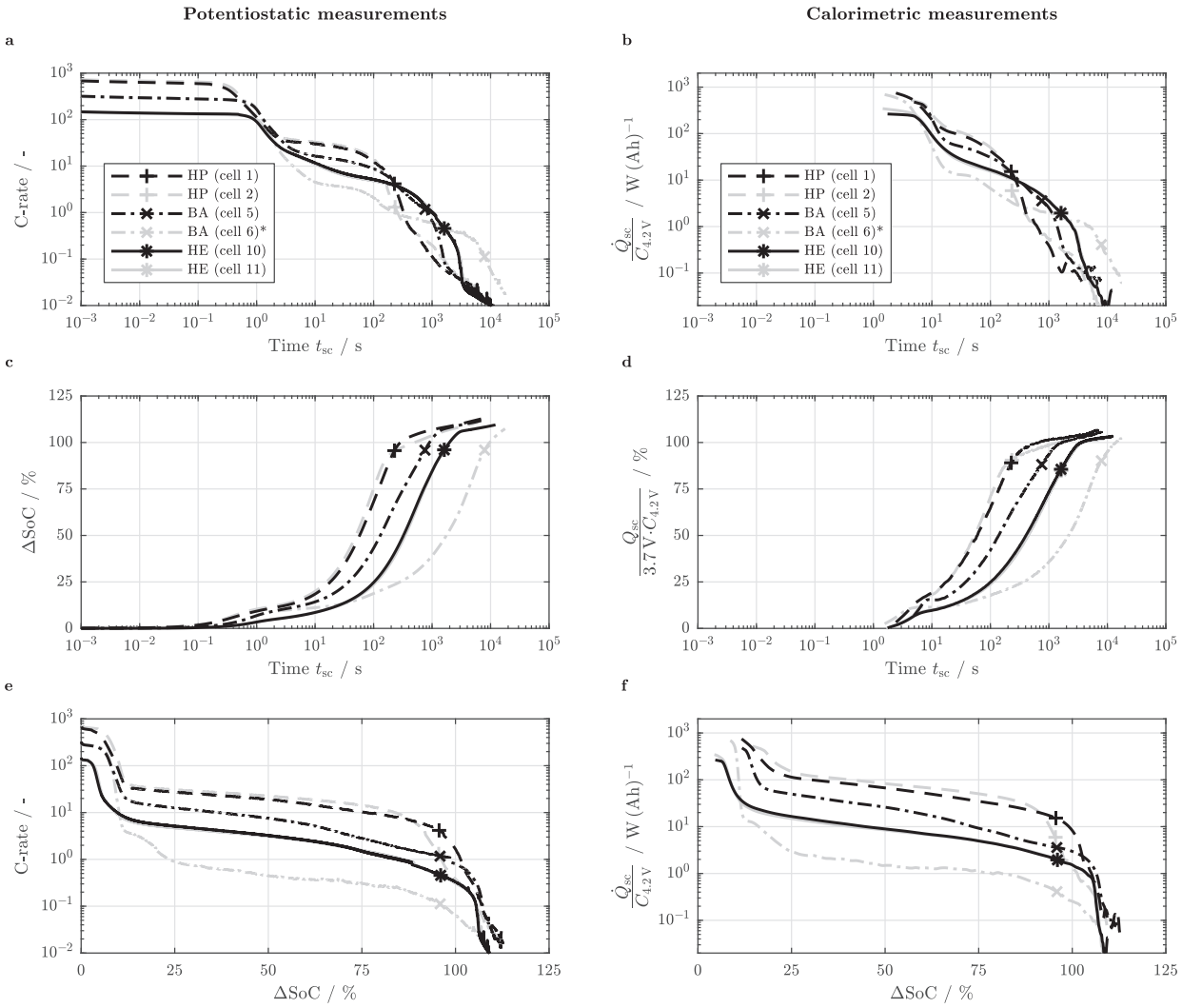

Figure 5. Cell behavior during a 0 V CV short circuit event applied to the HP (dashed lines), BA (dash-dotted lines), and HE loading (solid lines) with a CT design as a function of short circuit duration (a to d) and as a function of normalized discharged capacity (e and f) for the C-rate (a and e), capacity related heat generation rate (b and f), normalized discharged capacity (c), and electrical energy related heat (d) measured with the potentiostat (left: a, c, and e) and the calorimetric setup (right: b, d, and f). Markers indicate 0% SoC. Cell 6 shows a high-resistance behavior (*).

the overall magnitude of the withdrawn current at each plateau is almost identical, i.e. independent of the cell capacity (see Figs. 4a and 4e). With the heat rate following the cell current, a faster heat up can be observed for cells with a higher electrode loading and overall capacity based on the extended duration of each plateau (see Figs. 4c and 4d). After the cells passed the fully discharged state as defined by the discharged capacity determined prior to the test between the upper cutoff voltage and 3.0 V (indicated via markers in Fig. 4), the cells can still deliver decreasing cell currents and heat generation rates in the same order of magnitude before both drop by one or two magnitudes (see Figs. 4a, 4b, 4e, and 4f). This implies, that fully discharged cells can still contain a considerable amount of electrical and consequently thermal energy. Combined with the thermal stability of the materials and the heat produced based on exothermal side reactions, this may still pose a certain safety risk which, however, is at a comparably low level for the material combination studied in this work.[25]

Relating the current and heat generation rate to the measured capacity between 4.2 V and 3.0 V, a more pronounced difference between the investigated electrode loadings becomes apparent (see Figs. 5a, 5b, 5e, and 5f). Whilst the HP loading initially provides C-rates beyond 700C, the BA and HE loading fall in the range of 300C and 150C respectively. A spread between the lowest and highest electrode loading up to a magnitude (factor of ca. 5-10) can be observed in terms of C-rate and the adequately capacity related heat generation rate $\dot{Q}_{sc}/C_{4.2\,V}$ (W (Ah)$^{-1}$). In order to be able to better compare the three electrode loadings, an SoC-based representation is useful, whereas the cell is at 100% SoC at 4.2 V and at 0% SoC at 3.0 V following the 0.5C CC/CV procedure.

$$\Delta SoC = \frac{C_{sc}}{C_{4.2\,V}} \quad [23]$$

As can be seen from Figs. 5e and 5f, the three electrode loadings behave very similarly in terms of the C-rate and capacity related heat generation rate forming plateaus of similar size and shape but varying magnitude throughout the short circuit. All cells are fully depleted at a normalized discharged capacity ΔSoC of approximately 96% which is the discharged capacity of the cells at 4.15 V related to the fully

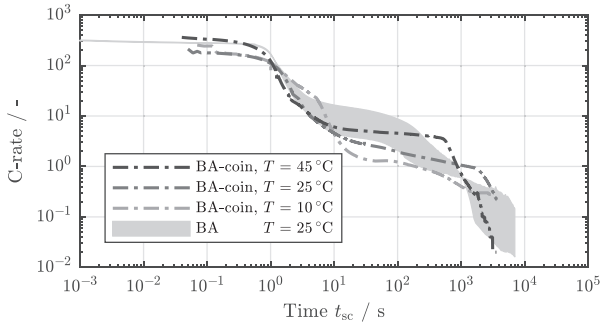

Figure 6. Comparison of cell behavior during a 0 V CV short circuit event applied to coin cells with a similar electrode loading as the BA loading at temperatures of 10°C, 25°C, and 45°C (data taken from Kriston et al.[14] used under CC BY-NC-ND, dash-dotted lines) to the cell behavior of single-layered pouch-type cells with a CT design and a BA loading at 25°C showing varying resistance characteristics (this work, gray shaded area).

charged state at 4.2 V. The first plateau consumes approximately 5% (HE) to 10% (HP) of the cell's capacity within less than a second. The second plateau consumes about 90% (HP) to 100% (HE) of the capacity passing 0% SoC. The third and last 'plateau' which rather resembles a change in curvature in this representation accounts for approximately another 5% (HE) to 15% (HP) of the cell's capacity. The increased magnitude in C-rate from the HE to the HP loading becomes further obvious when looking into the time-integrated normalized discharged capacity (see Fig. 5c). The observed spread in C-rate and capacity related heat generation rate results in a similar shift around a magnitude toward earlier times for the HP loading compared to the HE loading. This implies that the HP cell is fully discharged after just 225 s whilst the BA and HE loading last about 3.4 to 7.2 times as long respectively. This slow down in discharge also decelerates the relative heat up which appears as a shift to the right in Figs. 5c and 5d compared to the HP loading. By relating the generated heat to the cell's electrical energy, the share of thermal energy generated from the electrical energy can be evaluated (see Fig. 5d). With an effective cell voltage around 3.7 V between 100% and 0% SoC, the entire estimated electrical energy of the cell (ca. $3.7\,\mathrm{V} \cdot C_{4.2\,\mathrm{V}}$) is transformed to heat passing the 100% threshold due to the observed over-discharge. This confirms initial approximations for the total electrical and, hence, thermal energy content, as additional exothermal side reactions were suppressed based on the design of the experiment.

Influence of cell temperature.—When looking into previously published data of external short circuit tests on coin cells comprising a similar BA loading[14] and EC:DMC based electrolyte, the temperature has a similar effect on the short circuit behavior of a cell as the electrode loading itself (compare lines in Fig. 6 to Fig. 5a). By increasing the temperature or decreasing the electrode loading, the short circuit is accelerated. This means that both C-rate and capacity related heat generation rate at each plateau are raised toward higher levels resulting in a shorter duration of each plateau, which appears as a shift of the graph toward earlier times. This tendency can be confirmed for cells with a HP loading and a CT design in this work, where the temperature steps were set as 25°C, 45°C, and 55°C whilst applying a 0 V short circuit condition (see Table II). Raising the temperature as high as 55°C was considered to be of more interest in this work than lower temperatures such as 10°C as previously studied,[14] with a short circuit often resulting in a sudden temperature increase beyond the designated maximum operation temperature of the battery under non-isothermal conditions.

When comparing Fig. 7a to Fig. 6, a similar trend can be observed, whereas the impact of the temperature increase is reduced for the single-layered pouch-type cells with a HP loading compared to the coin cells with a BA-like loading. Even though the temperature spread between the measurements in this work and previous work lies in the same range (i.e. 30°C vs. 35°C[14]), the spread between the plateaus is smaller than previously shown, which especially holds for the second plateau. This could be based on an overall tendency of the coin cells behaving rather resistive in comparison to the investigated single-layered pouch-type cells in this work. This becomes apparent when comparing the coin cell behavior during the second plateau to the observed spread between a pouch-type cell that behaves analogously to other cells investigated in this work (upper boundary of gray area in Fig. 6) to a pouch-type cell that behaves in a high-resistance fashion (lower boundary of gray area in Fig. 6). Similar electrodes and separators were used within both coin cells and pouch-type cells resulting in similar effective transport lengths[31] and accompanied mass and charge transport based overpotentials. However, the assembly process between the coin cells and pouch-type cells is differing resulting in varying compressive forces and consequently diverging contact resistances. This discrepancy might be further increased by the chosen three-electrode configuration of the coin cells.[14]

With increasing the temperature in general, reaction overpotentials are reduced within the electrodes based on Butler-Volmer reaction kinetics increasing the observeable short circuit current. The second plateau being similarly influenced by the electrode loading and temperature further hints at a limitation in mass and charge transport within the liquid electrolyte. With the electrode loading mainly affecting the effective transport length and the temperature affecting the inherent transport properties of the electrolyte itself,[32,33] varying overpotentials are occurring which are based on ion movement. The HP loading being relatively less affected by temperature variations compared to the BA loading might further be a result of the reduced thickness and, hence, superior ion transport compared to the BA loading in the first place (see Table I). Possible mechanisms resulting in the observed characteristics of the short circuit behavior of the cells in each plateau are summarized at the end of the section helping to derive implications toward electrode and cell design. In this study, a further increase in temperature beyond 45°C does not considerably increase the current and heat rate of the short circuit. This becomes especially apparent when looking into Fig. 7c to f. Within the first plateau, the initial C-rate is increased by 9% from 45°C to 55°C which is similar to the increase from 25°C to 45°C (7%). However, the magnitude of the second plateau is not raised much further with respect to C-rate and capacity related heat generation rate beyond 45°C (see Figs. 7e and 7f). As a result, the normalized charge throughput and capacity related heat evolution are not shifted to much earlier times (see Figs. 7c and 7d), implying a certain limitation of the temperature impact.

Influence of cell voltage (state of charge).—As the cell's voltage is the driving force for the current to flow, its influence and consequently the cell's SoC was studied on cells with a BA loading and CT design at 25°C applying a 0 V short circuit condition (see Table II). The initial cell voltage was varied from 4.3 V, 4.15 V, 4.0 V, to 3.85 V resembling an SoC of approximately 108%, 96%, 82%, and 67%. As can be seen from Figs. 8a and 8b, the voltage has a mere influence on the cell's transient behavior up to 100 s to 200 s after the short circuit was triggered. Beyond this point, the higher the voltage and, hence, available cell capacity, the longer a cell can sustain the current level before it drops to the third plateau, which starts after a test duration of 1000 s to 2000 s. Whilst the discharged capacity and generated heat vary for the investigated cells (see Fig. 8c and 8d), the overall duration and magnitude of the first plateau remains almost unchanged. A slight variation in terms of the peak current can be observed, however, this might easily fall within the tolerance of the measurement itself and manufacturing tolerances accompanied with the investigated single-layered pouch-type cells (see Table II).

Referring to the observations made on the influence of electrode loading and temperature, the initial cell voltage or SoC does not affect the dynamics of the short circuit (i.e. the magnitude of current and heat rate) - it defines the overall charge and heat throughput during the short circuit. As the electrode morphology and electrolyte transport

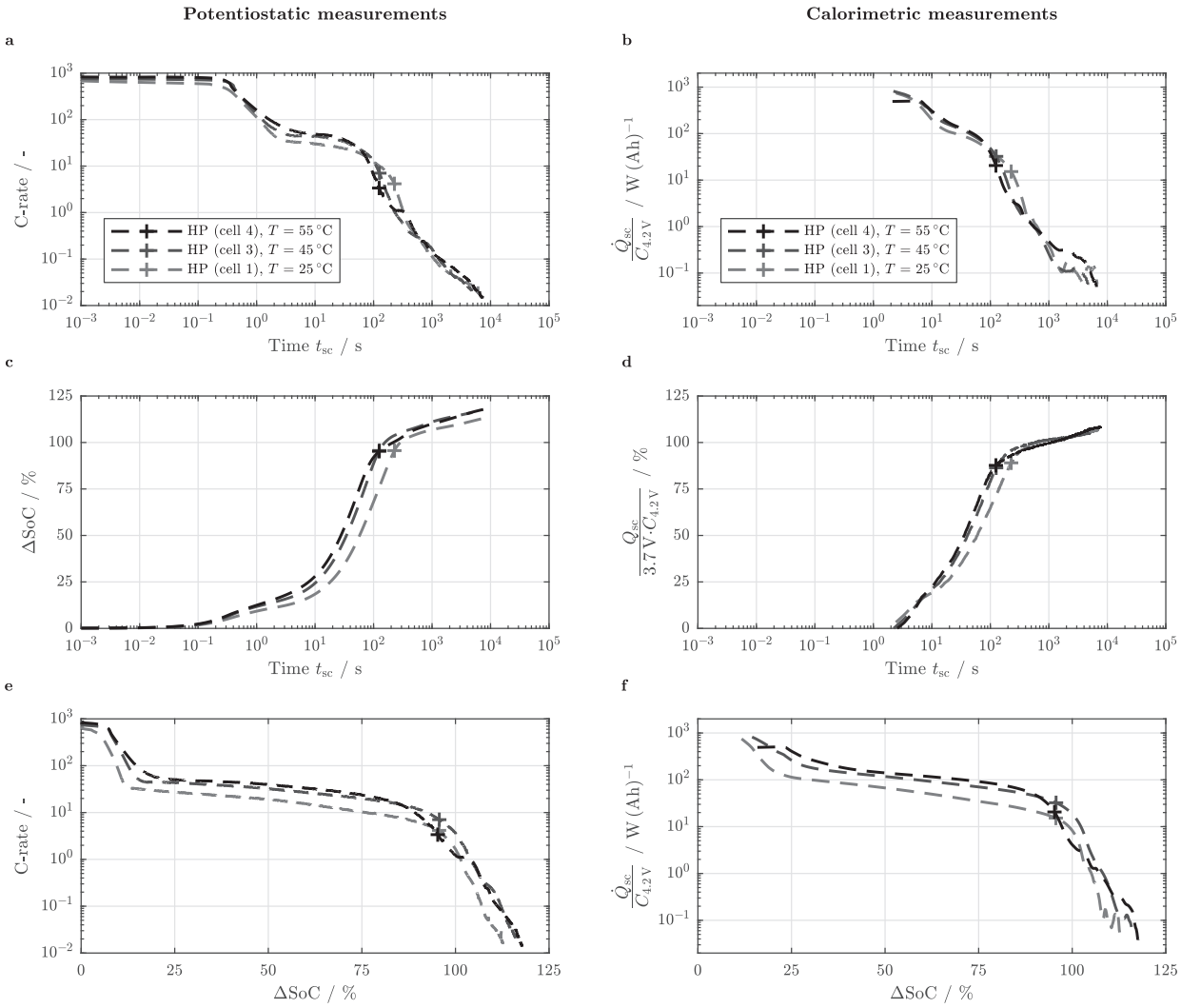

Figure 7. Cell behavior during a 0 V CV short circuit event applied to the HP loading with a CT design at temperatures of 25°C, 45°C, and 55°C as a function of short circuit duration (a to d) and as a function of normalized discharged capacity (e and f) for the C-rate (a and e), capacity related heat generation rate (b and f), normalized discharged capacity (c), and electrical energy related heat (d) measured with the potentiostat (left: a, c, and e) and the calorimetric setup (right: b, d, and f). Markers indicate 0% SoC.

properties are more or less unaffected by the cell's SoC, the magnitude of the second plateau remains unchanged (compare Figs. 8e and 8f to Figs. 5e and 5f and Figs. 7e and 7f). Due to the varying capacity, the second plateau is only changed in its duration. Interestingly, the magnitude of the initial cell current throughout the first plateau is also almost not influenced by the cell voltage which is contrary to previously stated theories.[14,30] Furthermore, the duration of the first plateau is not considerably altered based on the cell's SoC and consequently varying initial degrees of lithiation within the active material particles. Only the slope of the first plateau is marginally changing from the highest to the lowest SoC. Together with the observations made on the influence of electrode loading and cell temperature, each plateau seems to hint at different processes based on the interplay of mass and charge transport as well as reaction kinetics throughout the short circuit. Whilst the first plateau seems to be majorly affected by ohmic resistances throughout the electrodes and the separator and reaction kinetics of the active materials, the second plateau is likely to be dominated by a limited reaction related to ionic resistances especially in the liquid electrolyte. The influence of ionic resistances based on transport limitations within both solid and liquid phase throughout short circuit scenarios has been studied recently by the Newman group - however, solely based on simulation data.[34] Their work supports these assumptions with a rate limiting influence based on Li-ion depletion of the electrolyte and a simultaneously occurring saturation of the active material particle surface within the cathode during the second plateau increasing charge transfer based resistances. This will be further discussed at the end of the section. When further comparing the evolving C-rate and capacity related heat generation rate as a function of SoC (see Figs. 8g and 8h) to a representation based on the normalized discharged capacity ΔSoC (see Figs. 8e and 8f), the test data shows that cells starting from a lower SoC are even delivering a higher current and heat generation rate in the further process which is possible due to the monotonically decreasing nature of both quantities. This observation supports a theory of consecutively dominating mechanisms limiting the reaction and, hence, current during each plateau throughout the short circuit duration. This could be

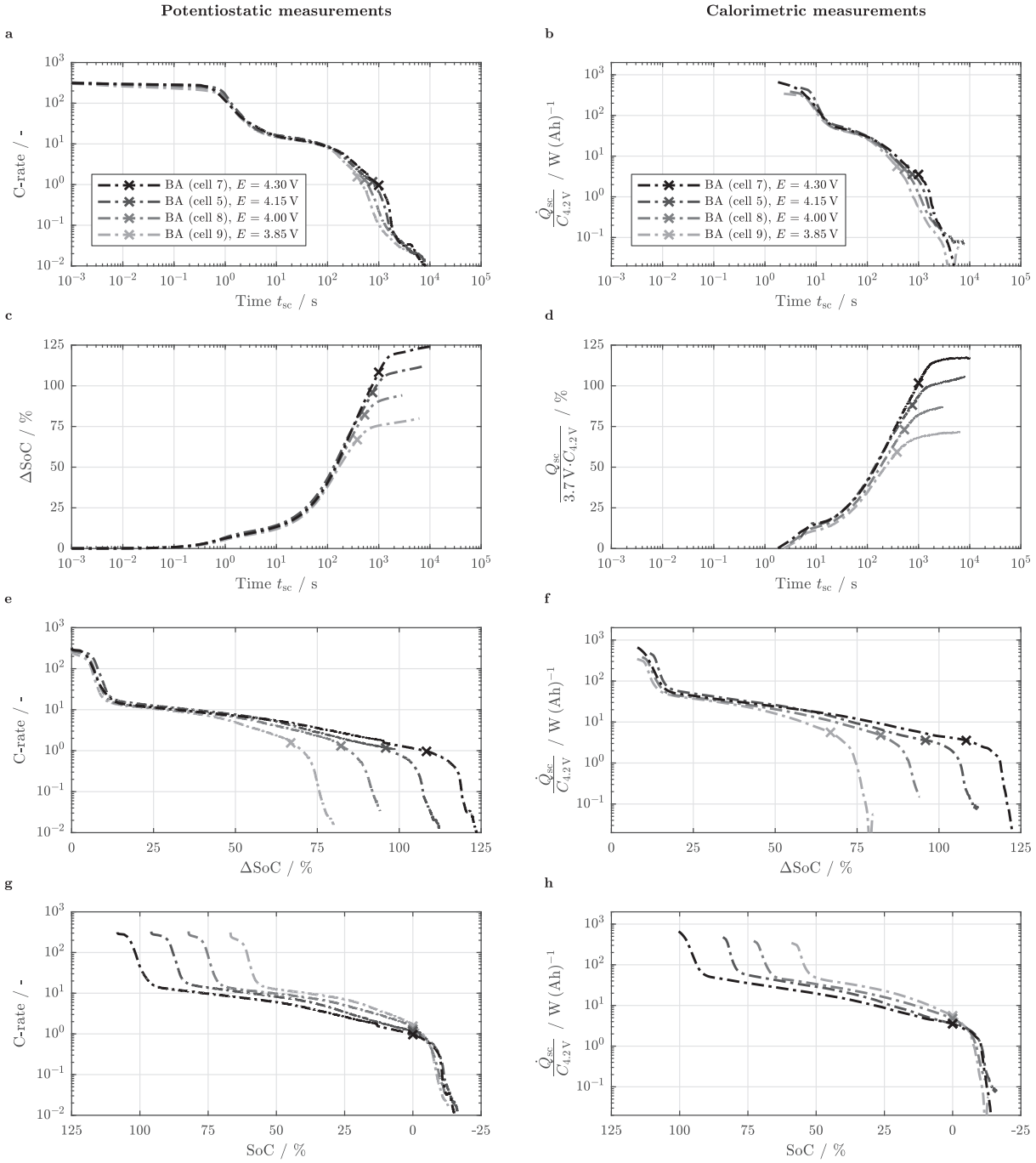

Figure 8. Cell behavior during a 0 V CV short circuit event applied to the BA loading with a CT design at initial cell voltages of 4.3 V, 4.15 V, 4.0 V, and 3.85 V as a function of short circuit duration (a to d), as a function of normalized discharged capacity (e and f), and as a function of SoC (g and h) for the C-rate (a, e, and g), capacity related heat generation rate (b, f, and h), normalized discharged capacity (c), and electrical energy related heat (d) measured with the potentiostat (left: a, c, e, and g) and the calorimetric setup (right: b, d, f, and h). Markers indicate 0% SoC.

e.g. based on the dimensions and morphology of the electrodes and active material particles.

At the end of the short circuit, all cells end up at a similar SoC between −11% and −16%. As the mean cell open circuit voltage as the driving force of the discharge process should be fairly constant throughout the short circuit duration (i.e. between 4.3 V and 3.0 V from 108% SoC to 0% SoC), the effective cell resistance must vary by orders of magnitude during the short circuit in order to explain the occurring C-rates from as high as 300C to as little as 1C at 0% SoC or C/100 at the end of the short circuit. Hence, it is most likely not the open circuit potential which is dominating the step-like characteristics of the short circuit but the effective resistance of the cell which seems to be mainly related to transport and kinetics related processes and limitations especially with ongoing short circuit

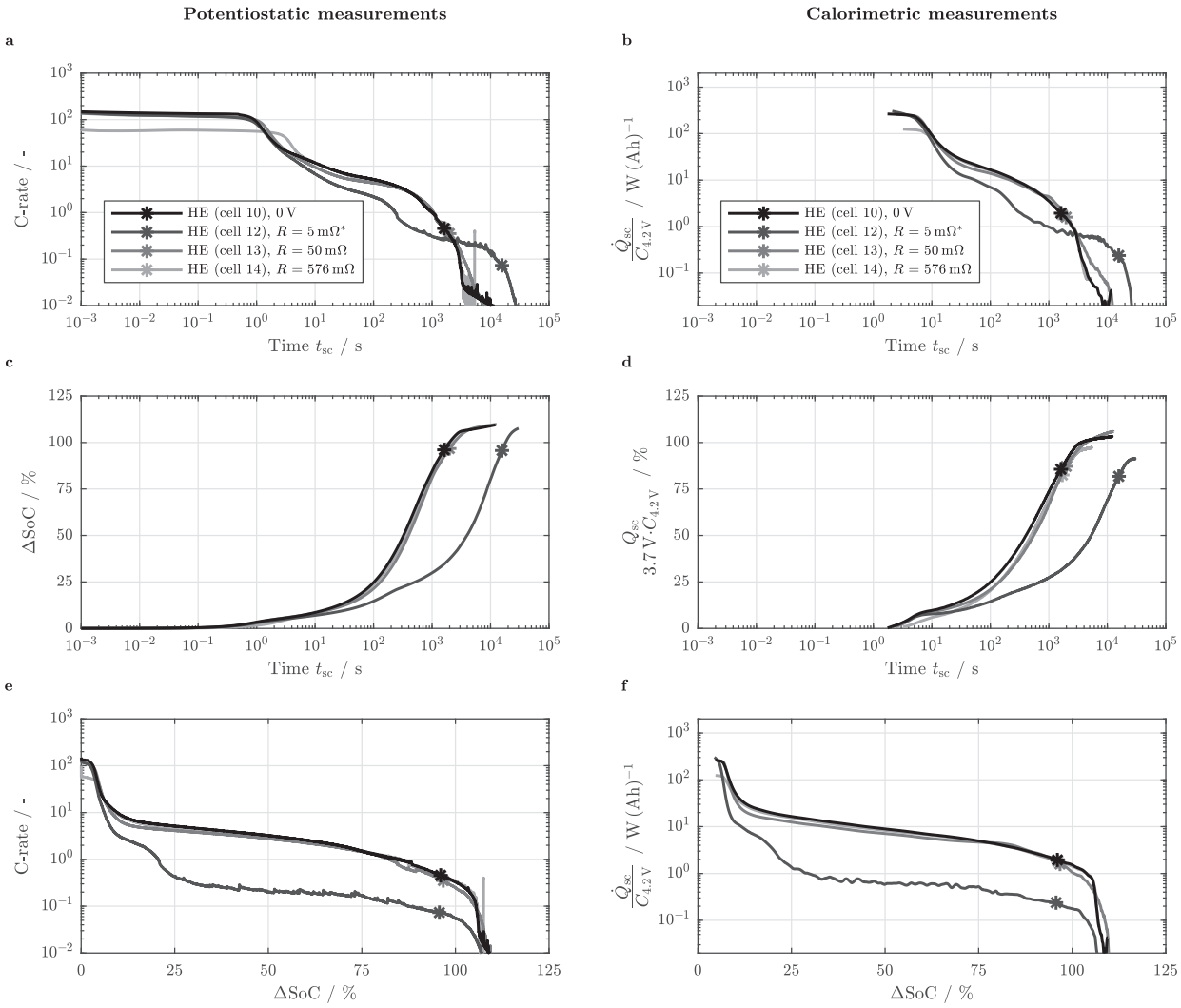

Figure 9. Cell behavior during both 0 V CV and 5 mΩ, 50 mΩ, and 576 mΩ external short circuit resistance events applied to the HE loading with a CT design as a function of short circuit duration (a to d) and as a function of normalized discharged capacity (e and f) for the C-rate (a and e), capacity related heat generation rate (b and f), normalized discharged capacity (c), and electrical energy related heat (d) measured with the potentiostat (left: a, c, and e) and the calorimetric setup (right: b, d and, f). Markers indicate 0% SoC. Cell 12 shows a high-resistance behavior (*).

duration. Instead, what is defined by the initial cell voltage is the overall heat produced in the process according to the available capacity (see Figs. 8c and 8d).

Influence of short circuit resistance.—Besides the open circuit voltage as the driving force and the effective resistance of the cell as the limiting factor for a current to flow, the external short circuit resistance defines the hardness of a short circuit. At 25°C, cells with a HE loading and a CT design were exposed to short circuit resistances ranging from 5 mΩ, 50 mΩ, to 576 mΩ (resistance ratio $R_{sc}/R_{1\,kHz}$ of ca. 0.01, 0.12, and 1.40) and were compared to the most severe short circuit scenario, represented by the 0 V CV condition (see Table II). Weighed with the planar electrode area of the investigated cells, these short circuit resistances represent 0.0087 mΩ m^2, 0.087 mΩ m^2 to 1 mΩ m^2. As an example, a cell with a total electrode area of approximately 0.5 m^2 resulting in a cell capacity of 10 Ah based on the BA loading,[14] would be correspondingly exposed to a short circuit of approximately 0.02 mΩ, 0.2 mΩ, and 2 mΩ, which would all fall in the classification of a hard external short defined by international standards and regulations.[8] As shown in Fig. 9, only a minor difference in the transient cell behavior can be identified between cells that behaved normally (i.e. cells 10, 13, and 14). As already observed when comparing cells 5 and 6 of the BA loading, cell 12 which was exposed to the lowest of the chosen external short circuit resistances also showed a high-resistance behavior during the test, whereas an influence of the externally connected precision resistor could be ruled out. Before and after the test, the 1 kHz impedance of each cell with and without the externally connected resistance was measured, which showed no evidence of a variation in the quality of the electrical connection for the investigated cells (i.e. cells 12 and 13). With the measured tab temperature not exceeding a heat up of 1°C, a melting of the contact area as previously observed[14] can be also ruled out. Even though several orders of magnitude of the external short circuit resistance were tested in this work, only the largest external resistance had a noticeably different impact on the cell's behavior, underlining the severity of the other chosen short circuit conditions. Before 5 s of the short circuit have passed, the initial cell current is considerably reduced which can be seen in Fig. 9a. The maximum cell current at

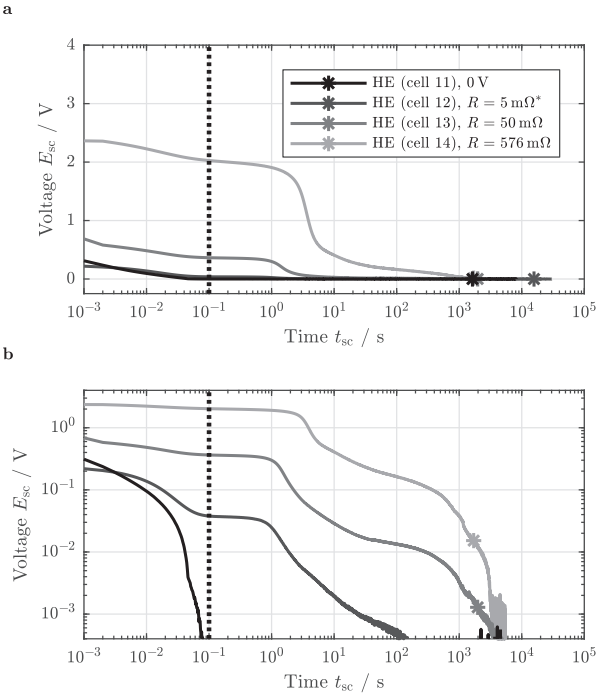

Figure 10. Cell voltage during both 0 V CV and 5 mΩ, 50 mΩ, and 576 mΩ external short circuit resistance events applied the HE loading with a CT design as a function of short circuit duration in a logarithmic (a) and double-logarithmic representation (b). Markers indicate 0% SoC. Cell 12 shows a high-resistance behavior (*).

the very beginning of the short circuit is 9.01 A, 8.37 A, 8.33 A, and 5.90 A respectively for the 0 V, 5 mΩ, 50 mΩ, and 576 mΩ condition representing 149C, 148C, 137C, and 99C (see Table II). A few seconds after the short circuit was triggered, almost no difference is observable in terms of C-rate, capacity related heat generation rate, discharged capacity and generated heat (see Figs. 9a to 9d). Only an influence on the magnitude of the first plateau can be observed. The second plateau remains almost unchanged (see Figs. 9e and 9f).

When comparing the transient cell voltage as a result of the chosen external short circuit conditions (see Fig. 10), a more pronounced difference between the cells can be observed. After the control of the potentiostat approached a stable voltage level of 100 µV after approximately 100 ms (see vertical dotted line in Fig. 10), the magnitude in varying external resistance values is reflected in the transient voltage response of the cells. Due to the increasing hardness of the short circuit and associated higher initial C-rate with decreasing external short circuit resistance, the first evolving voltage and current plateau is slightly reduced in size (see Fig. 9a and Fig. 10b). Even though the voltage response and consequently overvoltage varies between the different scenarios, the overall cell behavior in terms of charge throughput and generated heat remains almost unchanged, which supports a strongly dominating effective cell resistance during the short circuit event compared to the external short circuit resistance. These observations suggest that an external short circuit resistance in the range of 0.1 mΩ m^2 and below is almost identical to a worst-case 0 V scenario for the investigated HE loading. The intensity of the short circuit especially within the second plateau seems to be independent of the applied short circuit condition, approaching the fully discharged state at more or less the same test duration between 1500 s and 2000 s. Again, the overall heat produced throughout the test is solely dependent on the cell's capacity. With external short circuit resistances above 1 mΩ m^2, a stronger variation in cell behavior has been reported (approximately 2 mΩ m^2, 10 mΩ m^2, 20 mΩ m^2, and 30 mΩ m^2).[14]

Influence of cell design.—In order to evaluate the influence of a more inhomogeneous in-plane current density distribution on the overall cell behavior, cells with slimmer tabs (5 mm vs. 30 mm) aligned on the same side were exposed to a 0 V CV condition at 25°C (see Table II and Fig. 1c). With the electrode loading having the most significant influence on the overall magnitude of the resulting cell current and heat generation rate, again HP, BA, and HE loadings were studied. When comparing the cell behavior of the three electrode loadings between the CT and AT design in terms of absolute current and heat generation rate as a function of normalized discharged capacity (compare Figs. 11a and 11b to 11c and 11d), a stronger variation between the individual electrode loadings can be observed for the AT design (Figs. 11c and 11d). Whilst the HP loading does behave almost identical for both CT and AT designs, the BA and HE loading of the AT design show a stronger tendency toward a high-resistance behavior which means comparably lower currents and heat generation rates throughout the short circuit. Whilst the CT design shows similar values in terms of absolute current and heat generation rate throughout the second plateau for all three electrode loadings (see Figs. 11a and 11b), the AT design shows a variation over a magnitude (see Figs. 11c and 11d). Another indication toward the high-resistance behavior is the duration until the cells are fully discharged. For the AT design, the HP loading is similarly discharged within 160 s (CT: 225 s), whilst the BA and HE loading are approaching the fully discharged state after 1930 s (CT: 760 s) and over 12100 s (CT: 1610 s) which is 2.5 to 7.5 times slower than the CT design. Whilst the behavior of the AT and CT design is similar during the first plateau (i.e. before 1 s of the total short circuit duration), the cell designs vary significantly during the second plateau and the approach of the third plateau (compare Fig. 12 to Fig. 5). The observed difference of more than a magnitude in cell current and heat generation rate between the electrode loadings becomes even more distinct when looking into the C-rate and capacity related heat generation rate of the AT design (see Figs. 12e and 12f). Based on the approximately 100 times lower C-rate and capacity related heat generation rate throughout the second plateau, a stronger time delay between the HE loading compared to the HP loading for the AT design can be observed in terms of normalized discharged capacity and energy released compared to the CT design (see Figs. 12c and 12d as well as Figs. 5c and 5d). With the 1 kHz impedance of the two cell designs being in a similar range, the observed differences are most likely based on the increased inhomogeneity in current density distribution within the electrodes and a resulting larger effective cell resistance. This will be more closely evaluated in the following.

Effective overvoltage and cell resistance.—When relating the generated heat to the discharged capacity Q_{sc}/C_{sc} or referring the heat generation rate to the cell current $\dot{Q}_{sc}/I_{sc}$, an effective overvoltage can be calculated throughout the duration of the test. As an example, this is shown for both cell designs in Figs. 13a to 13d. Ideally, the calculated overvoltage would follow the open circuit voltage of the cell, which is not the case here due to the discussed measurement uncertainties of the calorimetric test setup. With the calorimetric measurement data showing a 7 s time delay, an adjustment period can be observed until the calculated polarization approaches stable values between 4 V and 3 V. This falls in the range below 10% (HE) to 20% ΔSoC (HP) depending on the electrode loading which correlates to more or less $3\Delta t_\infty$ (i.e. 21 s, see Fig. 5c). The variation in calculated overvoltage is rather low for time integrated data approaching a fairly constant value of approximately 3.3 V for all electrode loadings which ranges below the nominal cell voltage of 3.7 V (dotted line in Figs. 13a to 13d). The time derivative data shows a slightly higher deviation in the calculated overvoltage exceeding the initial cell voltage of 4.15 V which is physically not meaningful (Figs. 13c and 13d). However, both methods come to similar results throughout most of the short circuit duration with an increasing deviation beyond the fully discharged state based on the limited temperature resolution of the calorimetric test setup and interactions with the environment. The overvoltage again ranges around 3.3 V throughout the entire test duration. By relating the calculated overvoltage to the cell current $\dot{Q}_{sc}/I_{sc}^2$, an effective cell resistance

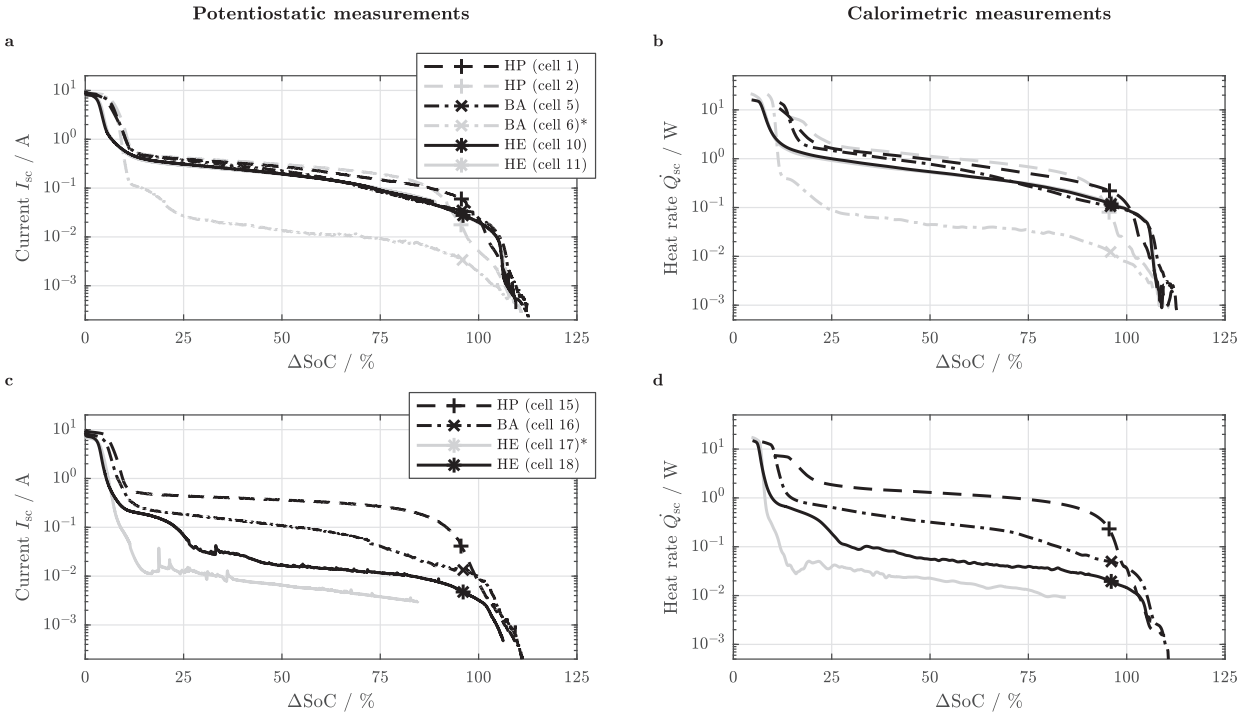

Figure 11. Cell behavior during a 0 V CV short circuit event applied to the HP (dashed lines), BA (dash-dotted lines), and HE loading (solid lines) with a CT (top: a and b) and AT design (bottom: c and d) as a function of normalized discharged capacity for the cell current and heat generation rate measured with the potentiostat (left: a and c) and the calorimetric setup (right: b and d). Markers indicate 0% SoC. Cells 6 and 17 show a high-resistance behavior (*).

can be derived which is shown in Figs. 13e and 13f for the CT and AT design. A considerable increase of the effective cell resistance up to three orders of magnitude can be observed throughout the short circuit duration for both designs (from approximately 10 Ω to 10 kΩ) which underlines the strong transient variability of the effective cell resistance. This observation supports the theory that it is primarily the effective cell resistance which causes the observed strongly varying, step-like characteristics of cell current and heat generation rate throughout the short circuit duration. Within this representation of the cell behavior, also the difference between cells that behave as expected (black lines) and cells that show a high-resistance behavior (gray lines) becomes apparent. All cells that behave unexpectedly, show a resistance increase above 100 Ω after a ΔSoC of just 20%. Furthermore the observed tendency of the AT design showing a higher resistance compared to the CT design especially for the BA and HE loading is also becoming apparent in this representation, with cell 18 of the HE loading bordering the characteristic high-resistance behavior of cells 6, 12 and 17. This means that an increasingly inhomogeneous current density distribution results in a rather restrained short circuit behavior which is very similar to a defective, i.e. highly resistive cell.

Results from post mortem analysis.—During opening the cells after the short circuit tests, visual differences for the electrode loadings and cell designs could be observed. Whilst both the HP and BA loading visually showed no abnormal characteristics for both CT and AT design, copper colored contours could be observed on the cathode surface for cells with a HE loading. Especially cell 10 exhibited distinct copper colored imprints along its middle axis (see upper photograph in Fig. 14a). The exact same contour could be also found on the anode as a black shadow (see mirrored lower photograph in Fig. 14d). Moreover, the anode and cathode coatings with a HP and BA loading were mechanically still well attached to the current collectors. For the HE loading, a poor mechanical integrity of the anode was observed which easily crumbled off the current collector during handling, especially for the AT design (cell 17). Furthermore, distinct holes of approximately 50-200 µm in diameter were visible across the cathode surface within a fairly homogeneous distance of a few mm between the holes (see Fig. 15). Investigations by both SEM and EDX on the HE electrode samples qualitatively confirmed the occurrence of copper on the cathode surface (see Figs. 14b and 14c) whereas the location of the EDX measurement was chosen at the edge of the copper colored contour (see Fig. 14a). This observation implies local anode potentials exceeding ∼ 3.1 V vs. Li/Li$^+$ in the course of the carried out short circuit test.[35–38] With an open circuit potential around ∼ 1.5 V vs. Li/Li$^+$ in the fully delithiated state, the graphite anode was most likely exposed to an overpotential larger than ∼ 1.6 V below 0% SoC. At a higher magnification, the structure of the copper traces shows to be cauliflower-like and is rather randomly spread across the electrode morphology. Interestingly, traces of copper could be also observed on the anode surface of the investigated HE cells (see Figs. 14c and 14d). These copper traces could have either been transferred to the anode from the cathode during the disassembly process or dissolved copper ions were deposited on the anode surface due to varying anode potentials throughout the short circuit duration. Whether the copper traces were then growing from the anode surface toward the cathode or from the cathode toward the anode remains unclear. The shape and morphology of the deposited copper particle as shown in the center of Fig. 14f, might indicate a growth starting from the anode surface. The detected oxide traces (blue/purple) on the surface of the magnified copper particle most likely resulted from an oxidation process of copper after the sample was transferred from the glove box to the SEM.

In order to better understand the occurrence of copper traces on the cathode surface and the overall cell behavior below 0% SoC, possible scenarios and underlying processes during such an over-discharge are evaluated in the following. Based on a differential voltage analysis of the cells (shown in the second part of this combined work), the electrode balancing between anode and cathode could be stud-

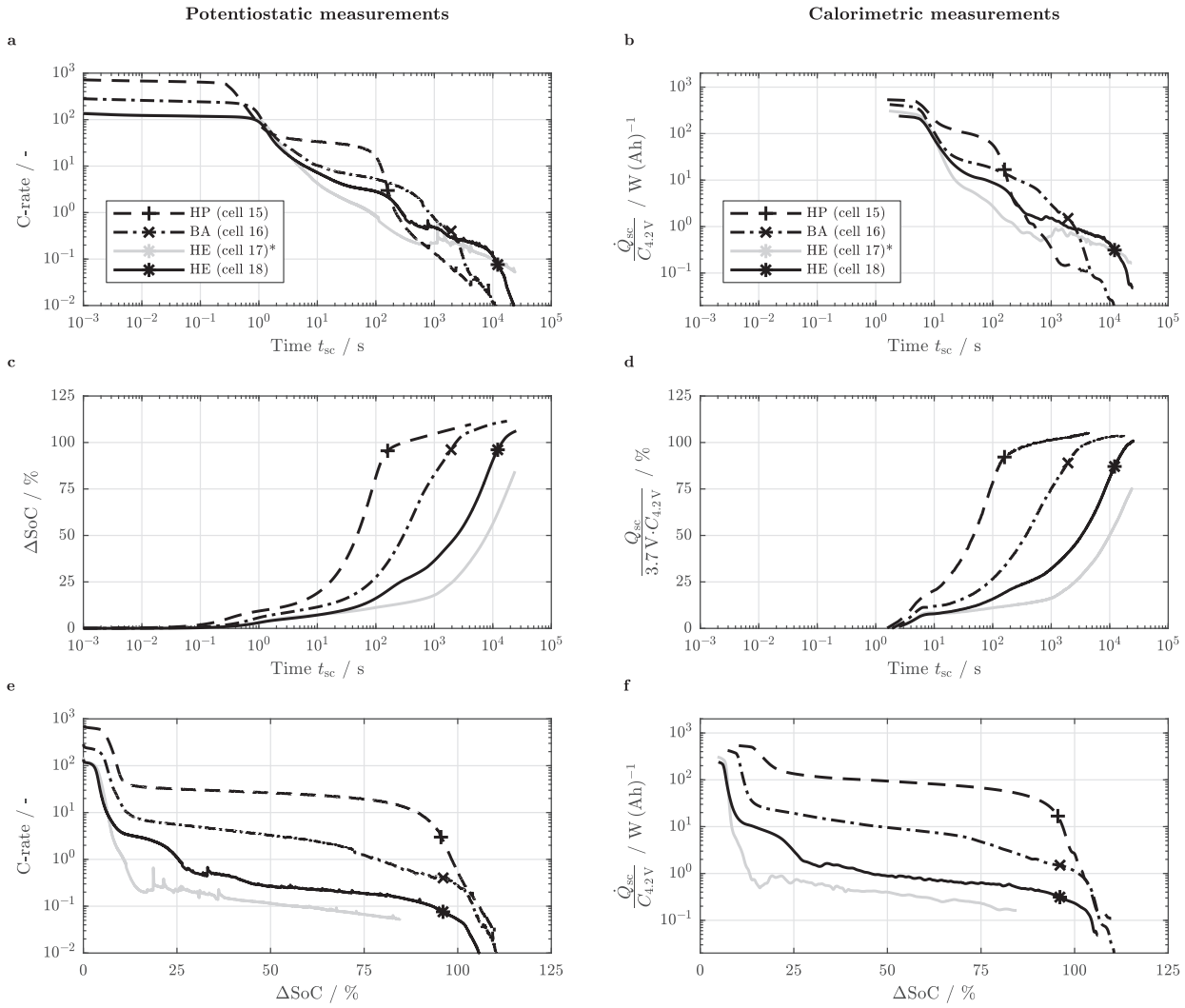

Figure 12. Cell behavior during a 0 V CV short circuit event applied to the HP (dashed lines), BA (dash-dotted lines), and HE loading (solid lines) with an AT design as a function of short circuit time (a to d) and as a function of normalized discharged capacity (e and f) for the C-rate (a and e), capacity related heat generation rate (b and f), normalized discharged capacity (c), and electrical energy related heat (d) measured with the potentiostat (left: a, c, and e) and the calorimetric setup (right: b, d, and f). Markers indicate 0% SoC. Cell 17 shows a high-resistance behavior (*).

ied based on measured (C/50) half-cell and full-cell potentials for each electrode loading prior to the short circuit tests. As more than the 2.4% (HE) to 3.4% (HP) of the capacity left within the anode at 0% SoC could be retrieved from the cells, a different process than a transfer of Li-ions from anode to cathode must have been initiated. With remaining vacancies for Li-ions at 0% cell SoC of 9.4% (HE) to 23.9% (HP) of the cathode's capacity between a cell voltage of 4.2 V and 3.0 V, an ongoing intercalation reaction of Li-ions seems possible. The source for the required Li-ions after the anode is fully depleted, could only be the electrolyte itself. This implies that an additional retrieval of 6.9% (HE) to 20.5% (HP) could be based on a depletion of Li-ions within the electrolyte, whereas the electrons for the intercalation reaction at the cathode surface would be supplied by an anodic dissoloution process of Cu at the negative electrode. Based on the rough pore volume within the electrodes and the separator filled with a 1 M $LiPF_6$ based electrolyte, approximately 10% to 15% of the cell's capacity could be retrieved from the electrolyte if the Li-ion concentration was completely depleted. This replacement of solvated Li-ions with Cu-ions would explain the ongoing discharge process beyond an SoC of −2.4% (HE) to −3.4% (HP). As soon as the cathode reaches its fully lithiated stage or the electrolyte is completely depleted, the only reaction occurring would then be a shuttle reaction of Cu-ions between the anode and cathode. This would fall in the range of the third evolving plateau which was observed especially for the BA and HE loading at currents below 1 mA or 0.1C (see Fig. 4a and Figs. 5a and 5e).

With a molar mass of 63.5 g mol^{-1} of copper and an estimated mass of roughly 280 mg of the copper foil within each cell based on the dimensions of the foil and the density of copper, an additional capacity of approximately 235 mAh could be retrieved from the cells if the whole copper current collector was dissolved into Cu^{2+}-ions and transferred to the cathode. With a capacity between approximately 1.9 mAh (HP) and 5.7 mAh (HE) that were additionally retrieved beyond the depletion of the anode, between 2.3 mg (HP) and 6.8 mg (HE) of copper were dissolved in the process. This implies that almost 3 times more copper must have been involved in the final stage of the short circuit for the HE loading compared to the HP loading. This would explain the observation made that the highest quantity, i.e. the

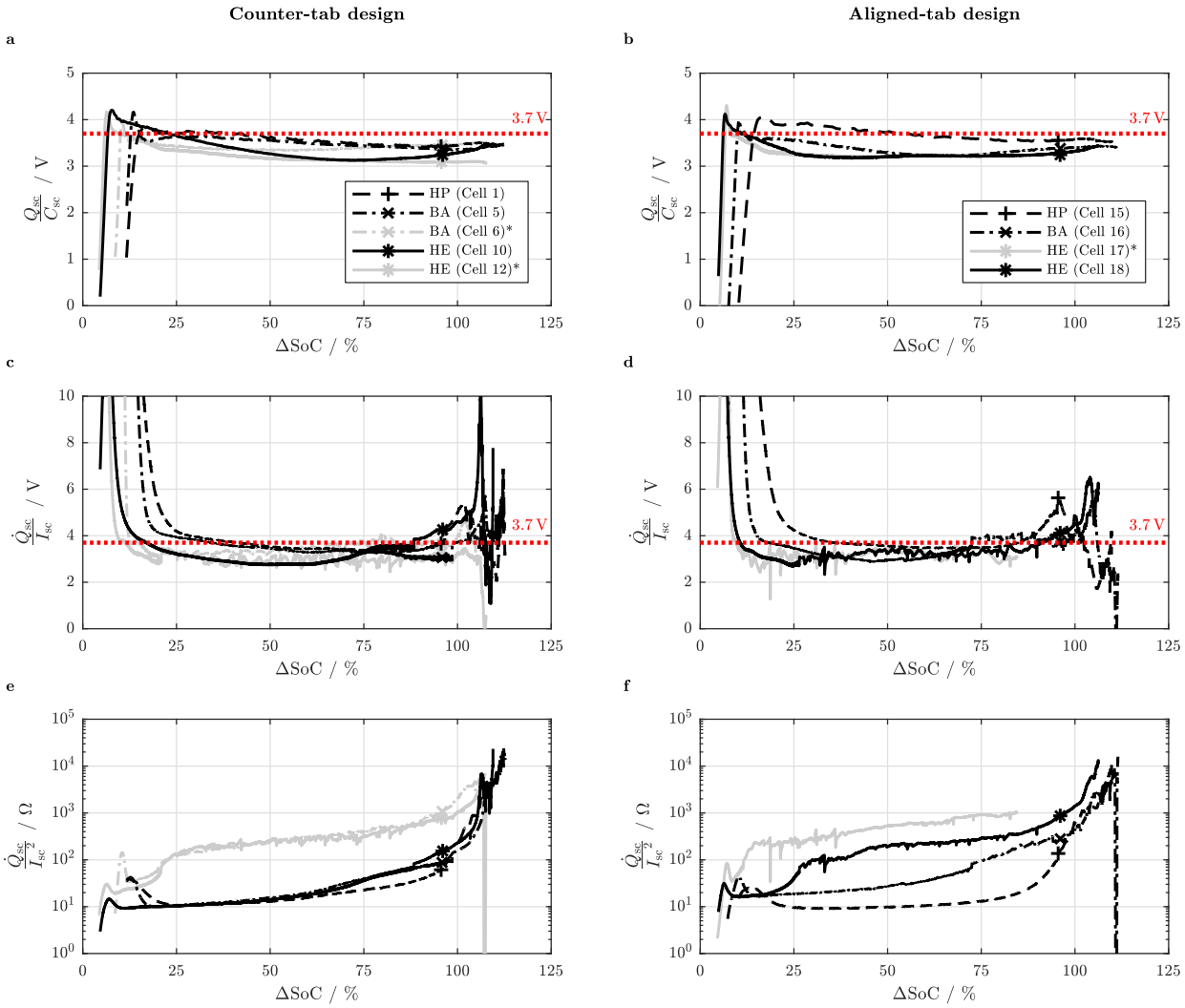

Figure 13. Calculated effective overpotential (a to d) and effective cell resistance (e and f) during a 0 V short circuit event applied to the HP (dashed lines), BA (dash-dotted lines), and HE loading (solid lines) with a CT (left: a, c and e) and AT design (right: b, d and f) based on the generated heat related to the discharged capacity (a and b) and based on the heat generation rate related to the cell current (c to f). Markers indicate 0% SoC. Cells 6, 12 and 17 show a high-resistance behavior (*).

clearest signal in the EDX measurement, could be observed for the HE loading whilst merely a Cu background noise could be detected for the HP loading.

An explanation for the higher tendency toward a high-resistance behavior of the BA and HE loadings especially for the AT design could be given based on the observed overall increased mechanical degradation of the anode composite electrode and an ongoing cracking of the cathode active material particles even resulting in particles that are split in half (see magnification in Fig. 15c). If the particle cracking on the cathode side is also responsible for the observed holes within the composite electrode is not clear (see Figs. 15a and 15b). Pristine electrodes and both HP and BA loadings gained from cell opening did not show such characteristics.

Discussion of underlying mechanisms and cell design implications.—Based on the experimental results presented in this work, correlations between the design of the investigated electrodes and cells toward a cell's short circuit behavior can be drawn which may allow for optimizing a cell's tolerance toward abusive short circuit scenarios.

In general, the cell's electrical energy content defines the amount of heat that will be generated throughout a short circuit as long as no additional exothermal side reactions are triggered. This implies that independent of a cell's characteristics toward e.g. delivering a comparably high energy density at predominantly low currents (i.e. high energy) or toward being able to sustain a comparably high power density at predominantly high currents (i.e. high power), only the cell's capacity and its voltage level are relevant for determining the amount of heat that will be produced throughout the short circuit. For a given combination of active materials, the cell's capacity is based on the electrode's active material loading and the size of the electrodes whereas the cell's voltage is defined by the equilibrium potential of both electrodes vs. Li/Li^+ which is only marginally affected by the electrode balancing in a given operating voltage range. However, what is altered by a cell's characteristics is the dynamics of the short circuit implying at what rate the cell is discharged and consequently how quickly the stored electrical energy is converted into thermal

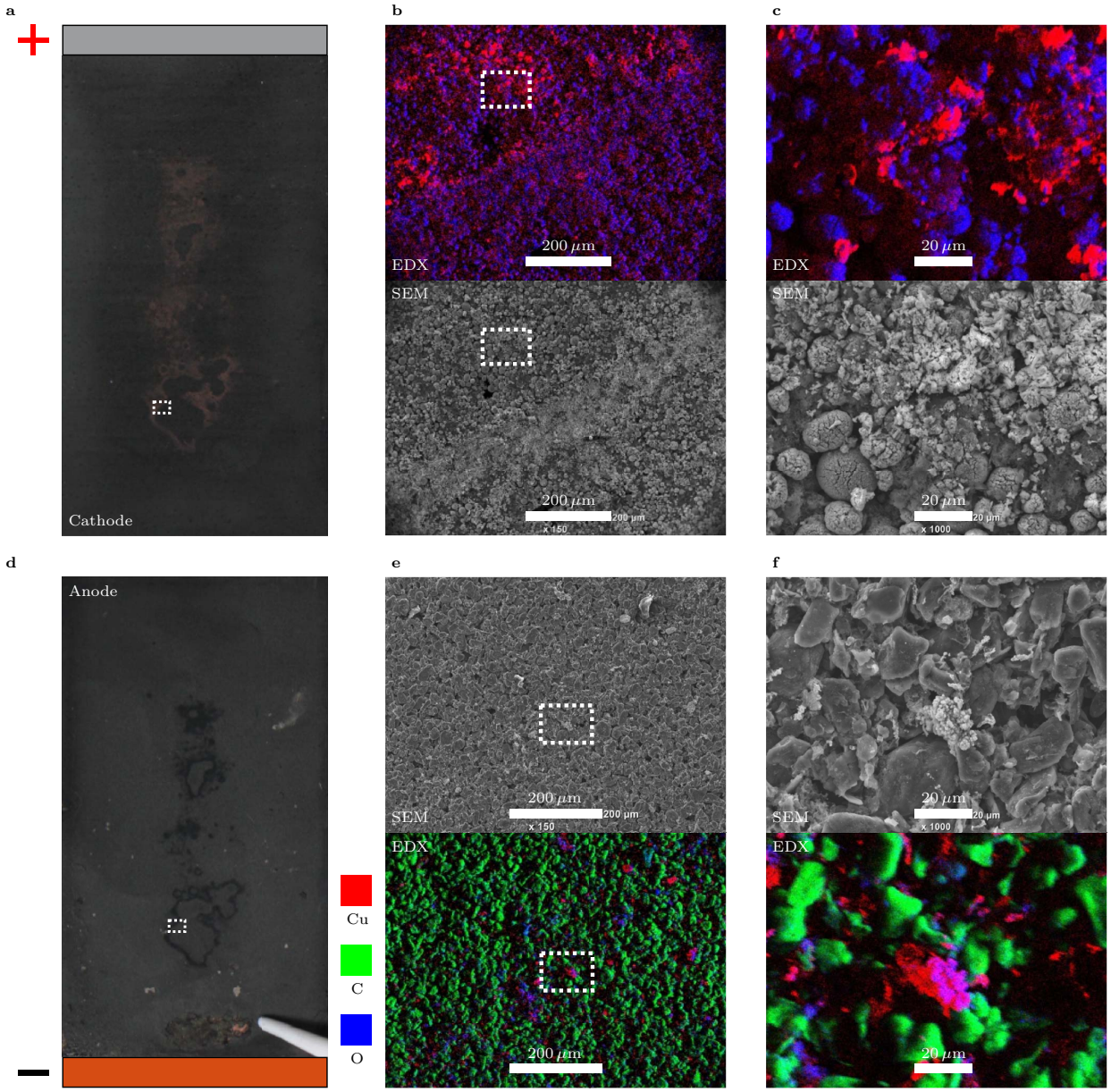

Figure 14. Photographs, SEM images and EDX measurements of both cathode (top: a to c) and anode samples (bottom: d to f) gained from opening cell 10 with a HE loading and a CT design at a magnification of 150 (b and e) and 1000 (c and f).

energy. This can be confirmed when looking into Figs. 4c and 4d and Figs. 5c and 5d. At a constant electrode size, the cell's capacity is only defined by the electrode loading which is over 4 times larger for the highest electrode loading (HE) compared to the lowest (HP) and therefore also generates over 4 times more heat (see Figs. 4c and 4d). With lower electrode loadings generally showing superior rate capability and, hence, power characteristics due to lower cell-internal resistances, the stored capacity and consequently thermal energy is withdrawn around 5-10 times faster for the lowest electrode loading compared to the highest (see Figs. 5c and 5d). In the following, possible mechanisms resulting in the observed short circuit characteristics are evaluated in order to derive implications toward both electrode and cell design.

Three stages of an external short circuit applied to Li-ion cells could be identified which can be characterized by distinct plateaus forming in current and heat generation rate throughout the discharge procedure both as a function of time and discharged capacity. The first plateau consuming around 5–10% ΔSoC within less than a second at currents ranging around 10 A for all electrode loadings and cell designs seems to be majorly affected by ohmic resistances (see $R_{1\,\mathrm{kHz}}$ before the test and $I_{\mathrm{sc,\,max}}$ during the test in Table II and Figs. 11a to 11d). With the electrodes studied in this work having the same electrode composition (see Table I) showing similar porosities (ca. 45–55%) and all cells comprising the same EC:DMC based electrolyte, the ohmic resistance within both solid and liquid phase scales with the coating thickness which is unaffected by the tab configuration. The

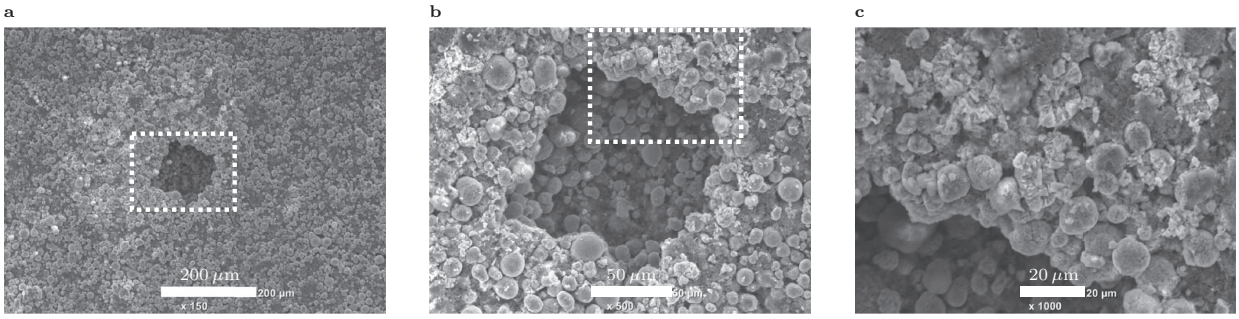

Figure 15. SEM images of a cathode sample gained from opening cell 17 with a HE loading and an AT design showing a representative hole-like structural defect at a magnification of 150 (a), 500 (b), and 1000 (c).

transport length for an electron or an ion to travel is consequently about 3.2 to 4.4 times longer within each electrode for the highest electrode loading compared to the lowest (see Table I) which might explain the considerable difference in initial C-rate between the two (HP: ca. 700C, HE: ca. 150C). With the same active materials used for all cells, the reaction surface area scales with the active material loading of the electrodes. This implies that the lowest electrode loading has a more than 4 times lower active material surface area available for charge transfer reactions occurring within both anode and cathode (see $C_{4.2\,V}$ in Table II). This circumstance could explain the deviation of the measured initial cell current from the theoretical value based on the open circuit voltage (i.e. 4.15 V) and high frequency resistance of the cells (HP: ca. 310 mΩ, HE: ca. 415 mΩ). Whilst the highest electrode loading delivers approximately 90% of the theoretical maximum short circuit current ($E_{cell}/R_{1\,kHz}$), the lowest electrode loading reaches only 74% (see $I_{sc,\,max}$ in Table II). An increased charge transfer overpotential based on the higher pore-wall flux with decreasing electrode loading might explain this observation.

For the current and heat rate to drop after the first plateau toward the second plateau by over a magnitude (see Figs. 11a to 11d) at a marginally reduced open circuit voltage ($E_{cell} > 4\,V$), an additional limitation must be triggered which is differing from a strictly ohmic nature. This process stabilizes for 90–100% ΔSoC over a few hundred seconds (HP) to several thousand seconds (HE). By means of simulation studies, the Newman group has recently shown that beyond 1 s of short circuit duration, a depletion of Li-ions within the electrolyte and a saturation of Li-ions at the surface of the active material particles is likely to occur within the positive electrode.[34] Such a combined scenario would considerably limit the reaction within the positive electrode and would consequently lead to a significantly reduced short circuit current as observed within this study. Furthermore, the impact of electron and ion transport toward the reaction site based on the electrode thickness would again explain the rather constant offset in C-rate and heat generation rate as a function of ΔSoC between the electrode loadings until the cells are fully discharged (see Figs. 5e and 5f). The observed more pronounced decrease in current and heat generation rate with increasing electrode loading for the AT design compared to the CT design is likely to be based on the current density distribution and corresponding stress and strain distribution along the electrodes.[39] Due to a more localized polarization around the 6 times thinner tabs which are furthermore placed right next to each other and not on opposite sides will most likely lead to comparably large currents in the tab vicinity which may result in an overuse of the active material in that area resulting in mechanical degradation of the electrodes (see Fig. 15) and consequently larger ohmic resistances in the further process. This can be confirmed when comparing the effective cell resistance of the CT design to the AT design in Figs. 13e and 13f. Interestingly, the effective cell resistance within the second plateau starts to noticeably increase beyond 50% ΔSoC for all electrode loadings of the CT design indicating a changing nature of the aforementioned reaction limitation (see Fig. 13e) which might be based e.g. on a dominating solid phase diffusion within the electrodes with decreasing cell SoC instead of an ongoing depletion of the liquid electrolyte. Whilst this is still more or less observable for the HP and BA loading of the AT design, the effective cell resistance of the HE loading is dominated by the increased ohmic contribution.

The third and last plateau forming beyond the fully discharged state (see upper plateau in discharged capacity and generated heat in Figs 4c and 4d) is rather independent of the cell characteristics and plays only a minor role in the short circuit with 5–15% ΔSoC consumed within thousands of seconds at comparably low currents, an open circuit voltage of the cell below 3 V and consequently low heat generation rates. With a fully depleted graphite anode, the ongoing discharge procedure is most likely based on the observed anodic copper dissolution reaction at the negative electrode until the NMC-111 cathode is fully lithiated and/or the electrolyte salt concentration is completely depleted throughout the electrodes.

So, a cell that would be categorized as high power with thin and/or highly porous electrodes and small active material particles resulting in a high specific surface area as well as wide tabs on opposing sides will also result in an accelerated short circuit behavior compared to a cell that is categorized as high energy with thick and/or dense electrodes and large active material particles resulting in a low specific surface area as well as slim tabs on the same side. In order to design a cell which is limiting the external short circuit current and heat generation rate due to its inherent electrode characteristics and tab configuration, a high energy cell with comparably long transport lengths for both electrons and ions combined with a large pore-wall flux at the active material particle surface as well as an inhomogeneous current density distribution along the electrodes might be desirable. Whilst the electrode morphology may also limit the current during an internal short circuit, the tab configuration should only have a minor influence unless a stacked electrode configuration is employed. This implies that by means of the cell design, the duration until a certain amount of heat has been generated during a short circuit can be modified in order to increase the time until a critical temperature threshold is exceeded and/or to reduce the cooling requirements of the thermal management to avoid the occurrence of such critical temperature levels. By further designing a cell with a high energy specific surface area of the cell housing (e.g. small cells) to guarantee limited temperature gradients and a good thermal interaction with the cell's environment, the short circuit current can be further restrained by keeping the cell's temperature as low as possible throughout the process.

However, the short circuit behavior of a cell is clearly not the only design criterion to meet throughout the cell design process resulting in a trade-off between the performance of a cell during normal operation and its tendency toward a self-restrained or unrestrained short circuit characteristics. Furthermore, all implications derived in this work are based on the observation of a complete reaction within both electrodes which is not interrupted e.g. by an evaporation of the electrolyte or by a shut-down mechanism of the separator triggered at elevated temperatures. Based on the geometric size of commercial cells and

limitations of thermal management systems fostering hot-spots within a cell, a premature termination of a short circuit current is likely to occur during external as well as internal short circuit scenarios. Such an event could then either prevent a further heat-up of the cell which would be considered as uncritical or result in further exothermal side reactions dominating the cell behavior which may ultimately result in a hazardous cell failure.

Conclusions

Within this work, 18 single-layered pouch-type graphite/NMC-111 Li-ion cells with varying area specific capacities (HP, BA, and HE) and tab configurations (CT and AT) were short circuited under quasi-isothermal test conditions. Besides the influence of electrode loading and cell design, the impact of cell temperature, initial cell voltage or cell SoC and external short circuit resistance were studied.

A potentiostat was used to apply the short circuit conditions at a constant voltage of 0 V or at varying short circuit resistances. For the purpose of providing a defined quasi-isothermal boundary condition, a calibrated calorimetric test setup was used which allows for an investigation of the heat generation rate whilst the cell temperature is kept almost constant. This test enables a quantitative investigation of the external short circuit behavior alone unaffected by superimposed thermal events such as thermal runaway.

In agreement with previous work, a strong step-like characteristics of the cell current as a function of time and discharged capacity could be observed during external short circuits which was directly reflected by the measured heat generation rate with a time delay related to the measurement setup. Three distinct plateaus in current and heat rate could be observed changing in duration and magnitude based on varying cell characteristics and test conditions. With higher electrode loadings and therefore cell capacities, the electrical and thermal energy released throughout the short circuit is increased which is resembled by a prolonged duration of each plateau in cell current and heat generation rate. The magnitude of each plateau, however is unaffected by the electrode loading for most of the investigated cells (CT). Based on the reduced 1 kHz impedance of the lower electrode loadings, the initial cell short circuit current is even slightly larger for cells with a lower capacity. Relating the measured electrical and thermal signals to the cell's capacity, the smallest electrode loading showed a significantly accelerated short circuit behavior compared to the highest electrode loading, showing larger C-rates resulting in both a faster relative discharge and heat generation rate by a factor up of to 10. Increasing the cell temperature from 25°C to 55°C had a similar effect on the short circuit dynamics as reducing the electrode loading. With increasing temperature, the short circuit is accelerated implying higher cell currents and heat generation rates especially within the first two plateaus. In this work, a temperature increase beyond 45°C did not considerably alter the cell behavior implying a limitation of the temperature influence. With varying initial cell voltages from 4.3 V to 3.85 V and therefore SoC from 108% to 67%, almost no influence on the dynamics of the short circuit could be observed especially within the first plateau. Similar to the electrode loading, the overall capacity defines the amount of generated heat which can be correlated to the duration of the second plateau. It could be observed that both transient current and heat generation rate are strongly depending on the amount of charge withdrawn from the cell almost unaffected by the SoC until a cell approaches the fully discharged state. This implies that for a lower initial SoC, larger currents and heat generation rates can be measured as a function of SoC compared to a cell shorted at a higher initial SoC. The magnitude of the external short circuit resistances ranging from about 0.01 $m\Omega\,m^2$ to 1 $m\Omega\,m^2$, influenced the cell behavior during the first plateau, i.e. within the first few seconds. Beyond that, almost no difference could be observed between the cells. Short circuit resistances below 0.1 $m\Omega\,m^2$ resemble a worst-case 0 V CV scenario. With slim tabs aligned on the same side of the electrodes (AT) compared to wide tabs on opposing sides (CT), the inhomogeneity of in-plane current density distribution is increased. As a result, the C-rate and capacity related heat generation rate are reduced by a factor up to 100 for the highest compared to the lowest electrode loading. This spread is about 10 times larger than observed for a homogeneous current density distribution. When comparing the calculated overvoltage and effective cell resistance for the two cell designs, a fairly constant overvoltage around 3.3 V can be observed, whereas the effective cell resistance rises from approximately 10 Ω to 10 kΩ with ongoing short circuit duration. Cells that behaved abnormally showing comparably lower cell currents and heat generation rates also revealed a more than 10 times larger effective cell resistance. With increasing inhomogeneity of the current density distribution, a higher tendency toward such a high-resistance behavior can be observed especially for higher electrode loadings. As part of a qualitative post mortem analysis, selected cells were opened and studied visually and by means of SEM and EDX. With an ongoing discharge of the cells beyond up to −20% SoC, a continued intercalation of the cathode active material particles and simultaneously occurring anodic copper dissolution is likely. Traces of copper could be qualitatively confirmed via EDX on both the cathode's and anode's surface especially for the highest electrode loading. The observed increased tendency for the occurrence of copper on the electrode surface with increasing electrode loading may be correlated to the amount of charge transferred between the two electrodes beyond the fully discharged state. The increased tendency toward a high-resistance behavior for higher electrode loadings might be based on the reduced mechanical integrity of the anode and the observed severe mechanical degradation of the cathode which seems to be triggered by an inhomogeneous current density distribution.

Due to the more self-restrained short circuit behavior, cells with a high energy characteristics comprising thick and/or dense electrodes, large active material particles and thin tabs placed next to each other are favorable compared to high power cells with thin and/or highly porous electrodes, small active material particles and wide tabs on opposite sides. Possible underlying mechanisms were discussed pointing out the significance of ohmic losses and charge transfer overpotentials within the first plateau, limited ion diffusion involving a depletion of Li-ions in the liquid electroylte accompanied by a saturation of Li-ions at the surface of the active material particles within the positive electrode during the second plateau and an ongoing intercalation reaction of the positive electrode based on an anodic copper dissolution reaction throughout the third plateau.

Further experimental work will focus on the comparison of external with internal short circuit conditions within the same calorimetric setup in order to evaluate the impact of the locality of a short circuit on its severity.

In the second forthcoming part of this combined work, the underlying mechanisms for the observed dynamics of the external short circuit behavior will be studied by means of a validated physical-chemical model.

Acknowledgments

The work presented here was financially supported by the German Federal Ministry of Education and Research (BMBF) under grant number 03XP0027G (*MiBZ*), 03XP0034G (*EffiForm*) and 03XP0081 (*ExZellTUM II*). The authors thank the group of Prof. Hubert A. Gasteiger (Chair of Technical Electrochemistry, Technical University of Munich) for the possibility to carry out SEM and EDX measurements. The authors further thank Marc Steen for his excellent support reviewing this manuscript.

Appendix

As the temperature within the center of the copper bars was measured instead of the mean copper bar temperature, an evaluation of this error is necessary. Based on the measurement setup including a thermal insulation of all components, the setup is exchanging only a small amount of heat with the environment. This allows for the assumption of no-flux or symmetry boundary conditions at the interface between each copper bar and the surrounding insulating material resulting in a one-dimensional heat conduction problem. Introducing the spatial coordinate x_i (m) along the normal direction of the cell's surface

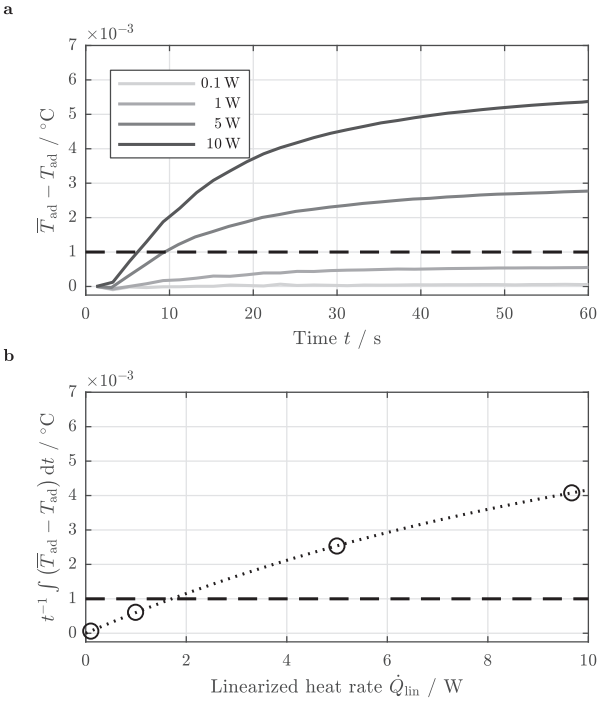

Figure A1. Measurement error accompanied with the placement of the temperature sensors as a function of time (a) and as a function of measured heat rate (b). The dashed line indicates the resolution of the measurement equipment around ±0.001°C.

(see Fig. 1a), the partial differential equation of this problem can be written as follows

$$\frac{\partial T_i}{\partial t} = a\frac{\partial^2 T_i}{\partial x_i^2} \qquad (i = 1,\ 2) \qquad [A1]$$

with T_i representing the spatio-temporal temperature within each copper bar and a ($m^2\ s^{-1}$) representing the thermal diffusivity of the material

$$a = \frac{k_{Cu}}{\rho_{Cu} \cdot c_{p,\,Cu}} \qquad [A2]$$

In Eq. A2, k_{Cu} (W $m^{-1}\ K^{-1}$) represents the thermal conductivity (CW004A: 394 W $m^{-1}\ K^{-1}$ at 20°C) and ρ_{Cu} (kg m^{-3}) the density of copper (CW004A: 8930 kg m^{-3} at 20°C). In order to solve Eq. A1 analytically, the dimensionless coordinate ξ_i is introduced by normalizing x_i with the thickness X of the copper bars (i.e. 45 mm, see Fig. 1a)

$$\xi_i = \frac{x_i}{X} \qquad (i = 1,\ 2) \qquad [A3]$$

Furthermore, the dimensionless spatio-temporal temperature Θ_i^* is introduced

$$\Theta_i^* = \frac{T_i - T_{0,\,i}}{T_{ref,\,i}} \qquad \forall \xi_i \in [0;\ 1] \qquad (i = 1,\ 2) \qquad [A4]$$

whereas $T_{0,\,i}$ is the initial, homogeneous temperature of each copper bar. Based on the chosen calibration procedure, a constant heat flux $\dot{q}_i$ (W m^{-2}) from the cell to each copper bar can be assumed. In this specific case, the constant reference temperature $T_{ref,\,i}$ can be defined as

$$T_{ref,\,i} = \frac{\dot{q}_i \cdot X}{k_{Cu}} \qquad (i = 1,\ 2) \qquad [A5]$$

Together with the Fourier number

$$Fo = \frac{a \cdot t}{X^2} \qquad [A6]$$

the partial differential equation in Eq. A1 can be rewritten in its dimensionless form

$$\frac{\partial \Theta_i^*(Fo,\ \xi_i)}{\partial Fo} = \frac{\partial^2 \Theta_i^*(Fo,\ \xi_i)}{\partial \xi_i^2} \qquad (i = 1,\ 2) \qquad [A7]$$

Based on the particular and homogeneous solution of this dimensionless partial differential equation, the general solution for the problem can be derived[29]

$$\Theta_i^*(Fo,\ \xi_i) = \left(\frac{\xi_i^2}{2} + Fo\right) - \left(\frac{1}{6} + \sum_{k=1}^{\infty}\frac{2\cos\delta_k}{\delta_k^2}\cos(\delta_k\xi_i)\exp\left(-\delta_k^2 Fo\right)\right) \qquad (i = 1,\ 2) \qquad [A8]$$

with δ_k representing the eigenvalues of the Fourier series

$$\delta_k = k\pi \qquad [A9]$$

approximated with k ranging from 1 and 100. Knowing the transient temperature T_i and the initial temperature $T_{0,\,i}$ at the center of each copper bar (i.e. $\xi_i = 0.5$), $T_{ref,\,i}$ and consequently q_i can be estimated. Based on this estimation, the difference between the mean temperature and the measured temperature can be evaluated via a spatial integration of the above equation within 0 and 1, resulting in

$$\overline{\Theta}_i^*(Fo) = Fo - \sum_{k=1}^{\infty}\frac{2\cos\delta_k\sin\delta_k}{\delta_k^3}\exp\left(-\delta_k^2 Fo\right) \qquad (i = 1,\ 2) \qquad [A10]$$

which allows to calculate $\overline{T}_i$ following Eq. A4 and consequently the measurement error in predicting the mean adiabatic temperature following Eq. 7

$$\overline{T}_{ad} - T_{ad} = \frac{\overline{T}_{ad,\,1} - T_{ad,\,1}}{2} + \frac{\overline{T}_{ad,\,2} - T_{ad,\,2}}{2} \qquad [A11]$$

The calculated error is shown in Fig. A1 as a function of time for the applied heat rates (a) and as a of function heat rate for the time-averaged error (b). With measured total heat rates below 5 W after 10 s even for the HE loading (see Fig. 3h), and an average heat rate around 0.1 W and below throughout the duration of the short circuit, the measurement error falls below the accuracy of the measurement equipment (dashed line in Figs. A1a and A1b) and can be therefore neglected.

ORCID

Alexander Rheinfeld https://orcid.org/0000-0003-0995-7266
Jörn Wilhelm https://orcid.org/0000-0002-5649-2580

References

1. Samsung, [Infographic] Galaxy Note7: What We Discovered. 2017; https://news.samsung.com/global/infographic-galaxy-note7-what-we-discovered.
2. J. Voelcker, Tesla Model S fire in Norway caused by short circuit in car. 2016; https://www.greencarreports.com/news/1102962_tesla-model-s-fire-in-norway-caused-by-short-circuit-in-car.
3. National Transportation Safety Board, Aircraft Incident Report: Auxiliary Power Unit Battery Fire, Japan Airlines Boeing 787-8, JA829J: 2013. https://www.ntsb.gov/investigations/AccidentReports/Reports/AIR1401.pdf.
4. R. Spotnitz and J. Franklin, *Journal of Power Sources*, **113**, 81 (2003).
5. T. M. Bandhauer, S. Garimella, and T. F. Fuller, *Journal of The Electrochemical Society*, **158**, R1 (2011).
6. Q. Wang, P. Ping, X. Zhao, G. Chu, J. Sun, and C. Chen, *Journal of Power Sources*, **208**, 210 (2012).
7. R. J. Brodd, *Batteries for Sustainability*, Springer New York: New York, NY, 2013.
8. V. Ruiz, A. Pfrang, A. Kriston, N. Omar, P. van den Bossche, and L. Boon-Brett, *Renewable and Sustainable Energy Reviews*, **81**, 1427 (2018).
9. K. Kitoh and H. Nemoto, *Journal of Power Sources*, **81–82**, 887 (1999).
10. M.-S. Wu, P.-C. J. Chiang, J.-C. Lin, and Y.-S. Jan, *Electrochimica Acta*, **49**, 1803 (2004).
11. F. Larsson and B.-E. Mellander, *Journal of the Electrochemical Society*, **161**, A1611 (2014).
12. Z. Chen, R. Xiong, J. Tian, X. Shang, and J. Lu, *Applied Energy*, **184**, 365 (2016).
13. R. Zhao, J. Liu, and J. Gu, *Applied Energy*, **173**, 29 (2016).
14. A. Kriston, A. Pfrang, H. Döring, B. Fritsch, V. Ruiz, I. Adanouj, T. Kosmidou, J. Ungeheuer, and L. Boon-Brett, *Journal of Power Sources*, **361**, 170 (2017).
15. H. Maleki and J. N. Howard, *Journal of Power Sources*, **191**, 568 (2009).
16. J. Lamb and C. J. Orendorff, *Journal of Power Sources*, **247**, 189 (2014).
17. P. T. Coman, E. C. Darcy, C. T. Veje, and R. E. White, *Journal of the Electrochemical Society*, **164**, A587 (2017).
18. C. J. Orendorff, E. P. Roth, and G. Nagasubramanian, *Journal of Power Sources*, **196**, 6554 (2011).
19. M. Zhang, J. Du, L. Liu, A. Stefanopoulou, J. Siegel, L. Lu, X. He, X. Xie, and M. Ouyang, *Journal of the Electrochemical Society*, **164**, A3038 (2017).
20. D. P. Finegan, B. Tjaden, M. M. T. Heenan, R. Jervis, M. Di Michiel, A. Rack, G. Hinds, D. J. L. Brett, and P. R. Shearing, *Journal of the Electrochemical Society*, **164**, A3285 (2017).
21. B. Mao, H. Chen, Z. Cui, T. Wu, and Q. Wang, *International Journal of Heat and Mass Transfer*, **122**, 1103 (2018).
22. D. D. MacNeil, Z. Lu, Z. Chen, and J. R. Dahn, *Journal of Power Sources*, **108**, 8 (2002).
23. L. Ma, M. Nie, J. Xia, and J. R. Dahn, *Journal of Power Sources*, **327**, 145 (2016).
24. M. N. Richard, *Journal of The Electrochemical Society*, **146**, 2068 (1999).

25. S. Hildebrand, A. Rheinfeld, A. Friesen, J. Haetge, F. M. Schappacher, A. Jossen, and M. Winter, *Journal of the Electrochemical Society*, **165**, A104 (2018).
26. K. G. Gallagher, S. E. Trask, C. Bauer, T. Woehrle, S. F. Lux, M. Tschech, P. Lamp, B. J. Polzin, S. Ha, B. Long, Q. Wu, W. Lu, D. W. Dees, and A. N. Jansen, *Journal of The Electrochemical Society*, **163**, A138 (2015).
27. J.-S. Hong, *Journal of The Electrochemical Society*, **145**, 1489 (1998).
28. H. Maleki, *Journal of The Electrochemical Society*, **146**, 947 (1999).
29. W. Polifke and J. Kopitz, *Wärmeübertragung: Grundlagen, analytische und numerische Methoden*, 2nd ed.; Ing-Maschinenbau; Pearson Studium: München u.a, 2009.
30. S. Okazaki, S. Higuchi, N. Kubota, and S. Takahashi, *Journal of Applied Electrochemistry*, **16**, 631 (1986).
31. J. B. Habedank, L. Kraft, A. Rheinfeld, C. Krezdorn, A. Jossen, and M. F. Zaeh, *Journal of the Electrochemical Society*, **165**, A1563 (2018).
32. L. O. Valøen and J. N. Reimers, *Journal of The Electrochemical Society*, **152**, A882 (2005).
33. H. Lundgren, M. Behm, and G. Lindbergh, *Journal of the Electrochemical Society*, **162**, A413 (2014).
34. J. Mao, W. Tiedemann, and J. Newman, *Journal of Power Sources*, **271**, 444 (2014).
35. K. R. Crompton and B. J. Landi, *Energy & Environmental Science*, **9**, 2219 (2016).
36. R. Guo, L. Lu, M. Ouyang, and X. Feng, *Scientific Reports*, **6**, 30248 (2016).
37. C. R. Birkl, M. R. Roberts, E. McTurk, P. G. Bruce, and D. A. Howey, *Journal of Power Sources*, **341**, 373 (2017).
38. C. Fear, D. Juarez-Robles, J. A. Jeevarajan, and P. P. Mukherjee, *Journal of the Electrochemical Society*, **165**, A1639 (2018).
39. B. Rieger, S. V. Erhard, S. Kosch, M. Venator, A. Rheinfeld, and A. Jossen, *Journal of the Electrochemical Society*, **163**, A3099 (2016).

3.4 Impact of rate limitations on external short circuit behavior of lithium ion cells

Within this section, the article titled *Quasi-Isothermal External Short Circuit Tests Applied to Lithium-Ion Cells: Part II. Modeling and Simulation* is presented. In the second part of this combined work, the previously presented experimental data is used to validate a widely accepted and applied homogenized physical-chemical model. This work is pivotal in presenting a means of correlating experimentally observed electrical and thermal short circuit characteristics of Li-ion cells with underlying rate limiting mechanisms.

Enhancing the approach discussed in section 3.1, a standard Newman-type model[290,291] is extended to account not only for a diffusion limitations within the liquid phase[295,296] but also within the solid phase. This approach guarantees smooth numerical calculation of the model at excessively high currents which would otherwise result in numerical instabilities with premature termination of the calculations. The chosen approach of accounting for a simplified Nernst diffusion layer thickness[343] is discussed and is shown to efficiently limit reaction kinetics at conditions approaching a depletion or saturation of Li-ions within the solid and liquid components with only slight modifications of the underlying Butler-Volmer equation. Such limitations have been similarly observed and discussed by alternative modeling approaches.[342]

Despite the simplicity of this modification and the chosen modeling approach accounting for only one representative particle size with a solid phase diffusion coefficient which is independent of solid phase concentration, the model shows very good agreement with the measurement data presented in the previous section. The experimentally observed transient characteristics in current and heat generation rate throughout various stages of the short circuit can be reliably described and correlated to the underlying solid and liquid phase concentration distribution throughout the electrodes and separator. In addition, individual overpotentials arising from mass and charge transport based processes as well reaction kinetics are calculated throughout the negative and positive electrode as well as the separator.[349] As already indicated by the experimental data, the initial phase of a short circuit is primarily defined by ohmic overpotentials throughout the liquid electrolyte as well as reaction based overpotentials within the negative electrode. The experimentally observed strong decline toward lower currents and heat generation rates with ongoing short circuit duration can be correlated to significant charge transfer based overpotentials within the positive electrode. These are at first caused by a simultaneous depletion of Li-ions within the liquid electrolyte near the current collector and a saturation at the surface of the active material particles near the separator. This solid phase saturation grows from the separator toward the current collector until the reaction within the entire positive electrode becomes limited by this effect. This change of rate limiting mechanisms within the positive electrode can be also experimentally observed by a slight change in the slope of the transient current and heat generation rate profile.

Minor discrepancies of the model in the very beginning of the short circuit can be ruled out by accounting for a concentration dependent solid phase diffusion coefficient within both electrodes. However, with a wide range of diffusion coefficients and concentration dependencies reported in literature, the exact behavior needs to be known in order to also depict the cell's short circuit characteristics with ongoing short circuit duration. A strong correlation between the solid phase diffusion coefficient of the cathode active material and a transition toward a stand-alone solid phase diffusion limited reaction kinetics within the positive electrode can be identified. This observation allows for a fit of this specific model parameter to the measurement data.

A sensitivity analysis emphasizes the importance of solid and liquid phase transport properties as well as the impact of electrode morphology including particle size, porosity, and tortuosity on a cell's short circuit characteristics. Simulation studies reveal the possibility of significantly decelerating the short circuit, reducing the overall level of short circuit current and, consequently, heat generation rate through provoking a dominating rate limitation within either the solid or the liquid phase of the positive electrode. This observation allows for a design optimization of electrodes and cells which guarantees a certain rate and cooling capability of the cell during what is considered as "normal" operation, whereas it instrinsically limits the current during a short circuit event.[350,351]
By further accounting for geometry related electrical effects along the current collectors as well as thermal effects across the cell, not only the external short circuit behavior of cells with defined electrode and cell geometries can be described, but also localized effects accompanied with local or internal short circuits can be evaluated. This will be more closely investigated in chapter 4.
The described approach of combining the development of both enhanced short circuit tests with modeling strategies in order to derive significant, validated simulation studies plays a key role in understanding the initiation of cell thermal runaway resulting from both external and internal short circuits. However, further work is yet required to correlate these results to both experiments and simulations investigating specifically local and field-like internal short circuits. Such combination of short circuit studies will eventually allow an understanding of the effect of a short circuit's locality on its severity in thermal runaway initiation.

Author contribution Alexander Rheinfeld developed the idea of quasi-isothermal short circuit tests, carried out half-cell measurements, developed and parametrized the model, carried out all simulation studies, and analyzed the data. Johannes Sturm helped with model parametrization, Andreas Noel helped to design the measurement setup and to establish testing protocols, and Jörn Wilhelm helped to the prepare the coin cell measurements. Akos Kriston and Andreas Pfrang shared their experience within the field of external short circuit measurements. The manuscript was written by Alexander Rheinfeld and was edited by Johannes Sturm, Andreas Noel, Jörn Wilhelm, Akos Kriston, Andreas Pfrang, and Andreas Jossen. All authors discussed the data and commented on the results.

Quasi-Isothermal External Short Circuit Tests Applied to Lithium-Ion Cells: Part II. Modeling and Simulation

Alexander Rheinfeld, Johannes Sturm, Andreas Noel, Jörn Wilhelm, Akos Kristion, Andreas Pfrang, Andreas Jossen

Journal of The Electrochemical Society 166 (2), pp. A151–A177, 2019

Permanent weblink:
http://dx.doi.org/10.1149/2.0071902jes

Quasi-Isothermal External Short Circuit Tests Applied to Lithium-Ion Cells: Part II. Modeling and Simulation

Alexander Rheinfeld,[1,*,z] Johannes Sturm,[1] Andreas Noel,[1] Jörn Wilhelm,[1] Akos Kriston,[2,] Andreas Pfrang,[2] and Andreas Jossen[1]**

[1]*Institute for Electrical Energy Storage Technology, Technical University of Munich (TUM), D-80333 Munich, Germany*
[2]*European Commission, Joint Research Centre (JRC), Directorate for Energy, Transport and Climate, Energy Storage Unit, 1755 LE Petten, The Netherlands*

Measurement data gained from quasi-isothermal external short circuit tests on single-layered pouch-type Li-ion cells presented in the first part of this combined work was used to validate a well-known homogenized physical-chemical model for different electrode loadings, cell temperatures, initial cell voltages, and external short circuit resistances. Accounting for diffusion-limited reaction kinetics, effective solid phase diffusion coefficients, and one representative active material particle size within each electrode, the model is capable of describing the experimentally observed characteristic change in magnitudes of current and heat generation rate throughout the short circuit. Underlying mechanisms for the observed characteristics are studied by evaluating the predicted concentration distribution across the electrodes and separator and by calculating the cell polarization due to ohmic losses, diffusion processes, and reaction kinetics. The importance of mass transport in the solid and liquid phase limiting reaction kinetics is discussed and evaluated in the context of a sensitivity analysis. Concentration dependent transport properties, electrode tortuosity, particle size, and electrode energy density are affecting different stages of a short circuit. Simulation results suggest a strong impact of electrode design on the short circuit dynamics allowing for an optimization regarding a cell's energy and power characteristics whilst guaranteeing a high short circuit tolerance.
 [DOI: 10.1149/2.0071902jes]

Manuscript submitted October 31, 2018; revised manuscript received December 11, 2018. Published January 15, 2019.

To date, lithium-ion batteries are the energy storage technology of choice for applications requiring a high gravimetric and volumetric energy density. Whilst the battery's energy density defines the runtime of a mobile device or the driving range of an electric vehicle at a given battery weight or volume, the battery's rate capability sets the limits for high performance scenarios such as acceleration, recuperation, and fast charging. Even though the work presented here focuses on Li-ion batteries, this circumstance is not restricted to this chemistry alone but holds true for all battery types. Increasing a battery's energy density can be achieved by applying advanced active materials[1] and by maximizing the active material content compared to the battery's electrochemically inactive components such as current collectors, separator, binder, and conductive agents.[2,3] An increase in the share of active materials can be achieved e.g. by designing dense[4] and/or thick electrodes[5] which, however, generally comes with a trade-off regarding a battery's rate capability.[6] This implies that batteries that are designed for applications requiring a high energy density can often supply this energy level only at comparably low currents. For mobile and automotive applications demanding ever increasing energy densities, this mostly does not pose a major problem during discharge as the battery is generally exposed to rather low currents on average.[7] However, with an increasing demand for fast charging, especially Li-ion batteries with a high energy density often do not allow for high continuous charge currents due to large local overpotentials occurring during operation resulting in anode potentials below 0 V vs. Li/Li^+ and consequently lithium-plating. In contrast, batteries that can deliver a sufficiently high power capability also at elevated currents, mostly suffer a reduced energy density. To overcome this trade-off with a given combination of active materials, electrochemically engineered electrodes are recently gaining more attention in the community. By adapting the morphology of the active material particles and electrodes as a whole, the rate capability can be improved due to reduced overpotentials based on ion movement within the cell's solid and liquid components.[1,8]

With increasing the total electrical energy content stored at a constant weight or volume of a battery, also the thermal energy content is increased which poses a certain risk in case of a battery failure. By employing active materials allowing for an increase in energy density of Li-ion batteries such as nickel-rich layered oxides, the thermal stability of the battery's active components is substantially reduced.[9–11] By adapting the morphology of the active materials and electrodes to also guarantee a high rate capability of the battery, this safety risk is even further increased. With an electrode morphology allowing for a high rate capability of a battery during normal operation, also the current and heat generation rate occurring during a short circuit are increased leading to an accelerated heat up with potential safety risks.[12] Furthermore, by employing active materials with a small active material particle size enhancing rate capability due to reduced solid phase diffusion based and reaction related overpotentials, the thermal stability is considerably compromised resulting from the decreased diffusion path and increased reaction surface area.[13,14]

A substantial number of experimental results,[5,6,15–18] simulation data,[19–22] and a combination of both[8,23–31] has been reported in literature to understand rate limiting effects within and beyond the designated operating window of Li-ion batteries at predominantly constant currents. However, only little data has been presented so far to adequately evaluate the underlying mechanisms of a battery's electrical and electrochemical response during abusive short circuit conditions.[12,32–35] With Li-ion battery short circuits being often synonymously used to refer to a worst-case internal short circuit within a cell, the focus of published work dealing with test development and experiments[36–39] as well as modeling and simulation[40–43] or both[44–53] has been predominantly focused on this event. Besides the recently increasing attention toward mechanical abuse conditions,[54] safety related modeling and simulation is mainly related the thermal response of a battery describing runaway related processes resulting from internal or external heat sources.[55–58] Even though short circuits are often considered as such a trigger heat source, the underlying mechanisms resulting in a certain current, electrode polarization, and consequently heat generation rate are mostly not further investigated.

Previous experimental results suggest a transient change of rate limiting mechanisms occurring during short circuit events.[12,32] With a cell delivering the maximum current possible at every moment of the discharge, hard external short circuits can be considered as the ultimate rate capability test of a cell. Therefore, previous work studying rate capability of materials,[27] electrodes,[5,6,15–18,27,31] and

*Electrochemical Society Student Member.
**Electrochemical Society Member.
[z]E-mail: alexander.rheinfeld@tum.de

cells[19–26,28–30] identifying reaction kinetics,[16,30] electron transport,[6] Li-ion transport in the solid[25,27,31] or liquid phase[5,15–18,20,23,24,29–31] or a combination[16,19,21,22,26,28,31] as the dominating rate limiting mechanism depending on the size of the active material particles,[17,19,27] electrode thickness[5,15,16,19–21,23,24,26,29–31] or electrode morphology,[6,18,20,22,31] are considered as the basis for the work presented here. Previous results suggest that a battery which exhibits a balanced contribution of resistances based on mass and charge transport as well as reaction kinetics shows a maximized rate capability for a set of materials and morphologies.[19,23] However, this might also imply that a battery which is optimized in terms of its rate capability also poses an increased risk when exposed to a short circuit.

Within this work, previously published experimental data of quasi-isothermal external short circuit tests applied to single-layered pouch-type Li-ion cells[12] is used to validate a well-known, widely accepted and applied physical-chemical modeling approach[59,60] at very high currents. The impact of varying electrode morphologies is studied for Li-ion cells comprising graphite anodes and $LiNi_{1/3}Co_{1/3}Mn_{1/3}O_2$ cathodes (NCM-111, in the following written as NMC-111) with nominal electrode loadings of 1 mAh cm^{-2} (i.e. high power loading, HP), 2 mAh cm^{-2} (i.e. balanced loading, BA), and 3.5 mAh cm^{-2} (i.e. high energy loading, HE). By further varying the cell's temperature, its initial voltage or initial state of charge (SoC), as well as the external short circuit resistance, the model is evaluated for its capability of simulating differing boundary and starting conditions. With the aid of the validated model, experimentally observed stages in current and heat generation rate during external short circuits are correlated to reaction kinetics as well as to mass and charge transport based processes and limitations within the electrodes. Based on the contribution of each mechanism to the observed overpotential,[26] a sensitivity analysis is carried out, on the one hand, to study the influence of the material's inherent transport properties on the transient short circuit behavior and, on the other hand, to evaluate the impact of electrode morphology which defines not only the effective transport length for electrons and ions but which also sets the limits for the cell's energy density.

Modeling

Within this section, the chosen modeling approach to describe the electrochemical response of Li-ion cells exposed to external short circuits is presented. In the first part, means of increasing the numerical stability when solving the model are evaluated and discussed, based on previously published findings. In the second part of the section, the model parameters used for describing the investigated cells are presented.

Diffusion limited currents.—Based on Newman's physical-chemical model,[59,60] cell-internal processes occurring in Li-ion batteries during both operation and resting periods can be reliably described, which has been demonstrated in the past for a manifold of electrode materials and load profiles. Recently, the applicability of the modeling approach to also describe large current densities occurring during abusive short circuit events has been discussed[33,34] but not validated. Provided that no further phenomena such as a possible deviation from electro-neutrality (at high currents or low salt concentrations[61]), solvent convection (at high salt concentrations and concentration gradients[62]), salt precipitation (at high salt concentrations[28]) or thermal decomposition reactions (at high temperatures[55,63,64]) are dominating the cell behavior and as long as the model equations can be solved without facing numerical issues, in theory the model should be also valid for describing a cell's response during hard external short circuit tests. Based on the theories of porous electrodes and concentrated solutions,[60] the applied pseudo two-dimensional (p2D) model accounts for a material balance and Ohm's law within both solid and liquid components as well as a charge balance based on Butler-Volmer reaction kinetics which can be summarized in five partial differential equations.

In order to guarantee a numerically stable operation of the model even at very high currents whilst following a physical concept, the Newman group recently adapted the original model by including an additional term in the Butler-Volmer equation resembling a diffusion limited depletion of Li-ions within the radial direction of the pores.[33,34] With this modification, the original Dualfoil model is reported to successfully run at virtually all currents as a complete depletion of Li-ions within the electrolyte can be efficiently suppressed.

The tendency of the original Newman model to develop such numerical issues is based on the nature of the applied Butler-Volmer equation, combined with the calculated exchange current density i_0 (A m^{-2}) as suggested by the Newman group[59,65] to derive the pore wall flux j_n (mol m^{-2} s^{-1})

$$j_n = \frac{i_0}{F}\left[\exp\left(\frac{\alpha_a F}{RT}\eta\right) - \exp\left(\frac{\alpha_c F}{RT}\eta\right)\right] \quad [1]$$

whereas α_a and α_c represent the anodic and cathodic charge-transfer coefficients of the reaction (with $\alpha_a + \alpha_c = 1$) following the reaction overpotential η (V). F describes Faraday's constant (96485 C mol^{-1}), R the universal gas constant (8.314 J mol^{-1}K^{-1}) and T the absolute temperature in Kelvin. To be able to include experimentally measured half-cell equilibrium potentials E_{eq} (V) in the Butler-Volmer equation, η is generally written in the form[59,65]

$$\eta = \Phi_s - \Phi_l - E_{eq} \quad [2]$$

based on the potentials Φ_s and Φ_l (V) in the solid and liquid phase of the electrodes. The exchange current density is commonly calculated as[59,65]

$$i_0 = F k_c^{\alpha_a} k_a^{\alpha_c} \left(\frac{c_l}{c_{l,\,ref}}\right)^{\alpha_a} \left(c_{s,\,max} - c_{s,\,surf}\right)^{\alpha_a} \left(c_{s,\,surf}\right)^{\alpha_c} \quad [3]$$

whereas k_a and k_c represent the anodic and cathodic reaction rate constants (m s^{-1}), c_l describes the salt concentration in the liquid electrolyte (mol m^{-3}) with a reference concentration $c_{l,\,ref}$ of 1 mol m^{-3}, and $c_{s,\,max}$ and $c_{s,\,surf}$ represent the maximum Li-ion concentration and surface concentration of the solid active material particles.

As previously stated by Latz and Zausch,[66] the commonly applied combination of Eqs. 1, 2, and 3 in Li-ion battery modeling struggles to describe a cell's behavior as soon as the liquid or solid phase is completely depleted at the reaction site (i.e. $c_l = 0$ or $c_{s,\,surf} = 0$), or the surface concentration of the active material particles approaches the maximum solid phase concentration (i.e. $c_{s,\,max} - c_{s,\,surf} = 0$). At these extremes, the exchange current density approaches 0 whilst the measured half-cell potential approaches a finite value. This singular behavior leads to numerical issues when calculating the pore-wall flux. As a result, the discharge process of a cell with a fully lithiated anode could simply not be described. Furthermore, a deep discharge of a cell during abusive short circuits would also result in numerical issues. To overcome this problem, Latz and Zausch suggested a reformulation of the Butler-Volmer equation based on nonequilibrium thermodynamics resulting in pre-exponential factors for both the anodic and cathodic reaction differing from the original equation.[66]

The approach suggested by the Newman group[33,34] aims at modifying only the cathodic reaction by including an additional pre-exponential factor in the original Butler-Volmer equation based on the concept of a limiting current density i_{lim}. For the investigated short circuit conditions, the cathodic reaction in the positive electrode was modified in order to avoid c_l approaching a complete depletion or becoming even negative.

$$i_n = j_n F = \frac{i_0\left[\exp\left(\frac{\alpha_a F}{RT}\eta\right) - \exp\left(\frac{\alpha_c F}{RT}\eta\right)\right]}{1 - \frac{i_0}{i_{lim}}\exp\left(\frac{\alpha_c F}{RT}\eta\right)} \quad [4]$$

The limiting current density i_{lim} in Eq. 4 is assumed to represent a diffusion limitation in the liquid electrolyte, which is fundamentally related to the thickness of the Nernst diffusion layer δ_l (m) at the interface between the liquid electrolyte and the surface of the solid active material particles.[67] Assuming a linear concentration profile within the Nernst diffusion layer separating the bulk electrolyte (c_l) from the reaction site ($c_{l,\,surf}$), the absolute value of the limiting current

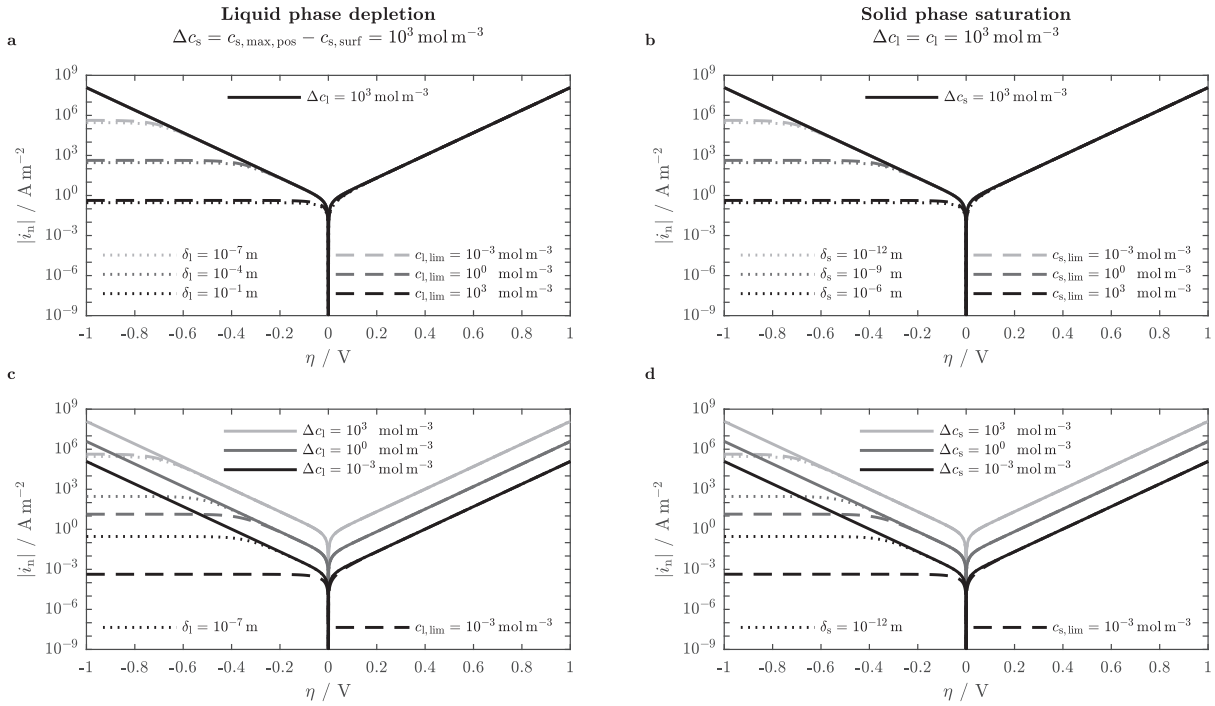

Figure 1. Influence of diffusion limited currents based on the Nernst diffusion layer thickness δ_i and limiting concentration $c_{i,\,\mathrm{lim}}$ in the liquid (i = l; left: a and c) and solid phase (i = s; right: b and d) on the reaction overpotential of the positive electrode at varying levels of limitation δ_i and $c_{i,\,\mathrm{lim}}$ and constant concentrations (top: a and b) as well as at varying concentrations and constant levels of limitation δ_i and $c_{i,\,\mathrm{lim}}$ (bottom: c and d) for $T = 25°\mathrm{C}$, $\alpha_a = \alpha_c = 0.5$, $k_a = k_c = k = 2 \times 10^{-11}\,\mathrm{m\,s^{-1}}$, $c_{s,\,max} = 50000\,\mathrm{mol\,m^{-3}}$, $D_l = 0.3 \times 10^{-9}\,\mathrm{m^2\,s^{-1}}$, $D_s = 0.3 \times 10^{-14}\,\mathrm{m^2\,s^{-1}}$, $c_{s,\,surf} = 49000\,\mathrm{mol\,m^{-3}}$ (a and c), and $c_l = 1000\,\mathrm{mol\,m^{-3}}$ (b and d).

density can be estimated via Fick's law[67]

$$|i_{\mathrm{lim}}| = F D_l \frac{c_l - c_{l,\,surf}}{\delta_l} = F D_l \frac{\Delta c_l}{\delta_l} \qquad [5]$$

whereas D_l represents the salt diffusion coefficient of solvated Li-ions in the liquid electrolyte ($\mathrm{m^2\,s^{-1}}$) and $c_{l,\,surf}$ approaches 0 in this case, so that $\Delta c_l = c_l$. With cathodic currents being negative by definition, i_{lim} also needs to be negative resulting in

$$i_n = \frac{i_0 \left[\exp\left(\frac{\alpha_a F}{RT}\eta\right) - \exp\left(\frac{\alpha_c F}{RT}\eta\right)\right]}{1 + \frac{i_0 \delta_l}{F D_l \Delta c_l} \exp\left(\frac{\alpha_c F}{RT}\eta\right)} \qquad [6]$$

For the main purpose of guaranteeing a smooth numerical calculation whilst still following a physical concept, Eq. 6 was suggested to be simplified by assuming a constant limiting concentration $c_{l,\,\mathrm{lim}}$ as suggested by the Newman group[34]

$$c_{l,\,\mathrm{lim}} = \frac{i_0 \delta_l}{F D_l} \qquad [7]$$

$$i_n = \frac{i_0 \left[\exp\left(\frac{\alpha_a F}{RT}\eta\right) - \exp\left(\frac{\alpha_c F}{RT}\eta\right)\right]}{1 + \frac{c_{l,\,\mathrm{lim}}}{\Delta c_l} \exp\left(\frac{\alpha_c F}{RT}\eta\right)} \qquad [8]$$

with $c_{l,\,\mathrm{lim}} \leq 1\,\mathrm{mol\,m^{-3}}$ showing the best results for the studied short circuit conditions.[34]

In the following, the suggested simplification is evaluated which has not been discussed so far. Comparing the effect of the simplified approach shown in Eq. 8 to the original concept of the Nernst diffusion layer shown in Eq. 6, δ_l is estimated based on Eq. 7.

Assuming $\alpha_a = \alpha_c = 0.5$ and $k_a = k_c = k$, whilst including Eq. 3 in Eq.7, δ_l calculates as

$$\delta_l = \left(\frac{D_l c_{l,\,\mathrm{lim}}}{k} \sqrt{\frac{c_{l,\,ref}}{\left(c_{s,\,max} - c_{s,\,surf}\right) c_{s,\,surf}}}\right) \frac{1}{\sqrt{c_l}} \qquad [9]$$

By further considering the liquid phase diffusion coefficient, the reaction rate constant and the Li-ion concentration at the surface of the active material particles as constant, δ_l inversely follows the square root of salt concentration $\sqrt{c_l}$ which itself changes with time t. This implies that with ongoing depletion of the salt concentration within the positive electrode during high discharge currents, the Nernst diffusion layer thickness increases, which in turn reduces the transfer current density. For a constant salt concentration at the reaction site (i.e. $c_{l,\,surf} = 0$), the thickness of the Nernst diffusion layer can be further approximated via[67]

$$\delta_l = \sqrt{\pi D_l t} \qquad [10]$$

which results in

$$\delta_l \sim \frac{1}{\sqrt{c_l}} \sim \sqrt{t} \qquad [11]$$

By introducing a constant limiting salt concentration $c_{l,\,\mathrm{lim}}$ as previously suggested[34] and presented in Eq. 7 and Eq. 8 to simplify Eq. 6, effectively the salt concentration c_l is assumed to follow the elapsed time in an inverse fashion approaching complete depletion with t approaching ∞. Hence, applying a constant $c_{l,\,\mathrm{lim}}$ limiting reaction kinetics is equivalent to using a Nernst diffusion layer thickness δ_l which is estimated to increase in size with time as stated in Eq. 10. Confirming the plausibility of the previously suggested modification (Eq. 6) and simplification (Eq. 8) of the Butler-Volmer equation, the suggested concept is further used within this work. The effect of both Nernst diffusion layer thickness as well as a limiting concentration

in the liquid electrolyte is visualized in Fig. 1 on the left (a and c). At a given Li-ion concentration in the liquid electrolyte and at the surface of the solid active material particles, the cathodic branch of the transfer current density is reduced to decreasing limiting current densities i_{lim} with increasing δ_l in Eq. 6 and $c_{l,\text{lim}}$ in Eq. 8 (compare dotted and dashed lines to solid line in Fig. 1a). To guarantee the same levels of i_{lim}, a constant ratio between δ_l and $c_{l,\text{lim}}$ is observed. With a reduction in c_l and consequently Δc_l whilst keeping the ratio between δ_l and $c_{l,\text{lim}}$ constant, a lower limitation can be observed for Eq. 6 compared to Eq. 8 (see Fig. 1c). The relationship between δ_l and $c_{l,\text{lim}}$ is summarized in Eq. 9 showing the same levels of current limitation for varying Δc_l. For a constant $c_{l,\text{lim}}$ of 10^{-3} mol m^{-3} (1 µM) and a surface concentration of 49000 mol m^{-3} as shown in Figs. 1a and 1c, δ_l grows from approximately 68 nm to 2.1 µm and 68 µm with Δc_l decreasing from 1000 mol m^{-3} (1 M) to 1 mol m^{-3} (1 mM) and 10^{-3} mol m^{-3} (1 µM), resembling a duration of ca. 5 µs to 5 ms and 5 s according to Eq. 10. At very low salt concentrations, the calculated Nernst diffusion layer is consequently likely to exceed the pore size representing rather a diffusion limitation across the electrode thickness instead of a diffusion limitation within the pores alone.

Extensive simulation studies carried out in this work with a commercial solver (COMSOL Multiphysics 5.3a) have revealed the necessity to further consider a limited solid phase saturation and solid phase depletion within the positive and negative electrode in order to guarantee numerical stability at all times. Following a similar approach as stated in Eq. 6 and Eq. 8, the cathodic current density can be further limited by referring $c_{s,\text{lim}}$ to Δc_s which is shown in Fig. 1 on the right (b and d). Due to the several orders of magnitude smaller solid phase diffusion coefficient, the estimated δ_s is also several orders of magnitude smaller than δ_l for similar values of $c_{s,\text{lim}}$ and $c_{l,\text{lim}}$ with $\Delta c_s = c_{s,\text{max}} - c_{s,\text{surf}}$. To be able to introduce this additional pre-factor in a straightforward manner without limiting the transfer current density too much, $c_{s,\text{lim}}$ is chosen several orders of magnitude smaller than $c_{l,\text{lim}}$, showing identical simulation results compared to a limitation in the liquid phase alone, whilst guaranteeing numerical stability throughout the calculation. With this additional modification, i_n in the positive electrode calculates as

$$i_n = \frac{i_0\left[\exp\left(\frac{\alpha_a F}{RT}\eta\right) - \exp\left(\frac{\alpha_c F}{RT}\eta\right)\right]}{1 + \left(\frac{c_{l,\text{lim}}}{\Delta c_l} + \frac{c_{s,\text{lim}}}{\Delta c_s}\right)\exp\left(\frac{\alpha_c F}{RT}\eta\right)} \quad [12]$$

Analogously, the anodic transfer current density in the negative electrode is limited by considering a limited depletion of the active material particles

$$i_n = \frac{i_0\left[\exp\left(\frac{\alpha_a F}{RT}\eta\right) - \exp\left(\frac{\alpha_c F}{RT}\eta\right)\right]}{1 + \frac{c_{s,\text{lim}}}{\Delta c_s}\exp\left(\frac{\alpha_a F}{RT}\eta\right)} \quad [13]$$

with $\Delta c_s = c_{s,\text{surf}}$ in this case. An additional diffusion limitation due to a liquid phase saturation in the negative electrode was not included at this stage, as it was not necessary to guarantee numerical stability and as, to the knowledge of the authors, the maximum solubility of $LiPF_6$ in organic solvents has not been addressed so far in literature. A similar approach as suggested in this work could be used to limit the calculated pore-wall flux during fast charging whereas a cathodic diffusion limitation would be required in the negative electrode and an anodic diffusion limitation could be incorporated in the positive electrode.

All simulation studies presented in this work were carried out with $c_{l,\text{lim}} = 1$ mol m^{-3} and $c_{s,\text{lim}} = 10^{-4}$ mol m^{-3} showing the best results by improving the numerical stability whilst minimizing the impact of the suggested modifications on the simulated short circuit behavior.

All relevant model equations are summarized in Table A1 in the appendix. Based on the calculated overpotentials occurring within the cell's components[26] (see Table A2 in the appendix) and the entropic coefficients for each electrode, the irreversible and reversible heat produced throughout the short circuit can be calculated accounting for a general energy balance[68,69] which is also explained in more detail in the appendix. Because quasi-isothermal test conditions are considered in this work ($\Delta T < 1\,^{\circ}$C),[12] the temperature is regarded to be constant throughout the simulations.

Parameterization.—For parameterizing the applied p2D model, experimental results and literature data were combined. Pristine graphite and NMC-111 electrode samples were used for half-cell potential measurements vs. Li/Li$^+$. By means of a differential voltage analysis (DVA) based on both half-cell and full-cell measurements, the utilization window of the electrodes was determined for each of the HP, BA, and HE loadings. Based on micrometer screw measurements and scanning electron microscopy of pristine electrode samples and electrode samples gained from post mortem analysis,[12] the thickness of the electrodes was determined and the size of the active material particles was estimated. Entropic coefficients,[70,71] reaction rate constants,[72] charge transfer coefficients and transport parameters within both liquid electrolyte[34,73–76] and solid active material particles[27,77] as well as tortuosity values of the electrodes and separator[78] were estimated in accordance with literature data.

Half-cell and full-cell measurements.—All investigated pouch-type cells and electrodes were supplied by the same manufacturer (CustomCells Itzehoe GmbH, Germany). CR2032-type coin cells were assembled in an argon filled glove box (M. Braun Inertgas-Systeme GmbH, Germany) containing graphite or NMC-111 electrode samples with a diameter of 14 mm and a metallic lithium electrode with a diameter of 15.6 mm (99.9% purity, 250 µm thickness, MTI Corporation, USA). To avoid electrical contact due to growth of lithium dendrites during operation, the two electrodes were separated by two glass fiber separators with a diameter of 16 mm (type 691 glass microfiber filter, 260 µm thickness each, VWR International, USA). Each coin cell was filled with 100 µL of electrolyte (Solvionic, France), containing 1 M lithium-hexaflourophosphate ($LiPF_6$) in ethylene carbonate (EC) : ethyl methyl carbonate (EMC) 3:7 (by weight). At least two coin cells were assembled for each electrode loading for both graphite and NMC-111. Following the formation procedure recommended by the manufacturer, the graphite and NMC-111 coin cells were charged and discharged at C/10 and C/5 for two cycles each followed by a final charge and discharge step at 1C between a lower and upper cutoff voltage of 0.1 V and 1.5 V (graphite) and 3.0 V and 4.3 V (NMC-111). The applied C-rate was chosen based on the estimated composite electrode loading (mg cm^{-2}) multiplied with the active material content (wt%) and specific capacity estimates (mAh g^{-1}) given by the manufacturer (see Table I).

The composite electrode loading was estimated by weighing both coated and uncoated/primed current collector samples prior to coin cell assembly. To determine the actual specific capacity of the active material, the coin cells were charged and discharged three times at C/50 between 0.01 V and 1.5 V (graphite) and 3.0 V and 4.2 V (NMC-111). The discharge capacity of the third C/50 cycle was considered to determine the specific capacity for each coin cell based on the estimated active material loading.

The mean values of all three electrode loadings shown in Table I are slightly higher than the manufacturer estimates which is well in line with previous studies.[11,79] Based on the measured specific capacities and the densities for both graphite and NMC-111 (see Table I), the maximum concentration $c_{s,\text{max}}$ (mol m^{-3}) can be determined. Assuming a complete utilization of the negative graphite electrode between 0.01 V and 1.5 V vs. Li/Li$^+$, $c_{s,\text{max,neg}}$ calculates as

$$c_{s,\text{max,neg}} = \frac{1}{F}\cdot 357.3\,\frac{\text{mAh}}{\text{g}}\cdot 3.6\,\frac{\text{As}}{\text{mAh}}\cdot 2.24\,\frac{\text{g}}{\text{cm}^3}\cdot 1\times 10^6\,\frac{\text{cm}^3}{\text{m}^3}$$
$$= 29862\,\frac{\text{mol}}{\text{m}^3} \quad [14]$$

In case of the positive NMC-111 electrode, $c_{s,\text{max,pos}}$ needs to be estimated based on the molar mass M_{pos} of $LiNi_{1/3}Co_{1/3}Mn_{1/3}O_2$

$$c_{s,\text{max,pos}} = \frac{1}{M_{\text{pos}}}\cdot 4.75\,\frac{\text{g}}{\text{cm}^3}\cdot 1\times 10^6\,\frac{\text{cm}^3}{\text{m}^3} = 49242\,\frac{\text{mol}}{\text{m}^3} \quad [15]$$

Table I. Coin cell electrode composition, material and electrode characteristics.

Description	Unit	Negative electrode (neg) Graphite			Positive electrode (pos) NMC-111		
Electrode composition							
Active material content[s]	wt%	96			86		
Binder content[s]	wt%	2			6		
Conductive carbon content[s]	wt%	2			8		
Material characteristics							
Particle size (D50)[m]	µm	11			7		
Specific capacity[s]	mAh g^{-1}	350			145		
Specific capacity[m]	mAh g^{-1}	357.3			157.4		
Active material density[l]	g cm^{-3}	2.24[79]			4.75[96]		
Binder density[l]	g cm^{-3}	1.76[96]			1.76[96]		
Conductive carbon density[l]	g cm^{-3}	2.00[96]			2.00[96]		
		HP	BA	HE	HP	BA	HE
Electrode characteristics							
Coating thickness[m]	µm	28	63	102	47	74	150
Area specific capacity[s]	mAh cm^{-2}	1.1	2.2	3.9	1.0	2.0	3.5
Area specific capacity[m]	mAh cm^{-2}	1.19	2.44	3.84	1.11	2.24	3.90

[l]literature.
[m]measured.
[s]supplier information.

with

$$M_{\text{pos}} = \left(6.9410 + \frac{1}{3}\cdot 58.6934 + \frac{1}{3}\cdot 58.9332 + \right.$$
$$\left. + \frac{1}{3}\cdot 54.9380 + 2\cdot 16\right)\frac{\text{g}}{\text{mol}} = 96.46\,\frac{\text{g}}{\text{mol}} \qquad [16]$$

Assuming a complete lithiation of $LiNi_{1/3}Co_{1/3}Mn_{1/3}O_2$ at the lower cutoff voltage of the C/50 cycling procedure, the stoichiometry of the positive electrode can be calculated knowing its capacity. At the beginning of lithiation at 4.2 V vs. Li/Li$^+$, the stoichiometry y in $Li_yNi_{1/3}Co_{1/3}Mn_{1/3}O_2$ calculates as

$$y = 1 - \frac{M_{\text{pos}}}{F}\cdot 157.4\,\frac{\text{mAh}}{\text{g}}\cdot 3.6\,\frac{\text{As}}{\text{mAh}} = 0.433 \qquad [17]$$

based on the measured specific discharge capacity of 157.4 mAh g^{-1}. To further study the electrode balancing for the investigated single-layered pouch-type cells within the designated operating window, the NMC-111 coin cells were charged and discharged at C/50 between 2.5 V and 4.4 V for another two cycles.

Pouch-type cells with a HP, BA, and HE electrode loading were charged and discharged two times between 3.0 V and 4.2 V at C/50 whereas the applied C-rate was based on the measured discharge capacity of the cells derived from a constant current (CC) check up procedure at C/2, followed by a constant voltage (CV) phase at the upper and lower cutoff voltage of the cells until the current dropped below C/100. The last C/50 cycle was used for both coin cells and pouch-type cells in order to fit the measured half-cell potentials of the coin cells to the full-cell potentials of the pouch-type cells. As the electrodes used within the coin cells originate from a different batch as those incorporated in the pouch-type cells, a scaling of the half-cell data to the full-cell data was necessary during DVA for all electrode loadings. The DVA performed during full-cell charging (i.e. lithiation of the graphite anode and delithiation of the NMC-111 cathode) is shown in Fig. 2. As can be seen from the figure, the measured area specific capacities of the pouch-type cells slightly differ from the values declared by the manufacturer (i.e. 0.83, 1.85, and 3.65 mAh cm^{-2} vs. 1.0, 2.0, and 3.5 mAh cm^{-2}). Furthermore, the balancing between the electrodes shifts with increasing electrode loading. This becomes especially apparent when looking into the utilization window of the graphite anode (see Figs. 2a, 2c, and 2e) and when comparing the transition from LiC_{12} to LiC_6 (indicated by the peak at a lithiation degree of approximately 0.5 in the graphite anode in Figs. 2b, 2d, and 2f). The stoichiometry values for both graphite and NMC-111 derived from DVA are presented in Table II for all electrode loadings at cell voltages of 4.2 V (100% SoC), 4.15 V (96% SoC), and 3.0 V (0% SoC). For the BA loading, initial stoichiometries for cell voltages of 4.3 V (108% SoC), 4.0 V (82% SoC), and 3.85 V (67% SoC) were additionally derived to account for a varying initial SoC prior to the short circuit in accordance with experimental data.[12] Together with the thickness of the composite electrodes l_i measured at three different locations of the electrodes gained from post-mortem analysis,[12] the electrode composition and densities of the materials (see Table I), the electrode's porosity ϵ_l and active material volume fraction ϵ_s can be further estimated and is also shown in Table II. Based on the carried out C/50 half-cell measurements and the stoichiometry values derived from DVA, the equilibrium potential of both electrodes vs. Li/Li$^+$ was determined by averaging between lithitation and delithiation. The equilibrium potentials for both negative and positive electrode are shown in Figs. A1a and A1b in the appendix.

Literature-derived parameters.—In order to account for reversible heat effects, entropic coefficients were taken from Reynier et al.[70] and Lu et al.[71] for lithiated graphite and NMC-111, respectively (see Figs. A1c and A1d in the appendix). Fitting functions further used within this work are given in Eq. A8 and Eq. A9.

To present a simple model which is able to describe a cell's short circuit behavior without accounting for complex three-dimensional electrode structures,[80,81] the presented homogenized p2D model is parameterized based on one representative particle size within each electrode assuming a constant solid phase diffusion coefficient for each active material. This implies that both the impact of a particle size distribution[22,82–84] and the influence of solid phase diffusion coefficients which vary with Li-ion concentration[85] are neglected in the model. The influence of electrode morphology was considered in this work by scaling the electrolyte's inherent transport properties with the ratio between porosity ϵ_l and tortuosity τ of the electrodes and of the separator which is also known as the inverse MacMullin number N_M (see Table AI in the appendix). The tortuosity is estimated based on the porosity applying the commonly used Bruggeman relation[86] ($\tau = \epsilon^{-\alpha_B}$, see Table I). The range of the Bruggeman exponents α_B was chosen in accordance with previously published findings.[78]

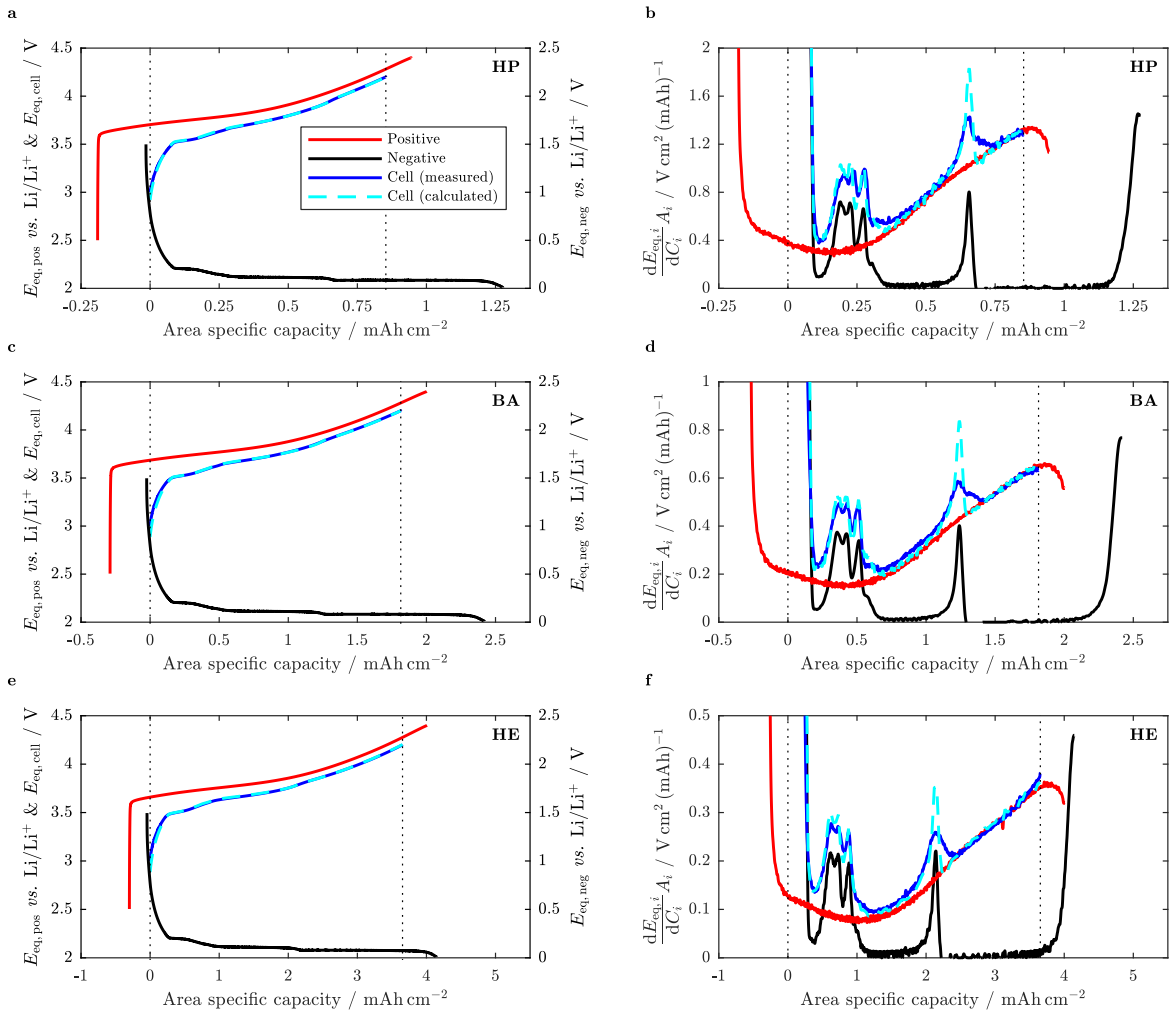

Figure 2. Derived electrode balancing for the HP (top: a and b), BA (middle: c and d), and HE (bottom: e and f) electrode loading based on the equilibrium voltage (left: a, c, and e) and differential voltage (right: b, d, and f) as a function of area specific capacity based on half-cell (graphite anode: lithiation, NMC-111 cathode: delithiation) and full-cell measurements (charge direction) at a constant current of C/50.

The fitted Bruggeman exponents vary between the three electrode loadings, which can be explained with uncertainties in porosity calculation and thickness measurements. Accounting for varying stoichiometries due to differing initial cell voltages and variations in electrode balancing (see Table II) as well as different temperatures, the solid phase diffusion coefficients were adapted allowing to fit the simulation data to experimental results (see Table III). The solid phase diffusion coefficients were chosen in accordance with reported data investigating the concentration dependency of Li-ion diffusion within both lithiated graphite[77,87,88] and NMC-111.[9,27] The plausibility of this approach is evaluated by implementing a concentration dependency of solid phase diffusion coefficients taken from literature[27,77] (see Figs. A1c and A1d in the appendix) as part of a sensitivity analysis at the end of the results section. Contrary to previous studies,[34,72] the reaction rate constants were considered independent from temperature as they showed almost no influence on the short circuit characteristics even when varied by up to one order of magnitude.

A mixture of 1 M $LiPF_6$ in ethylene carbonate (EC) : dimethyl carbonate (DMC) 1:1 (by weight) containing 2 wt% vinylene carbonate (VC) was used as electrolyte within the single-layered pouch-type cells.[12] With the electrolyte's transport properties depending on both salt concentration and temperature, literature data[34,73–76] is considered for describing the electrolyte's ionic conductivity κ_l (S m^{-1}), salt diffusion coefficient D_l (m^2 s^{-1}), cation transference number t_+ with respect to solvent, and thermodynamic factor TDF. To the knowledge of the authors, transport properties of electrolytes formed of $LiPF_6$ and organic solvents have not been studied so far at high concentrations (i.e. beyond 3.3 M[73]) or temperatures (i.e. beyond 60°C[73]). This can be best explained with the minor relevance of these conditions as long as a Li-ion cell is used within its designated operating window. As has been previously discussed, reported electrolyte properties are often presented as fitting functions following polynomial approximations which may cause problems if the electrolyte's transport properties are evaluated beyond the parameterization window.[8,81] This can result e.g. in an increasing ionic conductivity or diffusion coefficient at salt concentrations beyond the deflection point or the minimum of the polynomial fitting function, as shown in Figs. A2a and A2c in the appendix. To avoid this, fitting functions presented in literature are re-evaluated and amended for relevant concentration and temperature ranges (see Table AIII and Fig. A2 in the appendix). With the work of Valøen and Reimers[73] characterizing an EC:DMC based electrolyte with 10 vol% of polycarbonate (PC) from 7.7×10^{-6} M to 3.3 M $LiPF_6$ and from −10°C to 60°C, the simulation studies

Table II. Pouch-type cell material and electrode characteristics.

Description	Symbol	Unit	Negative electrode (neg) Graphite			Separator (sep) Polyolefin	Positive electrode (pos) NMC-111		
Material characteristics									
Equilibrium potential[m]	$E_{eq,\,i}$	V	see Fig. A1a			n/a	see Fig. A1b		
Anodic and cathodic reaction rate constant[l,72]	$k_{a/c,\,i}$	$m\,s^{-1}$	2×10^{-11}			n/a	2×10^{-11}		
Anodic and cathodic charge transfer coefficient[e]	$\alpha_{a/c,\,i}$	-	0.5			n/a	0.5		
Film resistance[l,34]	R_{film}	$\Omega\,m^{-2}$	0.0035			n/a	0		
Maximum solid phase concentration[c]	$c_{s,\,max,\,i}$	$mol\,m^{-3}$	29862			n/a	49242		
Solid phase eletronic conductivity[e]	$\sigma_{s,\,i}$	$S\,m^{-1}$	100			n/a	10		
Solid phase diffusion coefficient[e]	$D_{s,\,i}$	$m^2\,s^{-1}$	see Table III			n/a	see Table III		
Liquid phase ionic conductivity[l]	κ_l	$S\,m^{-1}$	Fitted function (see Table AIII and Figs. A2a and A2b)						
Liquid phase diffusion coefficient[l]	D_l	$m^2\,s^{-1}$	Fitted function (see Table AIII and Figs. A2c and A2d)						
Liquid phase transference number[l]	t_+	-	Fitted function (see Table AIII and Fig. A2e and A2f)						
Liquid phase thermodynamic factor[l]	TDF	-	Fitted function (see Table AIII and Figs. A2g and A2h)						
			HP	BA	HE		HP	BA	HE
Electrode characteristics									
Coating thickness[m]	l_i	µm	39	67	124	25	32	79	141
Porosity[c]	$\epsilon_{l,\,i}$	%	57.4	51.3	56.0	50	40.4	48.7	47.2
Active material volume fraction[c]	$\epsilon_{s,\,i}$	%	40.6	46.4	41.9	n/a	42.3	36.4	37.5
Tortuosity[e]	τ_i	-	$\epsilon_{l,\,neg}^{-2.7}$	$\epsilon_{l,\,neg}^{-1.8}$	$\epsilon_{l,\,neg}^{-1.5}$	$\epsilon_{l,\,sep}^{-1.8}$	$\epsilon_{l,\,pos}^{-1.7}$	$\epsilon_{l,\,pos}^{-1.1}$	$\epsilon_{l,\,pos}^{-0.8}$
Stoichiometry[c] at $E_{eq,\,cell}$ = 4.30 V / SoC = 108%			-	82.5	-		-	38.7	-
= 4.20 V = 100%			68.4	76.6	89.7		42.5	42.5	42.6
= 4.15 V = 96%	$\frac{c_s}{c_{s,\,max,\,i}}$	%	65.6	73.5	86.5		44.5	44.6	44.6
= 4.00 V = 82%			-	63.3	-		-	51.3	-
= 3.85 V = 67%			-	51.9	-		-	58.8	-
= 3.00 V = 0%			2.2	2.1	2.1	n/a	88.9	91.5	95.1

[c]calculated.
[e]estimated.
[l]literature.
[m]measured.

presented in this work are predominantly based on the reported findings.[73] Even though Mao et al.[34] have reported transport properties for an EC:DMC based electrolyte without the addition of PC as used within the pouch-type cells studied in this work, the origin and validity of these properties remains unclear. As part of a sensitivity analysis, the impact of the electrolyte's intrinsic transport properties on a cell's short circuit characteristics is studied at the end of this work for $LiPF_6$ in PC:EC:DMC,[73] EC:DMC,[34] EC:EMC,[74,75] and EC:DEC[76] (diethyl carbonate, DEC) based electrolytes.

The fully characterized (see Tables AI and AII in the appendix) and parameterized model (see Tables II and III as well as Table AIII in the appendix) was implemented in COMSOL Multiphysics 5.3a. Negative electrode, separator and positive electrode were discretized with 40, 40, and 80 nodes respectively as previously suggested.[34] The discretization in the positive electrode was chosen to be higher than in the negative electrode to be able to depict reported strong inhomogeneities in reaction and concentration.[34] The active material particles in both negative and positive electrode were discretized with an additional 20 nodes. Interpolation between the nodes was carried out following a cubic approach for all underlying variables. The applied discretization and interpolation schemes result in approximately 23500 degrees of freedom. With the chosen relative and absolute tolerance of 1×10^{-4}, the calculation takes approximately 15 min on a desktop computer (Intel Xeon E5-2687W 0 3.1 GHz with 64 GB RAM) until the current drops below C/100 which is considered the end of the short circuit procedure.

Table III. Fitted solid phase diffusion coefficients ($\times 10^{-14}\,m^2\,s^{-1}$) for both negative and positive electrode depending on stoichiometry, balancing, and temperature.

$D_{s,\,i}$ ($\times 10^{-14}\,m^2\,s^{-1}$)	Negative electrode (neg) Graphite			Positive electrode (pos) NMC-111		
	HP	BA	HE	HP	BA	HE
T = 25°C:						
initial $E_{eq,\,cell}$ = 4.30 V / SoC = 108%	-	8.0	-	-	0.2	-
= 4.15 V = 96%	8.0	8.0	8.0	0.55	0.25	0.15
= 4.00 V = 82%	-	8.0	-	-	0.3	-
= 3.85 V = 67%	-	8.0	-	-	0.4	-
T = 45°C:						
initial $E_{eq,\,cell}$ = 4.15 V / SoC = 96%	15.0	-	-	1.125	-	-
T = 55°C:						
initial $E_{eq,\,cell}$ = 4.15 V / SoC = 96%	20.0	-	-	1.5	-	-

Results and Discussion

Within this section, the presented modeling approach is validated first with respect to the predicted current and heat generation rate as a function of time and as a function of normalized discharged capacity. For this purpose, external short circuit conditions were simulated describing the behavior of single-layered pouch-type cells with varying electrode loadings (HP, BA, and HE) as well as at different cell temperatures (25°C, 45°C, and 55°C), initial cell voltages (4.30 V, 4.15 V, 4.00 V, and 3.85 V), and external short circuit resistances (0.0087 m Ω m^{-2}, 0.087 m Ω m^{-2}, and 1 m Ω m^{-2}) in accordance with experimental data presented in the first part of this combined work.[12] With the aid of the validated model, characteristics of external short circuits observed within both experiment and simulation are studied in more detail by evaluating the underlying mechanisms throughout the short circuit duration. These mechanisms are further evaluated by calculating each contribution to the overall cell polarization following the work of Nyman et al.[26] (see Table AII in the appendix). Based on these findings, a sensitivity study is presented, elaborating on the influence of transport properties and electrode morphology on a cell's short circuit characteristics.

Model validation.—In Fig. 3, model predictions (blue lines) are compared to previously reported measurement data (black lines) for all three electrode loadings at 25°C applying a 0 V short circuit condition (i.e. a first order Dirichlet boundary condition as presented in Table AI in the appendix). As can be seen from the figure, both the electrical (left: a, c, and e) and thermal behavior (right: b, d, and f) of all three electrode loadings can be reproduced very well with the model, not only as a function of short circuit duration t_{sc} (a to d) but also as a function of normalized discharged capacity ΔSoC (e and f). To determine C-rate (a and e), capacity related heat generation rate $\dot{Q}_{sc}/C_{4.2\,V}$ (W $(Ah)^{-1}$, b and f), ΔSoC (c, e, and f), and electrical energy related heat (d) in accordance with experimental data, the simulated current density (A m^{-2}), area specific heat rate (W m^{-2}), and area specific discharged capacity (Ah m^{-2}) are related to the cell's areal capacity $C_{4.2\,V}/A$ (Ah m^{-2}) between 4.2 V and 3.0 V (i.e. 0.83, 1.85, and 3.65 mAh cm^{-2} for the HP, BA, and HE loading as shown in Fig. 2).

When looking into Figs. 3a and 3e, the model is able to reliably follow the orders of magnitude in C-rate throughout the experimentally observed first and second plateau showing only minor discrepancies within the first few seconds of the short circuit or below 10% ΔSoC. As a shortcoming, the model is not able to describe the third plateau which was observed during experiments showing C-rates below 0.1 C beyond the fully discharged state (indicated via markers in Fig. 3). The experimentally observed over-discharge was previously attributed to a depletion of Li-ions within the electrolyte accompanied with a dissolution reaction of the anodic copper current collector allowing for an ongoing lithiation of the NMC-111 cathode even beyond complete depletion of the graphite anode. An additional side reaction describing the anodic copper dissolution process occurring beyond 3.1 V vs. Li/Li^+ was not implemented in the model which explains this discrepancy.

Adequately reproducing the experimentally observed similarity between the electrical and thermal behavior, the model correctly depicts the characteristic change in magnitudes of the capacity related heat generation rate throughout the first and second plateau (see Figs. 3b and 3f). However, a distinct delay between the measured and predicted heat generation rate can be observed. As previously described,[12] the chosen test setup showed a constant time delay of 21 s between calorimetric and potentiostatic data. This time delay can be explained with the thermal inertia of the used copper blocks increasing the heat capacity of the system to guarantee quasi-isothermal test conditions when determining the generated heat based on a transient temperature increment (ΔT<1°C). The reported time delay can be confirmed when comparing the model predictions with the measurement data (see Figs. 3b and 3d). The calculated heat generation rate which is primarily based on the simulated cell current density and calculated total overpotential throughout the electrodes as well as the voltage drop across the separator (see Eq. A5 to Eq. A7 in the appendix), shows a slightly higher deviation from the calorimetric measurements than the difference between the calculated C-rate and the potentiostatic measurements (see Figs. 3e and 3f). Based on the calculated adiabatic temperature increase as presented in the first part of this combined work, an integration error seems to occur in calculating the generated heat and, therefore, the calculation of heat generation rate. This integration error is ranging between 9% and 12% for the three electrode loadings (compare black and gray lines in Fig. 3d) which would also explain the previously discussed difference in the calculated effective overvoltage of the cells ranging between 3.3 V (HE) and 3.4 V (HP) compared to the nominal cell voltage of 3.7 V.[12]

It worth emphasizing here that the presented model is capable to qualitatively and quantitatively describe a cell's behavior during high currents without applying complex three-dimensional electrode models and without implementing extensions to the original Newman-type model such as a particle size distribution or a concentration dependency of solid phase transport parameters. This, however, is only the case provided that the only reaction that is occurring is a de-/intercalation reaction of Li-ions within the anodic and cathodic host lattice without any further side reactions which might be triggered at elevated temperatures. This implies that by solely depicting overall morphology and balancing related characteristics of the electrodes such as active material volume fraction, porosity, tortuosity, and stoichiometry, the homogenized model is able to describe the effect of electrode loading on the cell's short circuit characteristics, resulting in an increase in C-rate and capacity related heat generation rate with lower electrode loadings.

By further accounting for temperature dependent electrolyte transport properties according to Valøen and Reimers[73] (see Table AIII and Fig. A2 in the appendix), temperature dependent diffusion coefficients of the active materials (see Table III) and the temperature dependency of Butler-Volmer reaction kinetics (see Eq. 12 and Eq. 13 as well as Table AI in the appendix), the experimentally observed effect of temperature on the cell's short circuit behavior can be also described (see Fig. 4). Furthermore, a limited increase in C-rate and capacity related heat generation rate (not shown here) at temperatures beyond 45°C especially throughout the second plateau can be confirmed.

By accounting for a variation in stoichiometry within the active material particles (see Table II) and by considering varying solid phase diffusion coefficients (see Table III), the influence of initial cell voltage or SoC on the cell's short circuit behavior can be further evaluated (see Fig. 5). Confirming experimental results, the first plateau and the beginning of the second plateau are almost unaffected by the initial cell voltage or SoC whilst the duration of the short circuit scales with the discharged capacity.

By altering the boundary conditions at the positive terminal (see second order Neumann boundary condition in Table AI in the appendix), also the impact of varying external short circuit resistances can be analyzed in terms of C-rate, ΔSoC, and cell voltage (see Fig. 6).

Remaining deficiencies of the model especially within the first plateau can be reduced by adapting the model as discussed. This is exemplary shown for concentration dependent solid phase diffusion coefficients at the end of the results section as part of a sensitivity analysis. However, the accuracy of the presented model is satisfying, keeping in mind that a standard p2D model is used, which is only modified by accounting for a diffusion limited Butler-Volmer equation.

Rate limiting mechanisms.—With the presented model being capable of describing the experimentally observed characteristic change in magnitudes of both C-rate and capacity related heat generation rate, the model and the chosen set of parameters are considered to further identify and analyze the underlying mechanisms resulting in the observed cell behavior.

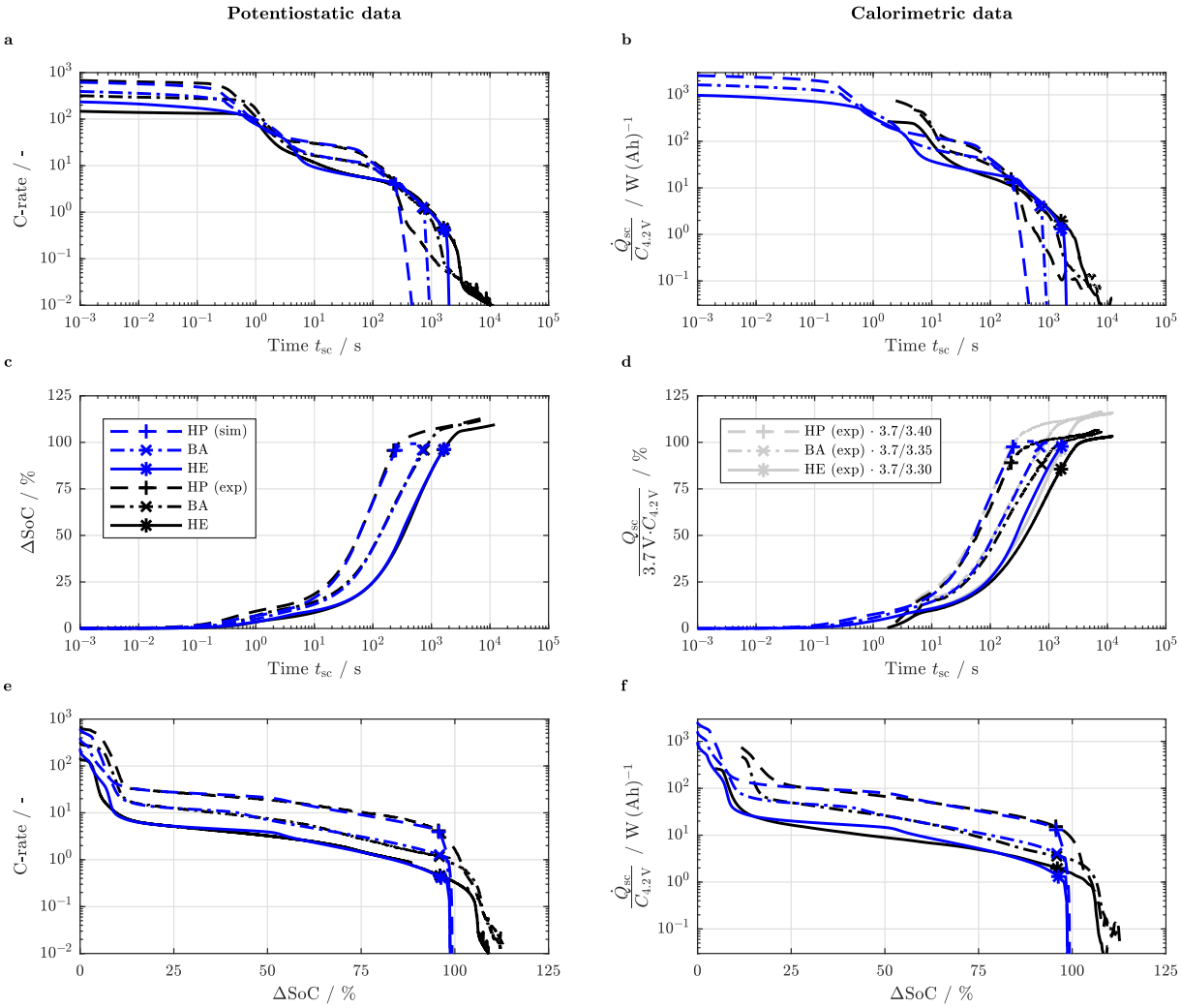

Figure 3. Comparison of measured (black lines and markers) and predicted (blue lines and markers) electrical (left: a, c, and e) and thermal cell behavior (right: b, d, and f) during a 0 V short circuit event for the HP (dashed lines), BA (dash-dotted lines), and HE loading (solid lines) at 25°C and an initial cell voltage of 4.15 V as a function of short circuit duration t_{sc} (a to d) and as a function of normalized discharged capacity ΔSoC (e and f) for the C-rate (a and e), capacity related heat generation rate (b and f), ΔSoC (c), and electrical energy related heat (d). The gray lines and markers in d represent qualitatively corrected measurement data. Markers indicate 0% SoC.

Evolution of Li-ion concentration distribution.—As rate limitation is generally regarded to be caused by a premature saturation or depletion of Li-ions in the solid and liquid components of a cell, the spatial Li-ion concentration throughout the electrodes and separator is studied at distinct times of the short circuit duration.

For this purpose, the BA loading with an initial cell voltage of 4.15 V or 96% SoC exposed to a 0 V short circuit condition at a temperature of 25°C is taken as a reference. From Fig. 3 and Fig. 5, three mentioned plateaus can be clearly identified: around 300 C in the beginning of the short circuit (below 1 s), around 10 C to 20 C with ongoing discharge (10 s to 100 s) and below 0.1 C at the end of the short circuit (1000 s to 10000 s). Neglecting an additional copper dissolution reaction within the anode, the observations made here focus on the first two plateaus and transition phases around 1 s to 10 s for the first plateau changing into the second and around 100 s to 1000 s for the second plateau passing into the third. When looking into the Li-ion concentration (see Fig. 7) in the liquid (left: a, c, e, and g) and in the solid components of the cell (right: b, d, f, and h) up to 0.32 s (a and b), between 0.5 s and 8 s (c and d), between 20 s to 160 s (e and f), and from 200 s to 800 s (g and h), characteristic concentration profiles for each plateau and transition phase can be observed in both the negative and positive electrode.

Throughout the first plateau (see Figs. 7a and 7b), the cell is discharged without major limitations in mass transport. Within the positive electrode, the salt concentration decreases forming a minimum near the separator whilst the Li-ion concentration at the surface of the active material particles increases forming a maximum at the boundary between the separator and electrode domain. Within the negative electrode, the salt concentration increases forming a maximum near the separator whilst the surface concentration of the active material particles decreases with the lowest concentration at the boundary between separator and electrode. However, the surface concentration varies in a slower fashion as a function of time compared to the positive electrode due to the larger diffusion coefficient of graphite (see Table III). The observed inhomogeneous Li-ion concentration is fundamentally based on a strongly non-uniform reaction across the electrodes with a larger pore-wall flux at the separator interface (not shown here). For the chosen set of parameters, the surface concentration approaches

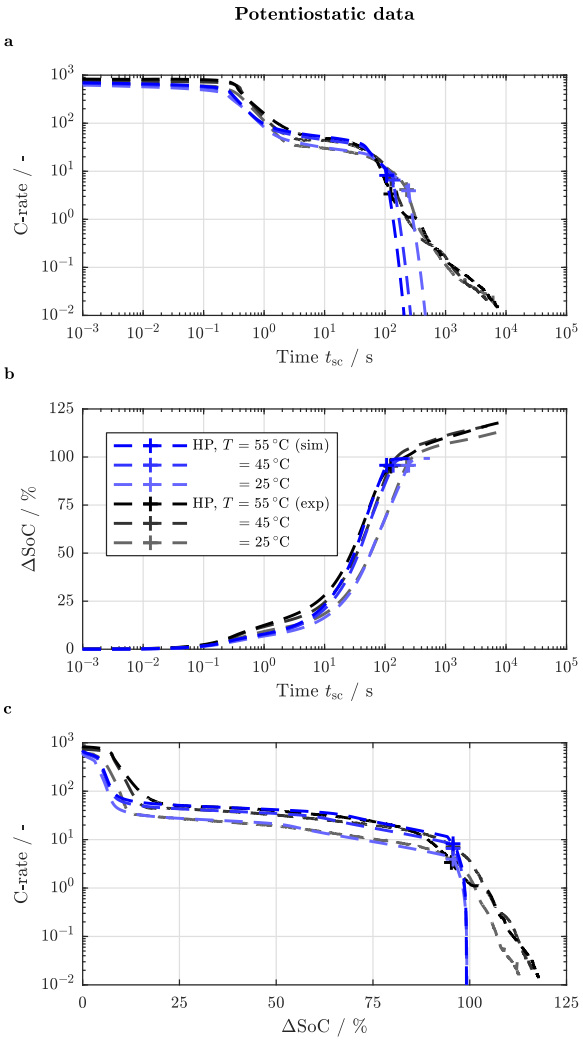

Figure 4. Comparison of measured (black lines and markers) and predicted (blue lines and markers) electrical cell behavior during a 0 V short circuit event for the HP loading at an initial cell voltage of 4.15 V and temperatures of 55°C, 45°C, and 25°C as a function of short circuit duration t_{sc} (a and b) and as a function of normalized discharged capacity ΔSoC (c) for the C-rate (a and c) and ΔSoC (b). Markers indicate 0% SoC.

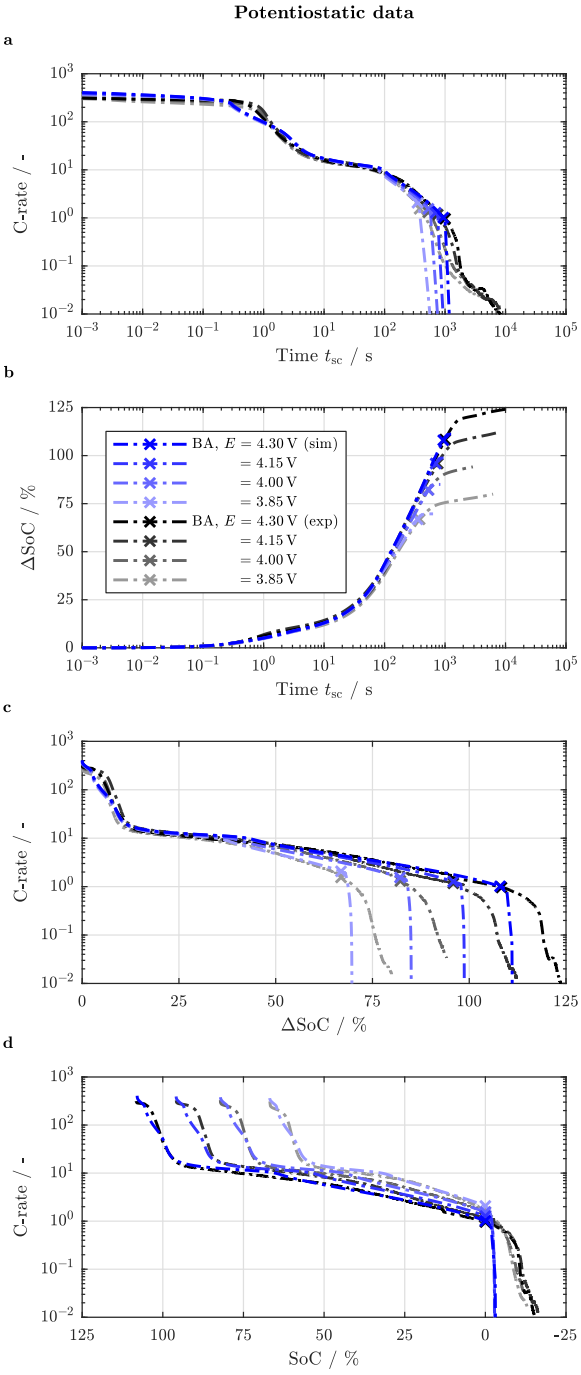

Figure 5. Comparison of measured (black lines and markers) and predicted (blue lines and markers) electrical cell behavior during a 0 V short circuit event for the BA loading at 25°C and initial cell voltages of 4.3 V, 4.15 V, 4.0 V, and 3.85 V as a function of short circuit duration t_{sc} (a and b), as a function of normalized discharged capacity ΔSoC (c), and as a function of SoC (d) for the C-rate (a, c, and d) and ΔSoC (b). Markers indicate 0% SoC.

the fully lithiated state throughout the entire positive electrode at the end of the first plateau, which results in large reaction and mass transport based overpotentials. As a result, the current and consequently also the heat generation rate drop toward the second plateau. During the observed transition period between the plateaus (see Figs. 7c and 7d), the salt concentration within the positive electrode approaches the fully depleted state with the minimum concentration forming at the current collector interface which allows the surface concentration within the positive electrode to decrease again based on the reduced pore-wall flux in this area and a simultaneously occurring homogenization of concentration gradients within the active material particles. Similarly, the surface concentration within the negative electrode slightly increases throughout the electrode whilst the maximum salt concentration moves from the separator to the current collector at concentrations exceeding 2 M (i.e. 2 mol L^{-1}). During the second plateau (see Figs. 7e and 7f), the minimum salt concentration is still located at the current collector interface and the maximum solid phase concentration is still located at the separator interface of the positive electrode. Whilst the region which is affected by a depletion in salt concentration is shrinking toward the current collector, the area which is affected by a saturation of the active material particles is growing from the separator toward the current collector until the active material particles are fully saturated at the surface within the entire

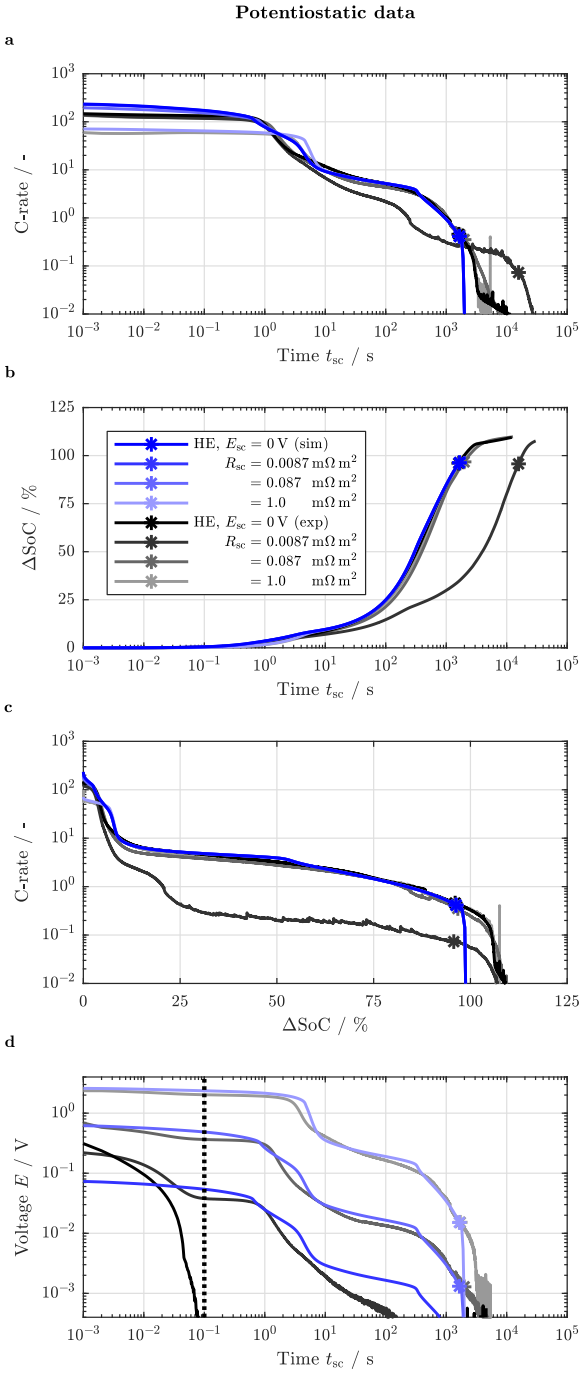

Figure 6. Comparison of measured (black lines and markers) and predicted (blue lines and markers) electrical cell behavior during a 0 V short circuit event and external short circuit resistances of 0.0087 mΩm^2, 0.087 mΩm^2, and 1 mΩm^2 for the HE loading at 25°C and an initial cell voltage of 4.15 V as a function of short circuit duration t_{sc} (a, b, and d) and as a function of normalized discharged capacity ΔSoC (c) for the C-rate (a and c), ΔSoC (b), and cell voltage (d). The vertical dotted line in d indicates the duration (100 ms) until a stable regulation of the used potentiostat was achieved. Markers indicate 0% SoC. The cell that was exposed to 0.0087 mΩm^2 during experiments showed an abnormal, high resistance behavior.

positive electrode. The reduced current density occurring throughout the second plateau allows for a homogenization in salt concentration throughout the electrodes. Despite the saturated surface concentration within the positive electrode, the ongoing discharge process results in a decreasing surface concentration within the negative electrode approaching the fully depleted state. This process is dominating the transition from the second plateau to the third plateau (see Figs. 7g and 7h), resulting in a strongly decreasing current and heat generation rate. At the end of the simulation of the short circuit, the surface concentration is completely depleted throughout the negative electrode resulting in a slightly decreasing surface concentration within the positive electrode whilst the comparably low cell currents allow for an ongoing homogenization in salt concentration approaching the initial concentration of 1 M (dashed line in Fig. 7g).

At the very end of the short circuit, the simulated potential at the boundary between current collector and negative electrode increases beyond 3.1 V[89] vs. Li/Li$^+$ (see Fig. 8) which supports the previously stated assumption of an ongoing intercalation reaction within the positive electrode based on an anodic copper dissolution reaction and salt depletion throughout the third plateau.[12]

Breakdown of cell polarization.—From the above, the transients in magnitudes of current and heat generation rate can be explained based on the salt and surface concentration at the boundaries of the positive electrode and the surface concentration at the boundaries of the negative electrode. Together with the resulting calculated polarization within the electrodes and the voltage drop across the separator as presented in Table AII in the appendix, a thorough evaluation of the observed short circuit behavior can be carried out.

This is exemplarily shown in Fig. 9 for the BA loading both as a function of short circuit duration t_{sc} (left: a, c, and e) and as a function of normalized discharged capacity ΔSoC (right: b, d, and f). When looking into the validation (top: a and b), the aforementioned three plateaus (I, II, and III) as well as the transition phases between the plateaus (I-II and II-III) can be identified. Plateau II can be further subdivided into two parts (IIa and IIb) based on a distinctly varying slope of the plateau which can be observed in both representations. Each phase shows different dominating voltage losses (middle: c and d) which can be correlated to the Li-ion concentration at the surface of the solid active material particles and to the average salt concentration in the liquid electrolyte at the boundaries of the electrodes (bottom: e and f). Within the first plateau, ohmic losses (Ω) within the liquid electrolyte throughout both electrodes and separator as well as Butler-Volmer (BV) reaction kinetics within the negative electrode (see Figs. 9c and 9d) are dominating the cell polarization. Even though the largest currents can be observed for the first plateau, ohmic losses within the solid phase range below 15 mΩ which is why they are not explicitly shown in the legend of Figs. 9c and 9d. The larger contribution of Butler-Volmer reaction kinetics within the negative electrode compared to the positive electrode can be explained with the additionally considered film resistance resulting in an increased voltage drop across the solid electrolyte interphase (see Table II and Table AI in the appendix), the negative electrode's approximately 30% smaller reaction surface area based on particle size, electrode thickness, and active material volume fraction as well as the 40% smaller exchange current density based on the balancing-related stoichiometry within the active materials (see Table I, Table II, and Table AI). Approaching the transition phase I-II, the polarization based on solid phase diffusion (D) within the active material particles of the positive electrode is substantially increasing. Due to the predicted premature saturation of the surface concentration throughout the entire positive electrode, the simulated transition phase I-II begins slightly earlier than observed during the measurements (see Figs. 9a and 9e), as also apparent in the ΔSoC based representation (see Figs. 9b and 9f). As soon as the minimum salt concentration is located at the current collector boundary of the positive electrode, the over-predicted limitation decreases and the simulation data again follows the measurement data very well. Due to the mass transport based limitation of the reaction within the positive electrode, the reaction overpotential increases considerably

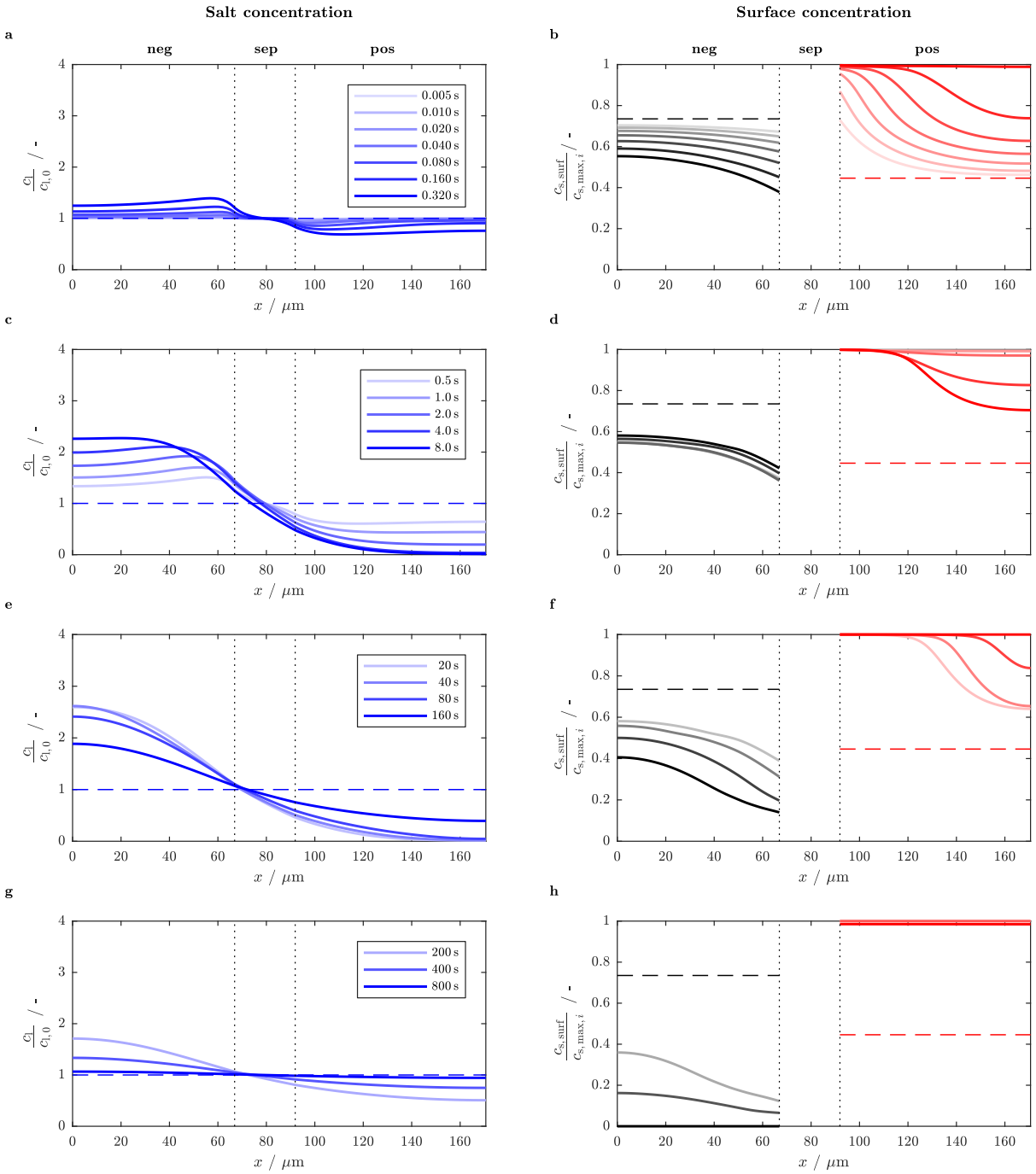

Figure 7. Predicted spatial distribution of normalized salt concentration within the liquid phase (left: a, c, e, and g) and normalized surface concentration within the solid phase (right: b, d, f, and h) during a 0 V short circuit event for the BA loading at 25°C and an initial cell voltage of 4.15 V during the first plateau (a and b) and the approach toward the second plateau (c and d) as well as throughout the beginning of the second plateau (e and f) and the end of the second plateau approaching the third plateau (g and h).

whilst the current drops and, hence, the ohmic based voltage drop decreases throughout the electrodes and separator following the current. After plateau I and the transition phase I-II consuming about 10% of the cell's capacity within less than 5 s, the reaction overpotential within the positive electrode remains dominating (ca. 3 V) throughout the first part of the second plateau (IIa) which forms due to a simultaneously occurring saturation of the active material particles near the separator and salt depletion near the current collector (see Figs. 7e and 7f as well as Figs. 9e and 9f). The occurring large liquid phase concentration gradients throughout the electrodes and separator as well as the salt concentration approaching depletion within the positive electrode result in an increasing diffusion based polarization within the liquid phase (dashed black, blue, and red lines in Figs. 9c and 9d). Similar to the total ohmic contribution of the solid phase,

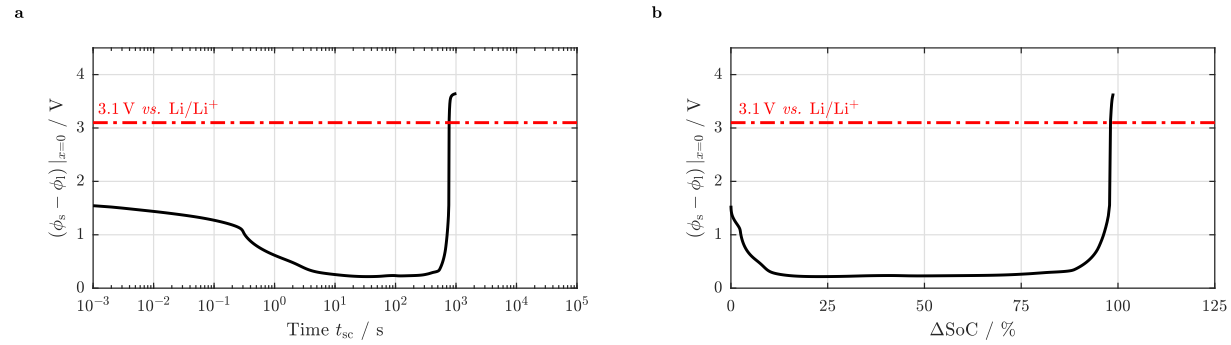

Figure 8. Simulated potential vs. Li/Li^+ of the negative electrode at the current collector interface ($x = 0$) as a function of short circuit duration t_{sc} (a) and as a function of normalized discharged capacity ΔSoC (b) indicating the likeliness of an anodic copper dissolution reaction[89] at the very end of the short circuit event with potentials exceeding 3.1 V vs. Li/Li^+.

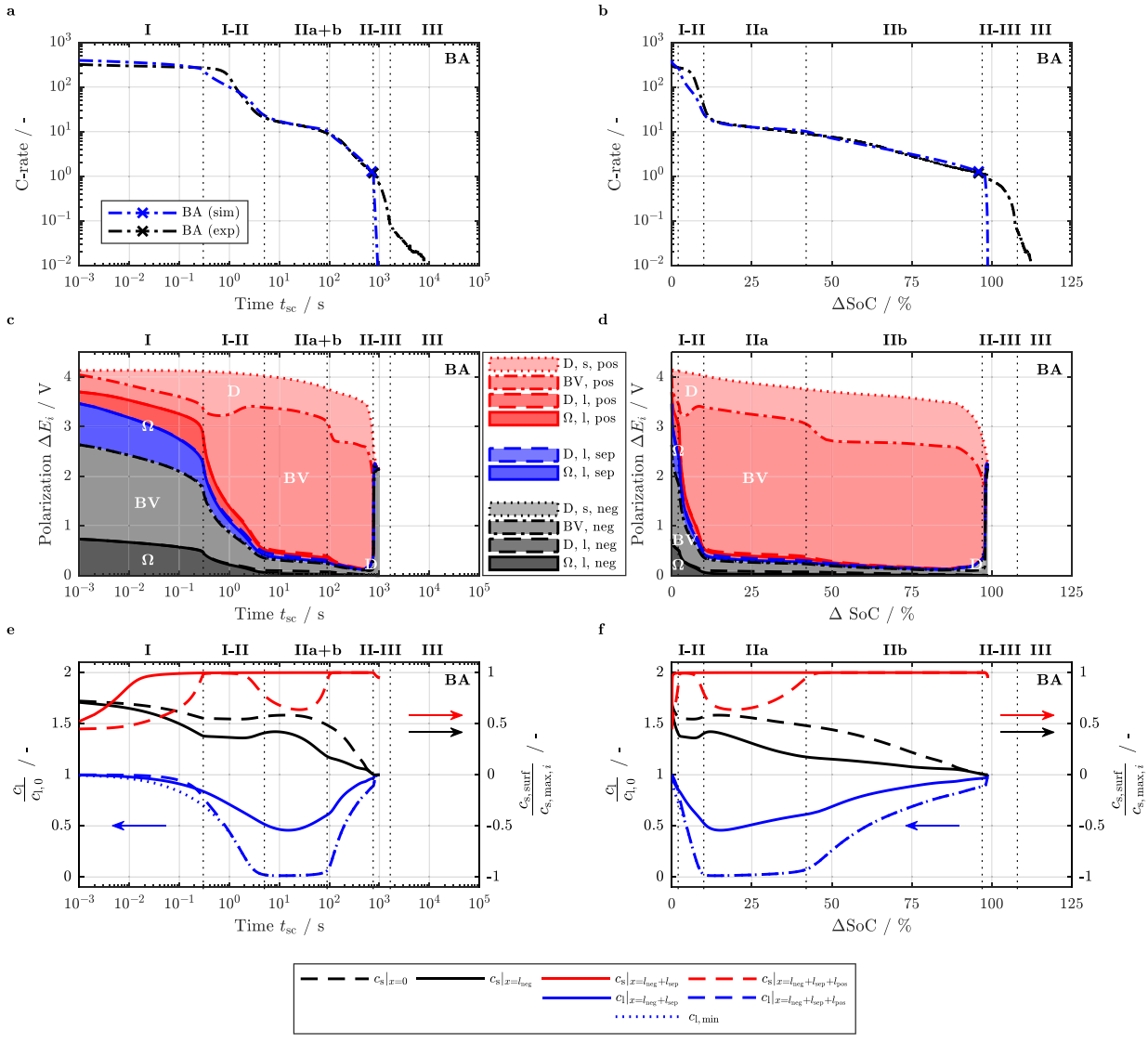

Figure 9. Measured and predicted phases of a short circuit during a 0 V short circuit event for the BA loading at 25°C and an initial cell voltage of 4.15 V observed in C-rate (top: a and b), the corresponding predicted polarization throughout the electrodes and separator (middle: c and d) resulting from the underlying normalized solid (surface) and liquid phase concentration (average) at distinct locations of the cell (bottom: e and f) as a function of short circuit duration (left: a, c, and e) and as a function of normalized discharged capacity (right: b, d, and f).

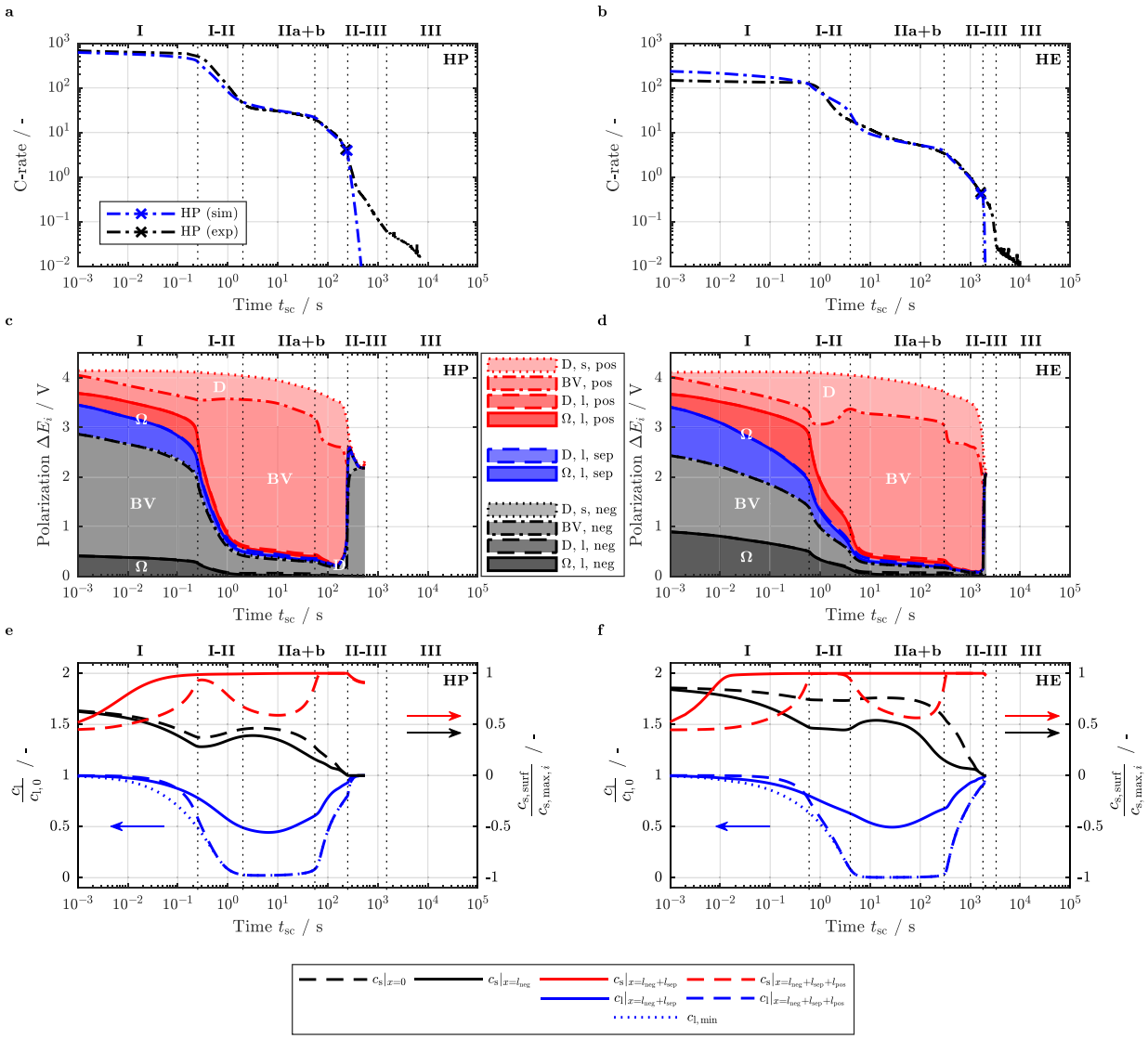

Figure 10. Measured and predicted phases of a short circuit during a 0 V short circuit event for the HP (left: a, c, and e) and HE loading (right: b, d, and f) at 25°C and an initial cell voltage of 4.15 V observed in C-rate (top: a and b), the corresponding predicted polarization throughout the electrodes and separator (middle: c and d) resulting from the underlying normalized solid (surface) and liquid phase concentration (average) at distinct locations of the cell (bottom: e and f) as a function of short circuit duration.

this polarization only plays a minor role during the entire short circuit (150 mΩ at its maximum in plateau II). After the first part (IIa) of the second plateau consuming another 32% of the cell's capacity within 85 s, the second part (IIb) is characterized by a fully saturated surface concentration within the entire positive electrode (see Figs. 9e and 9f). This change of dominating mass transport limitations is not only reflected in the slope of plateau IIa and IIb in Figs. 9a and 9b but also in the contribution of the positive electrode's solid phase diffusion to the observed cell polarization (ca. 1 V). Independent of the characteristics of mass transport limitation within the positive electrode (i.e. a combination of solid and liquid phase in IIa vs. solid phase alone in IIb), the reaction overpotential remains dominating. At the end of plateau IIb consuming 55% of the cell's capacity within 640 s, the mass transport within the solid phase and the reaction overpotential within the negative electrode become dominant due to the depleted surface concentration of the active material particles. With simulated anode potentials exceeding 3.1 V vs. Li/Li$^+$ at the negative electrode's current collector (see Fig. 8), the transition phase II-III is likely to be characterized by an ongoing Li-ion intercalation reaction within the positive electrode driven by the continuing de-intercalation reaction of the negative electrode and a simultaneously occurring anodic copper dissolution reaction until the positive electrode is completely lithiated throughout plateau III.

Influencing factors on cell polarization.—When comparing the HP and HE electrode loading to the BA loading as function of short circuit duration t_{sc} (see Fig. 10 and Fig. 9 on the left), the variations between the three loadings can be correlated to differences in the polarization behavior. The larger C-rate of the HP loading is primarily based on lower ohmic losses within the liquid electrolyte based on the reduced electrode thickness and the resulting smaller concentration gradients throughout the electrodes and separator. The more homogeneous electrode utilization further reduces the solid phase diffusion based polarization especially in the positive electrode of the HP loading. Based

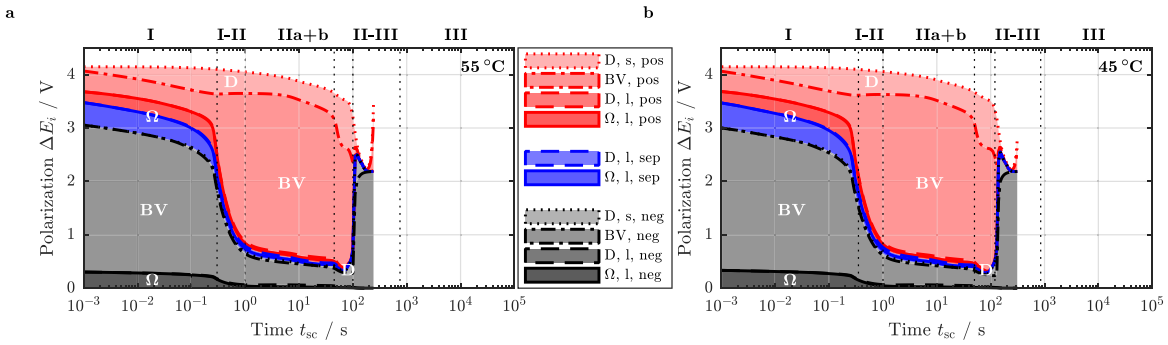

Figure 11. Predicted polarization during a 0 V short circuit event at an initial cell voltage of 4.15 V throughout the electrodes and separator for the HP loading at 55°C (a) and at 45°C (b) as a function of short circuit duration.

on the reduced electrode loading and, hence, smaller reaction surface area together with a reduced initial Li-ion concentration within the negative electrode due to the varied electrode balancing (see Table II), the reaction overpotential especially within the first plateau is considerably increased compared to the BA and HE loading. As a result of the logarithmic representation, the observed mass transport limitation of reaction kinetics within the negative electrode at the end of the short circuit becomes more pronounced at earlier times. Interestingly, the predicted transient change from plateau I to II can be described very well for the HP loading compared to the BA and HE loading based on a lacking occurrence of a solid phase diffusion limitation within the positive electrode during the transition phase I-II. Extensive simulation studies carried out as part of this work have shown that the solid phase diffusion coefficient within the positive electrode defines the initiation and the slope of plateau IIb which consumes the largest amount of charge throughout the short circuit. However, a larger diffusion coefficient would be beneficial to describe the transition phase I-II adequately for the BA and HE loading, avoiding a solid phase diffusion limitation within the transition phase. As the first plateau and the first transition phase only account for less than 10% of the cell's capacity, the focus of parameterization was laid on plateau IIb. This will be discussed in more detail as part of a sensitivity analysis.

When comparing the polarization of the HP loading at 55°C to 45°C (see Figs. 11a and 11b) and 25°C (see Fig. 10c), the experimentally observed limited impact of the cell's temperature beyond 45°C can be explained. An increase from 25°C to 45°C considerably reduces the ohmic losses within the liquid electrolyte based on an enhanced ionic conductivity (see Table AIII and Fig. A2 in the appendix) allowing for a larger charge transfer overpotential and consequently an increased pore-wall flux. This effect is further enhanced due to the reduced solid phase diffusion polarization based on the fitted temperature dependency of the solid phase diffusion coefficients.[34,72] Beyond 45°C, a marginal variation in the occurring polarization contributions can be observed, supporting the previously stated limited impact of temperature on the dynamics of the short circuit based on mass and charge transport.[12]

In Fig. 12, the influence of initial cell voltage or SoC on the occurring cell polarization is shown. The experimentally observed similarity between cells with varying initial cell voltage or SoC throughout phases I, I-II, and IIa, can be confirmed as the contribution of each mechanism to the entire cell polarization is fairly similar between 4.30 V (108% SoC) and 3.85 V (67% SoC). Despite the reduced overall polarization based on the lower cell voltage, especially the solid phase diffusion based polarization within the positive electrode is reduced due to higher initial concentrations and consequently reduced concentration gradients throughout the short circuit duration. Furthermore, the initial cell current is slightly lower for lower cell voltages, reducing ohmic losses within the liquid electrolyte. Due to the lower cell capacity, plateau IIb is considerably reduced approaching the transition phase II-III at earlier times.

With increasing external short circuit resistance, plateau I and the transition phase I-II are considerably affected (compare Fig. 13 to Fig. 10d) whereas plateau IIa and especially IIb are almost not influenced. This implies that as long as the short circuit resistance is small enough so that liquid phase depletion and solid phase saturation occur within the positive electrode, the second plateau will show the same characteristic shape.

To sum up, the presented standard p2D-model is able to shed light on the dominating mechanisms resulting in the experimentally observed characteristics occurring during quasi-isothermal external short circuit tests. The model based evaluation reveals that the first and second plateau as well as the transition phases between the two and the approach toward the third plateau are dominated by reaction kinetics within the negative electrode (I and II-III) as well was reaction kinetics within the positive electrode (I-II, IIa, and IIb). With the largest currents occurring within the first plateau, ohmic resistances

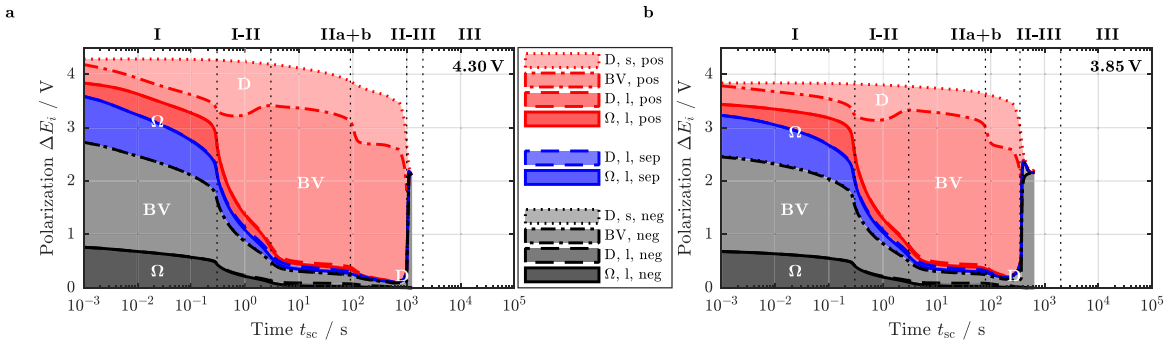

Figure 12. Predicted polarization during a 0 V short circuit event at initial cell voltages of 4.3 V (a) and 3.85 V (b) throughout the electrodes and separator for the BA loading at 25°C as a function of short circuit duration.

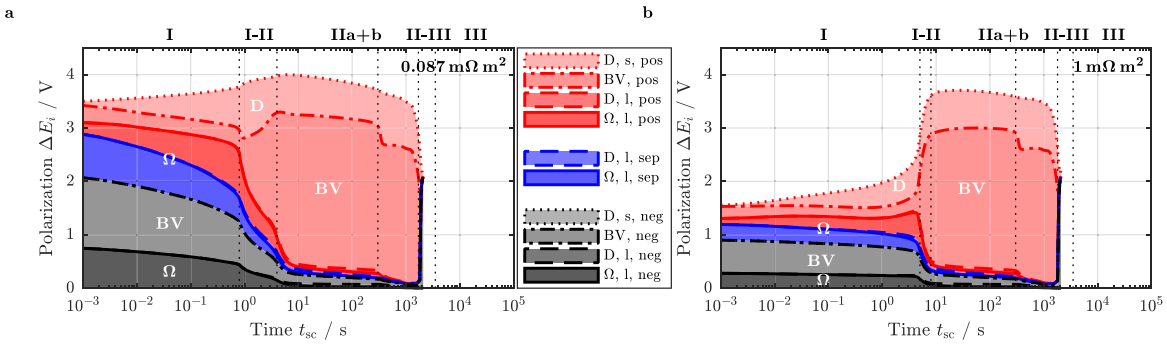

Figure 13. Predicted polarization during 0.087 mΩm^2 (a) and 1 mΩm^2 (b) external short circuit events at an initial cell voltage of 4.15 V and 25°C for the HE loading as a function of short circuit duration.

within the liquid electrolyte are forming a major contribution whilst solid phase diffusion polarization is becoming more important with ongoing duration of the short circuit. The characteristic second plateau with its two stages IIa and IIb is dominated by mass transport limited reaction kinetics throughout the entire positive electrode based on a combination of liquid phase depletion and solid phase saturation (IIa) as well as an exclusive solid phase limitation (IIb). Independent of the electrode loadings, cell temperatures, cell voltages, and external short resistances studied in this investigation, the sequence of rate limitation remains the same throughout the external short circuits. However, the contribution of each underlying mechanism based on the Li-ion concentration distribution throughout the electrodes and separator is varying for the investigated cells and applied short circuit conditions.

Sensitivity analysis.—As discussed within the model validation part and the analysis of rate limiting mechanisms, some discrepancies remain between the predicted and experimentally observed short circuit behavior for the chosen set of parameters, especially at early times combined with increasing electrode loadings. For this purpose, a sensitivity analysis is carried out for various transport parameters that have been reported in literature, accounting for a concentration dependency within both solid and liquid phase. In the second part of this sensitivity analysis, the influence of electrode characteristics defining the suitability of a cell toward high power or high energy applications is studied in terms of short circuit dynamics.

Influence of concentration dependent transport properties.—Only little work has been presented so far dealing with a concentration dependency of Li-ion diffusion coefficients within the active materials. Previous findings of Levi and Aurbach[77] and Markevich et al.[87] describing a considerable concentration dependency of the Li-ion diffusion coefficient within lithiated graphite have been recently confirmed by Malifarge et al.[88] The concentration dependency of Li-ion diffusion coefficients in NMC electrodes has been studied for varying compositions by Noh et al.[9] and explicitly for NMC-111 by Wu et al.[27] The experimental data supplied by Levi and Aurbach[77] and Wu et al.[27] as shown in Figs. A1e and A1f was fitted according to Eq. A10 and Eq. A11 in the appendix which is further used here. As can be seen from Figs. 14a and 14b, accounting for a concentration dependency of solid phase diffusion coefficients improves the prediction accuracy at the beginning of the short circuit, especially throughout transition phase I-II (compare Figs. 14a and 14b to Figs. 9a and 9b). This can be explained by the increased diffusion coefficient of NMC-111 (ca. 3.0×10^{-14} m^2 s^{-1} vs. the effective value of 0.25×10^{-14} m^2 s^{-1}) and the reduced diffusion coefficient of lithiated graphite (ca. 0.3×10^{-14} m^2 s^{-1} vs. the effective value of 8.0×10^{-14} m^2 s^{-1}) in the very beginning of the short circuit compared to the fitted constant diffusion coefficients used within this work. Based on the altered ratio of diffusion coefficients, the discussed solid phase diffusion limitation within the positive electrode during the transition phase I-II changes toward a solid phase diffusion limitation within the negative electrode at the end of plateau I (compare Figs. 14c to 14f to Figs. 9c to 9f). Associated with the larger solid phase diffusion coefficient of NMC-111 compared to the fitted value, the duration and the C-rate of plateau IIa are over-predicted resulting in an under-prediction of the duration of plateau IIb which, as a consequence, also shows a steeper decrease in predicted C-rate. With the reported high diffusion coefficient of lithiated graphite near complete depletion (ca. 30×10^{-14} m^2 s^{-1}) and the reported low diffusion coefficient of NMC-111 near complete saturation (ca. 0.03×10^{-14} m^2 s^{-1}), a second solid phase diffusion limitation within the negative electrode occurs only at the very end of plateau IIb, indicating the beginning of transition phase II-III. This observation supports the chosen ratio of the fitted constant diffusion coefficients in order to describe the cell's short circuit behavior throughout plateau II and especially IIb. The simulation results suggest that applying diffusion coefficients which vary in the range of up to three orders of magnitude may enhance the prediction accuracy especially at the very beginning of a short circuit, however, the exact behavior must be known for the investigated materials so that the simulation data can also follow the experimentally observed second plateau within which the largest amount of capacity is consumed and which also takes the longest amount of time. Taking into account the experimental data presented by Noh et al.[9] (gray markers in Fig. A1f in the appendix) and Wu et al.[27] (black markers in Fig. A1f in the appendix), a diffusion coefficient ranging between the two might fulfill the requirement of a comparably high diffusion coefficient in the beginning of the short circuit to describe plateau I and the transition phase I-II and a rather low diffusion coefficient at the end to depict the transition from plateau IIa into IIb. The fitted constant diffusion coefficients presented in this work represent effective diffusion coefficients which allow for a surprisingly high prediction accuracy, notwithstanding the simplicity of the approach.

Whilst concentration dependent Li-ion transport parameters within the solid phase are scarcely found in Li-ion battery modeling and simulation,[85] a concentration dependency of parameters describing Li-ion transport within the liquid phase is rather common practice for physical-chemical models describing ion transport throughout the electrodes and separator. To evaluate the relevance of the applied transport properties taken from Valøen and Reimers,[73] the presented data is compared to simulation studies based on liquid phase transport properties taken from Mao et al.,[34] Dees et al.,[74] Nyman et al.,[75] and Lundgren et al.[76] (see Table AIII and Fig. A2 in the appendix) in Fig. 15. As can be seen from from the figure, the liquid phase transport properties mainly affect the magnitude and the duration of the first part of the second plateau (IIa). Mainly following the level of ionic conductivity κ_l and partly also the magnitude of the salt diffusion coefficient D_l, the largest C-rate throughout plateau IIa can be observed for Valøen and Reimers,[73] as well as Mao et al.[34] With an approximately

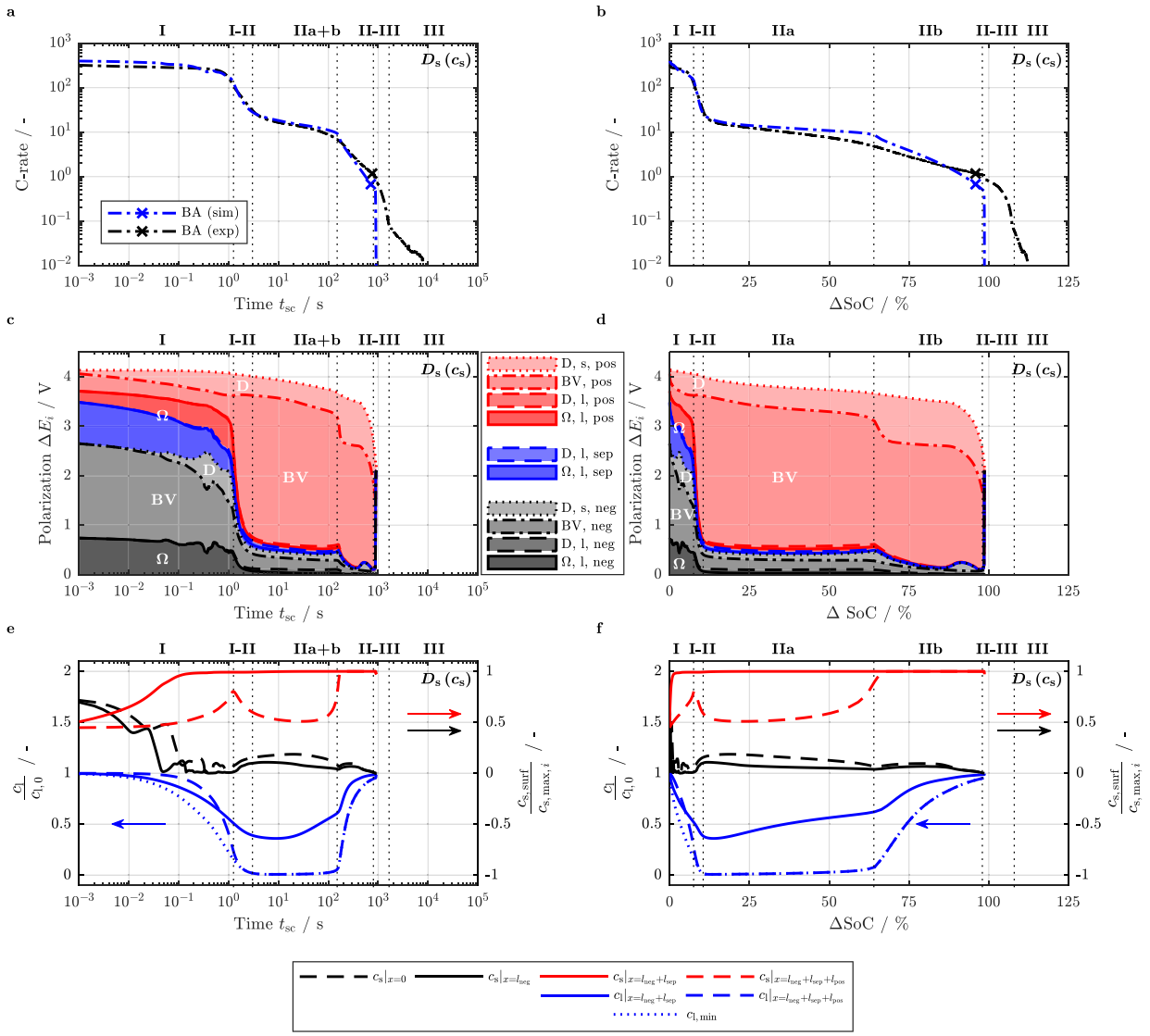

Figure 14. Measured and predicted phases of a short circuit during a 0 V short circuit event for the BA loading at 25°C and an initial cell voltage of 4.15 V observed in C-rate (top: a and b) accounting for concentration dependent solid phase diffusion coefficients D_s (c_s), the corresponding predicted polarization throughout the electrodes and separator (middle: c and d) resulting from the underlying normalized solid (surface) and liquid phase concentration (average) at distinct locations of the cell (bottom: e and f) as a function of short circuit duration (left: a, c, and e) and as a function of normalized discharged capacity (right: b, d, and f).

two times larger ohmic polarization throughout the liquid electrolyte (not explicitly shown here), the simulation data based on Lundgren et al.[76] shows the lowest C-rate throughout plateau IIa. With the ionic conductivity κ_l presented by Dees et al.[74] and Nyman et al.[75] ranging in between, also the C-rate is predicted to lie in this range. With the cation transference number t_+ reported to decrease with increasing salt concentration based on the work of Nyman et al.[75] and Lundgren et al.,[76] the liquid phase diffusion based overpotential in the negative electrode is increasing throughout plateau IIb which, however, seems to have only a minor impact on the transient short circuit behavior despite the predicted maximum salt concentration increasing beyond 4 M (Nyman et al.[75]), even approaching 5 M (Lundgren et al.[76]). Whether such high salt concentrations are even possible without salt precipitation to occur remains unclear. For all other reported data,[34,73,74] the predicted maximum salt concentration ranges below 3 M throughout the short circuit. The simulation data based on the transport properties reported by Mao et al.[34] for an EC:DMC based electrolyte is almost identical to simulation results based on the transport properties taken from Valøen and Reimers,[73] which supports the significance of the applied liquid phase transport properties for the model based short circuit evaluation presented in this work. Interestingly, the choice of the organic solvent used for the $LiPF_6$ based electrolyte seems to have a considerable impact on the dynamics of the short circuit with lower C-rates throughout plateau IIa and, hence, a decelerated energy release below a few hundred seconds or 60% ΔSoC for EC:EMC[74,75] and EC:DEC[76] based electrolytes compared to EC:DMC[34,73] based electrolytes. Whether this is truly the case remains to be evaluated by further experimental work.

Influence of electrode morphology.—As discussed in previous work,[12] a cell that is characterized as high power with thin and/or highly porous electrodes and small active material particles is likely to show an accelerated short circuit behavior compared to a cell that is categorized as high energy with thick and/or dense electrodes and

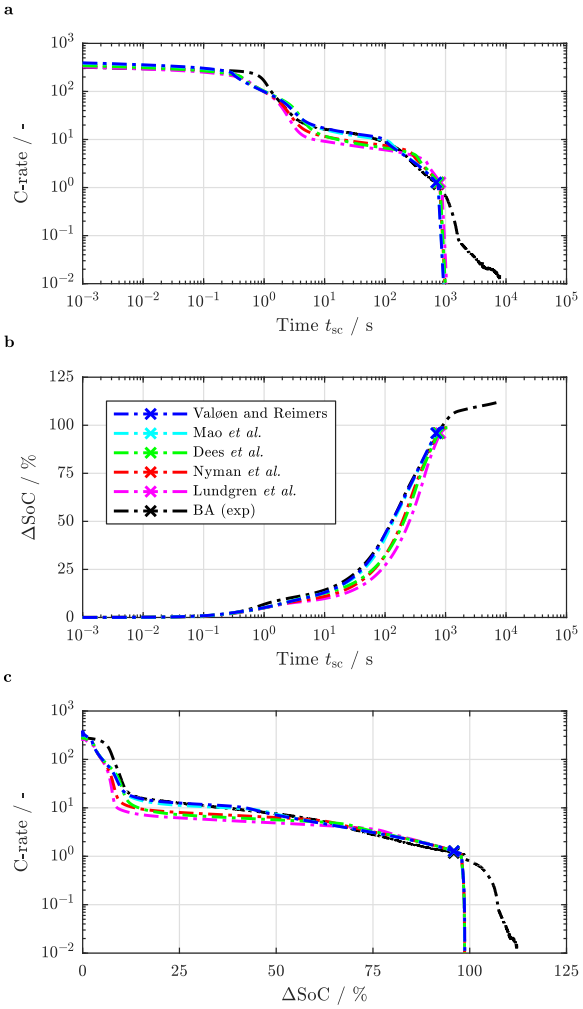

Figure 15. Influence of liquid phase transport properties reported by Valøen and Reimers,[73] Mao et al.,[34] Dees et al.,[74] Nyman et al.,[75] and Lundgren et al.[76] on the electrical cell behavior during a 0 V short circuit event for the BA loading at an initial cell voltage of 4.15 V and 25°C as a function of short circuit duration t_{sc} (a and b) and as a function of normalized discharged capacity ΔSoC (c) for the C-rate (a and c) and ΔSoC (b). Markers indicate 0% SoC.

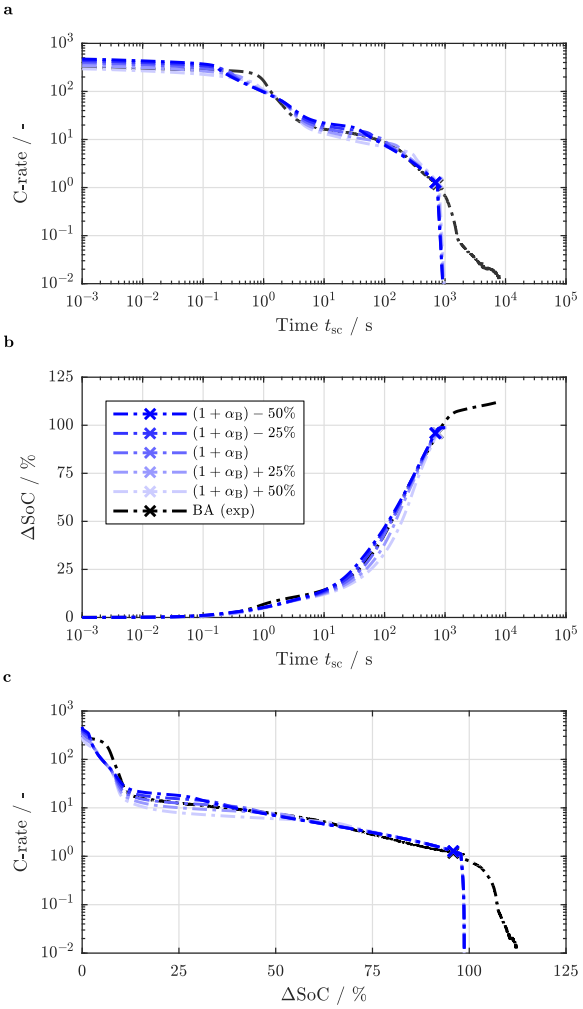

Figure 16. Influence of both positive and negative electrode tortuosity on the electrical cell behavior during a 0 V short circuit event for the BA loading at at an initial cell voltage of 4.15 V and 25°C as a function of short circuit duration t_{sc} (a and b) and as a function of normalized discharged capacity ΔSoC (c) for the C-rate (a and c) and ΔSoC (b). Markers indicate 0% SoC.

large active material particles. In order to evaluate the effect of a cell's energy and power characteristics on its short circuit behavior, the influence of electrode morphology is studied in more detail taking the BA loading as a reference.

Based on the Bruggeman relation, a lower porosity results in a higher tortuosity, thus reducing the effective ionic conductivity $\kappa_{l,\,eff}$ and the effective salt diffusion coefficient $D_{l,\,eff}$ (see Table AI in the appendix). Keeping the active material volume fraction ϵ_s constant in order to not alter the electrode loading, Archie's exponent[90] $(1+\alpha_B)$ within both negative and positive electrode is varied from −50% to +50% as can be seen in Fig. 16. Supporting the observations made from applying different concentration dependent liquid phase transport properties as shown in Fig. 15, primarily the level of plateau IIa is affected by this variation, shifting the beginning of plateau IIb toward earlier or later times for lower or higher tortuosities, respectively. As already observed for varying $LiPF_6$ based electrolytes in Fig. 15, the level of plateau IIb is not influenced by the liquid phase, which implies that cells comprising electrodes with a high tortuosity show a similarly decelerated short circuit behavior as cells which are filled with an electrolyte exhibiting inferior transport properties. Vice versa, cells comprising electrodes with a low tortuosity will show an accelerated short circuit behavior which also becomes apparent throughout plateau I. This observation underlines the importance of effective liquid phase transport properties defining a cell's behavior in the beginning of an external short circuit especially throughout plateau IIa.

With varying the size of both negative and positive active material particles (see Fig. 17), a different behavior can be observed compared to a variation or a scaling of liquid phase transport properties (see Fig. 15 and Fig. 16). Due to the related altered specific surface area within both electrodes, not only the level of plateau I is affected, but also the level of plateau II as a whole is raised or decreased with smaller or larger active material particles, respectively. This becomes especially apparent when looking into the amount of charge withdrawn throughout each plateau IIa and IIb (see Fig. 17c). Plateau IIa varies in a similar fashion as observed for a variation or a scaling of liquid phase transport properties (see Fig. 15c and Fig. 16c). Whilst the predicted level of plateau IIb is unaffected by the liquid phase, it changes with particle size. Reducing the particle size by as much as −50% results in a plateau II which is dominated by phase IIa characterized by a reaction limitation within the positive electrode based on mass transport within both liquid and solid phase. In contrast, increasing the particle size

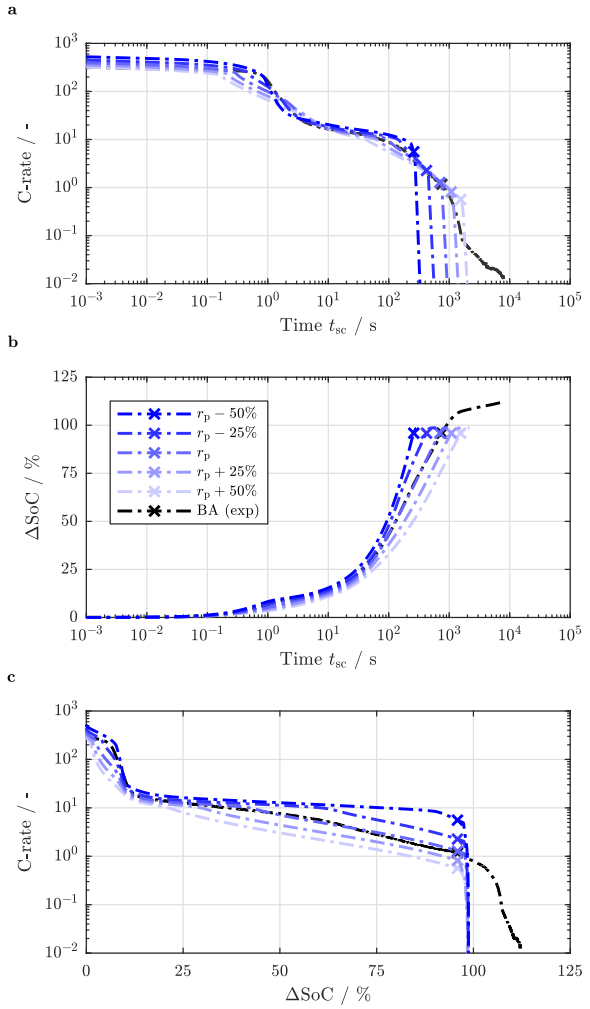

Figure 17. Influence of both positive and negative electrode active material particle size on the electrical cell behavior during a 0 V short circuit event for the BA loading at at an initial cell voltage of 4.15 V and 25°C as a function of short circuit duration t_{sc} (a to d), as a function of normalized discharged capacity ΔSoC (e), and as a function of area specific capacity (f) for the C-rate (a and e), cell current density (b and f), ΔSoC (c), and area specific capacity (d). Markers indicate 0% SoC.

by as much as +50% results in a plateau II which is dominated by phase IIb characterized by a reaction limitation within the positive electrode solely based on mass transport within the solid phase. This variation in dominating mechanisms also affects the amount of time until the cell is completely discharged (see Fig. 17b), which is not the case for a variation or a scaling of liquid phase transport properties (see Fig. 15b and Fig. 16b). This implies that cells comprising large active material particles resulting in a small specific surface area not only increases the share of plateau IIb in plateau II but also reduces the overall level of both plateaus resulting in a slower discharge and, hence, a longer duration until the entire electrical energy is withdrawn from the cell. Analogously, by reducing the particle size, the short circuit is accelerated resulting in a faster discharge and, consequently, faster heat up throughout the entire short circuit.

Lastly, keeping Bruggeman's and, hence, Archie's exponent as well as the active material particle radius constant within both electrodes whilst altering the volume fraction of the solid phase ϵ_s at the expense of porosity ϵ_l, again a slightly different behavior can be observed (see Fig. 18). With the level in C-rate throughout plateau IIb being strongly dependent on the particle radius (see Fig. 17c), it is unaffected by the electrode loading (see Fig. 18e). Reducing the porosity by densifying the electrodes in order to achieve higher electrode loadings at a constant coating thickness, the cell's energy density generally increases. Coming with a reduced porosity, the tortuosity is increased (see Table II) mainly affecting plateau IIa in C-rate. Furthermore, the increased volume fraction of the solid phase also scales the specific surface area available for reaction (see Table AI). Even though the specific surface area is increasing with a reduced porosity which should result in a larger C-rate for higher electrode loadings especially in plateau I (see Fig. 17a), the liquid phase and the associated scaled transport properties are dominating the behavior (see Fig. 18a). Reducing the electrode loading at a constant coating thickness by as much as −50% results in a dominating plateau IIb throughout almost the entire short circuit duration skipping plateau IIa which sets kind of a limit to the dynamics of the short circuit based on the employed active materials (see Fig. 18e). By increasing the electrode loading by as much as +50%, plateau IIa is dominating instead resulting in a suppression of plateau IIb. The lack of plateau IIb results in a strongly decelerated short circuit behavior throughout the entire duration of the short circuit implying a slower release of the stored specific electrical and, hence, thermal energy (see Fig. 18c). This does not only account for the C-rate and ΔSoC but also for the cell current density i_{sc} (mA cm^{-2}) and area specific discharged capacity C_{sc}/A (mA cm^{-2}) as shown on the right of Figs. 18b,18d, and 18f. This behavior is differing from the observed characteristics of the HP, BA, and HE loading which show the same sequence of plateaus unaffected by the area specific capacity (compare Fig. 18c to Fig. 3c). This effect can be explained by the applied strongly varying porosities (ca. 75% to 25% for −50% to +50% in capacity) based on the altered volume fractions of the active materials affecting electrode tortuosity, whilst fairly constant porosities and solid phase volume fractions were observed for the HP, BA, and, HE loading mainly varying in coating thickness (see Table II).

This sensitivity analysis underlines the importance of electrochemically engineered electrodes and cells that may allow for designing Li-ion cells which, on the one hand, comply with the energy and power characteristics required by a given application and, on the other hand, show a maximized level of safety during short circuit events. The complex interplay between transport properties within the cell's solid an liquid components and the morphology of the electrodes and separator, however, needs to be thoroughly evaluated to achieve this task.

By adapting the model parameters, not only the impact of different electrode morphologies and electrolytes can be described, but also different active materials such as the increasingly prominent combination of silicon-graphite compounds and nickel-rich layered oxides can be investigated in terms of the short circuit characteristics.[91] By further combining the presented p2D physical-chemical model with an electrical model describing the potential and current density distribution within the current collectors[72,92] as well a thermal model accounting for a temperature distribution within the cell's jelly roll or electrode stack,[91,92] also large-format Li-ion cells can be described during short circuit events. Such a combined modeling approach might help to identify critical short circuit conditions, which could result in the occurrence of thermal decomposition reactions and ultimately thermal runaway at a certain combination of temperature and SoC reached throughout the short circuit.[64] This information could be further used to design cells and electrodes depending on the topology of the battery pack with its inherent thermal management system in order to maximize the short circuit tolerance of the entire battery system.

Conclusions

Within this work, experimental data from quasi-isothermal external short circuit tests applied to single-layered pouch-type Li-ion cells with graphite anodes and NMC-111 cathodes published in the first part of this combined work was used to validate a well-known physical-chemical model at very high currents. Based on this validated model, the underlying mechanisms occurring within the electrodes and separator during external short circuit tests were evaluated. The impact of

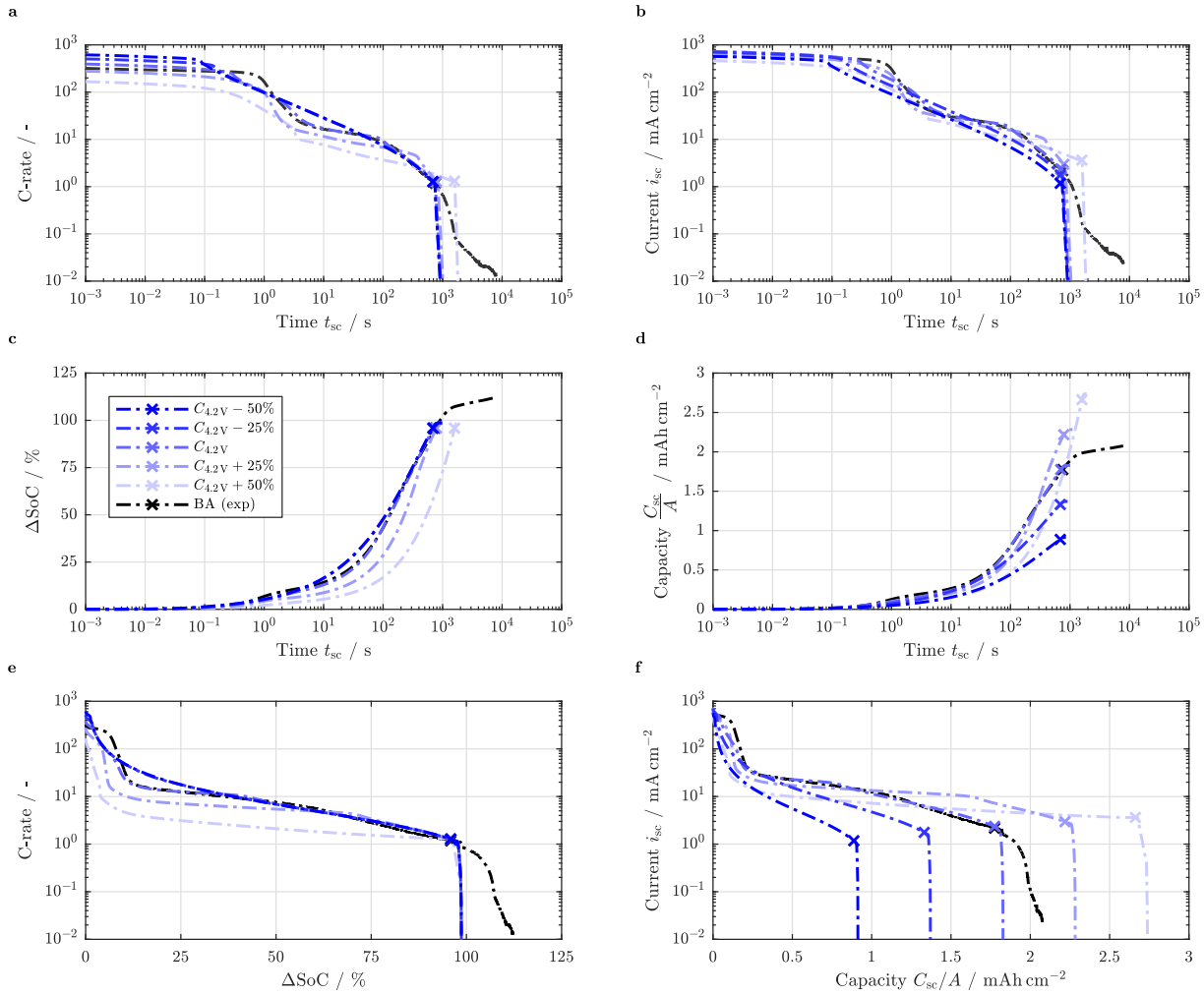

Figure 18. Influence of both positive and negative electrode loading at a constant coating thickness on the electrical cell behavior during a 0 V short circuit event for the BA loading at an initial cell voltage of 4.15 V and 25°C as a function of short circuit duration t_{sc} (a and b) and as a function of normalized discharged capacity ΔSoC (c) for the C-rate (a and c) and ΔSoC (b). Markers indicate 0% SoC.

transport properties reported in literature for both the liquid electrolyte and the solid active material particles was studied by means of a sensitivity analysis which was concluded by considerations on the effect of a cell's energy and power characteristics on its short circuit dynamics.

In order to guarantee a smooth calculation of the cell's short circuit behavior when using a commercial solver, a previously suggested modification of the Butler-Volmer equation based on a diffusion limitation within the liquid electrolyte was evaluated and extended by accounting for an additional solid phase diffusion limitation within both the negative and positive electrode. By means of this slight modification, applying liquid phase transport properties which depend on the local salt concentration and temperature, combined with effective solid phase diffusion coefficients depending solely on stoichiometry or electrode balancing as well as temperature, can reproduce the electrical and thermal short circuit behavior of a cell very well, with only minor discrepancies at the very beginning of a short circuit.

The three distinct plateaus which can be observed in a double-logarithmic representation of the short circuit current and heat generation rate as a function of time were correlated to the model-predicted underlying Li-ion concentration distribution throughout the electrodes as well as electrolyte and separator. Each of the three plateaus is characterized by distinct transport limitations within the solid and/or liquid phase within both electrodes which affect reaction kinetics and define the level in current and heat generation rate of each plateau. Accompanied with the analysis of the concentration distribution at distinct positions along the electrodes and separator, the cell polarization based on ohmic and diffusion related effects as well as reaction kinetics was calculated and shown to agree with previously published findings. Whilst the first plateau is characterized by comparably large ohmic losses within the liquid electrolyte accompanied with very large currents as well as a reaction limitation within the negative electrode, the second plateau is based on a distinct limitation in mass transport within the liquid and/or solid phase increasing the reaction overpotential in the positive electrode. In an SoC based representation of the short circuit behavior, the second plateau can be further divided into two parts, with the second part shown to be dominated by solid phase diffusion within the positive electrode allowing to determine effective solid phase diffusion coefficients. The previously stated theory[12] that the experimentally observed third and last plateau can be partially attributed to an anodic dissolution reaction of the copper current collector within the negative electrode, was supported by simulated anode potentials exceeding 3.1 V vs. Li/Li$^+$ at the end of the discharge.

The observed minor discrepancies between predicted and measured cell behavior at the very beginning of the short circuit could be ruled out by applying solid phase diffusion coefficients within both the negative and positive electrode depending on the local

Li-ion concentration within the active material particles. However, the exact dependency of the solid phase diffusion coefficients on Li-ion concentration needs to be known to also be able to properly describe the cell's behavior during the second plateau which is dominating the electrical and thermal short circuit behavior of the investigated cells.

Similar to varying liquid phase transport properties reported in literature for electrolytes based on $LiPF_6$ and organic solvents, the tortuosity scaling the ionic conductivity and salt diffusion coefficient mainly affects the first part of the second plateau with lower currents and heat generation rates for electrolytes showing inferior transport properties or electrodes with a high tortuosity. Increasing the size of the active material particles, the current and heat generation rate throughout the second part of the second plateau is reduced. By further increasing the electrode loading whilst keeping the coating thickness constant at the expense of porosity, resulting in a higher energy density of the cell, the level of the first part of the second plateau is reduced whilst its share throughout the second plateau is increased. Varying the electrode loading by increasing the coating thickness whilst keeping the electrode morphology constant affects the level of the first and second plateau as a whole whilst the ratio between the first part and the second part of the second plateau is unchanged.

These observations support the assumption that cells which can be characterized as high energy with thick and/or dense electrodes as well as large active material particles will result in a decelerated short circuit behavior compared to cells which can be described high power with thin and/or highly porous electrodes as well as small active material particles. Combining simulation studies with experiments ranging from normal operation to high performance and abusive scenarios may allow for designing electrodes and cells with a high energy density which can deliver the required rate capability at a maximum level of safety. This combined approach should be further investigated by experimentally validated modeling and simulation investigating not only the rate capability of materials, electrodes, and cells from normal to abusive conditions but also studying the thermal stability of the used components as well as the heat generated during operation. With such a validated model describing both the electrical and thermal safety characteristics for a combination of materials and electrodes, a truly conclusive electrode and cell design study can be carried out. Furthermore, the methodology presented within this combined work should be extended toward quasi-isothermal internal short circuit tests which will be the subject of future work.

Appendix

In order to be able to reproduce the simulation results presented in this work, the underlying model equations of the applied p2D model as well as parameters describing both liquid and solid phase are summarized.

Model equations.—In Table AI, an overview of main variables describing the Li-ion concentration c (mol m^{-3}) and the potential Φ vs. Li/Li$^+$ (V) of both liquid (l) and solid phase (s) associated with each computational domain is given. Furthermore, governing

Table AI. Main variables, governing partial differential equations, and additional analytic expressions solved within each domain of the p2D physical-chemical model as well as prevailing boundary and initial conditions.

Description	Negative electrode (neg) Graphite	Separator (sep) Polyolefin	Positive electrode (pos) NMC-111
Variables	$c_l(x,t)$, $c_s(x,r,t)$, $\Phi_l(x,t)$, $\Phi_s(x,t)$ $x \in [0; l_{neg}]$ $r \in [0; r_{p,neg}]$	$c_l(x,t)$, $\Phi_l(x,t)$ $x \in [l_{neg}; l_{neg}+l_{sep}]$	$c_l(x,t)$, $c_s(x,r,t)$, $\Phi_l(x,t)$, $\Phi_s(x,t)$ $x \in [l_{neg}+l_{sep}; l_{neg}+l_{sep}+l_{pos}]$ $r \in [0; r_{p,pos}]$
Governing partial differential equations			
Mass balance (liquid)	$\epsilon_{l,neg}\frac{\partial c_l}{\partial t} = \nabla(D_{l,eff}\nabla c_l) - \nabla\left(\frac{\mathbf{i}_l(1-t_+)}{F}\right)$	$\epsilon_{l,sep}\frac{\partial c_l}{\partial t} = \nabla(D_{l,eff}\nabla c_l)$	$\epsilon_{l,pos}\frac{\partial c_l}{\partial t} = \nabla(D_{l,eff}\nabla c_l) - \nabla\left(\frac{\mathbf{i}_l(1-t_+)}{F}\right)$
Mass balance (solid)	$\frac{\partial c_s}{\partial t} = \frac{1}{r^2}\frac{\partial}{\partial r}\left(D_{s,neg}r^2\frac{\partial c_s}{\partial r}\right)$	n/a	$\frac{\partial c_s}{\partial t} = \frac{1}{r^2}\frac{\partial}{\partial r}\left(D_{s,pos}r^2\frac{\partial c_s}{\partial r}\right)$
Ohm's law (liquid)	$\mathbf{i}_l = -\kappa_{l,eff}\nabla\Phi_l + \frac{2\kappa_{l,eff}RT}{F}(1-t_+)\left(1+\frac{\partial \ln f_\pm}{\partial \ln c_l}\right)\nabla \ln c_l$		
Ohm's law (solid)	$\mathbf{i}_s = -\sigma_{s,eff}\nabla\Phi_s$	n/a	$\mathbf{i}_s = -\sigma_{s,eff}\nabla\Phi_s$
Charge balance	$\nabla\mathbf{i}_l = -\nabla\mathbf{i}_s = \frac{3\epsilon_{s,neg}}{r_{p,neg}}i_n$	$\nabla\mathbf{i}_l = 0$	$\nabla\mathbf{i}_l = -\nabla\mathbf{i}_s = \frac{3\epsilon_{s,pos}}{r_{p,pos}}i_n$
Additional analytic expressions			
Ionic diffusivity	$D_{l,eff} = \frac{\epsilon_{l,neg}}{\tau_{neg}}D_l$	$D_{l,eff} = \frac{\epsilon_{l,sep}}{\tau_{sep}}D_l$	$D_{l,eff} = \frac{\epsilon_{l,pos}}{\tau_{pos}}D_l$
Ionic conductivity	$\kappa_{l,eff} = \frac{\epsilon_{l,neg}}{\tau_{neg}}\kappa_l$	$\kappa_{l,eff} = \frac{\epsilon_{l,sep}}{\tau_{sep}}\kappa_l$	$\kappa_{l,eff} = \frac{\epsilon_{l,pos}}{\tau_{pos}}\kappa_l$
Electronic conductivity	$\sigma_{s,eff} = \epsilon_{s,neg}\sigma_{s,neg}$	n/a	$\sigma_{s,eff} = \epsilon_{s,pos}\sigma_{s,pos}$
Reaction kinetics	$i_n = \frac{i_0\left[\exp\left(\frac{\alpha_a F}{RT}\eta\right) - \exp\left(\frac{\alpha_c F}{RT}\eta\right)\right]}{1+\frac{c_{s,lim}}{\Delta c_s}\exp\left(\frac{\alpha_a F}{RT}\eta\right)}$	n/a	$i_n = \frac{i_0\left[\exp\left(\frac{\alpha_a F}{RT}\eta\right) - \exp\left(\frac{\alpha_c F}{RT}\eta\right)\right]}{1+\left(\frac{c_{l,lim}}{\Delta c_l}+\frac{c_{s,lim}}{\Delta c_s}\right)\exp\left(\frac{\alpha_c F}{RT}\eta\right)}$
Exchange current density	$i_0 = Fk_{neg}\left(\frac{c_l}{c_{l,ref}}\right)^{\alpha_a}(c_{s,max,neg}-c_{s,surf})^{\alpha_a}(c_{s,surf})^{\alpha_c}$	n/a	$i_0 = Fk_{pos}\left(\frac{c_l}{c_{l,ref}}\right)^{\alpha_a}(c_{s,max,pos}-c_{s,surf})^{\alpha_a}(c_{s,surf})^{\alpha_c}$
Reaction overpotential	$\eta = \Phi_s - \Phi_l - \Delta\Phi_{s,film} - E_{eq,neg}$	n/a	$\eta = \Phi_s - \Phi_l - E_{eq,pos}$
Boundary conditions[*]			
Species 2nd (liquid)	$\nabla c_l\|_{x=0} = 0$	n/a	$\nabla c_l\|_{x=l_{neg}+l_{sep}+l_{pos}} = 0$
Species 2nd (solid)	$\frac{\partial c_s}{\partial r}\Big\|_{r=0} = 0 \quad \frac{\partial c_s}{\partial r}\Big\|_{r=r_{p,neg}} = -\frac{i_n}{FD_{s,neg}}$	n/a	$\frac{\partial c_s}{\partial r}\Big\|_{r=0} = 0 \quad \frac{\partial c_s}{\partial r}\Big\|_{r=r_{p,pos}} = -\frac{i_n}{FD_{s,pos}}$
Potential 2nd (liquid)	$\nabla\Phi_l\|_{x=0} = 0$	n/a	$\nabla\Phi_l\|_{x=l_{neg}+l_{sep}+l_{pos}} = 0$
Potential 1st (solid)	$\Phi_s\|_{x=0} = 0$	n/a	[**] $\Phi_s\|_{x=l_{neg}+l_{sep}+l_{pos}} = 10^{-6}$ V
Potential 2nd (solid)	$\nabla\Phi_s\|_{x=l_{neg}} = 0$	n/a	$\nabla\Phi_s\|_{x=l_{neg}+l_{sep}} = 0$ [**] $\nabla\Phi_s\|_{x=l_{neg}+l_{sep}+l_{pos}} = -\frac{E_{cell}}{R_{ext}\sigma_{s,eff}}$
Initial conditions			
Species (liquid)		$c_l(x,t=0) = c_{l,0}$	
Species (solid)	$c_s(x,r,t=0) = c_{s,0,neg}$	n/a	$c_s(x,r,t=0) = c_{s,0,pos}$
Potential (liquid)		$\Phi_l(x,t=0) = -E_{eq,neg}$	
Potential (solid)	$\Phi_s(x,t=0) = 0$		$\Phi_s(x,t=0) = E_{eq,pos} - E_{eq,neg}$

[*] indicated as first (Dirichlet) and second order (Neumann) boundary conditions.
[**] alternatively used for constant voltage (Dirichlet) and constant resistance (Neumann) short circuit conditions.

Table AII. Equation overview for calculating the overall polarization within each domain of the p2D physical-chemical model based on mass and charge transport as well as reaction kinetics.

Description	Symbol	Negative electrode (neg) Graphite	Separator (sep) Polyolefin	Positive electrode (pos) NMC-111
Definitions				
Bounds of integration	l_1	l_{neg}	$l_{neg}+l_{sep}$	$l_{neg}+l_{sep}+l_{pos}$
	l_0	0	l_{neg}	$l_{neg}+l_{sep}$
Specific surface	a	$\frac{3\epsilon_{s,\,neg}}{r_{p,\,neg}}$	n/a	$\frac{3\epsilon_{s,\,pos}}{r_{p,\,pos}}$
Total current	i_{tot}	$\int_{l_0}^{l_1}(ai_n)\,dx$	n/a*	$\int_{l_0}^{l_1}(ai_n)\,dx$
Polarization expressions				
Diffusion polarization (liquid)	$\Delta E_{D,\,l}$	$-\frac{1}{i_{tot}}\int_{l_0}^{l_1}\left(\mathbf{i}_l\frac{2RT}{F}(1-t_+)\left(1+\frac{\partial\ln f_{\pm}}{\partial\ln c_l}\right)\nabla\ln c_l\right)dx$		
Diffusion polarization (solid)	$\Delta E_{D,\,s}$	$\frac{1}{i_{tot}}\int_{l_0}^{l_1}\left(ai_n\left(E_{eq,\,neg}-E_{eq,\,neg,\,ave}\right)\right)dx$	n/a	$\frac{1}{i_{tot}}\int_{l_0}^{l_1}\left(ai_n\left(E_{eq,\,pos}-E_{eq,\,pos,\,ave}\right)\right)dx$
Ohmic losses (liquid)	$\Delta E_{\Omega,\,l}$	$\frac{1}{i_{tot}}\int_{l_0}^{l_1}\left(\frac{\mathbf{i}_l^2}{\kappa_{l,\,eff}}\right)dx$		
Ohmic losses (solid)	$\Delta E_{\Omega,\,s}$	$\frac{1}{i_{tot}}\int_{l_0}^{l_1}\left(\frac{\mathbf{i}_s^2}{\sigma_{s,\,eff}}\right)dx$	n/a	$\frac{1}{i_{tot}}\int_{l_0}^{l_1}\left(\frac{\mathbf{i}_s^2}{\sigma_{s,\,eff}}\right)dx$
Reaction overpotential	ΔE_{BV}	$\frac{1}{i_{tot}}\int_{l_0}^{l_1}\left(ai_n\left(\Phi_s-\Phi_l-E_{eq,\,neg}\right)\right)dx$	n/a	$\frac{1}{i_{tot}}\int_{l_0}^{l_1}\left(ai_n\left(\Phi_s-\Phi_l-E_{eq,\,pos}\right)\right)dx$
Overall polarization	$\sum\Delta E$	$\Delta E_{D,\,l}+\Delta E_{D,\,s}+\Delta E_{\Omega,\,l}+\Delta E_{\Omega,\,s}+\Delta E_{BV}$	$\Delta E_{D,\,l}+\Delta E_{\Omega,\,l}$	$\Delta E_{D,\,l}+\Delta E_{D,\,s}+\Delta E_{\Omega,\,l}+\Delta E_{\Omega,\,s}+\Delta E_{BV}$

*calculated total current within the positive electrode is used.

partial differential equations describing both mass and charge transport throughout the negative (neg) and positive electrode (pos) as well as the separator (sep) whilst accounting for a charge balance between both solid and liquid components are summarized. Together with additional analytical expressions describing effective transport parameters and reaction kinetics as well as the presented boundary and initial conditions, the model is fully described.

In order to evaluate the contribution of each underlying mechanism to the total polarization of the cell ΔE_{cell} (V), each individual voltage loss is calculated according to Nyman et al.[26] following the work of Rao and Newman[69] within all three domains as shown in Table AII. Based on the contribution of diffusion related losses (D) and ohmic losses (Ω) within the solid and liquid components of the cell as well as overpotentials associated with Butler-Volmer reaction kinetics (BV), the overall polarization $\sum\Delta E$ (V) within each electrode as well as the voltage drop across the separator can be calculated. Hence, the total polarization ΔE_{cell} occurring within the cell can be determined via[75]

$$\Delta E_{cell} = -\sum\Delta E_{neg}+\sum\Delta E_{sep}+\sum\Delta E_{pos} \quad [A1]$$

Essentially, ΔE_{cell} can be further calculated as[75]

$$\Delta E_{cell} = E_{cell}-E_{eq,\,cell,\,ave} = \Phi_s|_{l_{1,\,pos}}-\Phi_s|_{l_{0,\,neg}}+ -\frac{1}{i_{tot,\,pos}}\int_{l_{0,\,pos}}^{l_{1,\,pos}}\left(a_{pos}\,i_n\,E_{eq,\,pos,\,ave}\right)dx+ +\frac{1}{i_{tot,\,neg}}\int_{l_{0,\,neg}}^{l_{1,\,neg}}\left(a_{neg}\,i_n\,E_{eq,\,neg,\,ave}\right)dx \quad [A2]$$

with the average equilibrium potentials $E_{eq,\,neg,\,ave}$ and $E_{eq,\,pos,\,ave}$ vs. Li/Li$^+$ (V) occurring after an infinitely long relaxation period being a function of the average concentration within the active material particles $c_{s,\,ave}$. In contrast, the equilibrium potentials characterizing the reaction site $E_{eq,\,neg}$ and $E_{eq,\,pos}$ vs. Li/Li$^+$ are defined by the surface concentration of the active material particles $c_{s,\,surf}$. Both equations shown in Eq. A1 and Eq. A2 come to the same result which underlines the plausibility of the polarization expressions stated by Nyman et al.[75] even at very high currents.

Based on irreversible and reversible contributions neglecting heat of mixing effects,[34,68,69,93] the overall heat generation rate $\dot{q}_{cell}$ (W m^{-2}) can be approximated via

$$\dot{q}_{cell} = \dot{q}_{irrev,\,cell}+\dot{q}_{rev,\,cell} = \left(\dot{q}_{irrev,\,neg}+\dot{q}_{irrev,\,sep}+\dot{q}_{irrev,\,pos}\right)+\left(\dot{q}_{rev,\,neg}+\dot{q}_{rev,\,pos}\right) \quad [A3]$$

Together with the cell current density i_{cell} (A m^{-2}) as shown in Table AII

$$i_{cell} = i_{tot,\,pos} = -i_{tot,\,neg} \quad [A4]$$

the irreversible heat generation rate within the cell $\dot{q}_{irrev,\,cell}$ calculates as

$$\dot{q}_{irrev,\,cell} = i_{cell}\,\Delta E_{cell} = i_{cell}\,E_{cell}-\int_{l_{0,\,neg}}^{l_{1,\,neg}}\left(a_{neg}\,i_n\,E_{eq,\,neg,\,ave}\right)dx+ -\int_{l_{0,\,pos}}^{l_{1,\,pos}}\left(a_{pos}\,i_n\,E_{eq,\,pos,\,ave}\right)dx \quad [A5]$$

whereas the overall reversible heat generation rate $\dot{q}_{rev,\,cell}$ is estimated via

$$\dot{q}_{rev,\,cell} = \int_{l_{0,\,neg}}^{l_{1,\,neg}}\left(a_{neg}\,i_n\,T\,\frac{dE_{eq,\,neg,\,ave}}{dT}\right)dx+\int_{l_{0,\,pos}}^{l_{1,\,pos}}\left(a_{pos}\,i_n\,T\,\frac{dE_{eq,\,pos,\,ave}}{dT}\right)dx \quad [A6]$$

with the entropic coefficients $\frac{dE_{eq,\,neg,\,ave}}{dT}$ and $\frac{dE_{eq,\,pos,\,ave}}{dT}$ (V K^{-1}) of the negative and positive active materials which results in the often cited form[68]

$$\dot{q}_{cell} = \left[i_{cell}\,E_{cell}-\left(\int_{l_{0,\,neg}}^{l_{1,\,neg}}\left(a_{neg}\,i_n\,E_{eq,\,neg,\,ave}\right)dx+\int_{l_{0,\,pos}}^{l_{1,\,pos}}\left(a_{pos}\,i_n\,E_{eq,\,pos,\,ave}\right)dx\right)\right]+ +\left(\int_{l_{0,\,neg}}^{l_{1,\,neg}}\left(a_{neg}\,i_n\,T\,\frac{dE_{eq,\,neg,\,ave}}{dT}\right)dx+\int_{l_{0,\,pos}}^{l_{1,\,pos}}\left(a_{pos}\,i_n\,T\,\frac{dE_{eq,\,pos,\,ave}}{dT}\right)dx\right) \quad [A7]$$

Pre-studies have shown that despite the large currents, the contribution of heat of mixing effects within the active material particles approximated in accordance with Thomas and Newman[93] is ranging below the contribution of entropy related effects throughout the short circuit which is why it is not considered here.

Within this work, $\dot{q}_{sc} = \dot{q}_{tot}$ and $i_{sc} = -i_{cell}$. Together with the electrode area A of the experimentally investigated pouch-type cells (ca. 31 mm × 56 mm), the overall heat generation rate $\dot{Q}_{sc}$ (W) and short circuit current I_{sc} (A) can be calculated.

Solid phase parameters.—Applied half-cell potentials derived from averaging between lithiation and delithiation during a C/50 constant current operation are shown in Fig. A1a and A1b for the negative and positive electrode. The entropic coefficient of Li$_x$C was taken from experimental data reported by Reynier et al.[70] directly measuring the variation of the half-cell potential vs. Li/Li$^+$ with temperature. The entropic coefficient $\frac{dE_{eq,\,neg}}{dT}$ (V K^{-1}) was fitted according to Eq. A8 as a function of degree of lithiation x which is shown in Fig. A1c (solid line) together with the underlying experimental data (markers).

$$\frac{dE_{eq,\,neg}}{dT} = \frac{-3.8149\times10^{-4}x^5+1.058\times10^{-3}x^4-1.1235\times10^{-3}x^3+5.5727\times10^{-4}x^2-1.242\times10^{-4}x+9.0095\times10^{-6}}{x^5-2.9967x^4+3.2192x^3-1.4066x^2+1.8475\times10^{-1}x+1.3198\times10^{-2}} \quad [A8]$$

Similarly, experimental data gained from isothermal microcalorimetry reported by Lu et al.[71] was used for describing the entropic coefficient of Li$_y$Ni$_{1/3}$Co$_{1/3}$Mn$_{1/3}$O$_2$. The entropic coefficient $\frac{dE_{eq,\,pos}}{dT}$ (V K^{-1}) was fitted according to Eq. A9 as a function of degree of lithiation y which is shown in Fig. A1d (solid line) together with the underlying experimental data (markers).

$$\frac{dE_{eq,\,pos}}{dT} = \frac{-2.445\times10^{-3}y^2+3.4961\times10^{-3}y-1.4125\times10^{-3}}{y^2-2.7564y+3.9766} \quad [A9]$$

To describe a solid phase diffusion within the active material particles depending on a diffusion coefficient varying with Li-ion concentration along the pseudo-dimension r, experimental work of Levi and Aurbach[77] as well as Wu et al.[27] were used for Li$_x$C

Table AIII. Fitting functions for liquid phase transport properties based on electrolyte salt concentration c_l (mol m^{-3}) and temperature T (K).

Equation / Parameter	Valøen and Reimers[73] PC:EC:DMC 10:27:63 (vol:vol:vol)	Mao et al.[34] EC:DMC 1:1 (n/a:n/a)	Dees et al.[74] EC:EMC 3:7 (wt:wt)	Nyman et al.[75] EC:EMC 3:7 (wt:wt)	Lundgren et al.[76] EC:DEC 1:1 (wt:wt)
Ionic conductivity κ_l (S m^{-1})					
$\kappa_l = k_1 \cdot \left(\frac{c_l}{k_2}\right)^{(k_3-1)} \cdot \exp\left(-\left(\frac{c_l}{k_2}\right)^{k_3}\right)$ with $k_i = k_{i1}\exp\left(-\frac{k_{i2}}{T}\right)$					
k_{11}	4.7557×10^{2}	7.2999×10^{2}	9.0924×10^{2}	2.0743×10^{0}	8.9364×10^{2}
k_{12}	1.5570×10^{3}	1.6900×10^{3}	1.8246×10^{3}	0	1.8601×10^{3}
k_{21}	1.1730×10^{4}	2.0500×10^{3}	6.3255×10^{3}	1.6437×10^{3}	1.1258×10^{4}
k_{22}	5.7251×10^{2}	0	3.9753×10^{2}	0	5.9703×10^{2}
k_{31}	1.73	1.73	1.8	1.71	1.71
k_{32}	0	0	0	0	0
Salt diffusion coefficient D_l (m^2 s^{-1}):					
$D_l = d_1 \cdot \exp\left(-d_2 \cdot c_l + \frac{d_3}{d_4 + d_5 \cdot c_l - T}\right)$					
d_1	3.7290×10^{-9}	4.3880×10^{-7}	1.7041×10^{-5}	5.8289×10^{-10}	8.5689×10^{-9}
d_2	5.0646×10^{-4}	6.5000×10^{-4}	1.9023×10^{-4}	1.2626×10^{-3}	1.1645×10^{-3}
d_3	1.2500×10^{2}	2.0000×10^{3}	3.4528×10^{3}	0	8.9000×10^{2}
d_4	2.2879×10^{2}	0	-1.6595×10^{1}	0	0
d_5	5.0051×10^{-3}	0	1.6520×10^{-2}	0	0
Cation transference number t_+:					
$t_+ = t_1 + t_2 \cdot \tanh\left(\frac{c_l - t_3}{t_4}\right) + t_5 \cdot \tanh\left(\frac{c_l - t_6}{t_7}\right)$ with $t_i = t_{i1} \cdot \exp\left(\frac{t_{i2}}{t_{i3} - T}\right)$					
t_{11}	0.38	0.4	1.3742×10^{0}	2.7466×10^{-1}	5.2307×10^{-1}
t_{12}	0	0	3.8936×10^{3}	0	4.7331×10^{-2}
t_{13}	0	0	-3.0559×10^{3}	0	1.0137×10^{0}
t_{21}	0	0	4.9427×10^{-3}	-1.2798×10^{-1}	8.6228×10^{0}
t_{22}	0	0	-3.0545×10^{3}	0	0
t_{23}	0	0	-1.0117×10^{3}	0	0
t_{31}	0	0	-1.7559×10^{3}	1.9687×10^{3}	1.9319×10^{3}
t_{32}	0	0	1.7984×10^{2}	0	3.7635×10^{2}
t_{33}	0	0	1.9686×10^{2}	0	1.0734×10^{2}
t_{41}	0	0	5.3158×10^{3}	4.2195×10^{2}	9.3645×10^{2}
t_{42}	0	0	2.4728×10^{2}	0	1.4192×101
t_{43}	0	0	5.3978×10^{1}	0	2.3004×10^{2}
t_{51}	0	0	0	-1.4669×10^{-1}	-9.1458×10^{0}
t_{52}	0	0	0	0	0
t_{53}	0	0	0	0	0
t_{61}	0	0	0	9.5080×10^{1}	1.9067×10^{3}
t_{62}	0	0	0	0	3.7232×10^{2}
t_{63}	0	0	0	0	1.1446×10^{2}
t_{71}	0	0	0	4.6829×10^{2}	9.7011×10^{2}
t_{72}	0	0	0	0	1.5087×10^{1}
t_{73}	0	0	0	0	2.2748×10^{2}
Thermodynamic factor TDF:					
$(1-t_+) \cdot \mathrm{TDF} = (1-t_+) \cdot \left(1 + \frac{\partial \ln f_\pm}{\partial \ln c_l}\right) = f_1 \cdot {c_l}^{p_1} + f_2 \cdot {c_l}^{p_2} + f_3$ with $f_i = f_{i1} \cdot \exp\left(\frac{f_{i2}}{f_{i3} - T}\right)$					
p_1	1.5	0	2	2	2
p_2	0.5	0	1	1	1
f_{11}	2.4174×10^{-3}	0.6	2.7539×10^{-7}	2.8687×10^{-7}	7.8994×10^{-6}
f_{12}	-3.3972×10^{3}	0	-3.3210×10^{2}	0	1.0027×10^{3}
f_{13}	1.0732×10^{3}	0	0	0	0
f_{21}	-7.5895×10^{-3}	0	-1.5756×10^{-7}	7.4678×10^{-4}	2.8106×10^{-2}
f_{22}	0	0	-1.8453×10^{3}	0	1.1294×10^{3}
f_{23}	0	0	0	0	0
f_{31}	6.0100×10^{-1}	0	1.7116×10^{-1}	4.4103×10^{-1}	9.2607×10^{-1}
f_{32}	0	0	-2.8316×10^{2}	0	2.1001×10^{2}
f_{33}	0	0	0	0	0

and $Li_yNi_{1/3}Co_{1/3}Mn_{1/3}O_2$, respectively. Whilst Levi and Aurbach[77] carried out measurements based on potentiostatic intermittent titration technique (PITT), Wu et al.[27] performed a model based evaluation of measured cell relaxation related to solid phase diffusion. For the diffusion coefficient of Li_xC used within this work, an averaging between data gained from electrodes declared as "thin" and "ultrathin"[77] was performed whilst for the diffusion coefficient of $Li_yNi_{1/3}Co_{1/3}Mn_{1/3}O_2$, an averaging between the behavior of electrodes with two different particle sizes was carried out during both lithiation and delithiation. The fitted behavior is shown in Figs. A1e and A1f (solid black lines) together with the underlying averaged measurement data (black markers). The corresponding fitting functions of $D_{s,\,neg}$ and $D_{s,\,pos}$ (m^2 s^{-1}) are summarized in

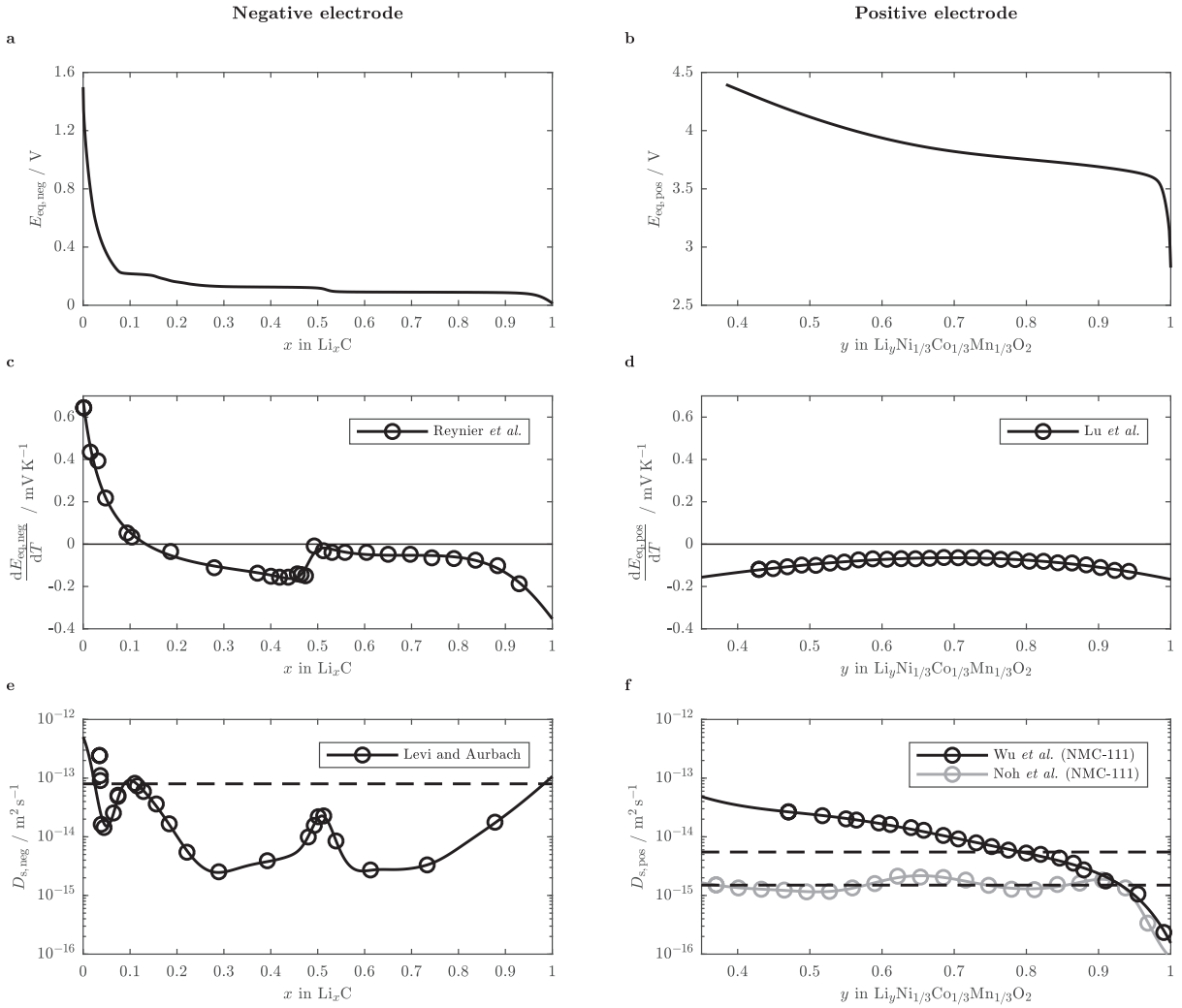

Figure A1. Measured half cell potentials vs. Li/Li$^+$ (top: a and b), fitted entropic coefficients according to experimental data taken from Reynier et al.[70] and Lu et al.[71] (middle: c and d), and fitted Li-ion diffusion coefficients taken from Levi and Aurbach[77] and Wu et al.[27] (bottom: e and f) for the negative (left: a, c, and e) and positive electrode (right: b, d, and f) as a function of degree of lithiation x and y. Markers indicate the considered measurement data. Dashed lines in e and f indicate the used range of effective diffusion coefficients at 25°C. Gray line and markers in f describe reported data from Noh et al.[9] as a comparison.

Eq. A10 and Eq. A11.

$$\begin{aligned}\log_{10} D_{\mathrm{s,\,neg}} = {} & -5.9401{\times}10^{-1}\exp\left(-\left(\frac{x-2.5720{\times}10^{-1}}{8.4006{\times}10^{-2}}\right)^2\right)+\\ & +5.1118{\times}10^{-1}\exp\left(-\left(\frac{x-5.1715{\times}10^{-1}}{1.0308{\times}10^{-1}}\right)^2\right)+\\ & -6.6628{\times}10^{-2}\exp\left(-\left(\frac{x-7.5004{\times}10^{-1}}{6.0470{\times}10^{-2}}\right)^2\right)+\\ & -1.9021{\times}10^{-1}\exp\left(-\left(\frac{x-5.7634{\times}10^{-1}}{4.1183{\times}10^{-2}}\right)^2\right)+\\ & +5.7993{\times}10^{-1}\exp\left(-\left(\frac{x-5.0993{\times}10^{-1}}{3.2647{\times}10^{-2}}\right)^2\right)+\\ & -1.0736{\times}10^{1}\exp\left(-\left(\frac{x-5.5128{\times}10^{-1}}{1.0588}\right)^2\right)+\\ & -1.2463\exp\left(-\left(\frac{x-4.7459{\times}10^{-2}}{3.0551{\times}10^{-2}}\right)^2\right)-4 \end{aligned} \quad [A10]$$

$$\begin{aligned}\log_{10} D_{\mathrm{s,\,pos}} = {} & -1.3922{\times}10^{12}\exp\left(-\left(\frac{y-4.0704}{5.8343{\times}10^{-1}}\right)^2\right)+\\ & -1.4516{\times}10^{1}\exp\left(-\left(\frac{y-1.0490}{1.8016}\right)^2\right)+\\ & -8.6982{\times}10^{-1}\exp\left(-\left(\frac{y-3.0124{\times}10^{-1}}{2.1998{\times}10^{-1}}\right)^2\right) \end{aligned} \quad [A11]$$

Furthermore, the fitted constant diffusion coefficients used within this work for the negative and positive electrode at 25°C are indicated Figs. A1e and A1f (black dashed lines) and compared to other reported data by Noh et al. for Li$_y$Ni$_{1/3}$Co$_{1/3}$Mn$_{1/3}$O$_2$ (gray solid line and markers in Fig. A1f).

Liquid phase parameters.—In order to complete the set of parameters used within this work, properties characterizing the ionic transport within the liquid electrolyte are required. Accompanied with high currents occurring during short circuit scenarios, large salt concentration gradients are likely to form throughout the electrodes and separator. With a reported significant impact of salt concentration on the inherent transport properties of electrolytes based on $LiPF_6$ and organic solvents such as ionic conductivity κ_l[34,73–76]

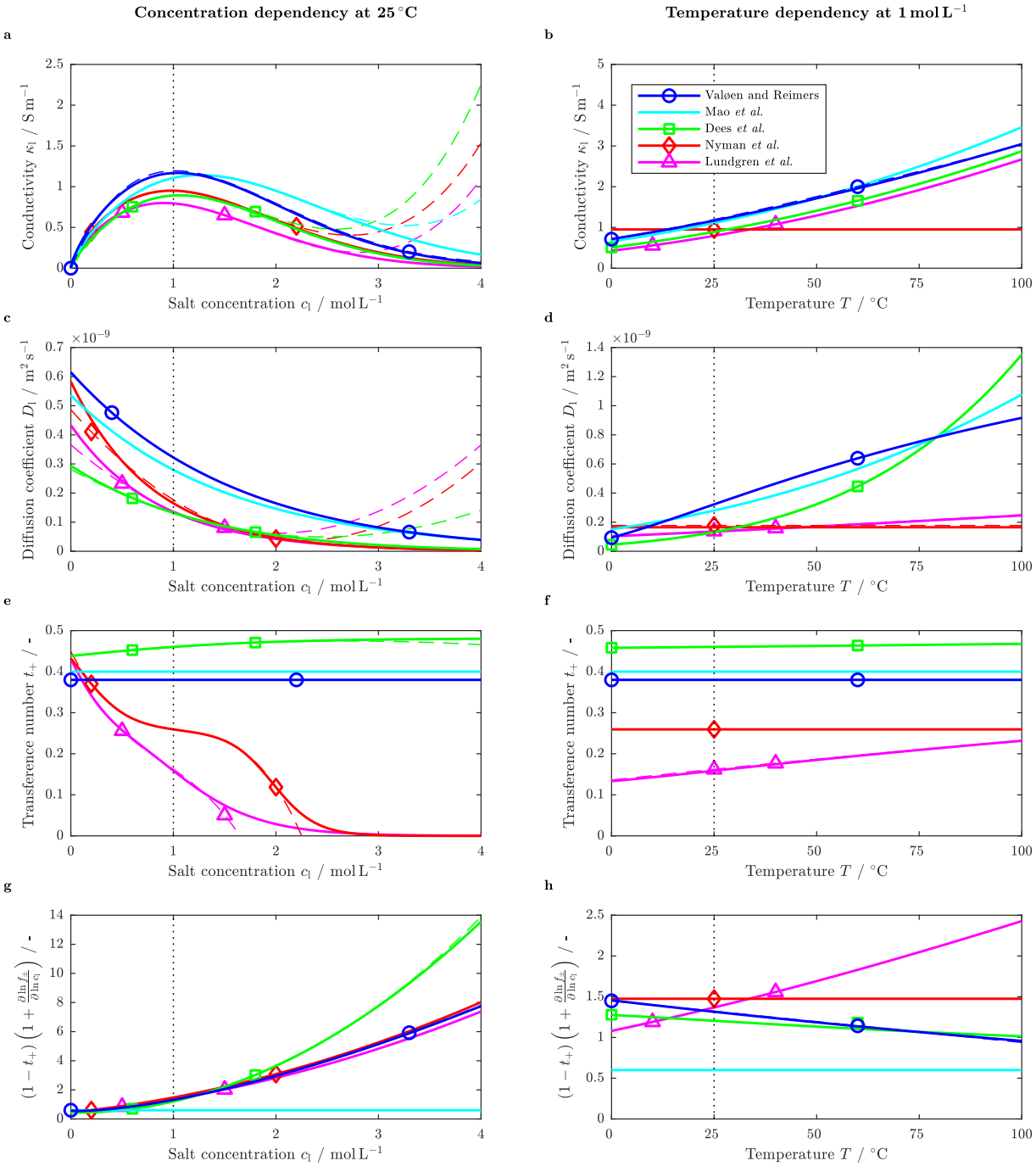

Figure A2. Fitting functions for the ionic conductivity κ_l (a and b), salt diffusion coefficient D_l (c and d), cation transference number t_+ (e and f), and thermodynamic factor TDF (g and h) as a function of the electrolyte's salt concentration c_l at 25°C (left: a, c, e, and g) and as a function of temperature T at 1 mol L^{-1} (right: b, d, f, and h) based on literature from Valøen and Reimers[73] (◯), Mao et al.,[34] Dees et al.[74] (□), Nyman et al.[75] (◊), and Lundgren et al.[76] (△). Markers indicate the considered range of validity.

(S m^{-1}), salt diffusion coefficient D_l[34,73–76] (m^2 s^{-1}), cation transference number t_+ related to the solvent,[74–76] and thermodynamic factor TDF,[73–76] a concentration dependency of these parameters is essential for describing the cell's behavior adequately. Based on the limited concentration range in terms of available data but also in terms of interest for most applications, fitted functions describing transport properties based on salt concentration are often given in a polynomial form which may result e.g. in an increasing κ_l[34,74–76] or D_l[74–76] beyond 3 M, which has not been observed experimentally[73] (see dashed lines in Figs. A2a and A2c). Furthermore, reported fitting functions of decreasing transference numbers[75,76] would even result in negative values at higher concentrations (see dashed lines in Fig. A2e) indicating the presence of negatively-charged clusters dominating ion transport.[94] In order to overcome these issues and to be able to compare the impact of different transport properties on a cell's short circuit behavior at high currents and large concentration gradients, reported fitting functions are re-evaluated and replaced whilst accounting for the reported concentration and temperature dependency.[34,73–76] The adapted

fitting functions are summarized in Table AIII and are shown in Fig. A2 (solid lines) in comparison to the initially reported fitting functions (dashed lines). It is worth stating here, that the initially reported fitting functions for an EC:EMC based electrolyte presented by Dees et al.[74] are based on Gering's advanced electrolyte model.[95] Furthermore, the initially reported fitting functions for both salt diffusion coefficient and transference number of an EC:DEC based electrolyte as discussed by Lundgren et al.[76] are re-evaluated for the temperature range between 25°C and 40°C due to the significantly altered behavior reported at 10°C which differs from the experimental observations made by Valøen and Reimers[73] at lower temperatures.

Acknowledgments

The work presented here was financially supported by the German Federal Ministry of Education and Research (BMBF) under grant number 03XP0027G (*MiBZ*), 03XP0034G (*EffiForm*) and 03XP0081 (*ExZellTUM II*) as well as by the European Union's Horizon 2020 research and innovation program under grant number 713771 (*EVERLASTING*). The authors further thank Marc Steen for his excellent support reviewing this manuscript.

ORCID

Alexander Rheinfeld https://orcid.org/0000-0003-0995-7266
Jörn Wilhelm https://orcid.org/0000-0002-5649-2580
Andreas Jossen https://orcid.org/0000-0003-0964-1405

References

1. N. Nitta, F. Wu, J. T. Lee, and G. Yushin, Li-ion battery materials: present and future, *Materials Today*, **18**, 252 (2015).
2. S. Kosch, A. Rheinfeld, S. V. Erhard, and A. Jossen, An extended polarization model to study the influence of current collector geometry of large-format lithium-ion pouch cells, *Journal of Power Sources*, **342**, 666 (2017).
3. H. Zheng, R. Yang, G. Liu, X. Song, and V. S. Battaglia, Cooperation between Active Material, Polymeric Binder and Conductive Carbon Additive in Lithium Ion Battery Cathode, *The Journal of Physical Chemistry C*, **116**, 4875 (2012).
4. H. Y. Tran, G. Greco, C. Täubert, M. Wohlfahrt-Mehrens, W. Haselrieder, and A. Kwade, Influence of electrode preparation on the electrochemical performance of $LiNi_{0.8}Co_{0.15}Al_{0.05}O_2$composite electrodes for lithium-ion batteries, *Journal of Power Sources*, **210**, 276 (2012).
5. M. Singh, J. Kaiser, and H. Hahn, Thick Electrodes for High Energy Lithium Ion Batteries, *Journal of the Electrochemical Society*, **162**, A1196 (2015).
6. B.-S. Lee, Z. Wu, V. Petrova, X. Xing, H.-D. Lim, H. Liu, and P. Liu, Analysis of Rate-Limiting Factors in Thick Electrodes for Electric Vehicle Applications, *Journal of the Electrochemical Society*, **165**, A525 (2018).
7. C. Campestrini, M. F. Horsche, I. Zilberman, T. Heil, T. Zimmermann, and A. Jossen, Validation and benchmark methods for battery management system functionalities: State of charge estimation algorithms, *Journal of Energy Storage*, **7**, 38 (2016).
8. J. B. Habedank, L. Kraft, A. Rheinfeld, C. Krezdorn, A. Jossen, and M. F. Zaeh, Increasing the Discharge Rate Capability of Lithium-Ion Cells with Laser-Structured Graphite Anodes: Modeling and Simulation, *Journal of the Electrochemical Society*, **165**, A1563 (2018).
9. H.-J. Noh, S. Youn, C. S. Yoon, and Y.-K. Sun, Comparison of the structural and electrochemical properties of layered $Li[Ni_xCo_yMn_z]O_2$(x = 1/3, 0.5, 0.6, 0.7, 0.8 and 0.85) cathode material for lithium-ion batteries, *Journal of Power Sources*, **233**, 121 (2013).
10. S.-M. Bak, K.-W. Nam, W. Chang, X. Yu, E. Hu, S. Hwang, E. A. Stach, K.-B. Kim, K. Y. Chung, and X.-Q. Yang, Correlating Structural Changes and Gas Evolution during the Thermal Decomposition of Charged $Li_xNi_{0.8}Co_{0.15}Al_{0.05}O_2$Cathode Materials, *Chemistry of Materials*, **25**, 337 (2013).
11. L. Ma, M. Nie, J. Xia, and J. R. Dahn, A systematic study on the reactivity of different grades of charged $Li[Ni_xMn_yCo_z]O_2$with electrolyte at elevated temperatures using accelerating rate calorimetry, *Journal of Power Sources*, **327**, 145 (2016).
12. A. Rheinfeld, A. Noel, J. Wilhelm, A. Kriston, A. Pfrang, and A. Jossen, Quasi-Isothermal External Short Circuit Tests Applied to Lithium-Ion Cells: Part I. Measurements, *Journal of The Electrochemical Society*, **165**, A3427 (2018).
13. Y.-S. Park and S.-M. Lee, Effects of particle size on the thermal stability of lithiated graphite anode, *Electrochimica Acta*, **54**, 3339 (2009).
14. J. Geder, H. E. Hoster, A. Jossen, J. Garche, and D. Y. Yu, Impact of active material surface area on thermal stability of $LiCoO_2$ cathode, *Journal of Power Sources*, **257**, 286 (2014).
15. H. Zheng, J. Li, X. Song, G. Liu, and V. S. Battaglia, A comprehensive understanding of electrode thickness effects on the electrochemical performances of Li-ion battery cathodes, *Electrochimica Acta*, **71**, 258 (2012).
16. N. Ogihara, Y. Itou, T. Sasaki, and Y. Takeuchi, Impedance Spectroscopy Characterization of Porous Electrodes under Different Electrode Thickness Using a Symmetric Cell for High-Performance Lithium-Ion Batteries, *The Journal of Physical Chemistry C*, **119**, 4612 (2015).
17. K. J. Lee, W. Bak, J.-J. Kim, M. A. Snyder, W. C. Yoo, and Y.-E. Sung, How Pore Parameters Affect Li Ion Depletion in Mesoporous Materials for Lithium-Ion Batteries, *The Journal of Physical Chemistry C*, **119**, 7604 (2015).
18. K. Kitada, H. Murayama, K. Fukuda, H. Arai, Y. Uchimoto, Z. Ogumi, and E. Matsubara, Factors determining the packing-limitation of active materials in the composite electrode of lithium-ion batteries, *Journal of Power Sources*, **301**, 11 (2016).
19. F. Jiang and P. Peng, Elucidating the Performance Limitations of Lithium-ion Batteries due to Species and Charge Transport through Five Characteristic Parameters, *Scientific reports*, **6**, 32639 (2016).
20. T. Danner, M. Singh, S. Hein, J. Kaiser, H. Hahn, and A. Latz, Thick electrodes for Li-ion batteries: A model based analysis, *Journal of Power Sources*, **334**, 191 (2016).
21. Z. Du, D. L. Wood, C. Daniel, S. Kalnaus, and J. Li, Understanding limiting factors in thick electrode performance as applied to high energy density Li-ion batteries, *Journal of Applied Electrochemistry*, **47**, 405 (2017).
22. S. T. Taleghani, B. Marcos, K. Zaghib, and G. Lantagne, A Study on the Effect of Porosity and Particles Size Distribution on Li-Ion Battery Performance, *Journal of the Electrochemical Society*, **164**, E3179 (2017).
23. M. Doyle, J. Newman, A. S. Gozdz, C. N. Schmutz, and J.-M. Tarascon, Comparison of Modeling Predictions with Experimental Data from Plastic Lithium Ion Cells, *Journal of The Electrochemical Society*, **143**, 1890 (1996).
24. P. Arora, M. Doyle, A. S. Gozdz, R. E. White, and J. Newman, Comparison between computer simulations and experimental data for high-rate discharges of plastic lithium-ion batteries, *Journal of Power Sources*, **88**, 219 (2000).
25. K. Smith and C.-Y. Wang, Solid-state diffusion limitations on pulse operation of a lithium ion cell for hybrid electric vehicles, *Journal of Power Sources*, **161**, 628 (2006).
26. A. Nyman, T. G. Zavalis, R. Elger, M. Behm, and G. Lindbergh, Analysis of the Polarization in a Li-Ion Battery Cell by Numerical Simulations, *Journal of The Electrochemical Society*, **157**, A1236 (2010).
27. S.-L. Wu, W. Zhang, X. Song, A. K. Shukla, G. Liu, V. Battaglia, and V. Srinivasan, High Rate Capability of $Li(Ni_{1/3}Mn_{1/3}Co_{1/3})O_2$Electrode for Li-Ion Batteries, *Journal of the Electrochemical Society*, **159**, A438 (2012).
28. J. N. Reimers, M. Shoesmith, Y. S. Lin, and L. O. Valoen, Simulating High Current Discharges of Power Optimized Li-Ion Cells, *Journal of the Electrochemical Society*, **160**, A1870 (2013).
29. R. Zhao, J. Liu, and J. Gu, The effects of electrode thickness on the electrochemical and thermal characteristics of lithium ion battery, *Applied Energy*, **139**, 220 (2015).
30. K. G. Gallagher, S. E. Trask, C. Bauer, T. Woehrle, S. F. Lux, M. Tschech, P. Lamp, B. J. Polzin, S. Ha, B. Long, Q. Wu, W. Lu, D. W. Dees, and A. N. Jansen, Optimizing Areal Capacities through Understanding the Limitations of Lithium-Ion Electrodes, *Journal of The Electrochemical Society*, **163**, A138 (2015).
31. S. Malifarge, B. Delobel, and C. Delacourt, Experimental and Modeling Analysis of Graphite Electrodes with Various Thicknesses and Porosities for High-Energy-Density Li-Ion Batteries, *Journal of the Electrochemical Society*, **165**, A1275 (2018).
32. A. Kriston, A. Pfrang, H. Döring, B. Fritsch, V. Ruiz, I. Adanouj, T. Kosmidou, J. Ungeheuer, and L. Boon-Brett, External short circuit performance of Graphite-$LiNi_{1/3}Co_{1/3}Mn_{1/3}O_2$and Graphite-$LiNi_{0.8}Co_{0.15}Al_{0.05}O_2$ cells at different external resistances, *Journal of Power Sources*, **361**, 170 (2017).
33. J. Mao, W. Tiedemann, and J. Newman, Simulation of Li-ion Cells by Dualfoil Model under Constant-Resistance Load, *ECS Transactions*, **58**, 71 (2014).
34. J. Mao, W. Tiedemann, and J. Newman, Simulation of temperature rise in Li-ion cells at very high currents, *Journal of Power Sources*, **271**, 444 (2014).
35. D. J. Noelle, M. Wang, A. V. Le, Y. Shi, and Y. Qiao, Internal resistance and polarization dynamics of lithium-ion batteries upon internal shorting, *Applied Energy*, **212**, 796 (2018).
36. C. J. Orendorff, E. P. Roth, and G. Nagasubramanian, Experimental triggers for internal short circuits in lithium-ion cells, *Journal of Power Sources*, **196**, 6554 (2011).
37. J. Lamb and C. J. Orendorff, Evaluation of mechanical abuse techniques in lithium ion batteries, *Journal of Power Sources*, **247**, 189 (2014).
38. T. D. Hatchard, S. Trussler, and J. R. Dahn, Building a "smart nail" for penetration tests on Li-ion cells, *Journal of Power Sources*, **247**, 821 (2014).
39. M. Zhang, J. Du, L. Liu, A. Stefanopoulou, J. Siegel, L. Lu, X. He, X. Xie, and M. Ouyang, Internal Short Circuit Trigger Method for Lithium-Ion Battery Based on Shape Memory Alloy, *Journal of The Electrochemical Society*, **164**, A3038 (2017).
40. S. Santhanagopalan, P. Ramadass, and J. Zhang, Analysis of internal short-circuit in a lithium ion cell, *Journal of Power Sources*, **194**, 550 (2009).
41. T. G. Zavalis, M. Behm, and G. Lindbergh, Investigation of Short-Circuit Scenarios in a Lithium-Ion Battery Cell, *Journal of The Electrochemical Society*, **159**, A848 (2012).
42. W. Zhao, G. Luo, and C.-Y. Wang, Modeling Nail Penetration Process in Large-Format Li-Ion Cells, *Journal of The Electrochemical Society*, **162**, A207 (2015).
43. W. Zhao, G. Luo, and C.-Y. Wang, Modeling Internal Shorting Process in Large-Format Li-Ion Cells, *Journal of The Electrochemical Society*, **162**, A1352 (2015).
44. H. Maleki and J. N. Howard, Internal short circuit in Li-ion cells, *Journal of Power Sources*, **191**, 568 (2009).
45. W. Fang, P. Ramadass, and Z. Zhang, Study of internal short in a Li-ion cell-II. Numerical investigation using a 3D electrochemical-thermal model, *Journal of Power Sources*, **248**, 1090 (2014).
46. K.-C. Chiu, C.-H. Lin, S.-F. Yeh, Y.-H. Lin, and K.-C. Chen, An electrochemical modeling of lithium-ion battery nail penetration, *Journal of Power Sources*, **251**, 254 (2014).

47. R. Zhao, J. Liu, and J. Gu, Simulation and experimental study on lithium ion battery short circuit, *Applied Energy*, **173**, 29 (2016).
48. B. Liu, S. Yin, and J. Xu, Integrated computation model of lithium-ion battery subject to nail penetration, *Applied Energy*, **183**, 278 (2016).
49. M. Zhang, L. Liu, A. Stefanopoulou, J. Siegel, L. Lu, X. He, and M. Ouyang, Fusing Phenomenon of Lithium-Ion Battery Internal Short Circuit. *Journal of The Electrochemical Society*, **164**, A2738 (2017).
50. J. Xu, Y. Wu, and S. Yin, Investigation of effects of design parameters on the internal short-circuit in cylindrical lithium-ion batteries, *RSC Advances*, **7**, 14360 (2017).
51. G. Liang, Y. Zhang, Q. Han, Z. Liu, Z. Jiang, and S. Tian, A novel 3D-layered electrochemical-thermal coupled model strategy for the nail-penetration process simulation, *Journal of Power Sources*, **342**, 836 (2017).
52. P. T. Coman, E. C. Darcy, C. T. Veje, and R. E. White, Modelling Li-Ion Cell Thermal Runaway Triggered by an Internal Short Circuit Device Using an Efficiency Factor and Arrhenius Formulations, *Journal of The Electrochemical Society*, **164**, A587 (2017).
53. X. Feng, X. He, L. Lu, and M. Ouyang, Analysis on the Fault Features for Internal Short Circuit Detection Using an Electrochemical-Thermal Coupled Model, *Journal of The Electrochemical Society*, **165**, A155 (2018).
54. J. Zhu, T. Wierzbicki, and W. Li, A review of safety-focused mechanical modeling of commercial lithium-ion batteries, *Journal of Power Sources*, **378**, 153 (2018).
55. R. Spotnitz and J. Franklin, Abuse behavior of high-power, lithium-ion cells, *Journal of Power Sources*, **113**, 81 (2003).
56. S. Pannala, J. A. Turner, S. Allu, W. R. Elwasif, S. Kalnaus, S. Simunovic, A. Kumar, J. J. Billings, H. Wang, and J. Nanda, Multiscale modeling and characterization for performance and safety of lithium-ion batteries, *Journal of Applied Physics*, **118**, 072017 (2015).
57. S. Abada, G. Marlair, A. Lecocq, M. Petit, V. Sauvant-Moynot, and F. Huet, Safety focused modeling of lithium-ion batteries: A review, *Journal of Power Sources*, **306**, 178 (2016).
58. J. Deng, C. Bae, J. Marcicki, A. Masias, and T. Miller, Safety modeling and testing of lithium-ion batteries in electrified vehicles, *Nature Energy*, **3**, 261 (2018).
59. M. Doyle, T. F. Fuller, and J. Newman, Modeling of Galvanostatic Charge and Discharge of the Lithium/Polymer/Insertion Cell, *Journal of The Electrochemical Society*, **140**, 1526 (1993).
60. J. Newman and K. E. Thomas-Alyea, *Electrochemical Systems*, 3rd ed., Wiley-Interscience: s.l., 2004.
61. T. J. Rademaker, G. R. A. Akkermans, D. L. Danilov, and P. H. L. Notten, On the Deviation of Electro-Neutrality in Li-Ion Battery Electrolytes, *Journal of The Electrochemical Society*, **161**, E3365 (2014).
62. K.-H. Xue and G. L. Plett, A convective transport theory for high rate discharge in lithium ion cells, *Electrochimica Acta*, **87**, 575 (2013).
63. T. D. Hatchard, D. D. MacNeil, A. Basu, and J. R. Dahn, Thermal Model of Cylindrical and Prismatic Lithium-Ion Cells, *Journal of The Electrochemical Society*, **148**, A755 (2001).
64. S. Hildebrand, A. Rheinfeld, A. Friesen, J. Haetge, F. M. Schappacher, A. Jossen, and M. Winter, Thermal Analysis of $LiNi_{0.4}Co_{0.2}Mn_{0.4}O_2$/Mesocarbon Microbeads Cells and Electrodes: State-of-Charge and State-of-Health Influences on Reaction Kinetics, *Journal of The Electrochemical Society*, **165**, A104 (2018).
65. T. F. Fuller, M. Doyle, and J. Newman, Simulation and Optimization of the Dual Lithium Ion Insertion Cell, *Journal of The Electrochemical Society*, **141**, 1 (1994).
66. A. Latz and J. Zausch, Thermodynamic derivation of a Butler–Volmer model for intercalation in Li-ion batteries, *Electrochimica Acta*, **110**, 358 (2013).
67. C. H. Hamann, A. Hamnett, and W. Vielstich, *Electrochemistry*, Wiley-VCH: Weinheim, 2007.
68. D. Bernardi, E. Pawlikowski, and J. Newman, A General Energy Balance for Battery Systems, *Journal of The Electrochemical Society*, **132**, 5 (1985).
69. L. Rao and J. Newman, Heat-Generation Rate and General Energy Balance for Insertion Battery Systems, *Journal of The Electrochemical Society*, **144**, 2697 (1997).
70. Y. Reynier, R. Yazami, and B. Fultz, The entropy and enthalpy of lithium intercalation into graphite, *Journal of Power Sources*, **119-121**, 850 (2003).
71. W. Lu, I. Belharouak, D. Vissers, and K. Amine, In Situ Thermal Study of $Li_{1+x}(Ni_{1/3}Co_{1/3}Mn_{1/3})_{1-x}O_2$Using Isothermal Micro-clorimetric Techniques, *Journal of The Electrochemical Society*, **153**, A2147 (2006).
72. S. V. Erhard et al., Simulation and Measurement of the Current Density Distribution in Lithium-Ion Batteries by a Multi-Tab Cell Approach, *Journal of The Electrochemical Society*, **164**, A6324 (2017).
73. L. O. Valøen and J. N. Reimers, Transport Properties of $LiPF_6$-Based Li-Ion Battery Electrolytes, *Journal of The Electrochemical Society*, **152**, A882 (2005).
74. D. Dees, E. Gunen, D. Abraham, A. Jansen, and J. Prakash, Electrochemical Modeling of Lithium-Ion Positive Electrodes during Hybrid Pulse Power Characterization Tests, *Journal of The Electrochemical Society*, **155**, A603 (2008).
75. A. Nyman, M. Behm, and G. Lindbergh, Electrochemical characterisation and modeling of the mass transport phenomena in $LiPF_6$–EC–EMC electrolyte, *Electrochimica Acta*, **53**, 6356 (2008).
76. H. Lundgren, M. Behm, and G. Lindbergh, Electrochemical Characterization and Temperature Dependency of Mass-Transport Properties of $LiPF_6$in EC: DEC, *Journal of the Electrochemical Society*, **162**, A413 (2014).
77. M. D. Levi and D. Aurbach, Diffusion Coefficients of Lithium Ions during Intercalation into Graphite Derived from the Simultaneous Measurements and Modeling of Electrochemical Impedance and Potentiostatic Intermittent Titration Characteristics of Thin Graphite Electrodes, *The Journal of Physical Chemistry B*, **101**, 4641 (1997).
78. J. Landesfeind, J. Hattendorff, A. Ehrl, W. A. Wall, and H. A. Gasteiger, Tortuosity Determination of Battery Electrodes and Separators by Impedance Spectroscopy, *Journal of The Electrochemical Society*, **163**, A1373 (2016).
79. M. Winter, J. O. Besenhard, M. E. Spahr, and P. Novák, Insertion Electrode Materials for Rechargeable Lithium Batteries, *Advanced Materials*, **10**, 725 (1998).
80. A. Latz and J. Zausch, Multiscale modeling of lithium ion batteries: Thermal aspects, *Beilstein journal of nanotechnology*, **6**, 987 (2015).
81. K. Higa, S.-L. Wu, D. Y. Parkinson, Y. Fu, S. Ferreira, V. Battaglia, and V. Srinivasan, Comparing Macroscale and Microscale Simulations of Porous Battery Electrodes, *Journal of The Electrochemical Society*, **164**, E3473 (2017).
82. R. Darling and J. Newman, Modeling a Porous Intercalation Electrode with Two Characteristic Particle Sizes, *Journal of The Electrochemical Society*, **144**, 4201 (1997).
83. M. Ender, An extended homogenized porous electrode model for lithium-ion cell electrodes, *Journal of Power Sources*, **282**, 572 (2015).
84. Z. Mao, M. Farkhondeh, M. Pritzker, M. Fowler, and Z. Chen, Multi-Particle Model for a Commercial Blended Lithium-Ion Electrode, *Journal of the Electrochemical Society*, **163**, A458 (2015).
85. C. Kupper and W. G. Bessler, Multi-Scale Thermo-Electrochemical Modeling of Performance and Aging of a $LiFePO_4$ /Graphite Lithium-Ion Cell, *Journal of The Electrochemical Society*, **164**, A304 (2017).
86. D. A. G. Bruggeman, Berechnung verschiedener physikalischer Konstanten von heterogenen Substanzen. I. Dielektrizitätskonstanten und Leitfähigkeiten der Mischkörper aus isotropen Substanzen, *Annalen der Physik*, **416**, 636 (1935).
87. E. Markevich, M. D. Levi, and D. Aurbach, Comparison between potentiostatic and galvanostatic intermittent titration techniques for determination of chemical diffusion coefficients in ion-insertion electrodes, *Journal of Electroanalytical Chemistry*, **580**, 231 (2005).
88. S. Malifarge, B. Delobel, and C. Delacourt, Guidelines for the Analysis of Data from the Potentiostatic Intermittent Titration Technique on Battery Electrodes, *Journal of The Electrochemical Society*, **164**, A3925 (2017).
89. K. R. Crompton and B. J. Landi, Opportunities for near zero volt storage of lithium ion batteries, *Energy & Environmental Science*, **9**, 2219 (2016).
90. G. E. Archie, The Electrical Resistivity Log as an Aid in Determining Some Reservoir Characteristics, *Transactions of the AIME*, **146**, 54 (1942).
91. J. Sturm, A. Rheinfeld, I. Zilberman, F. B. Spingler, S. Kosch, F. Frie, and A. Jossen, Modeling and simulation of inhomogeneities in a 18650 nickel-rich, silicon-graphite lithium-ion cell during fast charging, *Journal of Power Sources*, **412**, 204 (2019).
92. S. V. Erhard, P. J. Osswald, J. Wilhelm, A. Rheinfeld, S. Kosch, and A. Jossen, Simulation and Measurement of Local Potentials of Modified Commercial Cylindrical Cells, *Journal of The Electrochemical Society*, **162**, A2707 (2015).
93. K. E. Thomas and J. Newman, Heats of mixing and of entropy in porous insertion electrodes, *Journal of Power Sources*, **119-121**, 844 (2003).
94. D. M. Pesko, K. Timachova, R. Bhattacharya, M. C. Smith, I. Villaluenga, J. Newman, and N. P. Balsara, Negative Transference Numbers in Poly(ethylene oxide)-Based Electrolytes. *Journal of The Electrochemical Society*, **164**, E3569 (2017).
95. K. L. Gering, Prediction of electrolyte viscosity for aqueous and non-aqueous systems: Results from a molecular model based on ion solvation and a chemical physics framework, *Electrochimica Acta*, **51**, 3125 (2006).
96. T. Marks, S. Trussler, A. J. Smith, D. Xiong, and J. R. Dahn, A Guide to Li-Ion Coin-Cell Electrode Making for Academic Researchers, *Journal of The Electrochemical Society*, **158**, A51 (2011).

4 Heat Dissipation due to Thermal Design

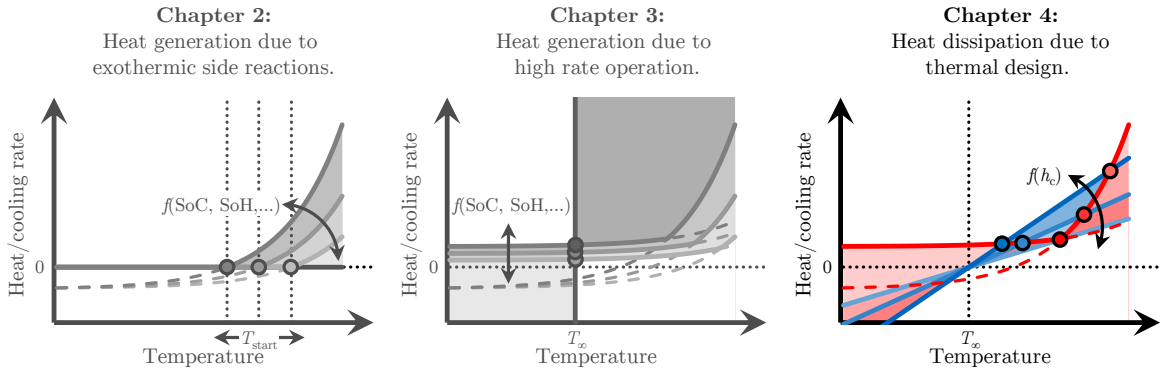

Figure 4.1: Outline of chapter 4.

With the evolution of Li-ion cell thermal runaway and its initiation characterized in chapter 2 and chapter 3, describing the interplay between the thermal design of cells of a given geometry with the prevailing cooling conditions is crucial in order to derive possible mitigation strategies which may prevent cell thermal runaway.

Due to the vast amount of cells differing in size and format to choose from as described section 1.2, a thorough experimental evaluation of a cell's heat generation, cooling capability, and associated cooling requirements is cumbersome. In order to be able to derive suitable combinations of cells and cooling strategies for a given application under all relevant operating conditions and extremes, multi-dimensional multiphysics modeling and simulation can be applied. To further be able to validate such modeling and simulation approaches accounting for a cell's geometric characteristics, novel experimental approaches are necessary, which allow for a maximum control of prevailing thermal boundary conditions.

Within this chapter, an approach to quantify the thermal interplay between cells of different sizes and formats with the surroundings is presented (see Fig. 4.1). By extending the physical-chemical short circuit model presented in section 3.4 to account for local electrical and thermal effects along the electrodes and across the cell's jelly roll or electrode stack, the external short circuit behavior of Li-ion cells with different formats and sizes is studied in section 4.1, focusing on the impact of the chosen cooling strategy on the local temperature evolution. In order to be able to also experimentally evaluate the thermal interaction of effects occurring within large-format Li-ion cells and between the cell and its surroundings, an experimental setup is presented and applied to validate a semi-empirical electro-thermal cell model of a large-format pouch-type Li-ion cell in section 4.2.

4.1 Influence of thermal design on external short circuit behavior of lithium-ion cells

Within this section, the article titled *Impact of Cell Size and Format on External Short Circuit Behavior of Lithium-Ion Cells at Varying Cooling Conditions: Modeling and Simulation* is presented. This work demonstrates the applicability of the short circuit model of the electrochemical unit cell presented in section 3.4 in order to describe the external short circuit behavior of larger sized Li-ion cells with different cooling capabilities at varying cooling conditions by combining the validated physical-chemical model with an electrical and a thermal model as part of the previously presented multidimensional modeling (MuDiMod) framwork.[115,118,124,126,352] This approach forms the basis for extensive simulation studies to optimize the thermal design of Li-ion batteries with regard to preventing a cell thermal runaway triggered by short circuit scenarios.

In order to allow for a computationally efficient calculation of the coupled electrochemical, electrical, and thermal short circuit behavior of larger sized cells as found in commercial applications such as consumer electronics or the automotive sector, a geometrical decoupling of the described modeling disciplines to each individual geometry and length scale is applied following the MuDiMod framework. This is essential, as the extremely large local currents require a substantial discretization effort which inevitably increases the computational time and, hence, directly affects the feasibility of extensive cell and thermal design studies. A previously described computationally lean and geometrically precise mapping between the planar electrodes and a spirally wound jelly roll found in cylindrical cells[126] is extended to also describe jelly roll configurations found in prismatic cells as well as stacked or z-folded electrode configurations which are characteristic for pouch-type cells.

With this model extension, an optimized number of physical-chemical model nodes can be included, which improves the model accuracy whilst still allowing for moderate computational demand. In total, three common cell formats, three cell sizes, two convective cooling strategies, and six different cooling intensities were studied resulting in 108 simulation runs allowing for a most thorough investigation of the cooling capability of the studied cells. Cylindrical, prismatic, and pouch-type cells with capacities ranging from 3 Ah, 9 Ah, to 27 Ah representing consumer-sized, HEV-sized, and PHEV-sized Li-ion cells were modeled applying surface and tab cooling at convection coefficients ranging from natural convection to convection coefficients representing a direct phase change of the coolant. The aspect ratio of each individual studied cell format was kept constant for all three cell sizes and was chosen in accordance with 26650 cylindrical cells, PHEV2 prismatic cells, and a mixture of PHEV1 and BEV1 pouch-type cells.[102] All simulated cells contain graphite and NMC-111 as anode and cathode active materials with an effective electrode loading of 1.85 $\mathrm{mAh\,cm^{-2}}$ as well as 1 M $LiPF_6$ in EC:DMC 1:1 (by weight) with 2 wt% VC as electrolyte in accordance with results presented in sections 3.3 and 3.4. Compared to the cooling capability of the electrochemical unit cell, the finite geometry of the studied cell formats and sizes considerably increases the effort that is required to cool the cells to a certain extent. Whilst keeping the electrochemical unit cell below the temperature threshold of exothermic side reactions can be achieved with moderate cooling effort throughout the entire short circuit duration, the considered minimum cooling requirement, avoiding an initiation of exothermic side reactions involving the NMC cathode above an SoC of 50 % (see section 2.2), cannot be guaranteed for both the maximum and average cell temperatures of the studied cell formats and sizes for the considered cooling strategies. Only surface cooled consumer-sized and HEV-sized pouch-type cells can be physically maintained within a safe temperature and SoC window with the applied convective cooling conditions. Whilst the average temperature of surface cooled consumer-sized prismatic cells and PHEV-sized

pouch-type cells as well as tab cooled consumer-sized cylindrical and prismatic cells can be still be maintained within this safe operating window, this does not hold for the maximum cell temperature. For all other cell formats and sizes, only the minimum cell temperature at the cooled surface can be maintained below the critical temperature threshold at 50 % SoC, implying the inevitable occurrence of critical exothermic side reactions which may lead to cell thermal runaway. The simulation results suggest that with increasing cell size and, hence, thermal resistivity of the cells, a cooling below a certain temperature threshold cannot be physically achieved in case the applied external short circuit cannot be limited or interrupted by cell-internal or external means.
With the aid of the presented model, a maximum cell size or minimum cooling requirement can be identified for a certain criterion based on the local cell temperature as well as the corresponding SoC distribution. Following this framework, the interplay between cell-internal heat generation and cell-external heat dissipation can be studied for a manifold of electrode and cell designs as well as cooling strategies, which allows a suitable combination of parameters that guarantees a maximum level of safety during various short circuit conditions to be derived. However, further work is required to validate multiphysics models especially for larger sized Li-ion cells in order to evaluate the true applicability of the model. An experimental approach aiming at such a model validation is presented within the following section focusing on the electro-thermal behavior of a large-format Li-ion cell within its designated operating window.

Author contribution Alexander Rheinfeld developed the idea of the carried out cell design study at varying cooling conditions, guided the continuous development of the MuDiMod framework, developed and parametrized the presented model, carried out all simulation studies, and analyzed the data. Johannes Sturm helped to develop the model and implemented the presented mapping between the electrical and thermal model within the MuDiMod framework. Alexander Frank helped to analyze the data. Stephan Kosch recently extended the MuDiMod framework by a nodal coupling between the electrochemical and electrical model and Simon V. Erhard initiated the idea of the framework and developed its first implementation. The manuscript was written by Alexander Rheinfeld and Johannes Sturm and was edited by Andreas Jossen. All authors discussed the data and commented on the results.

Impact of Cell Size and Format on External Short Circuit Behavior of Lithium-Ion Cells at Varying Cooling Conditions: Modeling and Simulation

Alexander Rheinfeld, Johannes Sturm, Alexander Frank, Stephan Kosch, Simon V. Erhard, Andreas Jossen

Journal of The Electrochemical Society 167 (1), p. 013511, 2020

Permanent weblink:
http://dx.doi.org/10.1149/2.0112001jes

Journal of The Electrochemical Society, 2020 **167** 013511

Impact of Cell Size and Format on External Short Circuit Behavior of Lithium-Ion Cells at Varying Cooling Conditions: Modeling and Simulation

Alexander Rheinfeld, [z] **Johannes Sturm, Alexander Frank, Stephan Kosch, Simon V. Erhard, and Andreas Jossen**

Institute for Electrical Energy Storage Technology, Technical University of Munich (TUM), D-80333 Munich, Germany

A multidimensional multiphysics model is presented to describe the external short circuit behavior of lithium-ion cells of various formats and sizes at different convective cooling conditions. For this purpose, a previously published homogenized physical-chemical model of the external short circuit behavior of a small-sized lithium-ion cell was combined with an electrical and a thermal model to describe in-plane inhomogeneities in current density and heat generation rate throughout the electrodes, together with the resulting temperature distribution within the cell's jelly roll or electrode stack. With the investigated cylindrical, prismatic, and pouch-type cell formats combined with cell capacities ranging from consumer-sized to automotive applications, a comprehensive cell design study is presented during external short circuits. The investigated surface and tab cooling strategies reveal a limited cooling capability of each cell format and size, which seems to be defined by the ratio of cooled surface area to electrode area as well as the thermal resistivity of the respective cell geometry. The simulation results show that only thin cells with a large ratio of cooling surface to electrode area can be physically maintained within an uncritical operating window of cell temperature and state of charge in case a low-resistance external short circuit is applied.

 [DOI: 10.1149/2.0112001JES]

Manuscript submitted June 19, 2019; revised manuscript received August 28, 2019. Published October 3, 2019. *This paper is part of the JES Focus Issue on Mathematical Modeling of Electrochemical Systems at Multiple Scales in Honor of Richard Alkire.*

Based on the comparably appealing combination of high energy and high power, lithium-ion batteries are the energy storage solution of choice for a manifold of today's applications, ranging from portable electronics to electric vehicles (EVs) and stationary energy storage systems. The increased electrochemical energy content required in order to achieve, for example, a longer battery run-time of portable electronics or an extended driving range of EVs, also comes with an increase in the thermal energy content which poses a significant hazard to customers and personnel involved in accidents. This tradeoff between energy increase and safety remains one of the main challenges of Li-ion battery research and development in order to achieve a high customer acceptance and, hence, market penetration. Besides the ever increasing demand for higher energy contents, key aspects of Li-ion battery safety are not fully understood so far, which hinders the efficient design of batteries that fulfill these two seemingly conflicting goals. Whilst Li-ion battery safety can be guaranteed on different levels of battery integration, the limited thermal stability of a cell's active and passive components can be often identified as the root cause for hazards that eventually need to be addressed on the cell, module, and battery pack or system level.

The vertical integration of battery safety, requires consideration of the topic throughout all relevant levels. This implies that a battery system needs to be designed in accordance with requirements defined by the applied materials and *vice versa*. The extremely complex interplay of safety relevant phenomena occurring on different length scales involving multiple mechanisms can often not be adequately described, which is why an experimental investigation of battery safety lacks true alternatives so far.

However, in order to efficiently design safe batteries, valid simulation tools are required to complement or even substitute costly and time-consuming safety and abuse tests. For commercial and larger sized Li-ion cells, such effort generally requires multidimensional modeling approaches describing multiphysics effects on varying length scales. Various approaches have been suggested throughout the past that can be generally divided into fully coupled continuum models[1] and models which decouple the prevailing length scale and geometry associated with a certain mechanism in order to reduce the computational effort,[2,3] such as the multidimensional modeling (MuDiMod) approach previously suggested by our group.[4–8] Multidimensional multiphysics models accounting for electrochemical, electrical, and thermal effects and interactions can be found rather frequently for what can be considered as "normal" operation of Li-ion cells. These models aim to describe local characteristics arising from in-plane polarization effects along the electrodes and a superimposed temperature distribution across the jelly roll or electrode stack. Such considerations then allow for deriving design criteria of cell properties linked to the electrochemical, electrical, and thermal behavior of the cell in order to guarantee a most optimized operation for a given application. Highly localized effects occurring during abnormal operation or abuse, such as those resulting from local short circuits triggered by an external deformation or penetration, can be adequately described by such an approach provided that no further reactions (e.g. exothermic side reactions) or effects (e.g. cell venting) are dominating the cell's behavior.[9–13]

Within this work, we extend the previously described MuDiMod approach[4–8] by accounting not only for a mapping between a spirally wound jelly roll and the cylindrical geometry it forms,[8] but by also describing prismatic and pouch-type cell geometries with either wound or stacked/folded electrode configurations. Furthermore, we include a validated physical-chemical short circuit model[14,15] describing the electrochemical behavior of the unit cell in order to depict the external short circuit behavior of cylindrical, prismatic, and pouch-type Li-ion cells of three different sizes, which are supposed to represent both consumer and automotive applications as can be found in hybrid electric vehicles (HEVs) and plug-in hybrid electric vehicles (PHEVs). Finally, a design study is carried out in order to evaluate the cooling capability of Li-ion cells depending on the cell's format and size as well as the applied cooling strategy, such as surface cooling and tab cooling, in terms of preventing a potential cell thermal runaway triggered by a low-resistance external short circuit.

Modeling and Simulation

Within this section, recent activities in multidimensional multiphysics modeling and simulation of Li-ion cells of different formats and sizes are briefly summarized. These works describe the context of the modeling approach presented here. For the reader's convenience, all relevant model parameters and equations are described in the appendix whereas the applied approach of multidimensional multiphysics coupling on varying length scales can be found in the

[z] E-mail: alexander.rheinfeld@tum.de

Table I. Overview of multidimensional multiphysics modeling approaches of Li-ion cells.

Cell format	Reference	Electrode configuration	Cell chemistry	Cell capacity	Electrode size/cm w_{ele}	Electrode size/cm h_{ele}	Model
Cylindrical	30	jelly roll	G/LMO	< 5 Ah	≈ 100	n.a.	2D-continuum
	31	jelly roll	G/NCA	19.9 Ah	323	13	3D-continuum
	41	jelly roll	G/LFP	> 5 Ah	≈ 111	11	720×p2D-EC/2D-E/3D-T
	8	jelly roll	SiC/NMC-811	3.35 Ah	61.5	5.8	197×p2D-EC/2D-E/3D-T
	4	jelly roll	G/LFP	2.5 Ah	169	5.6	19×p2D-EC/2D-E/2D-T
	60	jelly roll	G/LMO	≈ 2.9 Ah	158.2	6	18×p2D-EC/2D-E/1D-T
				≈ 24 Ah	620	14	
	38	jelly roll	G/LFP	2.3 Ah	169	5.6	1×p2D-EC/3D-T
	20	jelly roll	G/LMO	n.a.	19.1	5	56×p2D-EC/3D-E/3D-T
	27	jelly roll	G/LMO	0.5 Ah	≈ 100	n.a.	SPM-EC/2D-E/3D-T
Prismatic	32	jelly roll	G/NMC	40 Ah	512	20.5	3D-continuum (isothermal)
	41	jelly roll	G/LFP	> 5 Ah	≈ 111	11	672×p2D-EC/2D-E/3D-T
	61	jelly roll	G/NMC-111	25 Ah	n.a.	12.3	p2D-EC/3D-E/3D-T
	62	stack	G/LFP	16.5 Ah	6.7	10.5	p2D-EC/3D-E/3D-T
	63	stack	G/NCA	5 Ah	8	11	p2D-EC/3D-E/3D-T
	28	stack	G/NMC	5 Ah	12	7.5	42×SPM-EC/2D-E/2D-T
Pouch	1	stack	G/NCA	20 Ah	14	20	3D-continuum
	33	stack	G/LFP	10 Ah	10	11.5	3D-continuum
	7	stack	G/NMC-111	40 Ah	18	22	25×p2D/2D-E/2D-T
	6	stack	G/LCO	2.3 Ah	10	30	21×p2D/2D-E/2D-T/2D-M
	5	stack	G/NMC-111	0.8 Ah	49.8	9.8	11×p2D/ 2D-E
	20	stack	G/LMO	n.a.	50	2.4	1×p2D/3D-T
	39	stack	G/LFP	10 Ah	10	11.5	1×p2D-EC/3D-T
	40	stack	G/NMC-111	18.5 Ah	14.2	7.3	1×p2D-EC/3D-T
	3	stack	G/NCA	20 Ah	14.5	19.2	p2D-EC/2D-E/2D-T
	2	stack	G/LFP	n.a.	20	30	p2D/2D-E

p2D	homogenized pseudo two-dimensional Newman-type model
SPM	(enhanced) single particle model
EC	physical-chemical or empirical model describing the electrochemical unit cell
E	electrical model describing the current collectors
T	thermal model describing the jelly roll or electrode stack
M	mechanical model describing the jelly roll or electrode stack
2D/3D	two-/three-dimensional model geometry
G	Li_xC
SiC	3.5 wt% of Si in Li_xC
LCO	Li_yCoO_2
LFP	Li_yFePO_4
LMO	$Li_yMn_2O_4$
NCA	$Li_yNi_{0.8}Co_{0.15}Al_{0.05}O_2$
NMC-111	$Li_yNi_{1/3}Co_{1/3}Mn_{1/3}O_2$
NMC-811	$Li_yNi_{0.8}Co_{0.1}Mn_{0.1}O_2$

supplementary material for all three cell formats studied within this work.

Modeling the electrochemical-thermal behavior of the electrochemical unit cell together with polarization effects across and along the electrodes, as well as the thermal behavior of cell's jelly roll or electrode stack, the size of the differential algebraic equation (DAE) system is considerably increased. The associated computational effort to solve the DAE system, however, needs to be limited in order to not only guarantee an efficient simulation of the cell's behavior but to allow for a successful or converging calculation in the first place.

Based on the extremely large currents occurring during short circuits involving considerable gradients in potential and concentration across the electrode thickness,[16,17] discretizing and, hence, calculating the electrochemical response of the unit cell requires comparably large computational effort. Neglecting a spatial discretization between the electrodes by applying, for example, linear polarization models, such as suggested by Newman and Tiedeman[18] as well as its modifications,[19–22] seems not to be an appropriate choice as previously described rate limiting mechanisms defining a cell's short circuit behavior cannot be considered.[15] An adequately limited applicability during short circuit scenarios holds for equivalent circuit models (ECMs)[23–25] as well as single particle models (SPMs) and associated extensions.[26–29]

Recent works that are relevant for the considerations presented here are summarized in Table I. As can be seen from the table, there is a rather even split between works focusing on spirally wound electrode configurations (jelly roll), as found in cylindrical or prismatic cells, and stacked electrode configurations, as found in prismatic and pouch-type cells. With a wide variety of cell chemistries, capacities, and sizes, a manifold of multiphysics coupling schemes have also been applied, ranging from continuum models to geometrically decoupled models. Most of the presented models focus on simultaneously depicting the electrochemical processes occurring between anode and cathode based on solid and liquid phase concentrations and potentials, the electrical characteristics along the planar electrodes, and the thermal behavior across the cell's electrode configuration. Multidimensional continuum models[1,30–33] often lack computational efficiency as all considered variables ideally need to be solved within the same discretiza-

tion scheme, which is dominated by the smallest geometric entity (i.e. anode, separator, cathode, and current collector domains). Whilst such fine discretization is vital for describing the electrochemical response of the cell especially at higher currents, a coarser discretization would still allow for sufficient modeling accuracy in terms of the electrical and thermal cell behavior. This partly explains why this model type is not applied to the same extent as geometrically decoupled modeling approaches (see Table I). Such geometrical decoupling often involves studying electrochemical, electrical, thermal, and even mechanical effects on the corresponding lengths scales and exchanging only relevant variables between the individual models such as temperature, potential, current density distribution, and heat generation rate.

By describing mass and charge transport throughout the thickness of the electrodes and separator as well as diffusion limited reaction kinetics and diffusion processes within the active material particles (1D+1D, i.e. p2D[34,35]), the electrochemical cell behavior can be reliably described over a wide range of currents and temperatures.[15,16] By further accounting for a potential distribution and current flux along the current collectors (2D[2,18]), inhomogeneities in current density distribution and, hence, heat generation rate can be described. By finally accounting for sensible heat effects, heat conduction, and heat exchange of the cell with its surroundings, the resulting cell temperature and temperature distribution along the electrodes can be calculated based on a 2D[4,6,7] or 3D[8] thermal representation of the cell. Such considerations are essential as even under "normal" operation not only considerable variations in current density distribution and, consequently, state of charge (SoC) can be observed along the electrodes,[5] but also severe temperature gradients need to be considered which influence the local electrochemical and electrical cell behavior.[21,36,37] Whilst most of the presented geometrically decoupled multidimensional multiphysics models rely on a not further specified 2D electrical model of the current collector foils and a 1D to 3D thermal model of the cell's geometry or electrode configuration depending on the cooling condition and applicability of symmetry planes, the geometrical arrangement of the electrochemical models, such as p2D and SPM, greatly varies from coupling only one model node[38–40] to several hundred model nodes[8,41] to the planar electrical electrode model.

Within this work, very large currents and heat generation rates as well as cooling rates are applied to cells of various formats and sizes. This requires not only a high discretization of the used p2D physical-chemical modeling approach in order to describe the electrochemical unit cell,[15] but also demands for a precise, numerically efficient bi-directional mapping between the thermal and electrical/electrochemical response of the cell. Only few works have previously reported using a local coordinate mapping between a 2D electrical and 3D thermal model of a cylindrical cell.[24,27] Such mapping has been recently adapted for the MuDiMod approach[8] which is extended in this work to also describe the mapping between a spirally wound electrode configuration for a prismatic cell as well as a z-folded electrode configuration for a pouch-type cell (see supplementary material). Combining this coupling scheme with the previously published validated p2D short circuit model,[14,15] the desired cell design study can be carried out in order to evaluate the cooling capability of cells of different format and size during low-resistance external short circuits.

The validated physical-chemical model represents a Li-ion cell formed of graphite as anode and $LiNi_{1/3}Co_{1/3}Mn_{1/3}O_2$ (NCM-111, in the following written as NMC-111) as cathode active materials containing 1 M $LiPF_6$ in ethylene carbonate (EC) : dimethyl carbonate (DMC) 1:1 (by weight) with 2 wt% vinylene carbonate (VC) as electrolyte. An effective electrode loading of 1.85 mAh cm^{-2} (i.e. a balanced electrode loading, BA[14]) between an upper and lower cell voltage of 4.2 V and 3.0 V is considered, as represented by the material and electrode parameters summarized in the appendix. The geometric characteristics of the studied cylindrical, prismatic, and pouch-type cells with capacities of 3 Ah (consumer-sized), 9 Ah (HEV-sized), and 27 Ah (PHEV-sized) within this voltage range are shown in Table II. The aspect ratio of each individual cell format was kept constant for all considered cell sizes. Whilst a 26650 consumer-sized cell was used as the targeted geometry for the cylindrical cells, a PHEV2-format was considered for the prismatic cells, and a combination of a PHEV1-format and BEV1-format was applied for the pouch-type cells.[42] The PHEV/BEV cell geometry for the prismatic and pouch-type cells was taken from DIN 91252.[42] All cell formats are considered to contain electrodes and a counter-tab configuration with a continuous electrical interconnection along the electrode width w_{ele}. Whilst such electrode configuration can be more usually found within larger-sized cylindrical and prismatic Li-ion cells, a stacked or z-folded electrode configuration realistically requires individual electrode sheets with similarly individual or z-folded separator configurations. However, for model simplicity, a continuous electrode configuration is also considered for

Table II. Geometric characteristics of studied cell formats and sizes.

Cell size	Cell capacity	p2D-discretization $w_{ele} \times h_{ele}$	Description	Unit	Cylindrical	Prismatic	Pouch
Consumer	3 Ah	4 × 3	w_{ele}	mm	1361.9	1170.7	744.8
			h_{ele}	mm	59.5	69.2	108.8
			w_{jelly}, w_{stack}	mm		41.3	47.7
			h_{jelly}, h_{stack}	mm	59.5	69.2	108.8
			d_{jelly}, d_{stack}	mm	25.4	12.4	5.6
			A_{surf}/A_{ele}	%	2.9	4.1	6.4
			A_{tab}/A_{ele}	%	0.6	0.5	0.3
HEV	9 Ah	9 × 4	w_{ele}	mm	2834.5	2460.5	1549.2
			h_{ele}	mm	85.8	98.8	156.9
			w_{jelly}, w_{stack}	mm		59.0	68.7
			h_{jelly}, h_{stack}	mm	85.8	98.8	156.9
			d_{jelly}, d_{stack}	mm	36.7	17.7	8.4
			A_{surf}/A_{ele}	%	2.0	2.8	4.4
			A_{tab}/A_{ele}	%	0.4	0.4	0.2
PHEV	27 Ah	18 × 6	w_{ele}	mm	5898.8	5153.9	3222.4
			h_{ele}	mm	123.6	141.5	226.3
			w_{jelly}, w_{stack}	mm		84.5	99.2
			h_{jelly}, h_{stack}	mm	123.6	141.5	226.3
			d_{jelly}, d_{stack}	mm	52.9	25.4	12.1
			A_{surf}/A_{ele}	%	1.4	1.9	3.1
			A_{tab}/A_{ele}	%	0.3	0.3	0.2

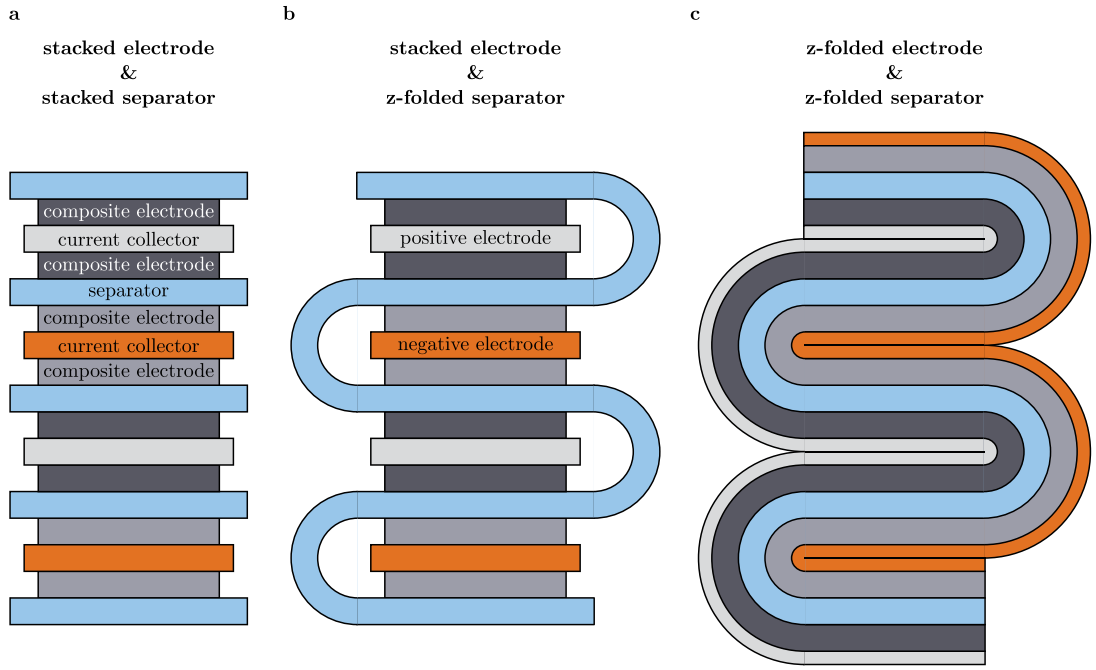

Figure 1. Modeled z-folded electrode and separator configuration forming the electrode stack of the pouch-type cell considered in this work (c) in comparison to common electrode and separator configurations including stacked, double-coated electrode sheets as well as individual separators (a) or a continuous, z-folded separator (b) in between the positive and negative electrodes.

the pouch-type cell assuming a z-folded electrode and separator configuration, as the polarization along the height of the electrode (i.e. between the tabs) is assumed to dominate the in-plane electrical behavior of the electrodes which is, hence, considered to be only marginally affected by the electrical electrode configuration along the width of the electrode. This essentially implies that the usually double-sided electrodes are considered to be coated only on one side with half the current collector thickness. This approach is schematically shown in Fig. 1c in comparison to a strictly stacked electrode and separator configuration (see Fig. 1a), as well as an electrode stack including a z-folded separator (see Fig. 1b).

For the applied cooling strategies, either the surface area of the cell or the tab area was used applying a convective boundary condition with convection coefficients h_c (W m^{-2} K^{-1}) ranging from natural convection (1 W m^{-2} K^{-1}) to an immediate phase change (10^5 W m^{-2} K^{-1}) at a constant coolant temperature of 25°C. This range is chosen in order to evaluate the cell's cooling behavior under physical extremes and does not necessarily reflect a realistic scenario (e.g. water would need to be held far below ambient pressure to realize such high heat transfer coefficients including boiling at 25°C). Furthermore, the applied convective cooling is considered to directly affect the surface of the cell's jelly roll or electrode stack which is not the case in real life as an additional cell housing would need to be considered. This assumption forms a best case which neglects the comparably low thermal resistivity of the cell's housing as well as geometrical imperfections of both cell and cooling system (e.g. unevenness resulting in a reduced thermal contact area). Radiation effects are further neglected as the cell is expected to be directly in contact with a cooler or the coolant. For the pouch-type cell, only the large surface area planar to the electrodes is considered for surface cooling whilst the entire lateral surface area of the jelly roll is considered for the prismatic and cylindrical cell under this cooling condition. Moreover, exothermic side reactions occurring at elevated temperatures as previously described[43–46] are not considered in this work in order to reduce computational time.

With the PHEV-sized cells requiring the largest discretization effort, the chosen 108 p2D models per electrode pair (or 8 p2D models per Ah) mark the upper limit of degrees of freedom that the solver and workstation are able to handle efficiently for the required discretization of the p2D model during high rate operation (COMSOL Multiphysics 5.3a, Intel Xeon E5-2687W 0 3.1 GHz with 64 GB RAM). A higher in-plane discretization was not feasible due to the large through-plane discretization effort required by the p2D models at very high currents. In our previous work, 158 p2D nodes per electrode pair were considered as the maximum for a lower discretization of the p2D models using the same computational resources.[8] In order to allow for maximum comparability, the same discretization of 8 p2D nodes per Ah was chosen for all cell models. Depending on numerical convergence, solving the PHEV-models required approximately two to three days per cell and cooling condition, whereas the consumer-sized models were generally solved within less than six hours.

Results and Discussion

Within this section, first of all the electrochemical-thermal short circuit behavior of a graphite/ NMC-111 electrochemical unit cell is studied. This is achieved by neglecting any electrical and thermal effects associated with geometric constraints of planar electrodes, which are usually spirally wound or stacked to form larger-sized Li-ion cells, as found in commercial applications. Assuming an ideal thermal contact of the electrodes to the cell's surroundings, the impact of various cooling conditions is studied by means of the p2D modeling approach described in the previous section and the appendix. By further accounting for geometrical characteristics of cylindrical, prismatic, and pouch-type Li-ion cells (see Table II), the external short circuit behavior of larger-sized Li-ion cells is studied by the MuDiMod approach described in the previous section, the appendix, and the supplementary material. The impact of a cell's size and format or configuration of the stacked or wound electrode is studied under various cooling conditions which are related to the simulation studies carried out with the p2D model of the electrochemical unit cell. These two approaches allow an examination of the impact of a cell's geometry on its cooling capabilities. The presented simulation results are further used as an

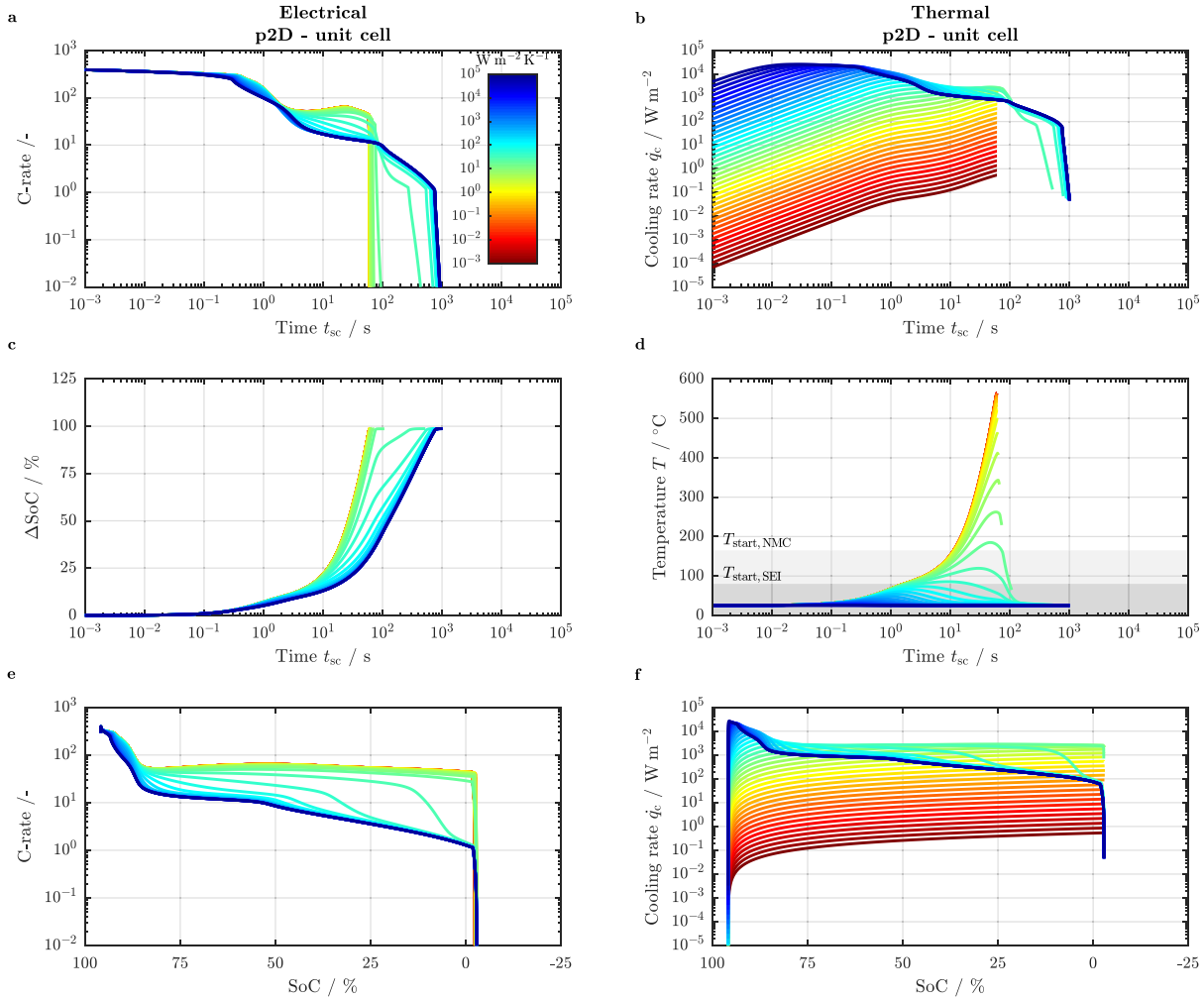

Figure 2. Predicted electrochemical (left: a, c, and e) and thermal response (right: b, d, and f) of the studied electrochemical unit cell under various cooling conditions with convection coefficients h_c ranging from 10^{-3} W m^{-2} K^{-1} to 10^5 W m^{-2} K^{-1} and a constant coolant temperature of 25°C as a function of short circuit duration t_{sc} (a to d) and as a function of SoC (e and f) for the C-rate (a and e), cooling rate $\dot{q}_c$ (b and f), ΔSoC (c), and temperature T (d). The coloring represents the chosen range of convection coefficients as defined in a.

indication of the feasibility of cooling cells of various sizes and formats during short circuit conditions, which may allow a reduction in the likelihood of cell thermal runaway.

Electrochemical-thermal short circuit behavior of the electrochemical unit cell.—By applying a "hard" external short circuit condition with a low resistance to the studied electrochemical unit cell within the p2D model as previously reported (i.e. applying a boundary condition approaching a cell voltage of 0 V),[15] the transient short circuit behavior of the cell can be studied in great detail. With electrode area specific convection coefficients h_c ranging from almost adiabatic conditions (10^{-3} W m^{-2} K^{-1}) to cooling conditions approaching isothermal operation involving immediate phase change, such as boiling or evaporation of the coolant (10^5 W m^{-2} K^{-1}), the dependency of the cell's short circuit behavior on the prevailing thermal boundary conditions can be evaluated, as shown in Fig. 2. As can be seen from the figure, a considerably strong convective cooling results in a short circuit behavior of the studied cells as recently reported under quasi-isothermal test conditions.[14,15] With lower heat transfer coefficients and, hence, lower cooling, the reported step-like characteristics in C-rate as a function of short circuit duration t_{sc} (s) and SoC changes toward higher C-rates, forming a peak-like shape around 30 s which correlates to approximately 50% SoC (see Figs. 2a and 2e). This increase in C-rate, which can be generally explained by enhanced transport properties of the liquid electrolyte[47] and increased solid phase diffusion coefficients of the active materials at elevated temperatures,[17] generally results in an accelerated short circuit behavior with a faster discharge as previously discussed (see Figs. 2a and 2c).[14,15] Based on this fast discharge converting the electrochemically stored energy into thermal energy, the temperature of the studied unit cell also quickly rises beyond the starting temperatures of exothermic side reactions involving the cell's components. The exothermic decomposition reaction of the graphite anode's solid electrolyte interphase (SEI) starts around 80°C with comparably low heat generation,[44,48,49] whereas, in the presence of non-aqueous electrolytes, cathode materials such as NMC start to exothermically decompose from as high as 180°C for NMC-111 to as low as 120°C for $LiNi_{0.8}Co_{0.1}Mn_{0.1}O_2$ (NMC-811) depending on the composition of NMC.[50] This decomposition reaction involving oxygen release is accompanied by comparably large heat rates that may result in electrolyte oxidation and, eventually, cell

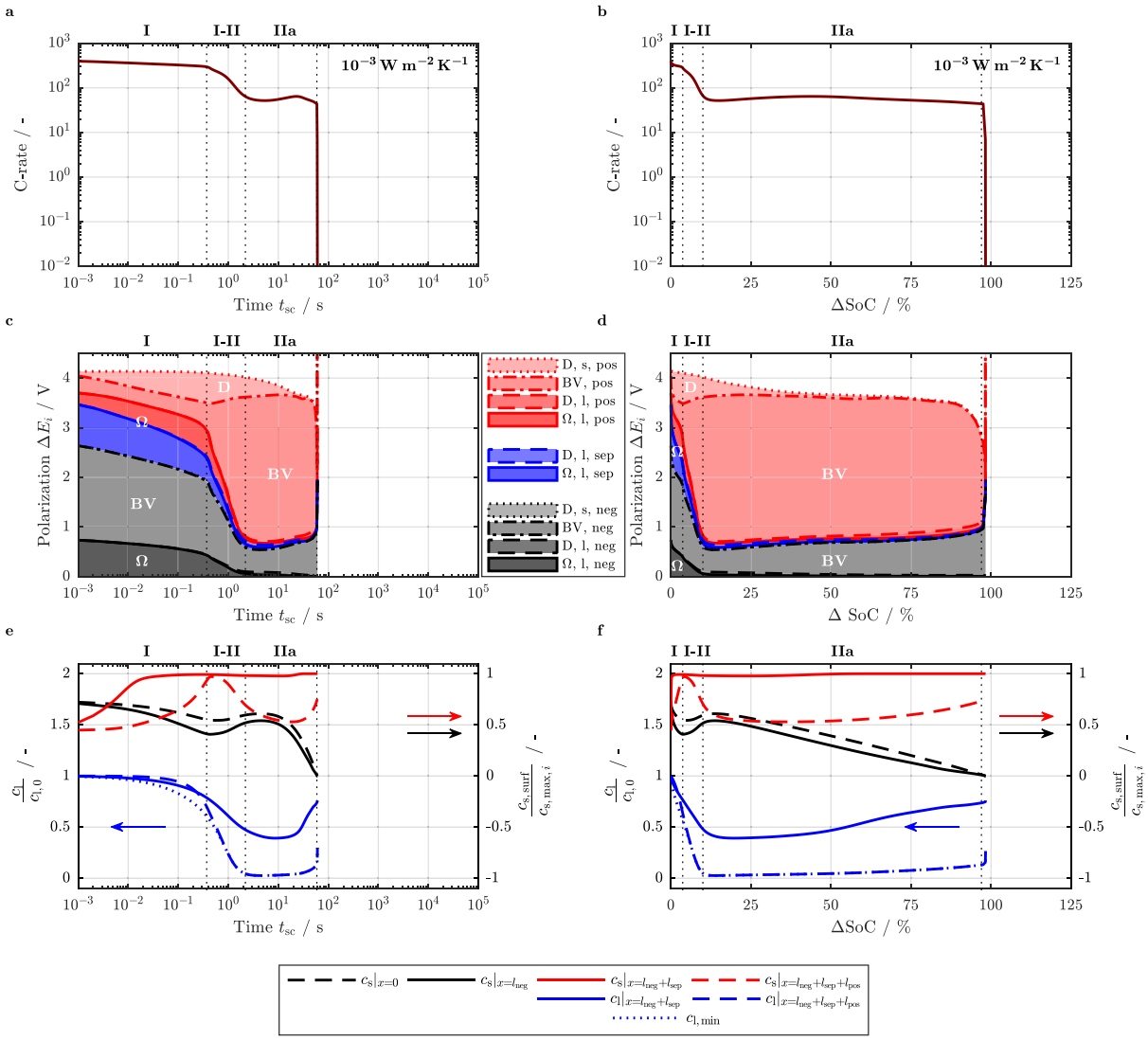

Figure 3. Predicted phases of a short circuit during a hard short circuit event for a cooling condition of 10^{-3} W m^{-2} K^{-1} with respect to electrode area and a coolant temperature of 25°C observed in C-rate (top: a and b), the corresponding polarization throughout the electrodes and separator (middle: c and d) resulting from the normalized solid (surface) and liquid phase concentration (average) at distinct locations of the cell (bottom: e and f) as a function of short circuit duration (left: a, c, and e) and as a function of normalized discharged capacity (right: b, d, and f). The overall polarization (middle: c and d) is primarily based on the contribution of diffusion related losses (D) and ohmic losses (Ω) within the solid (s) and liquid (l) components of the negative (neg) and positive electrode (pos) as well as throughout the separator (sep) including overpotentials associated with Butler-Volmer reaction kinetics (BV). Ohmic losses within the solid phase are negligible in comparison.

thermal runaway. Within this work, a starting temperature of approximately 165°C of the exothermic side reactions involving NMC is considered as previously reported for $LiNi_{0.4}Co_{0.2}Mn_{0.4}O_2$ (NMC-442) at 100% SoC.[46] This exemplary temperature threshold is chosen in order to not represent an overly optimistic scenario with rather high starting temperatures but to approach a more realistic application with moderate nickel contents within the NMC composition such as NMC-442, NMC-532, and NMC-622 or, in other words, to evaluate an NMC composition which is not limited to NMC-111 alone. The chosen starting temperature of 165°C was derived by Hildebrand et al. by means of a model-based data analysis from two-component calorimetric measurements formed of NMC-442 and electrolyte.[46]

With increasing convection coefficient and cell temperature, the electrode area specific cooling rate $\dot{q}_c$ (W m^{-2}) increases according to Newton's law of cooling (see Figs. 2b and 2f). Interestingly, there seems to be a threshold convection coefficient at which the cooling rate dominates the cell's short circuit behavior, resulting in a significantly decelerated discharge with lower C-rates and heat generation rates accompanied by a reduced cooling demand with ongoing short circuit duration. This correlates to a fading of the observed peak in C-rate resulting in the previously reported step-like behavior under quasi-isothermal conditions accompanied by a varying inclination in C-rate throughout the second plateau at approximately 80 s or 55% SoC (see blue line in Figs. 2a and 2e).[14,15] The discussed change in inclination of the C-rate, both as a function of short circuit

duration t_{sc} and SoC, can be correlated to a transient change in rate limiting mechanisms within the NMC cathode. In the beginning of the second plateau, rate limitation is based on a depletion of Li-ions within the liquid electrolyte near the current collector and a simultaneous saturation of the surface concentration of the active material particles near the separator. With ongoing short circuit duration, the short circuit behavior is exclusively dominated by solid phase diffusion limitations within the NMC cathode, resulting in a varying slope of the C-rate curve (see blue line Figs. 2a and 2e).[15] By varying the electrode area specific heat transfer coefficient h_c, a different behavior can be observed for non-isothermal conditions as shown in Fig. 2 and Fig. 2. Compared to the previously reported breakdown in cell polarization for isothermal conditions at high cooling rates (see Fig. A1 in the appendix),[15] an increase in temperature throughout the short circuit duration results in a minor contribution of solid phase diffusion polarization after the first plateau (I) and the transition toward the second plateau (I-II), especially within the cathode (see Fig. 3).

As a consequence, the overall cell polarization throughout the second plateau (II) is primarily dominated by reaction kinetics within the positive electrode based on a depletion in salt concentration within the liquid electrolyte near the current collector and a simultaneous approach of a fully saturated surface concentration within the active material particles near the separator (IIa). As the simulated temperatures exceed the starting temperature of exothermic side reactions, a limitation of charge transfer kinetics originating in a fully saturated positive electrode at the surface of the active material particles cannot be observed (previously reported as stage IIb,[15] see Fig. A1 in the appendix). Despite the compromised validity of the model at elevated temperatures neglecting exothermic side reactions, the predicted increased current levels also come with a stronger contribution from charge transfer overpotentials within the negative electrode throughout the short circuit duration which can be correlated to losses associated with the resistivity of the SEI. Furthermore, the observed peak in C-rate around 30 s or 50% SoC forms as soon as a fully saturated surface concentration is reached at the separator interface of the positive electrode even though ion transport within both solid and liquid components is enhanced with increasing temperature. A similar peak-like behavior during external short circuits has been previously reported via modeling and simulation[16,17,51] as well as experiments.[52]

With the observation of a strongly decelerated short circuit behavior by increasing the electrode area specific convection coefficient h_c, a threshold convection coefficient can be identified at which exothermic side reactions can be avoided completely or at least delayed toward uncritical SoCs (see Fig. 2). With this in mind, either the maximum temperature occurring throughout the short circuit or the temperature at a defined SoC can be evaluated as shown in Fig. 4.

Within this work, exothermic side reactions triggered within the NMC cathode at an SoC of 50% or less are considered as uncritical resulting in no cell thermal runaway, as previously observed via accelerating rate calorimetry measurements of pouch-type Li-ion cells formed of mesocarbon microbeads (MCMB) and NMC-442.[46] This can be explained with a reduced overall reactivity of both anode and cathode with lower heat generation rates at lower SoCs.[46] At this SoC, the starting temperature of the decomposition reaction of NMC-442 has been reported to slightly increase toward 170°C. However, for simplicity reasons, a constant starting temperature of 165°C is considered in this work for the NMC cathode. Even though exothermic side reactions involving SEI decomposition are triggered at lower temperatures,[48,49] such reactions are not considered to be sufficient enough to result in cell thermal runaway in this work, due to the comparably low heat released throughout this process.[53] Both the maximum temperature T_{max} occurring throughout the short circuit duration and the temperature at 50% SoC $T|_{50\%\,SoC}$ are studied in Fig. 4. As can be seen from the figure, with an electrode area specific convection coefficient ranging from approximately 20 W m^{-2} K^{-1} to 55 W m^{-2} K^{-1}, not only exothermic side reactions within the positive electrode can be delayed toward uncritical SoCs (i.e. $T|_{50\%\,SoC} < T_{start,\,NMC}$) but

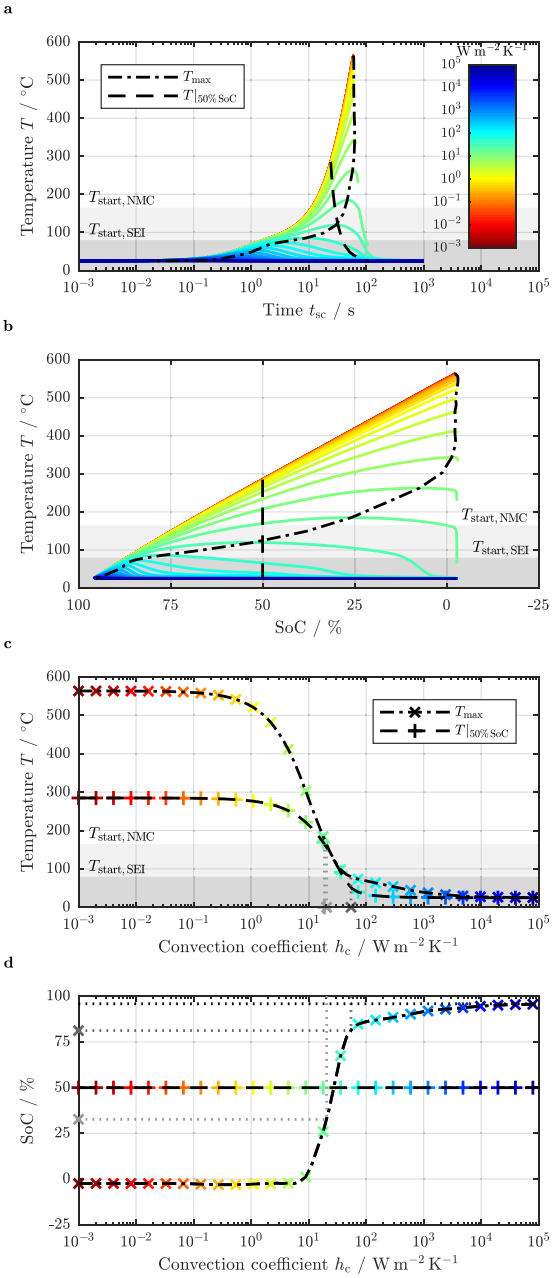

Figure 4. Predicted temperature of the electrochemical unit cell at a coolant temperature of 25°C as a function of short circuit duration t_{sc} (a), as a function of SoC (b), and as a function applied electrode area specific heat transfer coefficients h_c indicating the maximum occurring cell temperature T_{max} (dash-dotted line) and the cell temperature at 50% SoC $T|_{50\%\,SoC}$ (dashed line) for varying h_c (colors as defined in a) allowing for deriving cooling requirements to keep the unit cell within an uncritical temperature (c) and SoC window (d). Colored markers in c indicate the intersection of the dash-dotted (T_{max}: ×) and dashed lines ($T|_{50\%\,SoC}$: +) with the cell temperature curves shown in a and b as a function of h_c. The cell SoC corresponding to this intersection is shown in d. Gray markers in c and d indicate the minimum value of h_c and associated SoC to fall below a certain temperature threshold (i.e. $T_{start,\,SEI}$ or $T_{start,\,NMC}$) outlined as gray shaded areas in a, b, and c.

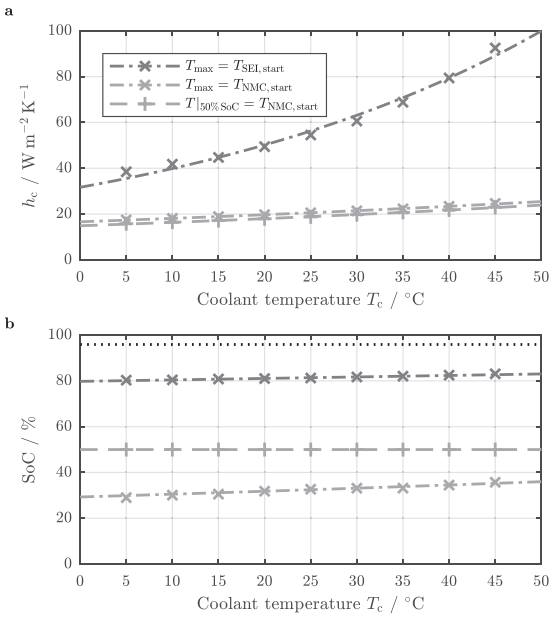

Figure 5. Comparison of electrode area specific convection coefficients h_c for predicted cooling requirements to avoid exothermic side reactions during hard short circuit events applied to the electrochemical unit cell as a function of coolant temperature ranging from 5°C to 45°C at an initial cell temperature of 25°C (a) and associated cell SoC (b) in accordance with Figs. 4c and 4d.

also exothermic side reactions within the anode can be ruled out completely (i.e. $T_{max} < T_{start,\,SEI}$, see Fig. 4c). Whilst electrode area specific convection coefficients h_c below 1 W m^{-2} K^{-1} merely reduce the resulting temperature of the unit cell due to the negligible cooling effect despite the large temperature difference between cell and coolant (see see Figs. 4a, 4b, and 4c), values above 100 W m^{-2} K^{-1} result in an asymptotic approach of the coolant temperature for both temperature criteria (see Fig. 4c). Between these two values, a strong variation in resulting cell temperature (see T_{max} and $T|_{50\%\,SoC}$ in Fig. 4c) and associated SoC (see T_{max} in Fig. 4d) can be observed, marking the range of interest for deriving appropriate cooling strategies. In order to allow for a complete avoidance of exothermic side reactions, the maximum temperature T_{max} needs to stay below the starting temperature of the SEI decomposition reaction $T_{start,\,SEI}$ of approximately 80°C. In order to achieve this, the short circuited cell needs to be cooled down below this temperature threshold within the first 15% ΔSoC or approximately 10 s of the short circuit. This leaves only little time between detecting a short circuit to applying an emergency cooling (see Figs. 2c and 2d and dash-dotted line as well as dark gray markers in Figs. 4c and 4d), starting from approximately 96% SoC in accordance with previous work.[15] In order to completely avoid exothermic side reactions involving the NMC cathode $T_{start,\,NMC}$ at approximately 165°C, the maximum temperature occurring throughout the short circuit must be maintained below this temperature within a ΔSoC of approximately 60%, which also implies a higher tolerance to a delay between short circuit detection and cell cooling (see dash-dotted line as well as light gray area and markers in Figs. 4c and 4d). The aforementioned criterion of approaching $T_{start,\,NMC}$ at 50% SoC can be therefore understood as a minimum cooling requirement to avoid cell thermal runaway whilst allowing for exothermic side reactions to occur within both anode and cathode. The range of the different cooling requirements are compared in Fig. 5a as a function of coolant temperature. As can be seen from

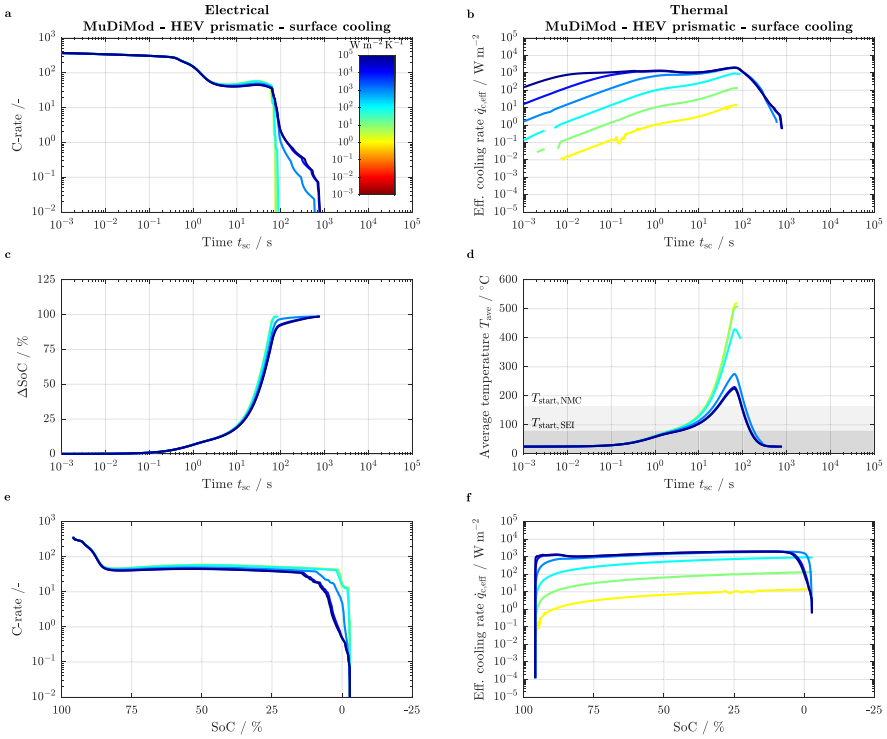

Figure 6. Predicted electrochemical (left: a, c, and e) and thermal response (right: b, d, and f) of the studied HEV-sized prismatic cell under various cooling conditions applying a surface cooling with convection coefficients h_c ranging from 1 W m^{-2} K^{-1} to 10^5 W m^{-2} K^{-1} and a constant coolant temperature of 25°C as a function of short circuit duration t_{sc} (a to d) and as a function of SoC (e and f) for the C-rate (a and e), the effectice cooling rate $\dot{q}_{c,\,eff}$ (b and f), ΔSoC (c), and average temperature T_{ave} (d).

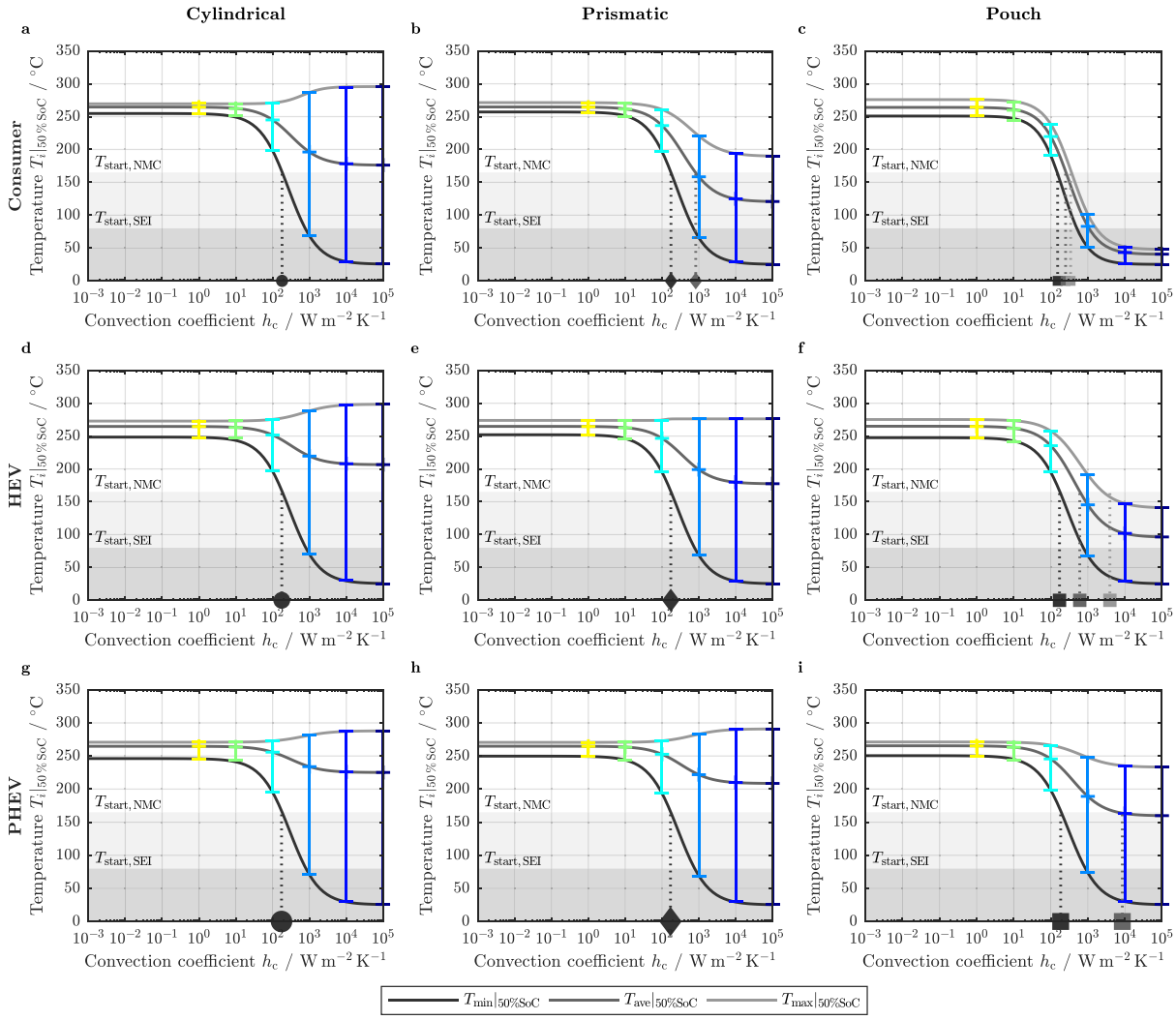

Figure 7. Predicted minimum, average, and maximum temperature of the studied cell formats and sizes in accordance with Table II for consumer-sized (top: a, b, and c), HEV-sized (middle horizontal: d, e, and f), and PHEV-sized (bottom: g, h, and i) cylindrical (left: a, d, and g), prismatic (middle vertical: b, e, and h), and pouch-type cells (right: c, f, and i) at an average cell SoC of 50% applying a surface cooling with convection coefficients h_c ranging from 1 W m^{-2} K^{-1} to 10^5 W m^{-2} K^{-1} and a constant coolant temperature of 25°C as a function of h_c. The vertical dotted lines and markers indicate a cooling below the threshold temperature $T_{\mathrm{start,\,NMC}}$ for each individual temperatures. Colors are chosen in accordance with Figs. 2, 4, and 6.

the figure, h_c is considerably dependent on the coolant temperature for T_{max} approaching $T_{\mathrm{start,\,SEI}}$. In order for both T_{max} and $T|_{50\%\,\mathrm{SoC}}$ to fall below $T_{\mathrm{start,\,NMC}}$, a reduced impact of the coolant temperature can be observed. This implies that for lower coolant temperatures, the likelihood of completely avoiding exothermic decomposition reactions can be considerably increased, approaching the minimum cooling requirements set by the $T|_{50\%\,\mathrm{SoC}} = T_{\mathrm{NMC}}$ criterion. However, this has almost no effect on the tolerable ΔSoC range, implying the necessity of a comparably immediate cooling of the cell in order to achieve this goal (see Fig. 5b). For both T_{max} and $T|_{50\%\,\mathrm{SoC}}$ to approach $T_{\mathrm{start,\,NMC}}$, similar values for h_c can be observed with a larger tolerable ΔSoC for T_{max} compared to $T|_{50\%\,\mathrm{SoC}}$ at slightly higher values of h_c.

In this work, $T|_{50\%\,\mathrm{SoC}} = T_{\mathrm{start,\,NMC}}$ is considered as the minimum cooling requirement in order to be able to avoid cell thermal runaway which will be studied in further detail for varying cell formats and sizes whilst applying a coolant temperature of 25°C.

Electrochemical-electrical-thermal short circuit behavior of different cell formats and sizes.—By applying the MuDiMod approach in order to describe the cell formats and sizes shown in Table II, the external short circuit behavior of larger sized cells used for commercial applications can be evaluated in comparison to the discussed short circuit characteristics of the unit cell. For this purpose, two cooling conditions are studied which have been recently discussed in literature, namely surface cooling[54,55] and tab cooling.[55,56] By accounting for the same short circuit condition for all cells representing a low external short circuit resistance (i.e. applying the same boundary condition approaching a cell voltage of 0 V), a most comparable evaluation of the interaction of cell format, size, and cooling condition can be achieved. Another approach would be to apply the same short circuit resistance to all cells implying lower overall current densities with increasing cell size. This would require an adaption of area specific short circuit resistances applied to the unit cell for each cell format and size in order

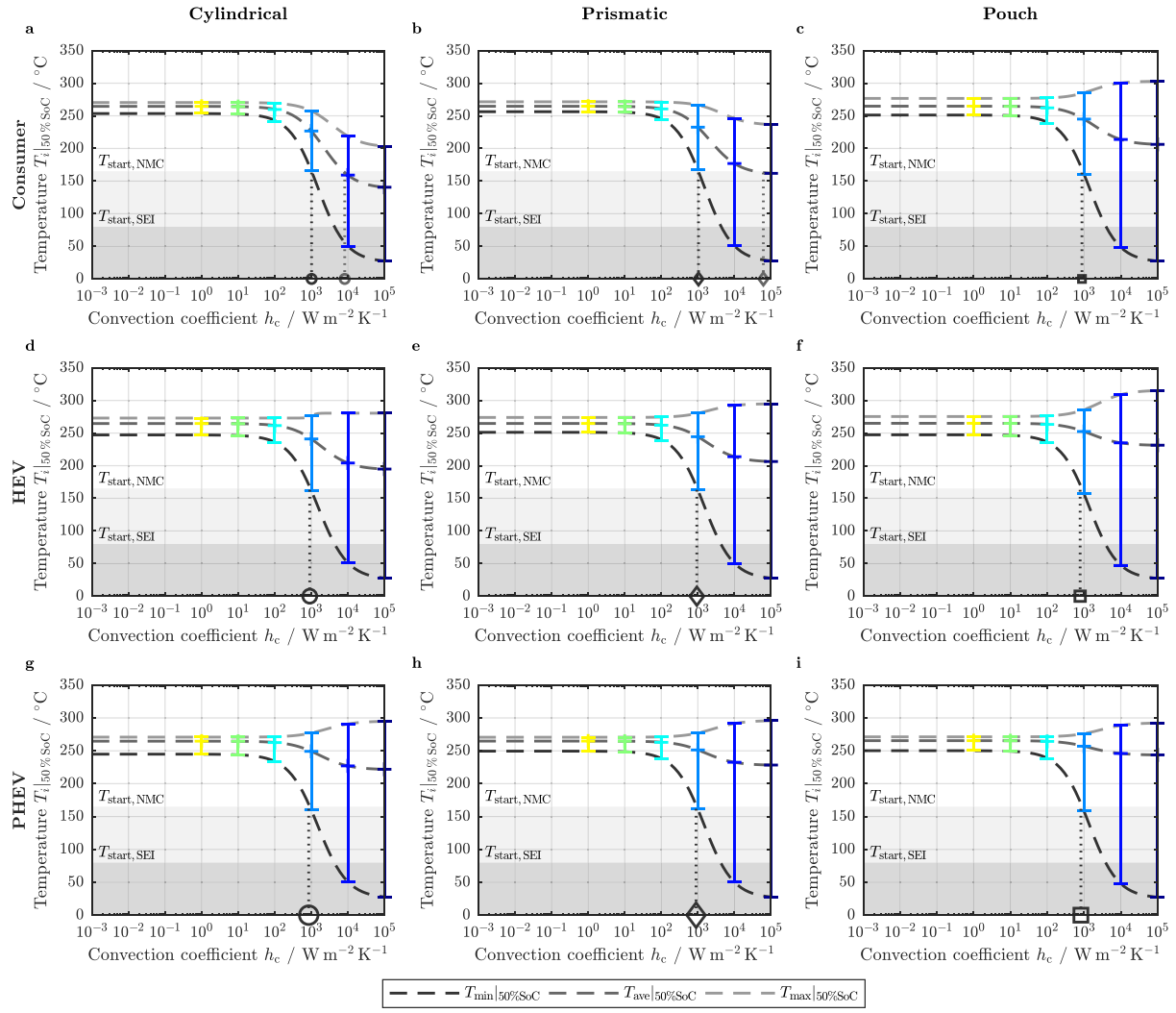

Figure 8. Predicted minimum, average, and maximum temperature of the studied cell formats and sizes in accordance with Table II for consumer-sized (top: a, b, and c), HEV-sized (middle horizontal: d, e, and f), and PHEV-sized (bottom: g, h, and i) cylindrical (left: a, d, and g), prismatic (middle vertical: b, e, and h), and pouch-type cells (right: c, f, and i) at an average cell SoC of 50% applying a tab cooling with convection coefficients h_c ranging from 1 W m^{-2} K^{-1} to 10^5 W m^{-2} K^{-1} and a constant coolant temperature of 25°C as a function of h_c. The vertical dotted lines and markers indicate a cooling below the threshold temperature $T_{\mathrm{start,\,NMC}}$ for each individual temperatures. Colors are chosen in accordance with Figs. 2, 4, and 6.

to allow for a straightforward comparison to the electrochemical unit cell.

The short circuit behavior of an HEV-sized prismatic cell is exemplarily shown in Fig. 6 applying a surface cooling with various convection coefficients at a coolant temperature of 25°C. When comparing Fig. 6 to Fig. 2, a strong difference between the thermally well-connected unit cell and the geometrically restricted prismatic cell becomes apparent. Whilst the unit cell's temperature cannot only be maintained below the temperature threshold of exothermic side reactions but can even be operated under isothermal conditions if the chosen cooling condition is sufficiently strong, the HEV-sized prismatic cell cannot be cooled to the same extent. This implies that even under conditions representing a direct phase change at the surface of the wound electrode configuration, keeping the cell's average temperature below $T_{\mathrm{start,\,NMC}}$ throughout the entire short circuit duration is not possible, let alone the cell's maximum temperature. Hence, exothermic side reactions involving the positive electrode which may result in cell thermal runaway must be expected to occur. The reason for this temperature increase can be found in a reduced effective cooling rate $\dot{q}_{\mathrm{c,\,eff}}$ (W m^{-2} K^{-1}) with respect to the coated electrode area (see Figs. 6b and 6f):

$$\dot{q}_{\mathrm{c,\,eff}} = \dot{q}_{\mathrm{c}} \cdot \frac{A_{\mathrm{surf/tab}}}{A_{\mathrm{ele}}} = \dot{q}_{\mathrm{c}} \cdot \frac{A_{\mathrm{surf/tab}}}{2 \cdot w_{\mathrm{ele}} \cdot h_{\mathrm{ele}}} \qquad [1]$$

whereas A_{surf} or A_{tab} represent the cooled area of the jelly roll or electrode stack, depending on the applied cooling strategy, and A_{ele} describes the double-sided electrode area of the investigated cell. This effective cooling rate is partly reduced by over a magnitude compared to the electrochemical unit cell (see Figs. 2b and 2f) which is based on the limited surface area available for cooling in the first place, and a reduced surface temperature resulting from an increased thermal resistivity in the second place. These two effects, which are related to geometric and thermophysical properties of the cell and its jelly roll or electrode stack, both directly affect the overall cooling performance:

$$\dot{Q}_{\mathrm{c}} = h_{\mathrm{c}} \cdot A_{\mathrm{surf/tab}} \cdot \left(T_{\mathrm{surf/tab}} - T_{\mathrm{c}}\right) \qquad [2]$$

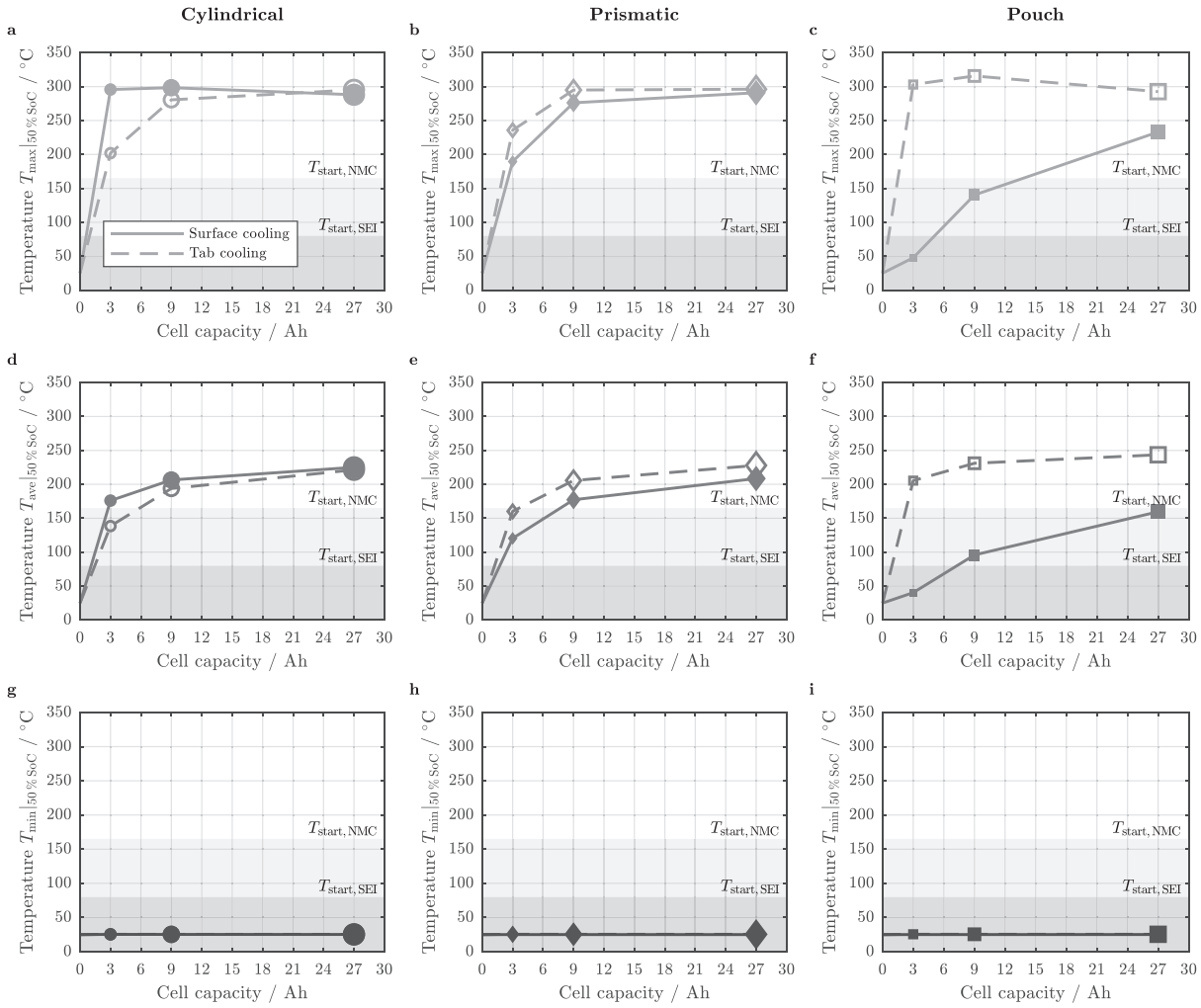

Figure 9. Approximated maximum (top: a, b, and c), average (middle horizontal: d, e, and f), and minimum cell temperature (bottom: g, h, and i) at maximum convective cooling (i.e. h_c approaching ∞) and a constant coolant temperature of 25°C of the studied cell formats and sizes in accordance with Table II for cylindrical (left: a, d, and g), prismatic (middle vertical: b, e, and h), and pouch-type cells (right: c, f, and i) at an average cell SoC of 50% applying a both surface and tab cooling as a function of cell capacity.

whereas T_{surf} or T_{tab} represent the local temperature of the cooled area depending on the applied cooling strategy and T_c describes the coolant temperature. The limited effect of the applied cooling conditions results in an almost unaffected short circuit behavior with similar C-rates and little variation in short circuit duration (see Figs. 6a, 6c, and 6e).

When studying the cell temperature at an average SoC of 50% in accordance with Fig. 4, the effect of cell format and size becomes obvious for both surface cooling (see Fig. 7) and tab cooling (see Fig. 8).

With the geometrical restrictions of the studied cells, considerable inhomogeneities are provoked which generally become more pronounced with growing cell size and increased cooling performance represented by larger convection coefficients h_c. However, even at low cooling rates approaching natural convection (ca. 1 W m^{-2} K^{-1}), a considerable difference between the minimum, average, and maximum cell temperature can be observed at 50% SoC, which can also not be ruled out completely even under adiabatic conditions (i.e. 0 W m^{-2} K^{-1}, not shown here). This can be explained with the polarization along the electrodes during operation involving an inhomogeneous current density distribution and, consequently, spatially varying heat generation rates, temperatures, cell polarization, and so forth building up throughout discharge. The impact of the chosen cell format and size as well as the applied cooling strategy becomes obvious when comparing the characteristics shown in Fig. 7 and Fig. 8 to the behavior of the unit cell shown in Fig. 4 as a function of convection coefficient. Whilst the minimum temperature can be maintained below $T_{\mathrm{start,\,NMC}}$ for all cells with the chosen range of convection coefficients, the average and especially the maximum cell temperature T_{ave} and T_{max} can only be controlled for smaller and thinner cells.

This can be explained with a relatively large surface area and a limited resistance for heat conduction. With the chosen model assumptions, only surface cooled pouch-type cells of consumer and HEV size can be maintained below $T_{\mathrm{start,\,NMC}}$ at 50% SoC. Whilst the average temperature of consumer-sized prismatic cells and PHEV-sized pouch-type cells can be physically reduced below this threshold, by applying a surface cooling, all other cell sizes and formats cannot be maintained below $T_{\mathrm{start,\,NMC}}$ for both T_{ave} and T_{max}. Due to the larger electrode length and reduced electrode height of cylindrical cells in comparison to prismatic and pouch-type cells, a slightly reversed pic-

ture can be observed between these three cell formats when applying a tab cooling, which allows the average cell temperature to be kept below $T_{\text{start, NMC}}$ for consumer-sized cylindrical and prismatic cells at convection coefficients exceeding 10000 W m^{-2} K^{-1}. All other studied combinations of format and size cannot be maintained below this threshold on average.

It becomes furthermore apparent that besides limitations of the applied convective cooling with 100000 W m^{-2} K^{-1} marking the somewhat upper range of physically possible heat transfer coefficients, both cell format and size also geometrically limit the heat that can be extracted from the cell. Whilst the temperature of the unit cell can be maintained isothermal if the cooling is chosen sufficiently strong, this seemingly cannot be achieved for larger sized cells showing an asymptotic approach of higher temperature levels for both average and maximum cell temperature. Furthermore, even though the average temperature is generally reduced with increasing convection coefficients, the maximum cell temperature at 50% SoC seems to partly increase depending on the cell's format and size combined with the chosen cooling strategy. This appears to be the case for all conditions in which a cooling of the cell's average temperature below $T_{\text{start, NMC}}$ is not possible. This effect can be only explained by vast inhomogeneities within the cell triggered by the temperature distribution fostering large local current densities and heat generation rates at higher temperature regions (e.g. center of the jelly roll or electrode stack), paired with a limited cooling capability which predominantly affects regions where comparably low currents and heat generation rates can be observed (e.g. surface near regions of the jelly roll or electrode stack). The temperature at maximum convective cooling (i.e. h_c approaching ∞) can be estimated by fitting the data shown in Fig. 7 and Fig. 8 via a hyperbolic tangent function (solid and dashed lines in Figs. 7 and Fig. 8), which is shown in Fig. 9 for the minimum, average, and maximum cell temperature. Following this approach, a critical cell size for each format and cooling condition can be derived which still allows for a complete cooling of the cell below a critical threshold temperature. Only surface cooled pouch-type cells can still be maintained below $T_{\text{start, NMC}}$ in terms of average and maximum temperatures for cell sizes beyond the considered HEV size. For all other combinations of cell format and cooling condition, only a cell size below the studied 3 Ah consumer size could possibly be kept below this temperature threshold at the applied short circuit condition.

Furthermore, the graphic representation showing the cooling performance in Fig. 9 allows a direct comparison of the effectiveness of surface cooling and tab cooling. Whilst the cylindrical cell can be physically maintained at lower temperatures via tab cooling, both prismatic and especially pouch-type cells can be cooled more efficiently via surface cooling. The general cooling capability of the three studied cell formats increases from cylindrical, to prismatic, and pouch-type cell with a stronger dependency on the applied cooling strategy (see spread between solid and dashed lines in Figs. 9a to 9f).

By further comparing the convection coefficients at which the minimum cell temperature falls below $T_{\text{start, NMC}}$ to the convection coefficient that needs to be applied to the unit cell for a cooling below this threshold, the loss in cooling efficiency due to geometrical restrictions becomes apparent (see Fig. 10). Whilst a convection coefficient of just under 20 W m^{-2} K^{-1} is sufficient for cooling the whole unit cell below $T_{\text{start, NMC}}$ at 50% SoC, a range between 150 W m^{-2} K^{-1} and 180 W m^{-2} K^{-1} must be applied for the surface cooling (see Fig. 10a) which increases toward 800 W m^{-2} K^{-1} and beyond 1000 W m^{-2} K^{-1} (see Fig. 10b) for the tab cooling, in order to reduce at least the cell's minimum temperature below this value depending the format and size of the cells. This increase by a factor of approximately 10 to 50 for the surface and tab cooling compared to the unit cell underlines not only the geometric restrictions of cooling larger sized cells but also reveals a superior cooling capability of surface cooling compared to tab cooling for the studied cells. However, this representation does not allow an easy distinction between the cooling capabilities of different cell formats and sizes.

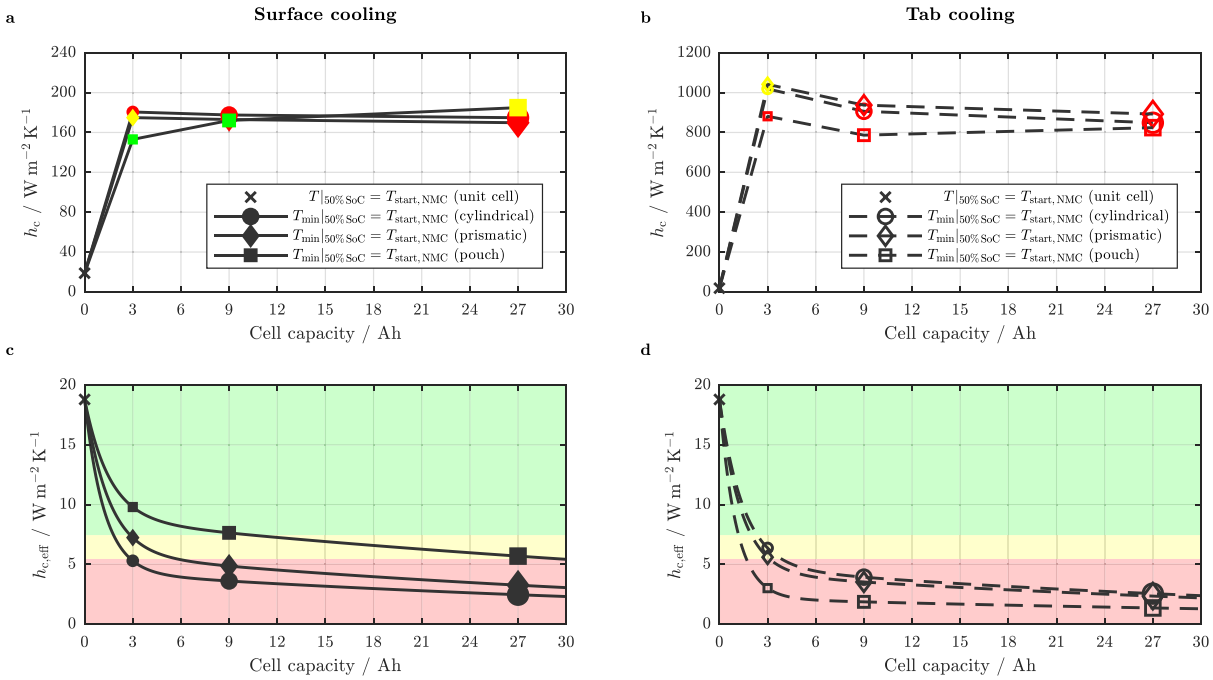

Figure 10. Approximated convection coefficients h_c (top: a and b) and approximated effective convection coefficients $h_{c,\,\text{eff}}$ (bottom: c and d) beyond which the temperature of the electrochemical unit cell and the minimum temperature of the studied cell formats and sizes (see Table II) fall below $T_{\text{start, NMC}}$ at an average cell SoC of 50% applying both a surface (left: a and c) and tab cooling (right: b and d) as a function of cell capacity. Green markers and area indicate a sufficient cooling to reduce both $T_{\text{ave}}|_{50\%\,\text{Soc}}$ and $T_{\text{max}}|_{50\%\,\text{Soc}}$ below $T_{\text{start, NMC}}$, yellow markers and area indicate a cooling of $T_{\text{ave}}|_{50\%\,\text{Soc}}$ below this threshold, and red markers and area indicate an insufficient cooling with both $T_{\text{ave}}|_{50\%\,\text{Soc}}$ and $T_{\text{max}}|_{50\%\,\text{Soc}}$ exceeding $T_{\text{start, NMC}}$.

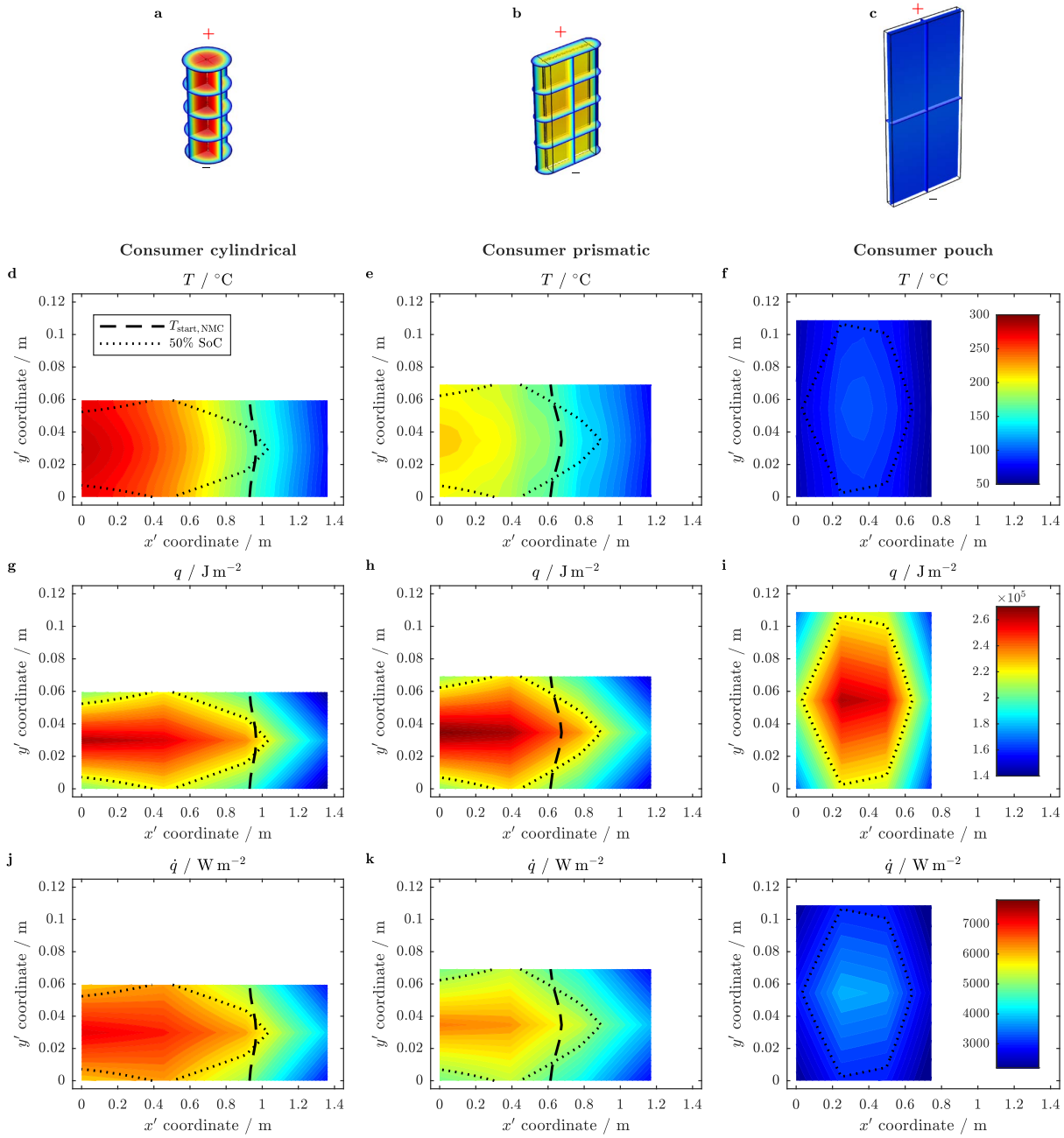

Figure 11. Predicted cell temperature for the 3D geometry of the jelly roll or electrode stack (a, b, and c) and for the mapped 2D representation along the electrodes with $x' = 0$ marking the beginning of the jelly roll or electrode stack (d, e, and f) based on the accumulated area specific heat q (g, h, and i) and the superimposed heat dissipation at an average SoC of 50% together with the area specific heat generation rate $\dot{q}$ (j, k, and l) for the cylindrical (left: a, d, g, and j), prismatic (middle: b, e, h, and k), and pouch-type consumer sized cells (right: c, f, i, and l) at a surface cooling of 1000 W m^{-2} K^{-1} and 25°C. The dashed and dotted lines indicate the threshold temperature $T_{\text{start, NMC}}$ and 50% SoC, respectively. The color range shown in f applies to all temperature data (a to f).

By further relating the cooled area A_{surf} or A_{tab} to the overall (double-sided) electrode area A_{ele} (see Table II), an effective cooling coefficient $h_{\text{c, eff}}$ can be derived in analogy to Eq. 1:

$$h_{\text{c, eff}} = h_{\text{c}} \cdot \frac{A_{\text{surf/tab}}}{A_{\text{ele}}} = h_{\text{c}} \cdot \frac{A_{\text{surf/tab}}}{2 \cdot w_{\text{ele}} \cdot h_{\text{ele}}} \quad [3]$$

Whilst $h_{\text{c, eff}} = h_{\text{c}}$ for the unit cell, the effective cooling coefficient strongly decreases for the surface and tab cooling of larger sized cells (compare Figs. 10a and 10b to 10c and 10d). When further rating a cell and cooling condition that allows for a cooling of both a cell's average and maximum temperature below $T_{\text{start, NMC}}$ at 50% SoC as uncritical (see green markers and area in Fig. 10) and an exceeding of both average and maximum temperatures as critical (see red markers

and area in Fig. 10), the combination of cell format, size, and applied cooling strategy can be assessed (see Figs. 10c and 10d). Hence, a cell and cooling condition resulting in an effective convection coefficient below 5.5 W m^{-2} K^{-1} at which the minimum cell temperature falls below $T_{start,\,NMC}$ can be regarded as critical (see red markers and area in Figs. 10c and 10d). An effective cooling coefficient beyond 7.5 W m^{-2} K^{-1} results in an uncritical behavior (see green markers and area in Figs. 10c and 10d). The range in between these two values, which is characterized by an average temperature below and a maximum temperature beyond $T_{start,\,NMC}$ at 50% SoC, marks a transition which needs to be considered more closely in terms of local temperatures and SoCs in order to be able to evaluate the likelihood of exothermic side reactions that may result in a cell thermal runaway (see yellow markers and area in Figs. 10c and 10d).

Such evaluation is exemplarily shown in Fig. 11 and Fig. 12 for consumer-sized cells with an applied surface cooling of $h_c = 1000$ W

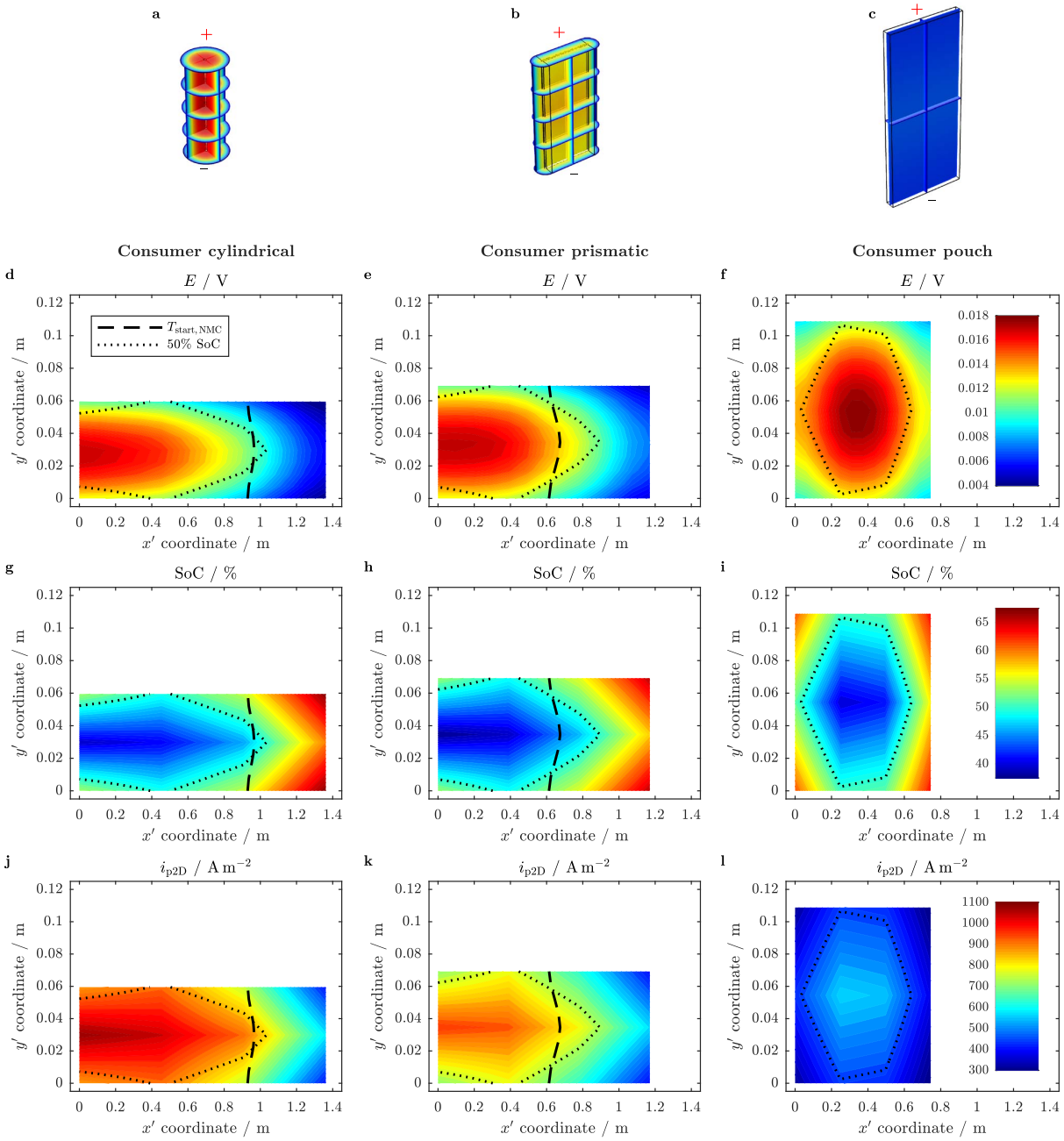

Figure 12. Predicted cell temperature for the 3D geometry of the jelly roll or electrode stack (a, b, and c) in accordance with Fig. 11 together with the corresponding local cell potential E (d, e, and f), cell SoC (g, h, and i), and the through-plane current density i_{p2D} (j, k, and l) at an average SoC of 50% for the cylindrical (left: a, d, g, and j), prismatic (middle: b, e, h, and k), and pouch-type consumer sized cells (right: c, f, i, and l) at a surface cooling of 1000 W m^{-2} K^{-1} and 25°C. The dashed and dotted lines indicate the threshold temperature $T_{start,\,NMC}$ and 50% SoC, respectively.

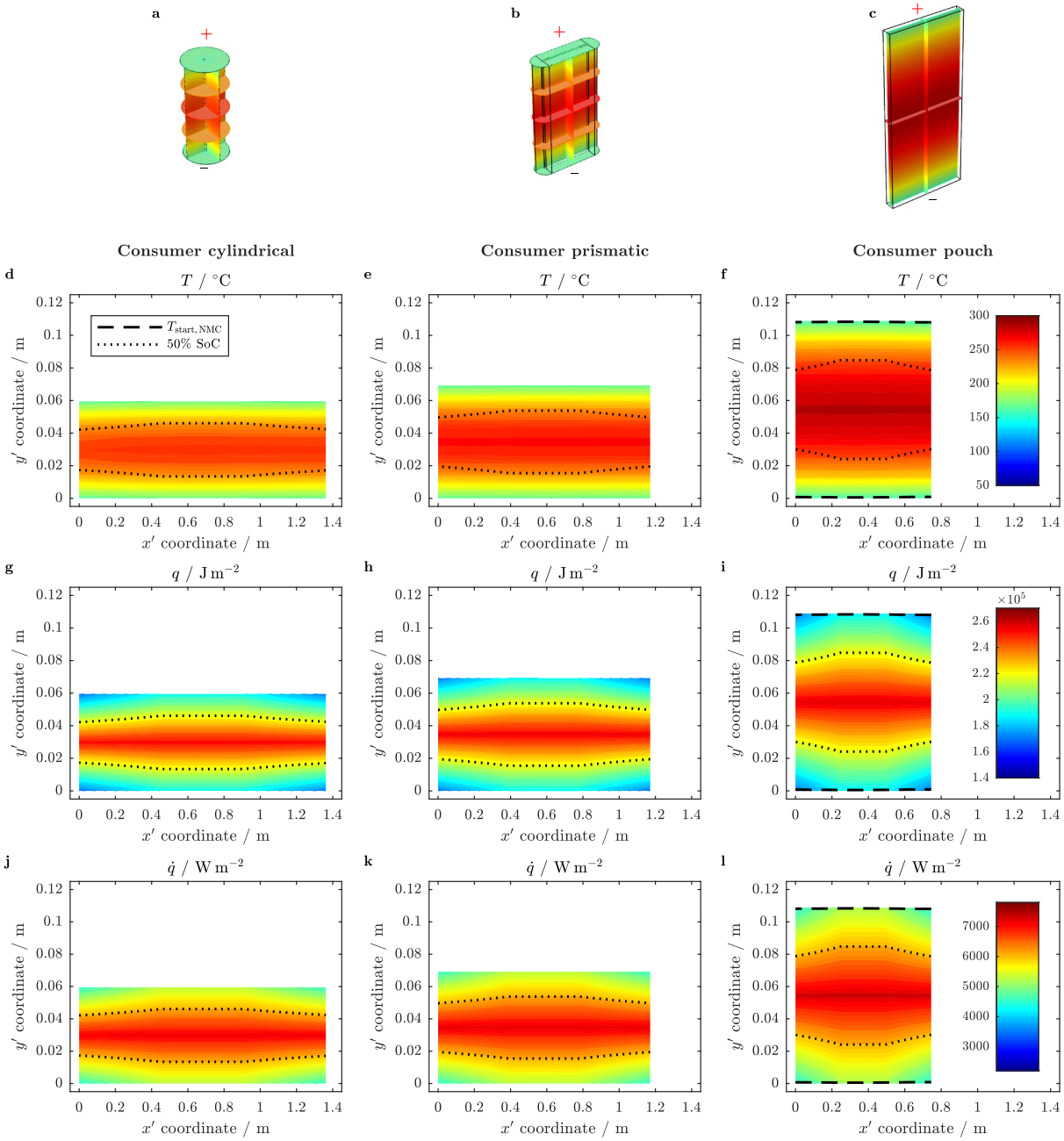

Figure 13. Predicted cell temperature for the 3D geometry of the jelly roll or electrode stack (a, b, and c) and for the mapped 2D representation (d, e, and f) based on the accumulated area specific heat q (g, h, and i) and the superimposed heat dissipation at an average SoC of 50% together with the area specific heat generation rate $\dot{q}$ (j, k, and l) for the cylindrical (left: a, d, g, and j), prismatic (middle: b, e, h, and k), and pouch-type consumer sized cells (right: c, f, i, and l) at a tab cooling of 1000 W m^{-2} K^{-1} and 25°C. The dashed and dotted lines indicate the threshold temperature $T_{\text{start, NMC}}$ and 50% SoC, respectively. The color range shown in f applies to all temperature data (a to f).

m^{-2} K^{-1} at 50% SoC. The derived distribution in temperature T (see Figs. 11a to 11f) is based on the accumulated area specific heat q (J m^{-2}) shown in Figs. 11g, 11h, and 11i and the underlying area specific heat generation rate $\dot{q}$ (W m^{-2}) shown in Figs. 11j, 11k, and 11l. As can be seen from Fig. 11, large temperature gradients form especially for the cylindrical and prismatic cell compared to the pouch-type cell which is also shown in Fig. 7. With the chosen model discretization of the coupled p2D physical-chemical/2D electrical electrode model (i.e. eight p2D models per Ah for all presented models), a coarser distribution in accumulated heat (see Figs. 11g, 11h, and 11i) and underlying heat generation rate (see Figs. 11j, 11k, and 11l) can be observed compared to the calculated 3D (see Fig. 11a, 11b,

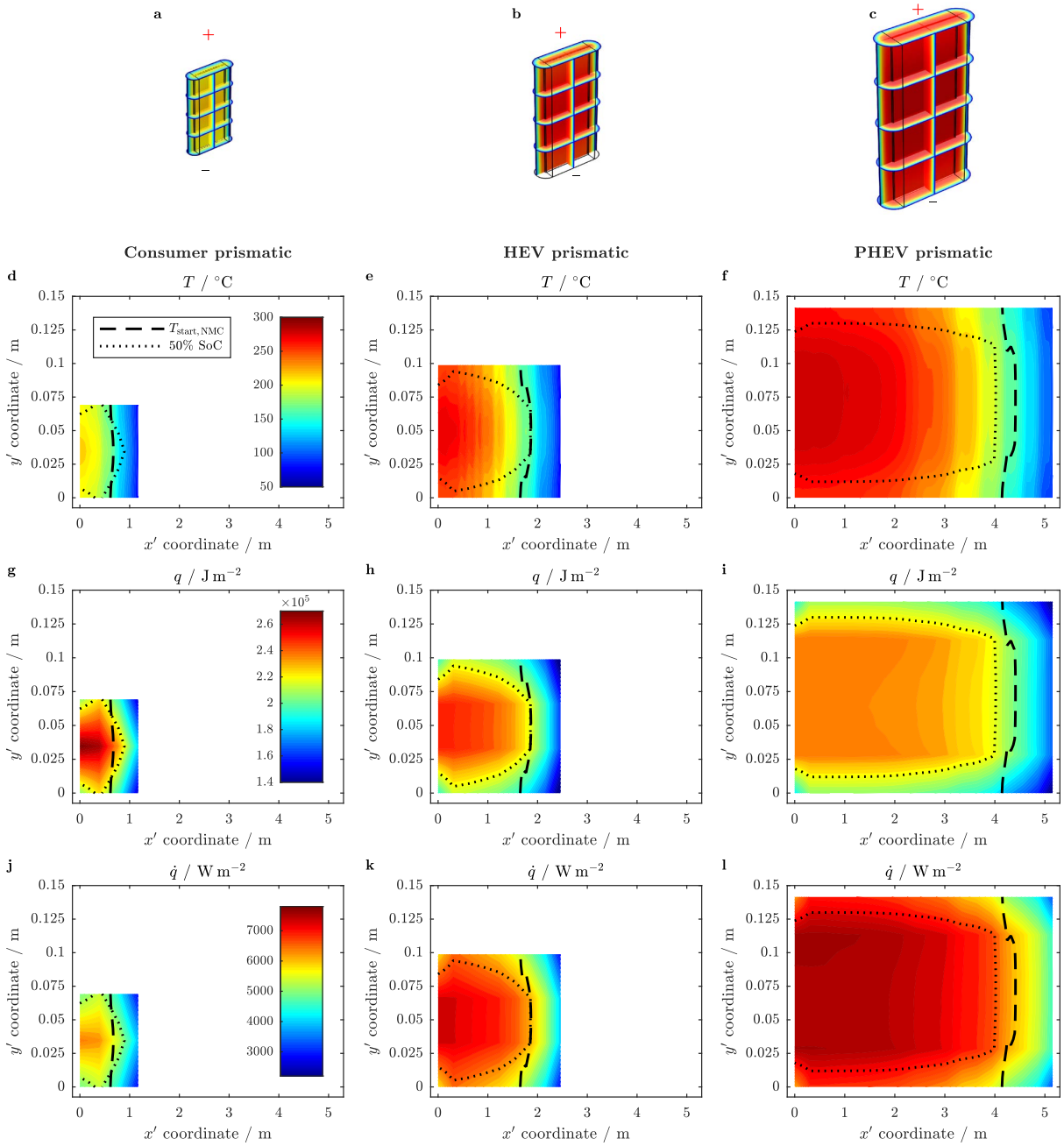

Figure 14. Predicted cell temperature for the 3D geometry of the jelly roll or electrode stack (a, b, and c) and for the mapped 2D representation along the electrodes (d, e, and f) based on the accumulated area specific heat q (g, h, and i) and the superimposed heat dissipation at an average SoC of 50% together with the area specific heat generation rate $\dot{q}$ (j, k, and l) for the consumer-sized (left: a, d, g, and j), HEV-sized (middle: b, e, h, and k), and PHEV-sized prismatic cells (right: c, f, i, and l) at a surface cooling of 1000 W m^{-2} K^{-1} and 25°C. The dashed and dotted lines indicate the threshold temperature $T_{\text{start, NMC}}$ and 50% SoC, respectively. The color range shown in f applies to all temperature data (a to f).

and 11c) and mapped 2D temperature distribution (see Figs. 11d, 11e, and 11f).

With the limited penetration depth of the applied cooling strategy, about two-thirds of the electrode width ranges above $T_{\text{start, NMC}}$ for the consumer-sized cylindrical cell, whereas this ratio is reduced to half of the electrode width for the prismatic cell. The pouch-type cell ranges completely below this threshold due to a comparably effective penetration of the cooling strategy (see dashed line in Fig. 11). When looking into the spatial distribution of electrochemical and electrical variables, such as local cell potential E (V, see Figs. 12d, 12e, and 12f), SoC (see Figs. 12g, 12h, and 12i), and through-plane current density i_{p2D} (A m^{-2}, see Figs. 12j, 12k, and 12l), it becomes obvious that the

current follows the temperature, resulting in the lowest SoCs at regions with the highest cell and electrode temperatures. With the presented cell formats and sizes, the 50% SoC boundary does not completely fill the area marked by the $T_{start,\,NMC}$ threshold for both cylindrical and prismatic cell types (compare dotted line to dashed line in Fig. 11 and Fig. 12). This would most likely result in considerable exothermic side reactions involving the positive electrode especially at tab-near regions within the cell's center at this very moment of the short circuit. With the average temperature of the prismatic cell ranging below the temperature of the cylindrical cell, the area which is affected by a potentially critical combination of temperature and SoC is smaller for the prismatic cell compared to the cylindrical cell. The consumer-sized pouch-type cell shows overall lower temperatures than $T_{start,\,NMC}$ at 50% SoC with a slightly unsymmetrical SoC distribution along the electrode width, which can be explained with the applied folding pattern and scaling of the chosen representative cell format from PHEV to HEV and consumer size. This involves an odd number of electrode layers which are z-folded to form the HEV and cylindrical cells based on the scaling from the PHEV1/BEV1 pouch-type cell whilst keeping the aspect ratio constant. As a result, the thermal representation of the cylindrical and HEV-sized electrode stack includes regions at the very end of the electrodes which are not heated. This provokes a slightly unsymmetrical temperature distribution, which affects the current density distribution and, hence, heat generation rate as shown in Fig. 11 and Fig. 12. By applying a tab cooling of 1000 W m^{-2} K^{-1} to the considered consumer-sized cells, all three cell formats surpass $T_{start,\,NMC}$ throughout almost the entire electrode area (see Fig. 13) at 50% SoC with the largest temperature gradients forming for the pouch-type cell, showing the highest maximum temperature among the three formats and also the lowest minimum temperature bordering $T_{start,\,NMC}$ directly at the tab region (see dashed line in Fig. 13f).

With the SoC inversely following the temperature distribution, showing the lowest SoCs at approximately half the electrode height (see dotted line in Fig. 13), an initiation of exothermic side reactions within the cell's center with a reaction front moving toward the tabs is likely, as the SoC reduction is seemingly not as fast as the temperature increase leading to potentially critical temperature and SoC combinations throughout the short circuit. With increasing cell size, the outpacing of a temperature increase beyond $T_{start,\,NMC}$ compared to an SoC decrease toward 50% or less becomes more pronounced which is exemplarily shown for the prismatic cell at a surface cooling of 1000 W m^{-2} K^{-1} (see Fig. 14). Despite the larger amount of area specific heat q accumulated throughout the short circuit within the cell's center of the consumer-sized prismatic cell compared to its HEV-sized and PHEV-sized representatives (see Figs. 14g to 14l), lower maximum temperatures can be observed which supports a superior cooling performance of smaller-sized cells due to a lower thermal resistivity.

Conclusions

The presented model helps to shed light on the short circuit performance of Li-ion cells of various formats and sizes under varying cooling conditions. With the suggested mapping procedure, exchanging temperature and heat generation rate between the 3D thermal model of the cell's jelly roll or electrode stack and the 2D electrical model of the planar electrodes, not only consumer-sized Li-ion cells but also larger, automotive cells can be described under extreme conditions such as short circuits, which demand a considerably detailed discretization especially for the p2D physical-chemical models between the two current collector foils. Whilst a thermally well-connected electrochemical unit cell can be rather easily maintained below a temperature threshold triggering exothermic side reactions and can be further shorted under quasi-isothermal operation as previously demonstrated,[14] larger sized cells pose a significant challenge to be maintained within a safe operating window, defined by the cell's local temperature and SoC. The limited heat dissipation throughout the cell's jelly roll or electrode stack make a sufficient cooling almost impossible for the chosen cell formats and sizes as well as the applied cooling conditions in case a short circuit is maintained. Even though the minimum cell temperature can be physically reduced to uncritical temperature levels, the average and maximum cell temperature within the cell's center can partly not be controlled, even though a physically maximized convective cooling is applied at moderate coolant temperatures. On the one hand, a reduced coolant temperature can enhance the cooling capability of the cooling system which might be able to push the cell's average and maximum temperature to lower values. On the other hand, a limited cell size combined with a maximized cooled surface area and minimized thermal resistivity improves the cooling capability of the cell itself. When applied and combined effectively, both of these measures can increase the likelihood of preventing cell thermal runaway as a result of external short circuits. Furthermore, alternative approaches focusing on altering the electrode design such as increasing the electrode loading by reducing the porosity, might intrinsically limit the short circuit current due to increased liquid phase limitations.[15,57,58] Such an approach, will be more closely investigated by our group in future. The question of an ideal cell design allowing for a maximum level of safety whilst guaranteeing the required energy and power characteristics, however, cannot be answered with such a cell model on its own. This requires further considerations of safety mechanisms included in the various cell designs and restrictions arising from module and pack integration.

The suggested criteria, outlining a critical temperature increase beyond the thermal stability window of the cell's active and passive components combined with a critical SoC threshold, need to be more thoroughly studied in future in order to be able to derive a safe operating window for various material combinations. This however, requires experimental data and models which are capable of reliably describing thermal decomposition reactions as a function of cell SoC or degree of lithiation within the active material particles, which can only be scarcely found in literature so far.[46] Such considerations need to be further evaluated in the context of aging which not only affects the reactivity of the individual exothermic side reactions,[46,59] but also increases the cell's electrical and electrochemical resistivity affecting short circuit currents and heat generation rates. Based on the presented difficulties of maintaining a cell within a safe temperature and SoC window during short circuit events, especially with increasing cell size, cell thermal runaway must be more thoroughly described including the cell's interactions with its surroundings (e.g. venting) in order to evaluate possibilities to design batteries which can tolerate cell thermal runaway without propagation to neighboring cells or modules.

With the aid of the presented model, also local or internal short circuits can be described which will be the focus of upcoming work of the group. Besides these activities, validating electro-thermal models under both normal operation and abusive conditions is also part of future activities which will allow for further improvement in the quality of the discussed modeling approaches.

Acknowledgment

The work presented here was financially supported by the German Federal Ministry of Education and Research (BMBF) under grant number 03XP0027G (*MiBZ*) as well as by the European Union's Horizon 2020 research and innovation program under grant number 713771 (*EVERLASTING*).

Appendix

$$\frac{dE_{eq,\,neg}}{dT} = \frac{-3.8149\times10^{-4}x^5 + 1.058\times10^{-3}x^4 - 1.1235\times10^{-3}x^3 + 5.5727\times10^{-4}x^2 - 1.242\times10^{-4}x + 9.0095\times10^{-6}}{x^5 - 2.9967x^4 + 3.2192x^3 - 1.4066x^2 + 1.8475\times10^{-1}x + 1.3198\times10^{-2}} \quad [A1]$$

Table A1. Model parameters for the physical-chemical model of the electrochemical unit cell (p2D-EC), the electrical model of the electrode layers (2D-E), and the thermal model of the jelly roll or electrode stack (3D-T). Model parameters of the p2D-EC model were chosen in acoordance with Ref. 15.

Description	Symbol	Unit	Negative electrode Cu (cc) & LiC (neg)	Separator polyolefin (sep)	Positive electrode NMC-111 (pos) & Al (cc)
p2D-EC model parameters					
Equilibrium potential[m,15]	$E_{\mathrm{eq},\,i}$	V	see Ref. 15	n/a	see Ref. 15
Entropic coefficient[l,64,65]	$\frac{\mathrm{d}E_{\mathrm{eq},\,i}}{\mathrm{d}T}$	V K^{-1}	fitted,[64] see Eq. A1	n/a	fitted,[65] see Eq. A2
Anodic and cathodic reaction rate constant[l,5]	$k_{\mathrm{a/c},\,i}$	m s^{-1}	2×10^{-11}	n/a	2×10^{-11}
Anodic and cathodic charge transfer coefficient[e]	$\alpha_{\mathrm{a/c},\,i}$	-	0.5	n/a	0.5
Film resistance[l,16]	R_{film}	Ω m^{-2}	0.0035	n/a	0
Maximum solid phase concentration[c]	$c_{\mathrm{s,\,max},\,i}$	mol m^{-3}	29862	n/a	49242
Solid phase electronic conductivity[e]	$\sigma_{\mathrm{s},\,i}$	S m^{-1}	100	n/a	10
Solid phase diffusion coefficient[e,15]	$D_{\mathrm{s},\,i}$	m^2 s^{-1}	fitted,[15] see Eq. A3	n/a	fitted,[15] see Eq. A4
Liquid phase ionic conductivity[l,47]	κ_{l}	S m^{-1}		modified from Ref. 47, see Eq. A5	
Liquid phase diffusion coefficient[l,47]	D_{l}	m^2 s^{-1}		modified from Ref. 47, see Eq. A6	
Liquid phase transference number[l,47]	t_+	-		0.38	
Liquid phase thermodynamic factor[l,47]	TDF	-		modified from Ref. 47, see Eq. A7	
Particle size (D50)[m]	$R_{\mathrm{p},\,i}$	μm	11	n/a	7
Coating and separator thickness[m]	l_i	μm	67	25	79
Porosity[c]	$\epsilon_{\mathrm{l},\,i}$	%	51.3	50	48.7
Active material volume fraction[c]	$\epsilon_{\mathrm{s},\,i}$	%	46.4	n/a	36.4
Tortuosity[e]	τ_i	-	$\epsilon_{\mathrm{l,\,neg}}^{-1.8}$	$\epsilon_{\mathrm{l,\,sep}}^{-1.8}$	$\epsilon_{\mathrm{l,\,pos}}^{-1.1}$
Stoichiometry[c] at $E_{\mathrm{eq,\,cell}} = 4.20$ V/SoC = 100%	$\frac{c_{\mathrm{s}}}{c_{\mathrm{s,\,max,\,i}}}$	%	76.6	n/a	42.5
$= 4.15$ V/SoC = 96%			73.5		44.6
2D-E model parameters					
Current collector electronic conductivity[l,66,67]	$\sigma_{\mathrm{cc},\,i}$	S m^{-1}	see Eq. A8[66]	n/a	see Eq. A9[67]
Current collector thickness[e]	$l_{\mathrm{cc},\,i}$	μm	12	n/a	18
Electrode width[e]	$w_{\mathrm{ele},\,i}$	mm	see Table II	n/a	see Table II
Electrode height[e]	$h_{\mathrm{ele},\,i}$	mm	see Table II	n/a	see Table II
3D-T model parameters			Cu / LiC		NMC-111 / Al
Density[l,68,69]	ρ_i	kg m^{-3}	8950[68] / 1347.33[69]	1008.98[69]	2328.5[69] / 2710[68]
Specific heat capacity[l,69]	$c_{p,\,i}$	J kg^{-1} K^{-1}	385 / 1437.4	1978.16	1269.21 / 903
Thermal conductivity[l,69]	λ_i	W m^{-1} K^{-1}	398 / 1.04	0.3344	1.58 / 238
Jelly roll/electrode stack width[e]	$w_{\mathrm{jelly/stack}}$	mm	see Table II		
Jelly roll/electrode stack height[e]	$h_{\mathrm{jelly/stack}}$	mm	see Table II		
Jelly roll/electrode stack thickness[e]	$d_{\mathrm{jelly/stack}}$	mm	see Table II		
Electrode layer thickness[c]	l_{layer}	μm	$l_{\mathrm{cc,\,neg}} + 2 \cdot \left(l_{\mathrm{neg}} + l_{\mathrm{sep}} + l_{\mathrm{pos}}\right) + l_{\mathrm{cc,\,pos}} = 372$		
Electrode layer density[c]	ρ_{layer}	kg m^{-3}	$\frac{\sum_i l_i \cdot \rho_i}{l_{\mathrm{layer}}} = 2029.77$		
Electrode layer specific heat capacity[c]	$c_{p,\,\mathrm{layer}}$	J kg^{-1} K^{-1}	$\frac{\sum_i l_i \cdot \rho_i \cdot c_{p,\,i}}{l_{\mathrm{layer}} \cdot \rho_{\mathrm{layer}}} = 1207.37$		
Electrode layer thermal conductivity (through-plane)[c]	$\lambda_\perp$	W m^{-1} K^{-1}	$\left(\frac{1}{l_{\mathrm{layer}}} \cdot \sum_i \frac{l_i}{\lambda_i}\right)^{-1} = 0.9829$		
Electrode layer thermal conductivity (in-plane)[c]	$\lambda_\parallel$	W m^{-1} K^{-1}	$\frac{\sum_i l_i \cdot \lambda_i}{l_{\mathrm{layer}}} = 25.445$		

[c]calculated.
[e]estimated.
[l]literature.
[m]measured.

Table A2. Main variables, governing partial differential equations, and additional analytic expressions solved within each domain of the p2D physical-chemical model of the electrochemical unit cell as well as prevailing boundary conditions and derived quantities.

Description	Negative electrode (neg)	Separator (sep)	Positive electrode (pos)
Variables and mathematical operators	$c_\mathrm{l}(x,t)$, $c_\mathrm{s}(x,r,t)$, $\Phi_\mathrm{l}(x,t)$, $\Phi_\mathrm{s}(x,t)$ $x \in [0; l_\mathrm{neg}]$ $r \in [0; r_\mathrm{p,\,neg}]$	$c_\mathrm{l}(x,t)$, $\Phi_\mathrm{l}(x,t)$ $x \in [l_\mathrm{neg}; l_\mathrm{neg}+l_\mathrm{sep}]$ $\nabla := \left(\frac{\partial}{\partial x}\right)$	$c_\mathrm{l}(x,t)$, $c_\mathrm{s}(x,r,t)$, $\Phi_\mathrm{l}(x,t)$, $\Phi_\mathrm{s}(x,t)$ $x \in [l_\mathrm{neg}+l_\mathrm{sep}; l_\mathrm{neg}+l_\mathrm{sep}+l_\mathrm{pos}]$ $r \in [0; r_\mathrm{p,\,pos}]$
Governing partial differential equations			
Mass balance (liquid)	$\epsilon_\mathrm{l,\,neg}\frac{\partial c_\mathrm{l}}{\partial t} = \nabla\left(D_\mathrm{l,\,eff}\nabla c_\mathrm{l}\right) - \nabla\left(\frac{\mathbf{i}_\mathrm{l}(1-t_+)}{F}\right)$	$\epsilon_\mathrm{l,\,sep}\frac{\partial c_\mathrm{l}}{\partial t} = \nabla\left(D_\mathrm{l,\,eff}\nabla c_\mathrm{l}\right)$	$\epsilon_\mathrm{l,\,pos}\frac{\partial c_\mathrm{l}}{\partial t} = \nabla\left(D_\mathrm{l,\,eff}\nabla c_\mathrm{l}\right) - \nabla\left(\frac{\mathbf{i}_\mathrm{l}(1-t_+)}{F}\right)$
Mass balance (solid)	$\frac{\partial c_\mathrm{s}}{\partial t} = \frac{1}{r^2}\frac{\partial}{\partial r}\left(D_\mathrm{s,\,neg}r^2\frac{\partial c_\mathrm{s}}{\partial r}\right)$	n/a	$\frac{\partial c_\mathrm{s}}{\partial t} = \frac{1}{r^2}\frac{\partial}{\partial r}\left(D_\mathrm{s,\,pos}r^2\frac{\partial c_\mathrm{s}}{\partial r}\right)$
Ohm's law (liquid)	$\mathbf{i}_\mathrm{l} = -\kappa_\mathrm{l,\,eff}\nabla\Phi_\mathrm{l} + \frac{2\kappa_\mathrm{l,\,eff}RT}{F}(1-t_+)\left(1+\frac{\partial \ln f_\pm}{\partial \ln c_\mathrm{l}}\right)\nabla \ln c_\mathrm{l}$		
Ohm's law (solid)	$\mathbf{i}_\mathrm{s} = -\sigma_\mathrm{s,\,eff}\nabla\Phi_\mathrm{s}$	n/a	$\mathbf{i}_\mathrm{s} = -\sigma_\mathrm{s,\,eff}\nabla\Phi_\mathrm{s}$
Charge balance	$\nabla\mathbf{i}_\mathrm{l} = -\nabla\mathbf{i}_\mathrm{s} = \frac{3\epsilon_\mathrm{s,\,neg}}{r_\mathrm{p,\,neg}}i_\mathrm{n}$	$\nabla\mathbf{i}_\mathrm{l} = 0$	$\nabla\mathbf{i}_\mathrm{l} = -\nabla\mathbf{i}_\mathrm{s} = \frac{3\epsilon_\mathrm{s,\,pos}}{r_\mathrm{p,\,pos}}i_\mathrm{n}$
Additional analytic expressions			
Ionic diffusivity	$D_\mathrm{l,\,eff} = \frac{\epsilon_\mathrm{l,\,neg}}{\tau_\mathrm{neg}}D_\mathrm{l}$	$D_\mathrm{l,\,eff} = \frac{\epsilon_\mathrm{l,\,sep}}{\tau_\mathrm{sep}}D_\mathrm{l}$	$D_\mathrm{l,\,eff} = \frac{\epsilon_\mathrm{l,\,pos}}{\tau_\mathrm{pos}}D_\mathrm{l}$
Ionic conductivity	$\kappa_\mathrm{l,\,eff} = \frac{\epsilon_\mathrm{l,\,neg}}{\tau_\mathrm{neg}}\kappa_\mathrm{l}$	$\kappa_\mathrm{l,\,eff} = \frac{\epsilon_\mathrm{l,\,sep}}{\tau_\mathrm{sep}}\kappa_\mathrm{l}$	$\kappa_\mathrm{l,\,eff} = \frac{\epsilon_\mathrm{l,\,pos}}{\tau_\mathrm{pos}}\kappa_\mathrm{l}$
Electronic conductivity	$\sigma_\mathrm{s,\,eff} = \epsilon_\mathrm{s,\,neg}\sigma_\mathrm{s,\,neg}$	n/a	$\sigma_\mathrm{s,\,eff} = \epsilon_\mathrm{s,\,pos}\sigma_\mathrm{s,\,pos}$
Reaction kinetics	$i_\mathrm{n} = \frac{i_0\left[\exp\left(\frac{\alpha_\mathrm{a}F}{RT}\eta\right) - \exp\left(\frac{\alpha_\mathrm{c}F}{RT}\eta\right)\right]}{1+\frac{c_\mathrm{s,\,lim}}{\Delta c_\mathrm{s}}\exp\left(\frac{\alpha_\mathrm{a}F}{RT}\eta\right)}$	n/a	$i_\mathrm{n} = \frac{i_0\left[\exp\left(\frac{\alpha_\mathrm{a}F}{RT}\eta\right) - \exp\left(\frac{\alpha_\mathrm{c}F}{RT}\eta\right)\right]}{1+\left(\frac{c_\mathrm{l,\,lim}}{\Delta c_\mathrm{l}}+\frac{c_\mathrm{s,\,lim}}{\Delta c_\mathrm{s}}\right)\exp\left(\frac{\alpha_\mathrm{c}F}{RT}\eta\right)}$
Exchange current density	$i_0 = Fk_\mathrm{neg}\left(\frac{c_\mathrm{l}}{c_\mathrm{l,\,ref}}\right)^{\alpha_\mathrm{a}} \cdot \left(c_\mathrm{s,\,max,\,neg} - c_\mathrm{s,\,surf}\right)^{\alpha_\mathrm{a}}\left(c_\mathrm{s,\,surf}\right)^{\alpha_\mathrm{c}}$	n/a	$i_0 = Fk_\mathrm{pos}\left(\frac{c_\mathrm{l}}{c_\mathrm{l,\,ref}}\right)^{\alpha_\mathrm{a}} \cdot \left(c_\mathrm{s,\,max,\,pos} - c_\mathrm{s,\,surf}\right)^{\alpha_\mathrm{a}}\left(c_\mathrm{s,\,surf}\right)^{\alpha_\mathrm{c}}$
Reaction overpotential	$\eta = \Phi_\mathrm{s} - \Phi_\mathrm{l} - \Delta\Phi_\mathrm{s,\,film} - E_\mathrm{eq,\,neg}$	n/a	$\eta = \Phi_\mathrm{s} - \Phi_\mathrm{l} - E_\mathrm{eq,\,pos}$
Boundary conditions[*]			
Species 2nd (liquid)	$\nabla c_\mathrm{l}\vert_{x=0} = 0$	n/a	$\nabla c_\mathrm{l}\vert_{x=l_\mathrm{neg}+l_\mathrm{sep}+l_\mathrm{pos}} = 0$
Species 2nd (solid)	$\frac{\partial c_\mathrm{s}}{\partial r}\Big\vert_{r=0} = 0 \quad \frac{\partial c_\mathrm{s}}{\partial r}\Big\vert_{r=r_\mathrm{p,\,neg}} = -\frac{i_\mathrm{n}}{FD_\mathrm{s,\,neg}}$	n/a	$\frac{\partial c_\mathrm{s}}{\partial r}\Big\vert_{r=0} = 0 \quad \frac{\partial c_\mathrm{s}}{\partial r}\Big\vert_{r=r_\mathrm{p,\,pos}} = -\frac{i_\mathrm{n}}{FD_\mathrm{s,\,pos}}$
Potential 2nd (liquid)	$\nabla\Phi_\mathrm{l}\vert_{x=0} = 0$	n/a	$\nabla\Phi_\mathrm{l}\vert_{x=l_\mathrm{neg}+l_\mathrm{sep}+l_\mathrm{pos}} = 0$
Potential[**] 1st (solid)	$\Phi_\mathrm{s}\vert_{x=0} = 0$ $\Phi_\mathrm{s}\vert_{x=0} = \Phi_\mathrm{cc,\,neg}$	n/a	$\Phi_\mathrm{s}\vert_{x=l_\mathrm{neg}+l_\mathrm{sep}+l_\mathrm{pos}} = 10^{-6}\,\mathrm{V}$ $\Phi_\mathrm{s}\vert_{x=l_\mathrm{neg}+l_\mathrm{sep}+l_\mathrm{pos}} = \Phi_\mathrm{cc,\,pos}$
Potential 2nd (solid)	$\nabla\Phi_\mathrm{s}\vert_{x=l_\mathrm{neg}} = 0$	n/a	$\nabla\Phi_\mathrm{s}\vert_{x=l_\mathrm{neg}+l_\mathrm{sep}} = 0$
Derived quantities			
Heat source	$\dot{q}_\mathrm{p2D} = \left[i_\mathrm{p2D}E_\mathrm{p2D} - \left(\int_{l_\mathrm{0,\,neg}}^{l_\mathrm{1,\,neg}}\left(a_\mathrm{neg}\,i_\mathrm{n}\,E_\mathrm{eq,\,neg,\,ave}\right)\mathrm{d}x + \int_{l_\mathrm{0,\,pos}}^{l_\mathrm{1,\,pos}}\left(a_\mathrm{pos}\,i_\mathrm{n}\,E_\mathrm{eq,\,pos,\,ave}\right)\mathrm{d}x\right)\right] + \left(\int_{l_\mathrm{0,\,neg}}^{l_\mathrm{1,\,neg}}\left(a_\mathrm{neg}\,i_\mathrm{n}\,T\,\frac{\mathrm{d}E_\mathrm{eq,\,neg,\,ave}}{\mathrm{d}T}\right)\mathrm{d}x + \int_{l_\mathrm{0,\,pos}}^{l_\mathrm{1,\,pos}}\left(a_\mathrm{pos}\,i_\mathrm{n}\,T\,\frac{\mathrm{d}E_\mathrm{eq,\,pos,\,ave}}{\mathrm{d}T}\right)\mathrm{d}x\right)$		

[*]indicated as first (Dirichlet) and second order (Neumann) boundary conditions.
[**]alternatively used for p2D model and coupled model.

Table A3. Main variables and governing partial differential equations solved within each domain of the 2D electrical model as well as prevailing boundary conditions including derived quantities.

Description	Negative current collector (cc, neg)		Positive current collector (cc, pos)
Variables and mathematical operators	$\mathbf{\Phi}_\mathrm{cc,\,neg}(x',y',t)$ $\boldsymbol{\sigma}_\mathrm{cc,\,neg} := \begin{bmatrix}\sigma_\mathrm{cc,\,neg} & 0\\ 0 & \sigma_\mathrm{cc,\,neg}\end{bmatrix}$	$x' \in [0; w_\mathrm{ele}]$ $y' \in [0; h_\mathrm{ele}]$ $\nabla := \left(\frac{\partial}{\partial x'}, \frac{\partial}{\partial y'}\right)^\mathrm{T}$	$\mathbf{\Phi}_\mathrm{cc,\,pos}(x',y',t)$ $\boldsymbol{\sigma}_\mathrm{cc,\,pos} := \begin{bmatrix}\sigma_\mathrm{cc,\,pos} & 0\\ 0 & \sigma_\mathrm{cc,\,pos}\end{bmatrix}$
Governing partial differential equations			
Charge balance	$\boldsymbol{\sigma}_\mathrm{cc,\,neg}\nabla^2\mathbf{\Phi}_\mathrm{cc,\,neg} = -\frac{2\cdot i_\mathrm{p2D}}{l_\mathrm{cc,\,neg}}$ $\int\left(\boldsymbol{\sigma}_\mathrm{cc,\,pos}\cdot\frac{\partial\mathbf{\Phi}_\mathrm{cc,\,pos}}{\partial y'}\vert_{y'=h_\mathrm{ele}}\cdot w_\mathrm{ele}\cdot\frac{l_\mathrm{cc,\,pos}}{2}\right)$		$\boldsymbol{\sigma}_\mathrm{cc,\,pos}\nabla^2\mathbf{\Phi}_\mathrm{cc,\,pos} = \frac{2\cdot i_\mathrm{p2D}}{l_\mathrm{cc,\,pos}}$ $\mathrm{d}x' = \sum_i i_\mathrm{p2D,\,i}\cdot A_\mathrm{p2D,\,i}$
Boundary conditions			
Potential 1st	$\mathbf{\Phi}_\mathrm{cc,\,neg}\vert_{y'=0} = 0$		$\mathbf{\Phi}_\mathrm{cc,\,pos}\vert_{y'=h_\mathrm{ele}} = 10^{-6}\,\mathrm{V}$
Potential 2nd	$\frac{\partial\mathbf{\Phi}_\mathrm{cc,\,neg}}{\partial x'}\vert_{x'=0\wedge x'=w_\mathrm{ele}} = 0$		$\frac{\partial\mathbf{\Phi}_\mathrm{cc,\,pos}}{\partial x'}\vert_{x'=0\wedge x'=w_\mathrm{ele}} = 0$
Derived quantities			
Heat source	$\dot{q}_\mathrm{cc,\,neg} = l_\mathrm{cc,\,neg}\cdot\boldsymbol{\sigma}_\mathrm{cc,\,neg}\cdot\left(\nabla\mathbf{\Phi}_\mathrm{cc,\,neg}\right)^2$		$\dot{q}_\mathrm{cc,\,pos} = l_\mathrm{cc,\,pos}\cdot\boldsymbol{\sigma}_\mathrm{cc,\,pos}\cdot\left(\nabla\mathbf{\Phi}_\mathrm{cc,\,pos}\right)^2$

$$\frac{dE_{eq,\,pos}}{dT} = \frac{-2.445\times10^{-3}y^2+3.4961\times10^{-3}y-1.4125\times10^{-3}}{y^2-2.7564y+3.9766} \quad [A2]$$

$$D_{s,\,neg} = 8\times10^{-14}\cdot\exp\left(\frac{2987\,K\cdot(T-298.15\,K)}{(T\cdot298.15\,K)}\right) \quad [A3]$$

$$D_{s,\,pos} = 0.25\times10^{-14}\cdot\exp\left(\frac{2987\,K\cdot(T-298.15\,K)}{(T\cdot298.15\,K)}\right) \quad [A4]$$

$$\kappa_l = 4.7557\times10^{2}\cdot\exp\left(\frac{-1.557\times10^{3}}{T}\right)\cdot\left(\frac{c_l}{1.173\times10^{4}\cdot\exp\left(\frac{-5.7251\times10^{2}}{T}\right)}\right)^{0.73}\cdot\exp\left(-\left(\frac{c_l}{1.173\times10^{4}\cdot\exp\left(\frac{-5.7251\times10^{2}}{T}\right)}\right)^{1.73}\right) \quad [A5]$$

$$D_l = 3.729\times10^{-9}\cdot\exp\left(-5.0646\times10^{-4}\cdot c_l+\frac{1.25\times10^{2}}{2.2879\times10^{2}+5.0051\times10^{-3}\cdot c_l-T}\right) \quad [A6]$$

$$(1-t_+)\cdot\mathrm{TDF} = (1-t_+)\cdot\left(1+\frac{\partial\ln f_{\pm}}{\partial c_l}\right) = 2.4174\times10^{-3}\cdot\exp\left(\frac{-3.3972\times10^{3}}{1.0732\times10^{3}-T}\right)\cdot c_l^{1.5}-7.5895\times10^{-3}\cdot c_l^{0.5}+6.01\times10^{-1} \quad [A7]$$

$$\sigma_{cc,\,neg} = \frac{5.96\times10^{7}}{1+3.383\times10^{-3}\,(T-293.15\,K)} \quad [A8]$$

$$\sigma_{cc,\,pos} = \frac{3.78\times10^{7}}{1+4.290\times10^{-3}\,(T-293.15\,K)} \quad [A9]$$

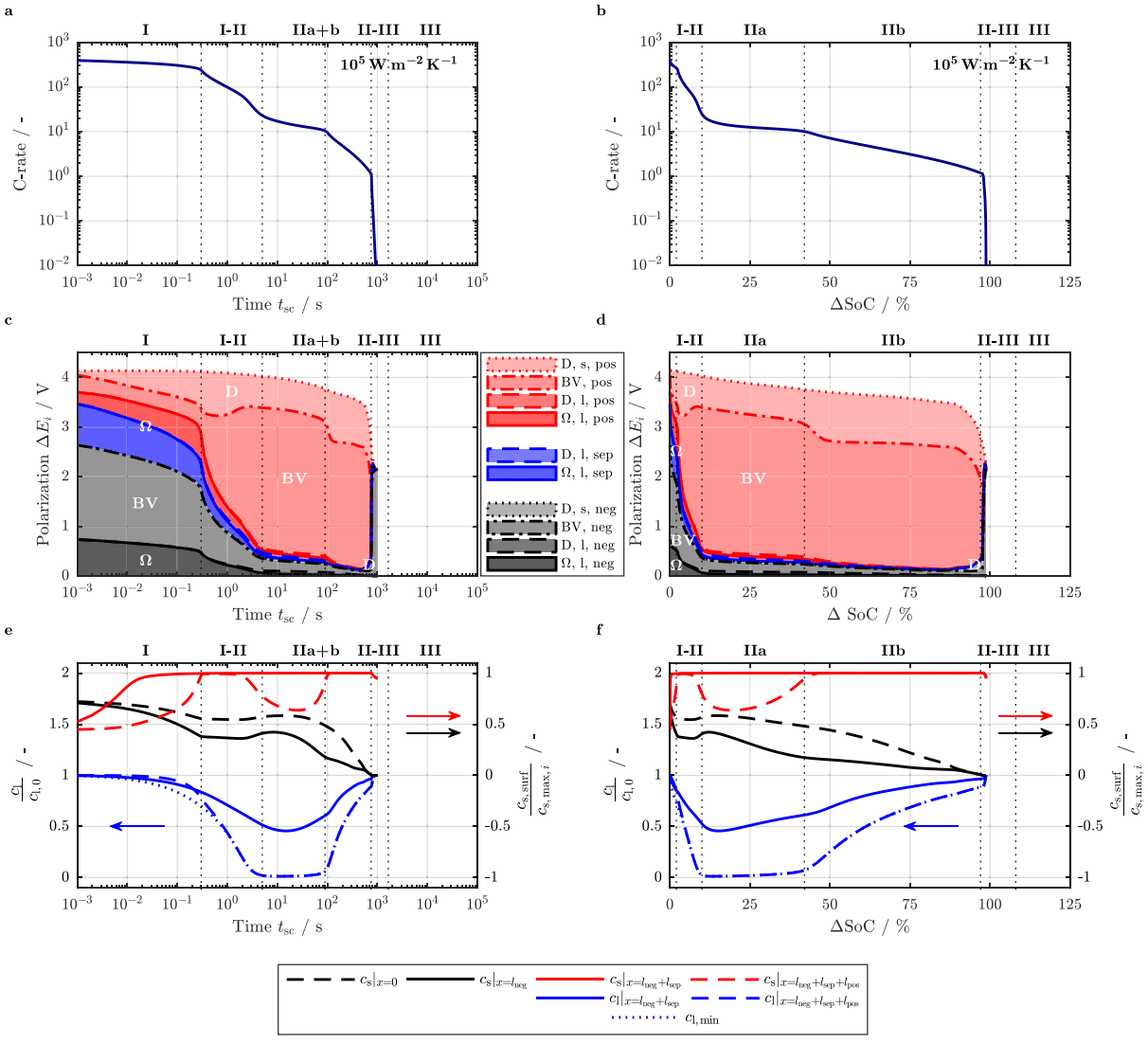

Figure A1. Predicted phases of a short circuit during a hard short circuit event for a cooling condition of 10^5 W m^{-2} K^{-1} with respect to electrode area and a coolant temperature of 25°C observed in C-rate (top: a and b), the corresponding polarization throughout the electrodes and separator (middle: c and d) resulting from the normalized solid (surface) and liquid phase concentration (average) at distinct locations of the cell (bottom: e and f) as a function of short circuit duration (left: a, c, and e) and as a function of normalized discharged capacity (right: b, d, and f).

Table A4. Main variables and governing partial differential equations solved within the 3D thermal model as well as prevailing boundary conditions and derived quantities.

Description	Jelly roll (spiral part)	Jelly roll (linear part) Electrode stack
Variables and mathematical operators	$\boldsymbol{T}\left(r'', \psi'', z'', t\right)$	$\boldsymbol{T}\left(x'', y'', z'', t\right)$
	$\boldsymbol{\lambda} = \begin{bmatrix} \lambda_\perp & 0 & 0 \\ 0 & \lambda_\parallel & 0 \\ 0 & 0 & \lambda_\parallel \end{bmatrix}$	$\boldsymbol{\lambda} = \begin{bmatrix} \lambda_\parallel & 0 & 0 \\ 0 & \lambda_\perp & 0 \\ 0 & 0 & \lambda_\parallel \end{bmatrix}$
	$\nabla := \left(\frac{\partial}{\partial r''}, \frac{\partial}{\partial \psi''}, \frac{\partial}{\partial z''}\right)^{\mathrm{T}}$	$\nabla := \left(\frac{\partial}{\partial x''}, \frac{\partial}{\partial y''}, \frac{\partial}{\partial z''}\right)^{\mathrm{T}}$
Governing partial differential equations		
Heat balance	$\rho_{\mathrm{layer}} c_{p,\,\mathrm{layer}} \frac{\partial \boldsymbol{T}}{\partial t} = \boldsymbol{\lambda} \nabla^2 \boldsymbol{T} + \frac{\dot{\boldsymbol{q}}}{l_{\mathrm{layer}}}$	
Boundary conditions		
Temperature 2nd	$-\boldsymbol{\lambda} \cdot \nabla \boldsymbol{T}\vert^{\Gamma} \cdot \mathbf{n} = 0 \vee -\boldsymbol{\lambda} \cdot \nabla \boldsymbol{T}\vert^{\Gamma} \cdot \mathbf{n} = h_{\mathrm{c}} \left(T_\infty - \boldsymbol{T}\vert^{\Gamma}\right)$	
Derived quantities		
Heat source	$\frac{\dot{\boldsymbol{q}}}{l_{\mathrm{layer}}} = \frac{\chi_{\mathrm{p2D}}}{l_{\mathrm{neg}} + l_{\mathrm{sep}} + l_{\mathrm{pos}}} \cdot \dot{\boldsymbol{q}}_{\mathrm{p2D}} + \frac{\chi_{\mathrm{cc,\,neg}}}{l_{\mathrm{cc,\,neg}}} \cdot \dot{\boldsymbol{q}}_{\mathrm{cc,\,neg}} + \frac{\chi_{\mathrm{cc,\,pos}}}{l_{\mathrm{cc,\,pos}}} \cdot \dot{\boldsymbol{q}}_{\mathrm{cc,\,pos}}$	

$^{\Gamma}$referring to the boundaries of the jelly roll or electrode stack.

ORCID

Alexander Rheinfeld https://orcid.org/0000-0003-0995-7266
Johannes Sturm https://orcid.org/0000-0001-8876-9989
Alexander Frank https://orcid.org/0000-0001-8069-2948
Stephan Kosch https://orcid.org/0000-0002-7469-9577
Andreas Jossen https://orcid.org/0000-0003-0964-1405

References

1. G.-H. Kim, K. Smith, K.-J. Lee, S. Santhanagopalan, and A. Pesaran, Multi-Domain Modeling of Lithium-Ion Batteries Encompassing Multi-Physics in Varied Length Scales, *Journal of The Electrochemical Society*, **158**, A955 (2011).
2. R. E. Gerver and J. P. Meyers, Three-Dimensional Modeling of Electrochemical Performance and Heat Generation of Lithium-Ion Batteries in Tabbed Planar Configurations, *Journal of The Electrochemical Society*, **158**, A835 (2011).
3. M. Guo and R. E. White, A distributed thermal model for a Li-ion electrode plate pair, *Journal of Power Sources*, **221**, 334 (2013).
4. S. V. Erhard, P. J. Osswald, J. Wilhelm, A. Rheinfeld, S. Kosch, and A. Jossen, Simulation and Measurement of Local Potentials of Modified Commercial Cylindrical Cells, *Journal of The Electrochemical Society*, **162**, A2707 (2015).
5. S. V. Erhard et al., Simulation and Measurement of the Current Density Distribution in Lithium-Ion Batteries by a Multi-Tab Cell Approach, *Journal of The Electrochemical Society*, **164**, A6324 (2017).
6. B. Rieger, S. V. Erhard, S. Kosch, M. Venator, A. Rheinfeld, and A. Jossen, Multi-Dimensional Modeling of the Influence of Cell Design on Temperature, Displacement and Stress Inhomogeneity in Large-Format Lithium-Ion Cells, *Journal of The Electrochemical Society*, **163**, A3099 (2016).
7. S. Kosch, Y. Zhao, J. Sturm, J. Schuster, G. Mulder, E. Ayerbe, and A. Jossen, A Computationally Efficient Multi-Scale Model for Lithium-Ion Cells, *Journal of The Electrochemical Society*, **165**, A2374 (2018).
8. J. Sturm, A. Rheinfeld, I. Zilberman, F. B. Spingler, S. Kosch, F. Frie, and A. Jossen, Modeling and simulation of inhomogeneities in a 18650 nickel-rich, silicon-graphite lithium-ion cell during fast charging, *Journal of Power Sources*, **412**, 204 (2019).
9. K.-C. Chiu, C.-H. Lin, S.-F. Yeh, Y.-H. Lin, and K.-C. Chen, An electrochemical modeling of lithium-ion battery nail penetration, *Journal of Power Sources*, **251**, 254 (2014).
10. W. Zhao, G. Luo, and C.-Y. Wang, Modeling Nail Penetration Process in Large-Format Li-Ion Cells, *Journal of The Electrochemical Society*, **162**, A207 (2015).
11. R. Zhao, J. Liu, and J. Gu, Simulation and experimental study on lithium ion battery short circuit, *Applied Energy*, **173**, 29 (2016).
12. J. Xu, Y. Wu, and S. Yin, Investigation of effects of design parameters on the internal short-circuit in cylindrical lithium-ion batteries, *RSC Advances*, **7**, 14360 (2017).
13. R. Zhao, J. Liu, and J. Gu, A comprehensive study on Li-ion battery nail penetrations and the possible solutions, *Energy*, **123**, 392 (2017).
14. A. Rheinfeld, A. Noel, J. Wilhelm, A. Kriston, A. Pfrang, and A. Jossen, Quasi-Isothermal External Short Circuit Tests Applied to Lithium-Ion Cells: Part I. Measurements, *Journal of The Electrochemical Society*, **165**, A3427 (2018).
15. A. Rheinfeld, J. Sturm, A. Noel, J. Wilhelm, A. Kriston, A. Pfrang, and A. Jossen, Quasi-Isothermal External Short Circuit Tests Applied to Lithium-Ion Cells: Part II. Modeling and Simulation, *Journal of The Electrochemical Society*, **166**, A151 (2019).
16. J. Mao, W. Tiedemann, and J. Newman, Simulation of Li-ion Cells by Dualfoil Model under Constant-Resistance Load, *ECS Transactions*, **58**, 71 (2014).
17. J. Mao, W. Tiedemann, and J. Newman, Simulation of temperature rise in Li-ion cells at very high currents, *Journal of Power Sources*, **271**, 444 (2014).
18. J. Newman and W. Tiedemann, Potential and Current Distribution in Electrochemical Cells: Interpretation of the Half–Cell Voltage Measurements as a Function of Reference–Electrode Location, *Journal of The Electrochemical Society*, **140**, 1961 (1993).
19. U. S. Kim, C. B. Shin, and C.-S. Kim, Effect of electrode configuration on the thermal behavior of a lithium-polymer battery, *Journal of Power Sources*, **180**, 909 (2008).
20. S. Allu, S. Kalnaus, W. Elwasif, S. Simunovic, J. A. Turner, and S. Pannala, A new open computational framework for highly-resolved coupled three-dimensional multiphysics simulations of Li-ion cells, *Journal of Power Sources*, **246**, 876 (2014).
21. A. Rheinfeld, S. Kosch, S. V. Erhard, P. J. Osswald, B. Rieger, and A. Jossen, Electro-Thermal Modeling of Large Format Lithium-Ion Pouch Cells: A Cell Temperature Dependent Linear Polarization Expression, *Journal of The Electrochemical Society*, **163**, A3046 (2016).
22. S. Kosch, A. Rheinfeld, S. V. Erhard, and A. Jossen, An extended polarization model to study the influence of current collector geometry of large-format lithium-ion pouch cells, *Journal of Power Sources*, **342**, 666 (2017).
23. K. Smith, G.-H. Kim, E. Darcy, and A. Pesaran, Thermal/electrical modeling for abuse-tolerant design of lithium ion modules, *International Journal of Energy Research*, **34**, 204 (2010).
24. M. Guo and R. E. White, Mathematical model for a spirally-wound lithium-ion cell, *Journal of Power Sources*, **250**, 220 (2014).
25. S. Goutam, A. Nikolian, J. Jaguemont, J. Smekens, N. Omar, P. van Dan Bossche, and J. van Mierlo, Three-dimensional electro-thermal model of li-ion pouch cell: Analysis and comparison of cell design factors and model assumptions, *Applied Thermal Engineering*, **126**, 796 (2017).
26. B. S. Haran, B. N. Popov, and R. E. White, Determination of the hydrogen diffusion coefficient in metal hydrides by impedance spectroscopy, *Journal of Power Sources*, **75**, 56 (1998).
27. N. Baba, H. Yoshida, M. Nagaoka, C. Okuda, and S. Kawauchi, Numerical simulation of thermal behavior of lithium-ion secondary batteries using the enhanced single particle model, *Journal of Power Sources*, **252**, 214 (2014).
28. G. Fan, K. Pan, G. L. Storti, M. Canova, J. Marcicki, and X. G. Yang, A Reduced-Order Multi-Scale, Multi-Dimensional Model for Performance Prediction of Large-Format Li-Ion Cells, *Journal of The Electrochemical Society*, **164**, A252 (2017).
29. S. Khaleghi Rahimian, S. Rayman, and R. E. White, Extension of physics–based single particle model for higher charge-discharge rates, *Journal of Power Sources*, **224**, 180 (2013).
30. K. Somasundaram, E. Birgersson, and A. S. Mujumdar, Thermal–electrochemical model for passive thermal management of a spiral-wound lithium-ion battery, *Journal of Power Sources*, **203**, 84 (2012).
31. K.-J. Lee, K. Smith, A. Pesaran, and G.-H. Kim, Three dimensional thermal-, electrical-, and electrochemical-coupled model for cylindrical wound large format lithium-ion batteries, *Journal of Power Sources*, **241**, 20 (2013).
32. W. Zhao, G. Luo, and C.-Y. Wang, Effect of tab design on large-format Li-ion cell performance, *Journal of Power Sources*, **257**, 70 (2014).

33. J. Li, Y. Cheng, L. Ai, M. Jia, S. Du, B. Yin, S. Woo, and H. Zhang, 3D simulation on the internal distributed properties of lithium-ion battery with planar tabbed configuration, *Journal of Power Sources*, **293**, 993 (2015).
34. M. Doyle, T. F. Fuller, and J. Newman, Modeling of Galvanostatic Charge and Discharge of the Lithium/Polymer/Insertion Cell, *Journal of The Electrochemical Society*, **140**, 1526 (1993).
35. J. Newman and K. E. Thomas-Alyea, *Electrochemical Systems*, 3rd ed., Wiley-Interscience: Hoboken, NJ, USA, 2004.
36. G. Zhang, L. Cao, S. Ge, C.-Y. Wang, C. E. Shaffer, and C. D. Rahn, In Situ Measurement of Radial Temperature Distributions in Cylindrical Li-Ion Cells, *Journal of The Electrochemical Society*, **161**, A1499 (2014).
37. T. Amietszajew, E. McTurk, J. Fleming, and R. Bhagat, Understanding the limits of rapid charging using instrumented commercial 18650 high-energy Li-ion cells, *Electrochimica Acta*, **263**, 346 (2018).
38. W. Q. Li, Z. G. Qu, Y. L. He, and Y. B. Tao, Experimental study of a passive thermal management system for high-powered lithium ion batteries using porous metal foam saturated with phase change materials, *Journal of Power Sources*, **255**, 9 (2014).
39. Y. Lai, S. Du, L. Ai, L. Ai, Y. Cheng, Y. Tang, and M. Jia, Insight into heat generation of lithium ion batteries based on the electrochemical-thermal model at high discharge rates, *International Journal of Hydrogen Energy*, **40**, 13039 (2015).
40. W. Mei, H. Chen, J. Sun, and Q. Wang, The effect of electrode design parameters on battery performance and optimization of electrode thickness based on the electrochemical–thermal coupling model, *Sustainable Energy & Fuels*, **3**, 148 (2019).
41. D. A. H. McCleary, J. P. Meyers, and B. Kim, Three-Dimensional Modeling of Electrochemical Performance and Heat Generation of Spirally and Prismatically Wound Lithium-Ion Batteries, *Journal of The Electrochemical Society*, **160**, A1931 (2013).
42. DIN Deutsches Institut für Normung e.V., Electrically propelled road vehicles - Battery systems - Design specifications for Lithium-Ion battery cells. 2016-11.
43. T. D. Hatchard, D. D. MacNeil, A. Basu, and J. R. Dahn, Thermal Model of Cylindrical and Prismatic Lithium-Ion Cells, *Journal of The Electrochemical Society*, **148**, A755 (2001).
44. R. Spotnitz and J. Franklin, Abuse behavior of high-power, lithium-ion cells, *Journal of Power Sources*, **113**, 81 (2003).
45. G.-H. Kim, A. Pesaran, and R. Spotnitz, A three-dimensional thermal abuse model for lithium-ion cells, *Journal of Power Sources*, **170**, 476 (2007).
46. S. Hildebrand, A. Rheinfeld, A. Friesen, J. Haetge, F. M. Schappacher, A. Jossen, and M. Winter, Thermal Analysis of $LiNi_{0.4}Co_{0.2}Mn_{0.4}O_2$/Mesocarbon Microbeads Cells and Electrodes: State-of-Charge and State-of-Health Influences on Reaction Kinetics, *Journal of The Electrochemical Society*, **165**, A104 (2018).
47. L. O. Valøen and J. N. Reimers, Transport Properties of $LiPF_6$-Based Li-Ion Battery Electrolytes, *Journal of The Electrochemical Society*, **152**, A882 (2005).
48. M. N. Richard and J. R. Dahn, Accelerating Rate Calorimetry Study on the Thermal Stability of Lithium Intercalated Graphite in Electrolyte. I. Experimental, *Journal of The Electrochemical Society*, **146**, 2068 (1999).
49. M. N. Richard and J. R. Dahn, Accelerating Rate Calorimetry Study on the Thermal Stability of Lithium Intercalated Graphite in Electrolyte. II. Modeling the Results and Predicting Differential Scanning Calorimeter Curves, *Journal of The Electrochemical Society*, **146**, 2078 (1999).
50. L. Ma, M. Nie, J. Xia, and J. R. Dahn, A systematic study on the reactivity of different grades of charged $Li[Ni_xMn_yCo_z]O_2$ with electrolyte at elevated temperatures using accelerating rate calorimetry, *Journal of Power Sources*, **327**, 145 (2016).
51. C. Kupper, S. Spitznagel, H. Döring, M. A. Danzer, C. Gutierrez, A. Kvasha, and W. G. Bessler, Combined modeling and experimental study of the high-temperature behavior of a lithium-ion cell: Differential scanning calorimetry, accelerating rate calorimetry and external short circuit, *Electrochimica Acta*, **306**, 209 (2019).
52. A. Kriston, A. Pfrang, H. Döring, B. Fritsch, V. Ruiz, I. Adanouj, T. Kosmidou, J. Ungeheuer, and L. Boon-Brett, External short circuit performance of Graphite-$LiNi_{1/3}Co_{1/3}Mn_{1/3}O_2$ and Graphite-$LiNi_{0.8}Co_{0.15}Al_{0.05}O_2$ cells at different external resistances, *Journal of Power Sources*, **361**, 170 (2017).
53. B. Barnett, D. Ofer, S. Sriramulu, and R. Stringfellow, In *Encyclopedia of Sustainability Science and Technology*, R. A. Meyers, Ed., Springer: New York, NY, USA, ; pp 6097, 2012.
54. T. M. Bandhauer, S. Garimella, and T. F. Fuller, Electrochemical-Thermal Modeling to Evaluate Battery Thermal Management Strategies: I. Side Cooling, *Journal of The Electrochemical Society*, **162**, A125 (2015).
55. I. A. Hunt, Y. Zhao, Y. Patel, and G. J. Offer, Surface Cooling Causes Accelerated Degradation Compared to Tab Cooling for Lithium-Ion Pouch Cells, *Journal of The Electrochemical Society*, **163**, A1846 (2016).
56. T. M. Bandhauer, S. Garimella, and T. F. Fuller, Electrochemical-Thermal Modeling to Evaluate Battery Thermal Management Strategies: II. Edge and Internal Cooling, *Journal of The Electrochemical Society*, **162**, A137 (2015).
57. C.-F. Chen, A. Verma, and P. P. Mukherjee, Probing the Role of Electrode Microstructure in the Lithium-Ion Battery Thermal Behavior, *Journal of The Electrochemical Society*, **164**, E3146 (2017).
58. D. J. Noelle, M. Wang, A. V. Le, Y. Shi, and Y. Qiao, Internal resistance and polarization dynamics of lithium-ion batteries upon internal shorting, *Applied Energy*, **212**, 796 (2018).
59. M. Fleischhammer, T. Waldmann, G. Bisle, B.-I. Hogg, and M. Wohlfahrt-Mehrens, Interaction of cyclic aging at high-rate and low temperatures and safety in lithium-ion batteries, *Journal of Power Sources*, **274**, 432 (2015).
60. J. N. Reimers, Accurate and Efficient Treatment of Foil Currents in a Spiral Wound Li-Ion Cell, *Journal of The Electrochemical Society*, **161**, A118 (2014).
61. H. Lundgren, P. Svens, H. Ekström, C. Tengstedt, J. Lindström, M. Behm, and G. Lindbergh, Thermal Management of Large-Format Prismatic Lithium-Ion Battery in PHEV Application, *Journal of The Electrochemical Society*, **163**, A309 (2016).
62. M. Xu, Z. Zhang, X. Wang, L. Jia, and L. Yang, A pseudo three-dimensional electrochemical–thermal model of a prismatic $LiFePO_4$ battery during discharge process, *Energy*, **80**, 303 (2015).
63. F. Bahiraei, A. Fartaj, and G.-A. Nazri, Electrochemical-thermal Modeling to Evaluate Active Thermal Management of a Lithium-ion Battery Module, *Electrochimica Acta*, **254**, 59 (2017).
64. Y. Reynier, R. Yazami, and B. Fultz, The entropy and enthalpy of lithium intercalation into graphite, *Journal of Power Sources*, **119–121**, 850 (2003).
65. W. Lu, I. Belharouak, D. Vissers, and K. Amine, In Situ Thermal Study of $Li_{1+x}[Ni_{1/3}Co_{1/3}\ Mn_{1/3}]_{1-x}O_2$ Using Isothermal Micro-clorimetric Techniques, *Journal of The Electrochemical Society*, **153**, A2147 (2006).
66. F. A. Wolff and J. H. Dellinger, The electrical conductivity of commercial copper, *Proceedings of the American Institute of Electrical Engineers*, **29**, 1981 (1910).
67. D. G. Giancoli, *Physics: Principles with application*, 4th edition, Prentice Hall: Englewood Cliffs, NJ, USA, 1995.
68. J. Christensen, V. Srinivasan, and J. Newman, Optimization of Lithium Titanate Electrodes for High-Power Cells, *Journal of The Electrochemical Society*, **153**, A560 (2006).
69. S. C. Chen, C. C. Wan, and Y. Y. Wang, Thermal analysis of lithium-ion batteries, *Journal of Power Sources*, **140**, 111 (2005).

Impact of Cell Size and Format on External Short Circuit Behavior of Lithium-Ion Cells at Varying Cooling Conditions – Modeling and Simulation

Alexander Rheinfeld,* Johannes Sturm, Alexander Frank, Stephan Kosch, Simon V. Erhard, and Andreas Jossen

Institute for Electrical Energy Storage Technology, Technical University of Munich (TUM), Arcisstrasse 21, D-80333 Munich, Germany

E-mail: alexander.rheinfeld@tum.de

Phone: +49 (0)89 289 26967. Fax: +49 (0)89 289 26968

Supplementary material

Multiphysical model coupling

The applied multiphysical coupling of the presented multidimensional model (MuDiMod) is illustrated in Fig. 1 referring to the cylindrical, prismatic, and pouch-type cell formats studied within this work. As the fundamental description of the MuDiMod framework has already been discussed elsewhere,[1–5] the applied extension of the MuDiMod approach aiming at a geometrically precise exchange of variables such as temperature and heat generation rate between the electrical (2D-E) and thermal (3D-T) representation of planar electrodes and spirally wound jelly roll or z-folded electrode stack configurations is presented here. In order to transfer the heat generation rates calculated within both physical-chemical model (p2D-EC) and electrical model to the thermal cell model, volume averaging and weighting ($\frac{l_i}{l_{\mathrm{layer}}}$) is applied accounting for individual thicknesses ($l_{\mathrm{cc,\,neg}}$, $l_{\mathrm{cc,\,pos}}$, and $l_{\mathrm{p2D}} = l_{\mathrm{neg}} + l_{\mathrm{sep}} + l_{\mathrm{pos}}$) with respect to the overall electrode layer thickness (l_{layer}) as shown in Table 1.

Table 1: Thickness ratio and weighting factors for calculating the heat generation rate transferred to the 3D thermal model of the jelly roll or electrode stack.

	$\dot{\boldsymbol{q}}_{\mathrm{p2D}}$	$\dot{\boldsymbol{q}}_{\mathrm{cc,\,neg}}$	$\dot{\boldsymbol{q}}_{\mathrm{cc,\,pos}}$
Thickness / μm	l_{p2D} 342	$l_{\mathrm{cc,\,neg}}$ 12	$l_{\mathrm{cc,\,pos}}$ 18
Thickness ratio $\frac{l_i}{l_{\mathrm{layer}}}$ / %*	χ_{p2D} 92.0	$\chi_{\mathrm{cc,\,neg}}$ 3.2	$\chi_{\mathrm{cc,\,pos}}$ 4.8

* $l_{\mathrm{layer}} = 372\,\mu\mathrm{m}$

By using volumetric fractions χ_i to transfer the calculated local heat generation rates, firstly from p2D to 2D and secondly from 2D to 3D, a lumped geometry of the jelly roll or electrode stack[6] (discretized via finite element method (FEM)) can be used instead of describing each individual layer separately.

Similar to previous works,[6–8] the coordinate mapping between the 2D electrodes and the 3D spirally wound jelly roll, such as common to cylindrical and prismatic cell formats, is based

on a correlation between arc length (Λ) and azimuthal angle (Ψ_{arc}). The difference between the cylindrical and prismatic cell format appears for the definition of the azimuthal angle, which accounts for both linearly stacked parts (w_{lin}) and outer spiral windings (see Figs. 1 and 2). Following the definition as previously discussed for a cylindrical cell format,[5] the correlation between Λ and Ψ_{arc} can be defined as follows:

$$\Lambda\left(\Psi_{\mathrm{arc}}\right) = \frac{l_{\mathrm{layer}}}{4\pi}\left[\left(\cosh\left(\arcsin\left(\Psi_{\mathrm{arc}}+4\pi\right)\right)\cdot\left(\Psi_{\mathrm{arc}}+4\pi\right)\right)+\arcsin\left(\Psi_{\mathrm{arc}}+4\pi\right)\right] \tag{1}$$

This definition is also applied to describe the prismatic cell format (see spiral part I and II in Fig. 2) with the extension of incorporating two linear definitions ($y'' \lesseqgtr 0$, see linear part I and II in Fig. 2) in the x''-y''-plane of the 3D model. This distinct correlation between arc-length and azimuthal angle is further used to define every point in the x''-y''-plane of the 3D geometry based on the azimuthal angle and the radial distance from the starting point of the jelly roll. Hence, every (x'', y'')-coordinate pair can be correlated to a (Ψ_{arc}, R_i)-coordinate pair according to Eq. 2:

$$\begin{bmatrix} x'' \\ y'' \end{bmatrix} = \begin{bmatrix} \cos\left(\Psi_{\mathrm{arc}}\right)\cdot\left(\Psi_{\mathrm{arc}}\cdot\frac{l_{\mathrm{layer}}}{2\pi}+R_i\right) \\ \sin\left(\Psi_{\mathrm{arc}}\right)\cdot\left(\Psi_{\mathrm{arc}}\cdot\frac{l_{\mathrm{layer}}}{2\pi}+R_i\right) \end{bmatrix} \quad \text{for} \quad \begin{matrix} \Psi_{\mathrm{arc}} \in [0;\Psi_{\mathrm{arc,tot}}] \\ R_i \in \left[2\cdot l_{\mathrm{layer}} : \frac{l_{\mathrm{layer}}}{10} : 3\cdot l_{\mathrm{layer}}\right] \end{matrix} \tag{2}$$

whereas R_i represents the initial distance of each curve to the center of the prismatic jelly roll.

When looking into the planar electrode geometry in the 2D model, the x'-coordinate along the width of the electrode w_{ele} directly corresponds to the arc-length and can be correlated to the azimuthal angle according to Eq. 1. Accordingly, the y'-coordinate along the height of the electrode h_{ele} directly corresponds to the height of the jelly roll h_{jelly} or z''-coordinate in the 3D model. The correlation between the x'-, x''-, and y''-coordinates together with the corresponding azimuthal angle is shown in the middle of Fig. 3 (b, d, f, and i) for the consumer-sized prismatic cell format. The previously discussed correlation for the consumer-

sized cylindrical cell format[5] is shown on the left of Fig. 3 (a, c, e, and h) in comparison.

In order to describe the coordinate mapping for the z-folded electrode configuration considered for the pouch-type cell in this work, each layer of the electrode stack is linked to the planar electrode accounting for the chosen width of the electrode stack (w_{stack}). After mapping the x'-coordinate to the y''-coordinate representing a whole w_{stack}, the coupling scheme moves to the next electrode pair and the thickness of the electrode stack represented by x'' is increased as shown in Fig. 3 j. The electrode area that is affected by folding the electrode pair (see Fig. 3 i) is assumed to be negligible compared to the electrode width. Analogous to the cylindrical and prismatic cell format, the height of the electrode represented by the y'-coordinate directly corresponds to the height of the electrode stack (h_{stack}) represented by the z''-coordinate.

With the presented approach of coordinate mapping, the local heat generation rate is extruded from the 2D representation of the electrodes to the 3D representation of the jelly roll or electrode stack, whilst the temperature is coupled back to both the 2D and the p2D models using the same mathematical operations (see Fig. 3).

For discretizing the mapping schemes, 3038, 5689, and 1600 nodes are considered along the electrode width for the cylindrical, prismatic, and pouch-type cell formats (representing an element size of ca. 0.4 mm, 0.2 mm, and 0.5 mm along the 1.36 m, 1.17 m, and 0.74 m wide electrodes). To discretize the radial direction of the prismatic jelly roll, 10 prismatically wound curves are defined by increasing the starting point ($R_i = 2 \cdot l_{\mathrm{layer}}$) in 37.2 µm-steps (i.e. $0.1 \cdot l_{\mathrm{layer}}$). The consumer-sized cylindrical cell shows as total number of 30.37 windings, whereas the prismatic cell is formed of 14.06 windings with $w_{\mathrm{lin}} = 28.92$ mm and the pouch-type cell comprises 16 electrode layers in total.

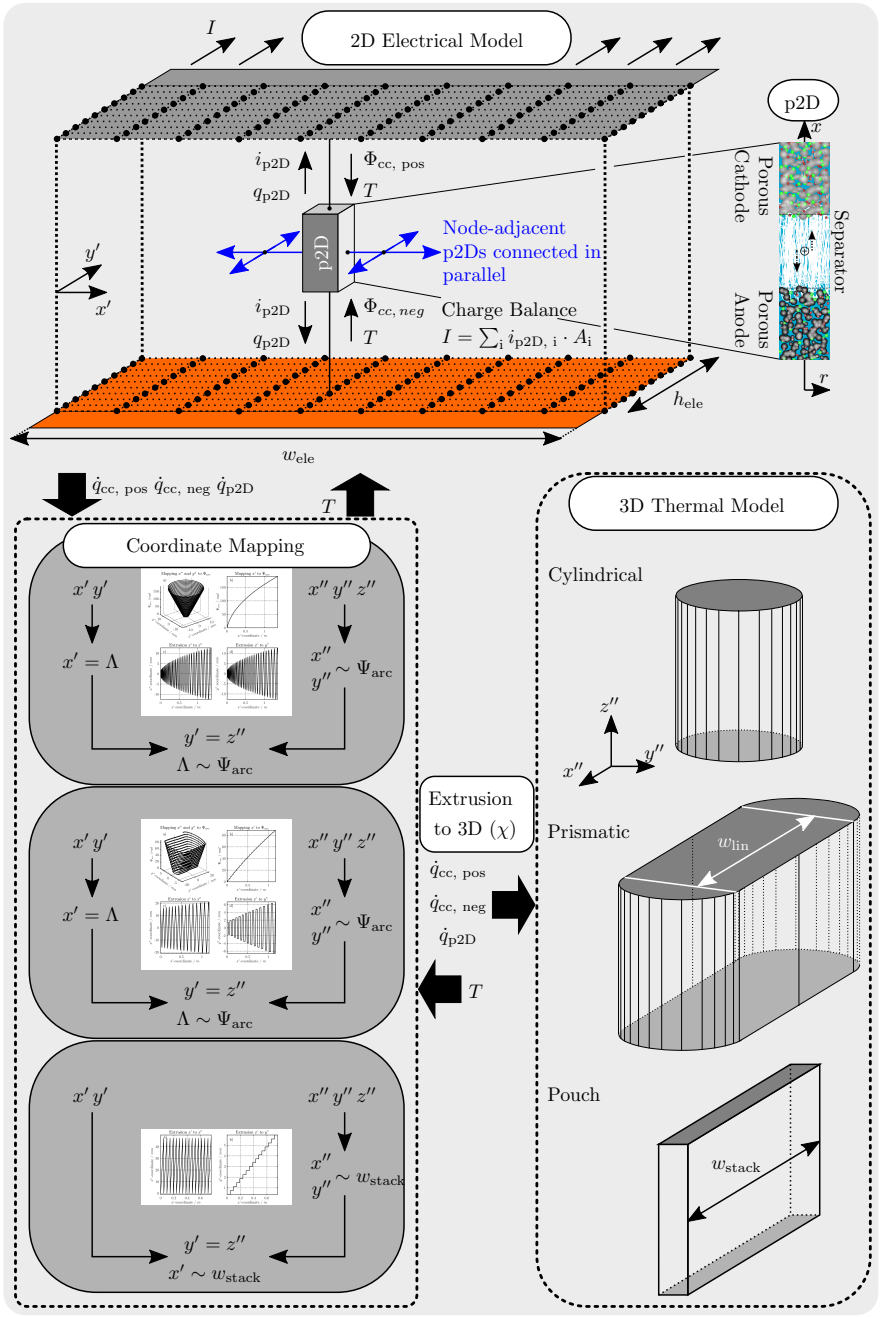

Figure 1: Applied multiphysical model coupling within the MuDiMod approach accounting for several p2D physical-chemical models connected in parallel, a 2D electrical, and 3D thermal model. The coordinate mapping between the 2D and 3D cartesian coordinates referring to Fig. 3 is shown for the cylindrical, prismatic, and pouch-type cell format which is used to exchange the locally calculated heat generation rates ("Extrusion to 3D (χ)", see Table 1) and the resulting temperature distribution between 2D and 3D.

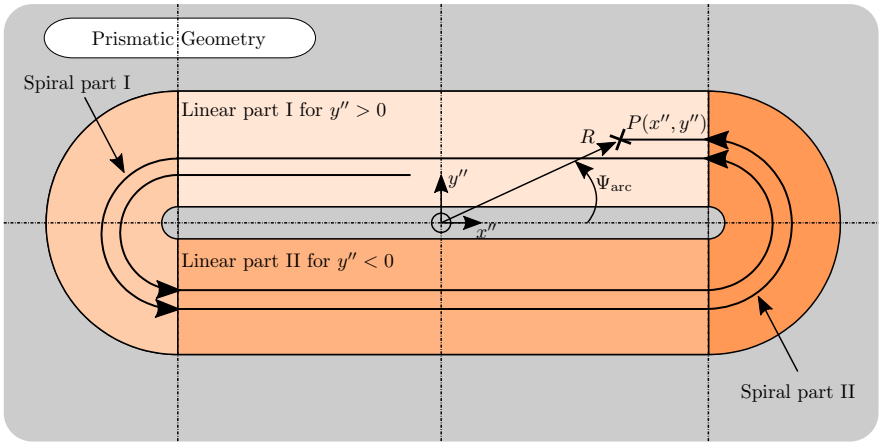

Figure 2: Mathematical definition of the azimuthal angle (Ψ_{arc}) within the 3D thermal model of a spirally wound electrode configuration for the prismatic cell format. The jelly roll is divided into two linear and two spiral parts to calculate Ψ_{arc} and the initial radial distance (R_i) of every point $P\,(x'', y'')$ in the x''-y''-plane of the 3D geometry.

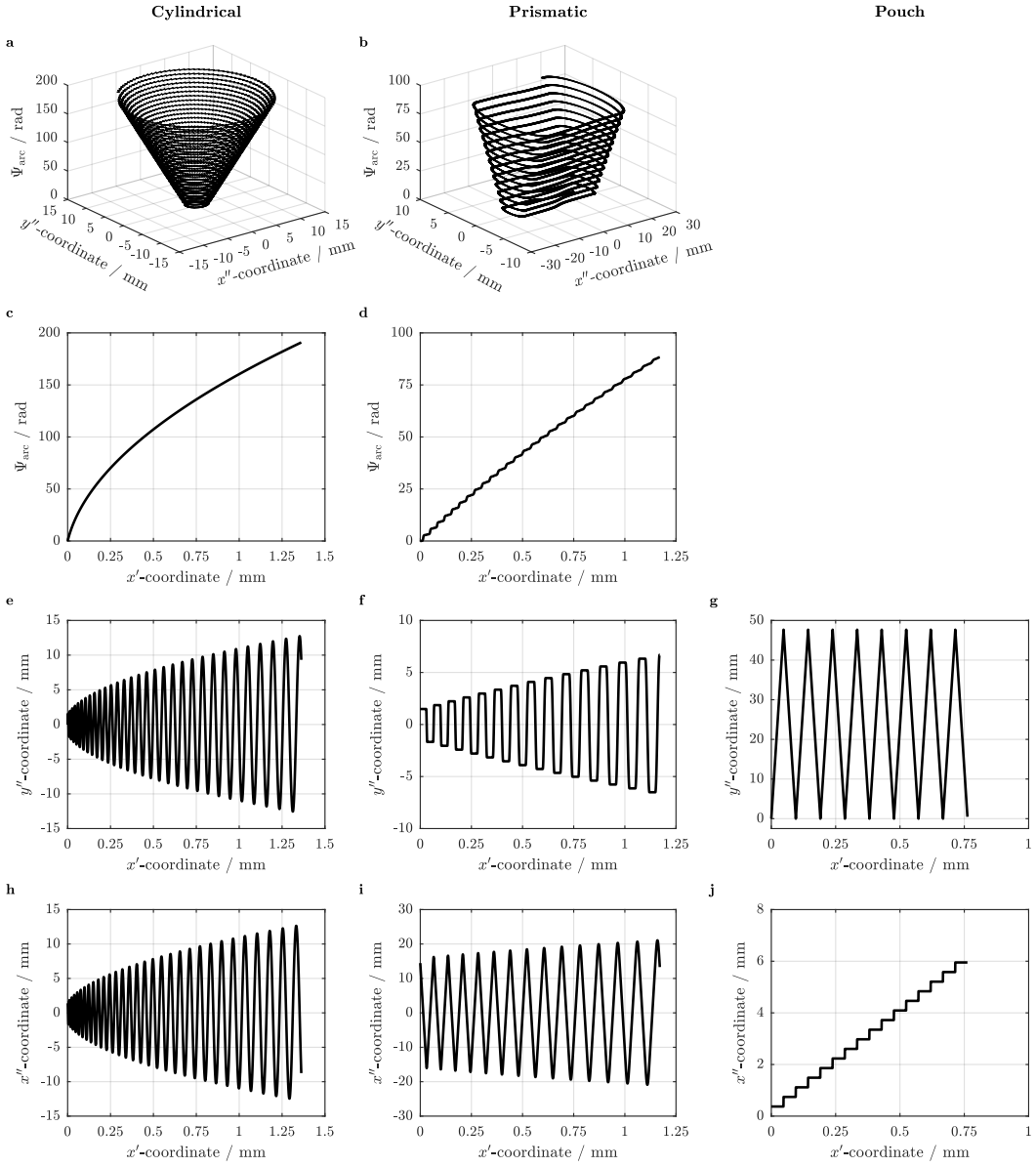

Figure 3: Coordinate mapping between the 2D- (x') and 3D-coordinates (x'', y'') as well as corresponding azimuthal angle (Ψ_{arc}) for the consumer-sized cylindrical (left: a, c, e, and h), prismatic (middle: b, d, f, and i), and pouch-type cell format (right: g and j). For the cylindrical and prismatic cell format a spirally wound electrode configuration is applied (i.e. a jelly roll) using the correlation between arc-length and electrode width ($x' = \Lambda$), whereas a z-folded electrode configuration (i.e. an electrode stack) is applied for the pouch-type cell format.

Discretization and solving

In this work, FEM is applied to discretize the underlying equations of the presented multidimensional model by using the commercial solver COMSOL Multiphysics® 5.3a. An individual spatial discretization is considered for the different length scales represented by each submodel which is summarized in Table 2.

Table 2: FEM mesh configurations.

Format	**Model**	**Geometry**	**Vertices**	**Elements** [I]	**Method**	$\sum$ **DoF** [II]
Consumer	**p2D**	All	21	20	FEM [VI]	
	2D	All	169	144 [III]	FEM [VII]	
	3D	Cylindrical	3042	4896 [V]		63583
		Prismatic	3771	5776 [V]	FEM [VIII]	69087
		Pouch	1134	800 [IV]		45258
HEV	**p2D**	All	21	20	FEM [VI]	
	2D	All	561	512 [III]	FEM [VII]	
	3D	Cylindrical	4524	7584 [IV]		151287
		Prismatic	5915	9480 [V]	FEM [VIII]	162483
		Pouch	1248	1680 [IV]		120458
PHEV	**p2D**	All	21	20	FEM [VI]	
	2D	All	1725	1632 [III]	FEM [VII]	
	3D	Cylindrical	7623	13240 [V]		401721
		Prismatic	10458	17480 [V]	FEM [VIII]	425861
		Pouch	3213	2560 [IV]		357272

[I] User defined settings incorporating a COMSOL built-in meshing algorithm

[II] Total degrees of freedom for the entire MuDiMod

[III] Rectangular, quadrilateral mesh elements [IV] Hexahedral mesh elements [V] Prism-mesh elements

[VI] Ref. 9 [VII] Ref. 10 [VIII] Ref. 11

As a result, a total of 401721, 425861, and 357272 degrees of freedom need to be considered when solving the differential algebraic equation system of the MuDiMod approach referring to cylindrical, prismatic, and pouch-type PHEV cell formats and sizes studied in this work. The resulting effective electrode widths and heights, which are discretized along the electrode with a single p2D model are shown in Tab. 3.

Table 3: Effective p2D electrode discretization within the 2D electrical model (in mm).

Format	Parameter	Cylindrical	Prismatic	Pouch
Consumer	Effective height (y')	29.8	34.6	54.4
	Effective width (x')	454.0	390.2	248.3
HEV	Effective height (y')	28.6	32.9	52.3
	Effective width (x')	354.3	307.6	193.6
PHEV	Effective height (y')	24.7	28.3	45.3
	Effective width (x')	347.0	303.2	189.6

A total of 12, 36, and 108 p2D models are used for the consumer, HEV, and PHEV-sized cells studied in this work which represents 8 p2D models per Ah. The solving process is based on COMSOL Multiphysics® built-in multifrontal massively parallel sparse direct solver (MUMPS)[12] with a relative and absolute tolerance of 10^{-3} and 10^{-4} at a maximum step-size of 1 s. All models are computed on a Intel Xeon E5-2687W 0 3.1 GHz with 64 GB RAM.

References

(1) Erhard, S. V.; Osswald, P. J.; Wilhelm, J.; Rheinfeld, A.; Kosch, S.; Jossen, A. Simulation and Measurement of Local Potentials of Modified Commercial Cylindrical Cells. *Journal of The Electrochemical Society* **2015**, *162*, A2707–A2719.

(2) Erhard, S. V. et al. Simulation and Measurement of the Current Density Distribution in Lithium-Ion Batteries by a Multi-Tab Cell Approach. *Journal of The Electrochemical Society* **2017**, *164*, A6324–A6333.

(3) Rieger, B.; Erhard, S. V.; Kosch, S.; Venator, M.; Rheinfeld, A.; Jossen, A. Multi-Dimensional Modeling of the Influence of Cell Design on Temperature, Displacement

and Stress Inhomogeneity in Large-Format Lithium-Ion Cells. *Journal of The Electrochemical Society* **2016**, *163*, A3099–A3110.

(4) Kosch, S.; Zhao, Y.; Sturm, J.; Schuster, J.; Mulder, G.; Ayerbe, E.; Jossen, A. A Computationally Efficient Multi-Scale Model for Lithium-Ion Cells. *Journal of The Electrochemical Society* **2018**, *165*, A2374–A2388.

(5) Sturm, J.; Rheinfeld, A.; Zilberman, I.; Spingler, F. B.; Kosch, S.; Frie, F.; Jossen, A. Modeling and simulation of inhomogeneities in a 18650 nickel-rich, silicon-graphite lithium-ion cell during fast charging. *Journal of Power Sources* **2019**, *412*, 204–223.

(6) Guo, M.; White, R. E. Mathematical model for a spirally-wound lithium-ion cell. *Journal of Power Sources* **2014**, *250*, 220–235.

(7) Reimers, J. N. Accurate and Efficient Treatment of Foil Currents in a Spiral Wound Li-Ion Cell. *Journal of The Electrochemical Society* **2014**, *161*, A118–A127.

(8) McCleary, D. A. H.; Meyers, J. P.; Kim, B. Three-Dimensional Modeling of Electrochemical Performance and Heat Generation of Spirally and Prismatically Wound Lithium-Ion Batteries. *Journal of The Electrochemical Society* **2013**, *160*, A1931–A1943.

(9) COMSOL Multiphysics, The heat transfer module user's guide. `https://www.comsol.com/`.

(10) COMSOL Multiphysics, Comsol multiphysics reference manual. `https://www.comsol.com/`.

(11) COMSOL Multiphysics, The batteries & fuel cells module user's guide. `https://www.comsol.com/`.

(12) Amestoy, P.; Buttari, A.; Guermouche, A.; L'Excellent, J.-Y.; Ucar, B. Mumps:

Multifrontal massively parallel sparse direct solver - version 5.1.2. https://mumps.enseeiht.fr/.

4.2 Electro-thermal validation of large-format lithium-ion cell models

Within this section, the article titled *Electro-Thermal Modeling of Large Format Lithium-Ion Pouch Cells: A Cell Temperature Dependent Linear Polarization Expression* is presented. This work aims to derive a computationally lean semi-empirical electro-thermal model in order to describe both the electrical and thermal behavior of a large format Li-ion pouch-type cell within its designated operating window. Besides the adaption and parametrization of the presented linear polarization model, the validation of both the cell's electrical and thermal response at a maximum control of thermal boundary conditions is shown. The described test bench, which focuses on the cell's thermal behavior, forms a powerful tool for not only experimental evaluation of the cell's response under varying cooling scenarios but also allows for a straightforward validation of multiphysics Li-ion cell models, which is crucial to reliably predict a cell's electro-thermal characteristics over a wide range of operating conditions.
Such a combined approach is vital in order to evaluate the cooling capability of Li-ion cells of different formats and sizes via both modeling and simulation as well as experimental validation, which also allows the tolerance of a Li-ion cell toward abusive short circuit scenarios to be estimated.
A large-format, 40 Ah pouch-type Li-ion cell containing a graphite anode and a blend of NMC and LMO as the cathode was studied via modeling and simulation as well as experimental parametrization and validation. The empirical linear polarization expression suggested by Newman and Tiedeman[353] was used due to its ease of parametrizing large format pouch-type Li-ion cell models in order to describe the cell's electrical response during moderate to high rate discharge operation. By further accounting for a cell temperature dependency of the measured current and voltage signals gained for parametrization purposes, an increased model accuracy could be achieved compared to previous approaches,[103] which did not consider this correction when using large format Li-ion cells for parametrization purposes. The inevitable heat up of the studied cell during parametrization measurements carried out at constant current operation affects the cell's electrochemical characteristics which limits the prediction accuracy of the model for varying cooling conditions if such a cell temperature correction is neglected. For the purpose of parametrizing the empirical linear polarization model, the studied cell was discharged from its fully charged state to its lower cut-off voltage with constant currents ranging from 1C, 2C, 3C, to 4C at ambient temperatures of 10 °C, 25 °C, and 40 °C within a climate chamber providing an undirected airflow across the cell's housing. In order to validate the presented model, a maximum control of thermal boundary conditions was guaranteed by a custom thermal test bench combining a directed laminar air flow across the cell's surface with a defined thermal interaction of the cell's terminals with the electrical interconnection to the measurement equipment. Both the cell's voltage characteristics as well as the surface temperature distribution measured via IR thermography were used to compare the predicted and measured cell response to constant current discharge profiles (1.25C, 2.5C, and 3.75C), an ambient temperature (30 °C), and cooling condition (air flow of $1\,\mathrm{m\,s^{-1}}$) varying from the parametrization measurements. Together with the cell's thermophysical parameters taken from literature, the presented model shows very good accuracy throughout model validation, especially compared to previous approaches.[103]
Whilst the chosen semi-empirical linear polarization approach is not suitable to describe a Li-ion cell's short circuit characteristics, the presented experimental validation of the thermal cell behavior can be used to develop multidimensional multiphysics models for various formats and sizes, as described in section 4.1, which are also valid under extreme conditions such as during short circuits until additional reactions or mechanisms affect the cell's behavior.

In order to further enhance the experimental setup, not only a wider temperature and velocity range of the controlled air flow across the cell's housing is required, but also further control strategies are necessary in order to apply different cooling conditions to the cell's terminals. Such adaption would allow for a calorimetry-like operation which could be used to optimize multidimensional multiphysics models.

Author contribution Alexander Rheinfeld developed the idea of a cell temperature dependent linear polarization expression, initiated the idea of the thermal test bench and supported its development, carried out all measurements, developed the model, carried out all simulation studies, and analyzed the data. Stephan Kosch helped to develop and parametrize the model. Simon V. Erhard helped to develop the model, initiated the idea of the thermal test bench, and guided its development. Patrick J. Osswald and Bernhard Rieger helped to analyze the data. The manuscript was written by Alexander Rheinfeld and was edited by Andreas Jossen. All authors discussed the data and commented on the results.

Electro-Thermal Modeling of Large Format Lithium-Ion Pouch Cells: A Cell Temperature Dependent Linear Polarization Expression

Alexander Rheinfeld, Stephan Kosch, Simon V. Erhard, Patrick J. Osswald, Bernhard Rieger, Andreas Jossen

Journal of The Electrochemical Society 163 (14), pp. A3046–A3062, 2016

Permanent weblink:
http://dx.doi.org/10.1149/2.0701614jes

Journal of The Electrochemical Society, **163** (14) A3046-A3062 (2016)
0013-4651/2016/163(14)/A3046/17/$33.00 © The Electrochemical Society

Electro-Thermal Modeling of Large Format Lithium-Ion Pouch Cells: A Cell Temperature Dependent Linear Polarization Expression

Alexander Rheinfeld,*,z Stephan Kosch,* Simon V. Erhard,* Patrick J. Osswald, Bernhard Rieger,* and Andreas Jossen

Institute for Electrical Energy Storage Technology, Technical University of Munich, 80333 Munich, Germany

In the work presented here, a well-known semi-empirical electro-thermal model of large format lithium-ion pouch cells is extended by accounting for a cell temperature dependency of electrode polarization gained from full cell measurement. For model parametrization, the cell was discharged at varying discharge rates and ambient temperatures within a climate chamber. By relating the measured cell potential to its current temperature, a cell temperature dependency of cell polarization is established. Evaluating the advantages of this approach, the extended model is compared to the initial model regarding the quality of predicting the electrical and thermal cell behavior. For further means of model validation, the cell was investigated at cooling conditions varying from the parametrization measurements via infrared thermography. It can be shown that a temperature dependency of electrode polarization shows superior quality especially when predicting the overall electrical and thermal cell performance at ambient conditions varying from the parametrization scenario. Controlling the thermal boundary conditions further allows to evaluate the impact of local heat generation on the temperature distribution. For a laminar, directed airflow of 1 m/s along the cell, the influence of local heat generation is minor in comparison to the thermal boundary conditions prevailing at the cell's surface and tabs.

Manuscript submitted September 1, 2016; revised manuscript received October 14, 2016. Published November 16, 2016.

With increasing maturity of electrochemical energy storage systems for high performance applications such as the electrification of the drivetrain in the automotive sector (xEVs), there is a growing demand for tools that allow for a reliable yet fast design of optimized, application-oriented energy storage solutions.

Based on a comparably high volumetric and gravimetric energy and power density combined with moderate costs, lithium-ion batteries currently form the most prominent technology in that respect. Yet, there is still need for major improvements primarily in terms of raising the energy and power density of battery cells without deteriorating their lifetime and safety whilst ensuring low cost. Hence, substantial effort has been put into gaining a deeper understanding of the dominating electrochemical and thermal processes as well as of the interdependencies taking place in Li-ion batteries. These investigations often resulted in various approaches to mathematically describe these processes and interdependencies not only phenomenologically but also mechanistically. Mechanistic, physicochemical battery models have shown to be a very powerful tool for describing the main electrochemical processes occurring and the electrical and thermal effects that are accompanied with these processes.[1,2] However, valid model parametrization and handling the tendency to high computational cost when describing larger battery cells or multiple cells are issues accompanied with this approach. Semi-empirical models describe the electrochemical processes occurring phenomenologically via applying parameters gained directly from measurement or simulation data but still consider mechanistical processes such as electrical and thermal conduction within the battery as well as heat dissipation to its surroundings.[3,4] They form a promising alternative for design studies of single and multiple battery cells due to the reduced model complexity. The relevance of such models is highly dependent on the quality of measurement data and its interpretation in terms of parameter extraction.

The work presented here focuses on means of reliable parametrization of the phenomenological part of a semi-empirical model and its subsequent validation. The presented modeling approach is based on the work of Newman and Tiedemann[3] and Gu[5] (NTG) by linearizing the cell's polarization behavior for estimating the two-dimensional potential and current density distribution within planar electrodes. The approach is extended by deriving a cell temperature dependent polarization expression for a large format 40 Ah Li-ion pouch cell under constant current discharge operation. In order to show the advantages accompanied with this approach, the presented methodology is benchmarked against the initial NTG-model which does not account for this dependency so far.

*Electrochemical Society Student Member.
zE-mail: alexander.rheinfeld@tum.de

Model Background

Considering a generally non-uniform potential distribution in the grid of a lead-acid battery even during uniform utilization of the electrodes[6] as well as a restricted linear interdependency between the polarization of an electrode pair and the current that is flowing between the electrodes during operation,[7] Tiedemann and Newman identified a way to efficiently describe the local electrochemical performance of large format batteries with planar electrodes.[8] By introducing the parameter γ_{el} (S m^{-2}) (equivalent to Y[6–8]), which represents the negative inverse slope $-m^{-1}$ (i.e. $-\mathrm{d}j/\mathrm{d}U$) of the linearized polarization curve of a single electrode or of an electrode pair, the local transfer current density j (A m^{-2}) can be estimated by directly multiplying this parameter with the local linearized polarization η_{lin} of the electrodes.

$$j = \gamma_{el} \cdot \left(U_{0,\,lin} - \phi_p + \phi_n\right) = \gamma_{el} \cdot \eta_{lin} \qquad [1]$$

In Eq. 1 $U_{0,\,lin}$ (V) represents the intercept of the linearized polarization curve at $j = 0$ and ϕ_i (V) is the local potential at the positive (p) and negative (n) electrode, respectively. This definition results in a positive or negative value for the transfer current density j during a discharge or charge operation. The correlation of the linearized polarization approach is schematically shown in Fig. 1. Following the nodal structure of the current collecting grid of the lead-acid battery, the local two-dimensional potential distribution was derived with the aid of a resistive network model applying Kirchhoff's first law. This linear interdependency was primarily treated to be temperature independent and was based on the findings from mathematically describing the physicochemical processes within and between ideally uniform electrode pairs. A significant dependency of this linearity on the cell potential and consequently state of charge (SoC) was depicted and a prospect of experimentally determining this interdependency was presented.[6–8] Later on, Gu took on the approach of determining this linear interdepency via measurement by investigating different Zn/NiOOH cells under non-constant current discharge, taking into account the dependency of the assumed linearity on the cell's depth of discharge (DoD).[5] Using the empirically determined parameters γ_{el} and $U_{0,lin}$, the linear polarization expression in Eq. 1 was applied to investigate the influence of electrode conductivity σ (S m^{-1}) on the power capability of electrodes with special attention toward the

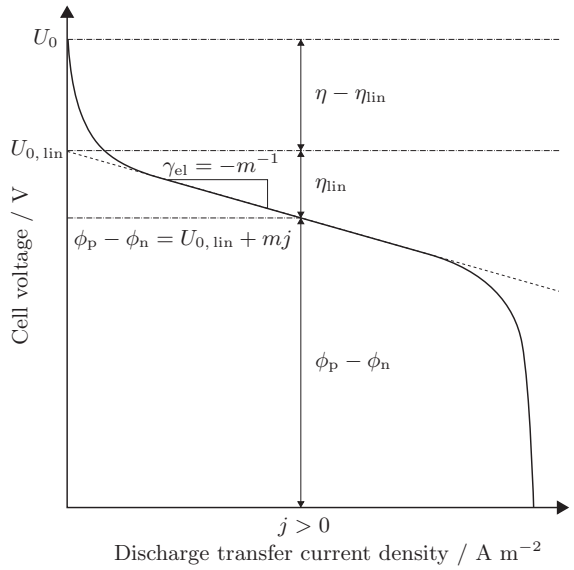

Figure 1. Schematic drawing of the polarization curve of a battery cell under discharge operation at a fixed state of charge and temperature visualizing the main idea of the linearization approach. The proportion of the magnitudes of the true cell polarization η and the linearized cell polarization η_{lin} is not representative.

two-dimensional inhomogeneity of transfer current and polarization effects. In a later work, Gu also referred to the parameter γ_{el} as the *polarization conductivity*.[9] A further application of this methodology was demonstrated by Newman and Tiedemann by mathematically describing the potential distribution within and between electrode pairs as a result of the polarization characteristics of working electrodes in batteries. The optimal location for placing reference electrodes and also how to correctly interpret the signals of the half-cell potential measurements gained during experiment were discussed.[3] Moving away from the assumption that the electrical current $\mathbf{i}_i$ (A m^{-2}) is only distributed within the electrodes in-plane due to the current collecting grid structure, Ohm's law was applied considering effective electrical conductivities σ_i (S m^{-1}) which represent the composite electrode structure formed of both active material and current collector

$$\mathbf{i}_i = -\sigma_i \nabla \phi_i \quad (i = \mathrm{n},\ \mathrm{p}) \qquad [2]$$

Assuming a two-dimensional polarization of the electrodes in Cartesian coordinates, here the ∇ operator is defined as

$$\nabla^{\mathrm{T}} := \left(\frac{\partial}{\partial x}, \frac{\partial}{\partial y} \right)$$

Considering a differential representation of the the electrodes with the composite electrode thickness t_i, a charge balance of the electric current flowing within the composite electrode structure and the ionic transfer current that is assumed to be flowing strictly perpendicular to the electrode planes (i.e. a scalar in a two-dimensional representation) can be established. Following the notation of the ionic transfer current density j, the general form of the charge balance can be derived for a discharge ($j > 0$) and charge operation ($j < 0$)

$$-t_{\mathrm{n}} \nabla \mathbf{i}_{\mathrm{n}} = j = t_{\mathrm{p}} \nabla \mathbf{i}_{\mathrm{p}} \qquad [3]$$

Including Ohm's law from Eq. 2, this charge balance can be also written as

$$t_{\mathrm{n}}\, \sigma_{\mathrm{n}}\, \nabla^2 \phi_{\mathrm{n}} = j = -t_{\mathrm{p}}\, \sigma_{\mathrm{p}}\, \nabla^2 \phi_{\mathrm{p}} \qquad [4]$$

Furthermore, the contributions to $\gamma_{\mathrm{el}}^{-1}$ (Ω m^2) were given in this work as the resistivity of the electrolyte solution within the porous electrodes of a cell and within the separator between them as well as the electrochemical resistivities of the two electrodes themselves. This approach allows to further distinguish between the positive and negative electrode considering these contributions in order to identify the limiting electrode of the system

$$\frac{1}{\gamma_{\mathrm{el}}} = \frac{1}{\gamma_{\mathrm{el,\,n}}} + \frac{1}{\gamma_{\mathrm{el,\,p}}} \qquad [5]$$

In their work, Newman and Tiedemann also introduced the term *electrochemical conductance* for describing the parameter γ_{el}. In this work, however, we will speak of γ_{el} as the area specific *electrochemical conductivity* of an electrode pair in order to merge the definitions introduced by Gu[9] and Newman and Tiedemann[3] and to point out the assumption that the distance between the two electrodes is negligible in comparison to their lateral dimensioning. Therefore, the electrochemical conductivity of an electrode pair is considered to be an area specific value. The inverse value of the electrochemical conductivity $\gamma_{\mathrm{el}}^{-1}$ shall be defined as the area specific *polarization resistivity* ρ_{pol} (Ω m^2) of an electrode pair accordingly. Consequently, we shall define the parameters G_{el} (S) as the *electrochemical conductance* and R_{pol} (Ω) as the *polarization resistance* of the electrode pair. Furthermore, we will refer to $U_{0,\,\mathrm{lin}}$ as the *linearized open circuit potential*.

The findings of these authors form the basis for numerous implementations in numerical[4,10–20] and analytical models[21–24] of predominantly large format Li-ion cells with planar electrodes and multiple cell arrangements formed of such cells.[25,26] Besides a dependency of the empirically determined fitting parameters γ_{el} and $U_{0,\,\mathrm{lin}}$ on the local SoC or DoD,[4,10–13,15,17,18,22,25,26] a dependency on the prevailing environmental temperature at a fixed cooling condition was presented.[14,16,19,23,24] However, an explicit cell temperature dependency of the NTG-model is still lacking today. Similarly, experimental cell polarization studies investigating the linear polarization behavior (often referred to as *V-I characteristics*),[27–31] also do not provide a generalized approach to determine this cell temperature dependency especially when higher current rates are considered.

Application to Li-ion battery modeling.—Looking into Li-ion batteries with graphite anodes and transition metal oxide cathodes, Kwon and coworkers were the first to apply the linear polarization approach to this cell type (i.e. a $LiMn_2O_4$ cathode) for modeling and simulation purposes.[10] Similar to the work of Gu,[5] γ_{el} and $U_{0,\,\mathrm{lin}}$ were principally regarded as fitting parameters to linearize the cell's polarization curve gained from experiments. Again, these parameters were considered to be dependent on the cell's local DoD. By comparing the simulated terminal voltage to experimental data, the authors showed the general applicability of the method for predicting the polarization behavior of planar Li-ion battery electrodes. Kim and Yi repeatedly adopted and modified Kwon's approach[10] to describe not only the electrical but also the thermal behavior of large format Li-ion batteries with planar electrodes during various modes of operation.[11–18] Accounting for the inhomogeneity of heat generation, Kim and coworkers extended the strictly isothermal modeling approach by including a unidirectional coupling of the accompanied heat generation to a two-dimensional thermal model of a pouch cell.[11] For proofing the validity of the modeling approach, the calculated temperature distribution was compared to infrared thermography measurements of the investigated cells. Later on, Kim and coworkers included an experimentally determined dependency of the considered fitting parameters γ_{el} and $U_{0,\,\mathrm{lin}}$ on the environmental temperature.[14] This approach allows for a more flexible utilization of the model over a wider temperature range. However, this approach does not reflect a full bidirectional coupling of the electrical/electrochemical model to the thermal one as no cell temperature dependent expressions are considered in the polarization behavior. Similar to the work of Chacko and Chung,[19] Yi and coworkers extended this model[14] via a three-dimensional representation of the thermal cell behavior.[15] Through an additional consideration of electrical and thermal contact resistances of the connected wires at the cell's terminals, they demonstrated a superior quality of the gained simulation results. Investigating the applicability of the presented approach[14] at very low environmental temperatures, Yi

and coworkers emphasized the strong temperature dependency of the electrochemical conductivity γ_{el} and the linearized open circuit potential $U_{0,\,lin}$.[16] Yet, the temperature dependency of these parameters was still considered to be strictly related to the difference in the environmental temperature during experimental parameter determination.

Experimental Li-ion cell polarization studies.—Onda and coworkers experimentally determined the polarization resistance R_{pol} of cylindrical 18650 sized $LiCoO_2$ cells via various test methods in order to quantify the resulting heat generation rate and temperature rise during discharge.[27,28] For that purpose, they considered a linear interdependency between the applied discharge current and the resulting cell polarization which they investigated at several ambient temperatures and varying SoCs. Besides that linear polarization behavior, they also took the true cell polarization at one specific discharge rate into account which is based on the voltage difference η between the cell's open circuit potential U_0 and its voltage $\phi_p - \phi_n$. Moreover, they also determined the cell's polarization resistance via applying an intermittent discharge profile in order to measure the voltage drop after 60 s as well as different AC impedance measurements. They showed that except for the AC impedance measurements, R_{pol} showed similar results at a given temperature and SoC. However, when calculating the cell's potential from the linearized polarization resistance, they considered the true open circuit potential U_0 instead of the fitting parameter $U_{0,\,lin}$ (see Fig. 1). This can lead to a general underestimation of the polarization at a discharge operation. Furthermore, they defined the polarization resistance gained from the true cell polarization as a quantity which is not depending on the applied current. This may lead to an underestimation or overestimation of the cell polarization if varying current rates are considered. Nieto and coworkers emphasized a significant temperature dependency of the polarization resistance. They applied constant current discharge pulses of 1 C to Li-ion pouch cells at various SoCs and temperatures in order to calculate the heat generation rate based on overpotential heat and entropic heat.[32] In accordance with the experimental approach of Onda and coworkers,[27,28] Abdul-Quadir and coworkers confirmed the general agreement of polarization resistance values gained from different experiments.[29] Based on these measurements, they further assumed a uniform heat generation and predicted the overall cell temperature due to the calculated reversible and irreversible heat generation rates at various discharge rates.[30] Liu and coworkers studied fresh and aged $LiMn_2O_4$ cells at varying charge and discharge currents and ambient temperatures.[33] Applying 10 s intermittent charge and discharge pulses, they determined the polarization resistance of the cell as a function of SoC, temperature and state of health (SoH). They identified a minor influence of the battery age on its polarization resistance and emphasized the significance of temperature dependency. Zhang and coworkers experimentally investigated the polarization behavior of a 25 Ah Li-ion pouch cell and compared it to the polarization characteristics of a small 288 mAh cell of the same cell format and electrode composition containing a blend of $Li(Ni_xCo_yMn_z)O_2$ and $LiMn_2O_4$ as the cathode material.[31] They demonstrated that the derived polarization resistivities ρ_{pol} from applying an intermittent current profile to the large 25 Ah cell agrees well with constant current operation studies of the small cell. As a continuation of this work, Wu and coworkers applied an intermittent current profile to the 25 Ah cell at a fixed discharge current rate of 0.5 C for 120 s at temperatures ranging from 25°C to 35°C in order to describe the two-dimensional electrical and three-dimensional cell temperature behavior as a function of the in-plane SoC and temperature distribution at various discharge rates.[34] Following the work of Yi,[15] special consideration was put on the experimental determination of the electrical contact resistance at the positive and negative tab respectively.

The combined work of Zhang[31] and Wu[34] forms a very comprehensive study investigating large format Li-ion cell polarization via both measurement and simulation. However, the applied polarization resistance gained from intermittent discharge pulses at a fixed discharge current does not resemble the initial linear polarization approach suggested within the NTG-model. Therefore, there is still need to combine the interpretation of experimental polarization studies with model parametrization when a linearized polarization approach is chosen.

On the one hand, the majority of the works describing Li-ion cell behavior by using a linearized polarization approach put their focus on model development and the derived simulation results. The parameter extraction is mostly based on linearizing the cell's polarization curve gained from varying constant current profiles at a various environmental temperatures. They only describe very briefly how the electrochemical conductivity γ_{el} and the linearized open circuit potential $U_{0,\,lin}$ were gained from experiment as input parameters for Eq. 1. On the other hand, most of the works dealing with experimentally investigating the polarization behavior of Li-ion cells, put their focus toward the determination of irreversible heat generation rates. They do not necessarily consider the implications of linearizing the cell's polarization curve in terms of parameter determination and interpretation.

In both cases, the identification of a dependency of the experimentally investigated linearized polarization behavior on the transient cell temperature is still lacking today.

Experimental

Based on its thin design and the accompanied limited temperature variation across its thickness combined with a comparably simple implementation in a spatially resolved model, a commercially available large format Li-ion pouch cell from Enertech International Inc. (SPB90210260V1) is investigated. The cell has a nominal capacity of 40 Ah containing stacked planar electrodes with a blend of $Li(Ni_xCo_yMn_z)O_2$ and $LiMn_2O_4$ as the cathode's active material and graphite as the anode's active material. Linear polarization expressions depending on the cell's initial temperature and DoD (so called *temperature independent* in this work) and furthermore depending the cell's transient temperature (so called *temperature dependent* in this work) are derived from experiments. Finally, both approaches are compared to each other in terms of model prediction accuracy during constant current discharge profiles at varying cooling conditions.

Extracting γ_{el} and $U_{0,\,lin}$ from measurements on commercial cells for model parametrization purposes is based on the premise that the measured tab potential reflects the difference in electrode potential of two ideal electrodes. That implies that the potential drop due to Ohmic resistances across the cell's current collecting components is negligible in comparison to the potential drop accompanied with the transfer current density j between the electrodes. As this assumption might hold for some cell types with small electronic resistances (e.g. large format pouch cells), this is not the only challenge as pointed out in the previous section. Studying the polarization behavior of the cell requires cell operation which will change the cell's SoC and may result in a temperature increase especially at high current loads. In accordance with the schematic representation of the cell polarization in Fig. 1 at a constant DoD and temperature T of the cell for varying discharge transfer current densities j, the generalized effect of changing these two parameters individually is shown in Fig. 2. Hence, if a cell is e.g. discharged and the cell temperature increases in a transient manner, both effects shown in Fig. 2 will affect the polarization characteristics of the cell simultaneously. Furthermore, the heat generation accompanied with cell operation is a function of the applied current. This can result in varying temperature values at each point of the polarization curve during the course of cell operation. Consequently, linearizing such a polarization curve will not allow for distinguishing between a dependency of the cell's DoD and a functionality of the cell's temperature. So, in order to determine the linearized polarization behavior of commercial cells in full detail, the ideal procedure would be to maintain the cell's temperature constant during the experiment in order to separate the effects. This can be achieved e.g. via cooling the cell excessively during a constant current operation or via choosing an intermittent discharge profile with long enough resting periods. Both procedures, however, seem to have disadvantages when putting them into practice. The excessive cooling procedure on the one hand will result in large temperature gradients across the cell and,

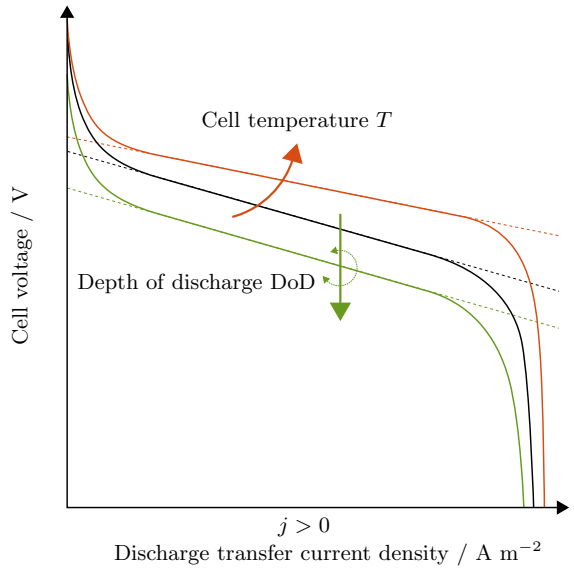

Figure 2. Schematic drawing of the influence of varying the cell's depth of discharge and temperature individually on the polarization curve. An increase in cell temperature generally leads to a flatter polarization curve whereas an increase in depth of discharge generally results in a drop of the polarization curve with varying slopes.

hence, makes it difficult to depict the actual cell temperature from measurement. The intermittent discharge procedure on the other hand needs to be designed long enough so that polarization representative Li^+ concentration profiles within the electrolyte and active material particles can be completely developed. At the same time, the procedure needs to be short enough so that the cell's temperature does not significantly vary during the experiment.

In order to allow for a most straightforward experimental determination of γ_{el} and $U_{0,\,lin}$, we decided to follow the procedure of applying different constant current discharge profiles at varying ambient temperatures as discussed in the previous section. By also tracking the cell's surface temperature rise during operation, a subsequent cell temperature correction of the examined cell polarization can be performed. This approach allows for a simple yet efficient determination of a cell temperature dependency of the fitting parameters γ_{el} and $U_{0,\,lin}$ of commercial Li-ion pouch cells without the need of adapting the test setup or the test sample.

Parametrization.—For studying the polarization behavior at reproducible ambient conditions, the investigated cell was placed within a VT 4021 climate chamber from Vötsch Industrietechnik GmbH at 10°C, 25°C, and 40°C. In total, eight four-wire Pt100 sensors with an accuracy of ±0.15 K at 0°C (DIN/IEC Class A) were placed on the cell's surface to trace its temperature during operation. At a frequency of 1 Hz, the data acquisition of the sensors was carried out with the aid of a NI CompactRIO 9024 controller comprising two NI 9217 analog input modules from National Instruments Corp. which allows for an accuracy of ±0.35 K and a resolution of 0.02 K in temperature measurement. In order to charge and discharge the cell, it was connected to a HPS battery test system from BaSyTec GmbH with an overall accuracy of ±0.05% and a resolution of 0.9 mV in voltage measurement and control and an overall accuracy of ±0.05% and a resolution of 18 mA in current measurement and control. In order to minimize the effect of electrical and thermal contact resistances, the cell was attached to two copper busbars at a defined torque of 10 Nm applied to a M5 screw placed within the center of the tab area. By polishing the contact area of the two copper busbars and cleaning both the cell's tabs and the busbars, remaining impurities were removed from the contact area. Prior to discharging the cell to 3 V at 40 A, 80 A, 120 A, and 160 A constant current load, the cell was charged to 4.2 V at a constant current of 40 A followed by a constant voltage charging phase until the charging current dropped to 0.4 A. In order to prevent significant artifacts within the voltage measurement from the previous charge process, a 4 h resting period was included between every charge and discharge process.[35,36] Following the published works that have been dealing with the effective heat transfer coefficient in climate chambers which is dominated by convection due to turbulent, undirected air flow,[37,38] we assume a convective heat transfer coefficient h of 25 Wm^{-2}K^{-1} at the cell's surface when it is placed in the climate chamber. Together with a total thickness of the cell t_{cell} of 9 mm and an overall thermal conductivity $k_\perp$ of roughly 1 Wm^{-1}K^{-1} perpendicular to the cell's planar surface,[39] we can calculate the Biot number in order to evaluate the validity of estimating the cell's overall temperature via measuring its surface temperature

$$Bi = \frac{h\,\frac{t_{cell}}{2}}{k_\perp} \approx 0.1 \qquad [6]$$

A Biot number $\ll 1$ suggests treating a body thermally as a lumped capacitance, which involves small temperature variations across the investigated dimension. The small value of 0.1 implies an error of around 2% when neglecting these variations.[40] This supports our presumption, that measuring the surface temperature of the investigated pouch cell at the prevailing cooling condition gives us enough insight into the overall cell temperature during operation.

Following the procedure pointed out in Fig. 1 and considering the applied cell current instead of area specific values, the linearized open circuit potential $U_{0,\,lin}$ and the overall electrochemical conductance G_{el} (i.e. $-\mathrm{d}I/\mathrm{d}U$) of the investigated cell were identified by means of linear regression. This procedure is shown in Fig. 3a for DoD values of 5%, 50%, and 89%. The extracted parameters are shown in Figs. 4a and 4b for the three investigated ambient temperatures as a function of the cell's DoD. The cell's capacity which is referred to when determining the overall DoD was found to be 41.41 Ah when discharging the cell at 4 A and 25°C. Both $U_{0,\,lin}$ and G_{el} are rising with increasing temperature which is in accordance with previous work.[14,34] The coefficient of determination R^2 shown in Fig. 4c shows a sufficient quality of the linear regression over the entire DoD range especially at higher ambient temperatures. Due to the lower overpotential at higher cell temperatures, the DoD range of linearizing the cell polarization also increases with rising ambient temperature.

As pointed out in the previous section, this procedure lacks the information of cell temperature which is required if a local cell temperature dependency shall be considered when describing the overall cell performance via modeling and simulation. What is more, the parameters gained are only representing one specific cooling scenario, namely convective cooling at 25 Wm^{-2}K^{-1} and ambient temperatures ranging from 10°C to 40°C. We included this information by relating the measured cell polarization to the averaged surface temperature gained from the eight Pt100 sensors placed on the surface of the cell. Within our studies, we found that the averaged surface temperature of the investigated pouch cell rises almost linearly with the applied current. This observation motivated us to perform a temperature correction of cell polarization by relating the cell's potential to its temperature as the linear character of the polarization curve remains. Applying the same approach of linear regression to the cell temperature related polarization behavior as shown in Fig. 3b, we found $U_{0,\,lin,\,T}$ (V K^{-1}) and $G_{el,\,T}$ (S K) which are shown in Figs. 4d and 4e. Hence, $G_{el,\,T}$ corresponds to $-\mathrm{d}I/\mathrm{d}(U/T)$. The coefficient of determination R^2 shown in Fig. 4f even indicates a slightly better quality of linear regression by following this approach especially at lower temperatures.

Validation test setup.—In order to not only parametrize our model but also to validate it, we applied infrared thermography to the investigated cell at current loads and ambient conditions varying from the parametrization measurements. Within our research, we identified

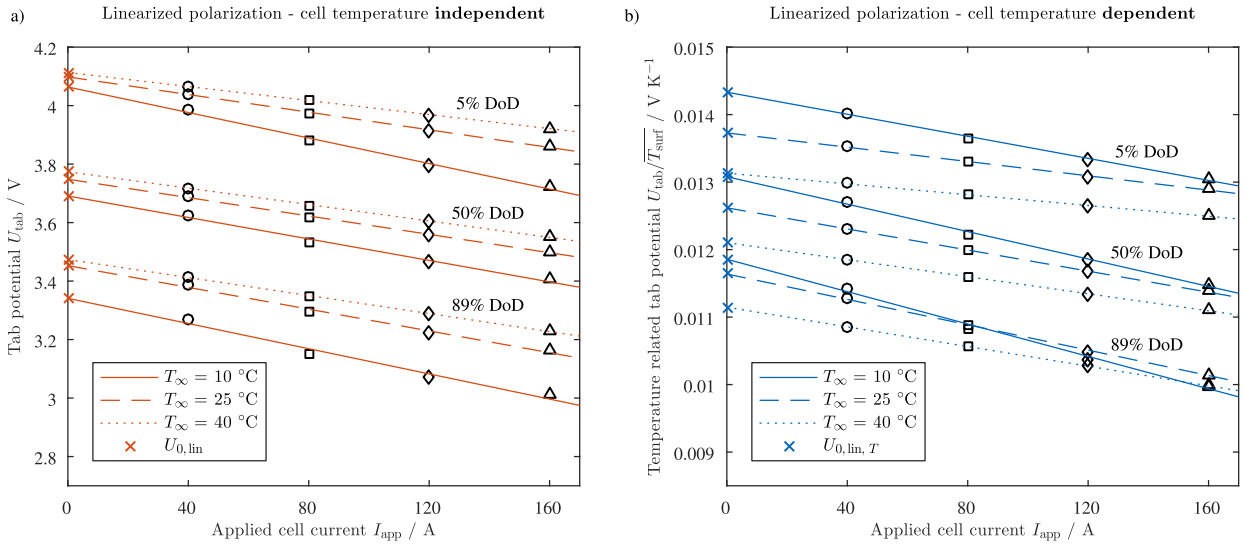

Figure 3. Linear regression of cell polarization between 40 A, 80 A, 120 A, and 160 A for DoD values of 5%, 50%, and 89% at temperatures of 10°C, 25°C, and 40°C of the surrounding ambient air within a climate chamber.

the need for reliably estimating the effective heat transfer coefficient during experiment for setting the right thermal boundary conditions within our model for validation purposes. Therefore, we designed a test bench, which contrary to climate chambers, allows for a laminar, directed airflow across the cell whilst being able to measure the cell's surface temperature via infrared thermopraphy. A schematic representation of the test setup can be found in Fig. 5. The test chamber comprises an infrared camera (IR) and the investigated cell including cell holder. The control unit guarantees an adjustment of the air's temperature and velocity flowing from the bottom of the cell to its top. For heating purposes, a resistance heating is included whereas a Peltier element is employed for cooling the airflow. Both the battery test

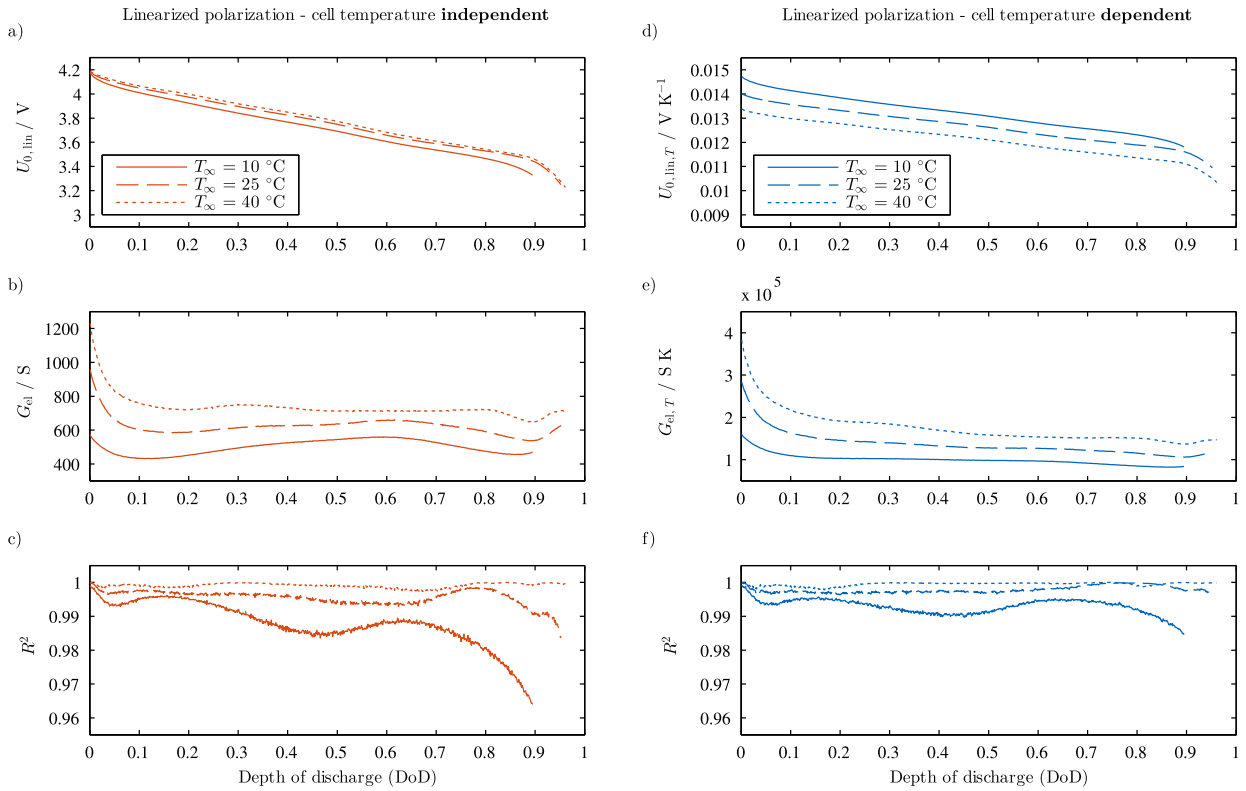

Figure 4. Fitting parameters gained from linearizing the cell's polarization behavior between 40 A, 80 A, 120 A, and 160 A and 10°C, 25°C, and 40°C of the surrounding ambient air within a climate chamber.

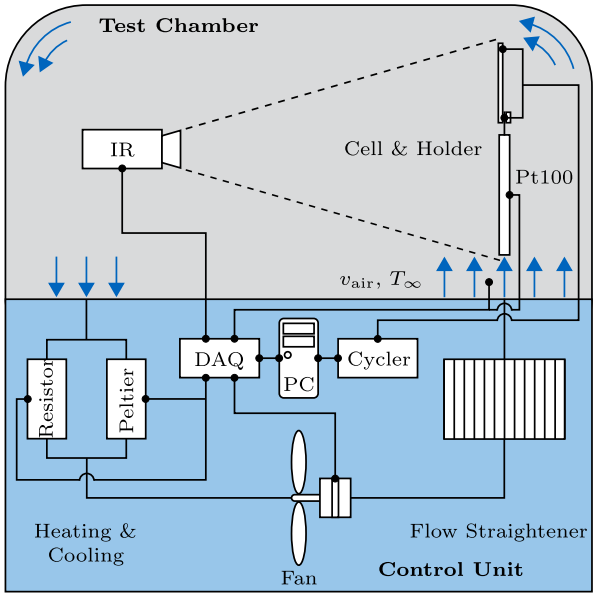

Figure 5. Schematic representation of the test setup chosen for model validation.

system (Cycler) and the data acquisition system (DAQ) are connected to a desktop computer (PC) which runs the software for monitoring and controlling purposes. Within this work, we chose an ambient temperature of 30°C and a velocity of the airflow v_{air} of 1 m/s along the cell's middle axis. The mean Nusselt number for a laminar flow along a flat plate can be estimated via[41]

$$Nu = 0.664\sqrt{Re}\sqrt[3]{Pr} \quad [7]$$

which is valid for a Reynolds number $< 10^5$

$$Re = \frac{v_{air}\, l}{\nu_{air}} \quad [8]$$

and a Prandtl number < 1 of the surrounding air. The convective heat transfer coefficient h can be then estimated via

$$h = \frac{Nu\, k_{air}}{l} \quad [9]$$

whereas l represents the characteristic length of the investigated plate-like geometry and ν_{air} ($m^2\,s^{-1}$) and k_{air} ($Wm^{-1}\,K^{-1}$) represent the kinematic viscosity and thermal conductivity of the surrounding air. With the characteristic length of 228.5 mm being defined by the cavity of the pouch housing comprising the electrode stack, a kinematic viscosity of $1.6 \times 10^{-5}\ m^2s^{-1}$, a Prandtl number of 0.72 and a thermal conductivity of 0.0259 $Wm^{-1}K^{-1}$ of air prevailing at 30°C and an ambient pressure of 1.013 bar, the resulting convective heat transfer coefficient calculates to 8.1 $Wm^{-2}K^{-1}$ at the cell's surface. With an absolute overall accuracy of ±2 K or ±2% of reading, a A655sc infrared camera from FLIR Systems Inc. was used within the test setup which allows for an optical resolution of 640 × 480 pixels and a noise-equivalent temperature difference of < 30 mK. With the aid of a 1524 reference thermometer equipped with a calibrated 5622 fast response platinum resistance thermometer from Fluke Corp. which results in a combined accuracy of ±0.019 K at 0°C, we found a maximum error of ±0.1 K in the reading of the infrared camera within a temperature range between 20°C and 40°C of the aforementioned test bench. In this configuration, the cell was discharged at discharge currents of 50 A, 100 A, and 150 A following the same charging procedure as performed for the parametrization measurements. Again, the cell was attached to two copper busbars for applying the electrical load current.

Model Development

In order to depict both the electrical and thermal cell behavior in sufficient detail whilst still limiting the computational cost, a multiphysically coupled and geometrically decoupled model is applied in this work. This is achieved by setting up two different models as previously shown.[15,19,34] A two-dimensional model describing the in-plane electrical conductance is combined with a simplified zero-dimensional model representing the through-plane electrochemical charge transfer within one effective electrode pair of the cell. A three-dimensional model of the cell geometry is considered in order to account for the heat transfer processes within the cell based on its anisotropic thermophysical properties and thermal boundary conditions. The three-dimensional approach is chosen in order to evaluate the error accompanied with measuring the cell's surface temperature for model parametrization purposes as described in the previous section. By transferring the heat generation rates from the two-dimensional representation to the three-dimensional model and mapping the temperature distribution from the three-dimensional model back to the two-dimensional model, a coupling between the two models is realized.

In this work, we consider an electrode pair as half a negative and half a positive double coated electrode layer separated by one separator sheet. The current that is flowing in one effective electrode pair is therefore derived via dividing the applied tab current I_{app} (A) by the number of electrode pairs n_{ep} within the cell. In this case, the cell is formed of 48 electrode pairs. Considering the electrical current to be only flowing within the current collector foils (cc) in planar direction,[22] Eq. 2 can be rewritten as

$$\mathbf{i}_i = -\sigma_{cc,\,i}\,\nabla\phi_i \quad (i = \mathrm{n},\ \mathrm{p}) \quad [10]$$

In accordance with Eq. 3 the charge balance between the two electrodes reads as

$$\frac{t_{cc,\,n}}{2}\,\sigma_{cc,\,n}\,\nabla^2\phi_n = j = -\frac{t_{cc,\,p}}{2}\,\sigma_{cc,\,p}\,\nabla^2\phi_p \quad [11]$$

The electrical resistivity of the negative and positive current collectors which are made of copper and aluminum respectively are considered to be dependent on the cell's temperature in order to reduce the model error accompanied with excessive temperature increase especially at moderate cooling conditions[42]

$$\frac{1}{\sigma_{cc,\,n}} = 1.68 \times 10^{-8}\,\Omega\,\mathrm{m}\,\left(1 + 0.00386\,\mathrm{K}^{-1}\,(T - 293.15\,\mathrm{K})\right) \quad [12]$$

$$\frac{1}{\sigma_{cc,\,p}} = 2.65 \times 10^{-8}\,\Omega\,\mathrm{m}\,\left(1 + 0.00492\,\mathrm{K}^{-1}\,(T - 293.15\,\mathrm{K})\right) \quad [13]$$

The same accounts for the negative and positive tab, which are treated to be made of the same material as the respective current collector foils. In order to further consider a cell temperature dependency of the electrochemical conductivity and the linearized open circuit potential, Eq. 1 is rewritten as

$$j = \frac{\gamma_{el,\,T}}{T}\,\left(T \cdot U_{0,\,lin,\,T} - \phi_p + \phi_n\right) \quad [14]$$

The cell temperature independent electrochemical conductivity γ_{el} and its cell temperature dependent counterpart $\gamma_{el,\,T}$ can be derived from the parametrization measurements described in the previous section by referring G_{el} and $G_{el,\,T}$ to the total electrochemically active electrode area of the cell stack A_{stack} (m^2). In this work, the positive electrode layer forms the smaller electrode of the electrode pair as pointed out in Table I. Hence, A_{stack} is defined as

$$A_{stack} = n_{ep}\,h_{el,\,p}\,w_{el,\,p} \quad [15]$$

with $h_{el,\,p}$ and $w_{el,\,p}$ resembling the height and width of the positive electrode layer. With the aid of Eq. 1 or Eq. 14, the local DoD can be determined by integrating the derived transfer current density and normalizing this value to the area specific capacity of the electrode

Table I. Geometric dimensions of the cell and the chosen test configuration.

Geometric entity	Index	Height (h_i)	Width (w_i)	Thickness (t_i)
Pouch cell	cell	260 mm	210 mm	9 mm
Pouch cavity	cav	228.5 mm	185 mm	9 mm
Neg. electrode layer*	el, n	221.4 mm	180.7 mm	152.4 µm
Pos. electrode layer*	el, p	216.9 mm	177.9 mm	153 µm
Negative tab	tab, n	40 mm	60 mm	300 µm
Positive tab	tab, p	40 mm	60 mm	400 µm
Busbar	bar	150 mm	65 mm	5 mm
Interconnection	int	50 mm	65 mm	5 mm

*double coated, mean thickness gained from micrometer measurements.

$Q_{\text{cell}}/A_{\text{stack}}$ (C m^{-2})

$$\text{DoD}(x,\, y) = \frac{A_{\text{stack}}}{Q_{\text{cell}}} \cdot \int_t j(x,\, y)\, dt \qquad [16]$$

whereas Q_{cell} (C) accounts for the electrical energy stored within the cell gained from discharging the cell at a current of 4 A and a temperature of 25°C. At a fully charged state of the cell, its DoD is 0. For model parametrization purposes, we assume $U_{0,\,\text{lin}}$ and γ_{el} as well as $U_{0,\,\text{lin},\,T}$ and $\gamma_{\text{el},\,T}$ to be functions of DoD and cell temperature T_0 prior to the discharge operation which is identical to the environmental temperature T_∞ in this case. To account for the lack of measurement data for DoD values larger than 0.96 due to the the limiting polarization during the 160 A discharge, both fitting parameters are assumed to approach 0 with DoD values larger than 0.96. Look up tables were derived from measurement data with the aid of cubic spline interpolation between data points. The extrapolation to 0 was carried out in the same manner. The resolution was set to 0.01 for a DoD ranging from 0 to 1 and 0.5°C for T_0 ranging from 10°C to 40°C. For the reader's convenience, polynomial fits of the derived polarization parameters are given in the appendix.

A Neumann boundary condition is chosen at the positive tab representing the applied discharge current

$$-\sigma_{\text{cc,\,p}} \left.\frac{\partial \phi_{\text{p}}}{\partial y}\right|_{y=h_{\text{el,\,n}}+h_{\text{tab,\,p}}} = \frac{I_{\text{app}}}{n_{\text{ep}}\, w_{\text{tab,\,p}}\, \frac{t_{\text{cc,\,p}}}{2}} \qquad [17]$$

A Dirichlet boundary condition at the negative tab is representing an electric reference point

$$\phi_{\text{n}}|_{y=h_{\text{el,\,n}}+h_{\text{tab\,n}}} = 0 \qquad [18]$$

Insulation boundary conditions are applied at the remaining edges of the electrode layers

$$\nabla \phi_i \cdot \mathbf{n} = 0 \quad (i = \text{n},\, \text{p}) \qquad [19]$$

whereas $\mathbf{n}$ is representing the normal vector of the boundary. Together with Eq. 11, the potential and transfer current density distribution can be calculated within the electrochemically active electrode area. The relevant boundary conditions are schematically illustrated in Fig. 6 on the left.

Based on the calculated electric and ionic charge transport, the volume specific heat generation rates within the cell can be derived. Joule heating within the current collectors can be calculated as follows

$$\begin{aligned} q'''_{\text{cc},\,i} &= -\mathbf{i}_i \cdot \nabla \phi_i = \sigma_{\text{cc},\,i}\, \nabla \phi_i \cdot \nabla \phi_i \\ &= \sigma_{\text{cc},\,i} \left(\frac{\partial \phi_i}{\partial x} \cdot \frac{\partial \phi_i}{\partial x} + \frac{\partial \phi_i}{\partial y} \cdot \frac{\partial \phi_i}{\partial y} \right) \quad (i = \text{n},\, \text{p}) \end{aligned} \qquad [20]$$

Here, the scalar value of $q'''_{\text{cc},\,i}$ (Wm^{-3}) represents the total volume specific heat generation rate within the respective current collector foil and does not account for its portion within the geometric entity that it is part of. As we consider the current collector foils to represent a certain

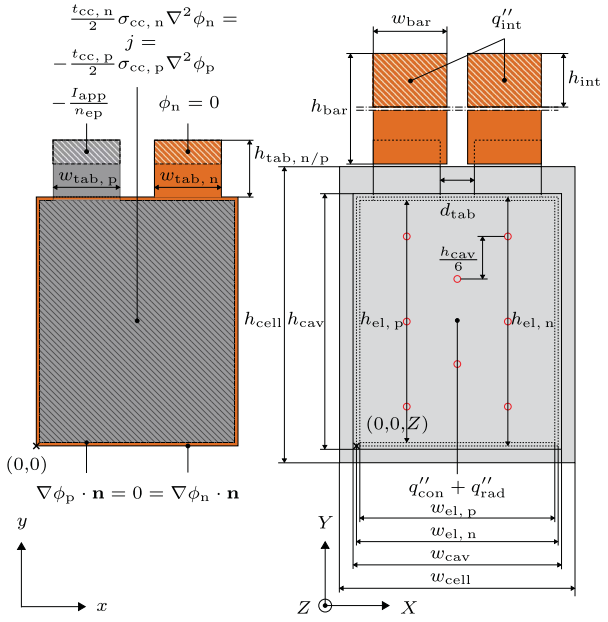

Figure 6. Dimensions of the investigated cell's electrodes, external housing and electrical interconnection as well as the applied boundary conditions. The red markers on the right indicate the positioning of the Pt100 sensors during parametrization measurements.

share of an electrode pair, this heat generation rate further needs to be scaled with its respective volume fraction as previously discussed.[43] With the corresponding thickness of one effective electrode pair t_{ep}

$$t_{\text{ep}} = \frac{t_{\text{cc,\,n}}}{2} + t_{\text{an}} + t_{\text{sep}} + t_{\text{ca}} + \frac{t_{\text{cc,\,p}}}{2} \qquad [21]$$

Eq. 20 further reads as

$$q'''_{\text{cc},\,i} = \sigma_{\text{cc},\,i}\, \nabla \phi_i \cdot \nabla \phi_i \frac{t_{\text{cc},\,i}}{2\, t_{\text{ep}}} \quad (i = \text{n},\, \text{p}) \qquad [22]$$

which holds for

$$q'''_{\text{cc,\,n}} := \forall x \in \left[0,\, w_{\text{el,\,n}}\right] \wedge \forall y \in \left[0,\, h_{\text{el,\,n}}\right] \qquad [23]$$

$$\begin{aligned} q'''_{\text{cc,\,p}} := \forall x \in &\left[\frac{w_{\text{el,\,n}} - w_{\text{el,\,p}}}{2},\, \frac{w_{\text{el,\,n}} + w_{\text{el,\,p}}}{2} \right] \wedge \\ \forall y \in &\left[\frac{h_{\text{el,\,n}} - h_{\text{el,\,p}}}{2},\, \frac{h_{\text{el,\,n}} + h_{\text{el,\,p}}}{2} \right] \end{aligned} \qquad [24]$$

based on the geometric configuration of the electrode layers as shown in Fig. 6. The sum of both heat generation rates described in Eq. 22 results in the overall Joule heating within the current collector foils. Similarly, Joule heating is also occurring within the cell's tabs. In accordance with Eqs. 20 and 22, the heat generation can be derived as

$$q'''_{\text{tab},\,i} = \sigma_{\text{cc},\,i}\, \nabla \phi_i \cdot \nabla \phi_i \frac{n_{\text{ep}}\, t_{\text{cc},\,i}}{2\, t_{\text{tab},\,i}} \quad (i = \text{n},\, \text{p}) \qquad [25]$$

which holds for

$$\begin{aligned} q'''_{\text{tab,\,n}} := \forall x \in &\left[\frac{w_{\text{el,\,n}} - d_{\text{tab}}}{2} - w_{\text{tab,\,n}},\, \frac{w_{\text{el,\,n}} - d_{\text{tab}}}{2} \right] \wedge \\ \forall y \in &\left[h_{\text{el,\,n}},\, h_{\text{el,\,n}} + h_{\text{tab,\,n}} \right] \end{aligned} \qquad [26]$$

$$q'''_{\text{tab, p}} := \forall x \in \left[\frac{w_{\text{el, n}} + d_{\text{tab}}}{2},\ \frac{w_{\text{el, n}} + d_{\text{tab}}}{2} + w_{\text{tab, p}}\right] \wedge \forall y \in \left[h_{\text{el, n}},\ h_{\text{el, n}} + h_{\text{tab, p}}\right] \quad [27]$$

with a distance between the two tabs d_{tab} of 32 mm.

Based on a general energy balance, Bernardi and coworkers described the major processes of heat generation within batteries.[44] Neglecting the enthalpy of mixing and effects of phase-change within a Li-ion battery combined with the assumption that only one reaction is taking place between the two current collecting foils, namely the charge transfer of Li-ions with the resulting area specific transfer current density j, the simplified volume specific enthalpy of reaction q'''_{ct} (Wm^{-3}) can be written as follows

$$q'''_{\text{ct}} = j\,\frac{U_0 - \phi_{\text{p}} + \phi_{\text{n}}}{t_{\text{an}} + t_{\text{sep}} + t_{\text{ca}}} + j\,\frac{T\,\frac{dU_0}{dT}}{t_{\text{an}} + t_{\text{sep}} + t_{\text{ca}}} \quad [28]$$

The two terms of this representation account for the polarization heat and entropic heat respectively. The polarization heat based on Ohmic losses, charge transfer overpotentials and mass transfer limitations between the electrodes can be derived by multiplying the charge transfer current with the overpotential η. It describes the energetic loss between reversible work $j\,U_0$ and electrical work $j\,(\phi_{\text{p}} - \phi_{\text{n}})$ or power in that case. Together with the entropic heat which is represented by the second term in Eq. 28, reversible isothermal cell operation can be described which is only based on the change in Gibbs enthalpy and entropy of the cell's active components. This heat generation is regarded to be occurring between the two current collecting foils. Therefore, the distance between the current collectors needs to be considered. Both open circuit potential U_0 (V) and entropic coefficient dU_0/dT (V K^{-1}) of the investigated Li-ion cell were determined via experiment and can be found in the appendix as a function of the cell's DoD. With that information, U_0 can be calculated for varying temperatures as

$$U_0|_{T=T_2} = U_0|_{T=T_1} + \frac{dU_0}{dT} \cdot (T_2 - T_1) \quad [29]$$

Again, for the considerations presented here, both overpotential heat and entropic heat need to be scaled with the respective volume fraction of the cell's geometry in which these sources of heat generation are assumed to be occurring. Consequently, Eq. 28 is rewritten for this purpose as

$$q'''_{\text{ct}} = j\,\frac{\eta + T\,\frac{dU_0}{dT}}{t_{\text{an}} + t_{\text{sep}} + t_{\text{ca}}} \cdot \frac{t_{\text{an}} + t_{\text{sep}} + t_{\text{ca}}}{t_{\text{ep}}} = j\,\frac{\eta + T\,\frac{dU_0}{dT}}{t_{\text{ep}}} \quad [30]$$

It is important to mention here that when calculating the heat generation q'''_{ct}, the overpotential η needs to be considered instead of the linearized overpotential η_{lin}. For the investigated cell, the overpotential could be then underestimated by 97 mV, 45 mV, and 25 mV throughout a discharge operation at ambient temperatures of 10°C, 25°C, and 40°C respectively as shown in Fig. 7. Considering the heat generation terms in Eqs. 22, 25, and 30 together with Fourier's law, the heat balance of the considered geometry can be derived. Based on the three-dimensional configuration shown in Fig. 6 on the right with its density ρ (kgm^{-3}), specific heat capacity c_p (Jkg^{-1}K^{-1}) and transient temperature variation, the heat balance reads as

$$\rho\,c_p\,\frac{\partial T}{\partial t} = k\,\nabla^2 T + q''' \quad [31]$$

whereas the ∇ operator is defined here as

$$\nabla^{\text{T}} := \left(\frac{\partial}{\partial X}, \frac{\partial}{\partial Y}, \frac{\partial}{\partial Z}\right)$$

For this purpose, the heat generation rates calculated from Eqs. 22, 25 and 30 within the two-dimensional model are transferred to the three-dimensional representation by assuming

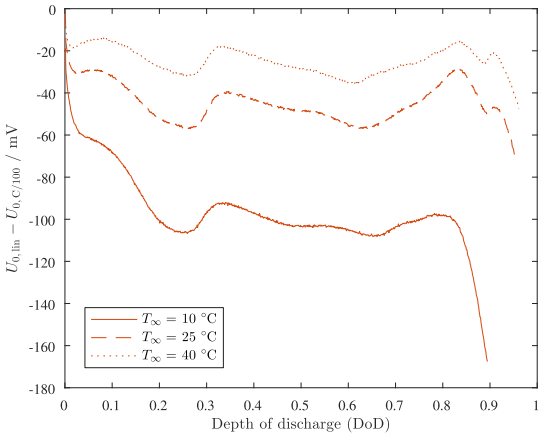

Figure 7. Difference between the linearized open circuit potential $U_{0,\text{lin}}$ gained from linear regression as shown in Fig. 3a and Fig. 4a and the open circuit potential $U_{0,\text{C/100}}$ gained from a 0.4 A constant current operation at 10°C, 25°C, and 40°C of the surrounding ambient air within a climate chamber.

$$q'''_{\text{cc},i}(X,Y,Z)\Big|_{\substack{\forall X=x\\ \forall Y=y\\ \forall Z\in[0,\,t_{\text{stack}}]}} = q'''_{\text{cc},i}(x,y) \quad (i = \text{n, p}) \quad [32]$$

$$q'''_{\text{tab},i}(X,Y,Z)\Big|_{\substack{\forall X=x\\ \forall Y=y\\ \forall Z\in\left[\frac{t_{\text{stack}}-t_{\text{tab},i}}{2},\,\frac{t_{\text{stack}}+t_{\text{tab},i}}{2}\right]}} = q'''_{\text{tab},i}(x,y) \quad [33]$$

$$q'''_{\text{ct}}(X,Y,Z)\Big|_{\substack{\forall X=x\\ \forall Y=y\\ \forall Z\in[0,\,t_{\text{stack}}]}} = q'''_{\text{ct}}(x,y) \quad [34]$$

whereas the thickness of the electrode stack t_{stack} can be derived by multiplying the thickness of an electrode pair t_{ep} with the number of active electrode pairs n_{ep} comprised in the cell. Within the stacked electrode configuration, the anisotropic thermal conductivity k (Wm^{-1}K^{-1}) is further defined as

$$k = \begin{pmatrix} k_{XX} & 0 & 0 \\ 0 & k_{YY} & 0 \\ 0 & 0 & k_{ZZ} \end{pmatrix} \quad [35]$$

In accordance with Chen and coworkers,[45] the effective thermal properties of the electrode stack are calculated by considering the volume fraction of each component within an electrode pair as described in Eq. 21 and by accounting for a series or parallel configuration of thermal resistivities

$$\rho\,c_p = \frac{\sum_i \rho_i\,c_{p,i}\,t_i}{\sum_i t_i} \quad [36]$$

$$k_{\parallel} = \frac{\sum_i t_i\,k_i}{\sum_i t_i} \quad [37]$$

$$k_{\perp} = \frac{\sum_i t_i}{\sum_i \frac{t_i}{k_i}} \quad [38]$$

The relevant geometrical and thermophysical properties for this approximation can be found in Table II. The derived values thereof are

Table II. Thermal and physical properties of the investigated cell's components.

Electrode stack	Symbol (unit)	Negative electrode		Separator (sep)	Positive electrode		Electrolyte (ele)
		Current collector (cc, n)	Composite electrode (an)		Composite electrode (ca)	Current collector (cc, p)	
		Copper	Graphite	Polyolefin	$Li(Ni_xCo_yMn_z)O_2$ + $LiMn_2O_4$	Aluminum	$LiPF_6$ in EC+DMC+EMC
Thickness[a]	t_i (µm)	13.5	69.4	24.5	65.5	22	-
Density[b]	ρ_i (kg m^{-3})	8933	1347.33	1008.98	2328.5	2702	1129.95
Specific heat capacity[b]	$c_{p,i}$ (J kg^{-1} K^{-1})	385	1437.4	1978.16	1269.21	903	2055.1
Thermal conductivity[b]	k_i (W m^{-1} K^{-1})	398	1.04	0.3344	1.58	238	0.6
Pouch case	Symbol (unit)	Outer protective layer (ol)		Metal layer (ml)		Inner sealant layer (il)	
		Polyamide (Nylon-6)		Aluminum		Polypropylene (PP)	
Thickness[c]	t_i (µm)	27		45		88	
Density	ρ_i (kg m^{-3})	1180[d]		2702[b]		885[d]	
Specific heat capacity	$c_{p,i}$ (J kg^{-1} K^{-1})	1470.7[e]		903[b]		1588.4[e]	
Thermal conductivity	k_i (W m^{-1} K^{-1})	0.31[f]		238[b]		0.16[f]	

[a]mean value gained from micrometer measurements at eight different locations.
[b]values in accordance with Ref. 45.
[c]values and configuration in accordance with Ref. 48.
[d]mean value in accordance with, Ref. 49 Tables 37.1 and 37.2.
[e]linear interpolation to room temperature in accordance with, Ref. 49 Table 9.1.
[f]mean value in accordance with, Ref. 49 Tables 10.1.

summarized in Table III together with other geometric entities within the cell. Following the same procedure, the values for the negative electrode and separator overlap, the laminate pouch casing around the cell's edges and seam as well as the sandwich layer on top of the electrode stack formed of pouch casing, half a negative electrode layer and one separator sheet were derived. Together with the respective boundary conditions in the three-dimensional model, the local transient cell temperature T can be determined. At the cell's surface, the area specific inward convective heat transfer q''_{con} and radiative heat transfer q''_{rad} (W m^{-2}) between the cell and and its surroundings (∞) are considered

$$q''_{con} = h\,(T_\infty - T) \quad [39]$$

$$q''_{rad} = \epsilon\sigma\left(T_\infty^4 - T^4\right) \quad [40]$$

Thermal conduction within the copper busbars attached to the cell's tabs as pointed out in Fig. 6 is considered whilst neglecting any thermal contact resistances. For this purpose, the convective heat transfer coefficient h in Eq. 39 is set to 25 W m^{-2} K^{-1} to account for an undirected, turbulent airflow during parametrization measurements and to 8.1 W m^{-2} K^{-1} to represent a directed, laminar airflow during validation measurements. The overall radiative emission coefficient ϵ is set to 0.95 as the cell's planar surface and its surroundings were varnished with a chalk spray prior to the measurements. In Eq. 40, σ represents the Stefan-Boltzmann constant. At the electrical interconnections at the top of the two busbars, we further assume a semi-infinite body due to the attached copper cables for times $t > 0$[40]

$$q''_{cab} = \sqrt{\frac{k\,\rho\,c_p}{\pi\,t}}\,(T_\infty - T) \quad [41]$$

Taking into account the area of the cables A_{cab}, i.e. 50 mm^2 in this case, a combined thermal boundary condition is derived

$$q''_{int} = \frac{A_{cab}}{w_{int}\,h_{int}}\,q''_{cab} + \left(1 - \frac{A_{cab}}{w_{int}\,h_{int}}\right)\left(q''_{con} + q''_{rad}\right) \quad [42]$$

On the side of the busbars opposing the electrical interconnections, thermal insulation is prevailing due to the fixture of the busbars

$$\nabla T \cdot \mathbf{n} = 0 \quad [43]$$

with $\mathbf{n}$ representing its normal vector.

The derived three-dimensional temperature distribution within the cell's electrode stack and tabs is then transferred back to the two-dimensional model by averaging the temperature distribution along the respective thickness t_i

$$T(x,y)\Big|_{\substack{\forall x=X\\ \forall y=Y}} = \frac{1}{t_i}\cdot\int_{t_i} T(X,Y,Z)\,dZ \quad [44]$$

The two-dimensional electrode and three-dimensional cell geometry as well as the introduced model equations were implemented in COMSOL Multiphysics 5.2. With the chosen spatial discretization, 1.75×10^5 degrees of freedom need to be solved at a relative tolerance of 1×10^{-6} with a maximum time step of 1s which consumes about 15 min of computational time for a 40 A (i.e. 1 C) discharge operation on a workstation with eight cores of 3.1 GHz and 32 GB of memory. By further coarsening the spatial discretization or by assuming a strictly two-dimensional thermal representation of the cell, the computational effort can be reduced significantly in order to suit the available computational resources.

Table III. Calculated effective thermal and physical properties of the investigated cell's geometric entities and corresponding heat generation rates.

Index	t_i (µm)	ρ_i (kg m^{-3})	$c_{p,i}$ (J kg^{-1} K^{-1})	$k_{\parallel,i}$ (W m^{-1} K^{-1})	$k_{\perp,i}$ (W m^{-3})	q'''_i
stack	8503.2	2033.6	1184.5	30.9	0.97	$q'''_{cc} + q'''_{ct}$
lap, ne	8503.2	1494.3	1450.9	15.83	0.66	$q'''_{cc,n}$
lap, sep	8503.2	1112.9	2045.3	0.56	0.54	-
tab, n	300	8933	385	398 (isotropic)		$q'''_{tab,n}$
tab, p	400	2702	903	238 (isotropic)		$q'''_{tab,p}$
case	160	1445.8	1211.9	67.08	0.25	-
top	260.65	1555.3	1196.8	51.16	0.34	-

Results and Discussion

In this section, the simulation data is compared to measurement data in order to proof the validity of the chosen cell temperature dependent polarization approach for spatially resolved electro-thermal

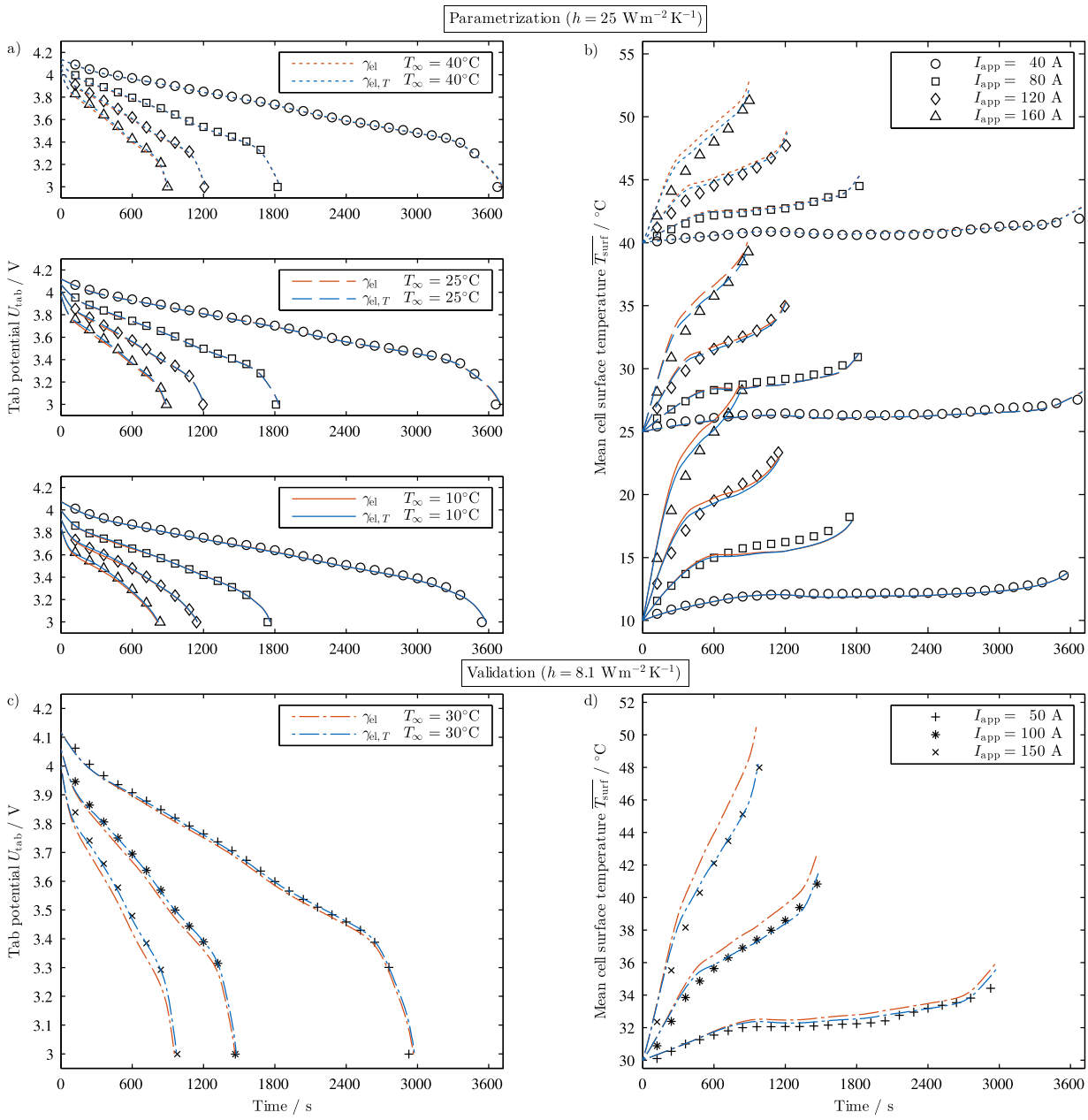

Figure 8. Comparison of simulation data (orange and blue lines) to measurement data (black symbols) for the tab potential U_{tab} and mean surface temperature $\overline{T_{surf}}$ for the parametrization scenario (a and b) as well as for the validation scenario (c and d).

models as suggested in Eq. 14 which will be further addressed as $\gamma_{el,T}$. Furthermore, it is benchmarked against the initial cell temperature invariant polarization expression stated in Eq. 1 which will be further referred to as γ_{el}. If we compare the simulated tab potential U_{tab} and mean surface temperature $\overline{T_{surf}}$ gained from averaging over the cavity of the pouch housing, both polarization approaches can depict the overall characteristic transient cell behavior for both parametrization (Figs. 8a and 8b) and validation scenarios (Figs. 8c and 8d). However, the cell temperature corrected approach shows a slightly better quality in predicting the cell behavior during the parametrization scenario especially for higher discharge currents which can be explained with a slightly superior quality of the linear regression for $\gamma_{el,T}$. Looking into the validation scenario shown in Figs. 8c and 8d, a more pronounced difference can be observed which we believe to be based on the capability of $\gamma_{el,T}$ to account for a variation in thermal boundary conditions when considering a local cell temperature dependency of electrode polarization. In order to show the observed difference quantitatively, we further calculated the mean absolute error (MAE) between simulation and measurement data via

$$\mathrm{MAE} = \frac{1}{n}\sum_{i=1}^{n} |f_i - y_i| \qquad [45]$$

with n representing the amount of data points considered which is every 10 s for the course of the discharge in this case, f_i describing the

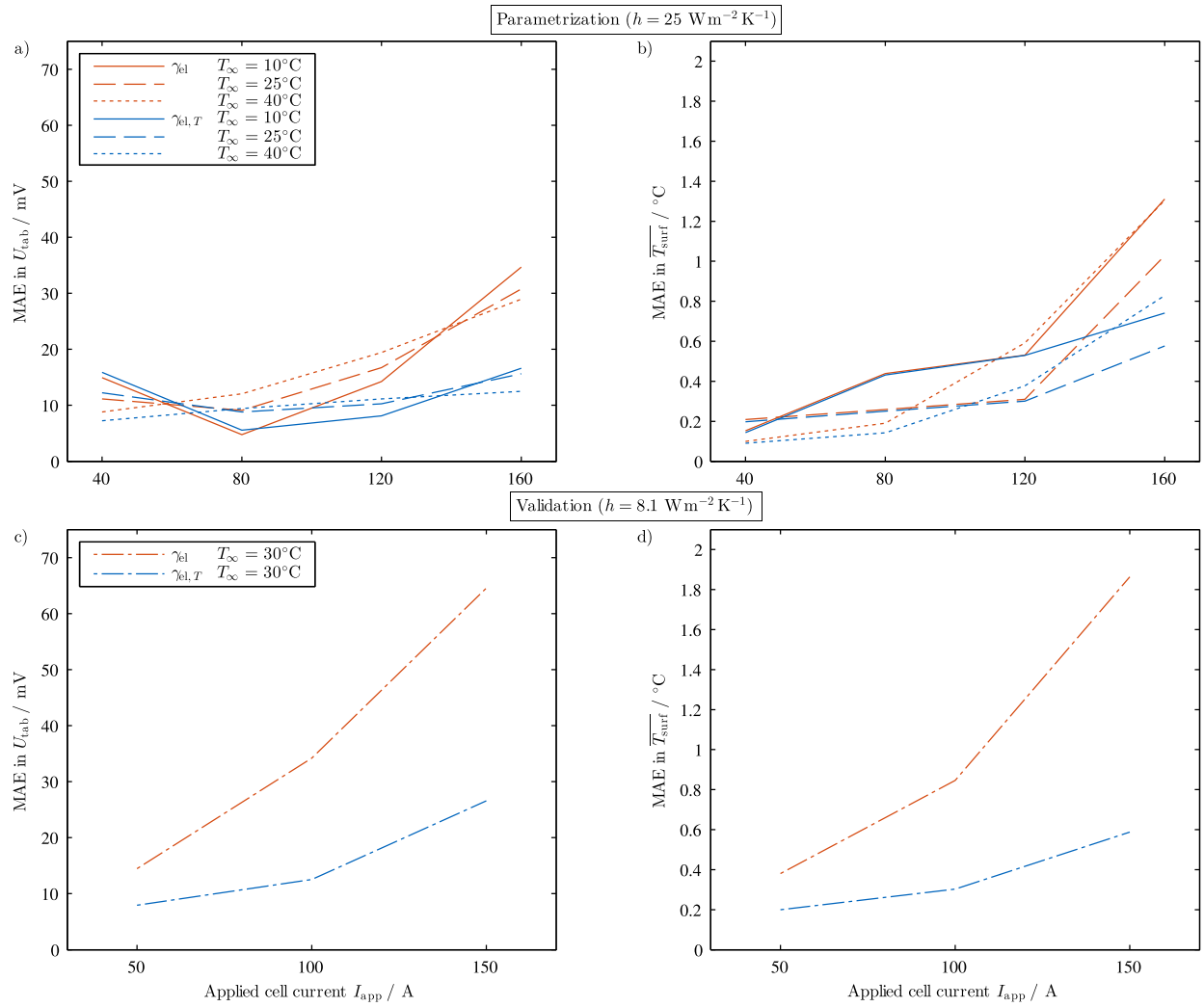

Figure 9. Mean absolute error between simulation and measurement data for the parametrization measurements (a and b) as well as for the validation measurements (c and d).

predicted value via simulation and y_i referring to the true value which is the measurement data. Whilst both polarization approaches show comparable performance during the simulation of the parametrization measurements (Figs. 9a and 9b), the difference becomes a lot more pronounced when the thermal boundary conditions are altered to a reduced convection during validation measurements (Figs. 9c and 9d). With a MAE of 64.6 mV and 26.5 mV in tab potential and 1.9°C and 0.6°C in mean surface temperature during a 150 A discharge operation, the overall simulation error can be reduced by a factor of approximately 3 when accounting for a cell temperature dependency of cell polarization.

With the aid of the derived simulation data, the overall error in measuring the tab potential instead of the mean electrode potential can be estimated for evaluating the quality of the carried out model parametrization. We can observe an underestimation of the mean electrode potential of about 6 mV at a 40 A discharge at 25°C which linearly increases with the applied current due to Ohmic losses within the current collecting components. The increase of 0.7 mV between discharge operations at 10°C to 40°C at 40 A can be adequately scaled to higher discharge currents. This error lies within the range of the MAE in the predicted tab potential U_{tab} as pointed out in Fig. 9a. Correcting the measurement data with the simulated offset, an iterative improvement of the parameter estimation can be obtained. When further estimating the overall error in measuring the cell's surface temperature at the eight positions indicated in Fig. 6 instead of the mean electrode stack temperature, an underestimation of the mean electrode temperature of about 0.08°C at 40 A and 25°C can be observed. This error and its decrease of 0.04°C between discharge operations at 10°C to 40°C at 40 A can also be almost linearly scaled to higher discharge currents. In contrast to the error in potential measurement, this error lies within the combined measurement accuracy of the applied test equipment for most of the investigated discharge scenarios. This satisfies the assumption of a sufficient accuracy when measuring the cell's surface temperature at the given cooling conditions.

If we consider the local temperature distribution within the cell and electrical interconnections as a further means of model validation, a considerable difference between infrared thermopraphy measurement data and simulation data can be observed with increasing discharge time (see Fig. 10). The observed trend of overall temperature overprediction for the cell temperature invariant polarization expression γ_{el} can also be seen here (a, c and e). Whilst the overall deviation in surface temperature is not as pronounced for the cell temperature dependent polarization expression $\gamma_{el,T}$ (b, d and f), the local characteristics of temperature distribution cannot be depicted in full detail for both

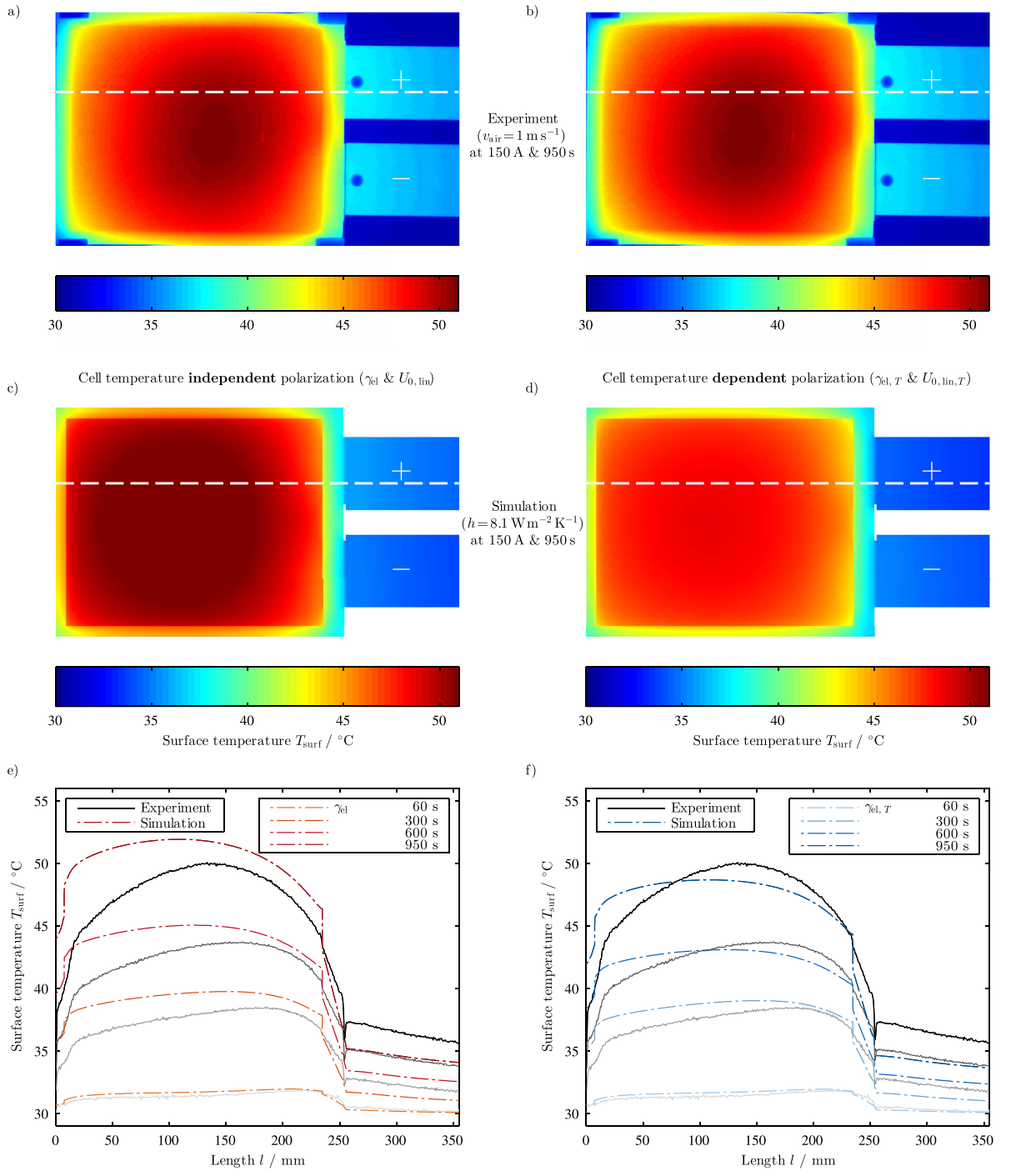

Figure 10. Comparison of simulated surface temperature distribution to infrared thermography measurements for both γ_{el} (a, c and e) and $\gamma_{el,T}$ (b, d and f). The cut lines through the two-dimensional temperature distribution at the end of a 150 A discharge operation at 950 s (a and c as well as b and d) are considered to illustrate the transient variation of the temperature distribution from 60 s, 300 s, and 600 s to 950 s (e and f).

cases. First of all, the simulated maximum cell temperature is quite near to half the height of the cavity of the pouch housing with a certain tendency toward its lower part whereas the measured maximum cell temperature is more shifted toward the tab area. Furthermore, both approaches similarly show a quite even temperature distribution across the cell's surface throughout the entire discharge operation which becomes more obvious with increasing discharge times. The simulated temperature level of the attached copper bars is also lower in comparison to measurement data with increasing discharge time.

Looking into the spatial distribution of the simplified volume specific enthalpy of reaction q'''_{ct} forming the major contribution to the overall heat generation within a Li-ion cell as calculated in Eq. 30, we

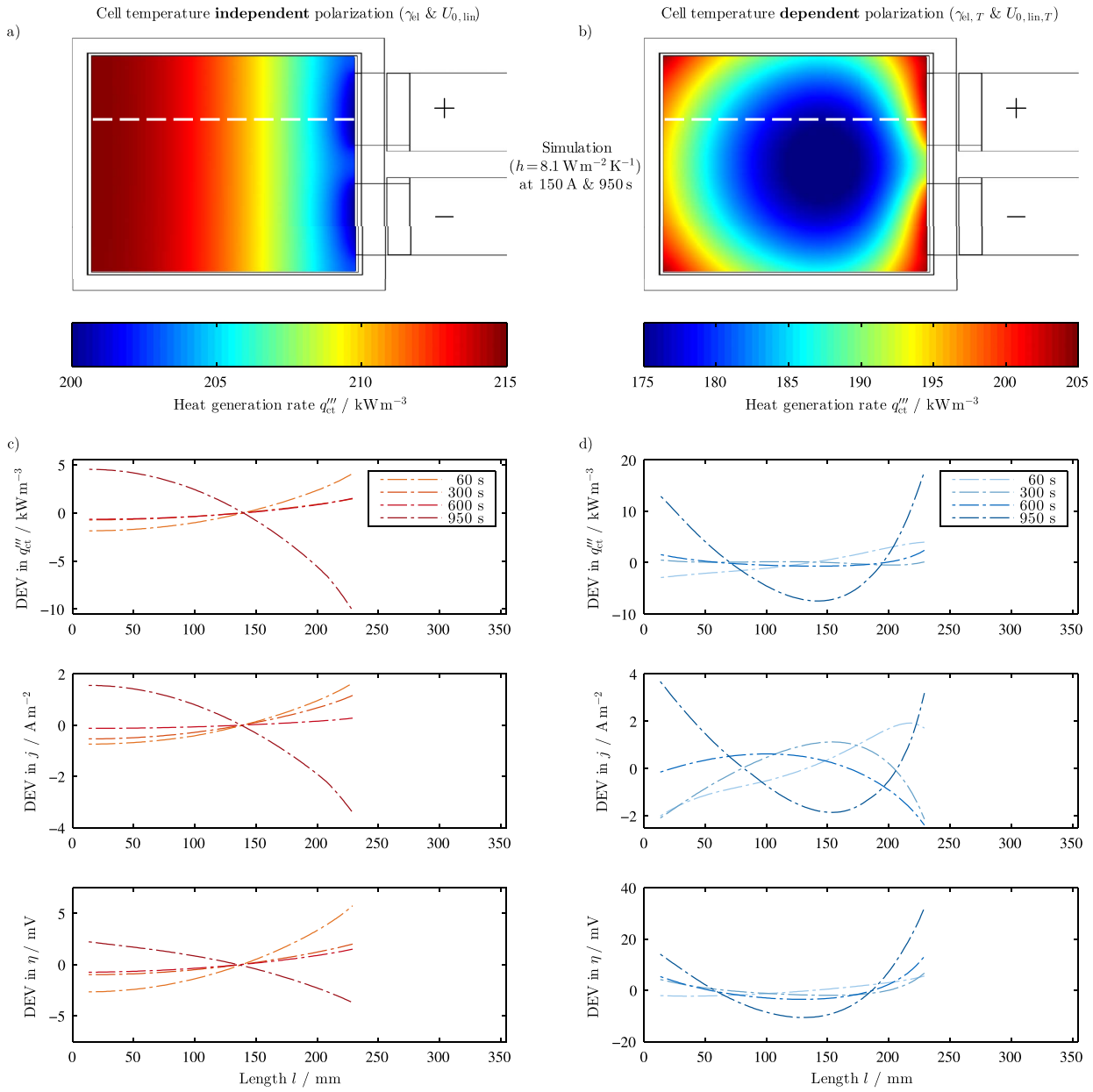

Figure 11. Comparison of simulated spatial distribution and local signed deviation from the arithmetic mean in heat generation rate q'''_{ct}, transfer current density j and overpotential η for both γ_{el} (a and c) and $\gamma_{el,T}$ (b and d). The cut lines through the two-dimensional distribution of heat generation rate at the end of a 150 A discharge operation at 950 s (a and b) are considered to illustrate the transient signed deviation from the arithmetic mean of the relevant variables from 60 s, 300 s, and 600 s to 950 s (c and d).

can observe quite a distinct difference between the two considered approaches (see Fig. 11). With the signed deviation from the arithmetic mean (DEV) in heat generation which is calculated by

$$\mathrm{DEV}_i = f_i - \frac{1}{n}\sum_{i=1}^{n} f_i \qquad [46]$$

we can observe a pronounced heat generation near the tab region for most of the discharge operation for the temperature invariant polarization expression which corresponds to the spatial distribution of DEV in transfer current density j and overpotential η (c) due to $q'''_{ct} \propto j\,\eta$ as stated in Eq. 30. At the end of the discharge operation, an inverse characteristics can be seen as the maxima in current density and overpotential shift toward the bottom of the electrodes following the similar trend of transfer current density and overpotential. This characteristics has been shown before by other groups.[34] Considering a cell temperature dependent linear polarization expression, we can now observe a significantly different behavior (b and d). In this case, the tab area is not as dominant during most of the discharge operation except for the beginning. At the end of the discharge, both tab area and bottom area of the cell are heated significantly as during most of the discharge operation, the maximum of transfer current density was situated around the center of the electrodes following the maximum cell temperature. With a minimum in overpotential at 300 s and 600 s

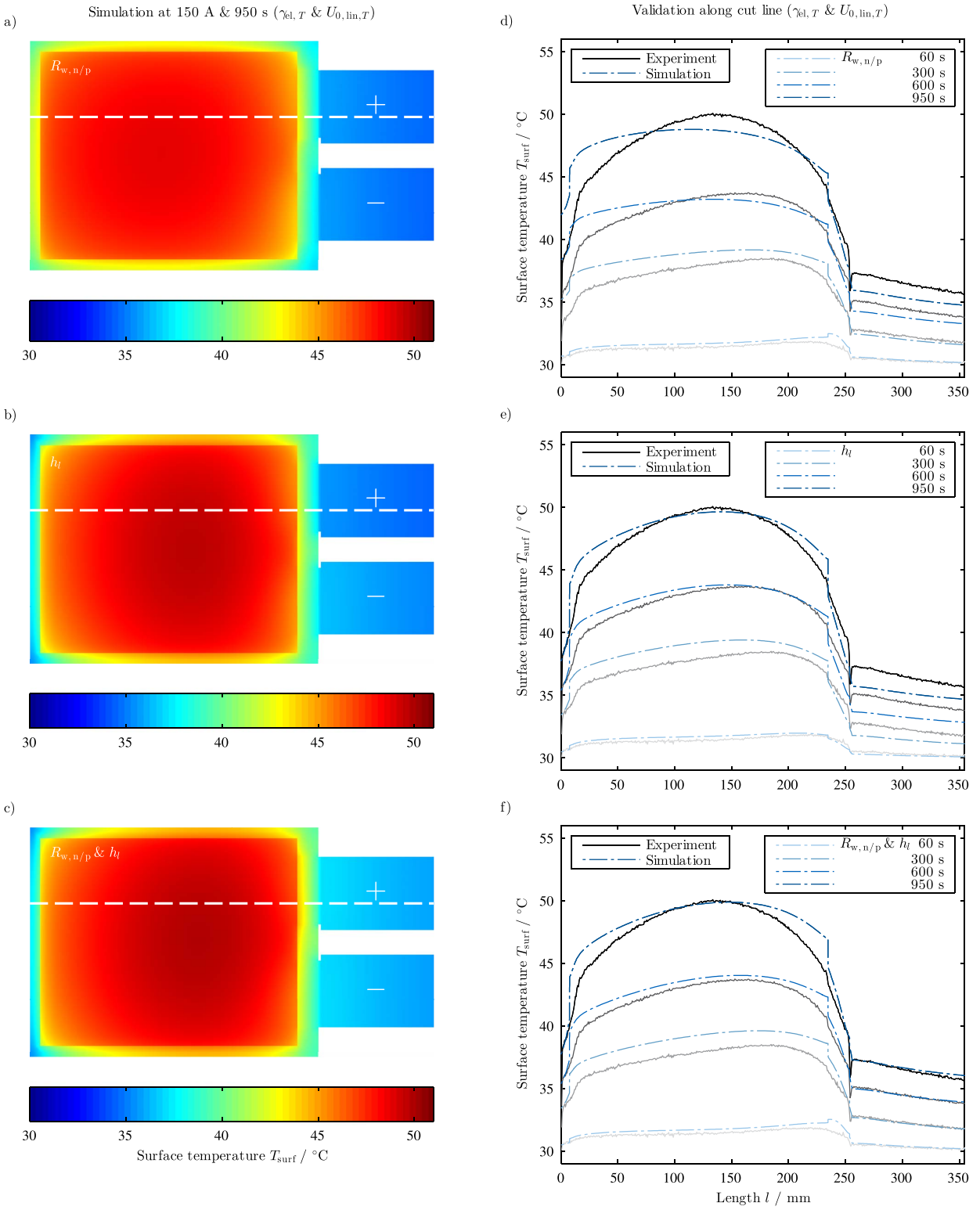

Figure 12. Comparison of simulated temperature distributions at the end of a 150 A discharge operation at 950 s (a, b and c) and along the cut lines indicated at 60 s, 300 s, 600 s, and 950 s (d, e and f) accounting for additional Ohmic losses at the tabs $R_{w,n/p}$ (a and d), a local heat transfer coefficient h_y (b and e) and both (c and f).

also following the maximum cell temperature, the deviation in heat generation is minor.

Even though the two polarization expressions show two completely different characteristics in the deviation of heat generation, its relative deviation is less than ca. 5% and 15% for γ_{el} and $\gamma_{el,T}$ throughout the entire discharge operation. This explains the observed similar characteristics in temperature distribution pointed out in Fig. 10. As we already considered variations in Joule heating between the negative and positive tabs and current collectors as well as thermal conduction from the tabs to the copper bars within our model, we assume that there are two more reasons for the observed temperature distribution being shifted toward the tab area that we have not accounted for as of yet in order to not superimpose the observations made so far. Firstly, we assume that even though we put substantial effort into cell preparation to avoid any major contact resistances between the copper bars and the cell's tabs, there are still some Ohmic losses that we could not prevent. We assume that these additional resistances are located within the cell's seam area based on the process of welding nickel plated copper and aluminum tabs to the cell's negative and positive current collector foils. Secondly, the test setup chosen in this work guarantees an airflow which is directed parallel to the cell's middle axis flowing from the bottom area to the tab area of the cell. Therefore, we assume that the heat transfer coefficient in the bottom area of the cell is higher due to a thinner laminar boundary layer. Similar to Eq. 7 we can find the following expression for this case [41]

$$Nu_l = 0.332\sqrt{Re_l}\sqrt[3]{Pr} \quad [47]$$

with

$$Re_l = \frac{v_{air}\, l}{\nu_{air}} \quad [48]$$

the local heat transfer coefficient h_l can be calculated

$$h_l = \frac{Nu_l\, k_{air}}{l} \quad [49]$$

whereas the length l is chosen to be zero at the bottom part of the cell's pouch seam. This approach results in values of the convective heat transfer coefficient h_l of 17.2 $W\,m^{-2}\,K$ at the bottom of the cavity of the pouch housing and 4.3 $W\,m^{-2}\,K$ at its tab area at a velocity of 1 $m\,s^{-1}$ of the directed airflow. We assume the welding resistances $R_{w,i}$ to be 15 $\mu\Omega$ for $R_{w,n}$ at the negative tab and 46 $\mu\Omega$ for $R_{w,p}$ at the positive tab.[46] We can calculate the total heat rate accompanied with these resistances $q_{w,i}$ (W) due to the applied tab current I_{app}

$$q_{w,i} = I_{app}^2 \cdot R_{w,i} \quad (i = n,\ p) \quad [50]$$

Including these resistance values as an additional boundary heat source within the seam area where the welding spots are located, we can see an overall increase in cell temperature especially at earlier times but also of the attached copper bars as pointed out in Figs. 12a and 12d. However, the shape of the temperature distribution across the cell does not vary significantly. If we then, in contrast, apply a local heat transfer coefficient as stated in Eq. 49, we can observe a drastic change in the shape of the simulated temperature distribution as shown Figs. 12b and 12e which resembles the general shape of the measured temperature distribution adequately. However, the temperature of the copper bars remains too low in comparison. Hence, if we combine these two boundary conditions as presented in Figs. 12c and 12f, we can see a temperature profile which matches to the temperature measurement very well. We assume that the remaining deviation from the measurement data is based on the applied effective thermophysical properties of the cell, which we did not measure in this work.

Therefore, we can state for the case presented here, that a cell temperature dependency of a linear polarization expression as suggested in this work is desirable to simulate the local electro-thermal cell behavior during varying cooling conditions which are not represented by the carried out parametrization measurements. In order to match the simulated temperature distribution to the measured one, not only special attention needs to be turned to the prevailing electrical and thermal boundary conditions due to the cell's electrical interconnections but also to the local convective cooling condition especially when forced convection is applied. The distribution in heat generation across the cell arising from localized charge transfer processes within the electrodes only seems to play a minor role in terms of the resulting temperature distribution. However, this effect needs to be further studied at varying electrical and thermal boundary conditions.

Conclusions

In this work, we extended a well-known polarization approach to account for a local cell temperature dependency of fitting parameters gained from constant current discharge experiments on large-format Li-ion pouch cells. We achieved this by referring the measured cell polarization to the simultaneously measured cell surface temperature and subsequently linearizing the resulting characteristics. This adoption shows a superior quality of predicting the overall tab potential and mean surface temperature at thermal boundary conditions varying from the initial parametrization measurements. For the chosen test configuration, we could reduce the model error by a factor of 3. In order to allow for a reliable model validation, we used a test bench which allows for an adjustable, directed airflow across the cell's middle axis. Controlling and knowing the prevailing flow condition, the convective heat transfer coefficient can be calculated from Nusselt, Reynolds and Prandtl correlations given in the literature. We demonstrated that a local cell temperature dependent linear polarization behavior results in substantially different spatial and temporal heat generation, charge transfer and overpotential characteristics within the electrodes compared to the initial cell temperature independent approach. We further showed that this difference does not majorly influence the observed surface temperature distribution. In order to align the simulated surface temperature distribution with the measured one, both a local heat transfer coefficient accounting for the direction of airflow and additional electrical resistances at the cell's terminals need to be considered.

In future work, we will discuss the observed influence of resistance variations at the cell's terminals on the surface temperature distribution via both simulation and experiment.

Acknowledgment

The work presented here was supported by the German Federal Ministry of Education and Research (03X4631P, *SafeBatt* and 03X4633A, *ExZellTUM*) and the Bavarian Ministry of Economic Affairs and Media, Energy and Technology under the auspices of the *EEBatt* project. The authors thank Alex Friesen, Jan Haetge, and Falko Schappacher from Münster Electrochemical Energy Technology (MEET) for providing essential geometric data from the investigated cell's components.

Appendix

For further studying the observed effects, polynomial fits of polarization parameters gained from parametrization measurements, measured open circuit potential U_0 (V) and entropic coefficient dU_0/dT ($V\,K^{-1}$) are provided. The polarization parameters are assumed to be dependent on the cell's DoD as well as the initial cell temperature at the beginning of the discharge process T_0 (K) with

$$f(\mathrm{DOD},\ T_0) = \sum_{n=1}^{10} a_{n-1}\,\mathrm{DoD}^{n-1} \quad [A1]$$

and

$$a_{n-1} = \sum_{m=1}^{3} a_{n-1}^{m-1}\,T_0^{m-1} \quad [A2]$$

The relevant coefficients are given in Table AI. U_0 and dU_0/dT are provided as functions of DoD in Table AII. For estimating these parameters, the cell was discharged at 40 A and 30°C until a capacity of 1 Ah was extracted from the cell. At this SoC, the cell was rested

Table AI. Coefficients of polynomial fit for derived polarization parameters as a function of DoD and T_0.

		Cell temperature **independent** polarization		Cell temperature **dependent** polarization	
		$U_{0,\mathrm{lin}}$ V	G_{el} S	$U_{0,\mathrm{lin},T}$ VK^{-1}	$G_{\mathrm{el},T}$ SK
	a_0^0	$1.69 \times 10^{+00}$	$-2.61 \times 10^{+04}$	3.57×10^{-02}	$-6.72 \times 10^{+06}$
a_0	a_0^1	1.58×10^{-02}	$1.61 \times 10^{+02}$	-1.02×10^{-04}	$4.01 \times 10^{+04}$
	a_0^2	-2.50×10^{-05}	-2.36×10^{-01}	9.81×10^{-08}	$-5.58 \times 10^{+01}$
	a_1^0	$-7.82 \times 10^{+01}$	$3.11 \times 10^{+05}$	-3.26×10^{-01}	$8.84 \times 10^{+07}$
a_1	a_1^1	4.94×10^{-01}	$-1.99 \times 10^{+03}$	2.06×10^{-03}	$-5.57 \times 10^{+05}$
	a_1^2	-7.92×10^{-04}	$3.12 \times 10^{+00}$	-3.29×10^{-06}	$8.56 \times 10^{+02}$
	a_2^0	$4.25 \times 10^{+02}$	$-1.00 \times 10^{+06}$	$1.69 \times 10^{+00}$	$-3.16 \times 10^{+08}$
a_2	a_2^1	$-2.77 \times 10^{+00}$	$6.61 \times 10^{+03}$	-1.10×10^{-02}	$2.07 \times 10^{+06}$
	a_2^2	4.49×10^{-03}	$-1.08 \times 10^{+01}$	1.80×10^{-05}	$-3.33 \times 10^{+03}$
	a_3^0	$4.36 \times 10^{+03}$	$-1.97 \times 10^{+06}$	$1.65 \times 10^{+01}$	$-5.07 \times 10^{+08}$
a_3	a_3^1	$-2.82 \times 10^{+01}$	$1.10 \times 10^{+04}$	-1.07×10^{-01}	$2.45 \times 10^{+06}$
	a_3^2	4.56×10^{-02}	$-1.35 \times 10^{+01}$	1.72×10^{-04}	$-2.13 \times 10^{+03}$
	a_4^0	$-5.59 \times 10^{+04}$	$1.66 \times 10^{+07}$	$-2.10 \times 10^{+02}$	$7.10 \times 10^{+09}$
a_4	a_4^1	$3.64 \times 10^{+02}$	$-1.01 \times 10^{+05}$	$1.37 \times 10^{+00}$	$-4.18 \times 10^{+07}$
	a_4^2	-5.89×10^{-01}	$1.43 \times 10^{+02}$	-2.22×10^{-03}	$5.73 \times 10^{+04}$
	a_5^0	$2.39 \times 10^{+05}$	$-2.10 \times 10^{+07}$	$8.87 \times 10^{+02}$	$-2.21 \times 10^{+10}$
a_5	a_5^1	$-1.55 \times 10^{+03}$	$1.26 \times 10^{+05}$	$-5.79 \times 10^{+00}$	$1.34 \times 10^{+08}$
	a_5^2	$2.52 \times 10^{+00}$	$-1.58 \times 10^{+02}$	9.42×10^{-03}	$-1.91 \times 10^{+05}$
	a_6^0	$-5.11 \times 10^{+05}$	$-4.06 \times 10^{+07}$	$-1.88 \times 10^{+03}$	$3.26 \times 10^{+10}$
a_6	a_6^1	$3.33 \times 10^{+03}$	$2.71 \times 10^{+05}$	$1.23 \times 10^{+01}$	$-2.00 \times 10^{+08}$
	a_6^2	$-5.40 \times 10^{+00}$	$-4.93 \times 10^{+02}$	-2.01×10^{-02}	$2.90 \times 10^{+05}$
	a_7^0	$5.91 \times 10^{+05}$	$1.29 \times 10^{+08}$	$2.16 \times 10^{+03}$	$-2.37 \times 10^{+10}$
a_7	a_7^1	$-3.85 \times 10^{+03}$	$-8.37 \times 10^{+05}$	$-1.42 \times 10^{+01}$	$1.47 \times 10^{+08}$
	a_7^2	$6.25 \times 10^{+00}$	$1.39 \times 10^{+03}$	2.31×10^{-02}	$-2.13 \times 10^{+05}$
	a_8^0	$-3.52 \times 10^{+05}$	$-1.18 \times 10^{+08}$	$-1.28 \times 10^{+03}$	$7.16 \times 10^{+09}$
a_8	a_8^1	$2.30 \times 10^{+03}$	$7.64 \times 10^{+05}$	$8.40 \times 10^{+00}$	$-4.41 \times 10^{+07}$
	a_8^2	$-3.73 \times 10^{+00}$	$-1.25 \times 10^{+03}$	-1.37×10^{-02}	$6.26 \times 10^{+04}$
	a_9^0	$8.49 \times 10^{+04}$	$3.67 \times 10^{+07}$	$3.08 \times 10^{+02}$	$-2.92 \times 10^{+08}$
a_9	a_9^1	$-5.55 \times 10^{+02}$	$-2.39 \times 10^{+05}$	$-2.02 \times 10^{+00}$	$1.67 \times 10^{+06}$
	a_9^2	9.00×10^{-01}	$3.90 \times 10^{+02}$	3.29×10^{-03}	$-1.46 \times 10^{+03}$

for 90 min in order to approach a nearly equilibriated state. The cell was subsequently cooled to 26°C and 22°C and rested until thermal equilibrium was achieved after 60 min. The cell was again heated to the initial 30°C in order to continue the discharge process. This procedure was repeated until the cell's cut off voltage of 3 V was reached. The exact procedure was previously explained.[47] Via linearizing the variation of the measured open circuit potential as a function of temperature, the entropic coefficient was finally derived. The parameters given in Table AII resemble the open circuit potential of the cell at 30°C.

Table AII. Coefficients of polynomial fit for measured open circuit potential U_0 and entropic coefficient dU_0/dT as a function of DoD.

	U_0 V	dU_0/dT VK^{-1}
a_0	$4.17 \times 10^{+00}$	-4.46×10^{-05}
a_1	$-1.67 \times 10^{+00}$	2.75×10^{-03}
a_2	$1.28 \times 10^{+01}$	-3.17×10^{-02}
a_3	$-7.22 \times 10^{+01}$	1.04×10^{-01}
a_4	$2.22 \times 10^{+02}$	4.92×10^{-02}
a_5	$-4.22 \times 10^{+02}$	-9.30×10^{-01}
a_6	$5.43 \times 10^{+02}$	$2.09 \times 10^{+00}$
a_7	$-4.82 \times 10^{+02}$	$-2.15 \times 10^{+00}$
a_8	$2.71 \times 10^{+02}$	$1.07 \times 10^{+00}$
a_9	$-7.03 \times 10^{+01}$	-2.07×10^{-01}

References

1. M. Doyle, T. F. Fuller, and J. Newman, *Journal of The Electrochemical Society*, **140**, 1526 (1993).
2. J. Christensen, D. Cook, and P. Albertus, *Journal of the Electrochemical Society*, **160**, A2258 (2013).
3. J. Newman and W. Tiedemann, *Journal of The Electrochemical Society*, **140**, 1961 (1993).
4. S. Allu, S. Kalnaus, W. Elwasif, S. Simunovic, J. A. Turner, and S. Pannala, *Journal of Power Sources*, **246**, 876 (2014).
5. H. Gu, *Journal of The Electrochemical Society*, **130**, 1459 (1983).
6. W. Tiedemann, J. Newman, and F. DeSua, Potential Distribution in the Lead-Acid Battery Grid. Power Sources 6. London, 1977; pp 15–23
7. W. Tiedemann and J. Newman. In *Proceedings of the Symposium on Battery Design and Optimization*; Gross, S., Ed.; Proceedings volume / The Electrochemical Society; The Electrochemical Society: Princeton and NJ, 1979; Vol. 79-1; pp 23–38
8. W. Tiedemann and J. Newman. In *Proceedings of the Symposium on Battery Design and Optimization*; Gross, S., Ed.; Proceedings volume / The Electrochemical Society; The Electrochemical Society: Princeton and NJ, 1979; Vol. 79-1; pp 39–49
9. H. Gu, *IEEE Aerospace and Electronic Systems Magazine*, **5**, 3 (1990).
10. K. H. Kwon, C. B. Shin, T. H. Kang, and C.-S. Kim, *Journal of Power Sources*, **163**, 151 (2006).
11. U. S. Kim, C. B. Shin, and C.-S. Kim, *Journal of Power Sources*, **180**, 909 (2008).
12. U. S. Kim, C. B. Shin, and C.-S. Kim, *Journal of Power Sources*, **189**, 841 (2009).
13. U. S. Kim, J. Yi, C. B. Shin, T. Han, and S. Park, *Journal of Power Sources*, **196**, 5115 (2011).
14. U. S. Kim, J. Yi, C. B. Shin, T. Han, and S. Park, *Journal of The Electrochemical Society*, **158**, A611 (2011).
15. J. Yi, U. S. Kim, C. B. Shin, T. Han, and S. Park, *Journal of the Electrochemical Society*, **160**, A437 (2013).
16. J. Yi, U. S. Kim, C. B. Shin, T. Han, and S. Park, *Journal of Power Sources*, **244**, 143 (2013).
17. U. S. Kim, J. Yi, C. B. Shin, T. Han, and S. Park, *Journal of the Electrochemical Society*, **160**, A990 (2013).
18. J. Yi, J. Lee, C. B. Shin, T. Han, and S. Park, *Journal of Power Sources*, **277**, 379 (2015).
19. S. Chacko and Y. M. Chung, *Journal of Power Sources*, **213**, 296 (2012).
20. S. Jung and D. Kang, *Journal of Power Sources*, **248**, 498 (2014).
21. P. Taheri, M. Yazdanpour, and M. Bahrami, *Journal of Power Sources*, **243**, 280 (2013).
22. P. Taheri, A. Mansouri, B. Schweitzer, M. Yazdanpour, and M. Bahrami, *Journal of the Electrochemical Society*, **160**, A1731 (2013).
23. P. Taheri, A. Mansouri, M. Yazdanpour, and M. Bahrami, *Electrochimica Acta*, **133**, 197 (2014).
24. M. Yazdanpour, P. Taheri, A. Mansouri, and M. Bahrami, *Journal of the Electrochemical Society*, **161**, A1953 (2014).
25. H. Sun, X. Wang, B. Tossan, and R. Dixon, *Journal of Power Sources*, **206**, 349 (2012).
26. J. Yi, B. Koo, and C. Shin, *Energies*, **7**, 7586 (2014).
27. K. Onda, H. Kameyama, T. Hanamoto, and K. Ito, *Journal of The Electrochemical Society*, **150**, A285 (2003).
28. K. Onda, T. Ohshima, M. Nakayama, K. Fukuda, and T. Araki, *Journal of Power Sources*, **158**, 535 (2006).
29. Y. Abdul-Quadir, T. Laurila, J. Karppinen, K. Jalkanen, K. Vuorilehto, L. Skogström, and M. Paulasto-Kröckel, *International Journal of Energy Research*, **38**, 1424 (2014).
30. Y. Abdul-Quadir, T. Laurila, J. Karppinen, and M. Paulasto-Kröckel, *International Journal of Energy Research*, **38**, 564 (2014).
31. J. Zhang, J. Huang, Z. Li, B. Wu, Z. Nie, Y. Sun, F. An, and N. Wu, *Journal of Thermal Analysis and Calorimetry*, **117**, 447 (2014).
32. N. Nieto, L. Diaz, J. Gastelurrutia, I. Alava, F. Blanco, J. Carlos Ramos, and A. Rivas, *Journal of the Electrochemical Society*, **160**, A212 (2012).
33. G. Liu, M. Ouyang, L. Lu, J. Li, and X. Han, *Journal of Thermal Analysis and Calorimetry*, **116**, 1001 (2014).
34. B. Wu, Z. Li, and J. Zhang, *Journal of the Electrochemical Society* , **162**, A181 (2014).
35. A. Barai, G. H. Chouchelamane, Y. Guo, A. McGordon, and P. Jennings, *Journal of Power Sources*, **280**, 74 (2015).
36. F. M. Kindermann, A. Noel, S. V. Erhard, and A. Jossen, *Electrochimica Acta*, **185**, 107 (2015).
37. G. Zhang, L. Cao, S. Ge, C.-Y. Wang, C. E. Shaffer, and C. D. Rahn, *Journal of the Electrochemical Society*, **161**, A1499 (2014).
38. J. Zhang, H. Ge, Z. Li, and Z. Ding, *Journal of Power Sources*, **273**, 1030 (2015).
39. T. M. Bandhauer, S. Garimella, and T. F. Fuller, *Journal of The Electrochemical Society*, **158**, R1 (2011).
40. W. Polifke and J. Kopitz, *Wärmeübertragung: Grundlagen, analytische und numerische Methoden: pp. 105–106, 315-316*, 2nd ed.; Ing-Maschinenbau; Pearson Studium: Munich, 2009
41. *VDI heat atlas: pp. 172–191, 713-716, 2nd ed.; VDI-Buch; Springer: Berlin and New York, 2010*
42. D. C. Giancoli, *Physics for scientists & engineers with modern physics*, 4th ed.; Pearson Prentice Hall: Upper Saddle River, N.J., 2009
43. S. V. Erhard, P. J. Osswald, J. Wilhelm, A. Rheinfeld, S. Kosch, and A. Jossen, *Journal of The Electrochemical Society*, **162**, A2707 (2015).

44. D. Bernardi, E. Pawlikowski, and J. Newman, *Journal of The Electrochemical Society*, **132**, 5 (1985).
45. S. C. Chen, C. C. Wan, and Y. Y. Wang, *Journal of Power Sources*, **140**, 111 (2005).
46. P. A. Schmidt, M. Schweier, and M. F. Zaeh, Joining of Lithium-Ion Batteries Using Laser Beam Welding: Electrical Losses of Welded Aluminum and Copper Joints. ICALEO. 2012; pp 915–923.
47. P. J. Osswald, M. d. Rosario, J. Garche, A. Jossen, and H. E. Hoster, *Electrochimica Acta*, **177**, 270 (2015).
48. P. Svens, M. Kjell, C. Tengstedt, G. Flodberg, and G. Lindbergh, *Energies*, **6**, 400 (2013).
49. J. E. Mark, *Physical properties of polymers handbook*, 2nd ed.; Springer: New York, 2006

5 Summary and Conclusion

Whilst a high energy and power density combined with a good rate capability, longevity, and low cost are essential requirements which make a Li-ion battery suitable for highly demanding applications such as experienced in the automotive sector, a battery's intrinsic safety is the foundation for all further considerations.
All of these attributes are ultimately defined by the design of Li-ion batteries including the chosen materials on the electrode level, as well as the selected format and size of a cell with its inherent thermal restrictions and safety features. For a given set of electrode materials, a variation in cell design can enhance or deteriorate the safety characteristics of a Li-ion battery associated with the likelihood of cell thermal runaway. Due to the thermal nature of this problem, heat generation and heat dissipation at elevated temperatures and currents from electrode to cell level must be investigated, defining both a Li-ion battery's performance and safety.

As a result of a lack in common understanding of what makes a Li-ion battery as safe or unsafe, the term "thermal runaway" has been excessively used in Li-ion battery research throughout the last years even though a generally accepted and commonly applied definition of the term is still missing today. A cell thermal runaway can be generally understood as a surpassing of a critical operating point or temperature beyond which the heat dissipation rate constantly ranges below the heat generation rate until all exothermic side reactions are completely converted. However, the often accompanied other thermal, chemical, and kinetic hazards pose a considerable danger to individuals exposed to a failing Li-ion battery which dominates the general perception of the topic.
On the one hand, an experimental separation of cause (e.g. a short circuit) and effect (e.g. exothermic side reactions) is difficult to achieve based on the self-accelerating nature of cell thermal runaway. On the other hand, key mechanisms dominating cell thermal runaway are not fully understood as of yet, which diminishes the validity and applicability of safety related models. So far, experimental design and testing, as well as modeling and simulation, have been rather treated as two individual disciplines within the context of Li-ion battery safety which impedes true progress in this field. A thorough literature review of current activities in the field of Li-ion battery safety in the beginning of this thesis reveals a strong need for combining the indispensable nature of measurement data with invaluable insights gained from simulation results.
With both the experimental and computational approaches presented within this thesis, the evolution, initiation, and possible mitigation of cell thermal runaway can be assessed which allows to derive design criteria guaranteeing a high level of Li-ion battery safety.

In order to be able to describe the evolution of a cell thermal runaway, underlying kinetics of exothermic side reactions must be fully described and understood. For this purpose, a model-based approach to derive kinetic triplets from two-component ARC measurements of electrolyte wetted NMC-442 and MCMB samples is presented in this thesis which allows the impact of a cell's SoC and SoH on the dynamics throughout thermal runaway evolution to be studied. With NMC-442 based cathode materials receiving growing attention within the field of Li-ion batteries, a kinetic description of the thermal decomposition reaction of this material including electrolyte oxidation is essential.

This allows deriving valid thermal runaway models describing this chemistry. The kinetic investigation of the exothermic side reactions revealed a higher reactivity of the NMC cathode compared to the MCMB anode throughout the entire considered range of temperature, SoC, and SoH. Whilst lower SoCs increase the thermal stability of the materials and cells, a lower SoH comes with a compromised thermal stability on the material and full-cell level due to a decrease in lithiation of the cathode with ongoing aging especially at lower SoCs which is also reflected by the change in the sample's reactivity as a function of temperature. Even though the presented full-cell simulations of ARC measurements show a certain discrepancy between the model predictions and measurement data due to possible shortcomings in sample preparation as well as a missing description of reactions such as SEI decomposition and possible interactions between anode and cathode, such work is crucial in order to make progress in the field of describing the evolution of cell thermal runaway as well as thermal propagation for NMC based Li-ion batteries. Investigating the SoC and especially the SoH dependency of the kinetics of exothermic side reactions is, furthermore, essential in order to evaluate the thermal stability and thermal runaway characteristics throughout the entire operating range and operational life of a Li-ion cell, which can be readily carried out with the presented approach.

With local and field-like internal short circuits being identified as a root cause of initiating cell thermal runaway, the high rate discharge operation and short circuit behavior of Li-ion cells containing graphite and NMC-111 as anode and cathode materials was studied via both experiments as well as modeling and simulation. Both high rate discharge at constant currents as well as short circuit conditions with varying discharge currents, based on an applied constant voltage or constant resistance at the cell's terminals, reveal similarly occurring characteristic rate limiting effects. These rate limitations need to be studied in order to understand the short circuit behavior of Li-ion cells and the associated heat generation rate, which may initiate a cell thermal runaway.
The high rate discharge operation of coin cells with laser-structured and unstructured anode morphologies revealed a dominant impact of salt concentration gradients throughout the electrodes and separator with a considerable Li-ion depletion within the cathode leading to a significantly reduced capacity retention. These concentration gradients could be reduced within a restricted current window by an enhanced ion transport throughout the laser-structured, bi-tortuous graphite anode, resulting in a higher relative capacity retention compared to a coin cell with an unstructured graphite electrode. With ongoing Li-ion depletion throughout the liquid phase of the positive electrode, this effect diminishes and becomes dominated by associated reaction overpotentials leading to a similar capacity retention for cells with both structured and unstructured graphite anodes at higher discharge rates.
Low-resistance external short circuit tests can be considered as ultimate rate capability tests within this context as the cell delivers the maximum current possible defined by its own internal resistivity. In order to measure the short circuit characteristics of Li-ion cells without interfering exothermic side reactions, a novel quasi-isothermal external short circuit test setup for small-sized pouch-type Li-ion cells was designed, which allows for a calorimetric evaluation of the generated heat throughout the applied external short circuits. By varying the cell's intrinsic characteristics, such as electrode loading and tab configuration, as well as test parameters, such as temperature, SoC, and external short circuit resistance, different rate limiting mechanisms could be observed throughout the carried out external short circuit tests. Applying a physical-chemical model accounting for diffusion limitations within both electrodes, underlying rate limiting mechanisms could be identified throughout the carried out short circuit tests. The transient change in the experimentally observed short circuit characteristics, revealing certain plateaus in current and heat generation rate, are mainly dominated by consecutive mass transport limitations and associated reaction overpotentials within the positive electrode.

Whilst similar Li-ion depletion effects within the liquid phase of the positive electrode can be observed as for the carried out rate capability tests, an additional solid phase saturation occurs within the positive electrode, defining the transition between individual plateaus. Low electrode loadings and higher temperatures accelerate the short circuit at higher overall C-rates throughout the short circuit duration, whereas a varying SoC and short circuit resistance merely affect the transient short circuit characteristics until the cells are fully discharged, which underlines the dominance of transient rate limiting mechanisms throughout the liquid and solid components with the corresponding time constants. By simulating a variation in electrode morphology, the possibility of a self-limiting short circuit behavior arising from a disproportionally increased solid or liquid phase limitation was observed which is worth further investigation.
The short circuit characteristics of Li-ion cells could only be studied in the presented detail by combining quasi-isothermal short circuit tests with physical-chemical modeling and simulation, which forms a promising method of evaluating the short circuit tolerance of a certain material combination without interfering exothermic side reactions — these can be more thoroughly studied by ARC measurements as also presented in this work.

By implementing the presented validated physical-chemical short circuit model within a multidimensional multiphysics framework, the external short circuit behavior of larger, commercially sized Li-ion cells was studied. By further accounting for varying cooling strategies, the possibility of mitigating a cell thermal runaway triggered by an external short circuit could be evaluated for various cell formats and sizes. For this purpose, a computationally lean model coupling between the electrical representation of the planar electrodes and the thermal model of a cell's jelly roll or electrode stack was presented. A thorough design study investigating the heat dissipation capabilities of cylindrical, prismatic, and pouch-type cells of different sizes relevant for consumer and automotive applications reveals a superior cooling capability of smaller sized cells with a large cooled surface area and a comparably thin design, as characteristic for pouch-type cells. Especially larger-sized cells show a geometrically limited heat dissipation capability which makes cooling below a critical temperature threshold impossible independent of the considered cooling strategies.
Whether or not these observations hold true, however, needs to be confirmed via experiments. In order to validate thermal models for cells of various formats and sizes, novel experimental methods are required which allow for a maximum control of thermal boundary conditions. Such an approach has been presented in this thesis for a semi-empirical electro-thermal model of a large-format pouch-type Li-ion cell. By applying a controlled laminar airflow across the cell's housing whilst measuring the thermal interaction of the cell's terminals with the electrical interconnection of the test equipment, the cell's surface temperature distribution measured via IR thermography can be considered in order to validate the predicted cell temperature at varying operating and cooling conditions.

By combining the experimental and computational methods presented within this thesis, a cell's thermal runaway characteristics can be most thoroughly evaluated. Starting on the material and electrode level, first of all the kinetics of exothermic side reactions need to be determined via the presented model based data analysis of two-component ARC measurements for the relevant SoC and SoH window of the considered materials, which can be validated by ARC measurements on full cells. By further studying the rate capability and short circuit characteristics of small-sized pouch-type Li-ion cells formed of the same electrode materials as studied within the ARC measurements, the corresponding validated physical-chemical model can be derived with the aid of the presented model adaptions and the discussed combination of rate capability tests and quasi-isothermal calorimetric measurements.

By including these models within the developed multidimensional multiphysics framework, the full cell behavior can be studied for all common cell formats and sizes. In order to validate the thermal cell model, the presented thermal test bench can be used, applying different cooling conditions and current profiles to the studied Li-ion cell.
With this fully parametrized and validated model, the investigated cell can finally be studied in terms of an evolution, initiation, and possible mitigation of cell thermal runaway under various abusive conditions with a focus on short circuit conditions which remains to be validated via cell abuse tests. In order to further describe thermal propagation based on heat dissipation mechanisms such as conduction and radiation, the fully validated cell model merely needs to be implemented in a model of a multiple cell arrangement.

In order to further extend and enhance this workflow, the quasi-isothermal calorimetric setup could be used to study local and field-like internal short circuits on the electrode level, which can be correlated to external short circuit tests, in order to evaluate the impact of the locality of a short circuit on its severity in terms of thermal runaway initiation. The presented multidimensional modeling framework could be then used to study the observed local or internal short circuit characteristics in order to derive the resistance at which the cell was shorted during the carried out experiment. Furthermore, the presented thermal test bench can be extended to allow for a wider range of temperatures and velocities of the controlled airflow, which together with a variable cooling condition at the cell's terminals would enable calorimetric operation. These research topics are currently being studied at the Institute for Electrical Energy Storage Technology of the Technical University of Munich.
Further research work in the field of validated battery safety modeling and simulation should aim at describing not only cell thermal runaway in an enclosed cell housing but should also consider the interaction of a cell with its surroundings due to emitted cell components as well as combustion such as occurring during cell venting and rupture.
Combining these extensions with the experimental and simulation based methods presented in this work, as well as electrochemical and mechanical aspects of triggering internal or local short circuits, the initiation and evolution of cell thermal runaway which may result in thermal propagation of modules and packs or systems can be studied, which allows to design intrinsically safe batteries that can tolerate cell thermal runaway in case runaway mitigation is not possible.

With all solid state Li-ion batteries being expected to reduce (or maybe even rule out) associated safety issues, a continuation of Li-ion battery's dominance in the electrochemical energy storage market is to be expected. However, if all solid state Li-ion batteries are indeed safer is to be questioned, as the targeted metallic lithium anode comes with its own safety issues as already experienced in lithium-metal primary batteries (e.g. low melting point of lithium, dendrite growth, etc.).[129,153,200]

Nevertheless, Li-ion battery safety will undoubtedly remain a key challenge in battery research within the near to mid-term future, which not only deserves but requires appropriate scientific attention.
Only with battery safety being an integral part of Li-ion battery research, economically and technologically appealing yet intrinsically safe Li-ion batteries can be developed so that a thorough market penetration and a general societal acceptance of advanced battery powered products, such as EVs, can be achieved.

References

1 Armand, M.; Tarascon, J.-M.: *Building better batteries*, in: *Nature 451 (7179)*, pp. 652–657, 2008

2 Buss, J.: *Automakers Need A Global Timetable For Phasing Out Internal-Combustion Engines - Oliver Wyman on Transportation & Logistics*, in: *Forbes*, 2018-03-27, URL: https://www.forbes.com/sites/oliverwyman/2018/03/27/automakers-need-a-global-timetable-for-phasing-out-internal-combustion-engines/#2b15c91f23c3, log-date: 06/10/2019

3 International Energy Agency: *CO_2 Emissions from Fuel Combustion 2018 - Highlights*, ed. by IEA Publications, 2018, URL: https://webstore.iea.org/co2-emissions-from-fuel-combustion-2018, log-date: 06/10/2019

4 Blomgren, G.E.: *The Development and Future of Lithium Ion Batteries*, in: *Journal of The Electrochemical Society 164 (1)*, A5019–A5025, 2017

5 Tarascon, J.M.; Armand, M.: *Issues and challenges facing rechargeable lithium batteries*, in: *Nature 414 (6861)*, pp. 359–367, 2001

6 Holden, J.; Goel, N.: *Uber Elevate - Fast-Forwarding to a Future of On-Demand Urban Air Transportation*, ed. by Uber Technologies, 2016, URL: https://www.uber.com/elevate.pdf, log-date: 06/10/2019

7 Grandl, G.; Ostgathe, M.; Cachay, J.; Doppler, S.; Salib, J.; Ross, H.: *The Future of Vertical Mobility - Sizing the market for passenger, inspection, and goods services until 2035*, ed. by Porsche Consulting, 2018, URL: https://www.porsche-consulting.com/fileadmin/docs/04_Medien/Publikationen/TT1371_The_Future_of_Vertical_Mobility/The_Future_of_Vertical_Mobility_A_Porsche_Consulting_study__C_2018.pdf, log-date: 06/10/2019

8 van Noorden, R.: *The rechargeable revolution: A better battery*, in: *Nature 507 (7490)*, pp. 26–28, 2014

9 Andre, D.; Kim, S.-J.; Lamp, P.; Lux, S.F.; Maglia, F.; Paschos, O.; Stiaszny, B.: *Future generations of cathode materials: an automotive industry perspective*, in: *Journal of Materials Chemistry A 3 (13)*, pp. 6709–6732, 2015

10 Schmuch, R.; Wagner, R.; Hörpel, G.; Placke, T.; Winter, M.: *Performance and cost of materials for lithium-based rechargeable automotive batteries*, in: *Nature Energy 3 (4)*, pp. 267–278, 2018

11 Küpper, D.; Kuhlmann, K.; Wolf, S.; Pieper, C.; Xu, G.; Ahmad, J.: *The Future of Battery Production for Electric Vehicles*, ed. by Boston Consulting Group, 2018, URL: https://www.bcg.com/de-de/publications/2018/future-battery-production-electric-vehicles.aspx, log-date: 06/10/2019

12 Nykvist, B.; Nilsson, M.: *Rapidly falling costs of battery packs for electric vehicles*, in: *Nature Climate Change 5 (4)*, pp. 329–332, 2015

13 McKerracher, C.; Morsy, S.; Kou, N.; Goldie-Scot, L.; O'Donovan, A.; Doherty, D.: *Electric Vehicle Outlook 2018*, ed. by Bloomberg New Energy Finance, 2018, URL: https://about.bnef.com/electric-vehicle-outlook/#toc-download, log-date: 06/10/2019

14 Goldie-Scot, L.: *A Behind the Scenes Take on Lithium-ion Battery Prices*, ed. by Bloomberg New Energy Finance, URL: https://about.bnef.com/blog/behind-scenes-take-lithium-ion-battery-prices/, log-date: 06/10/2019

15 Wood, D.L.; Li, J.; Daniel, C.: *Prospects for reducing the processing cost of lithium ion batteries*, in: *Journal of Power Sources 275*, pp. 234–242, 2015

16 Nitta, N.; Wu, F.; Lee, J.T.; Yushin, G.: *Li-ion battery materials: present and future*, in: *Materials Today 18 (5)*, pp. 252–264, 2015

17 Choi, J.W.; Aurbach, D.: *Promise and reality of post-lithium-ion batteries with high energy densities*, in: *Nature Reviews Materials 1 (4)*, p. 1401826, 2016

18 Gröger, O.; Gasteiger, H.A.; Suchsland, J.-P.: *Review – Electromobility: Batteries or Fuel Cells?*, in: *Journal of The Electrochemical Society 162 (14)*, A2605–A2622, 2015

19 Manthiram, A.; Knight, J.C.; Myung, S.-T.; Oh, S.-M.; Sun, Y.-K.: *Nickel-Rich and Lithium-Rich Layered Oxide Cathodes: Progress and Perspectives*, in: *Advanced Energy Materials 6 (1)*, p. 1501010, 2016

20 Azevedo, M.; Campagnol, N.; Hagenbruch, T.; Hoffman, K.; Lala, A.; Ramsbottom, O.: *Lithium and cobalt - a tale of two commodities*, ed. by McKinsey & Company, 2018, URL: https://www.mckinsey.com/~/media/mckinsey/industries/metals%20and%20mining/our%20insights/lithium%20and%20cobalt%20a%20tale%20of%20two%20commodities/lithium-and-cobalt-a-tale-of-two-commodities.ashx, log-date: 06/10/2019

21 Eddy, J.; Mulligan, C.; van de Staaij, J.; Klip, D.; Campagnol, N.; Hagenbruch, T.: *Metal mining constraints on the electric mobility horizon - Developed in collaboration with MineSpans and McKinsey Basic Materials Institute*, ed. by McKinsey & Company, 2018, URL: https://www.mckinsey.com/industries/oil-and-gas/our-insights/metal-mining-constraints-on-the-electric-mobility-horizon, log-date: 06/10/2019

22 Nitta, N.; Yushin, G.: *High-Capacity Anode Materials for Lithium-Ion Batteries: Choice of Elements and Structures for Active Particles*, in: *Particle & Particle Systems Characterization 31 (3)*, pp. 317–336, 2014

23 Michaelis, A. et al.: *VDMA Roadmap Battery Production Equipment 2030 - Update 2018*, ed. by VDMA Battery Production, 2018, URL: https://battprod.vdma.org/documents/7411591/31763313/Roadmap%20Battery%20Production%20Equipment%202030_Update%202018_english_1555386264179.pdf/4431e130-f9a1-8a25-60b2-b976c4c467d9, log-date: 06/10/2019

24 Kwade, A.; Haselrieder, W.; Leithoff, R.; Modlinger, A.; Dietrich, F.; Droeder, K.: *Current status and challenges for automotive battery production technologies*, in: *Nature Energy 3 (4)*, pp. 290–300, 2018

25 Notter, D.A.; Gauch, M.; Widmer, R.; Wäger, P.; Stamp, A.; Zah, R.; Althaus, H.-J.: *Contribution of Li-ion batteries to the environmental impact of electric vehicles*, in: *Environmental science & technology 44 (17)*, pp. 6550–6556, 2010

26 Feng, X.; Ouyang, M.; Liu, X.; Lu, L.; Xia, Y.; He, X.: *Thermal runaway mechanism of lithium ion battery for electric vehicles: A review*, in: *Energy Storage Materials 10*, pp. 246–267, 2018

27 International Organization for Standardization *(ISO 6469-3)*: *Electrically propelled road vehicles - Safety specifications - Part 3: Electrical safety*, 2018-10

28 Brandt, K.; Garche, J.: *General Battery Safety Considerations*, in: Garche, J.; Brandt, K. (eds.): *Electrochemical Power Sources: Fundamentals, Systems, and Applications*, Elsevier, Amsterdam, Netherlands, 2019

29 Lyness, C.: *Lithium-Secondary Cell: Sources of Risks and Their Effects - Sources of Risk*, in: Garche, J.; Brandt, K. (eds.): *Electrochemical Power Sources: Fundamentals, Systems, and Applications*, Elsevier, Amsterdam, Netherlands, 2019

30 International Organization for Standardization *(ISO 7010)*: *Graphical symbols - Safety colours and safety signs - Registered safety signs*, 2011-06

31 Liaw, B.Y.; Wang, F.Q.; Wei, Y.M.: *Managing Safety Risk by Manufacturers - Managing Safety Risk by Cell Manufacturers*, in: Garche, J.; Brandt, K. (eds.): *Electrochemical Power Sources: Fundamentals, Systems, and Applications*, Elsevier, Amsterdam, Netherlands, 2019

32 Brandt, K.; Schultheiß, J.; Schweizer-Berberich, M.: *Managing Safety Risk by Manufacturers - Managing of Risk by Battery Manufacturers*, in: Garche, J.; Brandt, K. (eds.): *Electrochemical Power Sources: Fundamentals, Systems, and Applications*, Elsevier, Amsterdam, Netherlands, 2019

33 Barnett, B.; Ofer, D.; Sriramulu, S.; Stringfellow, R.: *Lithium-Ion Batteries, Safety*, in: Meyers, R.A. (ed.): *Encyclopedia of Sustainability Science and Technology*, Springer, New York, NY, USA, 2012

34 Spotnitz, R.; Franklin, J.: *Abuse behavior of high-power, lithium-ion cells*, in: *Journal of Power Sources 113 (1)*, pp. 81–100, 2003

35 Barnett, B.; McCoy, C.H.; Ofer, D.; Sriramulu, S.: *Lithium-Secondary Cell: Sources of Risks and Their Effects - Risks due to Grown-In Internal Shorts*, in: Garche, J.; Brandt, K. (eds.): *Electrochemical Power Sources: Fundamentals, Systems, and Applications*, Elsevier, Amsterdam, Netherlands, 2019

36 Larsson, F.; Andersson, P.; Blomqvist, P.; Mellander, B.-E.: *Toxic fluoride gas emissions from lithium-ion battery fires*, in: *Scientific reports 7 (1)*, p. 10018, 2017

37 Abert, M.: *Lithium-Secondary Cell: Sources of Risks and Their Effects - Analysis of Gases Emitted in Safety Events*, in: Garche, J.; Brandt, K. (eds.): *Electrochemical Power Sources: Fundamentals, Systems, and Applications*, Elsevier, Amsterdam, Netherlands, 2019

38 Doughty, D.H.; Roth, E.P.: *A General Discussion of Li Ion Battery Safety*, in: *Interface magazine 21 (2)*, pp. 37–44, 2012

39 Xu, K.: *Nonaqueous Liquid Electrolytes for Lithium-Based Rechargeable Batteries*, in: *Chemical Reviews 104 (10)*, pp. 4303–4418, 2004

40 Dahn, J.; Ehrlich, G.M.: *LITHIUM-ION BATTERIES*, in: Reddy, T.B.; Linden, D. (eds.): *Linden's handbook of batteries*, McGraw-Hill, New York, NY, USA, 2011

41 Arora, P.; Zhang, Z.: *Battery Separators*, in: *Chemical Reviews 104 (10)*, pp. 4419–4462, 2004

42 Zhang, S.S.: *A review on the separators of liquid electrolyte Li-ion batteries*, in: *Journal of Power Sources 164 (1)*, pp. 351–364, 2007

43 Orendorff, C.J.: *The Role of Separators in Lithium-Ion Cell Safety*, in: *Interface magazine 21 (2)*, pp. 61–65, 2012

44 Lee, H.; Yanilmaz, M.; Toprakci, O.; Fu, K.; Zhang, X.: *A review of recent developments in membrane separators for rechargeable lithium-ion batteries*, in: *Energy & Environmental Science 7 (12)*, pp. 3857–3886, 2014

45 Choi, J.-A.; Kim, S.H.; Kim, D.-W.: *Enhancement of thermal stability and cycling performance in lithium-ion cells through the use of ceramic-coated separators*, in: *Journal of Power Sources 195 (18)*, pp. 6192–6196, 2010

46 Fleischhammer, M.: *Lithium-Secondary Cell: Sources of Risks and Their Effects - Risk Potentials by Materials*, in: Garche, J.; Brandt, K. (eds.): *Electrochemical Power Sources: Fundamentals, Systems, and Applications*, Elsevier, Amsterdam, Netherlands, 2019

47 Winter, M.: *The Solid Electrolyte Interphase – The Most Important and the Least Understood Solid Electrolyte in Rechargeable Li Batteries*, in: *Zeitschrift für Physikalische Chemie 223 (10-11)*, pp. 1395–1406, 2009

48 Lisbona, D.; Snee, T.: *A review of hazards associated with primary lithium and lithium-ion batteries*, in: *Process Safety and Environmental Protection 89 (6)*, pp. 434–442, 2011

49 Wang, Q.; Ping, P.; Zhao, X.; Chu, G.; Sun, J.; Chen, C.: *Thermal runaway caused fire and explosion of lithium ion battery*, in: *Journal of Power Sources 208*, pp. 210–224, 2012

50 Wen, J.; Yu, Y.; Chen, C.: *A Review on Lithium-Ion Batteries Safety Issues: Existing Problems and Possible Solutions*, in: *Materials Express 2 (3)*, pp. 197–212, 2012

51 Hong, J.-S.; Maleki, H.; Al Hallaj, S.; Redey, L.; Selman, J.R.: *Electrochemical-Calorimetric Studies of Lithium-Ion Cells*, in: *Journal of The Electrochemical Society 145 (5)*, pp. 1489–1501, 1998

52 Maleki, H.; Al Hallaj, S.; Selman, J.R.; Dinwiddie, R.B.; Wang, H.: *Thermal Properties of Lithium-Ion Battery and Components*, in: *Journal of The Electrochemical Society 146 (3)*, pp. 947–954, 1999

53 Ruiz, V.; Pfrang, A.: *JRC exploratory research: Safer Li-ion batteries by preventing thermal propagation - Workshop report: summary & outcomes (JRC Petten, Netherlands, 8-9 March 2018)*, ed. by Publications Office of the European Union, 2018, URL: `http://publications.jrc.ec.europa.eu/repository/bitstream/JRC113320/kjna29384enn.pdf`, log-date: 06/10/2019

54 Hoffmann, D.: *Safety Tests for Li-Secondary Batteries - Battery Safety Testing*, in: Garche, J.; Brandt, K. (eds.): *Electrochemical Power Sources: Fundamentals, Systems, and Applications*, Elsevier, Amsterdam, Netherlands, 2019

55 Doughty, D.H.; Crafts, C.C.: *FreedomCAR - Electrical Energy Storage System Abuse Test Manual for Electric and Hybrid Electric Vehicle Applications*, ed. by Sandia National Laboratories, 2006

56 Darcy, E.: *Screening Li-ion batteries for internal shorts*, in: *Journal of Power Sources 174 (2)*, pp. 575–578, 2007

57 National Transportation Safety Board: *Aircraft Incident Report: Auxiliary Power Unit Battery Fire - Japan Airlines Boeing 787-8, JA829J*, Nov. 21, 2014, URL: `https://www.ntsb.gov/investigations/AccidentReports/Reports/AIR1401.pdf`, log-date: 06/10/2019

58 Chiang, H.; Grzic, D.; Wu, A.: *Multi-Level Forensic and Functional Analysis of 787 Main/APU Lithium Ion Battery - Corporate Research*, ed. by Underwriters Laboratories Inc., May 28, 2014, URL: `https://www.ntsb.gov/investigations/AccidentReports/Documents/UL_Forensic_Report.pdf`, log-date: 06/10/2019

59 Samsung: *Samsung Announces Cause of Galaxy Note7 Incidents in Press Conference*, Jan. 23, 2017, URL: https://news.samsung.com/us/Samsung-Electronics-Announces-Cause-of-Galaxy-Note7-Incidents-in-Press-Conference, log-date: 06/10/2019

60 Schweidler, S.; Biasi, L. de; Schiele, A.; Hartmann, P.; Brezesinski, T.; Janek, J.: *Volume Changes of Graphite Anodes Revisited: A Combined Operando X-ray Diffraction and In Situ Pressure Analysis Study*, in: *The Journal of Physical Chemistry C 122 (16)*, pp. 8829–8835, 2018

61 Brissot, C.; Rosso, M.; Chazalviel, J.-N.; Lascaud, S.: *Dendritic growth mechanisms in lithium/polymer cells*, in: *Journal of Power Sources 81-82*, pp. 925–929, 1999

62 Rosso, M.; Brissot, C.; Teyssot, A.; Dollé, M.; Sannier, L.; Tarascon, J.-M.; Bouchet, R.; Lascaud, S.: *Dendrite short-circuit and fuse effect on Li/polymer/Li cells*, in: *Electrochimica Acta 51 (25)*, pp. 5334–5340, 2006

63 Bhattacharyya, R.; Key, B.; Chen, H.; Best, A.S.; Hollenkamp, A.F.; Grey, C.P.: *In situ NMR observation of the formation of metallic lithium microstructures in lithium batteries*, in: *Nature materials 9 (6)*, pp. 504–510, 2010

64 Zinth, V.; von Lüders, C.; Hofmann, M.; Hattendorff, J.; Buchberger, I.; Erhard, S.; Rebelo-Kornmeier, J.; Jossen, A.; Gilles, R.: *Lithium plating in lithium-ion batteries at sub-ambient temperatures investigated by in situ neutron diffraction*, in: *Journal of Power Sources 271*, pp. 152–159, 2014

65 Love, C.T.; Baturina, O.A.; Swider-Lyons, K.E.: *Observation of Lithium Dendrites at Ambient Temperature and Below*, in: *ECS Electrochemistry Letters 4 (2)*, A24–A27, 2015

66 Waldmann, T.; Hogg, B.-I.; Wohlfahrt-Mehrens, M.: *Li plating as unwanted side reaction in commercial Li-ion cells – A review*, in: *Journal of Power Sources 384*, pp. 107–124, 2018

67 Crompton, K.R.; Landi, B.J.: *Opportunities for near zero volt storage of lithium ion batteries*, in: *Energy & Environmental Science 9 (7)*, pp. 2219–2239, 2016

68 Guo, R.; Lu, L.; Ouyang, M.; Feng, X.: *Mechanism of the entire overdischarge process and overdischarge-induced internal short circuit in lithium-ion batteries*, in: *Scientific reports 6*, p. 30248, 2016

69 Birkl, C.R.; Roberts, M.R.; McTurk, E.; Bruce, P.G.; Howey, D.A.: *Degradation diagnostics for lithium ion cells*, in: *Journal of Power Sources 341*, pp. 373–386, 2017

70 Fear, C.; Juarez-Robles, D.; Jeevarajan, J.A.; Mukherjee, P.P.: *Elucidating Copper Dissolution Phenomenon in Li-Ion Cells under Overdischarge Extremes*, in: *Journal of The Electrochemical Society 165 (9)*, A1639–A1647, 2018

71 Feng, X.; Weng, C.; Ouyang, M.; Sun, J.: *Online internal short circuit detection for a large format lithium ion battery*, in: *Applied Energy 161*, pp. 168–180, 2016

72 Feng, X.; He, X.; Lu, L.; Ouyang, M.: *Analysis on the Fault Features for Internal Short Circuit Detection Using an Electrochemical-Thermal Coupled Model*, in: *Journal of The Electrochemical Society 165 (2)*, A155–A167, 2018

73 Feng, X.; Pan, Y.; He, X.; Wang, L.; Ouyang, M.: *Detecting the internal short circuit in large-format lithium-ion battery using model-based fault-diagnosis algorithm*, in: *Journal of Energy Storage 18*, pp. 26–39, 2018

74 Sazhin, S.V.; Dufek, E.J.; Gering, K.L.: *Enhancing Li-Ion Battery Safety by Early Detection of Nascent Internal Shorts*, in: *Journal of The Electrochemical Society 164 (1)*, A6281–A6287, 2017

75 International Electrotechnical Commission *(IEC 61508)*: *Functional safety of electrical/electronic/programmable electronic safety-related systems*, 2010-04-30

76 International Electrotechnical Commission *(IEC 61511)*: *Functional safety - Safety instrumented systems for the process industry sector*, 2018-01-23

77 International Organization for Standardization *(ISO 26262)*: *Road vehicles - Functional safety*, 2018

78 Jossen, A.; Weydanz, W.: *Moderne Akkumulatoren richtig einsetzen*, 2nd edition, Cuvillier Verlag, Göttingen, Germany, 2019

79 Kim, H.; Oh, S.-M.; Scrosati, B.; Sun, Y.-K.: *High-performance electrode materials for lithium-ion batteries for electric vehicles*, in: Scrosati, B.; Garche, J.; Tillmetz, W. (eds.): *Advances in Battery Technologies for Electric Vehicles*, Woodhead Publishing, Sawston, Cambridge, UK, 2015

80 Ohzuku, T.; Ueda, A.; Nagayama, M.; Iwakoshi, Y.; Komori, H.: *Comparative study of $LiCoO_2$, $LiNi_{1/2}Co_{1/2}O_2$ and $LiNiO_2$ for 4 volt secondary lithium cells*, in: *Electrochimica Acta 38 (9)*, pp. 1159–1167, 1993

81 Kanno, R.; Kubo, H.; Kawamoto, Y.; Kamiyama, T.; Izumi, F.; Takeda, Y.; Takano, M.: *Phase Relationship and Lithium Deintercalation in Lithium Nickel Oxides*, in: *Journal of Solid State Chemistry 110 (2)*, pp. 216–225, 1994

82 Yoon, C.S.; Jun, D.-W.; Myung, S.-T.; Sun, Y.-K.: *Structural Stability of $LiNiO_2$ Cycled above 4.2 V*, in: *ACS Energy Letters 2 (5)*, pp. 1150–1155, 2017

83 Yoon, C.S.; Kim, U.-H.; Park, G.-T.; Kim, S.J.; Kim, K.-H.; Kim, J.; Sun, Y.-K.: *Self-Passivation of a $LiNiO_2$ Cathode for a Lithium-Ion Battery through Zr Doping*, in: *ACS Energy Letters 3 (7)*, pp. 1634–1639, 2018

84 MacNeil, D.D.; Lu, Z.; Chen, Z.; Dahn, J.R.: *A comparison of the electrode/electrolyte reaction at elevated temperatures for various Li-ion battery cathodes*, in: *Journal of Power Sources 108 (1-2)*, pp. 8–14, 2002

85 Cho, J.; Kim, T.-J.; Kim, Y.J.; Park, B.: *High-Performance ZrO_2-Coated $LiNiO_2$ Cathode Material*, in: *Journal of The Electrochemical Society 4 (10)*, A159–A161, 2001

86 Martha, S.K.; Haik, O.; Zinigrad, E.; Exnar, I.; Drezen, T.; Miners, J.H.; Aurbach, D.: *On the Thermal Stability of Olivine Cathode Materials for Lithium-Ion Batteries*, in: *Journal of The Electrochemical Society 158 (10)*, A1115–A1122, 2011

87 Rossen, E.; Jones, C.; Dahn, J.: *Structure and electrochemistry of $Li_xMn_yNi_{1-y}O_2$*, in: *Solid State Ionics 57 (3-4)*, pp. 311–318, 1992

88 Liu, Z.; Yu, A.; Lee, J.Y.: *Synthesis and characterization of $LiNi_{1-x-y}Co_xMn_yO_2$ as the cathode materials of secondary lithium batteries*, in: *Journal of Power Sources 81-82*, pp. 416–419, 1999

89 Yoshio, M.; Noguchi, H.; Itoh, J.-I.; Okada, M.; Mouri, T.: *Preparation and properties of $LiCo_yMn_xNi_{1-x-y}O_2$ as a cathode for lithium ion batteries*, in: *Journal of Power Sources 90 (2)*, pp. 176–181, 2000

90 MacNeil, D.D.; Lu, Z.; Dahn, J.R.: *Structure and Electrochemistry of $Li[Ni_xCo_{1-2x}Mn_x]O_2$ ($0 \leq x \leq 1/2$)*, in: *Journal of The Electrochemical Society 149 (10)*, A1332–A1336, 2002

91 Ohzuku, T.; Makimura, Y.: *Layered Lithium Insertion Material of $LiCo_{1/3}Ni_{1/3}Mn_{1/3}O_2$ for Lithium-Ion Batteries*, in: *Chemistry Letters 30 (7)*, pp. 642–643, 2001

92 Yabuuchi, N.; Ohzuku, T.: *Novel lithium insertion material of $LiCo_{1/3}Ni_{1/3}Mn_{1/3}O_2$ for advanced lithium-ion batteries*, in: *Journal of Power Sources 119-121*, pp. 171–174, 2003

93 Noh, H.-J.; Youn, S.; Yoon, C.S.; Sun, Y.-K.: *Comparison of the structural and electrochemical properties of layered $Li[Ni_xCo_yMn_z]O_2$ (x = 1/3, 0.5, 0.6, 0.7, 0.8 and 0.85) cathode material for lithium-ion batteries*, in: *Journal of Power Sources 233*, pp. 121–130, 2013

94 Bak, S.-M. et al.: *Structural changes and thermal stability of charged $LiNi_xMn_yCo_zO_2$ cathode materials studied by combined in situ time-resolved XRD and mass spectroscopy*, in: *ACS applied materials & interfaces 6 (24)*, pp. 22594–22601, 2014

95 Ma, L.; Nie, M.; Xia, J.; Dahn, J.R.: *A systematic study on the reactivity of different grades of charged $Li[Ni_xMn_yCo_z]O_2$ with electrolyte at elevated temperatures using accelerating rate calorimetry*, in: *Journal of Power Sources 327*, pp. 145–150, 2016

96 Myung, S.-T.; Maglia, F.; Park, K.-J.; Yoon, C.S.; Lamp, P.; Kim, S.-J.; Sun, Y.-K.: *Nickel-Rich Layered Cathode Materials for Automotive Lithium-Ion Batteries: Achievements and Perspectives*, in: *ACS Energy Letters 2 (1)*, pp. 196–223, 2017

97 Kim, J.; Lee, H.; Cha, H.; Yoon, M.; Park, M.; Cho, J.: *Prospect and Reality of Ni-Rich Cathode for Commercialization*, in: *Advanced Energy Materials 8 (6)*, p. 1702028, 2018

98 Berdichevsky, G.; Kelty, K.; Straubel, J.B.; Toomre, E.: *The Tesla Roadster Battery System - Tesla Motors*, ed. by Tesla Motors, Dec. 19, 2007, URL: `http://large.stanford.edu/publications/coal/references/docs/tesla.pdf`, log-date: 06/10/2019

99 BMW Group: *With new high-voltage batteries for an even further extended range and retaining characteristic BMW sporty flair: the BMW i3 (120 Ah) and the BMW i3s (120 Ah).* Sept. 28, 2018, URL: `https://www.press.bmwgroup.com/global/article/detail/T0284828EN/with-new-high-voltage-batteries-for-an-even-further-extended-range-and-retaining-characteristic-bmw-sporty-flair:-the-bmw-i3-120-ah-and-the-bmw-i3s-120-ah?language=en`, log-date: 06/10/2019

100 Quinn, J.B.; Waldmann, T.; Richter, K.; Kasper, M.; Wohlfahrt-Mehrens, M.: *Energy Density of Cylindrical Li-Ion Cells: A Comparison of Commercial 18650 to the 21700 Cells*, in: *Journal of The Electrochemical Society 165 (14)*, A3284–A3291, 2018

101 Ciez, R.E.; Whitacre, J.F.: *Comparison between cylindrical and prismatic lithium-ion cell costs using a process based cost model*, in: *Journal of Power Sources 340*, pp. 273–281, 2017

102 DIN Deutsches Institut für Normung *(DIN 91252)*: *Electrically propelled road vehicles - Battery systems - Design specifications for Lithium-Ion battery cells*, 2016-11

103 Kim, U.S.; Shin, C.B.; Kim, C.-S.: *Effect of electrode configuration on the thermal behavior of a lithium-polymer battery*, in: *Journal of Power Sources 180 (2)*, pp. 909–916, 2008

104 Waldmann, T.; Bisle, G.; Hogg, B.-I.; Stumpp, S.; Danzer, M.A.; Kasper, M.; Axmann, P.; Wohlfahrt-Mehrens, M.: *Influence of Cell Design on Temperatures and Temperature Gradients in Lithium-Ion Cells: An In Operando Study*, in: *Journal of The Electrochemical Society 162 (6)*, A921–A927, 2015

105 Li, Z.; Zhang, J.; Wu, B.; Huang, J.; Nie, Z.; Sun, Y.; An, F.; Wu, N.: *Examining temporal and spatial variations of internal temperature in large-format laminated battery with embedded thermocouples*, in: *Journal of Power Sources 241*, pp. 536–553, 2013

106 Martiny, N.; Rheinfeld, A.; Geder, J.; Wang, Y.; Kraus, W.; Jossen, A.: *Development of an All Kapton-Based Thin-Film Thermocouple Matrix for In Situ Temperature Measurement in a Lithium Ion Pouch Cell*, in: *IEEE Sensors Journal 14 (10)*, pp. 3377–3384, 2014

107 Mutyala, M.S.K.; Zhao, J.; Li, J.; Pan, H.; Yuan, C.; Li, X.: *In-situ temperature measurement in lithium ion battery by transferable flexible thin film thermocouples*, in: *Journal of Power Sources 260*, pp. 43–49, 2014

108 Zhang, G.; Cao, L.; Ge, S.; Wang, C.-Y.; Shaffer, C.E.; Rahn, C.D.: *In Situ Measurement of Radial Temperature Distributions in Cylindrical Li-Ion Cells*, in: *Journal of The Electrochemical Society 161 (10)*, A1499–A1507, 2014

109 Waldmann, T.; Wohlfahrt-Mehrens, M.: *In-Operando Measurement of Temperature Gradients in Cylindrical Lithium-Ion Cells during High-Current Discharge*, in: *ECS Electrochemistry Letters 4 (1)*, A1–A3, 2015

110 Amietszajew, T.; McTurk, E.; Fleming, J.; Bhagat, R.: *Understanding the limits of rapid charging using instrumented commercial 18650 high-energy Li-ion cells*, in: *Electrochimica Acta 263*, pp. 346–352, 2018

111 Zhao, W.; Luo, G.; Wang, C.-Y.: *Effect of tab design on large-format Li-ion cell performance*, in: *Journal of Power Sources 257*, pp. 70–79, 2014

112 Waldmann, T.; Geramifard, G.; Wohlfahrt-Mehrens, M.: *Influence of current collecting tab design on thermal and electrochemical performance of cylindrical Lithium-ion cells during high current discharge*, in: *Journal of Energy Storage 5*, pp. 163–168, 2016

113 Zhang, G.; Shaffer, C.E.; Wang, C.-Y.; Rahn, C.D.: *In-Situ Measurement of Current Distribution in a Li-Ion Cell*, in: *Journal of The Electrochemical Society 160 (4)*, A610–A615, 2013

114 Osswald, P.J.; Erhard, S.V.; Wilhelm, J.; Hoster, H.E.; Jossen, A.: *Simulation and Measurement of Local Potentials of Modified Commercial Cylindrical Cells*, in: *Journal of The Electrochemical Society 162 (10)*, A2099–A2105, 2015

115 Erhard, S.V.; Osswald, P.J.; Wilhelm, J.; Rheinfeld, A.; Kosch, S.; Jossen, A.: *Simulation and Measurement of Local Potentials of Modified Commercial Cylindrical Cells*, in: *Journal of The Electrochemical Society 162 (14)*, A2707–A2719, 2015

116 Osswald, P.J.; Erhard, S.V.; Noel, A.; Keil, P.; Kindermann, F.M.; Hoster, H.; Jossen, A.: *Current density distribution in cylindrical Li-Ion cells during impedance measurements*, in: *Journal of Power Sources 314*, pp. 93–101, 2016

117 Osswald, P.J.; Erhard, S.V.; Rheinfeld, A.; Rieger, B.; Hoster, H.E.; Jossen, A.: *Temperature dependency of state of charge inhomogeneities and their equalization in cylindrical lithium-ion cells*, in: *Journal of Power Sources 329*, pp. 546–552, 2016

118 Erhard, S.V. et al.: *Simulation and Measurement of the Current Density Distribution in Lithium-Ion Batteries by a Multi-Tab Cell Approach*, in: *Journal of The Electrochemical Society 164 (1)*, A6324–A6333, 2017

119 Rieger, B.; Schuster, S.F.; Erhard, S.V.; Osswald, P.J.; Rheinfeld, A.; Willmann, C.; Jossen, A.: *Multi-directional laser scanning as innovative method to detect local cell damage during fast charging of lithium-ion cells*, in: *Journal of Energy Storage 8*, pp. 1–5, 2016

120 McCleary, D.A.H.; Meyers, J.P.; Kim, B.: *Three-Dimensional Modeling of Electrochemical Performance and Heat Generation of Spirally and Prismatically Wound Lithium-Ion Batteries*, in: *Journal of The Electrochemical Society 160 (11)*, A1931–A1943, 2013

121 Kim, G.-H.; Smith, K.; Lee, K.-J.; Santhanagopalan, S.; Pesaran, A.: *Multi-Domain Modeling of Lithium-Ion Batteries Encompassing Multi-Physics in Varied Length Scales*, in: *Journal of The Electrochemical Society 158 (8)*, A955–A969, 2011

122 Lee, K.-J.; Smith, K.; Pesaran, A.; Kim, G.-H.: *Three dimensional thermal-, electrical-, and electrochemical-coupled model for cylindrical wound large format lithium-ion batteries*, in: *Journal of Power Sources 241*, pp. 20–32, 2013

123 Samba, A.; Omar, N.; Gualous, H.; Capron, O.; van den Bossche, P.; van Mierlo, J.: *Impact of Tab Location on Large Format Lithium-Ion Pouch Cell Based on Fully Coupled Tree-Dimensional Electrochemical-Thermal Modeling*, in: *Electrochimica Acta 147*, pp. 319–329, 2014

124 Rieger, B.; Erhard, S.V.; Kosch, S.; Venator, M.; Rheinfeld, A.; Jossen, A.: *Multi-Dimensional Modeling of the Influence of Cell Design on Temperature, Displacement and Stress Inhomogeneity in Large-Format Lithium-Ion Cells*, in: *Journal of The Electrochemical Society 163 (14)*, A3099–A3110, 2016

125 Kosch, S.; Rheinfeld, A.; Erhard, S.V.; Jossen, A.: *An extended polarization model to study the influence of current collector geometry of large-format lithium-ion pouch cells*, in: *Journal of Power Sources 342*, pp. 666–676, 2017

126 Sturm, J.; Rheinfeld, A.; Zilberman, I.; Spingler, F.B.; Kosch, S.; Frie, F.; Jossen, A.: *Modeling and simulation of inhomogeneities in a 18650 nickel-rich, silicon-graphite lithium-ion cell during fast charging*, in: *Journal of Power Sources 412*, pp. 204–223, 2019

127 Hettesheimer, T. et al.: *Entwicklungsperspektiven für Zellformate von Lithium-Ionen-Batterien in der Elektromobilität*, ed. by Fraunhofer-Allianz Batterien, 2017, URL: `https://www.batterien.fraunhofer.de/content/dam/batterien/de/documents/Allianz_Batterie_Zellformate_Studie.pdf`, log-date: 06/10/2019

128 Venugopal, G.: *Characterization of thermal cut-off mechanisms in prismatic lithium-ion batteries*, in: *Journal of Power Sources 101 (2)*, pp. 231–237, 2001

129 Balakrishnan, P.G.; Ramesh, R.; Prem Kumar, T.: *Safety mechanisms in lithium-ion batteries*, in: *Journal of Power Sources 155 (2)*, pp. 401–414, 2006

130 Uchida, I.; Ishikawa, H.; Mohamedi, M.; Umeda, M.: *AC-impedance measurements during thermal runaway process in several lithium/polymer batteries*, in: *Journal of Power Sources 119-121*, pp. 821–825, 2003

131 Roth, E.P.; Doughty, D.H.; Pile, D.L.: *Effects of separator breakdown on abuse response of 18650 Li-ion cells*, in: *Journal of Power Sources 174 (2)*, pp. 579–583, 2007

132 Roth, E.P.; Orendorff, C.J.: *How Electrolytes Influence Battery Safety*, in: *Interface magazine 21 (2)*, pp. 45–49, 2012

133 Nagasubramanian, G.; Fenton, K.: *Reducing Li-ion safety hazards through use of non-flammable solvents and recent work at Sandia National Laboratories*, in: *Electrochimica Acta 101*, pp. 3–10, 2013

134 Kalhoff, J.; Eshetu, G.G.; Bresser, D.; Passerini, S.: *Safer Electrolytes for Lithium-Ion Batteries: State of the Art and Perspectives*, in: *ChemSusChem 8 (13)*, pp. 2154–2175, 2015

135 Mandal, B.K.; Padhi, A.K.; Shi, Z.; Chakraborty, S.; Filler, R.: *Thermal runaway inhibitors for lithium battery electrolytes*, in: *Journal of Power Sources 161 (2)*, pp. 1341–1345, 2006

136 Zhang, S.S.: *A review on electrolyte additives for lithium-ion batteries*, in: *Journal of The Electrochemical Society 162 (2)*, pp. 1379–1394, 2006

137 Park, G.; Nakamura, H.; Lee, Y.; Yoshio, M.: *The important role of additives for improved lithium ion battery safety*, in: *Journal of Power Sources 189 (1)*, pp. 602–606, 2009

138 Haregewoin, A.M.; Wotango, A.S.; Hwang, B.-J.: *Electrolyte additives for lithium ion battery electrodes: progress and perspectives*, in: *Energy & Environmental Science 9 (6)*, pp. 1955–1988, 2016

139 Richardson, T.J.: *SECONDARY BATTERIES – LITHIUM RECHARGEABLE SYSTEMS – LITHIUM-ION | Overcharge Protection Shuttles*, in: Garche, J.; Dyer, C.K.; Moseley, P.T.; Ogumi, Z.; Rand, D.A.J.; Scrosati, B. (eds.): *Encyclopedia of Electrochemical Power Sources*, Elsevier Science, 2009

140 Samsung SDI Energy Storage System: *Smart Battery Systems for Energy Storage - Lithium-ion*, 2016, URL: `http://www.samsungsdi.com/upload/ess_brochure/Samsung%20SDI%20brochure_EN.pdf`, log-date: 06/10/2019

141 Ruiz, V.; Pfrang, A.; Kriston, A.; Omar, N.; van den Bossche, P.; Boon-Brett, L.: *A review of international abuse testing standards and regulations for lithium ion batteries in electric and hybrid electric vehicles*, in: *Renewable and Sustainable Energy Reviews 81*, pp. 1427–1452, 2018

142 Oxford English Dictionary Online: *"runaway reaction"*, Oxford University Press, 2019, URL: `https://en.oxforddictionaries.com/definition/runaway_reaction`

143 Kosanke, K.L.; Kosanke, B.J.; Sturman, B.T.; Winokur, R.M.: *Encyclopedic Dictionary of Pyrotechnics - and Related Subjects*, 1st edition, Journal of Pyrotechnics, Inc., Whitewater, CO, USA, 2012

144 Semenov, N.N.: *Some Problems in Chemical Kinetics and Reactivity, Volume 2*, Princeton University Press, Princeton, NJ, USA, 2017

145 Tobishima, S.-i.; Yamaki, J.-i.: *A consideration of lithium cell safety*, in: *Journal of Power Sources 81-82*, pp. 882–886, 1999

146 Guo, Y.: *SAFETY | Thermal Runaway*, in: Garche, J.; Dyer, C.K.; Moseley, P.T.; Ogumi, Z.; Rand, D.A.J.; Scrosati, B. (eds.): *Encyclopedia of Electrochemical Power Sources*, Elsevier Science, 2009

147 Biensan, P.; Simon, B.; Pérès, J.; Guibert, A. de; Broussely, M.; Bodet, J.; Perton, F.: *On safety of lithium-ion cells*, in: *Journal of Power Sources 81-82*, pp. 906–912, 1999

148 Bandhauer, T.M.; Garimella, S.; Fuller, T.F.: *A Critical Review of Thermal Issues in Lithium-Ion Batteries*, in: *Journal of The Electrochemical Society 158 (3)*, R1–R25, 2011

149 Hatchard, T.D.; MacNeil, D.D.; Stevens, D.A.; Christensen, L.; Dahn, J.R.: *Importance of Heat Transfer by Radiation in Li-Ion Batteries during Thermal Abuse*, in: *Electrochemical and Solid-State Letters 3 (7)*, pp. 305–308, 1999

150 Doughty, D.H.; Pesaran, A.A.: *Vehicle Battery Safety Roadmap Guidance*, ed. by National Renewable Energy Laboratory, 2012

151 Schuster, E.; Ziebert, C.; Melcher, A.; Rohde, M.; Seifert, H.J.: *Thermal behavior and electrochemical heat generation in a commercial 40 Ah lithium ion pouch cell*, in: *Journal of Power Sources 286*, pp. 580–589, 2015

152 Townsend, D.I.; Tou, J.C.: *Thermal hazard evaluation by an accelerating rate calorimeter*, in: *Thermochimica Acta 37 (1)*, pp. 1–30, 1980

153 von Sacken, U.; Nodwell, E.; Sundher, A.; Dahn, J.R.: *Comparative thermal stability of carbon intercalation anodes and lithium metal anodes for rechargeable lithium batteries*, in: *Journal of Power Sources 54 (2)*, pp. 240–245, 1995

154 Zhang, Z.; Fouchard, D.; Rea, J.R.: *Differential scanning calorimetry material studies: implications for the safety of lithium-ion cells*, in: *Journal of Power Sources 70 (1)*, pp. 16–20, 1998

155 Maleki, H.; Deng, G.; Anani, A.; Howard, J.: *Thermal Stability Studies of Li-Ion Cells and Components*, in: *Journal of The Electrochemical Society 146 (9)*, pp. 3224–3229, 1999

156 Ribière, P.; Grugeon, S.; Morcrette, M.; Boyanov, S.; Laruelle, S.; Marlair, G.: *Investigation on the fire-induced hazards of Li-ion battery cells by fire calorimetry*, in: *Energy & Environmental Science 5 (1)*, pp. 5271–5280, 2012

157 Fu, Y.; Lu, S.; Li, K.; Liu, C.; Cheng, X.; Zhang, H.: *An experimental study on burning behaviors of 18650 lithium ion batteries using a cone calorimeter*, in: *Journal of Power Sources 273*, pp. 216–222, 2015

158 Kissinger, H.E.: *Reaction Kinetics in Differential Thermal Analysis*, in: *Analytical Chemistry 29 (11)*, pp. 1702–1706, 1957

159 Ozawa, T.: *A New Method of Analyzing Thermogravimetric Data*, in: *Bulletin of the Chemical Society of Japan 38 (11)*, pp. 1881–1886, 1965

160 Peng, P.; Jiang, F.: *Thermal safety of lithium-ion batteries with various cathode materials: A numerical study*, in: *International Journal of Heat and Mass Transfer 103*, pp. 1008–1016, 2016

161 MacNeil, D.D.; Larcher, D.; Dahn, J.R.: *Comparison of the Reactivity of Various Carbon Electrode Materials with Electrolyte at Elevated Temperature*, in: *Journal of The Electrochemical Society 146 (10)*, pp. 3596–3602, 1999

162 Wang, Q.; Sun, J.; Yao, X.; Chen, C.: *Thermal Behavior of Lithiated Graphite with Electrolyte in Lithium-Ion Batteries*, in: *Journal of The Electrochemical Society 153 (2)*, A329–A333, 2006

163 Wang, Q.; Sun, J.; Yao, X.; Chen, C.: *Thermal stability of $LiPF_6$/EC+DEC electrolyte with charged electrodes for lithium ion batteries*, in: *Thermochimica Acta 437 (1-2)*, pp. 12–16, 2005

164 Richard, M.N.; Dahn, J.R.: *Accelerating Rate Calorimetry Study on the Thermal Stability of Lithium Intercalated Graphite in Electrolyte. I. Experimental*, in: *Journal of The Electrochemical Society 146 (6)*, pp. 2068–2077, 1999

165 Peled, E.; Menkin, S.: *Review–SEI: Past, Present and Future*, in: *Journal of The Electrochemical Society 164 (7)*, A1703–A1719, 2017

166 Yang, H.; Bang, H.; Amine, K.; Prakash, J.: *Investigations of the Exothermic Reactions of Natural Graphite Anode for Li-Ion Batteries during Thermal Runaway*, in: *Journal of The Electrochemical Society 152 (1)*, A73–A79, 2005

167 Roth, E.; Doughty, D.: *Thermal abuse performance of high-power 18650 Li-ion cells*, in: *Journal of Power Sources 128 (2)*, pp. 308–318, 2004

168 Ryou, M.-H.; Lee, J.-N.; Lee, D.J.; Kim, W.-K.; Jeong, Y.K.; Choi, J.W.; Park, J.-K.; Lee, Y.M.: *Effects of lithium salts on thermal stabilities of lithium alkyl carbonates in SEI layer*, in: *Electrochimica Acta 83*, pp. 259–263, 2012

169 Richard, M.N.; Dahn, J.R.: *Accelerating Rate Calorimetry Study on the Thermal Stability of Lithium Intercalated Graphite in Electrolyte. II. Modeling the Results and Predicting Differential Scanning Calorimeter Curves*, in: *Journal of The Electrochemical Society 146 (6)*, pp. 2078–2084, 1999

170 Wang, Y.; Nakamura, S.; Ue, M.; Balbuena, P.B.: *Theoretical Studies To Understand Surface Chemistry on Carbon Anodes for Lithium-Ion Batteries: Reduction Mechanisms of Ethylene Carbonate*, in: *Journal of the American Chemical Society 123 (47)*, pp. 11708–11718, 2001

171 Chen, Z.; Qin, Y.; Ren, Y.; Lu, W.; Orendorff, C.; Roth, E.P.; Amine, K.: *Multi-scale study of thermal stability of lithiated graphite*, in: *Energy & Environmental Science 4 (10)*, p. 4023, 2011

172 Roth, E.; Doughty, D.; Franklin, J.: *DSC investigation of exothermic reactions occurring at elevated temperatures in lithium-ion anodes containing PVDF-based binders*, in: *Journal of Power Sources 134 (2)*, pp. 222–234, 2004

173 Du Pasquier, A.; Disma, F.; Bowmer, T.; Gozdz, A.S.; Amatucci, G.; Tarascon, J.-M.: *Differential Scanning Calorimetry Study of the Reactivity of Carbon Anodes in Plastic Li-Ion Batteries*, in: *Journal of The Electrochemical Society 145 (2)*, pp. 472–477, 1998

174 Maleki, H.; Deng, G.; Kerzhner-Haller, I.; Anani, A.; Howard, J.N.: *Thermal Stability Studies of Binder Materials in Anodes for Lithium-Ion Batteries*, in: *Journal of The Electrochemical Society 147 (12)*, pp. 4470–4475, 2000

175 Jiang, J.; Dahn, J.R.: *Effects of solvents and salts on the thermal stability of LiC_6*, in: *Electrochimica Acta 49 (26)*, pp. 4599–4604, 2004

176 Park, Y.-S.; Lee, S.-M.: *Effects of particle size on the thermal stability of lithiated graphite anode*, in: *Electrochimica Acta 54 (12)*, pp. 3339–3343, 2009

177 Geder, J.; Hoster, H.E.; Jossen, A.; Garche, J.; Yu, D.Y.W.: *Impact of active material surface area on thermal stability of $LiCoO_2$ cathode*, in: *Journal of Power Sources 257*, pp. 286–292, 2014

178 Kim, G.-Y.; Dahn, J.R.: *Effects of Electrode Density on the Safety of NCA Positive Electrode for Li-Ion Batteries*, in: *Journal of The Electrochemical Society 160 (8)*, A1108–A1111, 2013

179 Jiang, J.; Dahn, J.R.: *ARC studies of the thermal stability of three different cathode materials: $LiCoO_2$; $Li[Ni_{0.1}Co_{0.8}Mn_{0.1}]O_2$; and $LiFePO_4$, in $LiPF_6$ and LiBoB EC/DEC electrolytes*, in: *Electrochemistry Communications 6 (1)*, pp. 39–43, 2004

180 Wang, Y.; Jiang, J.; Dahn, J.R.: *The reactivity of delithiated $Li(Ni_{1/3}Co_{1/3}Mn_{1/3})O_2$, $Li(Ni_{0.8}Co_{0.15}Al_{0.05})O2$ or $LiCoO_2$ with non-aqueous electrolyte*, in: *Electrochemistry Communications 9 (10)*, pp. 2534–2540, 2007

181 Roth, E.P.: *Abuse Response of 18650 Li-Ion Cells with Different Cathodes Using EC:EMC/$LiPF_6$ and EC:PC:DMC/$LiPF_6$ Electrolytes*, in: *ECS Transactions 11 (19)*, pp. 19–41, 2008

182 Arai, H.; Tsuda, M.; Saito, K.; Hayashi, M.; Sakurai, Y.: *Thermal Reactions Between Delithiated Lithium Nickelate and Electrolyte Solutions*, in: *Journal of The Electrochemical Society 149 (4)*, A401–A406, 2002

183 MacNeil, D.D.; Christensen, L.; Landucci, J.; Paulsen, J.M.; Dahn, J.R.: *An Autocatalytic Mechanism for the Reaction of Li_xCoO_2 in Electrolyte at Elevated Temperature*, in: *Journal of The Electrochemical Society 147 (3)*, pp. 970–979, 2000

184 MacNeil, D.D.; Dahn, J.R.: *Test of Reaction Kinetics Using Both Differential Scanning and Accelerating Rate Calorimetries As Applied to the Reaction of Li_xCoO_2 in Non-aqueous Electrolyte*, in: *The Journal of Physical Chemistry A 105 (18)*, pp. 4430–4439, 2001

185 MacNeil, D.D.; Dahn, J.R.: *The Reaction of Charged Cathodes with Nonaqueous Solvents and Electrolytes: I. $Li_{0.5}CoO_2$*, in: *Journal of The Electrochemical Society 148 (11)*, A1205–A1210, 2001

186 Yamaki, J.-i.; Shinjo, Y.; Doi, T.; Okada, S.: *The Rate Equation for Oxygen Evolution by Decomposition of Li_xCoO_2 at Elevated Temperatures*, in: *Journal of The Electrochemical Society 161 (10)*, A1648–A1654, 2014

187 Julien, C.; Mauger, A.; Zaghib, K.; Groult, H.: *Comparative Issues of Cathode Materials for Li-Ion Batteries*, in: *Inorganics 2 (1)*, pp. 132–154, 2014

188 Bak, S.-M. et al.: *Correlating Structural Changes and Gas Evolution during the Thermal Decomposition of Charged $Li_xNi_{0.8}Co_{0.15}Al_{0.05}O_2$ Cathode Materials*, in: *Chemistry of Materials 25 (3)*, pp. 337–351, 2013

189 Nam, K.-W.; Yoon, W.-S.; Yang, X.-Q.: *Structural changes and thermal stability of charged $LiNi_{1/3}Co_{1/3}Mn_{1/3}O_2$ cathode material for Li-ion batteries studied by time-resolved XRD*, in: *Journal of Power Sources 189 (1)*, pp. 515–518, 2009

190 Konishi, H.; Yoshikawa, M.; Hirano, T.; Hidaka, K.: *Evaluation of thermal stability in $Li_{0.2}Ni_x Mn_{(1-x)/2}Co_{(1-x)/2}O_2$ (x = 1/3, 0.6, and 0.8) through X-ray absorption fine structure*, in: *Journal of Power Sources 254*, pp. 338–344, 2014

191 MacNeil, D.D.; Dahn, J.R.: *The Reaction of Charged Cathodes with Nonaqueous Solvents and Electrolytes: II. $LiMn_2O_4$ charged to 4.2 V*, in: *Journal of The Electrochemical Society 148 (11)*, A1211–A1215, 2001

192 Lu, Z.; Yang, L.; Guo, Y.: *Thermal behavior and decomposition kinetics of six electrolyte salts by thermal analysis*, in: *Journal of Power Sources 156 (2)*, pp. 555–559, 2006

193 Kawamura, T.; Kimura, A.; Egashira, M.; Okada, S.; Yamaki, J.-i.: *Thermal stability of alkyl carbonate mixed-solvent electrolytes for lithium ion cells*, in: *Journal of Power Sources 104 (2)*, pp. 260–264, 2002

194 Botte, G.G.; White, R.E.; Zhang, Z.: *Thermal stability of $LiPF_6$-EC:EMC electrolyte for lithium ion batteries*, in: *Journal of Power Sources 97-98*, pp. 570–575, 2001

195 Eshetu, G.G.; Grugeon, S.; Laruelle, S.; Boyanov, S.; Lecocq, A.; Bertrand, J.-P.; Marlair, G.: *In-depth safety-focused analysis of solvents used in electrolytes for large scale lithium ion batteries*, in: *Physical chemistry chemical physics : PCCP 15 (23)*, pp. 9145–9155, 2013

196 Eshetu, G.G.; Bertrand, J.-P.; Lecocq, A.; Grugeon, S.; Laruelle, S.; Armand, M.; Marlair, G.: *Fire behavior of carbonates-based electrolytes used in Li-ion rechargeable batteries with a focus on the role of the $LiPF_6$ and LiFSI salts*, in: *Journal of Power Sources 269*, pp. 804–811, 2014

197 Harris, S.J.; Timmons, A.; Pitz, W.J.: *A combustion chemistry analysis of carbonate solvents used in Li-ion batteries*, in: *Journal of Power Sources 193 (2)*, pp. 855–858, 2009

198 Wang, Y.; Zaghib, K.; Guerfi, A.; Bazito, F.F.C.; Torresi, R.M.; Dahn, J.R.: *Accelerating rate calorimetry studies of the reactions between ionic liquids and charged lithium ion battery electrode materials*, in: *Electrochimica Acta 52 (22)*, pp. 6346–6352, 2007

199 Ripp, C.; Hambitzer, G.; Zinck, L.; Borck, M.: *SECONDARY BATTERIES – LITHIUM RECHARGEABLE SYSTEMS – LITHIUM-ION | Inorganic Electrolyte Batteries*, in: Garche, J.; Dyer, C.K.; Moseley, P.T.; Ogumi, Z.; Rand, D.A.J.; Scrosati, B. (eds.): *Encyclopedia of Electrochemical Power Sources*, Elsevier Science, 2009

200 Inoue, T.; Mukai, K.: *Are All-Solid-State Lithium-Ion Batteries Really Safe?-Verification by Differential Scanning Calorimetry with an All-Inclusive Microcell*, in: *ACS applied materials & interfaces 9 (2)*, pp. 1507–1515, 2017

201 Jhu, C.-Y.; Wang, Y.-W.; Shu, C.-M.; Chang, J.-C.; Wu, H.-C.: *Thermal explosion hazards on 18650 lithium ion batteries with a VSP2 adiabatic calorimeter*, in: *Journal of hazardous materials 192 (1)*, pp. 99–107, 2011

202 Jhu, C.-Y.; Wang, Y.-W.; Wen, C.-Y.; Shu, C.-M.: *Thermal runaway potential of LiCoO2 and Li(Ni1/3Co1/3Mn1/3)O2 batteries determined with adiabatic calorimetry methodology*, in: *Applied Energy 100*, pp. 127–131, 2012

203 Wen, C.-Y.; Jhu, C.-Y.; Wang, Y.-W.; Chiang, C.-C.; Shu, C.-M.: *Thermal runaway features of 18650 lithium-ion batteries for $LiFePO_4$ cathode material by DSC and VSP2*, in: *Journal of Thermal Analysis and Calorimetry 109 (3)*, pp. 1297–1302, 2012

204 Feng, X.; Sun, J.; Ouyang, M.; He, X.; Lu, L.; Han, X.; Fang, M.; Peng, H.: *Characterization of large format lithium ion battery exposed to extremely high temperature*, in: *Journal of Power Sources 272*, pp. 457–467, 2014

205 Feng, X.; Fang, M.; He, X.; Ouyang, M.; Lu, L.; Wang, H.; Zhang, M.: *Thermal runaway features of large format prismatic lithium ion battery using extended volume accelerating rate calorimetry*, in: *Journal of Power Sources 255*, pp. 294–301, 2014

206 Golubkov, A.W.; Fuchs, D.; Wagner, J.; Wiltsche, H.; Stangl, C.; Fauler, G.; Voitic, G.; Thaler, A.; Hacker, V.: *Thermal-runaway experiments on consumer Li-ion batteries with metal-oxide and olivin-type cathodes*, in: *RSC Advances 4 (7)*, pp. 3633–3642, 2014

207 Golubkov, A.W.; Scheikl, S.; Planteu, R.; Voitic, G.; Wiltsche, H.; Stangl, C.; Fauler, G.; Thaler, A.; Hacker, V.: *Thermal runaway of commercial 18650 Li-ion batteries with LFP and NCA cathodes – impact of state of charge and overcharge*, in: *RSC Advances 5 (70)*, pp. 57171–57186, 2015

208 Fleischhammer, M.; Waldmann, T.; Bisle, G.; Hogg, B.-I.; Wohlfahrt-Mehrens, M.: *Interaction of cyclic ageing at high-rate and low temperatures and safety in lithium-ion batteries*, in: *Journal of Power Sources 274*, pp. 432–439, 2015

209 Mendoza-Hernandez, O.S.; Ishikawa, H.; Nishikawa, Y.; Maruyama, Y.; Umeda, M.: *Cathode material comparison of thermal runaway behavior of Li-ion cells at different state of charges including over charge*, in: *Journal of Power Sources 280*, pp. 499–504, 2015

210 Börner, M.; Friesen, A.; Grützke, M.; Stenzel, Y.P.; Brunklaus, G.; Haetge, J.; Nowak, S.; Schappacher, F.M.; Winter, M.: *Correlation of aging and thermal stability of commercial 18650-type lithium ion batteries*, in: *Journal of Power Sources 342*, pp. 382–392, 2017

211 Inoue, T.; Mukai, K.: *Roles of positive or negative electrodes in the thermal runaway of lithium-ion batteries: Accelerating rate calorimetry analyses with an all-inclusive microcell*, in: *Electrochemistry Communications 77*, pp. 28–31, 2017

212 Lammer, M.; Königseder, A.; Hacker, V.: *Holistic methodology for characterisation of the thermally induced failure of commercially available 18650 lithium ion cells*, in: *RSC Advances 7 (39)*, pp. 24425–24429, 2017

213 Galushkin, N.E.; Yazvinskaya, N.N.; Galushkin, D.N.: *Mechanism of Thermal Runaway in Lithium-Ion Cells*, in: *Journal of The Electrochemical Society 165 (7)*, A1303–A1308, 2018

214 Perea, A.; Paolella, A.; Dubé, J.; Champagne, D.; Mauger, A.; Zaghib, K.: *State of charge influence on thermal reactions and abuse tests in commercial lithium-ion cells*, in: *Journal of Power Sources 399*, pp. 392–397, 2018

215 Bugryniec, P.J.; Davidson, J.N.; Cumming, D.J.; Brown, S.F.: *Pursuing safer batteries: Thermal abuse of $LiFePO_4$ cells*, in: *Journal of Power Sources 414*, pp. 557–568, 2019

216 Feng, X.; Ren, D.; Zhang, S.; He, X.; Wang, L.; Ouyang, M.: *Influence of aging paths on the thermal runaway features of lithium-ion batteries in accelerating rate calorimetry tests*, in: *International Journal of Electrochemical Science*, pp. 44–58, 2019

217 Kitoh, K.; Nemoto, H.: *100 Wh Large size Li-ion batteries and safety tests*, in: *Journal of Power Sources 81-82*, pp. 887–890, 1999

218 Larsson, F.; Mellander, B.-E.: *Abuse by External Heating, Overcharge and Short Circuiting of Commercial Lithium-Ion Battery Cells*, in: *Journal of The Electrochemical Society 161 (10)*, A1611–A1617, 2014

219 Larsson, F.; Bertilsson, S.; Furlani, M.; Albinsson, I.; Mellander, B.-E.: *Gas explosions and thermal runaways during external heating abuse of commercial lithium-ion graphite-$LiCoO_2$ cells at different levels of ageing*, in: *Journal of Power Sources 373*, pp. 220–231, 2018

220 Finegan, D.P. et al.: *In-operando high-speed tomography of lithium-ion batteries during thermal runaway*, in: *Nature communications 6*, p. 6924, 2015

221 Finegan, D.P. et al.: *Identifying the Cause of Rupture of Li-Ion Batteries during Thermal Runaway*, in: *Advanced Science 5 (1)*, p. 1700369, 2018

222 Golubkov, A.W.; Planteu, R.; Krohn, P.; Rasch, B.; Brunnsteiner, B.; Thaler, A.; Hacker, V.: *Thermal runaway of large automotive Li-ion batteries*, in: *RSC Advances 8 (70)*, pp. 40172–40186, 2018

223 Wang, E.; Wu, H.-P.; Chiu, C.-H.; Chou, P.-H.: *The Effect of Battery Separator Properties on Thermal Ramp, Overcharge and Short Circuiting of Rechargeable Li-Ion Batteries*, in: *Journal of The Electrochemical Society 166 (2)*, A125–A131, 2019

224 Liu, X.; Stoliarov, S.I.; Denlinger, M.; Masias, A.; Snyder, K.: *Comprehensive calorimetry of the thermally-induced failure of a lithium ion battery*, in: *Journal of Power Sources 280*, pp. 516–525, 2015

225 Walker, W.Q.; Darst, J.J.; Finegan, D.P.; Bayles, G.A.; Johnson, K.L.; Darcy, E.C.; Rickman, S.L.: *Decoupling of heat generated from ejected and non-ejected contents of 18650-format lithium-ion cells using statistical methods*, in: *Journal of Power Sources 415*, pp. 207–218, 2019

226 Larsson, F.; Andersson, P.; Blomqvist, P.; Lorén, A.; Mellander, B.-E.: *Characteristics of lithium-ion batteries during fire tests*, in: *Journal of Power Sources 271*, pp. 414–420, 2014

227 Huang, P.; Wang, Q.; Li, K.; Ping, P.; Sun, J.: *The combustion behavior of large scale lithium titanate battery*, in: *Scientific reports 5*, p. 7788, 2015

228 Ping, P.; Wang, Q.; Huang, P.; Li, K.; Sun, J.; Kong, D.; Chen, C.: *Study of the fire behavior of high-energy lithium-ion batteries with full-scale burning test*, in: *Journal of Power Sources 285*, pp. 80–89, 2015

229 Wang, Z.; Ning, X.; Zhu, K.; Hu, J.; Yang, H.; Wang, J.: *Evaluating the thermal failure risk of large-format lithium-ion batteries using a cone calorimeter*, in: *Journal of Fire Sciences 37 (1)*, pp. 81–95, 2019

230 Zhang, X.; Sahraei, E.; Wang, K.: *Li-ion Battery Separators, Mechanical Integrity and Failure Mechanisms Leading to Soft and Hard Internal Shorts*, in: *Scientific reports 6*, p. 32578, 2016

231 Zhu, J.; Wierzbicki, T.; Li, W.: *A review of safety-focused mechanical modeling of commercial lithium-ion batteries*, in: *Journal of Power Sources 378*, pp. 153–168, 2018

232 Lamb, J.; Orendorff, C.J.: *Evaluation of mechanical abuse techniques in lithium ion batteries*, in: *Journal of Power Sources 247*, pp. 189–196, 2014

233 Cai, W.; Wang, H.; Maleki, H.; Howard, J.; Lara-Curzio, E.: *Experimental simulation of internal short circuit in Li-ion and Li-ion-polymer cells*, in: *Journal of Power Sources 196 (18)*, pp. 7779–7783, 2011

234 Ren, F.; Cox, T.; Wang, H.: *Thermal runaway risk evaluation of Li-ion cells using a pinch–torsion test*, in: *Journal of Power Sources 249*, pp. 156–162, 2014

235 Maleki, H.; Howard, J.N.: *Internal short circuit in Li-ion cells*, in: *Journal of Power Sources 191 (2)*, pp. 568–574, 2009

236 Finegan, D.P.; Tjaden, B.; Heenan, T.M.M.; Jervis, R.; Di Michiel, M.; Rack, A.; Hinds, G.; Brett, D.J.L.; Shearing, P.R.: *Tracking Internal Temperature and Structural Dynamics during Nail Penetration of Lithium-Ion Cells*, in: *Journal of The Electrochemical Society 164 (13)*, A3285–A3291, 2017

237 Mao, B.; Chen, H.; Cui, Z.; Wu, T.; Wang, Q.: *Failure mechanism of the lithium ion battery during nail penetration*, in: *International Journal of Heat and Mass Transfer 122*, pp. 1103–1115, 2018

238 Ramadass, P.; Fang, W.; Zhang, Z.: *Study of internal short in a Li-ion cell I. Test method development using infra-red imaging technique*, in: *Journal of Power Sources 248*, pp. 769–776, 2014

239 Kim, C.-S.; Yoo, J.-S.; Jeong, K.-M.; Kim, K.; Yi, C.-W.: *Investigation on internal short circuits of lithium polymer batteries with a ceramic-coated separator during nail penetration*, in: *Journal of Power Sources 289*, pp. 41–49, 2015

240 Hatchard, T.D.; Trussler, S.; Dahn, J.R.: *Building a "smart nail" for penetration tests on Li-ion cells*, in: *Journal of Power Sources 247*, pp. 821–823, 2014

241 Yokoshima, T.; Mukoyama, D.; Maeda, F.; Osaka, T.; Takazawa, K.; Egusa, S.; Naoi, S.; Ishikura, S.; Yamamoto, K.: *Direct observation of internal state of thermal runaway in lithium ion battery during nail-penetration test*, in: *Journal of Power Sources 393*, pp. 67–74, 2018

242 Yokoshima, T.; Mukoyama, D.; Maeda, F.; Osaka, T.; Takazawa, K.; Egusa, S.: *Operando Analysis of Thermal Runaway in Lithium Ion Battery during Nail-Penetration Test Using an X-ray Inspection System*, in: *Journal of The Electrochemical Society 166 (6)*, A1243–A1250, 2019

243 Abaza, A.; Ferrari, A.; Wong, H.K.; Lyness, C.; Moore, A.; Weaving, J.; Blanco-Martin, M.; Dashwood, R.; Bhagat, R.: *Experimental study of internal and external short circuits of commercial automotive pouch lithium-ion cells*, in: *Journal of Energy Storage 16*, pp. 211–217, 2018

244 International Electrotechnical Commission *(IEC TR 62660-4:2017)*: *Secondary lithium-ion cells for the propulsion of electric road vehicles - Part 4: Candidate alternative test methods for the internal short circuit test of IEC 62660-3*, 2017-02-13

245 Orendorff, C.J.; Roth, E.P.; Nagasubramanian, G.: *Experimental triggers for internal short circuits in lithium-ion cells*, in: *Journal of Power Sources 196 (15)*, pp. 6554–6558, 2011

246 International Electrotechnical Commission *(IEC 62660-3:2016)*: *Secondary lithium-ion cells for the propulsion of electric road vehicles - Part 3: Safety requirements*, 2016-08-29

247 International Electrotechnical Commission *(IEC 62133-2:2017)*: *Secondary cells and batteries containing alkaline or other non-acid electrolytes - Safety requirements for portable sealed secondary lithium cells, and for batteries made from them, for use in portable applications - Part 2: Lithium systems*, 2017-02-07

248 Zhang, M.; Du, J.; Liu, L.; Stefanopoulou, A.; Siegel, J.; Lu, L.; He, X.; Xie, X.; Ouyang, M.: *Internal Short Circuit Trigger Method for Lithium-Ion Battery Based on Shape Memory Alloy*, in: *Journal of The Electrochemical Society 164 (13)*, A3038–A3044, 2017

249 Zhang, M.; Liu, L.; Stefanopoulou, A.; Siegel, J.; Lu, L.; He, X.; Ouyang, M.: *Fusing Phenomenon of Lithium-Ion Battery Internal Short Circuit*, in: *Journal of The Electrochemical Society 164 (12)*, A2738–A2745, 2017

250 Finegan, D.P. et al.: *Characterising thermal runaway within lithium-ion cells by inducing and monitoring internal short circuits*, in: *Energy & Environmental Science 10 (6)*, pp. 1377–1388, 2017

251 Finegan, D.P. et al.: *Modelling and experiments to identify high-risk failure scenarios for testing the safety of lithium-ion cells*, in: *Journal of Power Sources 417*, pp. 29–41, 2019

252 Santhanagopalan, S.; Ramadass, P.; Zhang, J.: *Analysis of internal short-circuit in a lithium ion cell*, in: *Journal of Power Sources 194 (1)*, pp. 550–557, 2009

253 Zavalis, T.G.; Behm, M.; Lindbergh, G.: *Investigation of Short-Circuit Scenarios in a Lithium-Ion Battery Cell*, in: *Journal of The Electrochemical Society 159 (6)*, A848–A859, 2012

254 Wang, M.; Le, A.V.; Noelle, D.J.; Shi, Y.; Meng, Y.S.; Qiao, Y.: *Internal-short-mitigating current collector for lithium-ion battery*, in: *Journal of Power Sources 349*, pp. 84–93, 2017

255 Wu, M.-S.; Chiang, P.-C.J.; Lin, J.-C.; Jan, Y.-S.: *Correlation between electrochemical characteristics and thermal stability of advanced lithium-ion batteries in abuse tests – short-circuit tests*, in: *Electrochimica Acta 49 (11)*, pp. 1803–1812, 2004

256 Dong, T.; Wang, Y.; Peng, P.; Jiang, F.: *Electrical–thermal behaviors of a cylindrical graphite–NCA Li –ion battery responding to external short circuit operation*, in: *International Journal of Energy Research 43 (4)*, pp. 1444–1459, 2019

257 Kriston, A.; Pfrang, A.; Döring, H.; Fritsch, B.; Ruiz, V.; Adanouj, I.; Kosmidou, T.; Ungeheuer, J.; Boon-Brett, L.: *External short circuit performance of Graphite-LiNi$_{1/3}$Co$_{1/3}$Mn$_{1/3}$O$_2$ and Graphite-LiNi$_{0.8}$Co$_{0.15}$Al$_{0.05}$O$_2$ cells at different external resistances*, in: *Journal of Power Sources 361*, pp. 170–181, 2017

258 Leising, R.A.; Palazzo, M.J.; Takeuchi, E.S.; Takeuchi, K.J.: *Abuse Testing of Lithium-Ion Batteries: Characterization of the Overcharge Reaction of LiCoO$_2$/Graphite Cells*, in: *Journal of The Electrochemical Society 148 (8)*, A838–A844, 2001

259 Zeng, Y.; Wu, K.; Wang, D.; Wang, Z.; Chen, L.: *Overcharge investigation of lithium-ion polymer batteries*, in: *Journal of Power Sources 160 (2)*, pp. 1302–1307, 2006

260 Lin, C.-K.; Ren, Y.; Amine, K.; Qin, Y.; Chen, Z.: *In situ high-energy X-ray diffraction to study overcharge abuse of 18650-size lithium-ion battery*, in: *Journal of Power Sources 230*, pp. 32–37, 2013

261 Leising, R.A.; Palazzo, M.J.; Takeuchi, E.S.; Takeuchi, K.J.: *A study of the overcharge reaction of lithium-ion batteries*, in: *Journal of Power Sources 97-98*, pp. 681–683, 2001

262 Ohsaki, T.; Kishi, T.; Kuboki, T.; Takami, N.; Shimura, N.; Sato, Y.; Sekino, M.; Satoh, A.: *Overcharge reaction of lithium-ion batteries*, in: *Journal of Power Sources 146 (1-2)*, pp. 97–100, 2005

263 Takahashi, M.; Komatsu, K.; Maeda, K.: *The Safety Evaluation Test of Lithium-Ion Batteries in Vehicles - Investigation of Overcharge Test Method -*, in: *ECS Transactions 41 (39)*, pp. 27–41, 2012

264 Zhu, X.; Wang, Z.; Wang, C.; Huang, L.: *Overcharge Investigation of Large Format Lithium-Ion Pouch Cells with $Li(Ni_{0.6}Co_{0.2}Mn_{0.2})O_2$ Cathode for Electric Vehicles: Degradation and Failure Mechanisms*, in: *Journal of The Electrochemical Society 165 (16)*, A3613–A3629, 2018

265 Maleki, H.; Howard, J.N.: *Effects of overdischarge on performance and thermal stability of a Li-ion cell*, in: *Journal of Power Sources 160 (2)*, pp. 1395–1402, 2006

266 Wu, L.; Liu, Y.; Cui, Y.; Zhang, Y.; Zhang, J.: *In Situ Temperature Evolution and Failure Mechanisms of $LiNi_{0.33}Mn_{0.33}Co_{0.33}O_2$ Cell under Over-Discharge Conditions*, in: *Journal of The Electrochemical Society 165 (10)*, A2162–A2166, 2018

267 Spotnitz, R.M.; Weaver, J.; Yeduvaka, G.; Doughty, D.H.; Roth, E.P.: *Simulation of abuse tolerance of lithium-ion battery packs*, in: *Journal of Power Sources 163 (2)*, pp. 1080–1086, 2007

268 Lamb, J.; Orendorff, C.J.; Steele, L.A.M.; Spangler, S.W.: *Failure propagation in multi-cell lithium ion batteries*, in: *Journal of Power Sources 283*, pp. 517–523, 2015

269 Lopez, C.F.; Jeevarajan, J.A.; Mukherjee, P.P.: *Experimental Analysis of Thermal Runaway and Propagation in Lithium-Ion Battery Modules*, in: *Journal of The Electrochemical Society 162 (9)*, A1905–A1915, 2015

270 Feng, X.; Sun, J.; Ouyang, M.; Wang, F.; He, X.; Lu, L.; Peng, H.: *Characterization of penetration induced thermal runaway propagation process within a large format lithium ion battery module*, in: *Journal of Power Sources 275*, pp. 261–273, 2015

271 Spinner, N.S.; Field, C.R.; Hammond, M.H.; Williams, B.A.; Myers, K.M.; Lubrano, A.L.; Rose-Pehrsson, S.L.; Tuttle, S.G.: *Physical and chemical analysis of lithium-ion battery cell-to-cell failure events inside custom fire chamber*, in: *Journal of Power Sources 279*, pp. 713–721, 2015

272 Zhong, G.; Li, H.; Wang, C.; Xu, K.; Wang, Q.: *Experimental Analysis of Thermal Runaway Propagation Risk within 18650 Lithium-Ion Battery Modules*, in: *Journal of The Electrochemical Society 165 (9)*, A1925–A1934, 2018

273 Ramadesigan, V.; Northrop, P.W.C.; De, S.; Santhanagopalan, S.; Braatz, R.D.; Subramanian, V.R.: *Modeling and Simulation of Lithium-Ion Batteries from a Systems Engineering Perspective*, in: *Journal of The Electrochemical Society 159 (3)*, R31–R45, 2012

274 Abada, S.; Marlair, G.; Lecocq, A.; Petit, M.; Sauvant-Moynot, V.; Huet, F.: *Safety focused modeling of lithium-ion batteries: A review*, in: *Journal of Power Sources 306*, pp. 178–192, 2016

275 Deng, J.; Bae, C.; Marcicki, J.; Masias, A.; Miller, T.: *Safety modelling and testing of lithium-ion batteries in electrified vehicles*, in: *Nature Energy 3 (4)*, pp. 261–266, 2018

276 Greve, L.; Fehrenbach, C.: *Mechanical testing and macro-mechanical finite element simulation of the deformation, fracture, and short circuit initiation of cylindrical Lithium ion battery cells*, in: *Journal of The Electrochemical Society 214*, pp. 377–385, 2012

277 Sahraei, E.; Campbell, J.; Wierzbicki, T.: *Modeling and short circuit detection of 18650 Li-ion cells under mechanical abuse conditions*, in: *Journal of Power Sources 220*, pp. 360–372, 2012

278 Avdeev, I.; Gilaki, M.: *Structural analysis and experimental characterization of cylindrical lithium-ion battery cells subject to lateral impact*, in: *Journal of Power Sources 271*, pp. 382–391, 2014

279 Sahraei, E.; Meier, J.; Wierzbicki, T.: *Characterizing and modeling mechanical properties and onset of short circuit for three types of lithium-ion pouch cells*, in: *Journal of Power Sources 247*, pp. 503–516, 2014

280 Sahraei, E.; Kahn, M.; Meier, J.; Wierzbicki, T.: *Modelling of cracks developed in lithium-ion cells under mechanical loading*, in: *RSC Advances 5 (98)*, pp. 80369–80380, 2015

281 Sahraei, E.; Bosco, E.; Dixon, B.; Lai, B.: *Microscale failure mechanisms leading to internal short circuit in Li-ion batteries under complex loading scenarios*, in: *Journal of Power Sources 319*, pp. 56–65, 2016

282 Raffler, M.; Sevarin, A.; Ellersdorfer, C.; Heindl, S.F.; Breitfuss, C.; Sinz, W.: *Finite element model approach of a cylindrical lithium ion battery cell with a focus on minimization of the computational effort and short circuit prediction*, in: *Journal of Power Sources 360*, pp. 605–617, 2017

283 Xia, Y.; Li, T.; Ren, F.; Gao, Y.; Wang, H.: *Failure analysis of pinch–torsion tests as a thermal runaway risk evaluation method of Li-ion cells*, in: *Journal of Power Sources 265*, pp. 356–362, 2014

284 Wang, H. et al.: *Progressive mechanical indentation of large-format Li-ion cells*, in: *Journal of Power Sources 341*, pp. 156–164, 2017

285 Wang, L.; Yin, S.; Xu, J.: *A detailed computational model for cylindrical lithium-ion batteries under mechanical loading: From cell deformation to short-circuit onset*, in: *Journal of Power Sources 413*, pp. 284–292, 2019

286 Jana, A.; Ely, D.R.; García, R.E.: *Dendrite-separator interactions in lithium-based batteries*, in: *Journal of Power Sources 275*, pp. 912–921, 2015

287 Rieger, B.; Erhard, S.V.; Rumpf, K.; Jossen, A.: *A New Method to Model the Thickness Change of a Commercial Pouch Cell during Discharge*, in: *Journal of The Electrochemical Society 163 (8)*, A1566–A1575, 2016

288 Sturm, J.; Spingler, F.B.; Rieger, B.; Rheinfeld, A.; Jossen, A.: *Non-Destructive Detection of Local Aging in Lithium-Ion Pouch Cells by Multi-Directional Laser Scanning*, in: *Journal of The Electrochemical Society 164 (7)*, A1342–A1351, 2017

289 Smith, K.; Kim, G.-H.; Darcy, E.; Pesaran, A.: *Thermal/electrical modeling for abuse-tolerant design of lithium ion modules*, in: *International Journal of Energy Research 34 (2)*, pp. 204–215, 2010

290 Doyle, M.; Fuller, T.F.; Newman, J.: *Modeling of Galvanostatic Charge and Discharge of the Lithium/Polymer/Insertion Cell*, in: *Journal of The Electrochemical Society 140 (6)*, pp. 1526–1533, 1993

291 Newman, J.; Thomas-Alyea, K.E.: *Electrochemical Systems*, 3rd edition, Wiley-Interscience, Hoboken, NJ, USA, 2004

292 Kindermann, F.M.; Osswald, P.J.; Ehlert, G.; Schuster, J.; Rheinfeld, A.; Jossen, A.: *Reducing Inhomogeneous Current Density Distribution in Graphite Electrodes by Design Variation*, in: *Journal of The Electrochemical Society 164 (11)*, E3105–E3113, 2017

293 Sturm, J.; Ennifar, H.; Erhard, S.V.; Rheinfeld, A.; Kosch, S.; Jossen, A.: *State estimation of lithium-ion cells using a physicochemical model based extended Kalman filter*, in: *Applied Energy 223*, pp. 103–123, 2018

294 Rumpf, K.; Rheinfeld, A.; Schindler, M.; Keil, J.; Schua, T.; Jossen, A.: *Influence of Cell-to-Cell Variations on the Inhomogeneity of Lithium-Ion Battery Modules*, in: *Journal of The Electrochemical Society 165 (11)*, A2587–A2607, 2018

295 Mao, J.; Tiedemann, W.; Newman, J.: *Simulation of Li-ion Cells by Dualfoil Model under Constant-Resistance Load*, in: *ECS Transactions 58 (48)*, pp. 71–81, 2014

296 Mao, J.; Tiedemann, W.; Newman, J.: *Simulation of temperature rise in Li-ion cells at very high currents*, in: *Journal of Power Sources 271*, pp. 444–454, 2014

297 Zilberman, I.; Rheinfeld, A.; Jossen, A.: *Uncertainties in entropy due to temperature path dependent voltage hysteresis in Li-ion cells*, in: *Journal of Power Sources 395*, pp. 179–184, 2018

298 Bernardi, D.; Pawlikowski, E.; Newman, J.: *A General Energy Balance for Battery Systems*, in: *Journal of The Electrochemical Society 132 (1)*, pp. 5–12, 1985

299 Gerver, R.E.; Meyers, J.P.: *Three-Dimensional Modeling of Electrochemical Performance and Heat Generation of Lithium-Ion Batteries in Tabbed Planar Configurations*, in: *Journal of The Electrochemical Society 158 (7)*, A835–A843, 2011

300 Guo, M.; White, R.E.: *A distributed thermal model for a Li-ion electrode plate pair*, in: *Journal of Power Sources 221*, pp. 334–344, 2013

301 Yamauchi, T.; Mizushima, K.; Satoh, Y.; Yamada, S.: *Development of a simulator for both property and safety of a lithium secondary battery*, in: *Journal of Power Sources 136 (1)*, pp. 99–107, 2004

302 Chiu, K.-C.; Lin, C.-H.; Yeh, S.-F.; Lin, Y.-H.; Chen, K.-C.: *An electrochemical modeling of lithium-ion battery nail penetration*, in: *Journal of Power Sources 251*, pp. 254–263, 2014

303 Zhao, W.; Luo, G.; Wang, C.-Y.: *Modeling Nail Penetration Process in Large-Format Li-Ion Cells*, in: *Journal of The Electrochemical Society 162 (1)*, A207–A217, 2015

304 Zhao, R.; Liu, J.; Gu, J.: *Simulation and experimental study on lithium ion battery short circuit*, in: *Applied Energy 173*, pp. 29–39, 2016

305 Xu, J.; Wu, Y.; Yin, S.: *Investigation of effects of design parameters on the internal short-circuit in cylindrical lithium-ion batteries*, in: *RSC Advances 7 (24)*, pp. 14360–14371, 2017

306 Zhao, R.; Liu, J.; Gu, J.: *A comprehensive study on Li-ion battery nail penetrations and the possible solutions*, in: *Energy 123*, pp. 392–401, 2017

307 Zhao, W.; Luo, G.; Wang, C.-Y.: *Modeling Internal Shorting Process in Large-Format Li-Ion Cells*, in: *Journal of The Electrochemical Society 162 (7)*, A1352–A1364, 2015

308 Fang, W.; Ramadass, P.; Zhang, Z.: *Study of internal short in a Li-ion cell-II. Numerical investigation using a 3D electrochemical-thermal model*, in: *Journal of Power Sources 248*, pp. 1090–1098, 2014

309 Okamoto, Y.: *Ab Initio Calculations of Thermal Decomposition Mechanism of $LiPF_6$ -Based Electrolytes for Lithium-Ion Batteries*, in: *Journal of The Electrochemical Society 160 (2)*, A404–A409, 2013

310 Selman, J.R.; Al Hallaj, S.; Uchida, I.; Hirano, Y.H.: *Cooperative research on safety fundamentals of lithium batteries*, in: *Journal of Power Sources 97-98*, pp. 726–732, 2001

311 Hatchard, T.D.; MacNeil, D.D.; Basu, A.; Dahn, J.R.: *Thermal Model of Cylindrical and Prismatic Lithium-Ion Cells*, in: *Journal of The Electrochemical Society 148 (7)*, A755–A761, 2001

312 Kim, G.-H.; Pesaran, A.; Spotnitz, R.: *A three-dimensional thermal abuse model for lithium-ion cells*, in: *Journal of Power Sources 170 (2)*, pp. 476–489, 2007

313 Kim, S.U.; Albertus, P.; Cook, D.; Monroe, C.W.; Christensen, J.: *Thermoelectrochemical simulations of performance and abuse in 50-Ah automotive cells*, in: *Journal of Power Sources 268*, pp. 625–633, 2014

314 Peng, P.; Sun, Y.; Jiang, F.: *Thermal analyses of $LiCoO_2$ lithium-ion battery during oven tests*, in: *Heat and Mass Transfer 50 (10)*, pp. 1405–1416, 2014

315 Peng, P.; Jiang, F.: *Thermal behavior analyses of stacked prismatic $LiCoO_2$ lithium-ion batteries during oven tests*, in: *International Journal of Heat and Mass Transfer 88*, pp. 411–423, 2015

316 Huang, P.; Chen, H.; Verma, A.; Wang, Q.; Mukherjee, P.; Sun, J.: *Non-dimensional analysis of the criticality of Li-ion battery thermal runaway behavior*, in: *Journal of hazardous materials 369*, pp. 268–278, 2019

317 Liang, G.; Zhang, Y.; Han, Q.; Liu, Z.; Jiang, Z.; Tian, S.: *A novel 3D-layered electrochemical-thermal coupled model strategy for the nail-penetration process simulation*, in: *Journal of Power Sources 342*, pp. 836–845, 2017

318 Wang, S.; Lu, L.; Liu, X.: *A simulation on safety of $LiFePO_4/C$ cell using electrochemical–thermal coupling model*, in: *Journal of Power Sources 244*, pp. 101–108, 2013

319 Tanaka, N.; Bessler, W.G.: *Numerical investigation of kinetic mechanism for runaway thermo-electrochemistry in lithium-ion cells*, in: *Solid State Ionics 262*, pp. 70–73, 2014

320 Shurtz, R.C.; Engerer, J.D.; Hewson, J.C.: *Predicting High-Temperature Decomposition of Lithiated Graphite: Part I. Review of Phenomena and a Comprehensive Model*, in: *Journal of The Electrochemical Society 165 (16)*, A3878–A3890, 2018

321 Shurtz, R.C.; Engerer, J.D.; Hewson, J.C.: *Predicting High-Temperature Decomposition of Lithiated Graphite: Part II. Passivation Layer Evolution and the Role of Surface Area*, in: *Journal of The Electrochemical Society 165 (16)*, A3891–A3902, 2018

322 Abada, S.; Petit, M.; Lecocq, A.; Marlair, G.; Sauvant-Moynot, V.; Huet, F.: *Combined experimental and modeling approaches of the thermal runaway of fresh and aged lithium-ion batteries*, in: *Journal of Power Sources 399*, pp. 264–273, 2018

323 Coman, P.T.; Rayman, S.; White, R.E.: *A lumped model of venting during thermal runaway in a cylindrical Lithium Cobalt Oxide lithium-ion cell*, in: *Journal of Power Sources 307*, pp. 56–62, 2016

324 Coman, P.T.; Darcy, E.C.; Veje, C.T.; White, R.E.: *Modelling Li-Ion Cell Thermal Runaway Triggered by an Internal Short Circuit Device Using an Efficiency Factor and Arrhenius Formulations*, in: *Journal of The Electrochemical Society 164 (4)*, A587–A593, 2017

325 Coman, P.T.; Mátéfi-Tempfli, S.; Veje, C.T.; White, R.E.: *Modeling Vaporization, Gas Generation and Venting in Li-Ion Battery Cells with a Dimethyl Carbonate Electrolyte*, in: *Journal of The Electrochemical Society 164 (9)*, A1858–A1865, 2017

326 Lopez, C.F.; Jeevarajan, J.A.; Mukherjee, P.P.: *Characterization of Lithium-Ion Battery Thermal Abuse Behavior Using Experimental and Computational Analysis*, in: *Journal of The Electrochemical Society 162 (10)*, A2163–A2173, 2015

327 Feng, X.; He, X.; Ouyang, M.; Lu, L.; Wu, P.; Kulp, C.; Prasser, S.: *Thermal runaway propagation model for designing a safer battery pack with 25 Ah $LiNi_xCo_yMn_zO_2$ large format lithium ion battery*, in: *Applied Energy 154*, pp. 74–91, 2015

328 Liu, X.; Wu, Z.; Stoliarov, S.I.; Denlinger, M.; Masias, A.; Snyder, K.: *A Thermo-Kinetic Model of Thermally-Induced Failure of a Lithium Ion Battery: Development, Validation and Application*, in: *Journal of The Electrochemical Society 165 (11)*, A2909–A2918, 2018

329 Pannala, S. et al.: *Multiscale modeling and characterization for performance and safety of lithium-ion batteries*, in: *Journal of Applied Physics 118 (7)*, p. 072017, 2015

330 Zhang, C.; Santhanagopalan, S.; Sprague, M.A.; Pesaran, A.A.: *Coupled mechanical-electrical-thermal modeling for short-circuit prediction in a lithium-ion cell under mechanical abuse*, in: *Journal of Power Sources 290*, pp. 102–113, 2015

331 Liu, B.; Yin, S.; Xu, J.: *Integrated computation model of lithium-ion battery subject to nail penetration*, in: *Applied Energy 183*, pp. 278–289, 2016

332 Liu, B.; Jia, Y.; Li, J.; Yin, S.; Yuan, C.; Hu, Z.; Wang, L.; Li, Y.; Xu, J.: *Safety issues caused by internal short circuits in lithium-ion batteries*, in: *Journal of Materials Chemistry A 6 (43)*, pp. 21475–21484, 2018

333 Deng, J.; Bae, C.; Miller, T.; L'Eplattenier, P.; Bateau-Meyer, S.: *Accelerate Battery Safety Simulations Using Composite Tshell Elements*, in: *Journal of The Electrochemical Society 165 (13)*, A3067–A3076, 2018

334 Ren, D.; Liu, X.; Feng, X.; Lu, L.; Ouyang, M.; Li, J.; He, X.: *Model-based thermal runaway prediction of lithium-ion batteries from kinetics analysis of cell components*, in: *Applied Energy 228*, pp. 633–644, 2018

335 Yamaki, J.-i.; Shinjo, Y.; Doi, T.; Okada, S.; Ogumi, Z.: *The Rate Equation of Decomposition for Electrolytes with $LiPF_6$ in Li-Ion Cells at Elevated Temperatures*, in: *Journal of The Electrochemical Society 162 (4)*, A520–A530, 2015

336 Ping, P.; Wang, Q.; Huang, P.; Sun, J.; Chen, C.: *Thermal behaviour analysis of lithium-ion battery at elevated temperature using deconvolution method*, in: *Applied Energy 129*, pp. 261–273, 2014

337 Brown, W.E.; Dollimore, D.; Galwey, A.K.: *Theory of Solid State Reaction Kinetics*, in: Bamford, C.H.; Tipper, C. (eds.): *Reactions in the Solid State*, Elsevier, 1980

338 Kabza, A. et al.: *Studie zur Bewertung der Sicherheit von Lithium-Ionen Batterien über den gesamten Lebenszyklus*, ed. by Zentrum für Sonnenenergie- und Wasserstoff-Forschung Baden-Württemberg, 2017, URL: https://www.now-gmbh.de/content/4-bundesfoerderung-elektromobilitaet-vor-ort/2-projektfinder/20180820-elektromobilitaet-vor-ort/20150731-studie-batteriesicherheit/batsich_abschlussbericht_2017-05-10.pdf, logdate: 06/10/2019

339 Jiang, F.; Peng, P.: *Elucidating the Performance Limitations of Lithium-ion Batteries due to Species and Charge Transport through Five Characteristic Parameters*, in: *Scientific reports 6*, p. 32639, 2016

340 Gallagher, K.G. et al.: *Optimizing Areal Capacities through Understanding the Limitations of Lithium-Ion Electrodes*, in: *Journal of The Electrochemical Society 163 (2)*, A138–A149, 2016

341 Fuller, T.F.; Doyle, M.; Newman, J.: *Simulation and Optimization of the Dual Lithium Ion Insertion Cell*, in: *Journal of The Electrochemical Society 141 (1)*, pp. 1–10, 1994

342 Latz, A.; Zausch, J.: *Thermodynamic derivation of a Butler–Volmer model for intercalation in Li-ion batteries*, in: *Electrochimica Acta 110*, pp. 358–362, 2013

343 Hamann, C.H.; Hamnett, A.; Vielstich, W.: *Electrochemistry*, 2nd edition, Wiley-VCH, Weinheim, Germany, 2007

344 Habedank, J.B.; Endres, J.; Schmitz, P.; Zaeh, M.F.; Huber, H.P.: *Femtosecond laser structuring of graphite anodes for improved lithium-ion batteries: Ablation characteristics and process design*, in: *Journal of Laser Applications 30 (3)*, p. 032205, 2018

345 Nemani, V.P.; Harris, S.J.; Smith, K.C.: *Design of Bi-Tortuous, Anisotropic Graphite Anodes for Fast Ion-Transport in Li-Ion Batteries*, in: *Journal of The Electrochemical Society 162 (8)*, A1415–A1423, 2015

346 Li, J.; Liang, X.; Panat, R.; Park, J.: *Enhanced Battery Performance through Three-Dimensional Structured Electrodes: Experimental and Modeling Study*, in: *Journal of The Electrochemical Society 165 (14)*, A3566–A3573, 2018

347 Ebner, M.; Chung, D.-W.; García, R.E.; Wood, V.: *Tortuosity Anisotropy in Lithium-Ion Battery Electrodes*, in: *Advanced Energy Materials 4 (5)*, p. 1301278, 2014

348 Landesfeind, J.; Hattendorff, J.; Ehrl, A.; Wall, W.A.; Gasteiger, H.A.: *Tortuosity Determination of Battery Electrodes and Separators by Impedance Spectroscopy*, in: *Journal of The Electrochemical Society 163 (7)*, A1373–A1387, 2016

349 Nyman, A.; Zavalis, T.G.; Elger, R.; Behm, M.; Lindbergh, G.: *Analysis of the Polarization in a Li-Ion Battery Cell by Numerical Simulations*, in: *Journal of The Electrochemical Society 157 (11)*, A1236, 2010

350 Chen, C.-F.; Verma, A.; Mukherjee, P.P.: *Probing the Role of Electrode Microstructure in the Lithium-Ion Battery Thermal Behavior*, in: *Journal of The Electrochemical Society 164 (11)*, E3146–E3158, 2017

351 Noelle, D.J.; Wang, M.; Le, A.V.; Shi, Y.; Qiao, Y.: *Internal resistance and polarization dynamics of lithium-ion batteries upon internal shorting*, in: *Applied Energy 212*, pp. 796–808, 2018

352 Kosch, S.; Zhao, Y.; Sturm, J.; Schuster, J.; Mulder, G.; Ayerbe, E.; Jossen, A.: *A Computationally Efficient Multi-Scale Model for Lithium-Ion Cells*, in: *Journal of The Electrochemical Society 165 (10)*, A2374–A2388, 2018

353 Newman, J.; Tiedemann, W.: *Potential and Current Distribution in Electrochemical Cells - Interpretation of the Half–Cell Voltage Measurements as a Function of Reference–Electrode Location*, in: *Journal of The Electrochemical Society 140 (7)*, pp. 1961–1968, 1993

List of Publications

21. **Rheinfeld, A.**; Sturm, J.; Frank, A.; Kosch, S.; Erhard, S.V.; Jossen, A.: *Impact of Cell Size and Format on External Short Circuit Behavior of Lithium-Ion Cells at Varying Cooling Conditions: Modeling and Simulation*, in: *Journal of The Electrochemical Society 167 (1)*, p. 013511, 2020

20. Kraft, L.; Habedank, J.B.; Frank, A.; **Rheinfeld, A.**; Jossen, A.: *Modeling and Simulation of Pore Morphology Modifications using Laser-Structured Graphite Anodes in Lithium-Ion Batteries*, in: *Journal of The Electrochemical Society 167 (1)*, p. 013506, 2020

19. **Rheinfeld, A.**; Sturm, J.; Noel, A.; Wilhelm, J.; Kriston, A.; Pfrang, A.; Jossen, A.: *Quasi-Isothermal External Short Circuit Tests Applied to Lithium-Ion Cells: Part II. Modeling and Simulation*, in: *Journal of The Electrochemical Society 166 (2)*, pp. A151–A177, 2019

18. Sturm, J.; **Rheinfeld, A.**; Zilbermann, I.; Spingler, F.B.; Kosch, S.; Frie, F.; Jossen, A.: *Modeling and simulation of inhomogeneities in a 18650 nickel-rich, silicon-graphite lithium-ion cell during fast charging*, in: *Journal of Power Sources 412*, pp. 204–223, 2019

17. **Rheinfeld, A.**; Noel, A.; Wilhelm, J.; Kriston, A.; Pfrang, A.; Jossen, A.: *Quasi-Isothermal External Short Circuit Tests Applied to Lithium-Ion Cells: Part I. Measurements*, in: *Journal of The Electrochemical Society 165 (14)*, pp. A3427–A3448, 2018

16. Rumpf, K.; **Rheinfeld, A.**; Schindler, M.; Keil, J.; Schua, T.; Jossen, A.: *Influence of Cell-to-Cell Variations on the Inhomogeneity of Lithium-Ion Battery Modules*, in: *Journal of The Electrochemical Society 165 (11)*, pp. A2587–A2607, 2018

15. Zilbermann, I.; **Rheinfeld, A.**; Jossen, A.: *Uncertainties in entropy due to temperature path dependent voltage hysteresis in Li-ion cells*, in: *Journal of Power Sources 395*, pp. 179–184, 2018

14. Sturm, J.; Ennifar, H.; Erhard, S.V. **Rheinfeld, A.**; Kosch, S.; Jossen, A.: *State estimation of lithium-ion cells using a physicochemical model based extended Kalman filter*, in: *Applied Energy 223*, pp. 103–123, 2018

13. Habedank, J.B.; Kraft, L.; **Rheinfeld, A.**; Krezdorn, C.; Jossen, A.; Zaeh, M.F.: *Increasing the Discharge Rate Capability of Lithium-Ion Cells with Laser-Structured Graphite Anodes: Modeling and Simulation*, in: *Journal of The Electrochemical Society 165 (7)*, pp. A1563–A1573, 2018

12. Hildebrand, S.; **Rheinfeld, A.**; Friesen, A.; Haetge, J., Schappacher, F.M.; Jossen, A.; Winter, M.: *Thermal Analysis of $LiNi_{0.4}Co_{0.2}Mn_{0.4}O_2$/Mesocarbon Microbeads Cells and Electrodes: State-of-Charge and State-of-Health Influences on Reaction Kinetics*, in: *Journal of The Electrochemical Society 165 (2)*, pp. A104–A117, 2018

11. Sturm, J.; Spingler, F.B.; Rieger, B.; **Rheinfeld, A.**; Jossen, A.: *Non-Destructive Detection of Local Aging in Lithium-Ion Pouch Cells by Multi-Directional Laser Scanning*, in: *Journal of The Electrochemical Society 164 (7)*, pp. A1342–A1351, 2017

10. Kindermann, F.M.; Osswald, P.J.; Ehlert, G.; Schuster, J.; **Rheinfeld, A.**; Jossen, A.: *Reducing Inhomogeneous Current Density Distribution in Graphite Electrodes by Design Variation*, in: *Journal of The Electrochemical Society 164 (11)*, pp. E3105–E3113, 2017

9. Erhard, S.V.; Osswald, P.J.; Keil, P.; Höffer, E.; Haug, M.; Noel, A.; Wilhelm, J.; Rieger, B.; Schmidt, K.; Kosch, S.; Kindermann, F.M.; Spingler, F.B.; Kloust, H.; Thoennessen, T.; **Rheinfeld, A.**; Jossen, A.: *Simulation and Measurement of the Current Density Distribution in Lithium-Ion Batteries by a Multi-Tab Cell Approach*, in: *Journal of The Electrochemical Society 164 (1)*, pp. A6324–A6333, 2017

8. Kosch, S.; **Rheinfeld, A.**; Erhard, S.V.; Jossen, A.: *An extended polarization model to study the influence of current collector geometry of large-format lithium-ion pouch cells*, in: *Journal of Power Sources 342*, pp. 666–676, 2017

7. Rieger, B.; Erhard, S.V.; Kosch, S.; Venator, M.; **Rheinfeld, A.**; Jossen, A.: *Multi-Dimensional Modeling of the Influence of Cell Design on Temperature, Displacement and Stress Inhomogeneity in Large-Format Lithium-Ion Cells*, in: *Journal of The Electrochemical Society 163 (14)*, pp. A3099–A3110, 2016

6. **Rheinfeld, A.**; Kosch, S.; Erhard, S.V.; Osswald, P.J.; Rieger, B.; Jossen, A.: *Electro-Thermal Modeling of Large Format Lithium-Ion Pouch Cells: A Cell Temperature Dependent Linear Polarization Expression*, in: *Journal of The Electrochemical Society 163 (14)*, pp. A3046–A3062, 2016

5. Rieger, B.; Schuster, S.F.; Erhard, S.V.; Osswald, P.J.; **Rheinfeld, A.**; Willmann, C.; Jossen, A.: *Multi-directional laser scanning as innovative method to detect local cell damage during fast charging of lithium-ion cells*, in: *Journal of Energy Storage 8*, pp. 1–5, 2016

4. Osswald, P.J.; Erhard, S.V.; **Rheinfeld, A.**; Rieger, B.; Hoster, H.E.; Jossen, A.: *Temperature dependency of state of charge inhomogeneities and their equalization in cylindrical lithium-ion cells*, in: *Journal of Power Sources 329*, pp. 546–552, 2016

3. Erhard, S.V.; Osswald, P.J.; Wilhelm, J.; **Rheinfeld, A.**; Kosch, S.; Jossen, A.: *Simulation and Measurement of Local Potentials of Modified Commercial Cylindrical Cells II: Multi-Dimensional Modeling and Validation*, in: *Journal of The Electrochemical Society 162 (14)*, pp. A2707–A2719, 2015

2. Erhard, S.V.; Spingler, F.B.; **Rheinfeld, A.**; Kosch, S.; Rumpf, K.; Jossen, A.: *Physico-chemical Modelling of Li-ion Batteries: Parameter Analysis in the Frequency Domain*, in: *Lecture Notes on Impedance Spectroscopy 5*, pp. 53–62, 2015

1. Martiny, N; **Rheinfeld, A.**; Geder, J.; Wang, Y.; Kraus, W.; Jossen, A.: *Development of an All Kapton-Based Thin-Film Thermocouple Matrix for In Situ Temperature Measurement in a Lithium Ion Pouch Cell*, in: *IEEE Sensors Journal 14*, pp. 3377–3384, 2014

Acknowledgment

This thesis originates from my time as a research associate at the Institute for Electrical Energy Storage Technology (EES) at Technical University of Munich (TUM). First of all, I would like to thank Prof. Dr.-Ing. Andreas Jossen for giving me the opportunity to carry out the research work which forms the basis for the presented results. I appreciate the supervision I received throughout my time at the institute and until finishing this thesis. I am very grateful to have had the opportunity to explore various fields of Li-ion battery research, as well as the chance to take on responsibilities within the institute and beyond.

Furthermore, I thank Prof. Dr. rer. nat. Jürgen Garche for his mentoring throughout the years and his ongoing support in reviewing my research work (mostly at rather short notice), as well as for introducing me to and guiding me through the topic of Li-ion battery safety.

I would also like to thank all of my co-authors who not only inspired this work but who also made the presented results possible in the very first place. Thanks to the experimental input from Stephan Hildebrand, Alex Friesen, Jan Haetge, and Falko Schappacher from Münster Electrochemical Energy Technology (MEET, Prof. Dr. Martin Winter), the presented model based investigation of decomposition reactions was made possible. Furthermore, the work of Jan Habedank from the Institute for Machine Tools and Industrial Management of TUM on laser structured electrodes, enabled the presented rate limitation studies. Thanks to the in-depth discussions regarding cell short circuits and possible underlying mechanisms with both Akos Kriston and Andreas Pfrang from the European Commission's Joint Research Centre (JRC), I was motivated to study short circuits to the extent required, enabling model validation.

A very big thank you goes to all my former EES colleagues for making my time at the institute such a valuable experience. It was a pleasure to work with all of you and I am very grateful for the numerous friendships that developed from this. During this time, I had the pleasure of sharing offices with great people who supported me through all the ups and downs within the last years. By name, I thank Frank Kindermann who has been a true companion from day one, helping and advising me whenever he could. Special thanks goes to the guys from 3015, Simon Erhard, Patrick Osswald, and Bernhard Rieger for the short but inspiring time we were able to work together. I would also like to thank Ilya Zilbermann for accommodating and supporting me throughout the final part of my thesis. Furthermore, without the technical assistance especially from Korbinian Schmidt but also Jens Dietrich and Andreas Noel, the presented experimental results would certainly not have been possible to this extent — thank you very much for helping me to put my ideas into practice. A further thank you goes to my former students and EES colleagues Johannes Sturm and Alexander Frank who helped me, even beyond my time at the institute, to finish the manuscript of cell design studies.

Lastly, my biggest thanks goes to my girlfriend Nikki, as well as to my family and friends. Thank you for your love, your never-ending support, and your patience throughout this journey. To all of you I dedicate this thesis.